# OPTICAL FIBER-BASED PLASMONICS BIOSENSORS FOR BIOMEDICAL APPLICATIONS

EDITED BY: Santosh Kumar, Carlos Marques, Qiang Wu, Qinglin Wang and Sanjeev Kumar Raghuwanshi

PUBLISHED IN: Frontiers in Physics and Frontiers in Sensors

frontiers Research Topics

# frontiers



ISSN 1664-8714
ISBN 978-2-88974-680-4
DOI 10.3389/978-2-88974-680-4

## About Frontiers

Frontiers is more than just an open-access publisher of scholarly articles: it is a pioneering approach to the world of academia, radically improving the way scholarly research is managed. The grand vision of Frontiers is a world where all people have an equal opportunity to seek, share and generate knowledge. Frontiers provides immediate and permanent online open access to all its publications, but this alone is not enough to realize our grand goals.

## Frontiers Journal Series

The Frontiers Journal Series is a multi-tier and interdisciplinary set of open-access, online journals, promising a paradigm shift from the current review, selection and dissemination processes in academic publishing. All Frontiers journals are driven by researchers for researchers; therefore, they constitute a service to the scholarly community. At the same time, the Frontiers Journal Series operates on a revolutionary invention, the tiered publishing system, initially addressing specific communities of scholars, and gradually climbing up to broader public understanding, thus serving the interests of the lay society, too.

## Dedication to Quality

Each Frontiers article is a landmark of the highest quality, thanks to genuinely collaborative interactions between authors and review editors, who include some of the world's best academicians. Research must be certified by peers before entering a stream of knowledge that may eventually reach the public - and shape society; therefore, Frontiers only applies the most rigorous and unbiased reviews.
Frontiers revolutionizes research publishing by freely delivering the most outstanding research, evaluated with no bias from both the academic and social point of view. By applying the most advanced information technologies, Frontiers is catapulting scholarly publishing into a new generation.

## What are Frontiers Research Topics?

Frontiers Research Topics are very popular trademarks of the Frontiers Journals Series: they are collections of at least ten articles, all centered on a particular subject. With their unique mix of varied contributions from Original Research to Review Articles, Frontiers Research Topics unify the most influential researchers, the latest key findings and historical advances in a hot research area! Find out more on how to host your own Frontiers Research Topic or contribute to one as an author by contacting the Frontiers Editorial Office: frontiersin.org/about/contact

# OPTICAL FIBER-BASED PLASMONICS BIOSENSORS FOR BIOMEDICAL APPLICATIONS

Topic Editors:
**Santosh Kumar,** Liaocheng University, China
**Carlos Marques,** University of Aveiro, Portugal
**Qiang Wu,** Northumbria University, United Kingdom
**Qinglin Wang,** Liaocheng University, China
**Sanjeev Kumar Raghuwanshi,** Indian Institute of Technology Dhanbad, India

**Citation:** Kumar, S., Marques, C., Wu, Q., Wang, Q., Raghuwanshi, S. K., eds. (2022). Optical Fiber-Based Plasmonics Biosensors for Biomedical Applications. Lausanne: Frontiers Media. doi: 10.3389/978-2-88974-680-4

# Table of Contents

frontiers | Frontiers in Sensors

EDITORIAL
published: 17 May 2022
doi: 10.3389/fsens.2022.903826

# Editorial: Optical Fiber-Based Plasmonics Biosensors for Biomedical Applications

*Carlos Marques*[1] *and Santosh Kumar*[2]*

[1]Physics Department, University of Aveiro, Aveiro, Portugal, [2]Shandong Key Laboratory of Optical Communication Science and Technology, School of Physics Science and Information Technology, Liaocheng University, Liaocheng, China

**Keywords: biosensor, optical fiber, Plasmonics, biomedical, Optical Devices**

## Editorial on the Research Topic

## Optical Fiber-based Plasmonics Biosensors for Biomedical Applications

Today, healthcare problems have become the most essential and challenging matters worldwide. Many features in biomedical industries have been growing quickly in recent years, particularly in the underdeveloped areas.

The plasmonic-optical fiber sensors have shown extraordinary capabilities in realizing highly sensitive and accurate sensors for the measurement of biological analytes in the field of health monitoring and diagnosis.

This kind of sensor offers a unique ability for real-time monitoring of the molecular binding events. Plasmonics in optical fiber is a highly dynamic field feeding to multi-faceted research domains and involves several students, researchers, scientists, and engineers from different areas. The sensitivity of plasmonic structures to the changes in their local dielectric environment has led to the development of new sensing strategies and systems. It is a huge topic for many areas that need more than even research to increase the strength of this digital Era.

This Research Topic on "Optical Fiber-based Plasmonics Biosensors for Biomedical Applications" have contribution of papers in Frontiers in Sensors, Physical Sensors, Biosensors and Frontiers in Physics, Optics and Photonics and it was organized by Managing Editor Santosh Kumar, Liaocheng University, China and Guest Editors Carlos Marques, Qiang Wu, Qinglin Wang, and Sanjeev Kumar Raghuwanshi. The goal is to highlight the advancement of optical fiber-based plasmonics biosensors and devices in applications to sensors covering fields such as medicine, power industry, energy, fast optics and telecom. The Research Topic includes both comprehensive review articles and original technical contributions covering fundamental research and application. 17 invited feature papers will be published in this issue where the authors are from universities, government labs and industries.

The managing editor, Santosh Kumar, and guest editors thank the authors who submitted their papers to this Research Topic and the anonymous reviewers whose feedbacks ensure the high quality of the Journal, the Frontiers publication team, for helping this issue to be a success.

All Guest Editors hope that this special issue can provide and in-depth look at this hot-topic where future students, researchers, engineers and industrial applicators can take a valuable reference on Optical Fiber-based Plasmonics Biosensors for Biomedical Applications.

A list of these papers is listed below.

1. *$GeO_2$ Doped Optical Fiber Plasmonic Sensor for Refractive Index Detection* (Gangwar et al.).



***Edited and reviewed by:***
*Joel Villatoro, University of the Basque Country, Spain*

***Correspondence:**
*Santosh Kumar*
*santosh@lcu.edu.cn*

***Specialty section:***
*This article was submitted to Physical Sensors, a section of the journal Frontiers in Sensors*

***Received:*** *24 March 2022*
***Accepted:*** *29 March 2022*
***Published:*** *17 May 2022*

***Citation:***
*Marques C and Kumar S (2022) Editorial: Optical Fiber-Based Plasmonics Biosensors for Biomedical Applications. Front. Sens. 3:903826. doi: 10.3389/fsens.2022.903826*

2. *Cost-Efficient Hybrid WDM-MDM-Ro-FSO System for Broadband Services in Hospitals* (Liang et al.).
3. *Exploring Optimality of Piecewise Polynomial Interpolation Functions for Lung Field Modeling in 2D Chest X-Ray Images* (Kumar R. et al.).
4. *WDM-Based 160 Gbps Radio Over Fiber System With the Application of Dispersion Compensation Fiber and Fiber Bragg Grating* (Kumar D et al.).
5. *A Cost-Efficient RGB Laser-Based Visible Light Communication System by Incorporating Hybrid Wavelength and Polarization Division Multiplexing Schemes* (Xiang-Peng).
6. *Secrecy Performance Analysis of Hybrid RF/VLC Dual-Hop Relaying Systems* (Liu et al.).
7. *Developing Cost-Effective and High-Speed 40 Gbps FSO Systems Incorporating Wavelength and Spatial Diversity Techniques* (Modalavalasa et al.).
8. *Performance Evaluation of a 4 × 20-Gbps OFDM-Based FSO Link Incorporating Hybrid W-MDM Techniques* (Singh et al.).
9. *A Cost-Effective Photonic Radar Under Adverse Weather Conditions for Autonomous Vehicles by Incorporating a Frequency-Modulated Direct Detection Scheme* (Sharma et al.).
10. *Coherent Detection-Based Optical OFDM, 60 GHz Radio-over-Fiber Link Using Frequency Quadrupling, and Channel and Carrier Phase Estimation* (Thool et al.).
11. *Hybrid MDM-PDM Based Ro-FSO System for Broadband Services by Incorporating Donut Modes Under Diverse Weather Conditions* (Chaudhary et al.).
12. *Performance Investigation of a High Data Rate Mode Division Multiplexed-Free Space Optics Link Under Harsh Weather Conditions* (Singh et al.).
13. *Modeling and Performance Analysis of Simplified Two-Diode Model of Photovoltaic Cells* (Prakash et al.).
14. *Improved Dielectric Properties and Grain Boundary Effect of Phenanthrene Under High Pressure* (Wang et al.).
15. *Large Tunable 16-Tupled Millimeter Wave Generation Utilizing Optical Carrier Suppression With a Tunable Sideband Suppression Ratio* (Asha and Sandeep Dahiya).
16. *Nanoparticle-Based FM-MCF LSPR Biosensor With Open Air-Hole* (Yang et al.).
17. *Remote Chemical Sensing by SERS with Self-Assembly Plasmonic Nanoparticle Arrays on a Fiber* (Zhang et al.).

## AUTHOR CONTRIBUTIONS

All authors listed have made a substantial, direct, and intellectual contribution to the work and approved it for publication.

**Conflict of Interest:** The authors declare that the research was conducted in the absence of any commercial or financial relationships that could be construed as a potential conflict of interest.

**Publisher's Note:** All claims expressed in this article are solely those of the authors and do not necessarily represent those of their affiliated organizations, or those of the publisher, the editors and the reviewers. Any product that may be evaluated in this article, or claim that may be made by its manufacturer, is not guaranteed or endorsed by the publisher.

frontiers in Physics

ORIGINAL RESEARCH
published: 10 May 2021
doi: 10.3389/fphy.2021.691387

# WDM-Based 160 Gbps Radio Over Fiber System With the Application of Dispersion Compensation Fiber and Fiber Bragg Grating

*Suresh Kumar*[1], *Sonia Sharma*[1] *and Sandeep Dahiya*[2]*

[1] *Department of Electronics and Communication Engineering, University Institute of Engineering and Technology, Maharshi Dayanand University, Rohtak, India,* [2] *Department of Electronics and Communication Engineering, Bhagat Phool Singh Women University Khanpur-Kalan, Sonipat, India*

The demand for data transmission is rising expensively for the applications of biomedical sensors data, multimedia technologies, and ultrahigh-definition online video streaming. Such applications require larger bandwidth with minimum latency and seamless service delivery. Radio-over-fiber (RoF), integrated with wavelength division multiplexing (WDM) technology, is being considered one of the promising technologies. However, the integration of optical fiber and wireless communication also generates non-linear effects as and when the number of users increases. That results in the introduction of signal noise, unwanted frequencies, low quality of signals, and increased latency. In this paper, a 16-channel 160 Gbps data rate WDM-based RoF system has been simulated and evaluated for optimum performance at a variable input power level, from 5 to −15 dBm, with the application of dispersion compensation fiber (DCF) and fiber Bragg grating (FBG), with channel spacing of 50 and 100 GHz. The performance of the system is evaluated with the existing WDM-RoF system. The performance metrics parameters chosen for evaluation are bit error rate (BER), quality factor (Q-factor), and eye diagrams and simulated on opti-system simulator. The optimum performance has been observed at a power level of −5 dBm for all these elected evaluation parameters. It has also been observed that, for channel spacing of 100 GHz, the network performed better in comparison with 50 GHz.

**Keywords: self-phase modulation, mach zehnder modulator, RoF, cross-phase modulation (XPM), four wave mixing, FBG, stimulated brillouin scattering, stimulated raman scattering**

OPEN ACCESS

***Edited by:***
*Santosh Kumar,*
*Liaocheng University, China*

***Reviewed by:***
*Abhimanyu Nain,*
*Guru Jambheshwar University of Science and Technology, India*
*Ragini Singh,*
*Liaocheng University, China*

***Correspondence:**
*Sandeep Dahiya*
*sandeepdahiya@bpswomenuniversity.ac.in*

***Specialty section:***
*This article was submitted to Optics and Photonics, a section of the journal Frontiers in Physics*

***Received:*** *06 April 2021*
***Accepted:*** *15 April 2021*
***Published:*** *10 May 2021*

***Citation:***
*Kumar S, Sharma S and Dahiya S (2021) WDM-Based 160 Gbps Radio Over Fiber System With the Application of Dispersion Compensation Fiber and Fiber Bragg Grating. Front. Phys. 9:691387. doi: 10.3389/fphy.2021.691387*

## INTRODUCTION

With time, the need for superfast transmission speed of data is growing. Nowadays, it is difficult to imagine life without video calls, online high-resolution video streaming, biomedical sensors data aggregation, online gaming, virtual reality experience, artificial intelligence (AI), and the list goes on. All these technologies require high bandwidth, high transmission speed, and minimum disturbance possible. Optical fiber communication plays a vital role in our modern age communication systems.

In RoF technology, the modulated RF signal is carried by uplink and downlink between central station (CS) and base station (BS) [1, 2]. These data are transported, using an optical

fiber link. However, the optical fiber introduces various non-linearities while transmitting data through it [3]. These non-linearities produce both generative and degenerative effects in the communication system. Non-linear effects also enhance the fiber performance; hence, they offer innovative applications, such as fiber lasers, multiplexers, demultiplexers, etc. On the other hand, the disadvantage of the non-linear effects is that they limit the optical fiber communication. In RoF, the centralization of BS and reduced cell size offers uninterrupted high-data speed to serve a maximum number of customers. It also decreases the installation cost, operational cost, and maintenance cost of the system, and, hence, the overall fixed cost of the system installation decreases [4]. Dahiya et al. discussed the effects of PMD and have used a hybrid optical amplifier to achieve enhanced capacity in the polarization division multiplexed (PDM-QAM) system [5].

Jia et al. proposed a novel method for a link distance of 40 km and a data rate of 2.5 Gbps in a RoF system. The carrier suppression technique is used for downlink, while utilizing this carrier for uplink communication results in obviating the requirement of the optical source at the BS end. However, this method exhibited a power penalty of 1.2 dB [6]. Lin et al. employed a null-biased MZM for modulating the light into central carrier suppressed double side band (CCS-DSB) and a central carrier added DSB (CCA-DSB) master and a dual-mode colorless laser diode in order to establish 5G-based 39-GHz mm-wave over the fiber system for a perfect fusion between the fiber and mm-wave to deliver 36 Gbps for baseband and 4-Gbps free-space transmissions. A comparison of different injection-locking masters was also performed that revealed a CCS-DSB master injection-locked slave colorless laser diode, superior with best back-to-back performance in comparison with the CCA-DSB and the dual distributed feedback laser diodes (DFBLD) [7].

The combination of RoF with the WDM technology enhances cellular communication availability even in remote areas. In WDM, different wavelengths carry different signals, and many wavelengths travel through a single optical fiber. Therefore, different signals with different wavelengths are combined and then transmitted through a single optical fiber and then separated at the end [8]. This results in a high-data rate, the larger capacity of the system, more flexibility, a decrease in cost, and a simple network design, hence an enhanced optical communication system in all forms. Kim et al. evaluated WDM RoF applications, using SOA and implemented frequency up conversion by the FWM effect; they observed that the simultaneous up conversion of eight channels was achieved, almost a negligible crosstalk and with no error. This proves that WDM RoF technology is certainly a better choice of a broadband wireless access network [9].

A basic WDM RoF system is depicted in **Figure 1**. The electrical data received from an individual sensor is fed into the transmitter (present at the CS), which consists of an RF modulator, a continuous wave (CW) laser, and MZM. Then, it is fed to the multiplexer; likewise, all transmitters feed $\lambda_1 \ldots \lambda_n$ into the multiplexer. The multiplexer then combines all these wavelengths and then passes it on through an optical fiber to the demultiplexer. The demultiplexer separates all the wavelengths and passes them to the receiver BS. The BS consists of a photodiode and a filter. The signal is then transmitted through an antenna to other mobile stations.

The present research work involves the design of a 16/160 Gbps WDM-RoF system, utilizing the hybrid combination of DCF and FBG for the mitigation of non-linearities. Section Non-linearities in the propagation path categorizes the non-linearities that occur in the path link and the impact on the system quality. The designed simulation schematic is described in section Simulation Design, with the selected parameter values. The section Results and Discussion contains the result and discussion, and section Conclusion concludes the paper.

## NON-LINEARITIES IN THE PROPAGATION PATH

Fiber non-linearities are basically subdivided into two categories. The first one relates to the index, which includes the non-linearities that occur because of intensity-dependent disparities in the refractive index of the optical fiber and is broadly named as "Kerr effect." The Kerr effect is further subdivided into different non-linearities, known as "SPM," "XPM," and FWM. The second category is related to scattering non-linearities and because of inflexible stimulated scattering, which is further classified as SRS and SBS [10].

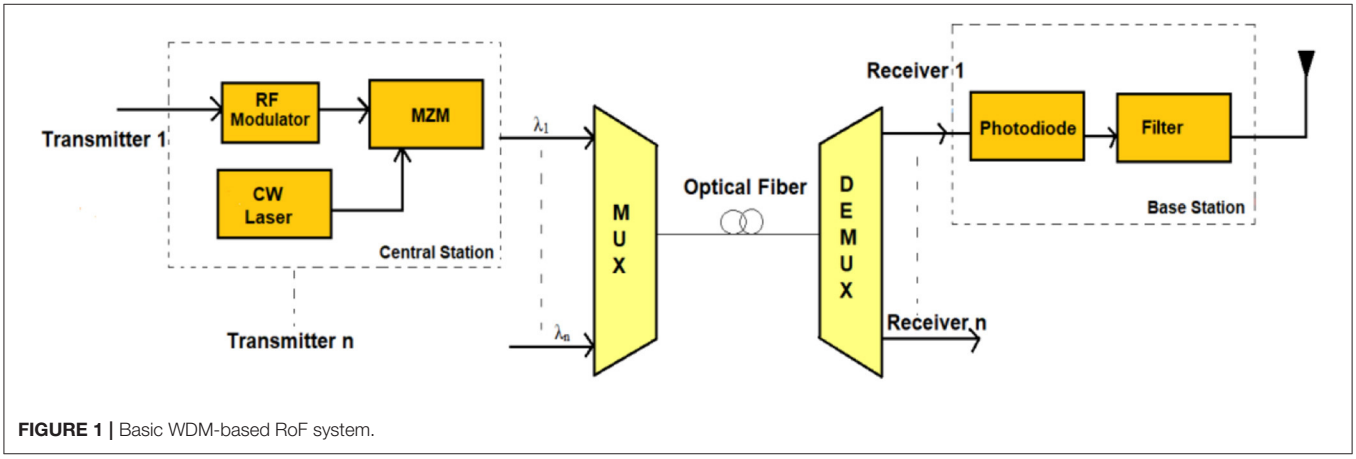


**FIGURE 1 |** Basic WDM-based RoF system.

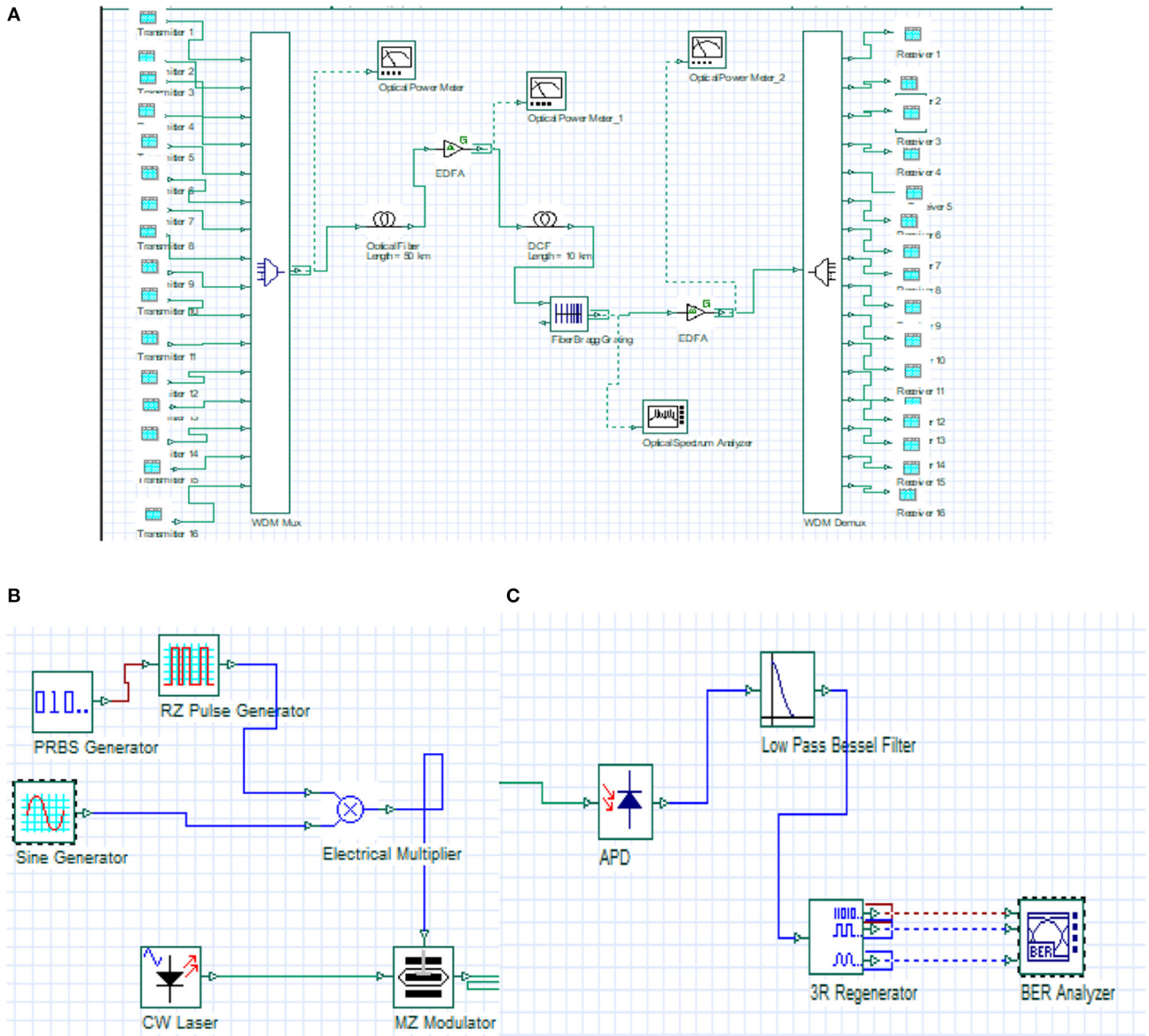


**FIGURE 2 |** Schematic representation of the simulation layout of the 16/160-Gbps WDM-RoF system, transmitter, and receiver subsystem. **(A)** The layout of the 16/160-Gbps WDM-RoF system. **(B)** Transmitter subsystem. **(C)** Receiver subsystem.

SPM—it is, basically, the self-induced phase shift, which is observed in the fiber when the optical signal is transmitted through the optical fiber. In other words, this phenomenon can also be termed as "phase modulation" of light due to the fact of varying light intensity. It results in the broadening of the signal spectrum. When the light signal travels through fiber, it leads to high intensity of light in the core, which further results in a higher refractive index. The variation of the refractive index with respect to time takes place due to variation in light signal intensity, and this further leads to phase changes, which are purely time dependent. Nain et al. investigated the performance of MZM and optical phase modulator (OPM) under the SPM effect in the RoF system [11].

XPM—in the XPM non-linearity, one wavelength of light can affect the phase of another light wavelength. Here, the refractive index non-linearity of one light signal is not only dependent on its own intensity but also gets affected by the intensity of other light signal beams while these are propagating into the fiber. It results in translation of power variations from one wavelength channel to the phase variations of another channel. Nain et al. evaluated the influence of the XPM crosstalk in SCM-based RoF systems. It has been observed that the crosstalk increases

**TABLE 1 |** The simulation parameters employed in the design of 16/160-Gbps WDM-RoF system.

| **Transmitter parameters** | **Value (unit)** |
|---|---|
| The bit rate of PRBS | 10 Gbps |
| The power of CW laser | −15 to 5 (dBm) |
| The frequency of sine generator | 2 to 32 (GHz) |
| The channel spacing | 50 and 100 (GHz) |
| The frequency of CW laser | 193.1–193.85 (THz) for 50 GHz<br>193.1–194.6 (THz) for 100 GHz |
| The laser line width | 10 (MHz) |
| The extinction ratio of MZM | 30 (dB) |
| **SMF parameters** | **Value (unit)** |
| Length | 50 (km) |
| The effective area | 80 ($\mu m^2$) |
| Dispersion | 16 (ps/nm/km) |
| The third-order dispersion slope | 0.074 (ps/$nm^2$/k) |
| Attenuation | 0.2 (dB/km) |
| **EDFA parameters** | **Value (unit)** |
| Gain | 25 (dB) |
| The noise figure | 4 (dB) |
| **DCF parameters** | **Value (unit)** |
| Length | 10 (km) |
| Dispersion | −80 (ps/nm/km) |
| Attenuation | 0.0051(dB/km) |
| **FBG parameters** | **Value (unit)** |
| The effective index | 1.45 |
| Length | 2 (mm) |
| The gauss parameter | 0.5 |
| The linear parameter | 0.0001 ($\mu m$) |
| **Receiver parameters** | **Value (unit)** |
| Responsivity | 1 (A/W) |
| Gain | 3 |
| The ionization ratio | 0.9 |
| Dark current | 10 (nA) |
| Thermal power density | 100e−24 (W/Hz) |
| The cutoff frequency of a filter | 0.75· bit rate (Hz) |
| The filter order | 4 |

for the greater transmission distance and higher modulation frequency [12].

FWM–it gets observed when channel spacing is comparatively less, i.e., wavelength channels are placed very close to each other. Channel spacing and a fiber type result in variation in the FWM effects. These wavelengths, while propagating through the fiber simultaneously, create another new wavelength, which is named as "idler" due to the effect of FWM. This new wavelength is entirely different from all other wavelengths, given as input to the system [13].

$$f_{xyz}=f_x+f_y+f_z\ (x,y\neq z) \tag{1}$$

where $f_x$,$f_y$,$f_z$ = frequency of input signals and $f_{xyz}$ = frequency of a resultant signal.

The equations below represent the high-order dispersion parameters of FWM in terms of propagation constant 'b' by Taylor series;

$$b=b_0+(\omega-\omega_0)\frac{db}{d\omega}+\frac{1}{2}(\omega-\omega_0)^2\frac{d^2b}{d\omega^2}+\frac{1}{6}(\omega-\omega_0)^3\frac{d^3b}{d\omega^3}+\frac{1}{24}(\omega-\omega_0)^4\frac{d^4b}{d\omega^4}+\ldots \tag{2}$$

Now, $\frac{db}{d\omega}=\delta$, where δ is the propagation delay per optical length. We will replace the values in Equation (2);

$$\triangle b=b-b_0=2\pi\left[(\triangle f)\,\delta+\pi\,(\triangle f)^2\frac{d\delta}{d\omega}+\frac{2\pi^2}{3}(\triangle f)^3\frac{d^2\delta}{d\omega^2}+\frac{\pi^3}{3}(\triangle f)^4\frac{d^3\delta}{d\omega^3}+\ldots\right. \tag{3}$$

Therefore, by 4, second-order dispersion is given by

$$b_2=\frac{d\delta}{d\omega}=\frac{\lambda^2}{2\pi c}\frac{d\delta}{d\lambda}=\frac{\lambda^2}{2\pi c}F_0 \tag{4}$$

Third order dispersion is given by

$$b_3=\frac{d^2\delta}{d\omega^2}=\frac{\lambda^2}{(2\pi c)^2}\left[\lambda^2\frac{d^2\delta}{d\lambda^2}+2\lambda\frac{d\delta}{d\lambda}\right]=\frac{\lambda^2}{(2\pi c)^2}\left[\lambda^2F_1-2\lambda F_0\right] \tag{5}$$

where $\triangle f$ = channel spacing and $F_0$ = fiber chromatic dispersion

The power of the resultant FWM signal is expressed as

$$P_F(L)=\frac{1024\pi^2}{\pi^4\lambda^2c^2}(D_X).\frac{P_x(0)\,P_y(0)\,P_z(0)}{A_{ef}^2}e^{-\alpha L}.\frac{(1-e^{\alpha L})^2}{\alpha^2}n \tag{6}$$

where $L$ = fiber length;
$\lambda$ = wavelength;
$c$ = speed of light;
$D$ = a degrading factor;
$X$ = non-linear susceptibility;
$P_x\ P_y\ P_z$ = power of the input signal with frequency $f_x$, $f_y$, and $f_z$, respectively;
$A_{ef}$ = the effective area of the optical fiber core;
$\alpha$ = loss coefficient; and
$n$ = the refractive index

When input channels increase, the FWM sideband products also increase. When an equal amount of power is given as input to all the channels and phase matching is maintained, then the following equation holds true:

$$\frac{P_{FWM}}{P_0}=(D_F\gamma L)^2P_i^2\,(mW) \tag{7}$$

where $\gamma$ denotes a non-linear coefficient, $P_i$ is the input power, and $D_F$is 2 for each channel having a different frequency.

With an increase in optical power levels, the FWM effects get observed significantly. Processes such as wavelength conversion and de-multiplexing are the basic applications of FWM. Kathpal

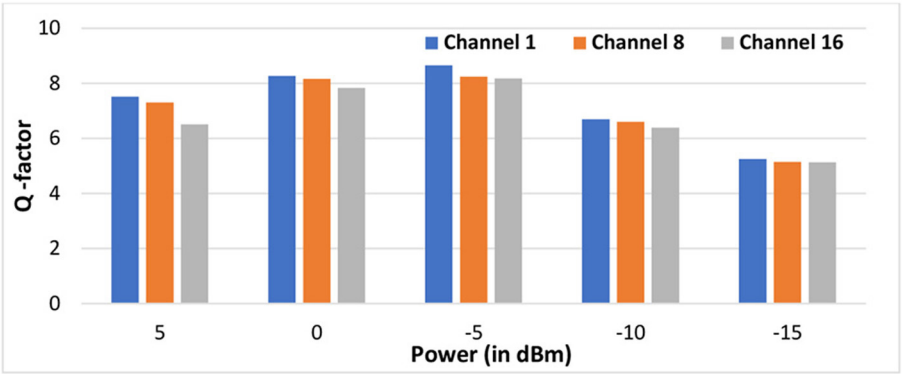


**FIGURE 3 |** Variation of Q factor with input power at 50 GHz channel spacing.

and Garg have presented the simulations of the studied 8/32 RoF-BF system and found out that the FWM effects are lesser when there is a reduction in the power level and enhancement in channel spacing [14].

SRS—in the WDM fiber communication system, SRS plays an important role. The photons of the light signal interact with the molecular vibrations of the fiber, and these also interact with the photons of the other light signals while using the same single fiber for the propagation of light. Because of these interactions, the generation of scattered light takes place. It has also been concluded that the wavelength of the resultant light is comparatively longer than all other light signals [15]. Nain et al. have observed that the SRS-induced crosstalk level varies due to variation in modulation frequency and optical power. It has also been noticed that the crosstalk remains almost unchanged with respect to variation in transmission link length [16].

SBS—it has been observed that the scattering of light is in the backward direction. In order to reduce the SBS effect, the possible solution is to keep the input power below the threshold of SBS or increase the spectral line width of the source itself. SBS effects are found to be related to the bandwidth of the input light signal and the type of the optical fiber [17].

Dispersion—it causes the light pulse to spread as it propagates through the fiber. Chromatic dispersion is one of the main factors responsible for the power penalty that limits the RoF link performance. Li et al. proposed two stages, heterodyning in a millimeter-wave RoF system, one at a millimeter-wave mixer and the other at FBG in BS. The system overall performed well with suppression of redundant frequency tones and no deterioration of power due to chromatic dispersion [18]. Li et al. proposed a carrier-phase-shifted DSB modulation in the RoF system to achieve high linearity without using additional RF or optical components and to reduce the effects of power fading due to dispersion. The RoF system has been verified with maximum frequency shifted to 10 and 15 GHz for 25- and 39-km ranges, with SFDR of 111.3 dB $Hz^{2/3}$, which is greater than the conventional SSB modulation by 10 dB [19].

Cui et al. presented a parallel configuration of the electro-optic phase and intensity modulator to reduce the effect of chromatic dispersion (CD) over a 34-km link for a wide bandwidth of 0–18 GHz. The CD-induced power fading has been sufficiently compensated by appropriate adjustment of optical power and the time delay among the signals from different modulators. Furthermore, the proposed link is compared with the DSB-based link, and enhancement of up to 31 dB $Hz^{2/3}$ in spurious free dynamic range (SFDR) has been observed [20]. Tsai et al. used an injection-locked colorless laser diode in a 40 Gbps 256-QAM-based OFDM system over a distance of 25 km. By careful adjustment of a bias current and pre-leveling of the modulation throughput, the dispersion-induced fading has been reduced prior to transmission [21]. Tsai et al. proposed a 60-GHz mm-WoF system via a directly modulated dual-mode laser diode (DMLD), with suppressed third order intermodulation dispersion for transmitting 16-QAM-modulated OFDM data at 6Gbps over a 4-km fiber and 3-m wireless distance. The power fading effect was restricted with improved BER and a power penalty of 1.1 dB [22]. The apodized and linearly chirped FBG (LCFBG) has been incorporated in the present system design so that the sidelobe levels and ripples in group delay response can be suitably reduced. The Gaussian apodization function is applied because of its maximum reflectivity and reduced side lobes characteristics.

## SIMULATION DESIGN

We have designed a 16-channel 160 Gbps WDM-RoF system with each channel operating at 10 Gbps, using Optisystem 16.1 [M/s Optiwave Systems Inc. (OPTIWAVE) at Ottawa, ON, Canada]. The diagram representing the 16/160 WDM-RoF setup is illustrated in **Figure 2A**. The transmitter section comprises 16 RF signals that are combined, using a WDM multiplexer, and are transmitted over an optical fiber at 60-km transmission distance.

**Figure 2B** depicts the transmitter subsystem. Each transmitter includes a pseudorandom bit sequence (PRBS) generator that generates binary data at a 10-Gbps data rate, which is given to the return-to-zero (RZ) pulse generator for baseband signal generation. The RZ coding format has been used due to its increased fairness to fiber non-linear effects. It is then multiplexed over the RF sinusoidal source. The MZM provides

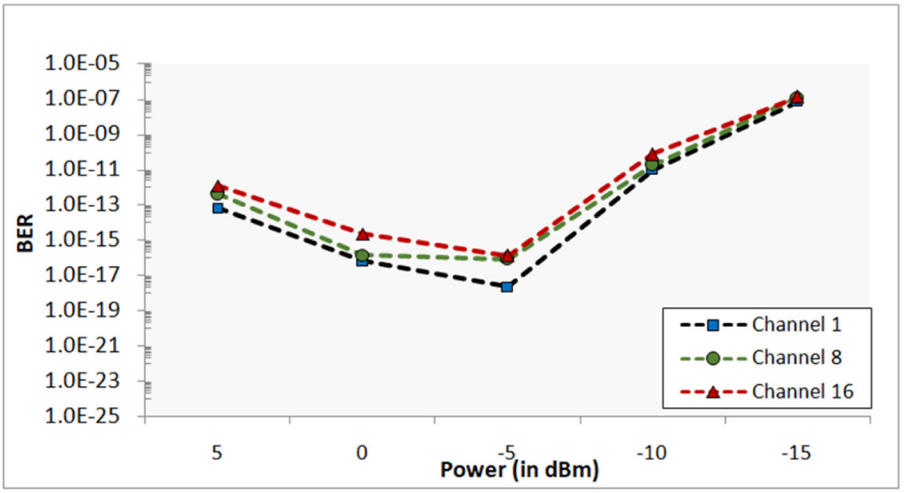


**FIGURE 4 |** Variation of BER with power at channel spacing of 50 GHz.

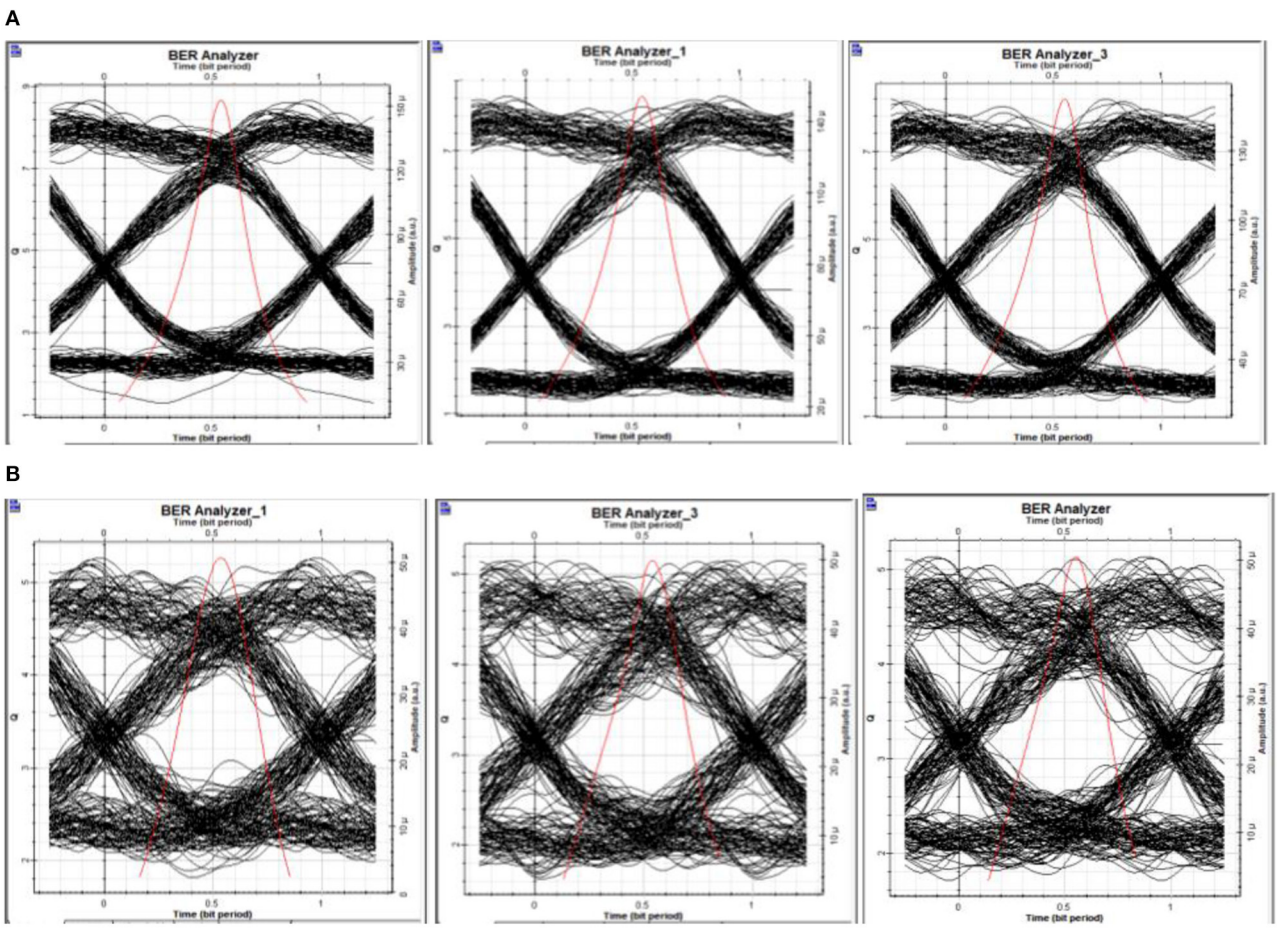


**FIGURE 5 |** The eye diagrams for conventional WDM-based RoF system for 50 GHz channel spacing. **(A)** The eye diagrams at channels 1, 8, and 16 at −5 dBm input power. **(B)** The eye diagrams at channels 1, 8, and 16 at −15 dBm input power.

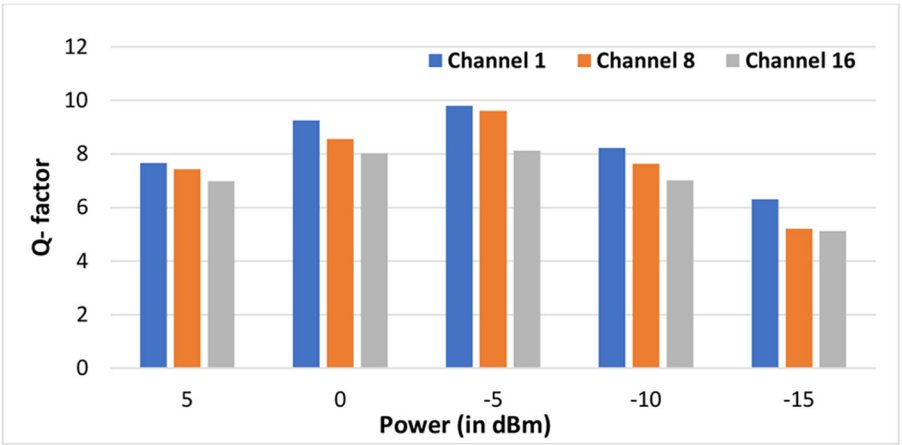


**FIGURE 6 |** Variation of Q factor with power at channel spacing of 50 GHz.

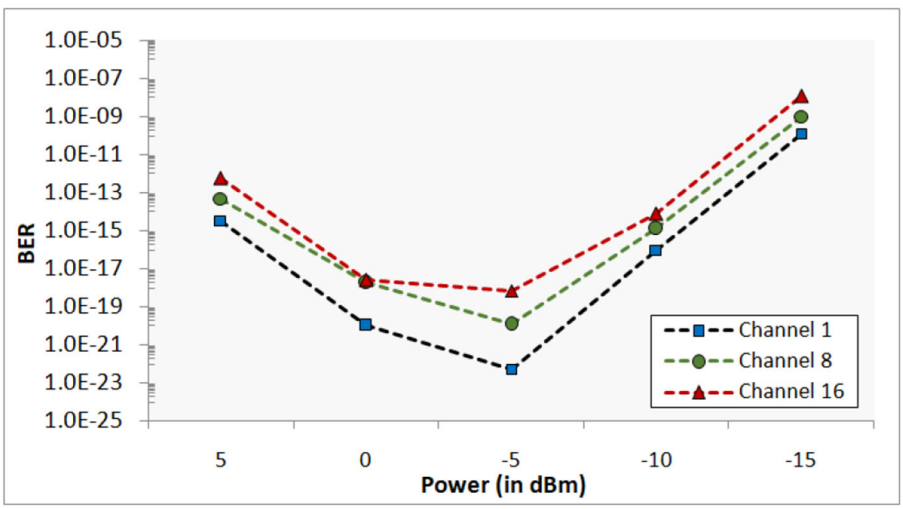


**FIGURE 7 |** Variation of BER with power at channel spacing of 100 GHz.

optical modulation, using a high-frequency optical carrier signal generated by the CW laser.

Optical signals of different wavelengths from all the CW lasers are modulated and, thereafter, combined, using the WDM multiplexer to enhance the data transmission capacity. This multiplexed signal is transmitted through a single-mode fiber (SMF). The SMF has been used, because, in comparison to multi-mode fiber (MMF), SMF is capable of carrying an optical signal at a higher data rate for a larger link length, although the optical signal also suffers due to higher order dispersion and non-linearities, which may result in limiting the transmission distance. In the present network simulation, erbium-doped fiber amplifier (EDFA) has been included because it can provide the necessary amplification of the optical signal while creating minimum internal noise.

The amplifier has been inserted after the SMF and acts as an in-line amplifier. Thereby, the EDFA provides amplification to the weak input signal and brings it to a precise level to compensate for the transmission losses. Furthermore, to compensate for the link losses and dispersion effects, DCF and FBG are also incorporated in the network system design. The amplified signal passes through DCF. Here, the DCF provides equal and opposite dispersion at the rate of −80 ps/nm/km so that the chromatic dispersion can be brought to nearly zero. FBGs are designed by exposing the fiber core to highly intense UV light. This results in an increase in the refractive index of the fiber core, which produces a fixed modulation index, known as "grating" [23]. This arrangement is found to be employing a low-cost filter in reducing the chromatic dispersion and also works as a wavelength selector. The apodized and linearly chirped FBG (LCFBG) has been incorporated in the present system design so

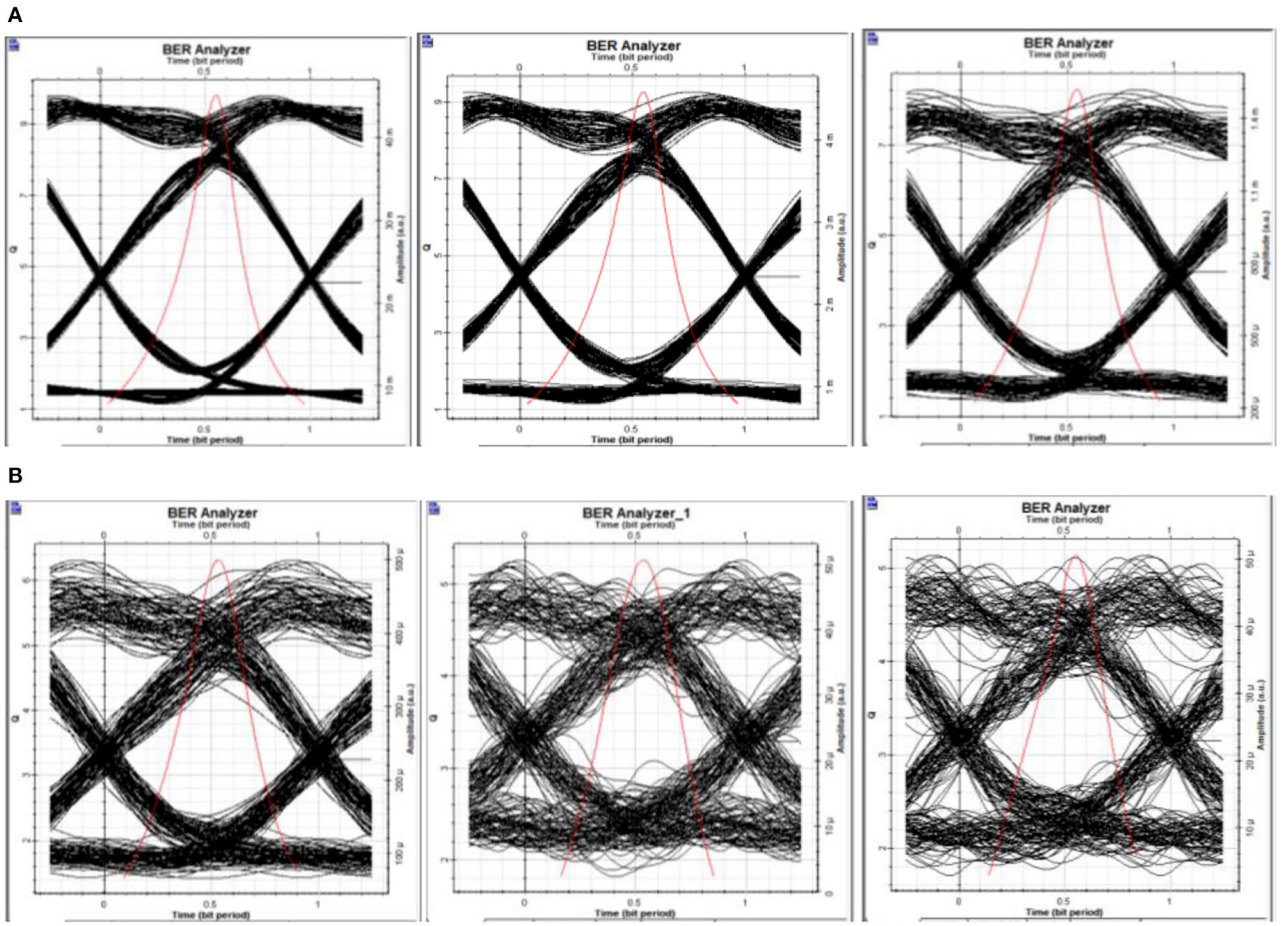


**FIGURE 8 |** The eye diagrams for the conventional WDM-based RoF system for 100 GHz channel spacing. **(A)** The eye diagrams at channels 1, 8, and 16 at −5 dBm input power. **(B)** The eye diagrams at channels 1, 8, and 16 at −15 dBm input power.

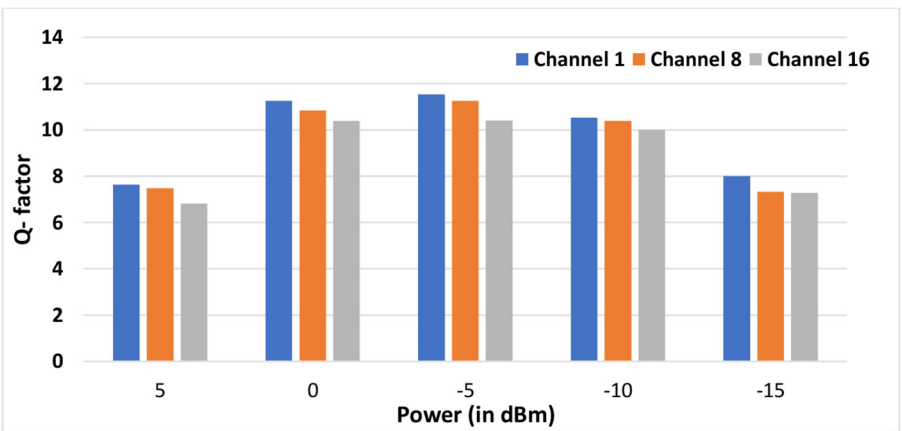


**FIGURE 9 |** Variation of Q factor with power at channel spacing of 50 GHz.

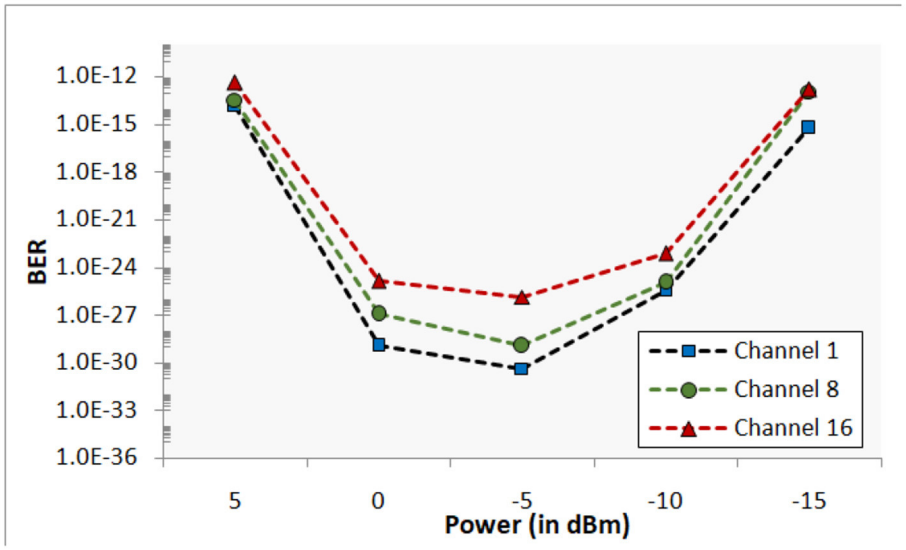


**FIGURE 10 |** Variation of BER with power at channel spacing of 50 GHz.

that the side lobe levels and ripples in the group delay response can be suitably reduced. The Gaussian apodization function is applied because of its maximum reflectivity and reduced side lobes characteristics.

Since the data from the biomedical sensors have to be of very high quality and least BER, therefore, for improved receiver sensitivity and required SNR, a preamplifier is used before the receiver. The signal, after passing through a WDM demultiplexer, is received by 16 remote stations.

The receiver subsystem shown in **Figure 2C** comprises of an avalanche photodiode detector (APD) for optical to electrical conversion, a fourth-order low-pass Bessel filter for noise removal, 3R regenerator for recreation of an original electrical signal, and BER analyzer for the visualization of the results. The optical power meter has also been used to examine the impact of non-linearities. **Table 1** below shows the simulation parameters used in the designed layout.

## RESULTS AND DISCUSSION

The simulated 16-channel WDM-RoF optical communication network has been analyzed, with variation in input transmission power, using performance metrics: Q factor, BER, and eye diagrams. Furthermore, the results are justified with the help of the eye diagrams. The two different network configurations—(i) the simple optical fiber link (ii) the optical fiber, with combination of DCF-FBG at two different channel spacing scenarios of 50 and 100 GHz—are taken into consideration.

**Figure 3** above shows the variation of Q factor with variation in input power for three different channels (channels 1, 8, and 16) at channel spacing of 50 GHz. The input power is varied from 5 to −15 dBm in a step size of 5 dBm.

From **Figure 3**, for a particular input power, the value of Q Factor shows a decreasing trend, with the increase in the number of input channels. Furthermore, with variation in input power from 5 to −15 dBm, the value of Q factor first increases from 7.42, 7.20, and 6.41 at 5 dBm to 8.58, 8.19, and 8.13 at −5 dBm for channels 1, 8, and 16, respectively. The Q factor decreases to 5.21, 5.1, and 5.06 for channels 1, 8, and 16, respectively, as the input power further decreases from −5 to −15 dBm. With the decrease in input power, the Q-factor increases up to optical power of −5 dBm; below which, the system performance has deteriorated. As the power decreases further, the FWM power generated to the existing channel power decreases, which, in turn, reduces the SNR.

**Figure 4** shows the BER curves corresponding to variation in input power. The variation in BER is in synchronization with Q Factor variation. The value of BER first decreases up to −5 dBm, with variation in input power, then increases thereby limiting the performance.

It is clear from the above graphs of Q-factor and BER that the optimum values have been obtained at input power of −5 dBm, and the least values of Q-factor and highest BER have been obtained at −15 dBm. This can be justified by observing the eye diagrams at −5 (good and optimal) and −15 dBm (worst) for channels 1, 8, and 16, respectively. **Figure 5** illustrates the eye diagrams of a conventional WDM-based RoF system at 50 GHz channel spacing.

The eye height at −5 dBm is 5.82E−5, 5.66E−5, and 5.55E−5 for channels 1, 8, and 16, respectively. It subsequently reduces with increase in number of channels. When power is reduced up to −15 dBm, the eye height observed is 1.12E−5, 1.05E−5, and 1.01E−5, respectively. The eye opening has considerably reduced with decrease in input power and increase in the number of channels.

**Figure 6** depicts a bar chart, showing the variation in Q factor for three different channels at 100 GHz channel spacing.

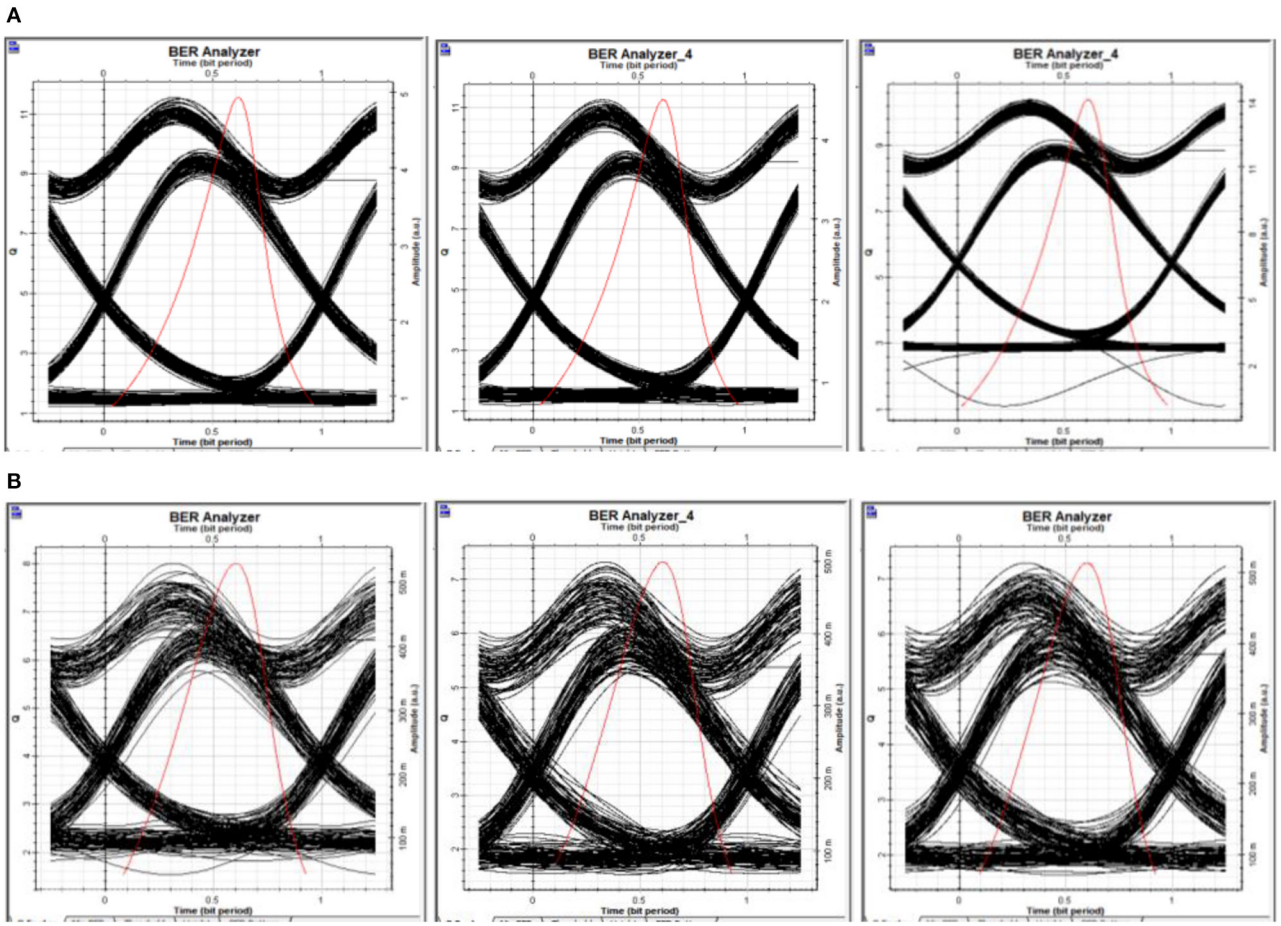


**FIGURE 11 |** The eye diagrams for WDM-based RoF system with DCF and FBG for 50 GHz channel spacing. **(A)** The eye diagrams at channels 1, 8, and 16 at −5 dBm input power. **(B)** The eye diagrams at channels 1, 8, and 16 at −15 dBm input power.

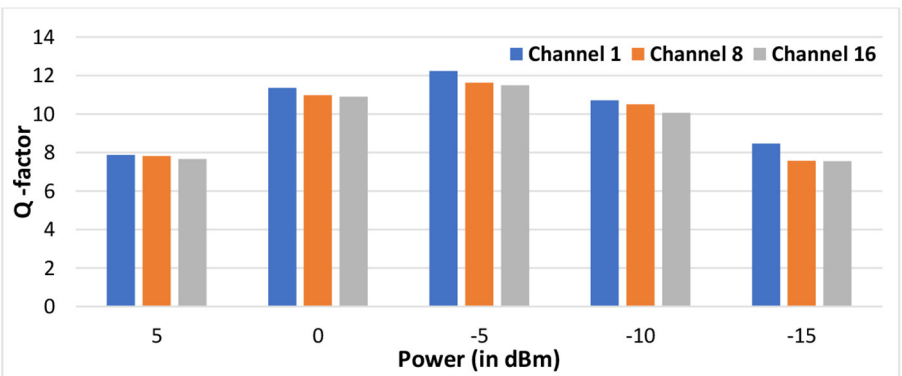


**FIGURE 12 |** Variation of Q factor with power at channel spacing of 100 GHz.

It is observed that, for a particular input power value and with increase in the number of input channels, the Q factor decreases. Furthermore, with variation in input power from 5 to −15 dBm, the value of Q factor first increases from 7.56, 7.33, and 6.88 at 5 dBm to 9.68, 9.59, and 8.04 at −5 dBm for channels 1, 8, and 16, respectively. The Q factor decreases to 6.25, 5.16, and 5.06 for channels 1, 8, and 16, respectively, as the input power further decreases from −5 to −15 dBm.

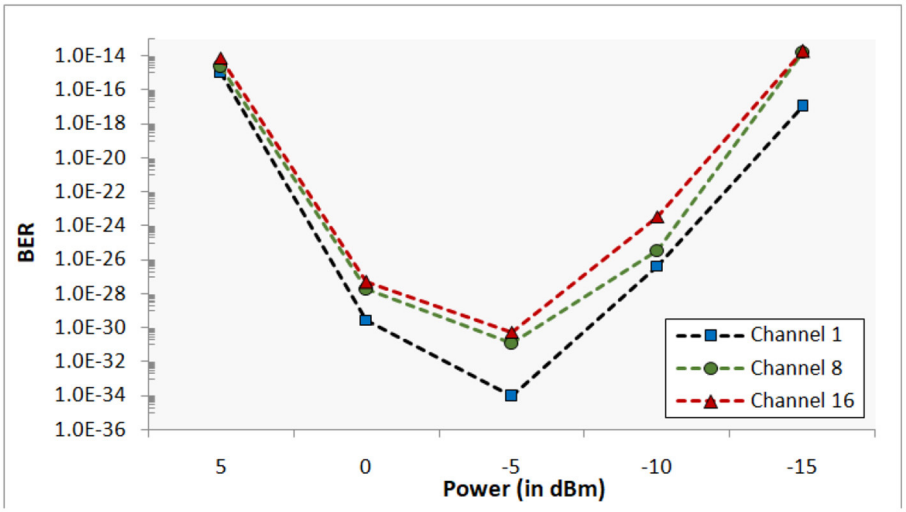


**FIGURE 13 |** Variation of BER with power at channel spacing of 100 GHz.

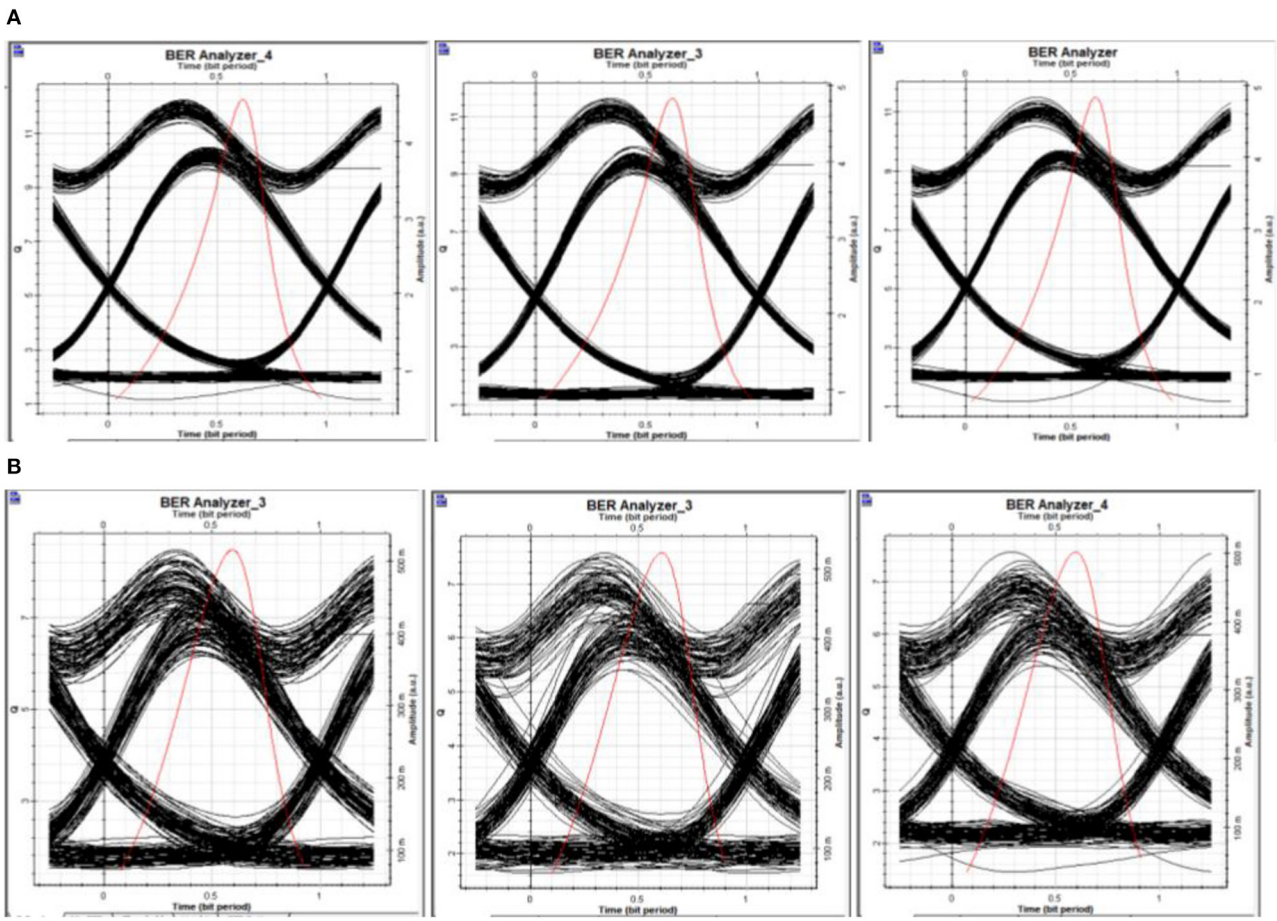


**FIGURE 14 |** The eye diagrams for WDM-based RoF system, with DCF and FBG for 100 GHz channel spacing. **(A)** The eye diagrams at channels 1, 8, and 16 at −5 dBm input power. **(B)** The eye diagrams at channels 1, 8, and 16 at −15 dBm input power.

**Figure 7** shows the variation of BER with input power. With increase in channel spacing, a decrease in BER is observed from 2.23E−18 to 5.41E−23 for channel 1 and, consequently, for the other channels at the optimum power level of −5 dBm. From **Figures 6**, **9**, the value of Q factor increases at a particular value of input power, with increase in channel spacing from 50 to 100 GHz. At input power of −5 dBm, an improvement of up to 16.51% is obtained in the Q factor.

**Figure 8** shows the eye diagrams of a conventional WDM-based RoF system at 100 GHz channel spacing.

The eye height for channels 1, 8, and 16 is 0.018, 0.0017, and 0.00056, respectively, at −5 dBm input power. It is observed that at −15 dBm, the eye height is 1.36E−4, 1.22E−5, and 1.12E−5 for the respective channels. With an increase in channel spacing to 100 GHz, clearer eye diagrams have been observed with a wider eye opening.

**Figure 9** given below depicts a bar chart, showing the variation in Q factor values for channels 1, 8, and 16 for a hybrid combination of DCF-FBG at channel spacing of 50 GHz. The input power is varied from 5 to −15 dBm. The value of Q factor first increases from 7.52, 7.41, and 6.71 at 5 dBm to 11.32, 11.13, and 10.21 at −5 dBm for channels 1, 8, and 16, respectively. The Q factor decreases to 8.02, 7.23, and 7.21 for channels 1, 8, and 16, respectively, as the input power further decreases from −5 to −15 dBm.

**Figure 10** shows the variation of BER with input power. The variation in BER is in synchronization with the variation in Q factor. The value of BER first decreases with variation in input power and then increases.

The eye diagrams for WDM-based RoF system with DCF and FBG at 50 GHz channel spacing are shown in **Figure 11**.

The height of the eye diagrams at −5 dBm is 2.12, 1.91, and 1.22 and, at −15 dBm, is 0.18, 0.16, and 0.13, respectively, at channels 1, 8, and 16. With the use of hybrid DCF-FBG combination in the designed model, enhanced qualitative performance is obtained.

**Figure 12** depicts a bar chart, showing the variation of Q factor for three different channels at channel spacing of 100 GHz. From **Figure 11**, the value of Q factor decreases with increase in the number of channels. Furthermore, as the input power is varied from 5 to −15 dBm, the value of Q factor first increases from 7.81, 7.72, and 7.59 at 5 dBm to 12.21, 11.59, and 11.48 at −5 dBm for channels 1, 8, and 16, respectively. The Q factor decreases to 8.42, 7.51, and 7.49 for channels 1, 8, and 16, respectively, as the input power further decreases from −5 to −15 dBm.

**Figure 13** shows BER vs. input power at 100 GHz channel spacing. The variation in BER is in synchronization with the variation in Q factor. The value of BER first decreases with variation in input power and then increases.

From **Figures 9**, **12**, with increase in channel spacing from 50 to 100 GHz, the value of Q factor increases at a particular value of input power. At input power of −5 dBm, an improvement of up to 10.42% is obtained in the Q factor.

The eye diagrams for WDM-based RoF system, with DCF and FBG at 100 GHz channel spacing, are shown in **Figure 14**.

At −5 dBm, the larger eye opening, with the height of 2.15, 2.09, and 2.07, is observed comparable to 0.18, 0.14, and 0.12 at −15 dBm, corresponding to channels 1, 8, and 16, respectively. It is clearly noticed from the eye diagrams that, with the inclusion of DCF and FBG in our designed layout, the impact of non-linearities, such as third-order harmonics, FWM, etc., in the propagation path, has been mitigated. From the above discussion, it can be concluded that the wider and clear opening of the diagram indicates that the quality of the signal received is optimum for further processing.

From the graphical results, the increased values of Q factor and the improved values of BER can be attributed to the hybrid DCF-FBG combination. It can be further concluded that the hybrid combination of DCF-FBG is successful in mitigating the higher-order dispersion harmonics and, thereby, limiting the impact of FWM. Furthermore, the numerical computations show that, at channel spacing of 100 GHz, there is an improvement of up to 41.52% in the value of Q factor at an input power of −5 dBm, using a hybrid combination of DCF-FBG, as compared with the conventional WDM-based RoF system, thereby justifying the selection of simulation parameters to offer the optimum results in the network design. The parameters have been varied with the stipulated design values, and the best performing values have been chosen in the table to give desired and best possible results.

## CONCLUSION

In the present work, a 16-channel, 160-Gbps WDM-RoF system has been evaluated for optimum performance, using Q factor and BER with varying input power at a channel spacing of 50 and 100 GHz, and is compared with the traditional RoF system. The data from biomedical sensors have to be captured, transported, and delivered, and the destination has to be of optimum quality. In order to mitigate the non-linearities, DCF-FBG hybrid combination has been used. From the qualitative analysis, with the reduction in input power, the Q factor first increases up to input power of −5 dBm, and, thereafter, it decreases with input power, whereas the BER first decreases up to −5 dBm and then increases thereafter with further variation in input power. The results also depicted that, at a given input power, the Q factor increases with an increase in channel spacing from 50 to 100 GHz, and an improvement of up to 16.51% is obtained. The WDM-RoF system with a hybrid combination of DCF-FBG performs efficiently at an input power of −5 dBm and provides an optimum BER performance, with an improvement of up to 41.52% in the value of Q factor, as compared with the conventional WDM-based RoF system. In further analysis of eye diagrams, the hybrid combination of DCF-FBG provides larger eye openings, with eye height of 2.15, 2.09, and 2.07 for channels 1, 8, and 16, respectively. With the considerable increase in channel spacing (50 to 100 GHz) and a simultaneous reduction in channel input power in the designed system, the effect of non-linearities has been sufficiently mitigated at an optimum power of −5 dBm.

## DATA AVAILABILITY STATEMENT

The raw data supporting the conclusions of this article will be made available by the authors, without undue reservation.

## AUTHOR CONTRIBUTIONS

SD proposed the idea and supervised the whole work. SK and SS carried out the analytical and numerical calculation. All authors contributed to the writing of the manuscript.

## REFERENCES


1. Singh S, Kumar S, Payal. Radio over fiber communication system: lateral shift in cellular communication. *Int J Emerg Technol.* (2020) 11:731–4.
2. Kumar S, Sharma D, Payal, Singh R. Performance analysis of radio over fiber link using mzm external modulator. In: Luhach A, Kosa J, Poonia R, Gao XZ, Singh D, editors. First *International Conference on Sustainable Technologies for Computational Intelligence (ICTSCI-2019).* Singapore: Springer; ASIC (2020). doi: 10.1007/978-981-15-0029-9_18
3. Payal, Kumar S. Nonlinear impairments in fiber optic communication systems: analytical review. In: *Futuristic Trends in Network and Communication Engineering (FTNCT-2018), Chapter-3, Vol. 958*. Singapore: Springer; CCIS (2019). p. 28–44.
4. Yadav J, Jaiswal AK, Kumar, M. Radio over fiber technology. *IOSR J Electron Commun Eng.* (2014) 9:83–7.
5. Dahiya S, Kumar S, Sharma D, Arora P. Mitigating polarization mode dispersion for enhanced capacity in polarization division multiplexed (PDM-QAM) optical fiber communication link using hybrid optical amplifier. In: *SPIE proceedings Optics Photonics for Information Processing XIV 115090L.* San Diego, CA (2020). doi: 10.1117/12.2566904
6. Jia Z, Yu J, Chang G. A full-duplex radio-over-fiber system based on optical carrier suppression and reuse. *IEEE Photon Technol Lett.* (2006) 18:1726–8. doi: 10.1109/LPT.2006.879946
7. Lin C, Chi Y, Tsai C, Wang H, Lin G. 39-GHz millimeter-wave carrier generation in dual-mode colorless laser diode for OFDM-MMWoF transmission. *IEEE J Select Top Quant Electron.* (2015) 21:609–18. doi: 10.1109/JSTQE.2015.2464276
8. Soni A, Pradesh M, Prajapati N, Sharma N. A review article of WDM based optical fiber communication with WDM system evolution. *Int J Adv Res Ideas Innovat Technol.* (2018) 4:739–43.
9. Kim HJ, Song JI. Simultaneous WDM RoF signal generation utilizing an all-optical frequency upconverter based on FWM in an SOA. *IEEE Photon Technol Lett.* (2011) 23:828–30. doi: 10.1109/LPT.2011.2140102
10. Amari A, Dobre OA, Venkatesan R, Kumar OS, Ciblat P, Jaouën Y. *A* survey on fiber nonlinearity compensation for 400 Gb/s and beyond optical communication systems. *IEEE Commun Surv Tutor.* (2017) 19:3097–113. doi: 10.1109/COMST.2017.2719958
11. Nain A, Kumar S. Performance investigation of different modulation schemes in RoF systems under the influence of self phase modulation. *J Opt Commun.* (2018) 39:343–7. doi: 10.1515/joc-2016-0155
12. Nain A, Kumar S, Singla S. Impact of XPM crosstalk on SCM-based RoF systems. *J Opt Commun.* (2017) 3:319–24. doi: 10.1515/joc-2016-0045
13. Bhatia R, Sharma AK, Saxena J. Improved analysis of four wave mixing with sub-plank higher-order dispersion parameters in optical communication systems. *Optik.* (2016) 127:9474–8. doi: 10.1016/j.ijleo.2016.07.035
14. Kathpal N, Garg AK. Analysis of radio over fiber system for mitigating four-wave mixing effect. *Digit Commun Netw.* (2020) 6:115–22. doi: 10.1016/j.dcan.2019.01.003
15. Kaur G, Singh ML, Patterh MS. Effect of fibre nonlinearities in a WDM transmission system. *Optik.* (2010) 121:889–96. doi: 10.1016/j.ijleo.2008.09.035
16. Nain A, Kumar S, Singla S. Performance estimation of WDM radio-over-fiber links under the influence of SRS induced crosstalk. In: *Proceeding of International Conference on Intelligent Communication.* Singapore: Springer (2017). p. 279–84. doi: 10.1007/978-981-10-1708-7_32
17. Ruzbarsky J, Turan J, Ovsenik L. Stimulated brillouin scattering in DWDM all optical communication systems. In: *26th IEEE International Conference Radioelektronika (Radioelektronika*), Kosice (2016). p. 395–8. doi: 10.1109/RADIOELEK.2016.7477354
18. Li J, Ning T, Pei L, Qi C. Millimeter-wave radio-over-fiber system based on two-step heterodyne technique. *Opt Lett.* (2009) 34:3136–8. doi: 10.1364/OL.34.003136
19. Li S, Zheng X, Zhang H, Zhou B. Compensation of dispersion-induced power fading for highly linear radio-over-fiber link using carrier phase-shifted double sideband modulation. *Opt Lett.* (2011) 36:546–8. doi: 10.1364/OL.36.000546
20. Cui Y, Xu K, Dai J, Sun X, Dai Y, Ji Y, et al. Overcoming chromatic-dispersion-induced power fading in ROF links employing parallel modulators. *IEEE Photon Technol Lett.* (2012) 24:1173–5. doi: 10.1109/LPT.2012.2192422
21. Tsai C, Chi Y, Lin G. Power fading mitigation of 40-Gbit/s 256-QAM OFDM carried by colourless laser diode under injection-locking. *Opt Express.* (2015) 23:29065–78. doi: 10.1364/OE.23.029065
22. Tsai C, Lin C, Lin C, Chi Y, Lin G. 60-GHz millimeter-wave over fiber with directly modulated dual-mode laser diode. *Sci Rep.* (2016) 6:27919. doi: 10.1038/srep27919
23. Ahlawat D, Arora P, Kumar S. Performance evaluation of proposed WDM optical link using EDFA and FBG combination. *J Opt Commun.* (2019) 40:101–7. doi: 10.1515/joc-2018-0044


**Conflict of Interest:** The authors declare that the research was conducted in the absence of any commercial or financial relationships that could be construed as a potential conflict of interest.

frontiers in Physics

ORIGINAL RESEARCH
published: 22 July 2021
doi: 10.3389/fphy.2021.732236

# Cost-Efficient Hybrid WDM-MDM-Ro-FSO System for Broadband Services in Hospitals

*Peidong Liang*[1], *Chentao Zhang*[1,2]*, *Jamel Nebhen*[3], *Sushank Chaudhary*[4] *and Xuan Tang*[4]

[1]Fujian (Quanzhou) – HIT Research Institute of Engineering and Technology, Quanzhou, China, [2]Department of Instrumental and Electrical Engineering, Xiamen University, Xiamen, China, [3]Prince Sattam bin Abdulaziz University, College of Computer Science and Engineering, Alkharj, Saudi Arabia, [4]Quanzhou Institute of Equipment Manufacturing, Haixi Institutes, Chinese Academy of Sciences, Jinjiang, China

The expansion of high-speed communication needs due to explosive growth of subscribers each year has led the researchers to design the next generation communication systems which can cope with the current growing demand. Millimeter waves, operated within the range of 30 GHz to 300 GHz, can become potential carrier for delivering large amount of data. However, in hospital scenarios, these radio waves are subjected to strict regulations due to direct impact on patients' health as well as high interference with other medical devices which again imposes critical challenge on patients. Thus, it is a challenge for the researchers to provide communication/broadband services for transmission of such sensitive biomedical sensor data in hospitals locations. Radio over Free space (Ro-FSO) systems may become the attractive solution to deliver millimeter waves over free space link with high speed. Further, to expand the capacity of Ro-FSO systems, mode division multiplexing (MDM) plays a vital role in addition to wavelength division multiplexing (WDM) scheme. In this work, we have demonstrated the MDM-WDM scheme to deliver four channels with each one having the capacity of 10 Gbps up-converted to 40 GHz over FSO link which is suitable for providing broadband and communication services within the hospital premises. Moreover, the proposed WDM-MDM-Ro-FSO link is evaluated under different fog conditions.

**Keywords: broadband services, radio over free space optics, mode division multiplexing, hospital scenarios, health monitoring**

OPEN ACCESS

***Edited by:***
*Santosh Kumar,*
*Liaocheng University, China*

***Reviewed by:***
*Akhilesh Pathak,*
*Chulalongkorn University, Thailand*
*Sudhanshu Arya,*
*Pukyong National University, South Korea*

***Correspondence:**
*Chentao Zhang*
*zctyyy@163.com*

***Specialty section:***
*This article was submitted to Optics and Photonics, a section of the journal Frontiers in Physics*

***Received:*** *28 June 2021*
***Accepted:*** *07 July 2021*
***Published:*** *22 July 2021*

***Citation:***
*Liang P, Zhang C, Nebhen J, Chaudhary S and Tang X (2021) Cost-Efficient Hybrid WDM-MDM-Ro-FSO System for Broadband Services in Hospitals. Front. Phys. 9:732236. doi: 10.3389/fphy.2021.732236*

## INTRODUCTION

The demand of wireless communication has increased rapidly since last decade which led to the development of optical wireless communication systems. International Telecom Union (ITU) [1] reported that the total number of mobile broadband subscribers increases every year by 20% that crossed four billion by the end of 2017. This growth further levitates the challenges for ITU to assign radio frequency (RF) spectrum for different cellular operators, both in rural and urban areas. However, in hospital scenarios it is not always feasible to provide broadband services due to interference of radio signals with sensitive medical appliances as well as having high impact on patients' health [2]. Thus, the use of radio waves is prohibited in hospital locations. However, broadband services are necessary in hospitals to transmit valuable data such as patients' monitoring reports from one location to another. Not only this, with high-speed broadband services doctors can connect with one another at any time and access the medical data bases from any location. This

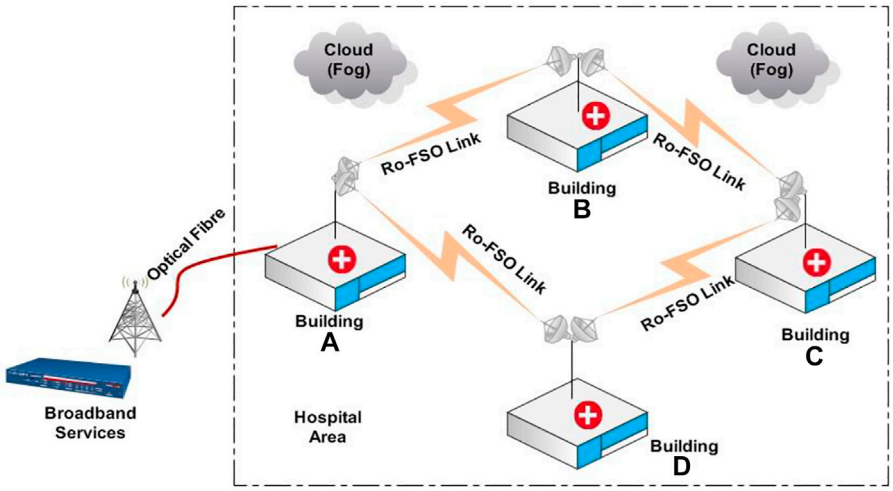


**FIGURE 1 |** Ro-FSO system in Hospital Infrastructure.

potential usage of broadband services further posits a big challenge for broadband providers to provide in the hospitals without compromising the health of patients. Ro-FSO or radio over free space can provide broadband services in hospitals as it integrates radio and optical networks as shown in **Figure 1**.

Ro-FSO permits the multiple transmission of RF signals without any expensive optical fiber infrastructure as well as license to RF operators [3]. Also, as data transmission in Ro-FSO is in the form of light signals which has no impact on patients' health as well as no interference with the medical devices, it becomes an attractive solution for providing broadband services in hospitals. Moreover, in hospital areas, it is not feasible to dig for installing optical fiber cables due to need of continuous working operations and less space, thus Ro-FSO becoming an apt substitute for replacing the optical fiber infrastructures. It also combines RoF or radio over fiber and FSO or free space optics. RoF allows sharing of various expensive RF operations like up-conversion and down-conversion, handoff, switching, etc. from central location to all the base stations which results in reduction of deployment cost [4]. Moreover, it can share large-bandwidth RF signals with low attenuation and power consumption. Whereas, FSO does not use optical fibers. Instead, it enables atmospheric data transmission with rapid adoption [5, 6]. Also, in contrast to RF transmission, it does not need any license. These combined features of RoF and FSO make Ro-FSO a compatible technology for providing broadband services in hospitals. Therefore, Ro-FSO is a relevant technology for seamless, rapid and cost-effective integration with RF wireless networks [7, 8]. However, Ro-FSO faces challenges of atmospheric turbulences such as scintillations, fog, rain, snow, etc. affecting the signal to noise ratio [9]. These atmospheric turbulences increase attenuation in the transmission path which results in shutdown of the network. Thus, researchers should consider these turbulences while designing the Ro-FSO network. Another emerging technology is MDM or mode division multiplexing that transmits through multiple channels using different modes. Apart from wavelength [10], polarization [11] and time [12] multiplexing schemes, MDM enables multimode data transmission by multiplexing through a single optical channel. In MDM, modes can be excited through various mechanisms such as spatial light modulators [13], offset launch [14], high-speed VCSEL arrays [15] and photonic crystal fibers (PCF) [16]. Researchers have used four OAM beams (1 = ±1 and 1 = ±3) to transmit 400 Gbps data through an FSO link of 120 m in 2016 [17]; MDM-OFDM scheme to transmit 80 Gbps data through an FSO link of 50 km in 2017 [7]; and MDM-based polarisation phase shift key scheme to transmit 80 Gbps data through an FSO link of 90 km in 2020 [18]. Researchers have also proposed hybrid multiplexing-based multi-channel communication systems including wavelength division multiplexing (WDM)-MDM [19], Optical code division multiplexing (OCDMA)-MDM [20] and WDM-PDM [21]. Combining MDM with WDM can increase aggregate capacity and improve spectral efficiency of Ro-FSO infrastructures which has potential application in hospital infrastructures. In this work, we have demonstrated Ro-FSO topology specially designed for medical locations by incorporating the WDM-MDM scheme which can transmit four channels with the each one having capacity of 10 Gbps up-converted to 40 GHz radio signal each over FSO link.

## MDM-RO-FSO MODELING

The schematic diagram of the proposed MDM-Ro-FSO is shown in **Figure 2**. Four channels are transmitted by using the hybrid WDM-MDM scheme. For the WDM scheme, two wavelengths (850 nm and 851 nm), each with 1 nm channel space, are used. The MDM scheme uses modal multiplexing of LG (Laguerre Gaussian) 00 and HG (Hermite Gaussian) 00. As shown in **Figure 2**, first and second channels are operated on LG 00 and HG 00 modes respectively with the wavelength of 850 nm while third and fourth channels are operated on LG 00 and HG 00 modes respectively with the wavelength of 851 nm. LG and HG modes are described by following **Eq. 1** and **Eq. 2** [22]:

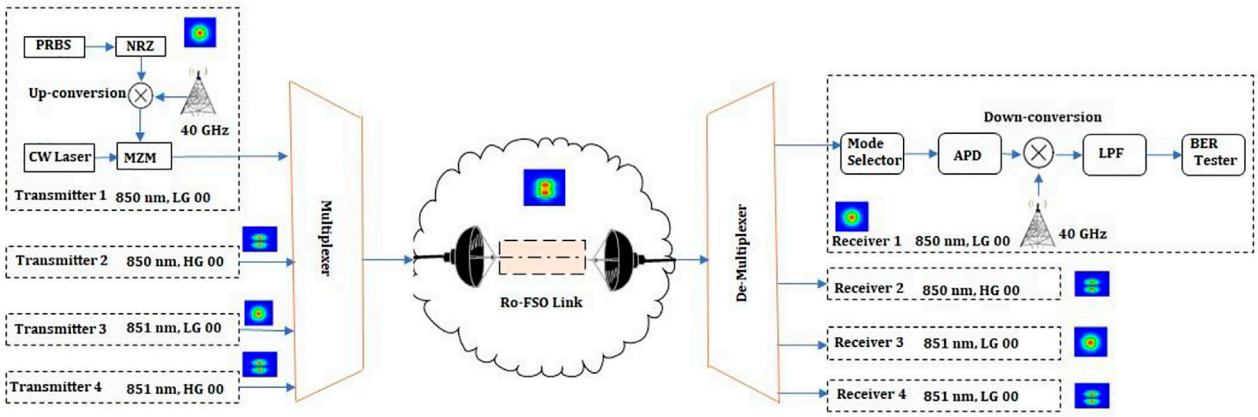


**FIGURE 2 |** Proposed 4 x 10 Gbps Ro-FSO Link.

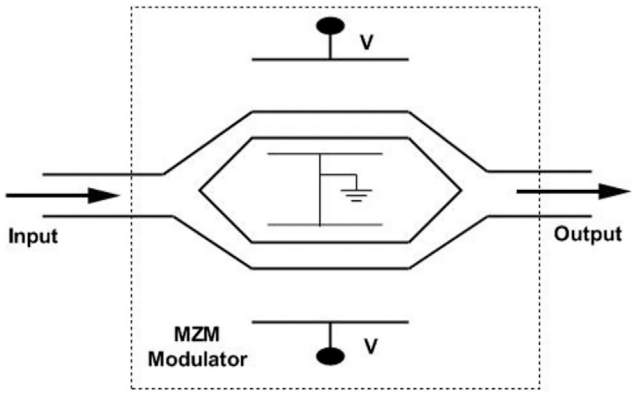


**FIGURE 3 |** Schematic model of MZM modulator.

$$\psi_{m,n}(r,\varphi) = \left(\frac{2r^2}{\omega_o^2}\right)^{\left|\frac{n}{m}\right|} L_m^n\left(\frac{2r^2}{\omega_o^2}\right)\exp\left(\frac{r^2}{\omega_o^2}\right)\times \exp\left(j\frac{\pi r^2}{\lambda R_0}\right)\left\{\begin{array}{l}\sin(|n|\varphi), n\geq 0\\ \cos(|n|\varphi), n\geq 0\end{array}\right\} \quad (1)$$

The above equation contains the azimuthal index *(X)* represented by *m* and the radial index (*Y)* represented by *n*. Curvature radius is represented by $R_o$, spot size by $w_o$ and the Laguerre Polynomial by *Ln, m*.

$$\psi_{m,n}(r,\phi) = H_m\left(\frac{\sqrt{2}x}{w_{o,x}}\right)\exp\left(-\frac{x^2}{w_{o\,x}^2}\right)exp\left(j\frac{\pi x^2}{\lambda R_{o\,x}}\right)\times H_n\left(\frac{\sqrt{2}y}{w_{o,y}}\right)\exp\left(-\frac{y^2}{w_{o\,y}^2}\right)\left(j\frac{\pi y^2}{\lambda R_{o\,y}}\right) \quad (2)$$

In the above equation, the X and Y indexes represent mode dependencies on their axes denoted by *m* and *n*, respectively. The radius of curvature is denoted by $R_o$ and *wo* is the spot size. Hermite polynomials are denoted by Hm and *Hn*.

Each channel has a non-return to zero (NRZ) data of 10 Gbps mixed with 40 GHz mm wave generated by sine generator with the help of mixer for the process of up-conversion. This 40 GHz mm wave is modulated over optical carrier by using Machzehnder modulator (MZM) derived from spatial continuous wavelength laser. The schematic diagram of MZM modulator is shown in **Figure 3**. The working principle *of MZM modulator*of MZM modulator is given by the following equation [23]:

$$E_{out}(t) = E_{in}(t).\cos(\Delta\theta(t)\times\exp(j.\Delta\Phi(t)) \quad (3)$$

where $E_{out}$ (t) is the electrical field at output port of modulator, $E_{in}$ (t) is the electrical field at input port of modulator, phase difference between two branches are represented by$\Delta\theta(t)$ which can be further represented as:

$$\Delta\theta(t) = \frac{\Pi}{2}\times(0.5 - ER\times(Modulation(t) - 0.5)) \quad (4)$$

where *Modulation (t)* is the electrical input signal.

In the above equation, the term *ER* can be defined as:

$$ER = 1 - \frac{4}{\Pi}\times\arctan\left(\frac{1}{\sqrt{extract}}\right) \quad (5)$$

where *extract* is the extinction factor which is set to be 30 dB. Similarly, signal phase change is defined as:

$$\Delta\Phi(t) = SC\times\Delta\theta(t)\times\frac{1+SF}{1-SF} \quad (6)$$

where the value of *SC* is 1 if the negative chirp value is enabled; otherwise, it will be -1 and *SF* is the symmetry factor.

The output of optical modulator is combined with the output of three modulators from different channels and transmitted over FSO link followed by optical amplifier with a gain of 16 dB. The link can be defined by the following equation [24]:

$$P_{Received} = P_{Transmitted}\frac{d_R^2}{(d_T+\theta_R)^2}10^{\alpha R/10} \quad (7)$$

**TABLE 1 |** Key parameters.

| Item | Parameter | Value |
|---|---|---|
| PRBS | Data rate | 10 Gbps |
| Sine generator | RF carrier | 40 GHz |
| Spatial laser | Wavelength | 850 and 851 nm |
| | Power | 0 dBm |
| | Linewidth | 10 MHz |
| Machzhender modulator | Extinction ratio | 30 dB |
| | Symmetry factor | 1 |
| FSO link | Transmitter aperture diameter | 10 cm |
| | Receiver aperture diameter | 20 cm |
| | Beam divergence | 2 $\mu$rad |
| Spatial APD photo diode | Width | 10 µm |
| | Responsivity | 1.2 A/W |
| | Gain | 3 |
| | Dark current | 10 nA |
| | Responsivity | 1 A/W |
| | Thermal noise power spectral density | 100e-024 W/Hz |
| | Ionization ratio | 0.9 |

The equation above represents receiver aperture diameter ($d_R$), transmitter aperture diameter ($d_T$), beam divergence ($\theta$), range ($R$) and atmospheric attenuation ($\alpha$). Gamma distribution model is used to model the atmospheric fading. The probability of given intensity ($I$) is described in the following equation [25]:

$$P(I) = \frac{2(\alpha.\beta)^{(\alpha+\beta)/2}}{\Gamma(\alpha)\Gamma(\beta)} I^{\left((\alpha+\beta)/2\right)-1} K_{\alpha-\beta}\left(2\sqrt{\alpha.\beta.I}\right) \quad (8)$$

In the above equation, small-scale eddies are represented by$1/\alpha$, large-scale eddies are represented by $1/\beta$, $\Gamma(\ldots)$is the Gamma function and $K_{\alpha-\beta}$is the modified Bessel function of second kind. $\alpha$ and $\beta$ can be derived mathematically as shown in **Eq. 9** and **Eq. 10**:

$$\alpha = \exp\left[\frac{0.49\sigma_R^2}{\left(1+1.11\sigma_R^{12/5}\right)^{5/6}}\right] - 1 \quad (9)$$

$$\beta = \exp\left[\frac{0.51\sigma_R^2}{\left(1+0.69\sigma_R^{12/5}\right)^{5/6}}\right] - 1 \quad (10)$$

where $\sigma_R^2$ is the Rytov variance which can be calculated from the following equation:

$$\sigma_R^2 = 1.23 C_n^2 k^{7/6} z^{11/6} \quad (11)$$

where $C_n^2$ is the index refraction structure, $k$ is the optical wavenumber and $z$ is the range.

Atmospheric attenuation for FSO link is considered as 0.14 dB/km in clear weather, 12 dB/km in low fog, 16 dB/km in medium fog and 22 dB/km in heavy fog [26, 27]. A splitter is used to split the FSO output

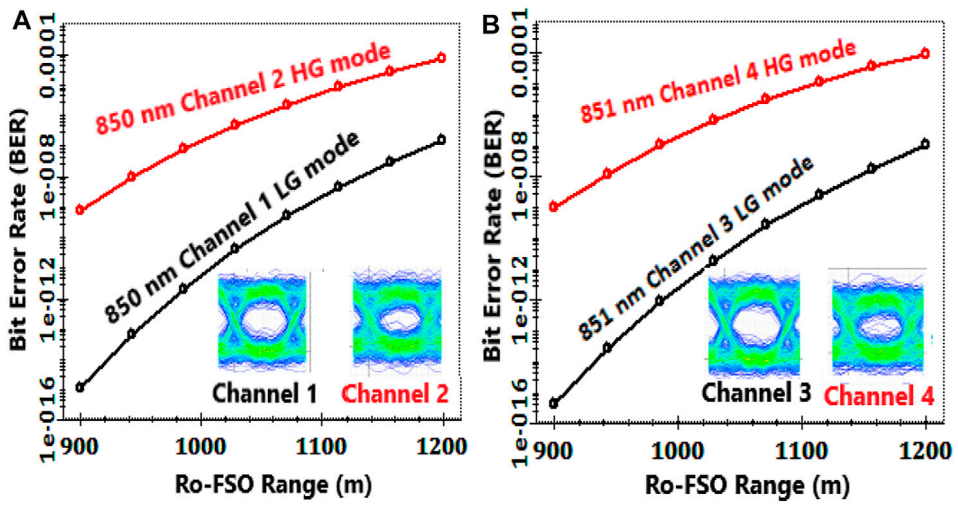


**FIGURE 4 |** Measurement of BER **(A)** Channels 1 and 2 **(B)** Channels 3 and 4.

into four receivers. Each receiver consists of a mode selector which selects the particular mode and wavelength. APD or avalanche photo diode is used for converting the optical signal to an electrical signal.

The shot noise and thermal noise is enabled in the APD whereas other background noises are assumed to be ideal in this work. After 40 GHz is mixed for the down-conversion process, the original baseband signal is recovered by using low pass filter.

The other key parameters are mentioned in **Table 1**.

## RESULTS AND DISCUSSION

The modeling of the proposed MDM-Ro-FSO model is done in OptiSystem™ software due to its accuracy. In this section, results obtained from the modeling are presented and discussed. First, Ro-FSO link is operated in clear weather conditions which mean no atmospheric turbulences are considered. The BER or bit error rate for all channels is measured as shown in **Figure 4**. At the distance of 1,200 m, the BER value for Channel 1 transmitted by using LG mode at 850 nm wavelength is computed as $10^{-7}$ whereas for Channel 2, which is transmitted by using HG 00 mode, it is computed as $10^{-5}$.

The result shows that HG mode is slightly more attenuated in FSO link as compared to LG mode. Similarly, the value of BER for Channel 3 transmitted by using LG 00 mode with 851 nm is also computed as $10^{-7}$ whereas for Channel 4, which is transmitted by using HG 00 mode, it is computed as $10^{-5}$. This shows that all the

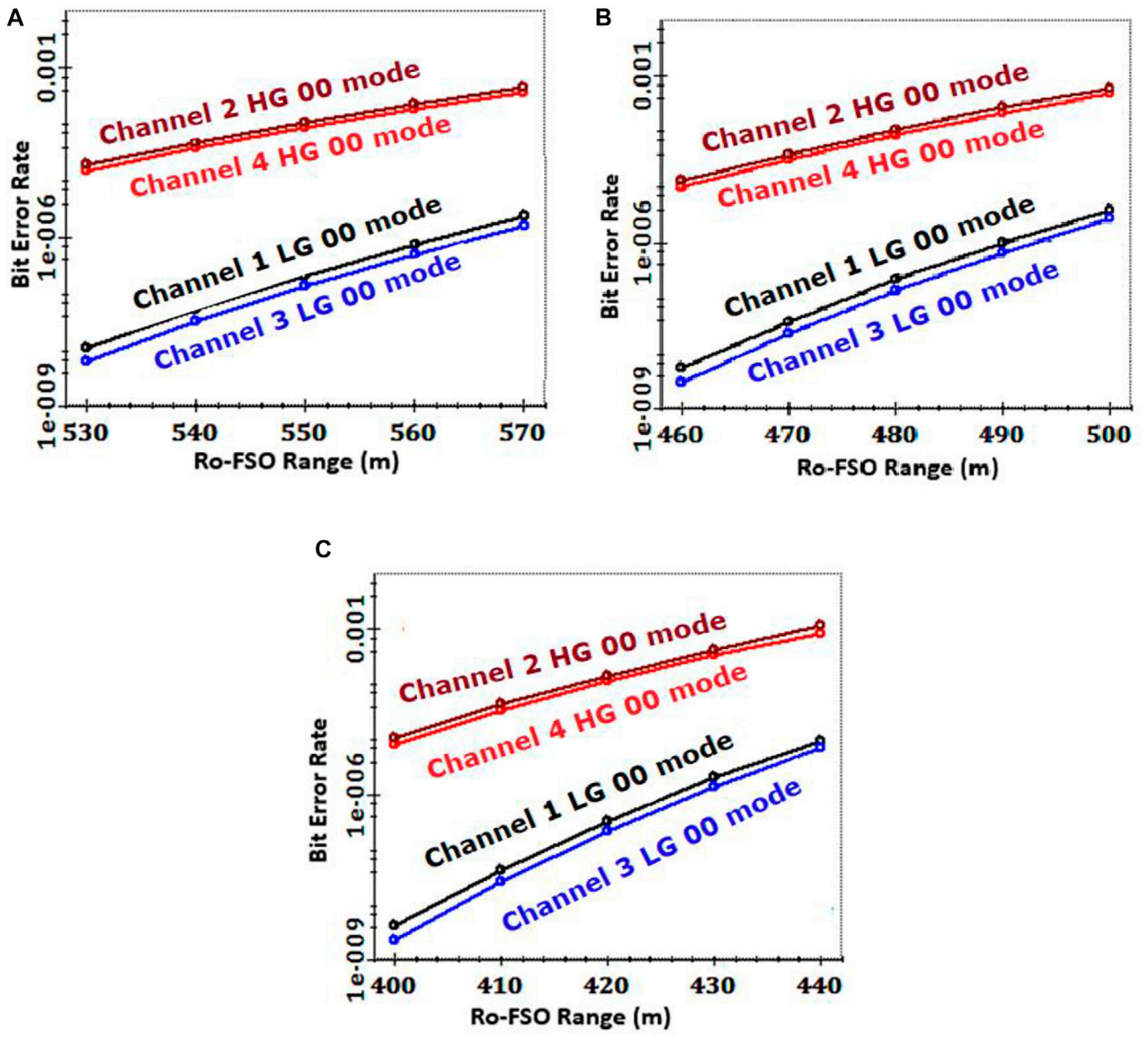


**FIGURE 5 |** Measurement of BER **(A)** low fog **(B)** medium fog **(C)** heavy fog.

channels are transmitted successfully over 1,200 m Ro-FSO link with acceptable BER ($\leq 10^{-3}$).

After that, the proposed MDM-Ro-FSO link is operated under the influence of different fog conditions that is low, medium and high. For low fog conditions, the value of atmospheric attenuation is considered as 12 dB/km whereas for medium fog conditions it is considered as 16 dB/km and for heavy fog conditions, it is considered as 22 dB/km. **Figure 5** (a), (b) and (c) show the measurement of BER of all channels under low, medium and heavy fog. When the Ro-FSO link is operated under low fog, the BER value for channel 1 and 3 is computed as $10^{-6}$ whereas for channel 2 and 4, it is measured as $10^{-4}$ at the Ro-FSO link distance of 570 m. However, when the Ro-FSO link is operated under medium fog, the BER value for channel 1 and 3 is computed as $10^{-5}$ whereas for channel 2 and 4, it is measured as $10^{-3}$ at the Ro-FSO link distance of 500 m. Similarly, when the Ro-FSO link is operated under heavy fog, the BER value for channel 1 and 3 is measured as $10^{-5}$ whereas for channel 2 and 4, it is measured as $10^{-3}$ at the Ro-FSO link distance of 440 m only.

## CONCLUSION

In this work, low-cost high-speed Ro-FSO system is proposed for providing broadband services in hospital scenarios. WDM and MDM schemes are incorporated to transmit four channels with the capacity of 10 Gbps each up-converted to 40 GHz mm wave over Ro-FSO link. The MDM scheme uses LG 00 and HG 00 modes whereas WDM uses 850 and 851 nm wavelengths. The reported results indicate successful transmission of all channels. When the RO-FSO link is operated in clear weather, all the channels are successfully transmitted up to 1,200 m. However, when the Ro-FSO link is operated in low, medium and heavy fog, the transmission distance is limited to 570, 500 and 440 m, respectively with acceptable ($\leq 10^{-3}$). Further research of the current work can include real-time experiments and performance evaluation of MDM-Ro-FSO under different atmospheric conditions.

## DATA AVAILABILITY STATEMENT

The raw data supporting the conclusions of this article will be made available by the authors, without undue reservation.

## AUTHOR CONTRIBUTIONS

PL: Conceptualization, methodology, investigation, writing—original draft, supervision, resources, project administration, funding acquisition. CZ: Methodology, investigation, writing—original draft, supervision, funding acquisition. JN: Methodology, investigation, data curation, visualization. SC: Investigation, data curation, writing—original draft. XT: Writing—review andediting, validation, conceptualization.

## FUNDING

This work is supported by National Key Research and Development Program of China under Grant no. 2018YFB1305700 and Scientific and Technological Program of Quanzhou City under Grant No. 2019CT009.

## REFERENCES

1. Internation Telecomunications Union. ICT facts and figures 2017. *Itu* (2017) 1–8.
2. Riurean S, Antipova T, Rocha Á, Leba M, and Ionica A. VLC, OCC, IR and LiFi Reliable Optical Wireless Technologies to be Embedded in Medical Facilities and Medical Devices. *J Med Syst* (2019) 43:308. doi:10.1007/s10916-019-1434-y
3. Dat PT, Bekkali A, Kazaura K, Wakamori K, and Matsumoto M. A universal platform for ubiquitous wireless communications using radio over FSO system. *J Lightwave Technol* (2010) 28:2258–67. doi:10.1109/jlt.2010.2049641
4. Bohata J, Komanec M, Spáčil J, Ghassemlooy Z, Zvánovec S, and Slavík R. 24-26 GHz radio-over-fiber and free-space optics for fifth-generation systems. *Opt Lett* (2018) 43:1035–8. doi:10.1364/ol.43.001035
5. Khalighi MA, and Uysal M. Survey on free space optical communication: A communication theory perspective. *IEEE Commun Surv Tutorials* (2014) 16: 2231–58. doi:10.1109/comst.2014.2329501
6. Chaudhary S, and Amphawan A. The role and challenges of free-space optical systems. *J Opt Commun* (2014) 35:327–34. doi:10.1515/joc-2014-0004
7. Chaudhary S, and Amphawan A. High-speed millimeter communication through radio-over-free-space-optics network by mode-division multiplexing. *Opt Eng* (2017) 56:116112. doi:10.1117/1.oe.56.11.116112
8. Singh M, and Malhotra J. Performance comparison of high-speed long-reach mode division multiplexing-based radio over free space optics transmission system using different modulation formats under the effect of atmospheric turbulence. *Opt Eng* (2019) 58:046112. doi:10.1117/1.oe.58.4.046112
9. Dev K, Nebuloni R, Capsoni C, Fiser O, and Brazda V. Estimation of optical attenuation in reduced visibility conditions in different environments across free space optics link. *IET Microwaves, Antennas & Propagation* (2017) 11: 1708–13. doi:10.1049/iet-map.2016.0872
10. Xu H, Liu L, and Shi Y. Polarization-insensitive four-channel coarse wavelength-division (de)multiplexer based on Mach-Zehnder interferometers with bent directional couplers and polarization rotators. *Opt Lett* (2018) 43:1483–6. doi:10.1364/ol.43.001483
12. Pan Y, Yan L, Yi A, Chen Z, Jiang L, Pan W, et al. Transmission of three-polarization-multiplexed 25-Gb/s DPSK signals over 300-km fiber link. *Opt Lett* (2016) 41:1620–3. doi:10.1364/ol.41.001620
13. Geng Z, Corcoran B, Zhu C, and Lowery AJ. Time-lenses for time-division multiplexing of optical OFDM channels. *Opt Express* (2015) 23:29788–801. doi:10.1364/oe.23.029788
14. Mendoza-Yero O, Mínguez-Vega G, Martínez-León L, Carbonell-Leal M, Fernández-Alonso M, Doñate-Buendía C, et al. Diffraction-based phase calibration of spatial light modulators with binary phase Fresnel lenses. *J Display Technol* (2016) 12:1027–32. doi:10.1109/jdt.2016.2580902
15. Wang X, Ge D, Ding W, Wang Y, Gao S, Zhang X, et al. Hollow-core conjoined-tube fiber for penalty-free data transmission under offset launch conditions. *Opt Lett* (2019) 44:2145–8. doi:10.1364/ol.44.002145
16. Sheffi N, and Sadot D. Energy-efficient VCSEL array using power and offset allocation of spatial multiplexing in graded-index multimode fiber. *J Lightwave Technol* (2017) 35:2098–108. doi:10.1109/jlt.2017.2656238
17. Chaudhary S, and Amphawan A. Selective excitation of LG 00, LG 01, and LG 02 modes by a solid core PCF based mode selector in MDM-Ro-FSO transmission systems. *Laser Phys* (2018) 28:075106. doi:10.1088/1555-6611/aabd15

18. Ren Y, Wang Z, Liao P, Li L, Xie G, Huang H, et al. Experimental characterization of a 400 Gbit/s orbital angular momentum multiplexed free-space optical link over 120 m. *Opt Lett* (2016) 41:622–5. doi:10.1364/ol.41.000622
19. Grover A, Sheetal A, and Dhasarathan V. Performance analysis of mode division multiplexing based free space optics system incorporating on–off keying and polarization shift keying under dynamic environmental conditions. *Wireless Networks* (2020) 1–11.
20. Chaudhary S, Tang X, and Wei X. Comparison of Laguerre-Gaussian and Donut modes for MDM-WDM in OFDM-Ro-FSO transmission system. *AEU - Int J Elect Commun* (2018) 93:208–14. doi:10.1016/j.aeue.2018.06.024
21. Upadhyay KK, Shukla NK, and Chaudhary S. A high speed 100 Gbps MDM-SAC-OCDMA multimode transmission system for short haul communication. *Optik* (2020) 202:163665. doi:10.1016/j.ijleo.2019.163665
22. Minz M, Mishra D, Sonkar RK, and Khan MM. Grating-assisted MDM-PDM hybrid (de) multiplexer for optical interconnect applications. In: *Nanophotonics and Micro/Nano Optics V*. China: SPIE/COS Photonics Asia (2019). p. 111930C.
23. Ghatak A, and Thyagarajan K, *An introduction to fiber optics*. United Kingdom: Cambridge university press (1998). doi:10.1017/cbo9781139174770
24. Design O. *Optiwave Corporation 7 Capella Court Ottawa*. Ontario: Canada.
25. Bloom S, Korevaar E, Schuster J, and Willebrand H. Understanding the performance of free-space optics [Invited]. *J Opt Netw* (2003) 2:178–200. doi:10.1364/jon.2.000178
26. Andrews LC, and Phillips RL. *Laser beam propagation through random media*, vol. 152. WA: SPIE press Bellingham (2005).
27. Kim II, McArthur B, and Korevaar EJ. Comparison of laser beam propagation at 785 nm and 1550 nm in fog and haze for optical wireless communications. In: *Optical Wireless Communications*, III. China: SPIE (2001). p. 26–37.
28. Majumdar AK. Free-space laser communication performance in the atmospheric channel. *J Optic Comm Rep* (2005) 2:345–96. doi:10.1007/s10297-005-0054-0

**Conflict of Interest:** The authors declare that the research was conducted in the absence of any commercial or financial relationships that could be construed as a potential conflict of interest.

frontiers in Physics

ORIGINAL RESEARCH
published: 30 July 2021
doi: 10.3389/fphy.2021.683479

# Secrecy Performance Analysis of Hybrid RF/VLC Dual-Hop Relaying Systems

*Jiaoli Liu*[1], *Jinyuan Wang*[1,2,3]*, *Bingyuan Zhang*[1] and *Qinglin Wang*[1]*

[1]Shandong Key Laboratory of Optical Communication Science and Technology, School of Physics Science and Information Technology, Liaocheng University, Liaocheng, China, [2]Key Laboratory of Broadband Wireless Communication and Sensor Network Technology, Nanjing University of Posts and Telecommunications, Nanjing, China, [3]Shanghai Key Laboratory of Trustworthy Computing, East China Normal University, Shanghai, China

In this article, the secrecy performance of a hybrid radio frequency (RF)/visible light communication (VLC) system is studied. In this hybrid system, the source node (i.e., Alice) transmits information to the relay node *via* the outdoor RF link. Nakagami-m fading and path loss are considered for the RF link. The relay node includes an outdoor component and an indoor component, which are connected by using a wired medium. The outdoor component receives and recovers information by using the decode-and-forward (DF) relaying scheme and then transmits it to the indoor component. The indoor component then converts the received electrical signal into an optical signal by using a light-emitting diode. A legitimate receiver (i.e., Bob) deployed on the floor receives the optical signal. An eavesdropper (i.e., Eve) deployed in the RF or VLC link wiretaps the confidential information. In this study, we use the secrecy outage probability (SOP) and the probability of strictly positive secrecy capacity (SPSC) to evaluate the system performance. We then obtain the closed-form expression for a lower bound on the SOP and an exact closed-form expression for the probability of SPSC when the RF and VLC links are wiretapped, respectively. Numerical results are presented to validate the accuracy of our derivations. We further discuss the effects of the noise standard deviation, the equivalent threshold of the signal-to-noise ratio, and the floor radius on the system secrecy performance when the VLC link is eavesdropped upon. For the case when the RF link is eavesdropped upon, the impacts of the distance between Alice and the relay, the path loss exponent, the fading factor, and the distance between Alice and Eve on secrecy performance are also provided.

**Keywords: visible light communications, radio frequency communications, secrecy outage probability, probability of strictly positive secrecy capacity, hybrid RF/VLC systems**

OPEN ACCESS

***Edited by:***
*Haohai Yu,*
*Shandong University, China*

***Reviewed by:***
*Qiong Wu,*
*Jiangnan University, China*
*Shuai Ma,*
*China University of Mining and Technology, China*
*Zhaohui Yang,*
*King's College London, United Kingdom*

***Correspondence:**
*Jinyuan Wang*
*jywang@njupt.edu.cn*
*Qinglin Wang*
*wangqinglin@lcu.edu.cn*

***Specialty section:***
*This article was submitted to Optics and Photonics, a section of the journal Frontiers in Physics*

***Received:*** *21 March 2021*
***Accepted:*** *28 June 2021*
***Published:*** *30 July 2021*

***Citation:***
*Liu J, Wang J, Zhang B and Wang Q (2021) Secrecy Performance Analysis of Hybrid RF/VLC Dual-Hop Relaying Systems. Front. Phys. 9:683479. doi: 10.3389/fphy.2021.683479*

## 1 INTRODUCTION

In the past ten years, the research on conventional radio frequency (RF) wireless communication has intensified [1]. With the rapid development of solid-state lighting, the visible light communication (VLC) technology has emerged as a promising technology in recent years [2]. VLC has a wider modulation bandwidth, less susceptibility to electromagnetic interference, and a larger capacity than RF communications. In VLC, both illumination and communication are simultaneously implemented [3]. The performance of VLC, however, heavily depends on the line-of-sight (LoS)

connection, and it also has a limited coverage area. Therefore, the performance of VLC suffers severe degradation in the absence of the LoS link. Moreover, the light emitted by a light-emitting diode (LED) in VLC is easily blocked by obstacles [4]. In contrast, RF communication has higher transmission reliability even in the absence of the LoS link [5–10]. To address the issues mentioned above, hybrid VLC/RF technology is proposed to tackle the aforementioned problems. The VLC technology can overcome the shortcomings of RF spectrum shortage and large power consumption, while the RF technology compensates for the dependence of VLC on LoS to improve the communication coverage and also reduces the power consumption. Besides, VLC and RF signals do not interfere with each other [7].

There are several studies on hybrid wireless systems combining RF and VLC technologies. In reference [3], a random geometric framework for the coexistence of VLC and RF networks was proposed, and its coverage and achievable rate analysis for typical users were studied. In reference [5], the power and bandwidth allocation problem for the energy efficiency maximization of the VLC/RF hybrid system was solved, and the impact of the system parameters on the energy efficiency of the mixed system was investigated. The research in reference [7] showed that compared with the network that only uses RF or VLC, a hybrid RF/VLC network can reduce the probability of interruption by reducing the area power consumption. An effective beamforming design was also discussed in reference [8].

Since the physical layer security (PLS) utilizes the randomness of the wireless channel and noise, it is often considered to be a viable solution to ensure secure communication and prevent eavesdropping and jamming attacks [11]. In reference [9], PLS characteristics of the hybrid RF/VLC system were studied, the problem of minimizing the power consumption was also studied, and a zero-forcing beamforming strategy and a minimum power allocation algorithm were proposed. The PLS of indoor heterogeneous VLC/RF networks based on known and unknown channel state information (CSI) was further analyzed in reference [12]. In reference [13], the PLS transmission for VLC with simultaneous lightwave information and power transfer was investigated.

Besides, dual-hop relay technology has been considered to be another efficient technology that can be used to increase the capacity and expand the coverage of low-power wireless networks [14]. In such systems, the signal propagates from the source node to the destination node through a relay node, so that the connection can be realized in the case of high path loss and deep attenuation in the traditional direct transmission between the source node and the destination node. In references [4, 10], the dual-hop hybrid systems with energy harvesting relays were investigated. Specifically, the authors of reference [4] optimized the VLC/RF hybrid system from the perspective of maximizing the data rate, while the authors of reference [10] investigated the data packet transmission performance of the VLC/RF hybrid system. Furthermore, in reference [14], the performance of hybrid free-space optical (FSO) communication and RF dual-hop systems based on amplify-and-forward relaying and CSI-assisted relaying were analyzed, and the closed-form expressions for the outage probability and the average bit error rate were derived in the high signal-to-noise ratio (SNR) regime. In reference [15], the expressions of the outage probability, bit error rate, and average capacity of the hybrid RF/FSO system were derived for the first time. For amplify-and-forward relay, the outage probability and bit error probability of the hybrid RF/FSO system were also obtained in reference [16]. There are many studies on the PLS of the dual-hop system. It is noteworthy that the authors of references [17–20] considered the mixed RF/FSO transmission systems. The lower bound of the secrecy outage probability (SOP) and the closed-form expression of the probability of strictly positive secrecy capacity (SPSC) when an eavesdropper is eavesdropping on the FSO link were derived in reference [17]. Furthermore, for a mixed RF/FSO downlink simultaneous wireless information and power transfer system, reference [18] derived the exact and asymptotic expressions of the SOP. The closed-form expressions for the lower bound of the SOP and the exact average secrecy capacity of mixed RF/FSO systems were also derived in reference [19], where an eavesdropper node eavesdrops on the FSO hop. In reference [20], the secrecy outage performance of a mixed RF/FSO system with imperfect CSI was analyzed. To the best of the authors' knowledge, in the aforementioned works, Shannon's capacity is often employed to evaluate the performance of the VLC link [11, 12]. However, in the actual VLC environment, the visible-light signal is an optical intensity signal, which means that the signal amplitude of the VLC system is non-negative. Furthermore, in the VLC system, it is necessary to consider illumination while transmitting data; therefore, the average optical intensity should be a fixed value according to the users' dimming requirement [21]. Therefore, Shannon's capacity is not suitable for VLC. Based on the considerations above, it is necessary to analyze the secrecy performance of the hybrid RF/VLC dual-hop relaying systems.

In this study, we analyze the PLS performance of a hybrid RF/VLC system. The main contributions are summarized as follows:

- Based on the system model, when the VLC link is eavesdropped upon, the probability density functions (PDFs) of the channel gain for the RF and VLC channels are derived, respectively. Using those PDFs, we then derive the closed-form expressions for the lower bound of the SOP and the probability of SPSC. It is also shown that the performance gap between theoretical results and simulation results is small, which verifies the accuracy of the derived expression. Moreover, the SOP increases with the noise standard deviation of Bob and decreases with the noise standard deviation of Eve. The SNR threshold degrades the system secrecy performance. The performance of the probability of SPSC mainly depends on the VLC, which deteriorates with Bob's noise standard deviation and improves with Eve's noise standard deviation or the radius of the floor.
- For the case when the RF link is eavesdropped upon, the PDFs and cumulative distribution functions (CDFs) of the instantaneous SNR at the relay node and the Eve node have been derived. Based on these statistic distributions, we also derive the closed-form expressions for the lower bound of the SOP and the probability of SPSC. The results further show that the performance gap between theoretical results and simulation results is also small, which verifies the accuracy of the derived expressions. In this case, the performance of the probability of SPSC mainly depends on the RF link, and all theoretical results of the probability of SPSC

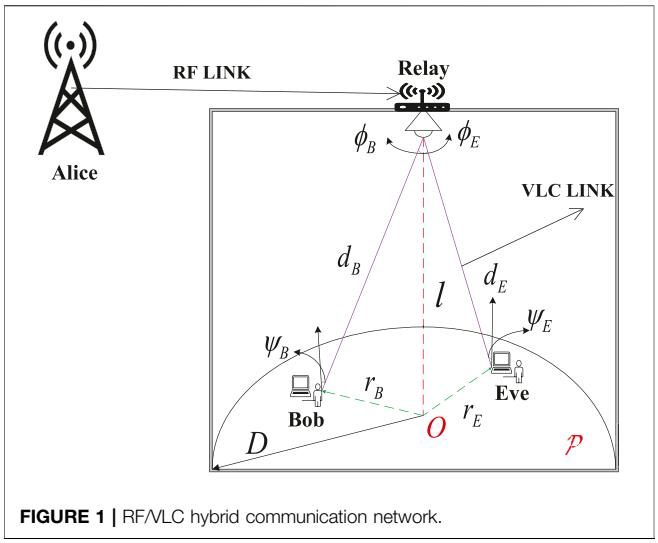


**FIGURE 1 |** RF/VLC hybrid communication network.

match the simulation results very well. Numerical results further confirm that the system secrecy performance is degraded with the distance between the Alice and relay nodes and the channel fading factor and improved by increasing the path loss exponent.

This article is arranged as follows. In **Section 2**, the system model of the hybrid VLC/RF system is presented. In **Section 3**, we derive the lower bound of the SOP and the exact expression of the probability of SPSC when the VLC link is eavesdropped upon. The secrecy performance analysis when the RF link is eavesdropped upon is presented in **Section 4**. **Section 5** presents some numerical results. Finally, the conclusion of this article is given in **Section 6**.

## 2 SYSTEM MODEL

As shown in **Figure 1**, we consider a dual-hop hybrid RF/VLC network, which includes an outdoor RF link and an indoor VLC link. The hybrid network is composed of a source node (Alice), a relay node, an eavesdropper (Eve), and a legitimate receiver (Bob). The relay node includes an outdoor component and an indoor component, which are connected by using a wired medium. In this study, we assume that the outdoor component receives and recovers information by using the DF relaying scheme and then transmits it to the indoor component. The indoor component converts the received electrical signal to an optical signal by using an LED. There is no direct communication between Alice and Bob; information must be transmitted through the relay node. The communication arranges two transmission time slots. In the first time slot, Alice transmits confidential information $x$ to the outdoor component of the relay over the RF channel. In the second time slot, the indoor component of the relay forwards the optical signal $X$ to Bob through the indoor VLC channel. Both Bob and Eve deploy photodiodes to receive information and perform photoelectric conversion. When Alice transmits to Bob, Eve attempts to intercept the secret information.

### 2.1 RF Link

In the first time slot, the received signal at the relay can be written as follows:

$$y = \sqrt{P_s} h_{SR} x + n_R, \tag{1}$$

where $P_s$ represents the transmission power at Alice, $h_{SR}$ represents the channel gain of the RF link, $x$ is the transmitted confidential information, and $n_R$ is additive white Gaussian noise (AWGN) with zero mean and variance $N_0$.

The instantaneous SNR $\gamma_{SR}$ at the relay is given by the following:

$$\gamma_{SR} = P_s |h_{SR}|^2 / N_0. \tag{2}$$

In the RF link, $|h_{SR}|^2$ in **Eq. 2** can be expressed as follows:

$$|h_{SR}|^2 = |g_R|^2 G_R, \tag{3}$$

where $g_R$ and $G_R$ denote the fast fading and path loss, respectively. It should be noted that the two terms are independent of each other. The envelope of $g_R$ is assumed to experience a Nakagami-m fading, and thus the squared envelope $|g_R|^2$ follows a gamma distribution. Therefore, the PDF of $|g_R|^2$ can be written as follows [22]:

$$f_{|g_R|^2}(x) = \frac{x^{m_R - 1}}{\Gamma(m_R)} m_R^{m_R} \exp(-m_R x), x \geq 0, \tag{4}$$

where $m_R$ represents the fading factor, and $\Gamma(m_R) = \int_0^{+\infty} x^{m_R - 1} e^{-x} dx$ represents the gamma function.

Furthermore, $G_R$ in **Eq. 3** can be modeled as follows [22]:

$$G_R = \left(\frac{d_0}{d_1}\right)^{\lambda}, \tag{5}$$

where $\lambda$ denotes the path loss exponent, $d_0$ denotes the reference distance, and $d_1$ is the distance between Alice and the relay.

Therefore, the PDF of $|h_{SR}|^2$ can be written as follows:

$$f_{|h_{SR}|^2}(y) = \frac{1}{G_R} \left(\frac{y}{G_R}\right)^{m_R - 1} \frac{1}{\Gamma(m_R)} m_R^{m_R} \times \exp\left(-m_R \cdot \frac{y}{G_R}\right), y \geq 0. \tag{6}$$

By using (8.351.1) in reference [23], the cumulative distribution function (CDF) of $|h_{SR}|^2$ can be written as follows:

$$F_{|h_{SR}|^2}(y) = \frac{1}{\Gamma(m_R)} \gamma\left(m_R, \frac{m_R y}{P_R}\right), y \geq 0, \tag{7}$$

where $\gamma(\cdot, \cdot)$ is the lower incomplete gamma function defined by (8.350.1) in reference [23].

### 2.2 VLC Link

In the second time slot, we consider an indoor VLC link. To facilitate the analysis, it is assumed that the receiving area $\mathcal{P}$ is a disk with a radius $D$. As shown in **Figure 1**, the LED is projected at the center of the disk. Besides, we assume that both Bob and Eve are uniformly distributed within the area $\mathcal{P}$. According to the

settings above, the PDF of Bob's (or Eve's) position is given by the following:

$$f_U(u) = \frac{1}{\pi D^2}, u \in \mathcal{P}, \tag{8}$$

$$f_W(w) = \frac{1}{\pi D^2}, w \in \mathcal{P}, \tag{9}$$

where $U$ represents the position of Bob and $W$ represents the position of Eve.

In the second time slot, the received signals at Bob and Eve can be expressed as follows:

$$Y_k = H_k X + Z_k, k = \text{B for Bob}, k = \text{E for Eve}, \tag{10}$$

where $X$ represents the input optical intensity, $Z_k \sim N(0, \sigma_k^2)$ is the AWGN at Bob (or Eve), and $\sigma_k^2$ is the variance of the corresponding noise.

Because the information is modulated as the instantaneous optical intensity, $X$ must meet the non-negative constraint as follows [21]:

$$X \geq 0. \tag{11}$$

Although the optical intensity can be adjusted according to the dimming requirements, the average optical intensity cannot change with time. Therefore, the dimmable average optical intensity constraint is given by the following [21]:

$$E(X) = \xi P, \tag{12}$$

where $\xi$ indicates the dimming target, and $P$ indicates the nominal optical intensity of the LED. Because the user can adjust the optical intensity at will, the dimming target must satisfy the following [21]:

$$0 \leq \xi \leq 1. \tag{13}$$

Without loss of generality, we assume that both Bob and Eve can be illuminated by the LED, and thus, the illumination angle $\psi_k$ cannot exceed the field of view of the PD $\Psi_c$, that is, $0 < \psi_k < \Psi_c$. In indoor VLC, the channel gain $H_k$ can be written as follows [24]:

$$H_k = \frac{(m+1)A}{2\pi d_k^2} T_S g \cos^m(\phi_k) \cos(\psi_k), k = \text{B or E}, \tag{14}$$

where $d_k$ and $\phi_k$ represent the distance and the irradiance angle between the LED and Bob (or Eve), $A$ is the physical area of the PD, $m$ denotes the order of the Lambertian emission, $g$ is the PD's concentrator gain, and $T_S$ represents the optical filter gain. Also, assuming that the normal vector between the transceiver plane and the ceiling is vertical, we can obtain $\cos(\phi_k) = \cos(\psi_k) = l/d_k$, where $l$ represents the vertical distance between the LED and the receiving plane. Therefore, the channel gain in **Eq. 14** can be further written as follows:

$$H_k = \frac{(m+1)AT_S g l^{m+1}}{2\pi} \left(r_k^2 + l^2\right)^{-\frac{m+3}{2}}, \tag{15}$$

where $r_k$ is the distance between the projection point $O$ and the $k^{\text{th}}$ receiver.

According to **Eqs. 8** and **9**, the CDF of $r_k$ can be expressed as follows:

$$\begin{aligned} F_{r_k}(r_k) &= \Pr\{r \leq r_k\} \\ &= \Pr\{\rho \leq r_k, 0 \leq \theta \leq 2\pi\} \\ &= \int_0^{2\pi} \int_0^{r_k} \frac{1}{\pi D^2} \rho \mathrm{d}\rho \mathrm{d}\theta \\ &= \frac{r_k^2}{D^2}, 0 < r_k \leq D. \end{aligned} \tag{16}$$

Furthermore, the PDF of $r_k$ can be obtained as follows:

$$f_{r_k}(r_k) = \frac{\mathrm{d}F_{r_k}(r_k)}{\mathrm{d}r_k} = \frac{2r_k}{D^2}, 0 \leq r_k \leq D, \tag{17}$$

where $\frac{\mathrm{d}F_{r_k}(r_k)}{\mathrm{d}r_k}$ is the derivative of $F_{r_k}(r_k)$ with respect to $r_k$.

The PDF of the channel gain $H_k$ is then written as follows:

$$f_{H_k}(h) = \left|\frac{\mathrm{d}}{\mathrm{d}h} r_k\right| f_{r_k}(r_k), \tag{18}$$

where $|.|$ is a symbol for the absolute value.

Substituting **Eq. 15** and **Eq. 17** into **Eq. 18**, we can obtain the PDF of $H_k$ as follows:

$$f_{H_k}(h) = \Xi h^{-\frac{2}{m+3}-1}, v_{\min} \leq h \leq v_{\max}, \tag{19}$$

where $\Xi$, $v_{\min}$, and $v_{\max}$ are given by the following:

$$\Xi = \frac{2}{(m+3)D^2} \left(\frac{(m+1)AT_S g l^{m+1}}{2\pi}\right)^{\frac{2}{m+3}}, \tag{20}$$

$$v_{\min} = \frac{(m+1)AT_S g l^{m+1}}{2\pi} \left(D^2 + l^2\right)^{-\frac{m+3}{2}}, \tag{21}$$

$$v_{\max} = \frac{(m+1)AT_S g l^{m+1}}{2\pi} l^{-(m+3)}. \tag{22}$$

# 3 SECRECY PERFORMANCE ANALYSIS WHEN VLC LINK IS EAVESDROPPED UPON

## 3.1 SOP Analysis

In this subsection, we analyze the SOP of the hybrid RF/VLC system. Because there are no eavesdroppers in the RF link, the instantaneous SC of the first hop is its instantaneous channel capacity, that is,

$$\begin{aligned} C_{\text{hop},1} &= \frac{1}{2} \ln\left(1 + \gamma_{\text{SR}}\right) \\ &= \frac{1}{2} \ln\left(1 + \frac{P_s}{N_0} |h_{\text{SR}}|^2\right). \end{aligned} \tag{23}$$

In the VLC link, we need to consider the average and non-negative constraints simultaneously. Therefore, Shannon's capacity is not applicable to the VLC link [25]. For VLC with constraints as in **Eqs 11**, **12**, a lower bound on the instantaneous SC is given by the following [26]:

$$C_{\text{hop},2} = \frac{1}{2}\ln\left(\frac{\sigma_{\text{E}}^2}{2\pi\sigma_{\text{B}}^2}\cdot\frac{e\xi^2P^2H_{\text{B}}^2 + 2\pi\sigma_{\text{B}}^2}{H_{\text{E}}^2\xi^2P^2 + \sigma_{\text{B}}^2}\right) = \frac{1}{2}\ln\left(\frac{1+J_{\text{B}}}{1+J_{\text{E}}}\right). \tag{24}$$

Furthermore, according to **Eq. 19**, $J_{\text{B}} = \frac{e\xi^2P^2H_{\text{B}}^2}{2\pi\sigma_{\text{B}}^2}$ and $J_{\text{E}} = \frac{\xi^2P^2H_{\text{E}}^2}{\sigma_{\text{E}}^2}$, the PDFs of $J_{\text{B}}$ and $J_{\text{E}}$ are given by the following [13]:

$$\begin{cases} f_{J_{\text{B}}}(j) = \frac{\Xi}{2}\left(\frac{2\pi\sigma_{\text{B}}^2}{e\xi^2P^2}\right)^{-\frac{1}{m+3}} j^{-\frac{1}{m+3}-1},\ J_{\text{B,min}} \le j \le J_{\text{B,max}}, \\ f_{J_{\text{E}}}(j) = \frac{\Xi}{2}\left(\frac{\sigma_{\text{E}}^2}{\xi^2P^2}\right)^{-\frac{1}{m+3}} j^{-\frac{1}{m+3}-1},\ J_{\text{E,min}} \le j \le J_{\text{E,max}}, \end{cases} \tag{25}$$

where $J_{\text{B,min}} = \frac{e\xi^2P^2\nu_{\text{min}}^2}{2\pi\sigma_{\text{B}}^2}$, $J_{\text{B,max}} = \frac{e\xi^2P^2\nu_{\text{max}}^2}{2\pi\sigma_{\text{B}}^2}$, $J_{\text{E,min}} = \frac{\xi^2P^2\nu_{\text{min}}^2}{\sigma_{\text{E}}^2}$, and $J_{\text{E,max}} = \frac{\xi^2P^2\nu_{\text{max}}^2}{\sigma_{\text{E}}^2}$.

As is known, the hybrid system is equivalent to a series network, so the capacity of the system is determined by the worse channel [27]. Therefore, the instantaneous SC of the entire hybrid system is the minimum of $C_{\text{hop},1}$ and $C_{\text{hop},2}$, which can be expressed as follows[1]:

$$C_{\text{I}} = \min\left\{C_{\text{hop},1}, C_{\text{hop},2}\right\}. \tag{26}$$

The SOP is an important performance metric to evaluate the PLS of a wireless communication system. It is defined as the probability that the instantaneous SC is lower than the target capacity $C_{\text{th}}$. Therefore, SOP can be expressed as follows:

$$P_{\text{SOP}} = \Pr\{C_{\text{I}} < C_{\text{th}}\}. \tag{27}$$

Substituting **Eq. 26** into **Eq. 27**, the SOP is rewritten as follows:

$$\begin{aligned} P_{\text{SOP}} &= \Pr\left\{\min\left(C_{\text{hop},1}, C_{\text{hop},2}\right) < C_{\text{th}}\right\} \\ &= 1 - \Pr\left\{\min\left(C_{\text{hop},1}, C_{\text{hop},2}\right) \ge C_{\text{th}}\right\} \\ &= 1 - \Pr\left\{C_{\text{hop},1} \ge C_{\text{th}}\right\}\Pr\left\{C_{\text{hop},2} \ge C_{\text{th}}\right\}, \end{aligned} \tag{28}$$

where $\Pr\{C_{\text{hop},1} \ge C_{\text{th}}\}$ is given by the following:

$$\begin{aligned} &\Pr\left\{C_{\text{hop},1} \ge C_{\text{th}}\right\} \\ &= \Pr\left\{\frac{1}{2}\ln\left(1 + \frac{P_{\text{s}}}{N_0}|h_{\text{SR}}|^2\right) \ge C_{\text{th}}\right\} \\ &= 1 - \Pr\left\{\frac{1}{2}\ln\left(1 + \frac{P_{\text{s}}}{N_0}|h_{\text{SR}}|^2\right) < \frac{1}{2}\ln(\gamma_{\text{th}})\right\} \\ &= 1 - \Pr\left\{|h_{\text{SR}}|^2 < \frac{(\gamma_{\text{th}}-1)N_0}{P_{\text{s}}}\right\} \\ &= 1 - F_{|h_{\text{SR}}|^2}\left(\frac{(\gamma_{\text{th}}-1)N_0}{P_{\text{s}}}\right), \end{aligned} \tag{29}$$

and $\Pr\{C_{\text{hop},2} \ge C_{\text{th}}\}$ is given by the following:

$$\begin{aligned} \Pr\left\{C_{\text{hop},2} \ge C_{\text{th}}\right\} &= 1 - \Pr\left\{C_{\text{hop},2} < C_{\text{th}}\right\} \\ &= 1 - \Pr\left\{\frac{1}{2}\ln\left(\frac{1+J_{\text{B}}}{1+J_{\text{E}}}\right) < \frac{1}{2}\ln(\gamma_{\text{th}})\right\}, \end{aligned} \tag{30}$$

where $C_{\text{th}} = \frac{1}{2}\ln(\gamma_{\text{th}})$ denotes the threshold of the targeted SC and $\gamma_{\text{th}} \ge 1$ denotes the equivalent threshold of the SNR [13]. It should be noted that it is challenging to obtain a closed-form expression of **Eq. 30**. In indoor VLC, it is reasonable to assume that $J_{\text{B}} \gg 1$ and $J_{\text{E}} \gg 1$. When $J_{\text{B}} > J_{\text{E}}$, we have $(1+J_{\text{B}})/(1+J_{\text{E}}) < J_{\text{B}}/J_{\text{E}}$. Therefore, an upper bound of **Eq. 30** is given by the following:

$$\Pr\left\{C_{\text{hop},2} \ge C_{\text{th}}\right\} \le 1 - \Pr\{J_{\text{B}} < J_{\text{E}}\gamma_{\text{th}}\}. \tag{31}$$

From **Eqs 28**, **29**, and **31**, the SOP is lower-bounded by the following:

$$\begin{aligned} P_{\text{SOP}} &= 1 - \left(1 - F_{|h_{\text{SR}}|^2}\left(\frac{(\gamma_{\text{th}}-1)N_0}{P_{\text{s}}}\right)\right) \times \left(1 - \Pr\{J_{\text{B}} < J_{\text{E}}\gamma_{\text{th}}\}\right) \\ &\triangleq P_{\text{SOP}_{\text{L}}}. \end{aligned} \tag{32}$$

In **Eq. 25**, $J_{\text{B}}$ and $J_{\text{E}}$ are independent of each other. Moreover, the value of $P_{\text{SOP}_{\text{L}}}$ depends on the value of $\gamma_{\text{th}}$. **Figure 2** shows four cases of the integral region of $\Pr(J_{\text{B}} < J_{\text{E}}\gamma_{\text{th}})$. Based on the four cases, $\Pr(J_{\text{B}} < J_{\text{E}}\gamma_{\text{th}})$ is derived as follows:

$$\Pr\left(J_{\text{B}} < J_{\text{E}}\gamma_{\text{th}}\right) = \begin{cases} 0, & \text{if } \gamma_{\text{th}} \le \frac{J_{\text{B,min}}}{J_{\text{E,max}}} \\ D_1, & \text{if } \frac{J_{\text{B,min}}}{J_{\text{E,max}}} < \gamma_{\text{th}} \le \frac{J_{\text{B,min}}}{J_{\text{E,min}}} \\ D_2, & \text{if } \frac{J_{\text{B,max}}}{J_{\text{E,max}}} < \gamma_{\text{th}} < \frac{J_{\text{B,max}}}{J_{\text{E,min}}} \\ 1, & \text{if } \gamma_{\text{th}} \ge \frac{J_{\text{B,max}}}{J_{\text{E,min}}}, \end{cases} \tag{33}$$

where $D_1$ and $D_2$ are given by the following:

$$\begin{aligned} D_1 &= \int_{\frac{J_{\text{B,min}}}{\gamma_{\text{th}}}}^{J_{\text{E,max}}} f_{J_{\text{E}}}(z)\int_{J_{\text{B,min}}}^{\gamma_{\text{th}}z} f_{J_{\text{B}}}(y)\text{d}y\text{d}z \\ &= \varepsilon(m+3)^2 J_{\text{B,min}}^{-\frac{1}{m+3}}\left[\left(\frac{J_{\text{B,min}}}{\gamma_{\text{th}}}\right)^{-\frac{1}{m+3}} - J_{\text{E,max}}^{-\frac{1}{m+3}}\right] \\ &\quad - \frac{\varepsilon}{2}(m+3)^2\gamma_{\text{th}}^{-\frac{1}{m+3}}\left[\left(\frac{J_{\text{B,min}}}{\gamma_{\text{th}}}\right)^{-\frac{2}{m+3}} - J_{\text{E,max}}^{-\frac{2}{m+3}}\right] \end{aligned} \tag{34}$$

and

$$\begin{aligned} D_2 &= \int_{J_{\text{E,min}}}^{\frac{J_{\text{B,max}}}{\gamma_{\text{th}}}} f_{J_{\text{E}}}(z)\int_{J_{\text{B,min}}}^{\gamma_{\text{th}}z} f_{J_{\text{B}}}(y)\text{d}y\text{d}z + \int_{\frac{J_{\text{B,max}}}{\gamma_{\text{th}}}}^{J_{\text{E,max}}} f_{J_{\text{E}}}(z)\int_{J_{\text{B,min}}}^{J_{\text{B,max}}} f_{J_{\text{B}}}(y)\text{d}y\text{d}z \\ &= \varepsilon(m+3)^2 J_{\text{B,min}}^{-\frac{1}{m+3}}\left[J_{\text{E,min}}^{-\frac{1}{m+3}} - \left(\frac{J_{\text{B,max}}}{\gamma_{\text{th}}}\right)^{-\frac{1}{m+3}}\right] - \frac{\varepsilon}{2}(m+3)^2\gamma_{\text{th}}^{-\frac{1}{m+3}}\left[J_{\text{E,min}}^{-\frac{2}{m+3}} - \left(\frac{J_{\text{B,max}}}{\gamma_{\text{th}}}\right)^{-\frac{2}{m+3}}\right] \\ &\quad + \varepsilon(m+3)^2\left(J_{\text{B,min}}^{-\frac{1}{m+3}} - J_{\text{B,max}}^{-\frac{1}{m+3}}\right) \times \left[\left(\frac{J_{\text{B,max}}}{\gamma_{\text{th}}}\right)^{-\frac{1}{m+3}} - J_{\text{E,max}}^{-\frac{1}{m+3}}\right], \end{aligned} \tag{35}$$

where $\varepsilon = \frac{\Xi^2}{4}\left(\frac{2\pi\sigma_{\text{B}}^2\sigma_{\text{E}}^2}{e\xi^4P^4}\right)^{-\frac{1}{m+3}}$.

[1]Note that the instantaneous SC in reference [18] is defined as the difference of channel capacities between the Alice–relay–Bob channel and the Alice–relay–Eve channel. Different from reference [18], the instantaneous SC in our study is defined as the minimum SC of the two hops, which is similar to that in reference [17].

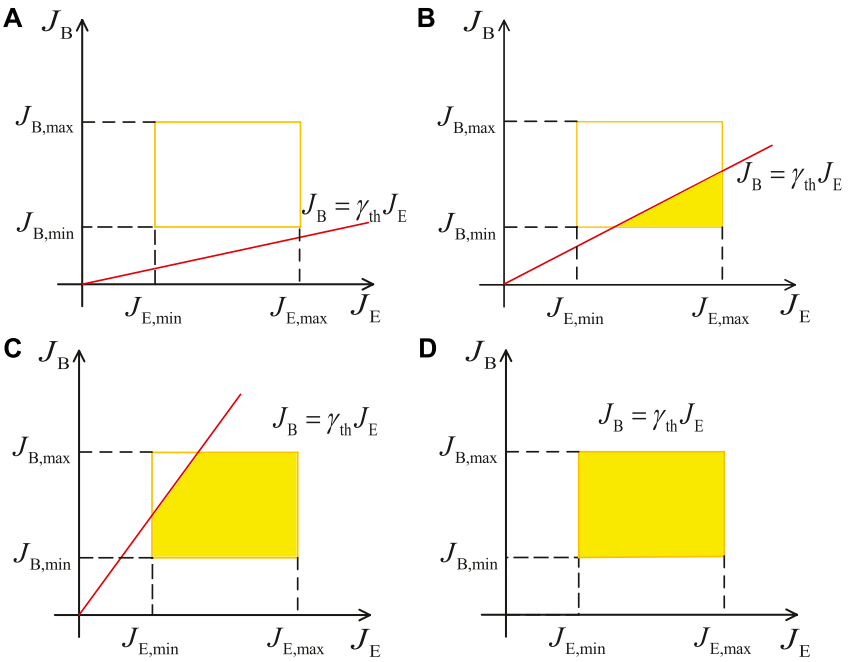


**FIGURE 2 |** Four cases of the integral of $\Pr(J_B < J_E\gamma_{th})$. **(A)** $\gamma_{th} \le \frac{J_{B,min}}{J_{E,max}}$. **(B)** $\frac{J_{B,min}}{J_{E,max}} < \gamma_{th} \le \frac{J_{B,min}}{J_{E,min}}$. **(C)** $\frac{J_{B,max}}{J_{E,max}} < \gamma_{th} < \frac{J_{B,max}}{J_{E,min}}$. **(D)** $\gamma_{th} \ge \frac{J_{B,max}}{J_{E,min}}$.

The lower bound of the SOP can be further derived as follows:

$$P_{\mathrm{SOP_L}} = \begin{cases} F_{|h_{\mathrm{SR}}|^2}\left(\dfrac{(\gamma_{\mathrm{th}}-1)N_0}{P_s}\right), & \text{if } \gamma_{\mathrm{th}} \le \dfrac{J_{\mathrm{B,min}}}{J_{\mathrm{E,max}}} \\ 1-\left(1-F_{|h_{\mathrm{SR}}|^2}\left(\dfrac{(\gamma_{\mathrm{th}}-1)N_0}{P_s}\right)\right)(1-D_1), & \text{if } \dfrac{J_{\mathrm{B,min}}}{J_{\mathrm{E,max}}} < \gamma_{\mathrm{th}} \le \dfrac{J_{\mathrm{B,min}}}{J_{\mathrm{E,min}}} \\ 1-\left(1-F_{|h_{\mathrm{SR}}|^2}\left(\dfrac{(\gamma_{\mathrm{th}}-1)N_0}{P_s}\right)\right)(1-D_2), & \text{if } \dfrac{J_{\mathrm{B,min}}}{J_{\mathrm{E,min}}} < \gamma_{\mathrm{th}} < \dfrac{J_{\mathrm{B,max}}}{J_{\mathrm{E,min}}} \\ 1, & \text{if } \gamma_{\mathrm{th}} \ge \dfrac{J_{\mathrm{B,max}}}{J_{\mathrm{E,min}}}, \end{cases} \tag{36}$$

Substituting **Eq. 34** and **Eq. 35** into **Eq. 36**, the expression for the lower bound of the SOP can be obtained as **Eq. 37**, as shown below:

$$P_{\mathrm{SOP_L}} = \begin{cases} \dfrac{P_R}{\Gamma(m_R)}\gamma\left(m_R, \dfrac{m_R}{P_R}\left(\dfrac{(\gamma_{\mathrm{th}}-1)N_0}{P_s}\right)\right), & \text{if } \gamma_{\mathrm{th}} \le \dfrac{J_{\mathrm{B,min}}}{J_{\mathrm{E,max}}} \\ 1-\dfrac{P_R}{\Gamma(m_R)}\gamma\left(m_R, \dfrac{m_R}{P_R}\left(\dfrac{(\gamma_{\mathrm{th}}-1)N_0}{P_s}\right)\right)+\dfrac{P_R}{\Gamma(m_R)}\gamma\left(m_R, \dfrac{m_R}{P_R}\left(\dfrac{(\gamma_{\mathrm{th}}-1)N_0}{P_s}\right)\right) & \\ \quad \times \varepsilon(m+3)^2 J_{\mathrm{B,min}}^{\frac{1}{m+3}}\left[\left(\dfrac{J_{\mathrm{B,min}}}{\gamma_{\mathrm{th}}}\right)^{-\frac{1}{m+3}} - J_{\mathrm{E,max}}^{-\frac{1}{m+3}}\right] & \text{if } \dfrac{J_{\mathrm{B,min}}}{J_{\mathrm{E,max}}} < \gamma_{\mathrm{th}} \le \dfrac{J_{\mathrm{B,min}}}{J_{\mathrm{E,min}}} \\ \quad -\dfrac{\varepsilon}{2}(m+3)^2\gamma_{\mathrm{th}}^{-\frac{1}{m+3}}\left[\left(\dfrac{J_{\mathrm{B,min}}}{\gamma_{\mathrm{th}}}\right)^{-\frac{2}{m+3}} - J_{\mathrm{E,max}}^{-\frac{2}{m+3}}\right], & \\ 1-\dfrac{P_R}{\Gamma(m_R)}\gamma\left(m_R, \dfrac{m_R}{P_R}\left(\dfrac{(\gamma_{\mathrm{th}}-1)N_0}{P_s}\right)\right)+\dfrac{P_R}{\Gamma(m_R)}\gamma\left(m_R, \dfrac{m_R}{P_R}\left(\dfrac{(\gamma_{\mathrm{th}}-1)N_0}{P_s}\right)\right) & \\ \quad \times \varepsilon(m+3)^2 J_{\mathrm{B,min}}^{\frac{1}{m+3}}\left[J_{\mathrm{E,min}}^{-\frac{1}{m+3}} - \left(\dfrac{J_{\mathrm{B,max}}}{\gamma_{\mathrm{th}}}\right)^{-\frac{1}{m+3}}\right] & \text{if } \dfrac{J_{\mathrm{B,min}}}{J_{\mathrm{E,min}}} < \gamma_{\mathrm{th}} < \dfrac{J_{\mathrm{B,max}}}{J_{\mathrm{E,min}}} \\ \quad -\dfrac{\varepsilon}{2}(m+3)^2\gamma_{\mathrm{th}}^{-\frac{1}{m+3}}\left[J_{\mathrm{E,min}}^{-\frac{2}{m+3}} - \left(\dfrac{J_{\mathrm{B,max}}}{\gamma_{\mathrm{th}}}\right)^{-\frac{2}{m+3}}\right] & \\ \quad +\varepsilon(m+3)^2\left(J_{\mathrm{B,min}}^{-\frac{1}{m+3}} - J_{\mathrm{B,max}}^{-\frac{1}{m+3}}\right)\times\left[\left(\dfrac{J_{\mathrm{B,max}}}{\gamma_{\mathrm{th}}}\right)^{-\frac{1}{m+3}} - J_{\mathrm{E,max}}^{-\frac{1}{m+3}}\right], & \\ 1, & \text{if } \gamma_{\mathrm{th}} \ge \dfrac{J_{\mathrm{B,max}}}{J_{\mathrm{E,min}}} \end{cases} \tag{37}$$

Remark 1. *According to* ***Eq. 33****, with the increase in* $\sigma_B$*, the channel gain* $H_B$ *decreases, and the integral range of* $\Pr(J_B < J_E\gamma_{th})$ *is enlarged. In this circumstance, the value of SOP in* ***Eq. 37*** *increases with* $\sigma_B$*. Similarly, we can conclude that the SOP degrades with the increase in* $\sigma_E$*.*

Remark 2. *With the increase in* $\gamma_{th}$*, the value of the lower bound of the SOP in* ***Eq. 37*** *is enlarged. Moreover, when* $\gamma_{th} \ge J_{B,max}/J_{E,min}$*, the lower bound of the SOP becomes one; hence, the information cannot be transmitted securely.*

## 3.2 Probability of SPSC Analysis

In secure communications, the probability of SPSC is a fundamental benchmark that is employed to emphasize the existence of SC [17]. In this subsection, we derive the probability of SPSC of the hybrid RF/VLC system. The probability of SPSC is defined as follows:

$$\begin{aligned} P_{\mathrm{SPSC}} &= \Pr\left\{\min\left(C_{\mathrm{hop},1}, C_{\mathrm{hop},2}\right) > 0\right\} \\ &= \Pr\left\{C_{\mathrm{hop},1} > 0\right\}\Pr\left\{C_{\mathrm{hop},2} > 0\right\}. \end{aligned} \tag{38}$$

According to **Eq. 23**, $\Pr\{C_{\mathrm{hop},1} > 0\}$ is expressed as follows:

$$\begin{aligned} \Pr\left\{C_{\mathrm{hop},1} > 0\right\} &= \Pr\left\{\frac{1}{2}\ln\left(1+\frac{P_s}{N_0}|h_{\mathrm{SR}}|^2\right) > 0\right\} \\ &= \Pr\left\{\frac{P_s}{N_0}|h_{\mathrm{SR}}|^2 > 0\right\} \\ &= 1, \end{aligned} \tag{39}$$

and $\Pr\{C_{\mathrm{hop},2} > 0\}$ is expressed as follows:

$$\begin{aligned} \Pr\left\{C_{\mathrm{hop},2} > 0\right\} &= \Pr\left\{\frac{1}{2}\ln\left(\frac{1+J_B}{1+J_E}\right) > 0\right\} \\ &= \Pr\{J_B > J_E\}. \end{aligned} \tag{40}$$

Remark 3. *Since* $\Pr\{C_{hop,1} > 0\}$ *is always equal to one, the performance of the probability of SPSC mainly depends on the VLC link.*

It should be noted that the value of **Eq. 40** also depends on the integral region. **Figure 3** shows four cases of the integral region in **Eq. 40**. Based on the four cases, the probability of SPSC in **Eq. 40** can be written as follows:

$$P_{\mathrm{SPSC}} = \begin{cases} 1, & \text{if } \dfrac{J_{\mathrm{B,min}}}{J_{\mathrm{E,max}}} \geq 1 \\ C_1, & \text{if } \dfrac{J_{\mathrm{B,min}}}{J_{\mathrm{E,max}}} < 1 \leq \dfrac{J_{\mathrm{B,min}}}{J_{\mathrm{E,min}}} \\ C_2, & \text{if } \dfrac{J_{\mathrm{B,min}}}{J_{\mathrm{E,min}}} < 1 < \dfrac{J_{\mathrm{B,max}}}{J_{\mathrm{E,min}}} \\ 0, & \text{if } \dfrac{J_{\mathrm{B,max}}}{J_{\mathrm{E,min}}} \leq 1. \end{cases} \tag{41}$$

Since $J_{\mathrm{B}}$ and $J_{\mathrm{E}}$ are independent of each other, $C_1$ and $C_2$ are given by the following:

$$\begin{aligned} C_1 &= 1 - \int_{J_{\mathrm{B,min}}}^{J_{\mathrm{E,max}}} f_{J_{\mathrm{E}}}(z) \int_{J_{\mathrm{B,min}}}^{z} f_{J_{\mathrm{B}}}(y)\mathrm{d}y\mathrm{d}z \\ &= 1 + \varepsilon(m+3)^2 J_{\mathrm{B,min}}^{-\frac{1}{m+3}} \left[ J_{\mathrm{E,max}}^{-\frac{1}{m+3}} - J_{\mathrm{B,min}}^{-\frac{1}{m+3}} \right] - \frac{\varepsilon}{2}(m+3)^2 \left[ J_{\mathrm{E,max}}^{-\frac{2}{m+3}} - J_{\mathrm{B,min}}^{-\frac{2}{m+3}} \right] \end{aligned} \tag{42}$$

and

$$\begin{aligned} C_2 &= \int_{J_{\mathrm{E,min}}}^{J_{\mathrm{B,max}}} f_{J_{\mathrm{E}}}(z) \int_{z}^{J_{\mathrm{B,max}}} f_{J_{\mathrm{B}}}(y)\mathrm{d}y\mathrm{d}z \\ &= \varepsilon(m+3)^2 \left[ J_{\mathrm{B,max}}^{-\frac{2}{m+3}} - J_{\mathrm{B,max}}^{-\frac{1}{m+3}} J_{\mathrm{E,min}}^{-\frac{1}{m+3}} \right] - \frac{\varepsilon}{2}(m+3)^2 \left[ J_{\mathrm{B,max}}^{-\frac{2}{m+3}} - J_{\mathrm{E,min}}^{-\frac{2}{m+3}} \right]. \end{aligned} \tag{43}$$

Finally, the closed-from expression of the probability of SPSC can be expressed as follows:

$$P_{\mathrm{SPSC}} = \begin{cases} 1, & \text{if } \dfrac{J_{\mathrm{B,min}}}{J_{\mathrm{E,max}}} \geq 1 \\ 1 + \varepsilon(m+3)^2 J_{\mathrm{B,min}}^{-\frac{1}{m+3}} \left[ J_{\mathrm{E,max}}^{-\frac{1}{m+3}} - J_{\mathrm{B,min}}^{-\frac{1}{m+3}} \right] - \dfrac{\varepsilon}{2}(m+3)^2 \left[ J_{\mathrm{E,max}}^{-\frac{2}{m+3}} - J_{\mathrm{B,min}}^{-\frac{2}{m+3}} \right], & \text{if } \dfrac{J_{\mathrm{B,min}}}{J_{\mathrm{E,max}}} < 1 \leq \dfrac{J_{\mathrm{B,min}}}{J_{\mathrm{E,min}}} \\ \varepsilon(m+3)^2 \left[ J_{\mathrm{B,max}}^{-\frac{2}{m+3}} - J_{\mathrm{B,max}}^{-\frac{1}{m+3}} J_{\mathrm{E,min}}^{-\frac{1}{m+3}} \right] - \dfrac{\varepsilon}{2}(m+3)^2 \left[ J_{\mathrm{B,max}}^{-\frac{2}{m+3}} - J_{\mathrm{E,min}}^{-\frac{2}{m+3}} \right], & \text{if } \dfrac{J_{\mathrm{B,min}}}{J_{\mathrm{E,min}}} < 1 < \dfrac{J_{\mathrm{B,max}}}{J_{\mathrm{E,min}}} \\ 0, & \text{if } \dfrac{J_{\mathrm{B,max}}}{J_{\mathrm{E,min}}} \leq 1. \end{cases} \tag{44}$$

Remark 4. *Opposite to Remark* 1, *with the increase in* $\sigma_B$, *the channel gain* $H_B$ *is decreased, and the integral range of* $\Pr\{C_{hop,2} > 0\}$ *is enlarged. In this circumstance, the value of the probability of SPSC can decrease with the increase in* $\sigma_B$. *Besides, we can conclude that the probability of the SPSC can increase with the increase in* $\sigma_E$.

Remark 5. *As the radius D increases, the probability of Eve being placed far away from Bob increases and the probability of Eve eavesdropping on confidential information decreases. Therefore, the channel gain* $H_B$ *is decreased, and the integral range of* $\Pr\{C_{hop,2} > 0\}$ *is enlarged. According to Remark* 3, *the performance of the probability of SPSC mainly depends on the VLC link. Therefore, the performance of the system will be improved.*

# 4 SECRECY PERFORMANCE ANALYSIS WHEN RF LINK IS EAVESDROPPED UPON

In **Section 3**, the SOP and the probability of the SPSC have been analyzed when the VLC link is eavesdropped upon. However, in practice, the RF link is more vulnerable to unauthorized users, so it is necessary to analyze the secrecy performance of the hybrid RF/VLC system when the RF link is eavesdropped upon. The system model is shown in **Figure 4**.

## 4.1 SOP Analysis

In this subsection, we analyze the SOP of a hybrid RF/VLC system when the RF link is eavesdropped upon. The instantaneous SC of the first hop is given by the following:

$$C_{\mathrm{hop},1}^{'} = \left\{ \frac{1}{2} \left( \ln(1+\gamma_{\mathrm{SR}}) - \ln(1+\gamma_{\mathrm{SE}}) \right) \right\}^{+}, \tag{45}$$

where $\{x\}^+ = \max\{x, 0\}$, $\gamma_{\mathrm{SE}}$ represents the instantaneous SNR at Eve and it can be expressed as follows:

$$\gamma_{\mathrm{SE}} = P_{\mathrm{s}} \left| h_{\mathrm{SE}} \right|^2 / N_0. \tag{46}$$

Similarly, the $h_{\mathrm{SE}}$ represents the channel gain between Alice and Eve, where $\left|h_{\mathrm{SE}}\right|^2$ can be written as follows:

$$\left|h_{\mathrm{SE}}\right|^2 = \left|g_{\mathrm{R}}^{'}\right|^2 G_{\mathrm{E}}, \tag{47}$$

where the PDF of $\left|g_{\mathrm{R}}^{'}\right|^2$ is as follows:

$$f_{\left|g_{\mathrm{R}}^{'}\right|^2}(x) = \frac{x^{m_{\mathrm{E}}-1}}{\Gamma(m_{\mathrm{E}})} m_{\mathrm{E}}^{m_{\mathrm{E}}} \exp(-m_{\mathrm{E}} x), x \geq 0, \tag{48}$$

where $m_{\mathrm{E}}$ represents the fading factor between Alice and Eve. Furthermore, $G_{\mathrm{E}}$ in **Eq. 47** can be modeled as follows [22]:

$$G_{\mathrm{E}} = \left( \frac{d_0}{d_1^{'}} \right)^{\lambda}, \tag{49}$$

where $d_1^{'}$ is the distance between Alice and Eve. Therefore, the PDF and the CDF of $\gamma_{\mathrm{S}j}$ ($j \in \{\mathrm{R}, \mathrm{E}\}$) are as follows:

$$\begin{cases} f_{\gamma_{\mathrm{S}j}}(z) = \dfrac{N_0}{P_{\mathrm{s}} G_j} \left( \dfrac{N_0}{P_{\mathrm{s}} G_j} z \right)^{m_j - 1} \dfrac{1}{\Gamma(m_j)} m_j^{m_j} \exp\left( -\dfrac{m_j N_0}{P_{\mathrm{s}} G_j} z \right), & z \geq 0 \\ F_{\gamma_{\mathrm{S}j}}(z) = \dfrac{1}{\Gamma(m_j)} \gamma\left( m_j, \dfrac{m_j N_0}{P_{\mathrm{s}} G_j} z \right), & z \geq 0. \end{cases} \tag{50}$$

Because there are no eavesdroppers in the VLC link, the instantaneous SC of the first hop is its instantaneous channel capacity, that is, a lower bound on the instantaneous SC of the second hop is written by using the following [21]:

$$C_{\mathrm{hop},1}^{'} = \frac{1}{2} \ln\left( 1 + \frac{e}{2\pi} \left( \frac{H_{\mathrm{B}} \xi P}{\sigma_{\mathrm{B}}} \right)^2 \right) = \frac{1}{2} \ln(1 + J_{\mathrm{B}}). \tag{51}$$

Similarly, the instantaneous SC of the entire hybrid system is the minimum of $C_{\mathrm{hop},1}^{'}$ and $C_{\mathrm{hop},2}^{'}$, which is expressed as follows:

$$C_{\mathrm{I}}^{'} = \min\left\{ C_{\mathrm{hop},1}^{'}, C_{\mathrm{hop},2}^{'} \right\}. \tag{52}$$

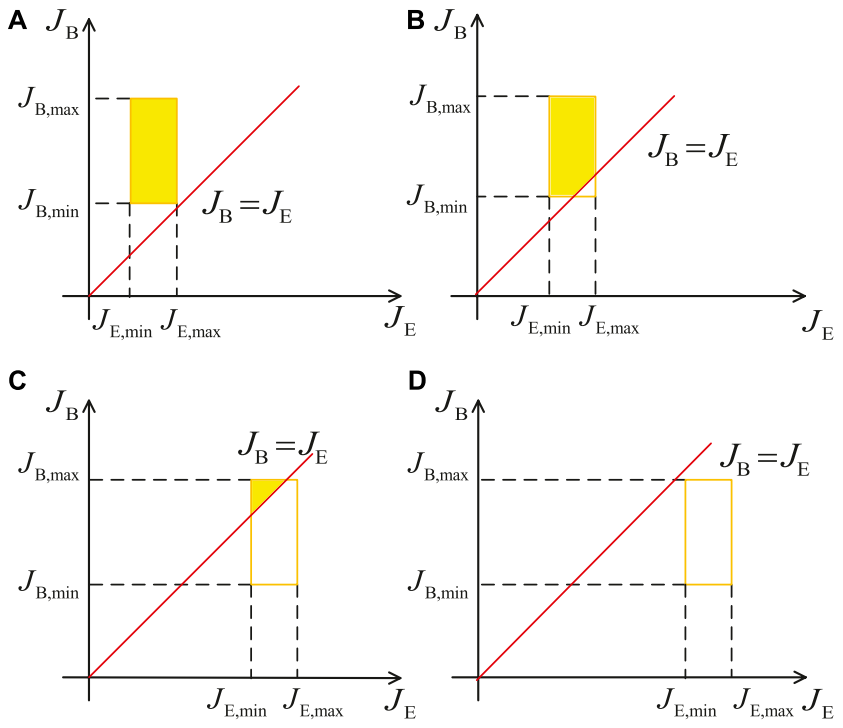


**FIGURE 3 |** Four cases of the integral of $\Pr\{C_{RD} > 0\}$. **(A)** $1 \le \frac{J_{B,min}}{J_{E,max}}$. **(B)** $\frac{J_{B,min}}{J_{E,max}} < 1 \le \frac{J_{B,min}}{J_{E,min}}$. **(C)** $\frac{J_{B,max}}{J_{E,max}} < 1 < \frac{J_{B,max}}{J_{E,min}}$. **(D)** $1 \ge \frac{J_{B,max}}{J_{E,min}}$ [3].

We have known that SOP can be given by $P_{SOP} = \Pr\{C_I' < C_{th}\}$. Furthermore, the SOP can be rewritten as follows:

$$\begin{aligned} P_{SOP} &= \Pr\left\{\min\left(C'_{hop,1}, C'_{hop,2}\right) < C_{th}\right\} \\ &= 1 - \Pr\left\{C'_{hop,1} \ge C_{th}\right\}\Pr\left\{C'_{hop,2} \ge C_{th}\right\}, \end{aligned} \tag{53}$$

where

$$\begin{aligned} &\Pr\left\{C'_{hop,1} \ge C_{th}\right\} \\ &= \Pr\left\{\frac{1}{2}\ln\left(\frac{1+\gamma_{SR}}{1+\gamma_{SE}}\right) \ge \frac{1}{2}\ln\gamma_{th}\right\} \\ &= 1 - \Pr\left\{\gamma_{SR} < \gamma_{th}\gamma_{SE} + \gamma_{th} - 1\right\} \end{aligned} \tag{54}$$

and

$$\begin{aligned} \Pr\left\{C'_{hop,2} \ge C_{th}\right\} &= \Pr\left\{\frac{1}{2}\ln\left(1+J_B\right) \ge \frac{1}{2}\ln\gamma_{th}\right\} \\ &= 1 - \Pr\left\{J_B < \gamma_{th} - 1\right\}. \end{aligned} \tag{55}$$

Substituting **Eqs 54** and **55** into **Eq. 53**, we have the following:

$$P_{SOP} = \begin{cases} \int_0^{\infty} F_{\gamma_{SR}}\left(\gamma_{SE}\gamma_{th} + \gamma_{th} - 1\right) f_{\gamma_{SE}}\left(\gamma_{SE}\right) d\gamma_{SE}, \\ \qquad \text{if } \gamma_{th} - 1 < J_{B,min} \\ 1 - \left(1 - \int_0^{\infty} F_{\gamma_{SR}}\left(\gamma_{SE}\gamma_{th} + \gamma_{th} - 1\right) f_{\gamma_{SE}}\left(\gamma_{SE}\right) d\gamma_{SE}\right)\left(1 - \int_{J_{B,min}}^{\gamma_{th}-1} f_{J_B}(y)dy\right), \\ \qquad \text{if } J_{B,min} \le \gamma_{th} - 1 < J_{B,max} \\ 1 - \left(1 - \int_0^{\infty} F_{\gamma_{SR}}\left(\gamma_{SE}\gamma_{th} + \gamma_{th} - 1\right) f_{\gamma_{SE}}\left(\gamma_{SE}\right) d\gamma_{SE}\right)\left(1 - \int_{J_{B,min}}^{J_{B,max}} f_{J_B}(y)dy\right), \\ \qquad \text{if } \gamma_{th} - 1 \ge J_{B,max}. \end{cases} \tag{56}$$

It is mathematically difficult to obtain the exact close-form expression for SOP as shown in **Eq. 56**. Therefore, we alternatively evaluate the lower bound of SOP. We assume that $\gamma_{SE} \gg 1$ and $\gamma_{SR} \gg 1$, and when $\gamma_{SR} > \gamma_{SE}$, we have $(1+\gamma_{SR})/(1+\gamma_{SE}) < \gamma_{SR}/\gamma_{SE}$. Therefore, we can derive the lower bound of SOP as follows:

$$P_{SOP} \ge P_{SOP_L} \triangleq \begin{cases} A, & \text{if } \gamma_{th} - 1 < J_{B,min} \\ A + \varepsilon'\left[J_{B,min}^{-\frac{1}{m+3}} - (\gamma_{th}-1)^{-\frac{1}{m+3}}\right] \times (1-A), & \text{if } J_{B,min} \le \gamma_{th} - 1 < J_{B,max} \\ A + \varepsilon'\left[J_{B,min}^{-\frac{1}{m+3}} - J_{B,max}^{-\frac{1}{m+3}}\right] \times (1-A), & \text{if } \gamma_{th} - 1 \ge J_{B,max}, \end{cases} \tag{57}$$

where

$$\begin{aligned} A = &\frac{1}{\Gamma(m_R)}\frac{1}{\Gamma(m_E)}\left(\frac{m_E G_R}{\gamma_{th} m_R G_E}\right)^{m_E} \frac{\Gamma(m_R + m_E)}{m_R\left(1 + \frac{m_E G_R}{\gamma_{th} m_R G_E}\right)^{m_R + m_E}} \\ &\times F\left(1, m_R + m_E; 1 + m_R; \frac{1}{\frac{m_E G_R}{\gamma_{th} m_R G_E} + 1}\right). \end{aligned} \tag{58}$$

$\varepsilon' = (m+3)\frac{\Xi}{2}\left(\frac{2\pi\sigma_B^2}{e\xi^2 P^2}\right)^{-\frac{1}{m+3}}$, $F(a,b;c;z)$ is the Gauss hypergeometric function.

Remark 6. *With the increase in $d_1$, the Alice–relay link path loss is reduced, which results in the decreasing of the instantaneous SNR $\gamma_{SR}$, and the value of the $\Pr\{C'_{hop,1} \ge C_{th}\}$ is reduced due to the channel advantages of the Alice–relay link over the Alice–Eve. Therefore, the value of the lower bound of the SOP also increased.*

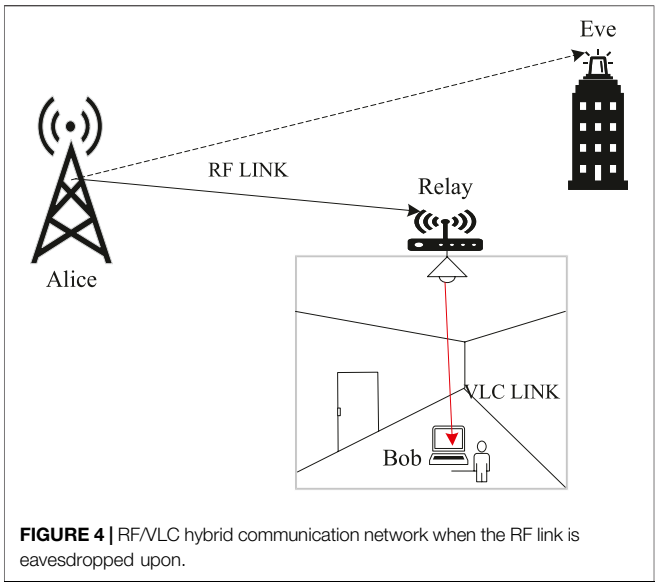


**FIGURE 4 |** RF/VLC hybrid communication network when the RF link is eavesdropped upon.

Remark 7. *According to* ***Eqs 2***, ***46***, and ***54****, it is seen that by increasing λ, the value of the* $\Pr\{C'_{hop,1} \geq C_{th}\}$ *is also increased, and then the lower bound of the SOP is decreased.*

Remark 8. *By increasing* $m_E$*, the value of the* $C'_{hop,1}$ *is decreased and the value of the* $\Pr\{C'_{hop,1} \geq C_{th}\}$ *is also decreased. According to* ***Eq. 53****, we can conclude that the value of the SOP is increased.*

## 4.2 Probability of SPSC Analysis

Similarly, the probability of SPSC of the hybrid RF/VLC system when an eavesdropper eavesdrops on the RF link can be written as follows:

$$\begin{aligned} P_{\text{SPSC}} &= \Pr\left\{\min\left(C'_{\text{hop},1}, C'_{\text{hop},2}\right) > 0\right\} \\ &= \Pr\left\{C'_{\text{hop},1} > 0\right\}\Pr\left\{C'_{\text{hop},2} > 0\right\}. \end{aligned} \tag{59}$$

According to **Eq. 45**, $\Pr\{C_{\text{hop},1}' > 0\}$ is expressed as follows:

$$\begin{aligned} \Pr\left\{C'_{\text{hop},1} > 0\right\} &= \Pr\left\{\frac{1}{2}\ln\left(\frac{1+\gamma_{\text{SR}}}{1+\gamma_{\text{SE}}}\right) > 0\right\} \\ &= \Pr\{\gamma_{\text{SR}} > \gamma_{\text{SE}}\}, \end{aligned} \tag{60}$$

and $\Pr\{C_{\text{hop},2}' > 0\}$ is expressed as follows:

$$\begin{aligned} \Pr\left\{C_{\text{hop},2}' > 0\right\} &= \Pr\left\{\frac{1}{2}(1+J_{\text{B}}) > 0\right\} \\ &= \Pr\{J_{\text{B}} > 0\} = 1. \end{aligned} \tag{61}$$

Based on **Eqs 60** and **61**, the closed-from expression of the probability of SPSC in **Eq. 59** can be written as follows:

$$P_{\text{SPSC}} = \frac{1}{\Gamma(m_{\text{R}})}\frac{1}{\Gamma(m_{\text{E}})}\left(\frac{G_{\text{R}}m_{\text{E}}}{m_{\text{R}}G_{\text{E}}}\right)^{m_{\text{E}}}\frac{\Gamma(m_{\text{R}}+m_{\text{E}})}{m_{\text{E}}\left(1+\frac{G_{\text{R}}m_{\text{E}}}{m_{\text{R}}G_{\text{E}}}\right)^{m_{\text{R}}+m_{\text{E}}}}F\left(1, m_{\text{R}}+m_{\text{E}}; 1+m_{\text{E}}; \frac{\frac{G_{\text{R}}m_{\text{E}}}{m_{\text{R}}G'_{\text{R}}}}{\frac{G_{\text{R}}m_{\text{E}}}{m_{\text{R}}G_{\text{E}}}+1}\right). \tag{62}$$

Remark 9. *Similar to Remark 6, the probability of the SPSC decreases by increasing* $d_1$*. However, with the increase in* $d'_1$*, the value of the* $\Pr\{C'_{hop,1} > 0\}$ *is also increased. Therefore, the probability of the SPSC is increased by increasing* $d'_1$*.*

Remark 10. *Since the value of the* $\Pr\{C'_{hop,2} > 0\}$ *is always equal to one, the probability of SPSC mainly depends on the RF link.*

**TABLE 1 |** Main simulation parameters.

| | Parameters | Symbols | Values |
|---|---|---|---|
| RF | Reference distance | $d_0$ | 1 km |
| | Noise variance | $N_0$ | 1 |
| | Transmission power at Alice | $P_s$ | 60 dB |
| VLC | Physical filter gain of the PD | $A$ | 1 $cm^2$ |
| | Optical filter gain of the PD | $T_S$ | 1 |
| | Concentrator gain of the PD | $g$ | 3 |
| | Vertical distance between the LED and the floor | $l$ | 4 m |
| | Order of Lambertian emission | $m$ | 2 |

# 5 NUMERICAL RESULTS

In this section, we present the numerical results of hybrid RF/VLC systems. Here, the theoretical results of the derived lower bound of the SOP and the probability of SPSC are verified by using Monte-Carlo simulation, which is performed by generating $10^4$ random samples. Unless otherwise specified, the main simulation parameters of the hybrid system are listed in **Table 1**. It should be noted that all numerical results are obtained by using MATLAB.

## 5.1 Results When VLC Link Is Eavesdropped Upon

**Figure 5** shows the SOP versus Bob's noise standard deviation $\sigma_{\text{B}}$ with different Eve's noise standard deviations $\sigma_{\text{E}}$ when $P$ = 60 dB, $\xi$ = 0.2, and $\gamma_{\text{th}}$ = 3. It is seen that the SOP performance deteriorates with the increase in $\sigma_{\text{B}}$, and this is because the larger the value of $\sigma_{\text{B}}$, the smaller the channel gain $H_{\text{B}}$. A larger $H_{\text{B}}$ also leads to better secrecy performance, while a smaller $H_{\text{B}}$ degrades the secrecy performance. Besides, with the increase in $\sigma_{\text{E}}$, the value of SOP is reduced; therefore, by increasing $\sigma_{\text{E}}$, $H_{\text{E}}$ is reduced, and a smaller $H_{\text{E}}$ leads to higher secrecy as in *Remark 1*.

**Figure 6** shows the SOP versus Bob's noise standard deviation $\sigma_{\text{B}}$ with different $\gamma_{\text{th}}$ when $P$ = 60 dB, $\xi$ = 0.2, and $\sigma_{\text{E}}$ = 3. As it is seen, the SOP increases with the increase in $\sigma_{\text{B}}$, which is consistent with that in **Figure 5**. Moreover, it can be observed that the value of SOP becomes larger with the increase in $\gamma_{\text{th}}$, which means that the system secrecy performance is degraded, which coincides with *Remark 2*.

From **Figure 5** and **Figure 6**, it can be clearly observed that simulation results are in close agreement with the theoretical results, which validates our theoretical analysis of SOP as correct.

**Figure 7** shows the probability of SPSC versus Bob's noise standard deviation $\sigma_{\text{B}}$ with different Eve's noise standard deviations $\sigma_{\text{E}}$ when $P$ = 60 dB and $\xi$ = 0.2. It can be seen that the performance of the probability of SPSC deteriorates with the increase in $\sigma_{\text{B}}$, and this is because a larger value of $\sigma_{\text{B}}$ results in a

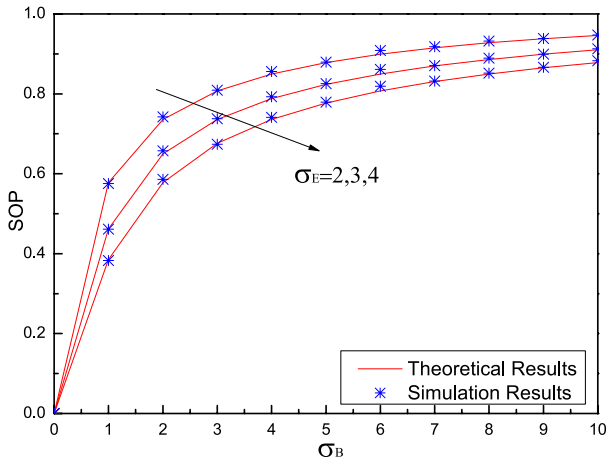


**FIGURE 5 |** SOP versus $\sigma_B$ with different $\sigma_E$ when $P$ = 60 dB, $\xi$ = 0.2, and $\gamma_{th}$ = 3.

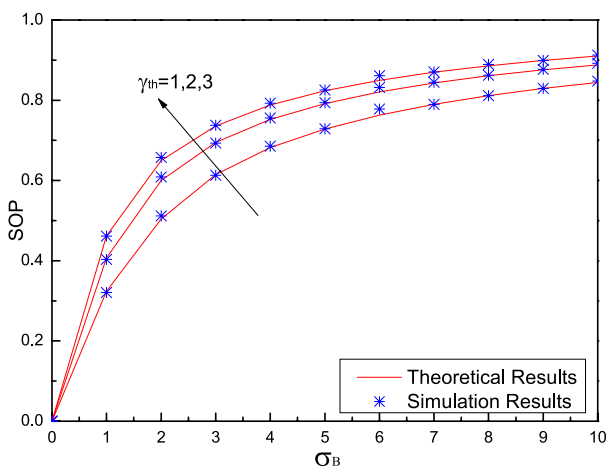


**FIGURE 6 |** SOP versus $\sigma_B$ with different $\gamma_{th}$ when $P$ = 60 dB, $\xi$ = 0.2, and $\sigma_E$ = 3.

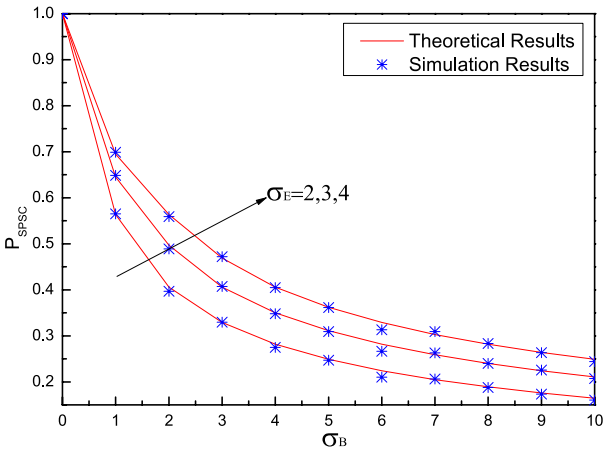


**FIGURE 7 |** $P_{SPSC}$ versus $\sigma_B$ with different $\sigma_E$ when $P$ = 60 dB and $\xi$ = 0.2.

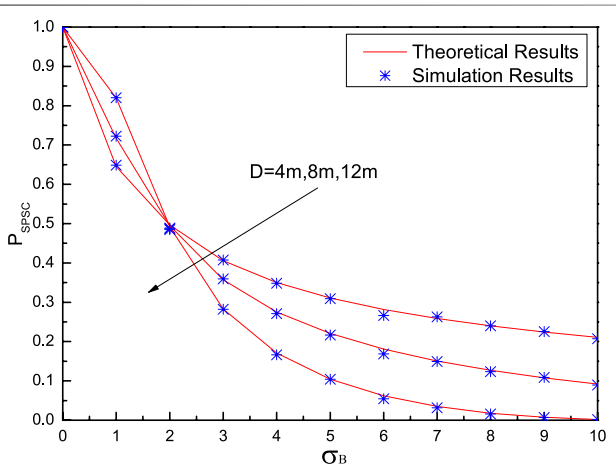


**FIGURE 8 |** $P_{SPSC}$ versus $\sigma_B$ with different $D$ when $P$ = 60 dB and $\xi$ = 0.2.

smaller channel gain $H_B$. A larger $H_B$ leads to better secrecy performance, whereas a smaller value leads to worse secrecy performance. Moreover, it can be observed from the plot that the probability of SPSC is increased by increasing $\sigma_E$ from $\sigma_E = 2$ to $\sigma_E = 4$. This means that by increasing $\sigma_E$, $H_E$ is reduced, and a smaller $H_E$ leads to better secrecy performance. This is consistent with *Remark 4*.

**Figure 8** shows the probability of SPSC versus Bob's noise standard deviation $\sigma_B$ with different floor radii $D$ when $P$ = 60 dB and $\xi$ = 0.2. It can be seen from **Figure 8** that when $\sigma_B \leq 2$, the probability of SPSC decreases with the increase in $D$. This is because when $\sigma_B \leq 2$, a larger $\sigma_E$ ($\sigma_E = 3$) leads to a smaller $H_E$, and thus, secrecy performance mainly depends on Bob's and Eve's SNRs. When $\sigma_B > 2$, it is seen that by increasing $D$ from 4 to 12 m, the value of the probability of SPSC is increased. This is also consistent with *Remark 5*. Expanding the floor radius, $D$, also decreases the probability of Eve eavesdropping on information, which improves the performance of the hybrid system.

Moreover, it can be found from **Figure 7** and **Figure 8** that all theoretical results match simulation results very well, which indicates the correctness of the theoretical analysis.

## 5.2 Results When RF Link Is Eavesdropped Upon

**Figure 9** shows SOP versus the distance between nodes Alice and relay $d_1$ with different path loss exponents $\lambda$ when $P$ = 60 dB, $m_E = 2$, $\sigma_B = 2$, $m_B = 2$, and $d_1' = 2$ (eavesdropping on the RF link). It can be seen that the SOP performance is deteriorated by increasing $d_1$, which is intuitive because a larger value of $d_1$ results in a smaller channel gain, $h_{SR}$, which then results in a worse secrecy performance. This conclusion is consistent with *Remark 6*. Moreover, with the increase in path loss exponent $\lambda$,

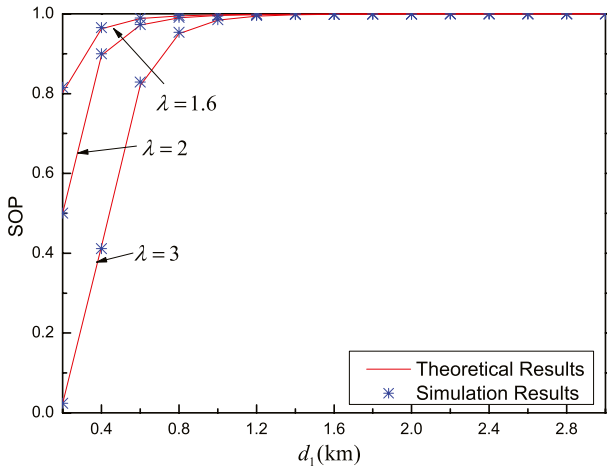


**FIGURE 9 |** SOP versus $d_1$ with different $\lambda$ when $P$ = 60 dB, $m_E$ = 2, $\sigma_B$ = 2, $m_B$ = 2, and $d_1'$ = 2 (eavesdropping on the RF link).

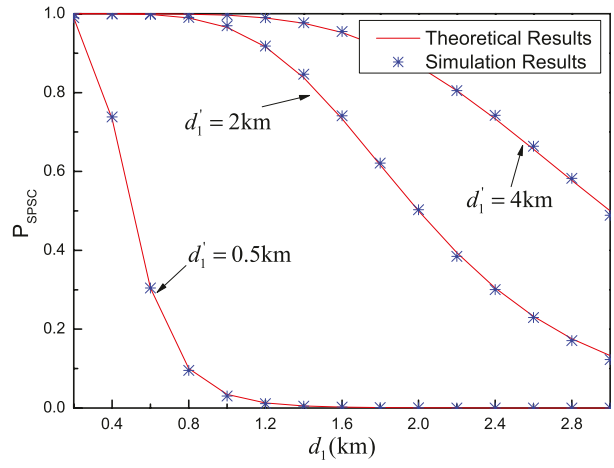


**FIGURE 11 |** $P_{SPSC}$ versus $d_1$ with different $d_1'$ when $P$ = 60 dB, $\lambda$ = 3, $\sigma_B$ = 2, $m_B$ = 2, and $m_E$ = 2 (eavesdropping on the RF link).

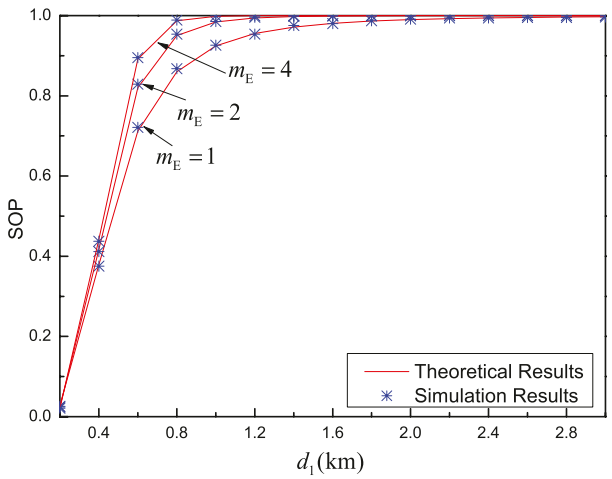


**FIGURE 10 |** SOP versus $d_1$ with different $m_E$ when $P$ = 60 dB, $\lambda$ = 3, $\sigma_B$ = 2, $m_B$ = 2, and $d_1'$ = 2 (eavesdropping on the RF link).

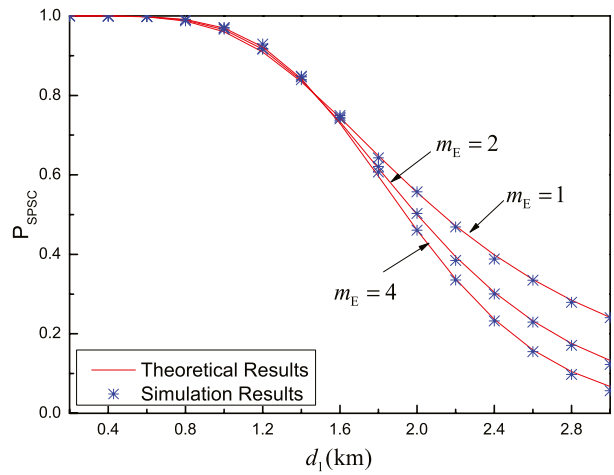


**FIGURE 12 |** $P_{SPSC}$ versus $d_1$ with different $d_1'$ when $P$ = 60 dB, $\lambda$ = 3, $\sigma_B$ = 2, $m_B$ = 2, and $d_1'$ = 2 (eavesdropping on the RF link).

the value of SOP becomes smaller, which means that the system secure transmission performance is improved. This verifies the conclusion in *Remark 7*.

**Figure 10** shows the SOP versus the distance between nodes Alice and relay $d_1$ with different Alice–Eve channel fading factors $m_E$ when $P$ = 60 dB, $\lambda$ = 3, $\sigma_B$ = 2, $m_B$ = 2, and $d_1'$ = 2 (eavesdropping on the RF link). As it is seen, by increasing $d_1$, the SOP performance is degraded with the increase in $d_1$. This is also consistent with that in **Figure 9**. Besides, by increasing $m_E$, the value of SOP also becomes large. This is because the larger the value of $m_E$, the smaller the Alice–Eve channel fading which, in turn, deteriorates the secrecy performance. This verifies the conclusion in *Remark 8*.

From **Figure 9** and **Figure 10**, it should be emphasized that the performance gap between theoretical results and simulation results is small, which verifies the accuracy of the derived expression, which indicates that the scaling for the lower bound of SOP is reasonable.

**Figure 11** shows the probability of SPSC versus the distance between nodes Alice and relay $d_1$ with different distances between node Alice and Eve $d_1'$ when $P$ = 60 dB, $\lambda$ = 3, $\sigma_B$ = 2, $m_B$ = 2, and $m_E$ = 2 (eavesdropping on the RF link). It is seen that the SPSC performance is decreased by increasing $d_1$. This also indicates that the system secrecy performance is reduced when the relay node receives less confidential information. This conclusion is consistent with that in **Figure 9**. By increasing $d_1'$, Eve eavesdrops on less information. Therefore, the larger the value of $d_1'$, the better the performance. This is also consistent with *Remark 9*.

**Figure 12** shows the probability of SPSC versus the distance between nodes Alice and relay $d_1$ with different Alice–Eve

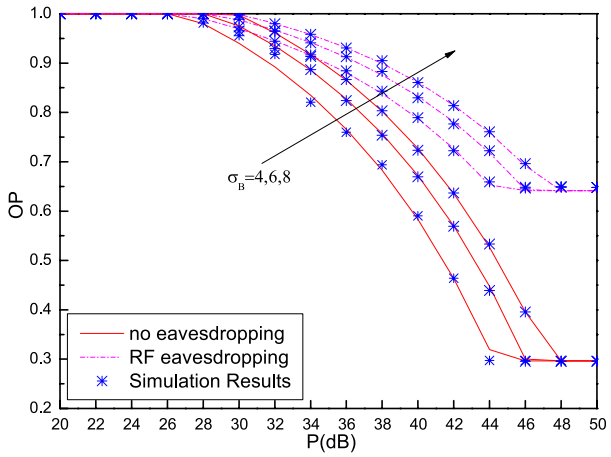


**FIGURE 13 |** OP performance of systems with and without an RF eavesdropper when $\xi = 0.2$ and $\gamma_{th} = 3$.

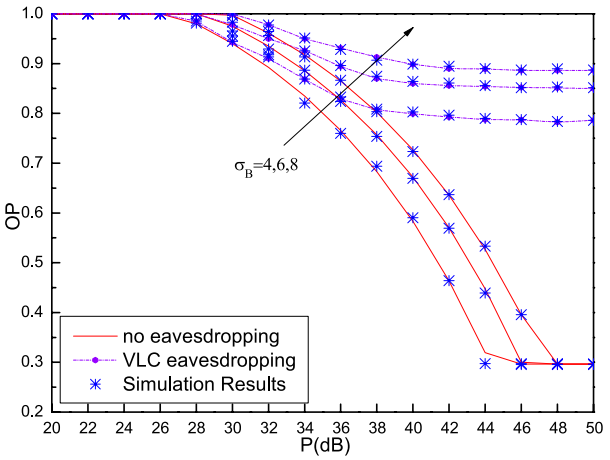


**FIGURE 14 |** OP performance of systems with and without a VLC eavesdropper when $\xi = 0.2$ and $\gamma_{th} = 3$.

channel fading factors $m_E$ when $P = 60$ dB, $\lambda = 3$, $\sigma_B = 2$, $m_B = 2$, and $d_1' = 2$ (eavesdropping on the RF link). Similar to **Figure 11**, the probability of the SPSC performance degrades with the increase in $d_1$. Moreover, for $m_E$ smaller than 1.6 (km), the probability of the SPSC increases with the increase in the Alice–Eve channel fading factor $m_E$. However, if $d_1$ is larger than 1.6 (km), the probability of the SPSC increases with the decrease in the Alice–Eve channel fading factor $m_E$. This is because for small $d_1$, the relay node has a stronger ability to receive confidential information than Eve. For a larger $d_1$, Eve eavesdrops on more confidential information.

From **Figure 11** and **Figure 12**, all theoretical results of the probability of the SPSC match the simulation results very well, which verifies the accuracy of the derived theoretical expression of the probability of the SPSC. Therefore, the derived expression can be used directly to evaluate the system performance with time-intensive simulations.

## 5.3 Comparisons for Systems With and Without Eavesdroppers

**Figure 13** depicts OP performance for systems with and without an RF eavesdropper when $\xi = 0.2$ and $\gamma_{th} = 3$. It is seen that the OP performance decreases with the increase in $P$, and this is because the larger the value of $P$, the larger the capacity of the second hop becomes. Besides, with the increase in larger $\sigma_B$, the OP performance is deteriorated, which is consistent with *Remark 1*. Furthermore, for fixed $P$ and $\sigma_B$, the system with an RF eavesdropper achieves worse OP performance than the system without an eavesdropper. It is because the existence of the eavesdropper increases the security risk of the system.

**Figure 14** illustrates the OP performance for systems with and without a VLC eavesdropper when $\xi = 0.2$ and $\gamma_{th} = 3$. As it is seen, the value of OP decreases with the increase in $P$, which is consistent with that in **Figure 13**. Moreover, it can be observed that for fixed $\sigma_B$ and $P$, the value of OP becomes larger when the VLC link is eavesdropped upon.

# 6 CONCLUSION

In this article, we have studied the performance of a hybrid RF/VLC DF-based relaying network, in which two scenarios are taken into account: in one scenario, the VLC link is wiretapped, and in the other scenario, the RF link is wiretapped. The major conclusions of the study are given as follows:

1. We assume that the RF link experiences Nakagami-m fading and has path loss, and the non-negative and average optical intensity constraint in the VLC link is considered. The closed-form expressions of the lower bound of SOP and the probability of SPSC are derived, respectively. Numerical results show that theoretical results match simulation results well.
2. When the VLC link is eavesdropped upon, Bob's (or Eve's) noise standard deviation $\sigma_B$ (or $\sigma_E$), the equivalent threshold of the SNR $\gamma_{th}$, and the floor radius $D$ have strong impacts on the performance of SOP or the probability of SPSC. The increase in the $\sigma_B$ and $\gamma_{th}$ degrades the system secrecy performance, while the increase in $\sigma_E$ and $D$ will improve the secrecy performance.
3. If the RF link is eavesdropped upon, we can conclude that with the increase in $d_1$, the system secrecy performance is degraded, whereas the increase in $\lambda$ and $d_1'$ improves the secrecy performance.
4. The derived theoretical expressions in this study will enable communication system designers to quickly and accurately evaluate PLS performance of the hybrid RF/VLC system without time-intensive and laborious Monte-Carlo simulations.

In this study, the secrecy performance of the hybrid RF/indoor VLC system is analyzed. In future work, we will establish the channel model for outdoor VLC and continue to study the secrecy performance of the hybrid RF/outdoor VLC system. Moreover, we will also explore some secrecy performance improvement schemes of the hybrid system.

## DATA AVAILABILITY STATEMENT

The original contributions presented in the study are included in the article/Supplementary Material; further inquiries can be directed to the corresponding authors.

## AUTHOR CONTRIBUTIONS

JW and QW designed the research. JW, QW, and JL contributed with data acquisition, analysis, and discussion of results. BZ contributed to the data analysis. JL wrote the manuscript with input from all other authors.

## FUNDING

This work is supported by the National Nature Science Foundation of China (61701254 and 11604133), the Science and Technology Plan of Youth Innovation Team for Universities of Shandong Province (2019KJJ019), the Introduction and Cultivation Plan of Youth Innovation Talents for Universities of Shandong Province, the Fund of the Shandong Key Laboratory of Optical Communication Science and Technology in Liaocheng University (SDOC201901), and the Open Project of Shanghai Key Laboratory of Trustworthy Computing.

## REFERENCES

1. Yang Z, Chen M, Wong KK, Poor HV, and Cui S. Federated Learning for 6G: Applications, Challenges, and Opportunities. *arXiv preprint arXiv:2101.01338* (2021).
2. Wang J-Y, Yang Z, Wang Y, and Chen M. On the Performance of Spatial Modulation Based Optical Wireless Communications. *IEEE Photon Technol Lett* (2016) 28:1. doi:10.1109/LPT.2016.2585502
3. Tabassum H, and Hossain E. Coverage and Rate Analysis for Co-existing RF/VLC Downlink Cellular Networks. *IEEE Trans Wireless Commun* (2018) 17: 2588–601. doi:10.1109/TWC.2018.2799204
4. Rakia T, Yang H-C, Gebali F, and Alouini M-S. Optimal Design of Dual-Hop VLC/RF Communication System with Energy Harvesting. *IEEE Commun Lett* (2016) 20:1979–82. doi:10.1109/LCOMM.2016.2595561
5. Kashef M, Ismail M, Abdallah M, Qaraqe KA, and Serpedin E. Energy Efficient Resource Allocation for Mixed RF/VLC Heterogeneous Wireless Networks. *IEEE J Select Areas Commun* (2016) 34:883–93. doi:10.1109/JSAC.2016.2544618
6. Hammouda M, Akin S, Vegni AM, Haas H, and Peissig J. Link Selection in Hybrid RF/VLC Systems under Statistical Queueing Constraints. *IEEE Trans Wireless Commun* (2018) 17:2738–54. doi:10.1109/TWC.2018.2802937
7. Kong J, Ismail M, Serpedin E, and Qaraqe KA. Energy Efficient Optimization of Base Station Intensities for Hybrid RF/VLC Networks. *IEEE Trans Wireless Commun* (2019) 18:4171–83. doi:10.1109/TWC.2019.2922611
8. Hsiao Y-C, Wu Y-C, and Lin C. Energy-efficient Beamforming Design for MU-MISO Mixed RF/VLC Heterogeneous Wireless Networks. *IEEE Trans Signal Process* (2019) 67:3770–84. doi:10.1109/TSP.2019.2920612
9. Marzban MF, Kashef M, Abdallah M, and Khairy M. Beamforming and Power Allocation for Physical-Layer Security in Hybrid RF/VLC Wireless Networks. In: 2017 13th International Wireless Communications and Mobile Computing Conference (IWCMC). Piscataway, New Jersey: IEEE (2017). p. 258–63.
10. Rakia T, Yang HC, Gebali F, and Alouini MS. Dual-hop VLC/RF Transmission System with Energy Harvesting Relay under Delay Constraint. In: 2016 IEEE Globecom Workshops (GC Wkshps). Piscataway, New Jersey: IEEE (2016). p. 1–6.
11. Al-Khori J, Nauryzbayev G, Abdallah MM, and Hamdi M. Secrecy Performance of Decode-And-Forward Based Hybrid RF/VLC Relaying Systems. *IEEE Access* (2019) 7:10844–56. doi:10.1109/ACCESS.2019.2891678
12. Kumar A, Garg P, and Gupta A. PLS Analysis in an Indoor Heterogeneous VLC/RF Network Based on Known and Unknown CSI. *IEEE Syst J* (2021) 15: 68–76. doi:10.1109/JSYST.2020.2964033
13. Wang J-Y, Qiu Y, Lin S-H, Wang J-B, Wang Q, and Zhang B. Performance Analysis and Improvement for Secure VLC with SLIPT and Random Terminals. *IEEE Access* (2020) 8:73645–58. doi:10.1109/ACCESS.2020.2988470
14. Zedini E, Soury H, and Alouini M-S. On the Performance Analysis of Dual-Hop Mixed FSO/RF Systems. *IEEE Trans Wireless Commun* (2016) 15: 3679–89. doi:10.1109/TWC.2016.2524685
15. Yang L, Hasna MO, and Gao X. Performance of Mixed RF/FSO with Variable Gain over Generalized Atmospheric Turbulence Channels. *IEEE J Select Areas Commun* (2015) 33:1913–24. doi:10.1109/JSAC.2015.2432471
16. Soleimani-Nasab E, and Uysal M. Generalized Performance Analysis of Mixed RF/FSO Cooperative Systems. *IEEE Trans Wireless Commun* (2016) 15: 714–27. doi:10.1109/TWC.2015.2477400
17. Pan X, Ran H, Pan G, Xie Y, and Zhang J. On Secrecy Analysis of DF Based Dual Hop Mixed RF-FSO Systems. *IEEE Access* (2019) 7:66725–30. doi:10.1109/ACCESS.2019.2914227
18. Lei H, Dai Z, Park K-H, Lei W, Pan G, and Alouini M-S. Secrecy Outage Analysis of Mixed RF-FSO Downlink SWIPT Systems. *IEEE Trans Commun* (2018) 66:6384–95. doi:10.1109/TCOMM.2018.2865944
19. Lei H, Dai Z, Ansari IS, Park K-H, Pan G, and Alouini M-S. On Secrecy Performance of Mixed RF-FSO Systems. *IEEE Photon J.* (2017) 9:1–14. doi:10.1109/JPHOT.2017.2723422
20. Lei H, Luo H, Park K-H, Ren Z, Pan G, and Alouini M-S. Secrecy Outage Analysis of Mixed RF-FSO Systems with Channel Imperfection. *IEEE Photon J.* (2018) 10:1–13. doi:10.1109/JPHOT.2018.2835562
21. Wang J-B, Hu Q-S, Wang J, Chen M, and Wang J-Y. Tight Bounds on Channel Capacity for Dimmable Visible Light Communications. *J Lightwave Technol* (2013) 31:3771–9. doi:10.1109/JLT.2013.2286088
22. Simon MK, and Alouini MS. *Digital Communication over Fading Channels*. 2nd ed., Vol. 95. Hoboken, New Jersey: John Wiley & Sons (2005).
23. Jeffrey A, and Zwillinger D. *Table of Integrals, Series, and Products*. Amsterdam, Netherlands: Elsevier (2007).
24. Komine T, and Nakagawa M. Fundamental Analysis for Visible-Light Communication System Using LED Lights. *IEEE Trans Consumer Electron* (2004) 50:100–7. doi:10.1109/TCE.2004.1277847
25. Yin L, and Haas H. Physical-layer Security in Multiuser Visible Light Communication Networks. *IEEE J Select Areas Commun* (2018) 36:162–74. doi:10.1109/JSAC.2017.2774429
26. Wang J-Y, Liu C, Wang J-B, Wu Y, Lin M, and Cheng J. Physical-layer Security for Indoor Visible Light Communications: Secrecy Capacity Analysis. *IEEE Trans Commun* (2018) 66:6423–36. doi:10.1109/TCOMM.2018.2859943
27. Ai Y, Mathur A, Cheffena M, Bhatnagar MR, and Lei H. Physical Layer Security of Hybrid Satellite-FSO Cooperative Systems. *IEEE Photon J* (2019) 11:1–14. doi:10.1109/JPHOT.2019.2892618

**Conflict of Interest:** The authors declare that the research was conducted in the absence of any commercial or financial relationships that could be construed as a potential conflict of interest.

**Publisher's Note:** All claims expressed in this article are solely those of the authors and do not necessarily represent those of their affiliated organizations, or those of the publisher, the editors and the reviewers. Any product that may be evaluated in this article, or claim that may be made by its manufacturer, is not guaranteed or endorsed by the publisher.

frontiers in Physics

ORIGINAL RESEARCH
published: 26 August 2021
doi: 10.3389/fphy.2021.731405

# A Cost-Efficient RGB Laser-Based Visible Light Communication System by Incorporating Hybrid Wavelength and Polarization Division Multiplexing Schemes

*CAI Xiang-Peng**

*Navigation college, Quanzhou Normal University, Quanzhou, Fujian, China*

Visible light communication (VLC) has been proven a promising technology to counter the limitations of radio frequency (RF) communication technology such as high interference and high latency issues. VLC offers high bandwidth as well as immunity to interference from other electromagnetic spectrums. Due to these features, VLC can be an excellent solution for biomedical and healthcare applications for transmission of body sensor signals and other crucial patient information. In this work, a highly efficient VLC system is designed to transmit six channels, with each one carrying 10 Gbps of data, over a 500 m optical fiber link and a 200 cm VLC link. To make the VLC system cost effective, simple and efficient on-off keying (OOK) (non-return to zero) is used as the encoding scheme. Moreover, to further enhance the capacity and bandwidth of the proposed VLC system, hybrid wavelength division multiplexing (WDM) and polarization division multiplexing (PDM) schemes are incorporated by using red, green, and blue lasers. The reported results show the successful transmission of all channels (6 × 10 Gbps) over 500 m optical fiber and 200 cm of VLC link.

**Keywords: visible light communication, wavelengh-division multiplexing (WDM), polarization division multiplexing (PDM), on off keying, biomedical application**

OPEN ACCESS

***Edited by:***
*Santosh Kumar,*
*Liaocheng University, China*

***Reviewed by:***
*Muhammad Saadi,*
*University of Central Punjab, Pakistan*
*Jawad Raza,*
*National College of Business Administration and Economics, Pakistan*

***Correspondence:**
*CAI Xiang-Peng*
*cxp263263@163.com*

***Specialty section:***
*This article was submitted to Optics and Photonics, a section of the journal Frontiers in Physics*

***Received:*** *27 June 2021*
***Accepted:*** *05 July 2021*
***Published:*** *26 August 2021*

***Citation:***
*Xiang-Peng CAI (2021) A Cost-Efficient RGB Laser-Based Visible Light Communication System by Incorporating Hybrid Wavelength and Polarization Division Multiplexing Schemes. Front. Phys. 9:731405. doi: 10.3389/fphy.2021.731405*

## INTRODUCTION

Incessant demand of higher data rates and multifold user support in existing networks has forced researchers to look beyond radio frequencies (RF), which are bandwidth-limited, toward optical wireless systems (OWC) that offer nearly unlimited bandwidth (>400 THz) via mounting an infrared and ultraviolet region of the electromagnetic spectrum [1]. Among different employed OWC systems, the visible light communication (VLC) system stands out as an apt future solution for terrestrial communication due to its ubiquitous influence and as light-emitting diodes (LEDs) are readily engaged in innumerable commercial applications ranging from lighting systems to multimedia display units in offices as well as homes, vehicles, and mobile phones. The VLC system offers innumerable features that consist of energy-efficient operation, higher data rates, zero RF or electromagnetic interference, and a physical layer of data security [2, 3]. Even with so many advantages, LEDs have a limited data rate due to strong internal polarization fields in common c-plane LEDs and hence are not considered suitable for higher speeds (in the gigabit range) [4–6]. Newly developed micro-LEDs offer a higher data rate in the order of 3 Gbps, but due to low illumination levels their use as light sources is not appropriate [7, 8]. On the other hand, laser diodes (LDs) have a high modulation bandwidth and high output power that allow them

to be better candidates for proposing an optimum solution in a high-speed and long-reach VLC system [9]. Hu et al. displayed a VLC link with the link range of 300 m by using a 650-*nm* laser diode and data rate of 10 Mbps [10]. Another group of researchers reported construction of a WDM-VLC system over a link range of 10 m using red and green lasers with a 500 Mbps data rate [11]. Another work reported using a 450-nm laser diode and QAM-OFDM-based VLC over a range of 5 m for a data rate of 9 Gbps [12]. Wei et al. [13] demonstrated a RGB laser diode-based VLC system over a bidirectional 1 m. Yeh et al. [14] demonstrated a 1,250 Mbps VLC system using a yellow phosphorous LD over a range of 1 m. Advanced modulation formats such as OFDM or QAM used with VLC systems are proved to be better in terms of high data rate but with increased cost and complexity of the system. In order to keep the system at minimal cost, on-off keying (OOK) is proved to be efficient in terms of low complexity and cost effectiveness. In 2016, researchers demonstrated a 2-m VLC link with a data rate of 266 Kbps using OOK [15]. In 2017, Lu et al. reported a GaN-based VLC system employing NRZ-OOK with a 600 Mbps data rate over a transmission range of 0.6 m [16]. For harnessing VLC with indoor white lightning, a new type of red, green, and blue (RGB) LDs are employed. In 2011, researchers reported highly bright white light generated from LDs by mixing red, green blue, and yellow light components [17]. To enhance data rate, researchers have employed various multiplexing techniques namely wavelength division multiplexing (WDM), multiple input multiple output (MIMO), and polarization division multiplexing (PDM). In 2015 [18], Tsonev et al. proposed a 100 Gbps system using an RGB LD-based WDM-VLC system by using 36 parallel data streams. Chi et al. [19] in 2016 proposed and demonstrated an RGB LED-based VLC system with a PS-Manchester and WDM scheme with a data rate of 3.35 Gbps and a 1 m indoor transmission range. Another study in 2017 [20] proposed a WDM-based VLC system over a 1 m span with a data rate of 4.05 Gbps. Recently in 2020 [21], Messa et al. experimentally demonstrated detection of a WDM-VLC signal via a single photodiode with the use of MIMO signal processing. These studies conclude that implementation of RGB-LD-based WDM-VLC can significantly enhance system performance. For further enhancement of the capacity of the proposed system, another multiplexing technique is proposed such as the PDM technique. In 2015 [22], Kwoon et al. experimentally demonstrated enhancement of data rate up to 2.04 Gbps by employing the PDM scheme in the VLC system. Hsu et al. in 2018 [23] demonstrated an OFDM-PDM based VLC system with a data rate of 1.4 Gbps. Recently in 2020 [24], authors have demonstrated the transmission of 1.2 Gbps and 1.12 Gbps of data over a 3 and 4 m free space link by using dual polarized green and blue LED-based light streams. On the other hand, hybrid multiplexing schemes are used by many researchers to increase the bandwidth and capacity of optical communication systems [25–35]. In this work, the OOK modulation technique is used for realization of a low-cost VLC system. Further to increase the capacity of the system, hybrid WDM and PDM multiplexing schemes are proposed using RGB LDs. The remainder of this paper is described as follows: *Hybrid WDM-PDM-VLC Modeling* shows the modeling of the proposed WDM-PDM VLC system, *Results and Discussion* represents the results and discussion, and *Conclusion* shows the overall conclusion of this work.

## HYBRID WAVELENGTH DIVISION MULTIPLEXING-POLARIZATION DIVISION MULTIPLEXING-VISIBLE LIGHT COMMUNICATION MODELING

The schematic diagram of the proposed 6 × 10 Gbps hybrid WDM-PDM-based VLC system, modelled in OptiSystem software, is shown **Figure 1**.

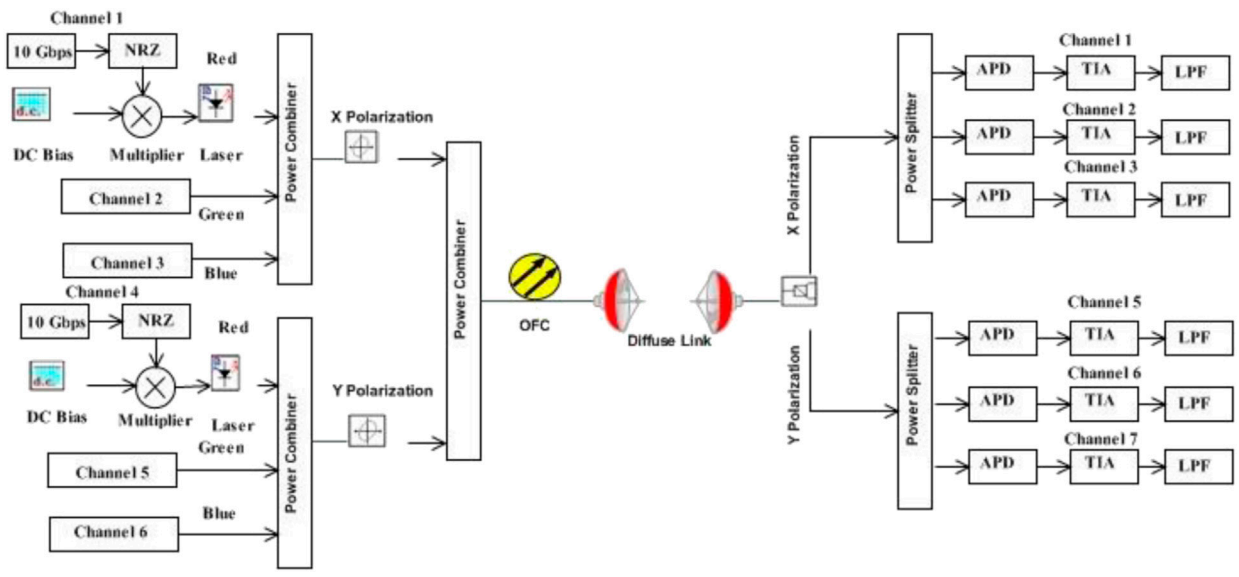


**FIGURE 1 |** Transmission of six channels over a VLC link using hybrid WDM and PDM schemes.

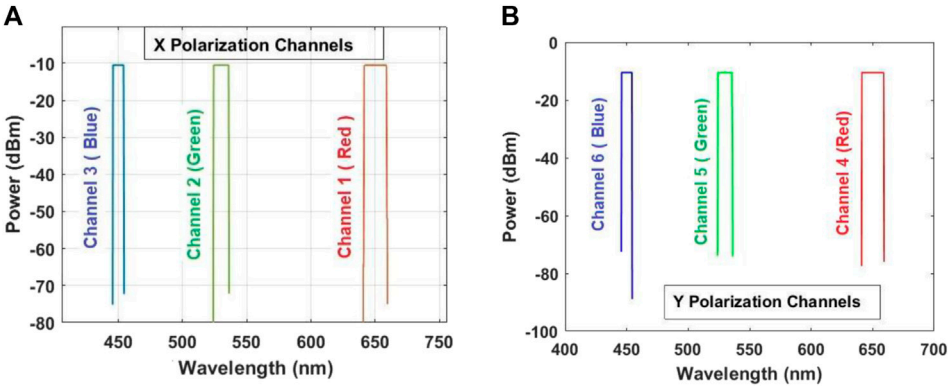


**FIGURE 2 |** Measured optical spectrum, **(A)** X polarization channels, **(B)** Y polarization channels.

**TABLE 1 |** Modeling parameters for the proposed WDM-PDM-VLC link.

| Component | Parameters | Value |
|---|---|---|
| Laser diode | Wavelengths | 650 nm, 530 nm, and 450 nm |
| | Extension ratio | 10 dB |
| | Power | 0 dB |
| | Linewidth | 10 MHz |
| DC bias generator | Amplitude | 1 a.u |
| Diffuse link | Transmitter half angle | 60 deg |
| | Irradiance half angle | 0 deg |
| | Incidence half angle | 0 deg |
| | Detection surface area | 1 $cm^2$ |
| | Optical concentration factor | 1 deg |
| | Index concentration factor | 1.5 |
| | Propagation delay | 0 ps/m |
| Avalanche photo diode | Gain` | 3 |
| | Responsivity | 1A/W |
| | Ionization ration | 0.9 |
| | Dark current | 10 nA |
| | Thermal noise | 100e-024 W/Hz |
| TIA | Voltage gain | 600 Ω |
| | Input capacitance | 3 pF |
| | Feedback resistance | 0.01e+009 |
| Simulation window | Sequence length | 1,024 |
| | Samples per bit | 64 |
| | No. of samples | 65,536 |

As shown in **Figure 1**, six channels are transmitted by using hybrid WDM and PDM schemes. A red laser (650 nm), green laser (530 nm), and blue laser (450 nm) are used for the WDM scheme whereas X polarization with a $0^0$ phase shift in azimuthal and Y polarization with a $90^0$ phase shift in azimuthal are used for the PDM scheme. Each channel generates a pseudo random bit stream of 10 Gbps which is encoded using the NRZ modulation format and then the signal is fed to the directly modulated (DM) laser. To ensure the laser diode (LD) operates above threshold, a direct current (D.C.) bias is fed into it. The output of the first three channels are combined together and subjected to a $0^0$ azimuthal phase (X polarization) whereas the output of the remaining three channels are combined and fed to the $90^0$ phase shift in azimuthal (Y polarization). **Figure 2** represents the measured optical spectrum of three channels for each state (X and Y polarizations).

These outputs from each polarization state are combined and transmitted over 500 m optical fiber and diffuser. For the modeling of the diffuse link, the transmitter source is assumed as a Lambertian disk which is irradiating a detector surface located at an axial distance *h* from the source. The Lambertian order which is based on transmitter half angle can be expressed mathematically as follows [36]:

$$m = \frac{-\log 2}{log\left[\cos\left(Transmitter\ half\ angle\right)\right]} \tag{1}$$

whereas optical concentrator gain can be mathematically expressed as:

$$Gain = \frac{I^2}{\sin\left(CR\right)^2} \tag{2}$$

where $I$ is defined as the internal refractive index of the lens and $CR$ is defined as the field of view.

At the receiver side, a polarization splitter is used to de-multiplex the polarized signal for each state (X and Y polarizations). For each receiving channel, an avalanche photo diode (APD) is used to detect the light from the diffuser. The down-sampling frequency of APD is set to corresponding wavelengths transmitted at the transmitter side. The output of APD is amplified by using a *trans*-impedance amplifier followed by the low pass filter (LPF). At the output of LPF, bit error rate BER) is measured by using a bit error tester. The received signal at the receiver is expressed as [37, 38]:

$$y\left(t\right) = x\left(t\right) \otimes h\left(t\right) + n\ \left(t\right) \tag{3}$$

where $y(t)$ represents the received signal, $x(t)$ represents the transmitted signal, $h(t)$ represents the impulse response of the transmitted signal, and $n(t)$ represents the additive noise which is composed of shot noise, thermal noise, and dark current noise. However, in this work, background noise is assumed to be negligible. The other modeling parameters considered for the proposed WDM-PDM-VLC link are mentioned in **Table 1**.

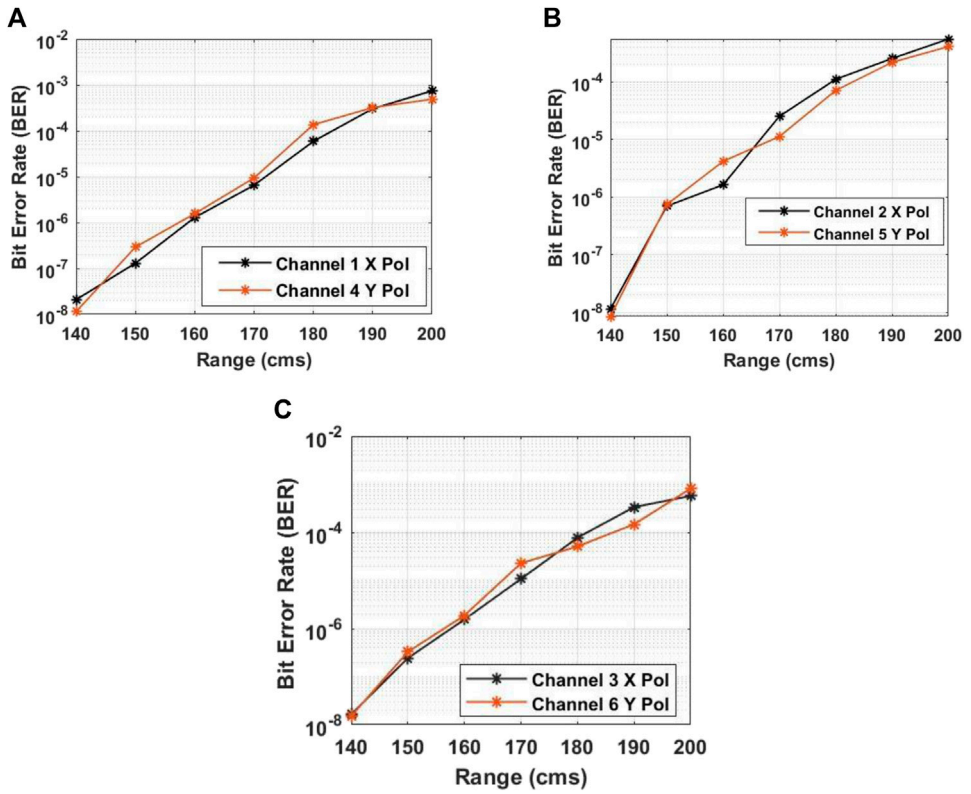


**FIGURE 3 |** Measured BER for each polarization channel, **(A)** channels 1 and 4, **(B)** channels 2 and 5, and **(C)** channels 3 and 6.

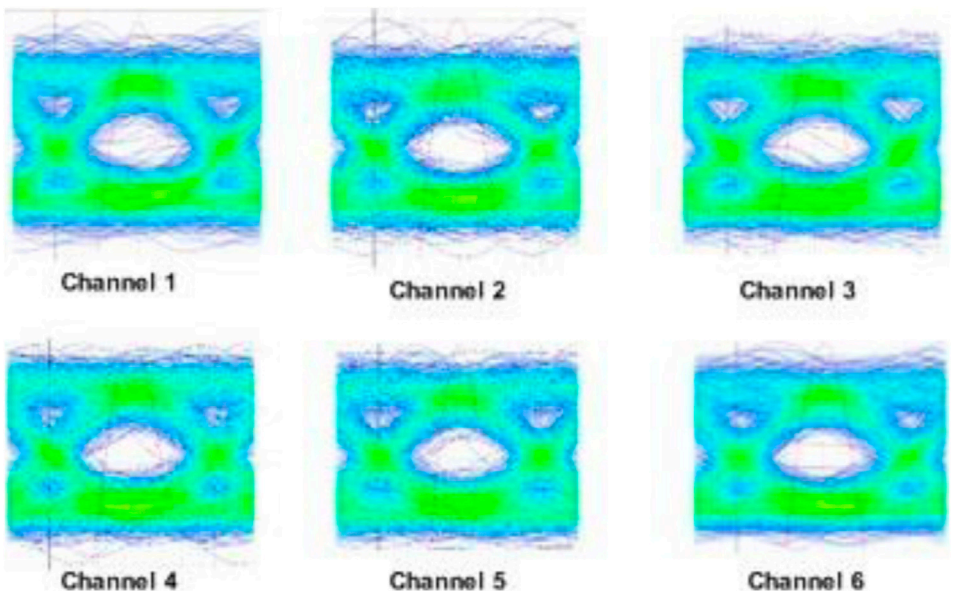


**FIGURE 4 |** Computed eye diagrams for all channels at the diffuse link of 200 cm.

## RESULTS AND DISCUSSION

This section comprises the results from the modeling of the proposed WDM-PDM-VLC link. BER is used to evaluate the performance of the proposed WDM-PDM-VLC link. **Figure 3** shows the computed BER for all the channels with respect to diffuse link range. It shows that channel 1 which is transmitted over 640 nm with X polarization and channel 4 which is transmitted over 650 nm with Y polarization achieved a BER of less than $10^{-3}$ at a diffuse link range of 200 cm. For channel 1 and channel 4, the BER is measured as $10^{-8}$ at the diffuse link range of 140 cm. As the diffuse link ranges increase further, BER also increases for both channels. Similarly, channel 2 (transmitted over 530 nm with X polarization) and channel 5 (transmitted over 530 nm with Y polarization) have also achieved a BER less than $10^{-3}$.

Channels 2 and 4 have also measured a BER of $10^{-8}$ at the diffuse link range of 140 cm. The values of BER for channel 3 which is transmitted over 430 nm with X polarization and channel 6 which is transmitted over 430 nm with Y polarization are also measured as less than $10^{-3}$. This satisfies the acceptable BER threshold of $\approx 10^{-3}$ as per FCC limits. The measured eye diagrams for all the channels at the diffuse link range of 200 cm are shown in **Figure 4**. It shows that eye diagrams are open enough to receive the 10 Gbps of data over a diffuse link up to 200 cm with an acceptable BER.

## CONCLUSION

In this work, six channels each carrying 10 Gbps of NRZ-encoded data are transmitted over a 500 m optical fiber and diffuse link range up to 200 cm by incorporating WDM and PDM schemes. RGB lasers are used for the WDM scheme whereas X and Y polarization states are used for the PDM scheme. For X polarization, an azimuthal phase shift of $0^0$ is used whereas for Y polarization, a azimuthal phase shift of $90^0$ is used. The performance of the proposed WDM-PDM-VLC link is evaluated in terms of BER and eye diagrams. The reported results show the successful transmission of all channels over a 500 m optical fiber link and 200 cm diffuse link with an acceptable BER $\approx 10^{-3}$. This work can be extended by considering real-time test beds to transmit high-speed data over a VLC link.

## DATA AVAILABILITY STATEMENT

The raw data supporting the conclusion of this article will be made available by the authors, without undue reservation.

## AUTHOR CONTRIBUTIONS

CX-P has conceived of the presented idea, designed the model and performed the computations and wrote the original draft.

## FUNDING

This work is supported by Education and Scientific research project of middle and young teachers in Fujian (JAT200541).

## REFERENCES

1. Rahaim MB, and Little TDC. Toward Practical Integration of Dual-Use VLC within 5G Networks. *IEEE Wireless Commun* (2015) 22:97–103. doi:10.1109/mwc.2015.7224733
2. Ghassemlooy Z, Alves LN, Zvanovec S, and Khalighi M-A. In: *Visible Light Communications: Theory and Applications*. Florida, United States: CRC Press (2017).
3. Chaudhary S, Tang X, Ghassemlooy Z, Lin B, Wei X, and Liaw S-K. "A 3× 25 Mbps WDM-Ro-VLC System for Amateur Radio Applications," in *2019 2nd West Asian Colloquium Opt Wireless Commun (Wacowc)*, 2019. p. 6–10.
4. Lin C, Lin B, Tang X, Shen X, Xu J, and Chaudhary S. A Blur Equalization Method for Screen-To-Camera Based Optical Camera Communications. In: *18th International Conference on Optical Communications and Networks*, 2019. Huangshan, China: ICOCN) (2019). p. 1–3. doi:10.1109/icocn.2019.8934224
5. Lin C, Lin B, Tang X, Zhou Z, Zhang H, and Chaudhary S. Multilevel Brightness Modulation Scheme Based on a LED Array and K-Means Clustering Algorithm for Optical Camera Communications. In: *17th International Conference on Optical Communications and Networks (ICOCN2018)* (2019). p. 1104820. doi:10.1117/12.2522829
6. Lin C, Lin B, Tang X, Zhou Z, Zhang H, Chaudhary S, et al. An Indoor Visible Light Positioning System Using Artificial Neural Network. In: *Asia Communications and Photonics Conference*, 2018. Hangzhou, China: ACP) (2018). p. 1–3. doi:10.1109/acp.2018.8596227
7. Rashidi A, Monavarian M, Aragon A, Rishinaramangalam A, and Feezell D. Nonpolar ${m}$ -Plane InGaN/GaN Micro-scale Light-Emitting Diode with 1.5 GHz Modulation Bandwidth. *IEEE Electron Device Lett* (2018) 39:520–3. doi:10.1109/led.2018.2803082
8. Ferreira RXG, Xie E, McKendry JJD, Rajbhandari S, Chun H, Faulkner G, et al. High Bandwidth GaN-based Micro-LEDs for Multi-Gb/s Visible Light Communications. *IEEE Photon Technol Lett* (2016) 28:2023–6. doi:10.1109/lpt.2016.2581318
9. Wu T-C, Chi Y-C, Wang H-Y, Tsai C-T, Huang Y-F, and Lin G-R. Tricolor R/G/B Laser Diode Based Eye-Safe White Lighting Communication beyond 8 Gbit/s. *Sci Rep* (2017) 7:11. doi:10.1038/s41598-017-00052-8
10. Hu G-y., Chen C-y., and Chen Z-q. Free-space Optical Communication Using Visible Light. *J Zhejiang Univ - Sci A* (2007) 8:186–91. doi:10.1631/jzus.2007.a0186
11. Lin W-Y, Chen C-Y, Lu H-H, Chang C-H, Lin Y-P, Lin H-C, et al. 10m/500Mbps WDM Visible Light Communication Systems. *Opt Express* (2012) 20:9919–24. doi:10.1364/oe.20.009919
12. Chi Y-C, Hsieh D-H, Tsai C-T, Chen H-Y, Kuo H-C, and Lin G-R. 450-nm GaN Laser Diode Enables High-Speed Visible Light Communication with 9-Gbps QAM-OFDM. *Opt Express* (2015) 23:13051–9. doi:10.1364/oe.23.013051
13. Wei L-Y, Hsu C-W, Chow C-W, and Yeh C-H. "20.231 Gbit/s Tricolor red/green/blue Laser Diode Based Bidirectional Signal Remodulation Visible-Light Communication System," *Photon Res* (2018) 6:422. doi:10.1364/PRJ.6.000422
14. Yeh C-H, Chow C-W, and Wei L-Y. 1250 Mbit/s OOK Wireless White-Light VLC Transmission Based on Phosphor Laser Diode. *IEEE Photon J.* (2019) 11:1–5. doi:10.1109/jphot.2019.2911411
15. Che F, Wu L, Hussain B, Li X, and Yue CP. A Fully Integrated IEEE 802.15. 7 Visible Light Communication Transmitter with On-Chip 8-W 85% Efficiency Boost LED Driver. *J Lightwave Technology* (2016) 34:2419–30.
16. Lu Z, Tian P, Chen H, Baranowski I, Fu H, Huang X, et al. Active Tracking System for Visible Light Communication Using a GaN-based Micro-LED and NRZ-OOK. *Opt Express* (2017) 25:17971–81. doi:10.1364/oe.25.017971
17. Neumann A, Wierer JJ, Davis W, Ohno Y, Brueck SRJ, and Tsao JY. Four-color Laser white Illuminant Demonstrating High Color-Rendering Quality. *Opt Express* (2011) 19:A982–A990. doi:10.1364/oe.19.00a982

18. Tsonev D, Videv S, and Haas H. Towards a 100 Gb/s Visible Light Wireless Access Network. *Opt Express* (2015) 23:1627–37. doi:10.1364/oe.23.001627
19. Chi N, Zhang M, Zhou Y, and Zhao J. 3375-Gb/s RGB-LED Based WDM Visible Light Communication System Employing PAM-8 Modulation with Phase Shifted Manchester Coding. *Opt Express* (2016/09/19 2016) 24: 21663–73. doi:10.1364/oe.24.021663
20. Zhang M, Shi M, Wang F, Zhao J, Zhou Y, Wang Z, et al. 4.05-Gb/s RGB LED-Based VLC System Utilizing PS-Manchester Coded Nyquist PAM-8 Modulation and Hybrid Time-Frequency Domain Equalization. In: *Optical Fiber Communication Conference*. California, United States: W2A (2017). p. 42. doi:10.1364/ofc.2017.w2a.42
21. Messa A, Cossu G, Presi M, Schidl S, Schneider-Hornstein K, Zimmermann H, et al. Detecting WDM Visible Light Signals by a Single Multi-Color Photodiode with MIMO Processing. *Opt Lett* (2020/03/01 2020) 45:1160–3. doi:10.1364/ol.385641
22. Kwon D-H, Kim S-J, Yang S-H, and Han S-K. Optimized Pre-equalization for Gigabit Polarization Division Multiplexed Visible Light Communication. *Opt Eng* (2015) 54:076101. doi:10.1117/1.oe.54.7.076101
23. Hsu C-W, Yeh C-H, and Chow C-W. Using Adaptive Equalization and Polarization-Multiplexing Technology for Gigabit-Per-Second Phosphor-LED Wireless Visible Light Communication. *Opt Laser Technology* (2018) 104:206–9. doi:10.1016/j.optlastec.2018.02.004
24. Yang Y-C, Yeh C-H, Liaw S-K, Chow C-W, Hsu W-H, and Wang B-Y, "Analysis and Investigation of Dual-Polarized Color LED Based Visible Light Communication System, in *Photonics*. 2021. p. 210. doi:10.3390/photonics8060210
25. Amphawan A, Chaudhary S, Neo T-K, Kakavand M, and Dabbagh M. Radio-over-free Space Optical Space Division Multiplexing System Using 3-core Photonic crystal Fiber Mode Group Multiplexers. In: *Wireless Networks* (2020). p. 1–15. doi:10.1007/s11276-020-02447-4
26. Chaudhary S, and Amphawan A. High-speed MDM-Ro-FSO System by Incorporating Spiral-Phased Hermite Gaussian Modes. *Photon Netw Commun* (2018) 35:374–80. doi:10.1007/s11107-017-0752-6
27. Chaudhary S, Lin B, Tang X, Wei X, Zhou Z, Lin C, et al. 40 Gbps-80 GHz PSK-MDM Based Ro-FSO Transmission System. *Opt Quant Electron* (2018) 50:321. doi:10.1007/s11082-018-1592-z
28. Chaudhary S, and Sharma A. 6 X 20Gbps Long Reach WDM-PI Based High Altitude Platform Inter-satellite Communication System. *Int J Computer Appl* (2015) 122. doi:10.5120/21861-5192
29. Chaudhary S, Sharma A, and Chaudhary N. 6× 20 Gbps Hybrid WDM–PI Inter-satellite System under the Influence of Transmitting Pointing Errors. *J Opt Commun* (2016) 37:375–9. doi:10.1515/joc-2015-0099
30. Chaudhary S, Sharma A, Tang X, Wei X, and Sood P. A Cost Effective 100 Gbps FSO System under the Impact of Fog by Incorporating OCDMA-PDM Scheme. *Wireless Personal Commun* (2020) 1–10. doi:10.1007/s11277-020-07784-3
31. Chaudhary S, Tang X, Sharma A, Lin B, Wei X, and Parmar A. A Cost-Effective 100 Gbps SAC-OCDMA-PDM Based Inter-satellite Communication Link. *Opt Quant Electron* (2019) 51:148. doi:10.1007/s11082-019-1864-2
32. Chaudhary S, Tang X, and Wei X. Comparison of Laguerre-Gaussian and Donut Modes for MDM-WDM in OFDM-Ro-FSO Transmission System. *AEU - Int J Electronics Commun* (2018) 93:208–14. doi:10.1016/j.aeue.2018.06.024
33. Sarangal H, Singh A, Malhotra J, and Chaudhary S. A Cost Effective 100 Gbps Hybrid MDM-OCDMA-FSO Transmission System under Atmospheric Turbulences. *Opt Quant Electron* (2017) 49:184. doi:10.1007/s11082-017-1019-2
34. Upadhyay KK, Shukla NK, and Chaudhary S. A High Speed 100 Gbps MDM-SAC-OCDMA Multimode Transmission System for Short Haul Communication. *Optik* (2020) 202:163665. doi:10.1016/j.ijleo.2019.163665
35. Upadhyay KK, Srivastava S, Shukla NK, and Chaudhary S. High-speed 120 Gbps AMI-WDM-PDM Free Space Optical Transmission System. *J Opt Commun* (2019) 40:429–33. doi:10.1515/joc-2017-0086
36. Kahn JM, and Barry JR. Wireless Infrared Communications. *Proc IEEE* (1997) 85:265–98. doi:10.1109/5.554222
37. Qiu Y, Chen H-H, and Meng W-X. Channel Modeling for Visible Light Communications-A Survey. *Wirel Commun Mob Comput* (2016) 16:2016–34. doi:10.1002/wcm.2665
38. Serena P, and Bononi A. An Alternative Approach to the Gaussian Noise Model and its System Implications. *J Lightwave Technology* (2013) 31: 3489–99.

**Conflict of Interest:** The author declares that the research was conducted in the absence of any commercial or financial relationships that could be construed as a potential conflict of interest.

**Publisher's Note:** All claims expressed in this article are solely those of the authors and do not necessarily represent those of their affiliated organizations, or those of the publisher, the editors and the reviewers. Any product that may be evaluated in this article, or claim that may be made by its manufacturer, is not guaranteed or endorsed by the publisher.

frontiers in Physics

ORIGINAL RESEARCH
published: 27 August 2021
doi: 10.3389/fphy.2021.744160

# Developing Cost-Effective and High-Speed 40 Gbps FSO Systems Incorporating Wavelength and Spatial Diversity Techniques

*Satish Kumar Modalavalasa*[1], *Rajan Miglani*[1], *Sushank Chaudhary*[2]*, *Faisel Tubbal*[3,4] and *Raad Raad*[3]

[1]Department of Electrical and Electronics Engineering, Lovely Professional University, Punjab, India, [2]Quanzhou Institute of Equipment Manufacturing, Chinese Academy of Sciences, Jinjiang, China, [3]School of Electrical, Computer and Telecommunication Engineering, University of Wollongong, Wollongong, NSW, Australia, [4]Technological Projects Department, The Libyan Center for Remote Sensing and Space Science, Tripoli, Libya

Free-space optical (FSO) communication systems are being anticipated to offer promising alternatives to existing radio networks in delivering high-speed data access to end-users. Ease of installation, robust features, and cost-effective operation have been the hallmark of FSO systems, and these features will play an obvious role in deciding the ways in which futuristic smart communication models will operate. Despite these arrays of features, FSO links suffer severe performance degradation due to channel-induced impairments caused by atmospheric effects such as rain, haze, and fog. In this work, we have investigated and compared the performance of 40 Gbps FSO links for different channel conditions ranging from clear weather to severe attenuation by incorporating spatial and wavelength diversity as performance booster techniques. The use of an erbium-doped fiber amplifier (EDFA) with FSO links has also been proposed here. Using performance metrics like bit error rate (BER) and eye patterns, it has been found that the use of EDFA not only helps in compensating for the link losses but also aids in realizing an all-optical processing based last-mile access system. The proposed FSO system will be capable of bridging the existing backbone fiber networks with end-users with minimal changes to the existing hardware regime, thereby proving to be extremely cost-effective in sharp contrast to radio-frequency generations which require major infrastructure overhaul.

**Keywords: MIMO, free-space optics, wavelength diversity, EDFA amplification, cooperative diversity**

OPEN ACCESS

***Edited by:***
*Santosh Kumar,*
*Liaocheng University, China*

***Reviewed by:***
*A. K. M. Sharoar Jahan Choyon,*
*University of New Mexico, United States*
*Dharmendra Kumar,*
*Madan Mohan Malaviya University of Technology, India*

***Correspondence:**
*Sushank Chaudhary*
*sushankchaudhary@gmail.com*

***Specialty section:***
*This article was submitted to Optics and Photonics, a section of the journal Frontiers in Physics*

***Received:*** *19 July 2021*
***Accepted:*** *27 July 2021*
***Published:*** *27 August 2021*

***Citation:***
*Modalavalasa SK, Miglani R, Chaudhary S, Tubbal F and Raad R (2021) Developing Cost-Effective and High-Speed 40 Gbps FSO Systems Incorporating Wavelength and Spatial Diversity Techniques. Front. Phys. 9:744160. doi: 10.3389/fphy.2021.744160*

## INTRODUCTION

Often labeled as wireless optical fibers, optical wireless communication has huge potential to serve the ever-increasing demand for high-speed data services. Over the last few decades, the per capita demand for data has increased manifolds, and this pattern only seems to become more and more aggressive in the near future [1–3]. The recent surge in popularity of free-space optical (FSO) systems as a commercial alternative to radio-frequency (RF) systems is attributed to a wide range of advantages such as 1) massive bandwidth of the order of THz, 2) adaptability with present-day radio systems as RF/FSO systems [4, 5], 3) license-free spectrum, 4) negligible interference from the adjacent carriers, and 5) plug–play character which makes the FSO systems very convenient to install and relocate [6, 7]. FSO systems have begun witnessing commercial and large-scale deployment in

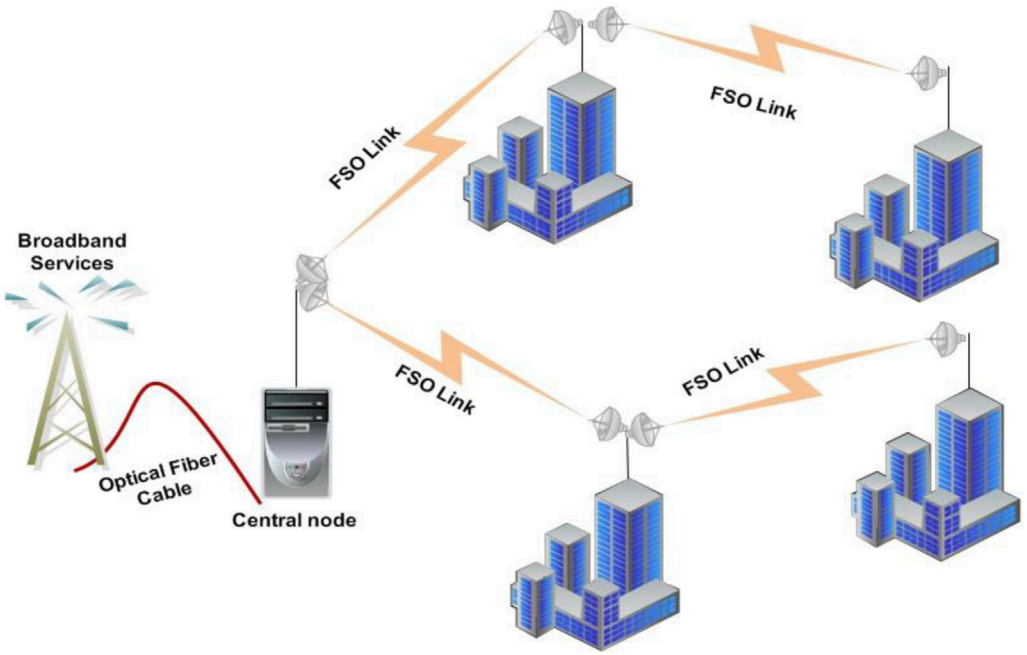


**FIGURE 1 |** Architecture of FSO for broadband services.

cases of disaster management, LAN connectivity within campuses, vehicle-to-vehicle communication, and backhaul services for futuristic cellular networks [8, 9]. However, it is anticipated that FSO links can play a game-changer role in cost-effective connectivity for far-flung areas, especially in developing countries like India in the fields of e-governance, telemedicine, and education [10]. **Figure 1** shows the typical FSO topology for providing broadband services in urban areas where the new installation of optical fiber is not possible. The underlying principle of end-user privacy in contemporary networks is based on data encryption and user authentication achieved through a complex mechanism of exchange of digital keys [11, 12]. The FSO channel link is a line-of-sight (LoS) communication model that requires straight-line alignment of transmitter and receiver for data transmission. This restricts the system from a wide-range broadcast of the information signal.

The role of the transmission channel is, therefore, extremely critical in determining the efficiency and uptime of communication links [13]. Additionally, the selection of the type of transmitter and transmitted wavelength is an important criterion in FSO systems. An optical wireless system consists of a light source that could be LED or LASER for transmitting optically modulated information over the channel, while on the receiver side, a photodiode collects the photons to reproduce the original information. However, it is relevant to point out that the received signal experiences absorption and scattering due to the presence of atmospheric phenomena such as rain, fog, and haze which causes signal degradation, thus leading to loss of transmitted information [4, 6]. Equally devastating is signal fading induced by the inhomogeneities present in the transmitting medium [8, 11]. The presence of these inhomogeneities leads to fluctuations in refractive indices along with the propagating medium, hence leading to a situation known as atmospheric turbulence that causes beam divergence and scintillation effects [7, 14]. Various mitigation techniques like the higher order modulation schemes, diversity combining, channel-coding schemes, and spectrum slicing have been proposed in the past to improve the performance and robustness of the FSO system [15–20]. The transmitter diversity, along with channel-coding techniques, deals with the performance enhancement by reducing the erroneous data induced by the characteristics of the fading channel [17, 21–23]. The use of different modulation schemes can also alter the system performance as it has been reported that higher modulation schemes like binary phase-shift keying (BPSK) are more immune to channel adversities than the conventional on-off keying (OOK) schemes [19, 21]. The diversity in the channel brings in the concept of multiple input multiple output (MIMO), which uses multiple transmitters/receivers to improve the transmission reliability [24, 25]. The adoption of diversity schemes not only proved to be a major cost-effective factor in improving the link reliability in FSO systems but also helps improve bandwidth capacity, quality factor (Q), and reduced latency [26–28]. Additional technology measures such as coherent reception, higher modulation techniques, artificial intelligence, and machine learning have also been suggested in recent literature as catalysts to enhance link performance in FSO systems; however, on the flip side, the technological intricacy and budgetary constraints of these techniques are major deterrents toward their commercial implementation [29, 30]. As a well-evolved and matured technology, spatial diversity and wavelength diversity proved to be efficient measures in countering

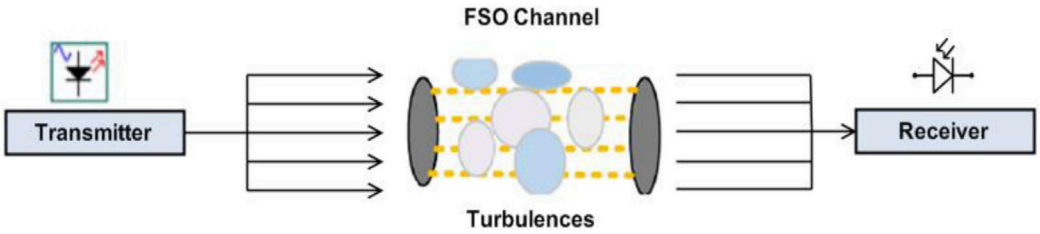


**FIGURE 2 |** Illustration for cooperative diversity using the MIMO technique.

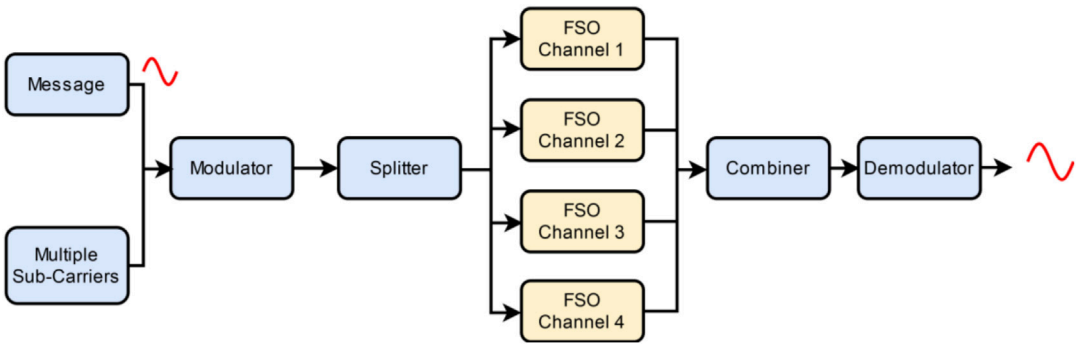


**FIGURE 3 |** Block diagram of an FSO MIMO system with multiple subcarriers.

atmospheric adversities [28]. Diversity schemes are also known for their ability to deliver higher throughput and low bit error rates [30]. The usage of readily available hardware, which is easy to install and comes with improved end factors, cuts down the overall cost for the setup, as the available resources are being shared for multiuser scenarios [31].

The organization of this paper is as follows: *Link Design Analytics* contains the description of the methodology that has been employed to design the link described in *System Description* and the analysis of the link for various quality factors is elaborated in *Results and Discussion*, followed by the conclusive report of the paper in *Conclusion*.

## LINK DESIGN ANALYTICS

Conventionally, MIMO systems have been used to increase the data transmission rates; as in FSO systems, the MIMO approach has been used to improve the probability of correct data reception by transmitting the same information through multiple lines-of-sight channels [32–36]. The systematic idea of approach toward MIMO is illustrated in **Figure 2**, which explains the transmission of information through different atmospheric conditions. The optical carriers used in MIMO systems are tuned at a particular wavelength, and this selection could affect the system properties. Therefore, wavelength selection is a crucial part of the FSO system design [37, 38].

Wavelength diversity refers to the use of different transmission wavelengths and these diverse subcarriers, while propagating through channels, undergo different levels of fading [39, 40]. However, if the information received over different channels is combined at the receiver, the detection probability of correct information increases [37]. The block diagram for the proposed MIMO-FSO system is illustrated in **Figure 3**, where the different blocks of the system are placed according to their functional positions. Since wavelength diversity and spatial diversity have a proven track as performance enhancement catalysts in the FSO system [24], in this paper, the use of wavelength diversity along with MIMO systems has been proposed to provide seamless last-mile connectivity.

It is important to underline here that FSO signals have to deal with absorption, scattering, and geometrical loss of orientation while propagating. All of these factors contribute toward atmospheric attenuation, which can be summed as follows [32, 38]:

$$(dB/km) = (absorption) + (scattering) + (geometrical) \quad (1)$$

The geometric losses include the attenuation due to beam divergence and the transmitter positioning with the receiver. The attenuation phenomenon can be described using Beer-Lambert law that states the relationship between transmitted wavelength and link distance, which is represented as follows [14, 41]:

$$(\lambda, L) = \exp(\lambda, L) \quad (2)$$

where λ is the wavelength, L is the propagation distance, and H is the loss coefficient. Kim's attenuation model for FSO links to relate attenuation with visibility and operational wavelength is as follows [34, 42]:

**TABLE 1 |** Various atmospheric conditions and their parametric values.

| Atmospheric conditions | Attenuation (dB/km) |
|---|---|
| Clear Sky | 0.468 |
| Rainy/Partially Hazy | 12 |
| Dense fog/Very Hazy | 25 |

$$\alpha\,(dB/Km) = \frac{3.91}{V}\left(\frac{\lambda}{550}\right)^{-q} \tag{3}$$

where V refers to meteorological visibility, λ is the operating wavelength, and q is the factor that depends on the size distribution of atmospheric particles. When it comes to attenuation that occurs due to rain, the equation based on the rate of rainfall can be given as follows [40]:

$$\alpha\,(dB/Km) = 1.07 \times R^{0.67} \tag{4}$$

Here, the rate of rainfall is represented by R and the attenuation depends proportionally on this factor.

The atmospheric effects that are considered for the FSO channel corresponding to various attenuation values are presented in **Table 1**, which will be used as a reference for the analysis of the proposed link [19].

Although the inclusion of multiple sub-carrier wavelengths helps improve reception quality, it forms a wideband signal after multiplexing and consumes greater amounts of bandwidth in contrast to the transmission of data over a single carrier [40, 43]. This tradeoff between system resources and performance is an exception for next-generation optical networks as optical links by default possess huge spectral bandwidth [36, 44]. Also, the wavelength diversified MIMO-FSO system could be improved further by incorporating the erbium-doped fiber amplifier (EDFA)–based link compensation [45]. The detailed block diagram of the EDFA optical amplifier working for the input optical signal is shown in **Figure 4** [46]. Usage of EDFA is helpful in avoiding the losses that incur due to change of signal from optical to electrical, and vice versa, for the purpose of amplification [47].

The optical signal traveling through the open-air medium is collected at a certain point using the collimating lens setup, which is then filtered with a bandpass filter that restricts the outlier wavelengths and forwards the filter output through a gain optimizer setup. The setup helps amplify the signal by an input from a pump LASER emitting the wavelength that is the same as the output toned by a bandpass filter [48]. The coupled output is passed through erbium-doped fiber that helps in the amplification of optical signals without loss of intended information. At the final stage, the signal may be passed through another optical bandpass filter which gives the final amplified signal as an output [46]. Later, a set of collimating optics can be used to transmit the modulated optical signal for detection and further analysis. This practice not only helps in delivering an all-optical system that is capable of compensating for the loss of signal quality due to atmospheric adversities but also readily integrates with the existing optical backbone networks [48–50].

The novelty and scope of the proposed link analyzed and reported in the paper can be summarized as follows:

- Design of a hybrid MIMO-FSO incorporating wavelength diversity over the adverse channel
- Performance analysis of a hybrid model when extended for the use of multiple users
- Gauging performance behavior of the proposed hybrid FSO when coupled with an EDFA-based all-optical post-amplification

## SYSTEM DESCRIPTION

The proposed link presented in this paper and illustrated in **Figure 5** has been designed and analyzed using a specialized link design tool, OptiSystem™ 16.0, which is an industry graded experimental platform [51]. The parameters used for the link design and subsequent investigation have been stated in **Table 2**. As shown in **Figure 5**, the pseudo-random bit sequence generator (PRBS) produces a stream of bits at the rate of 10 Gbps which are then modulated using Mach Zehnder (MZ) modulator before being relayed over the FSO channel.

Meanwhile, continuous wave (CW) laser generates four subcarriers of different wavelengths, which act as optical carriers for modulation. The modulated signal is propagated

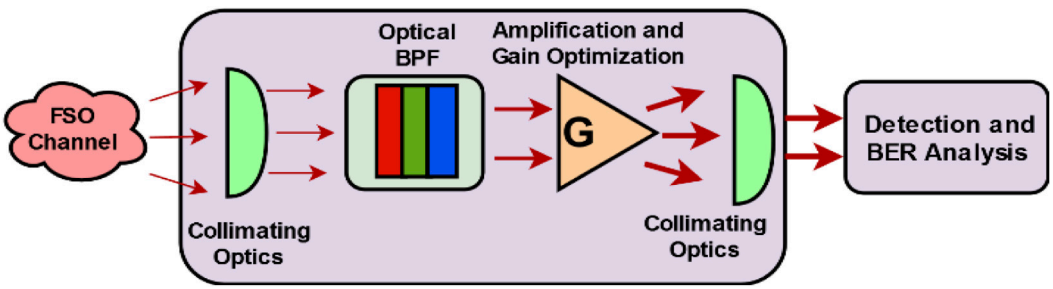


**FIGURE 4 |** Block diagram of an EDFA optical amplifier.

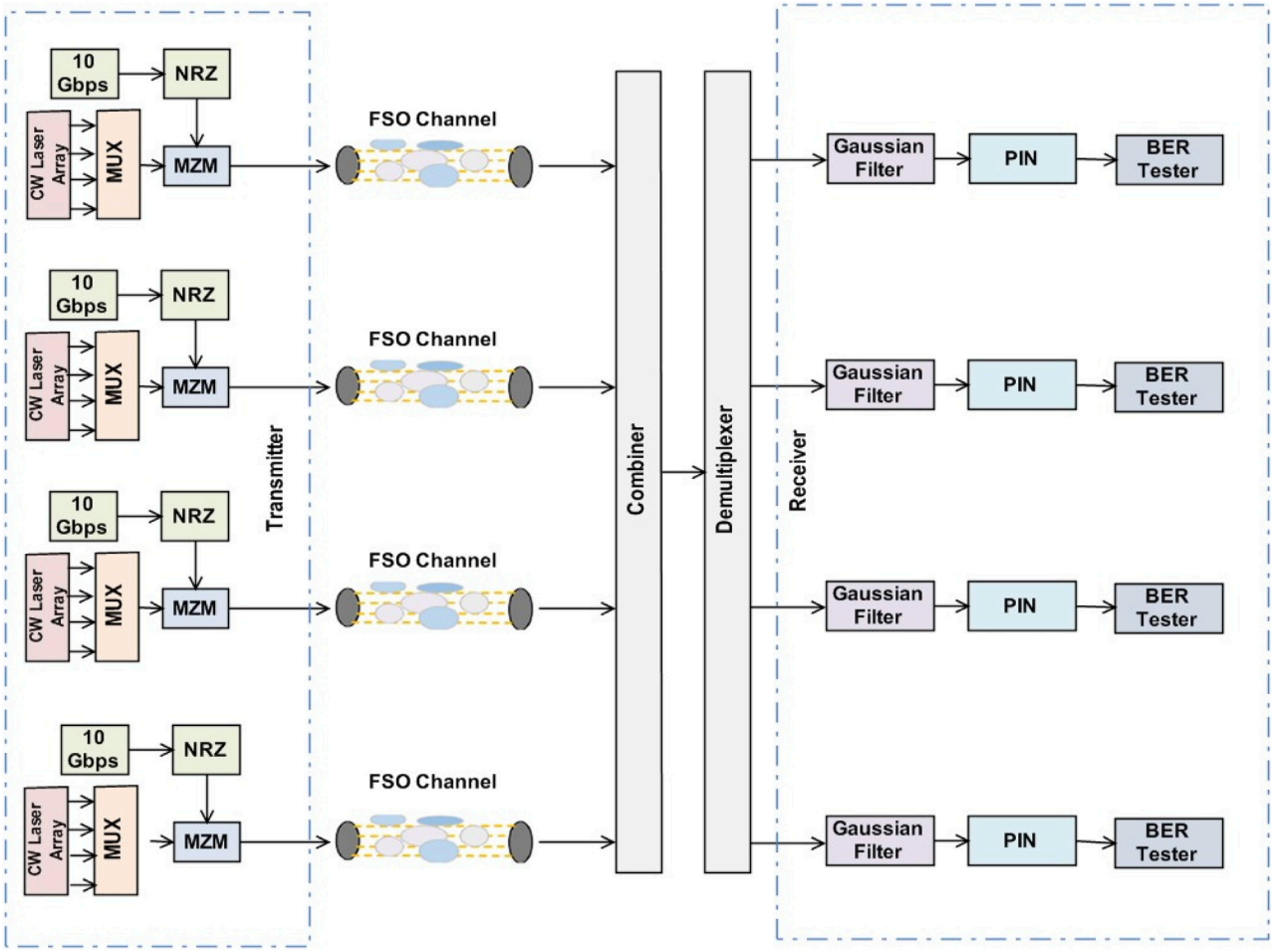


**FIGURE 5 |** Proposed system layout of an MIMO FSO communication setup.

**TABLE 2 |** Link design parameters.

| Aspect | Range |
|---|---|
| Transmitted power | 0–20 dB m [2, 38] |
| Bit rate | 10 Gbps [4] |
| Sample rate | $3.2 \times 10^{11}$ Hz [38] |
| Coding scheme | NRZ [5] |
| Line width | 10 MHz |
| Channel modelling parameters | |
| Samples per bit | 32 [33] |
| Light source | Continuous laser [18] |
| Optical modulator | Mach-Zehnder [7] |
| Transmission wavelength | 1,550–1,553 nm [17] |
| Link range | 100–2000 m [34, 40] |
| Channel spacing | 1 nm [19] |
| Attenuation (α) | 0.468–25 dB/mm [4] |
| Scintillation model | Gamma-Gamma [6] |
| Refraction index parameter ($C_n^2$) | $5 \times 10^{-15}$ $m^{-2/3}$ [33] |
| Photodiode | PIN [11] |
| Responsivity | 1 A/W [24] |
| Transmitter aperture diameter | 5 cm [38] |
| Receiver aperture diameter | 20 cm [35] |
| Bessel filter order | 4 [36] |

over four different paths (spatial diversity), thus leading to a hybrid diversity FSO link, which includes both wavelength and spatial diversity.

The receiver side uses a power combiner to collect the information received from four independent channels. This process essentially improves the prospectus of recovering reliable information by combining and averaging out power received from different paths [50]. In our investigation, we have set the number of simultaneous users to four while the rest of the procedure related to signal modulation and transmission over diversified wavelengths remains the same. This arrangement helps in incrementing the transmission rates without any significant compromise on the quality of signal reception. The system presented in **Figure 5** is capable of attaining transmission rates of up to 40 Gbps (4 × 10 Gbps). The comparative analysis of the proposed link over different sets of test conditions has been presented in *Results and Discussion*.

As set out in **Table 2**, the proposed link has been investigated for its performance behavior for the link range varying between

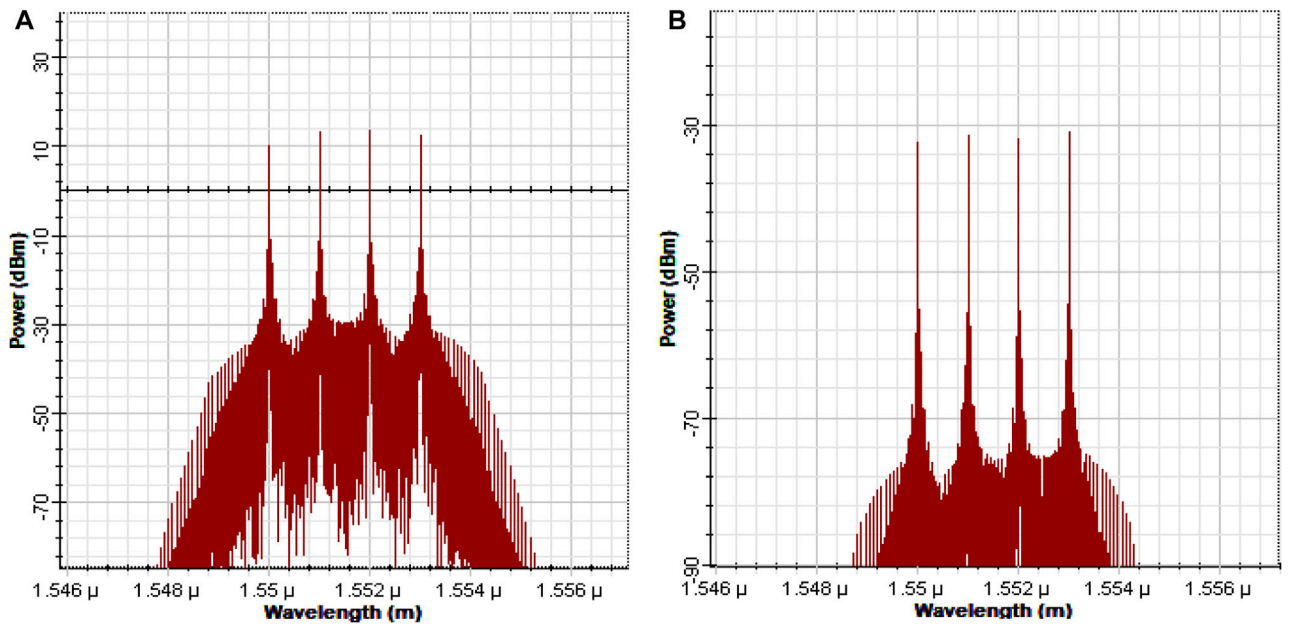


**FIGURE 6 |** The spectrum of signal **(A)** transmitter section and **(B)** receiver section.

1,000 and 2000 m, while the channel turbulence is characterized by the gamma-gamma model. The PDF of its intensity I is given as follows [24]:

$$P(I) = \frac{2(\alpha\beta)^{(\alpha+\beta)/2}}{\Gamma(\alpha)\Gamma(\beta)} I^{\frac{(\alpha+\beta)}{2}-1} K_{\alpha-\beta}\left(2\sqrt{\alpha\beta I}\right), I > 0 \quad (5)$$

where $\Gamma(.)$ is the gamma function, K (α,β) is the Bessel function of second order and the parameter I is referred to as irradiative intensity of the transmission, while α and β characterize the presence of small and large turbulence cells in the channel and are mathematically related as follows:

$$\alpha = \frac{1}{\exp\left[\frac{0.49\,\sigma^2}{\left(1+1.11\,\sigma^{\frac{12}{5}}\right)^{\frac{7}{6}}}\right] - 1} \quad (6)$$

$$\beta = \frac{1}{\exp\left[\frac{0.51\,\sigma^2}{\left(1+0.69\,\sigma^{\frac{12}{5}}\right)^{\frac{5}{6}}}\right] - 1} \quad (7)$$

where the value of $\sigma^2$ represents variance is associated with the respective turbulence consideration for the available distribution of channel elements.

The turbulence regime within the channel can be characterized by the parameter $C_n^2$, also known as the refractive index structure parameter. The mathematical formulation for the static turbulence can be represented as follows [1]:

$$C_n^2 = \left[7.9 \times 10^{-5}\left(\frac{P}{T}\right)\right]^2 C_t^2 \quad (8)$$

where $C_t^2$ represents the mean square temperature between two points within the link, T is the absolute temperature in Kelvin, and P is pressure in Pascals. The values of $C_n^2 \approx 10^{-15}\ m^{-2/3}$ symbolize a moderate turbulence regime [6]. The received signals are filtered using a Bessel filter of order four and then analyzed for quality reception using a bit error analyzer. Various design properties such as transmission bit rate, symbol rate, choice of wavelength, modulation type, and signal recovery setup act as key influencing factors that dictate the system performance.

## RESULTS AND DISCUSSION

The proposed link has been investigated for a different set of parameters described previously in **Tables 1** and **2**. The spectrum of the signal captured at the transmitter and then at the receiver is shown in **Figures 6A,B** respectively. The captured spectrum also characterizes a hybrid FSO link wherein the data is transmitted over four different optical sub-carriers with wavelengths in the range of 1,550–1,553 nm. In this particular case, the receiver is 2000 m away from the transmitter while the link attenuation is 12 dB/km. Analysis of **Figures 6A,B** illustrates a comparative decrease in power levels of all four carriers after propagating through the FSO channel.

In contrast to the transmission power, the received signal shows degraded power levels that are attributed to channel losses like scattering and absorption. It is imperative to mention here that the transmission power levels cannot be increased beyond a certain threshold value due to the limitation imposed by underlying opto-electronics. Hence transmission power cannot be used as a mitigation tool to overcome link losses. Moreover, keeping in view the eye and skin

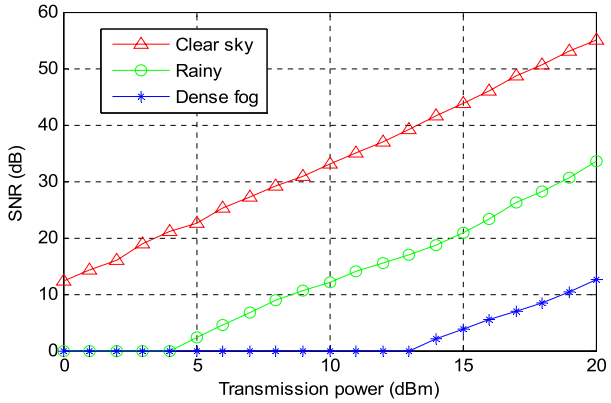


**FIGURE 7 |** Graph of SNR v/s transmitted power for different atmospheric conditions.

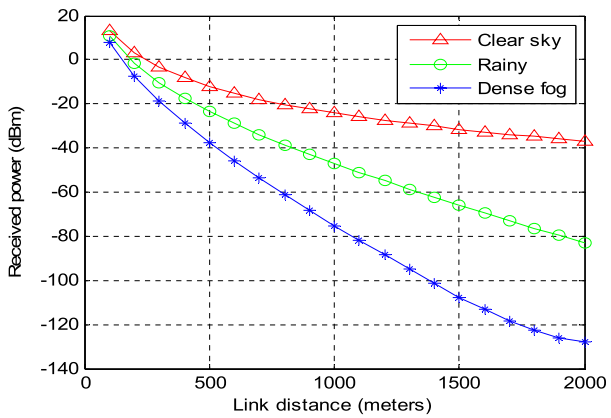


**FIGURE 8 |** Relation between received signal power and link distance.

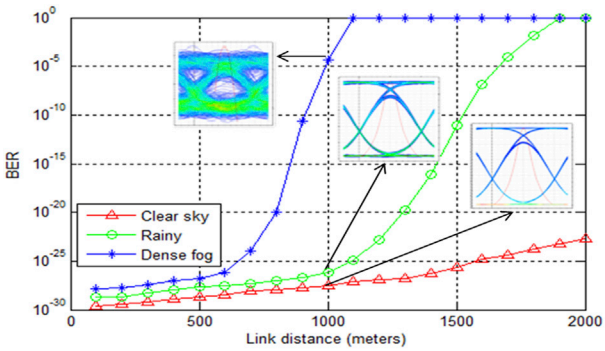


**FIGURE 9 |** Relationship between received BER and link distance for various atmospheric conditions.

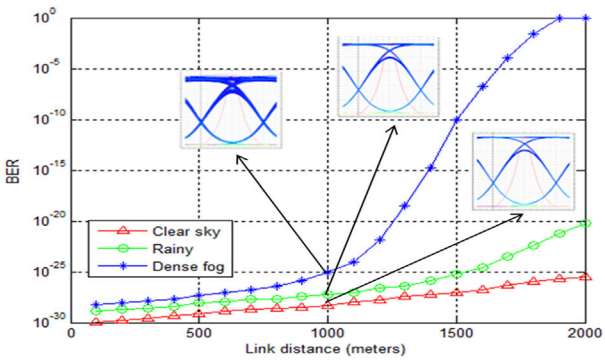


**FIGURE 10 |** Relationship between received BER and link distance at various atmospheric conditions with EDFA.

safety standards set by different governing agencies, the transmission powers must be within the prescribed human eye safe limits.

**Figure 7** indicates the pattern of signal to noise ratio (SNR) observed for the proposed system for variable transmission power while the link length is 1,000 m. It can be seen here that with the increase in transmission power, the performance of the link, i.e., achievable SNR, improves. Previously, transmission power solely cannot be used as a mitigation factor due to eye safety regulation. Hence, for the same reason, we have proposed wavelength and spatial diversity to complement our strategy in delivering cost-viable and high-speed FSO links that can address the needs of last-mile connectivity. From **Figure 7**, we also observe that for transmission power of 15 dB m, the SNR recorded at the receiver reaches 43 dB (approximately) under ideal channel conditions, while under adverse weather conditions, the recorded SNR nose dives to approximately 4 dB.

**Figure 8** highlights the relation between received signal power and link distance for different meteorological conditions. It can be clearly seen here that as on expected lines, the received power degrades as link distance increases. For the link range of 1,000 m, the received power reduces from −21 dB m to −78 dB m (approx.) as link attenuation increases from 0.468 dB/km to 25 dB/km, respectively.

The relationship between link distance and bit error rate (BER) under different atmospheric conditions is presented in **Figure 9**, where we observe that under clear atmospheric conditions, i.e., when link attenuation is 0.468 dB/km, the BER of the proposed system is recorded to be around $2.62 \times 10^{-28}$, while the link range is 1,000 m. However, as the link conditions worsen (25 dB/km), the BER increases to $4.3 \times 10^{-5}$ for the same link conditions. The BER degradation is further confirmed by the eye diagrams for different link conditions shown in **Figure 9**. The eye-opening patterns determine the quality of the received signal. The improved eye-opening (eye height) then corresponds to a successful reception of the transmitted information. The distortions in the eye diagrams indicate loss of coherence which may lead to possibly erroneous detection.

The BER performance analysis of the proposed system using EDFA-based post-amplification is presented in

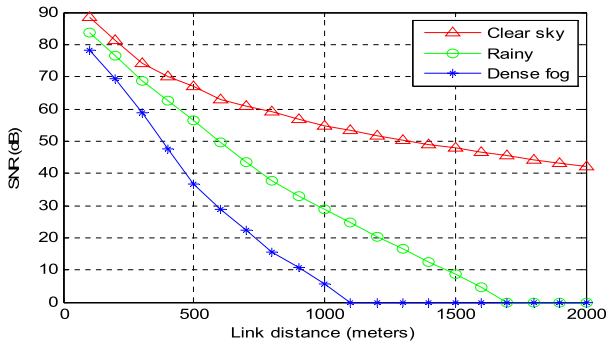


**FIGURE 11 |** Relationship between SNR and link distance for different meteorological conditions without link compensation.

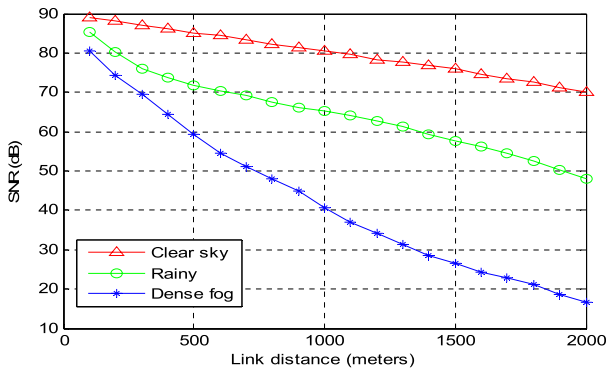


**FIGURE 12 |** Relationship between SNR and link distance for different meteorological conditions while using EDFA.

**Figure 10**. As seen from **Figure 10**, a consistently low BER pattern is observed for clear weather conditions for the entire link range of up to 2000 m. This is followed by a near similar performance under moderately adverse channel conditions. However, significant BER performance variation is witnessed when severe channel conditions prevail. For extremely adverse channel conditions (25 dB/km) and forward error correction (FEC)-BER limit of $10^{-9}$ as a performance benchmark, it can be seen from **Figure 9** that an EDFA-compensated FSO link delivers a link range of approximately 1,520 m. This link range is approximated 600 m more than the uncompensated FSO link shown in **Figure 9**, which is found to be restricted to a link range of 926 m under similar link conditions. The relation between the signal to noise ratio (SNR dB) and link range is presented in **Figure 11** and **Figure 12** for various weather conditions. At reference link range of 1,000 m, the uncompensated FSO link shown in **Figure 11** is found to deliver SNR (dB) of 54.87 dB, 28.77, and 5.48 dB for clear, moderate, and severe channel conditions, respectively. The performance enhancement in SNR (dB) using the post-amplification using EDFA can be ascertained from **Figure 12**, wherein SNR value of 40.7 dB can be achieved at the link range of 1,000 m under extremely adverse channel conditions (25 dB/km).

Thus, a significant improvement in the received SNR compared to the uncompensated FSO link is witnessed here. Moreover, from **Figure 12**, it can be observed further that for a link distance of 2000 m, the EDFA-compensated link delivers decent SNR while the uncompensated link is rendered useless under similar channel conditions. The detailed comparison of link performances illustrated in **Figure 10 Figure 11** has been complied in **Table 3**. It can be seen from **Table 3** that BER of EDFA-compensated FSO links degrades merely by a factor of $10^{-3}$ from $10^{-29}$ under clear weather conditions to $10^{-26}$ for severe conditions. The uncompensated link, however, witnesses massive deviations as BER are found to vary between $10^{-28}$ and $10^{-5}$. Similar improvements in Q-factor and receiver SNR (dB) can also be observed for compensated FSO links in contrast to non-compensated links over varied atmospheric conditions. The admissible values of FEC (Forward Error Correction) for BER is ~$10^{-3}$, and for SNR, it is ~20 dBm, for which the communication system proves to be working fine. FEC refers to the performance threshold which must be achieved by the system in order to provide end-to-end connectivity for voice and data related services [52, 53]. As mentioned in **Table 3**, the BER and SNR rates of the proposed link are pretty much beyond the FEC threshold limits.

## CONCLUSION

In this paper, we have presented a holistic analysis of the proposed hybrid FSO link that uses the principle of spatial and wavelength diversity to overcome atmosphere-induced limitations. It has been observed that the link performance degrades as the attenuation levels increase, thus rendering the link useless. However, the inclusion of EDFA-based all-optical compensation plays a critical role in propelling the performance under adverse channel conditions. For attenuation levels as high as 25 dB/km and with the use of EDFA, the proposed link witnesses link range improvement of approximately 600 m

**TABLE 3 |** Output values of different parameters at 1,000 m link distance.

| Attenuation (dB/km) | Without EDFA | | | With EDFA | | |
|---|---|---|---|---|---|---|
| | Q-factor | SNR (dB) | BER | Q-factor | SNR (dB) | BER |
| 0.468 | 11.26 | 54.87 | $2.62 \times 10^{-28}$ | 13.46 | 80.62 | $5.14 \times 10^{-29}$ |
| 12 | 10.2 | 28.77 | $6.82 \times 10^{-27}$ | 11.08 | 65.2 | $5.81 \times 10^{-28}$ |
| 25 | 5.68 | 5.48 | $4.3 \times 10^{-5}$ | 7.48 | 40.7 | $9.14 \times 10^{-26}$ |

over uncompensated FSO links considering the FEC-BER limit as a benchmark. Also, the proposed link incorporates multiple users, thus delivering an effective transmission rate of 40 Gbps. At this data rate, the proposed link is a promising answer to deliver cost-effective, high-speed data access to end-users. The possible future scope of the work could be its inclusion in future mobile generations of 5G and 6G as it is capable of delivering applications like virtual calling and holographic streaming. With aspects of decreased latency and increased reliability, the proposed system could be part of future driverless vehicles in which the response time should be minimal. Open access internet provision at public places with increased range and connectivity could be another possible future implementation of the proposed work.

## DATA AVAILABILITY STATEMENT

The raw data supporting the conclusions of this article will be made available by the authors without undue reservation.

## AUTHOR CONTRIBUTIONS

SM: writing original draft, methodology, simulations; RM: writing—review and editing, software, supervision; SC: writing—review and editing, data curation, supervision; FT: visualization, data curation; RR: formal analysis, project administration.

## REFERENCES


1. Khalighi MA, and Uysal M. Survey on Free Space Optical Communication: A Communication Theory Perspective. *IEEE Commun Surv Tutorials* (2014) 16: 2231–58. doi:10.1109/COMST.2014.2329501
2. Chaudhary S, Tang X, Sharma A, Lin B, Wei X, and Parmar A. A Cost-Effective 100 Gbps SAC-OCDMA-PDM Based Inter-satellite Communication Link. *Opt Quant Electron* (2019) 51(5):1–10. doi:10.1007/s11082-019-1864-2
3. Arezumand H, Zamiri-Jafarian H, and Soleimani-Nasab E. Exact and Asymptotic Analysis of Partial Relay Selection for Cognitive RF-FSO Systems with Non-zero Boresight Pointing Errors. *IEEE Access* (2019) 7: 58611–25. doi:10.1109/ACCESS.2019.2914480
4. Wani MY, Pathak H, Kaur K, and Kumar A. Free Space Optical Communication System under Different Weather Conditions. *J Opt Commun* (2019) 72:52–4. doi:10.1515/joc-2019-0064
5. Upadhya A, Dwivedi VK, and Singh G. Multiuser Diversity for Mixed RF/FSO Cooperative Relaying in the Presence of Interference. *Opt Commun* (2019) 442:77–83. doi:10.1016/j.optcom.2019.02.040
6. Miglani R, and Malhotra JS. Investigation on R-S Coded Coherent OFDM Free Space Optical (CO-OFDM-FSO) Communication Link over Gamma-Gamma Channel. *Wireless Pers Commun* (2019) 109:415–35. doi:10.1007/s11277-019-06571-z
7. Kaur S, Bhardwaj P, and Bhardwaj P. Performance of FSO Communication in the Atmospheric Turbulence for Various Modulation Schemes. *Ijett* (2018) 55(3):142–7. doi:10.14445/22315381/ijett-v55p226
8. Of N, and La ADE. Communications. *Revolutionary Russia* (2008) 21(2):237. doi:10.1080/09546540802461498
9. Jeyaseelan J, Sriram Kumar D, and Caroline BE. Disaster Management Using Free Space Optical Communication System. *Photon Netw Commun* (2019) 39: 1–14. doi:10.1007/s11107-019-00865-9
10. Torkestani SS, Sahuguede S, Julien-Vergonjanne A, and Cances JP. Indoor Optical Wireless System Dedicated to Healthcare Application in a Hospital. *IET Commun* (2012) 6(5):541–7. doi:10.1049/iet-com.2010.1116
11. Bhattacharya I. Advances in Optical Science and Engineering. *Springer Proc Phys* (2015) 166:467–77. doi:10.1007/978-81-322-2367-2
12. Odeyemi KO, and Owolawi PA. Physical Layer Security in Mixed Rf/FSO System under Multiple Eavesdroppers Collusion and Non-collusion. *Opt Quant Electron* (2018) 50:1. doi:10.1007/s11082-018-1565-2
13. Upadhyay KK, Shukla NK, and Chaudhary S. A High Speed 100 Gbps MDM-SAC-OCDMA Multimode Transmission System for Short Haul Communication. *Optik* (2020) 202:163665. doi:10.1016/j.ijleo.2019.163665
14. Ghassemlooy Z, and Popoola WO. *Terrestrial Free-Space Optical Communications, Mobile and Wireless Communications Network Layer and Circuit Level Design*. SA Fares and F Adachi, Editors. IntechOpen (2010). doi:10.5772/7698
15. Chaudhary S, Tang X, Wei X, Tang X, and Wei X. Comparison of Laguerre-Gaussian and Donut Modes for MDM-WDM in OFDM-Ro-FSO Transmission System. *AEU - Int J Electronics Commun* (2018) 93(6): 208–14. doi:10.1016/j.aeue.2018.06.024
16. Amphawan A, Chaudhary S, and Chan VWS. 2x20 Gbps - 40 GHz OFDM Ro-FSO Transmission with Mode Division Multiplexing. *JEOS:RP* (2014) 9:1–6. doi:10.2971/jeos.2014.14041
17. Sharma M, Chadha D, and Chandra V. Performance Analysis of MIMO-OFDM Free Space Optical Communication System with Low-Density Parity-Check Code. *Photon Netw Commun* (2016) 32(1):104–14. doi:10.1007/s11107-015-0579-y
18. Majumdar AK. Mitigation Techniques for Improved Free-Space Optical (FSO) Communications. *Springer Ser Opt Sci* (2015) 186.
19. Israr A, Israr A, Khan F, and Khan F. Optimal Modulation Technique for MIMO FSO Link. *Wireless Pers Commun* (2019) 109(695)–714. doi:10.1007/s11277-019-06586-6
20. Zou L, Wang L, Xing C, Cui J, and Zhao S. Turbulence Mitigation with MIMO Equalization for Orbital Angular Momentum Multiplexing Communication. *Int Conf Wirel Commun Signal Process WCSP* (2016) 1(1):1–4. doi:10.1109/WCSP.2016.7752455
21. Miglani R, and Malhotra JS. Statistical Analysis of Fso Links Employing Multiple Transmitter/receiver Strategy over Double-Generalized and Gamma-Gamma Fading Channel Using Different Modulation Techniques. *J Opt Commun* (2019) 40(3):295–305. doi:10.1515/joc-2017-0066
22. Das A, Bag B, Bose C, and Chandra A. Performance Analysis of MIMO FSO Link with Alamouti Coding and Switch-And-Examine Combining. *Photon Netw Commun* (2018) 36(3):350–60. doi:10.1007/s11107-018-0790-8
23. Fang J, Bi M, Xiao S, Yang G, Liu L, Zhang Y, et al. Polar-coded MIMO FSO Communication System over Gamma-Gamma Turbulence Channel with Spatially Correlated Fading. *J Opt Commun Netw* (2018) 10(11):915–23. doi:10.1364/JOCN.10.000915
24. Abou-Rjeily C. Performance Analysis of FSO Communications with Diversity Methods: Add More Relays or More Apertures?. *IEEE J Select Areas Commun* (2015) 33(9):1890–902. doi:10.1109/JSAC.2015.2432526
25. Vu BT, Thang TC, and Pham AT. BER Analysis of MIMO/FSO Systems Using Rectangular QAM over Gamma-Gamma Channels. *Int Conf Ubiquitous Futur Networks, ICUFN* (2013) 987:370–4. doi:10.1109/ICUFN.2013.6614844
26. Dayal N, Singh P, and Kaur P. Long Range Cost-Effective WDM-FSO System Using Hybrid Optical Amplifiers. *Wireless Pers Commun* (2017) 97:6055–67. doi:10.1007/s11277-017-4826-7
27. Pham TV, Thang TC, and Pham AT. Average Achievable Rate of Spatial Diversity MIMO-FSO over Correlated Gamma-Gamma Fading Channels. *J Opt Commun Netw* (2018) 10(8):662–74. doi:10.1364/JOCN.10.000662
28. Sharda P, and Bhatnagar MR. Diversity-Multiplexing Tradeoff for MIMO-FSO System under Different Transmission Scenarios with Limited Quantized Feedback. *IEEE Access* (2020) 8:114266–86. doi:10.1109/ACCESS.2020.3004135
29. Al-Gailani SA, Mohd Salleh MF, Salem AA, Shaddad RQ, Sheikh UU, Algeelani NA, et al. A Survey of Free Space Optics (FSO) Communication Systems, Links, and Networks. *IEEE Access* (2021) 9:7353–73. doi:10.1109/ACCESS.2020.3048049
30. Huang L, Liu S, Dai P, Li M, Chang G-K, Shi Y, et al. Unified Performance Analysis of Hybrid FSO/RF System with Diversity Combining. *J Lightwave Technol* (2020) 38(24):6788–800. doi:10.1109/JLT.2020.3018125

31. Sarangal H, Singh A, Malhotra J, and Chaudhary S. A Cost Effective 100 Gbps Hybrid MDM-OCDMA-FSO Transmission System under Atmospheric Turbulences. *Opt Quant Electron* (2017) 49:184. doi:10.1007/s11082-017-1019-2
32. Dubey A, and Prakash D. Performance Improvement of FSO Communication System Using MIMO Technique. *Ijitee* (2019) 8(10):3470–2. doi:10.35940/ijitee.j9722.0881019
33. Chatti I, Baklouti F, Chekir F, and Attia R. Comparative Analysis of MIMO-Based FSO and MIMO-Based MGDM Communications. *Opt Rev* (2019) 26: 631–43. doi:10.1007/s10043-019-00537-z
34. Shaker FK, Ali MAA, and Ameer FSA. Utilization of MIMO Concept for Optical Communication System under Fog Condition. Transactions on Electrical Engineering (2019) 17:130–5.
35. Yang P, Zhu J, Xiao Y, and Chen Z. Antenna Selection for MIMO System Based on Pattern Recognition. *Digital Commun Networks* (2019) 5(1):34–9. doi:10.1016/j.dcan.2018.10.001
36. Liu Y, and Li H. Research on Transmission Performance of Multi-Input Multi-Output Free Space Optical Communication System Channel. *Opt Rev* (2019) 26(0):303–9. doi:10.1007/s10043-019-00495-6
37. Shah D, and Kothari D. Performance Analysis of Free Space Optical Link with Wavelength Diversity under Weak and Moderate Turbulence Conditions. *Sens Lett* (2019) 17(2):137–43. doi:10.1166/sl.2019.4058
38. Badar N, Jha RK, and Towfeeq I. Performance Analysis of an 80 (8 × 10) Gbps RZ-DPSK Based WDM-FSO System under Combined Effects of Various Weather Conditions and Atmospheric Turbulence Induced Fading Employing Gamma-Gamma Fading Model. *Opt Quant Electron* (2018) 50(1):1–11. doi:10.1007/s11082-017-1306-y
39. Ding J, Yu S, Fu Y, Ma J, and Tan L. New Approximate and Asymptotic Closed-form Expressions for the Outage Probability and the Average BER of MIMO-FSO System with MRC Diversity Technique over Gamma-Gamma Fading Channels with Generalized Pointing Errors. *Opt Commun* (2020) 456: 124633. doi:10.1016/j.optcom.2019.124633
40. Kumar Giri R, and Patnaik B. Bit Error Rate Performance Analysis of Hybrid Subcarrier Intensity Modulation-Based Fso with Spatial Diversity in Various Weather Conditions. *J Opt Commun* (2019) 40(3):307–14. doi:10.1515/joc-2017-0073
41. Chowdhury R, and Choyon AKMSJ. Design of 320 Gbps Hybrid AMI-PDM-WDM FSO Link and its Performance Comparison with Traditional Models under Diverse Weather Conditions. *J Opt Commun* (2021) 1:0135. doi:10.1515/joc-2020-0135
42. Sharoar Jahan Choyon AKM, and Chowdhury R. Performance Comparison of Free-Space Optical (FSO) Communication Link under OOK, BPSK, DPSK, QPSK and 8-PSK Modulation Formats in the Presence of Strong Atmospheric Turbulence. *J Opt Commun* (2020) 1:1. doi:10.1515/joc-2019-0250
43. Dubey V, Chadha D, and Chandra V. Experimental Validation of Multiple Gain Combiner in Single-Relay Cooperative FSO Communication Systems. *Photon Netw Commun* (2019) 37(1):110–9. doi:10.1007/s11107-018-0800-x
44. Miglani R, and Malhotra JS. Evaluation of Link-Compensated 32 × 40 Gbit/s DWDM Free Space Optical (FSO) Transmission. *J Opt* (2018) 47(4):467–74. doi:10.1007/s12596-018-0484-8
45. Ciaramella E, Arimoto Y, Contestabile G, Presi M, D'Errico A, Guarino V, et al. 1.28 Terabit/s (32x40 Gbit/s) Wdm Transmission System for Free Space Optical Communications. *IEEE J Select Areas Commun* (2009) 27(9): 1639–45. doi:10.1109/JSAC.2009.091213
46. Honde V, Mhatre A, Tonde S, Barkul S, and Pund P. Performance Analysis of WDM Network Based on EDFA Amplifier with Different Pumping Techniques Performance Analysis of WDM Network Based on EDFA Amplifier with. *Int J Recent Innov Trends Comput Commun* (2016) 4(4):480–5.
47. Bayaki E, Michalopoulos DS, and Schober R. EDFA-based All-Optical Relaying in Free-Space Optical Systems. *IEEE Trans Commun* (2012) 60(12):3797–807. doi:10.1109/TCOMM.2012.090512.110198
48. Liu H, Huang B, Zacarias JCA, Wen H, Chen H, Fontaine NK, et al. Turbulence-Resistant FSO Communication Using a Few-Mode Pre-amplified Receiver. *Sci Rep* (2019) 9(1):1–7. doi:10.1038/s41598-019-52698-1
49. Trinh PV, Dang NT, and Pham AT. All-Optical Relaying FSO Systems Using EDFA Combined with Optical Hard-Limiter over Atmospheric Turbulence Channels. *J Lightwave Technol* (2015) 33(19):4132–44. doi:10.1109/JLT.2015.2466432
50. Priyadarshani R, Bhatnagar MR, Bohata J, Zvanovec S, and Ghassemlooy Z. Experimental and Analytical Investigations of an Optically Pre-amplified FSO-MIMO System with Repetition Coding over Non-identically Distributed Correlated Channels. *IEEE Access* (2020) 8:12188–203. doi:10.1109/ACCESS.2020.2964149
51. Zhu J, Xiao X, and Luo Y. An experiment Teaching Method Based on the Optisystem Simulation Platform. *Proc SPIE* (2017) 10452:198. doi:10.1117/12.2269886
52. Nguyen D-N, Bohata J, Komanec M, Zvanovec S, Ortega B, and Ghassemlooy Z. Seamless 25 GHz Transmission of LTE 4/16/64-QAM Signals over Hybrid SMF/FSO and Wireless Link. *J Lightwave Technol* (2019) 37(24):6040–7. doi:10.1109/JLT.2019.2945588
53. Kakati D, and Arya SC. Performance of 120 Gbps Single Channel Coherent DP-16-QAM in Terrestrial FSO Link under Different Weather Conditions. *Optik* (2019) 178:1230–9. doi:10.1016/j.ijleo.2018.10.035


**Conflict of Interest:** The authors declare that the research was conducted in the absence of any commercial or financial relationships that could be construed as a potential conflict of interest.

**Publisher's Note:** All claims expressed in this article are solely those of the authors and do not necessarily represent those of their affiliated organizations, or those of the publisher, the editors and the reviewers. Any product that may be evaluated in this article, or claim that may be made by its manufacturer, is not guaranteed or endorsed by the publisher.

frontiers in Physics

ORIGINAL RESEARCH
published: 31 August 2021
doi: 10.3389/fphy.2021.743545

# Performance Investigation of a High Data Rate Mode Division Multiplexed-Free Space Optics Link Under Harsh Weather Conditions

*Mehtab Singh*[1,2], *Sahil Nazir Pottoo*[3], *Suvidhi*[4], *Sanjeev Dewra*[5], *Rishabh*[6], *Amit Grover*[5]*, *A. Manikandan*[7] *and Anu Sheetal*[8]

[1]Department of Engineering and Technology, Guru Nanak Dev University, Jalandhar, India, [2]Department of Electronics and Communication Engineering, SIET, Amritsar, India, [3]Center for Interdisciplinary Programs, Indian Institute of Technology Hyderabad, Telangana, India, [4]Department of Computer Science and Engineering, Punjab Engineering College (Deemed to be University), Chandigarh, India, [5]Department of Electronics and Communication Engineering, Shaheed Bhagat Singh State University, Ferozepur, India, [6]Department of Computer Application, ABES Engineering College, Ghaziabad, India, [7]Department of Electronics and Communication Engineering, Vivekanandha College of Technology for Women, Tiruchengode, India, [8]Department of Engineering and Technology, Guru Nanak Dev University, Gurdaspur, India

OPEN ACCESS

**Edited by:**
*Santosh Kumar,*
*Liaocheng University, China*

**Reviewed by:**
*Sushank Chaudhary,*
*Quanzhou Institute of Equipment manufacturing, Chinese academy of Sciences, China, China*
*Dr. Shyam Akashe,*
*ITM University, India*

***Correspondence:**
*Amit Grover*
*amitgrover321@gmail.com*

**Specialty section:**
*This article was submitted to Optics and Photonics, a section of the journal Frontiers in Physics*

**Received:** *18 July 2021*
**Accepted:** *27 July 2021*
**Published:** *31 August 2021*

**Citation:**
*Singh M, Pottoo SN, Suvidhi, Dewra S, Rishabh, Grover A, Manikandan A and Sheetal A (2021) Performance Investigation of a High Data Rate Mode Division Multiplexed-Free Space Optics Link Under Harsh Weather Conditions. Front. Phys. 9:743545. doi: 10.3389/fphy.2021.743545*

The requirement of high data rate information transmission is rising exponentially for supporting different services including social networking, web streaming, and biomedical sensor data transmission. Such services required high channel bandwidth with secure information transmission and immunity to electromagnetic interference. Radio over free space optics (RoFSO) is witnessed as a promising technological solution to provide high data rate transmission over free space channel. We report on the design of a 2×10 Gb/s-10 GHz RoFSO transmission system using the mode division multiplexing technique and evaluate its transmission performance over varying levels of dust weather conditions. The comparison of non-return to zero (NRZ) and return to zero (RZ) binary digital optical modulation techniques is carried out in the proposed system. It is found that the proposed system using NRZ modulation serves 14.5 km transmission range; however, in the case of RZ modulation, it was restricted to 10 km for a target bit error rate (BER) of $10^{-6}$, thus resulting in a noticeable link enhancement of 4.5 km. Also, we demonstrate NRZ-based MDM-RoFSO link performance and availability in dust weather conditions using the BER, maximum reachable link range, and eye diagram as key performance parameters. We obtain a reliable transmission of 20 Gb/s-20 GHz data through HG00 and HG01 channels over a link range of 2500–108 m depending on the external dust weather condition. Furthermore, since this investigation shows the feasibility of RoFSO for small size cells, which is an essential feature of 5G mobile network, the proposed system can thus be implemented as a backhaul/fronthaul link for high-band (above 6 GHz) 5G services and for providing secure transmission of biomedical sensor data.

**Keywords: HG, biomedical sensor data, MDM, RoFSO, 5G technology**

## INTRODUCTION

In the present-day telecommunications sector, the base transceiver station (BTS)-BTS connection is established through fiber optic trunk cables in which voice/data are transmitted at high speed using radio over fiber (RoF) technology. Also, in order to establish a BTS-user communication link, a radio-frequency (RF) network is deployed. Nevertheless, fiber installation constrictions both in urban and rural areas, excessive infrastructure costs, and hefty spectrum pricing in the case of RF technology make such approaches unattractive and unfavorable for the establishment of next-generation wireless networks. To overcome this trouble, a radio over free space optics (RoFSO) link, where the RF signal will be transmitted between BTS-BTS or BTS-user using an optical carrier (up-conversion) and air/free space as the medium, is a viable solution. RoFSO technology provides unlicensed spectrum operation, interference, and interception-free transmission within a short deployment period and little expense [1]. To enhance the spectral efficiency and information-carrying capacity of RoFSO links, the mode division multiplexing (MDM) technique is incorporated in which independent RF signals are transmitted over distinct spatial modes of a single frequency laser beam [2–6]. Recently, Satea et al. proposed that FSO systems employing multiple channels with erbium-doped fiber amplifiers (EDFAs) work efficiently under high attenuation environments such as heavy fog and dust [7]. Alaa et al. analyzed the FSO system performance in fog and sandstorm conditions by changing the operating wavelength, receiver diameter aperture, photodetector type, and the modulation technique. They found that both the dense fog and dust triggered 87 and 95% power loss, respectively, at a transmission range of 1 km [8]. Maged et al. put forth an experimental evaluation of an all-optical hybrid FSO/RF link carrying 5G signals in a dust channel. They reported that the RF link with low bandwidth works well in dense dust and the FSO operates once the weather improves beyond a definite threshold. As a consequence, the FSO/RF parallel link can be a first-rate choice towards overcoming dust effects [9]. Matthew et al. proposed a novel visibility and dust absorption model after using visibility and absorption measurements made farther from the source (10–100 km) to demonstrate the impact of reduced dust particle size over the regional distance from the source [10]. Haichao et al. described that in addition to wavelength, particle sizes of sand and dust affect the laser beam attenuation [11]. Zabih et al. reported that the FSO link performance can be improved by increasing the launched optical power and selecting adequate line speed under sandstorm conditions [12]. The current research in RoFSO is mainly focused on fog- and smoke-induced attenuation [13–16]. Intensive investigation and modeling of the dust effects on the RoFSO channel are yet to grab the attention of researchers. Very limited or basically no attempt has been made in this course, and the development and investigation of MDM-based RoFSO transmission for dust environment has not been reported till date. In arid and semiarid regions, the effect of dust will remain paramount for any upcoming installation of the RoFSO network in 5G and smart city applications [17]. It is straightforward that the propagation prediction under dust storms regarding signal attenuation, maximum reachable distance, and error performance will be the solemn challenge for the setting up of the RoFSO communication network.

This work reports the designing and performance evaluation of an MDM-RoFSO transmission for varying levels of dust and clear climate conditions. This research article is structured as follows: *FSO Evaluation in Dust Channel* discusses the numerical model for dust storm characteristics and attenuation in FSO. *Simulation Setup Description* describes the proposed simulation

**TABLE 1 |** Dust storm classification established on a visibility basis.

| Type of dust | Severe dust storm | Dust storm | Blowing dust | Dust haze |
|---|---|---|---|---|
| **Depiction** | Dense | Moderate | Light | Very light |
| **Visibility, *V* (km)** | < 0.2 | 0.2–1 | 1–10 | ≤ 10 |

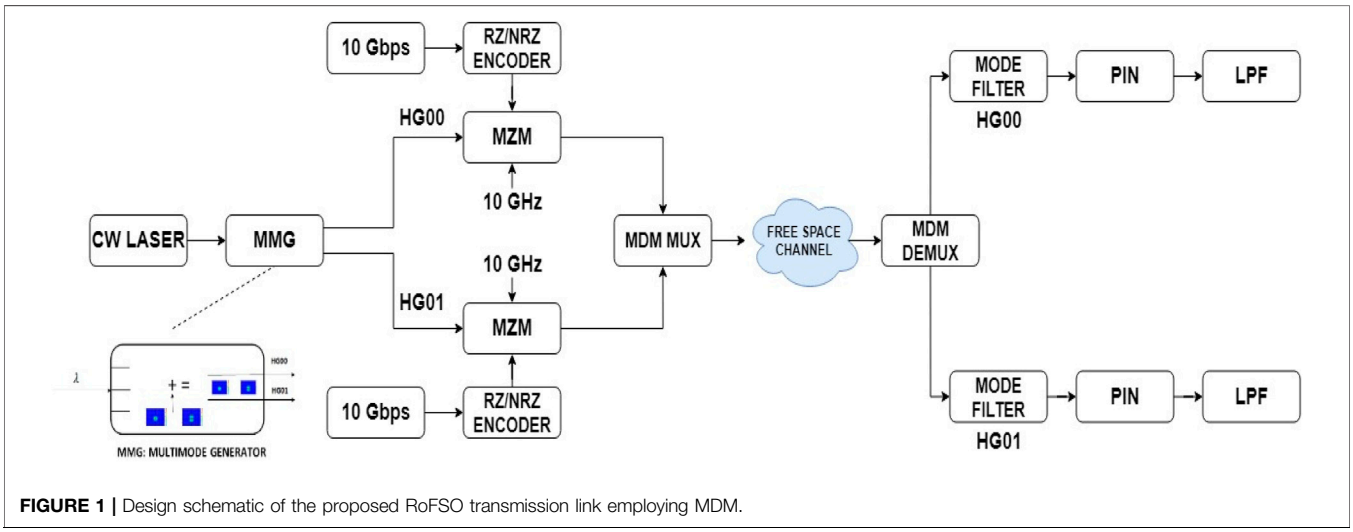


**FIGURE 1 |** Design schematic of the proposed RoFSO transmission link employing MDM.

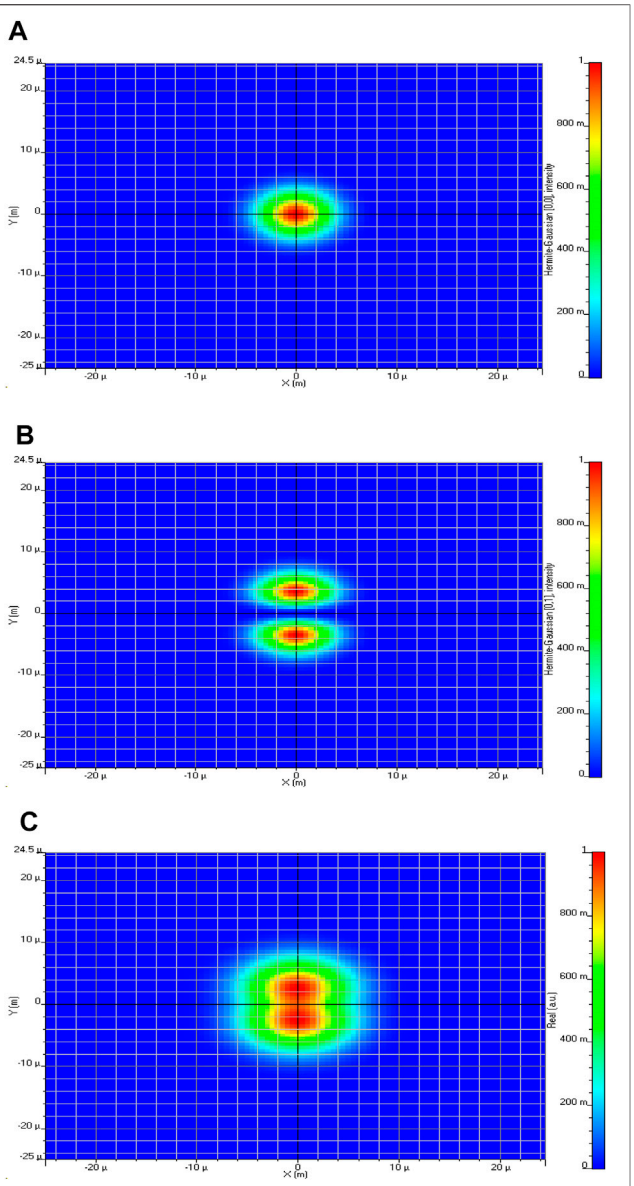


**FIGURE 2 |** Spatial intensity pattern of the **(A)** HG00 mode, **(B)** HG01 mode, and **(C)** transmitted MDM signal.

setup and parameters. *Results and Discussion* presents the simulation results, and *Conclusion* concludes the paper.

## FSO EVALUATION IN DUST CHANNEL

In FSO, the chosen signal wavelength belongs to the atmospheric transmission window which provides low molecular absorption since absorption cross-section $\sigma_a$ is negligible, that is, $\sigma_a \sim 0$ [18]. Therefore, the contribution of absorption to the total attenuation coefficient is meager in comparison to the scattering effect [19]. Different environmental factors for instance fog, rain, storm, snow, smoke, and dust causes scattering of optical beam [20, 21]. To

**TABLE 2 |** Simulation parameters considered for the proposed link design [30, 31].

| Parameter | Value |
|---|---|
| Operating frequency | 193.1 THz |
| Input power | 14 dBm |
| Laser linewidth | 100 e-012 MHz |
| Bit rate | 10 Gbps/channel |
| Transmitter aperture diameter | 10 cm |
| Receiver aperture diameter | 20 cm |
| Beam divergence angle | 0.25 mrad |
| PIN responsivity | 1 A/W |
| LPF cutoff frequency | 0.75×bit rate |
| Sequence length | 1,024 |
| Sample per bit | 32 |

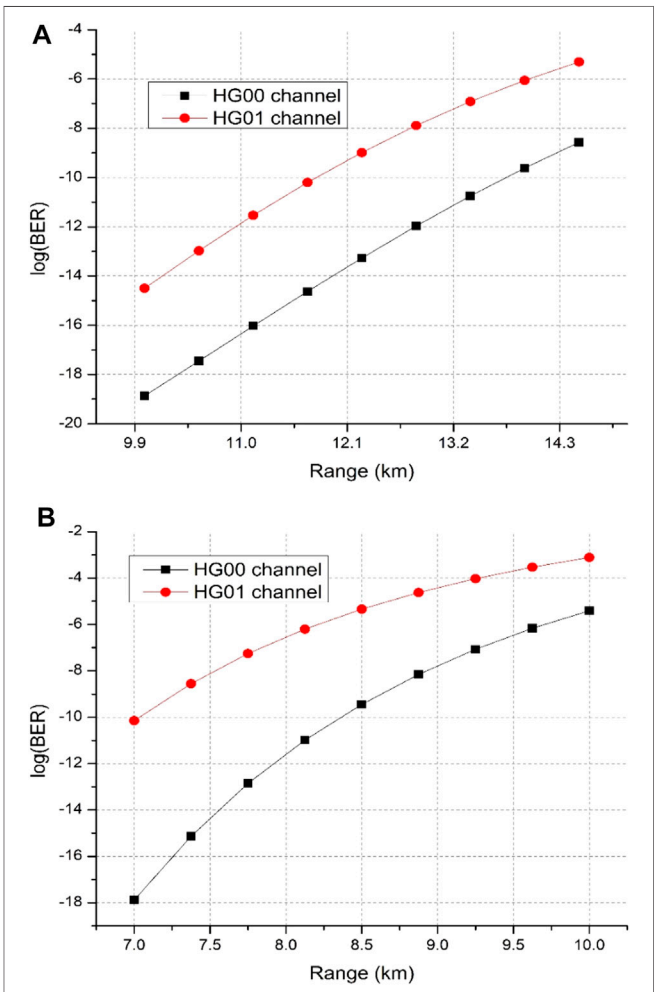


**FIGURE 3 |** log (BER) v/s transmission distance for clear weather using **(A)** NRZ modulation and **(B)** RZ modulation.

investigate the consequences of these conditions on the FSO, one of two existing approaches can be employed. The first approach utilizes theoretic-based theorems such as Mie theory. Nevertheless, this approach involves some parameters that may not be accessible at the installation site, for example, refractive index, particle size, and distribution. [22].

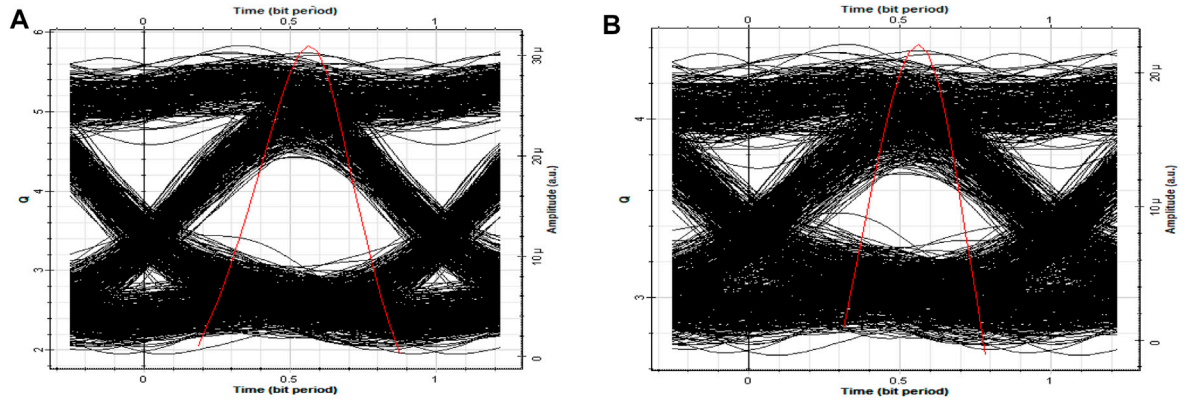


**FIGURE 4 |** Eye diagram using the proposed NRZ-based MDM-RoFSO link at 14.5 km transmission distance under clear weather for the **(A)** HG00 channel and **(B)** HG01 channel.

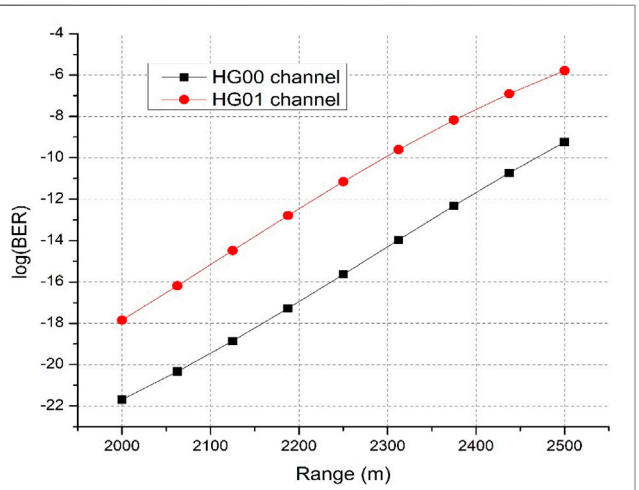


**FIGURE 5 |** log (BER) v/s transmission distance for very light dust. ($V \leq 10km$).

The second approach used in the literature for the calculation of attenuation in FSO for real-world applications rests on experimental remark [22]. This technique is based on experiential models established by means of visibility range statistics to identify the propagation path characteristics [23]. Link visibility information can be acquired from meteorological stations situated near the setup area. In [24], visual range is described as the distance to an entity at which the picture distinction falls to 2% of the original ocular contrast (100%) along the transmission distance usually referred to as the Koschmieder law. This 2% falloff value recognized as the visual threshold $T_{vis}$ is adopted here so as to follow the Koschmieder law as opposed to the $T_{vis} = 5\%$ considered in aviation operations [25, 26]. The visibility is computed at 550 nm wavelength since the highest solar radiation concentration occurs here. Visibility indicates the degree of sternness of the dust gale. Small visibility specifies the elevated concentration of dust elements in the free space, and vice versa.

Depending on the visibility, dust storms are classified into four groups as specified in **Table 1**. Type 1 is dust haze (very light dust) wherein widespread dust particles drift up and happen to remain suspended evenly in the atmosphere as a result of dust storm that begins at a large distance from the monitoring point. The visibility associated with this occasion is about 10 km or less. Type 2 is blowing dust (light dust) in which the dust is blown in the direction of monitoring position by the action of winds. As a result, the visibility drops between 1 and 10 km. Type 3 is dust storm (moderate dust) where strong winds bluster additional dust elements inside the observation area and the visibility decreases between 0.2 and 1 km. Finally, type 4 is severe dust storm (dense dust) which arises after a large volume of dust particles are blown by violent winds, and the visibility further drops below 0.2 km. The visibility $V$(km) in terms of $\alpha$ and $T_{vis}$ takes the form [22]:

$$V = -\frac{10\,log\,T_{vis}}{\alpha}, \tag{1}$$

where $\alpha$ is the specific atmospheric attenuation coefficient expressed in (dB/km) and is determined from the light wave transmittance $T$ at 550 nm and transmission distance $d$ (km) using the Beer-Lambert law as [27]:

$$\alpha = \frac{10\,log\,T}{4.343d}. \tag{2}$$

Moreover in [28], the FSO signal attenuation model as a function of the visibility for desert environment that is prone to frequent dust storms is obtained as:

$$\alpha = 52 \times V^{-1.05} \tag{3}$$

**Eq. 3** holds under the condition that the operating wavelength used in FSO communication is 1,550 nm since it provides lowest atmospheric attenuation and minor absorption loss, besides its technology is mature in terms of fabrication of optoelectronic devices.

## SIMULATION SETUP DESCRIPTION

The proposed MDM-based RoFSO link setup employing RZ and NRZ binary digital optical modulation is illustrated in **Figure 1**,

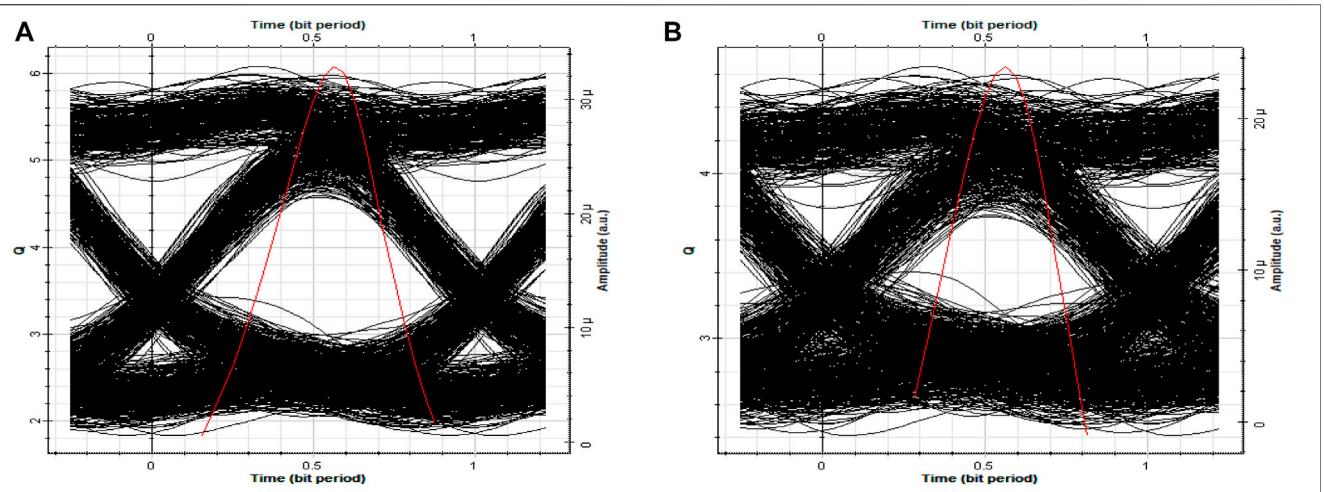


**FIGURE 6 |** Eye diagram using the proposed NRZ-based MDM-RoFSO system at 2,500 m transmission distance under very light dust for the **(A)** HG00 channel and **(B)** HG01 channel.

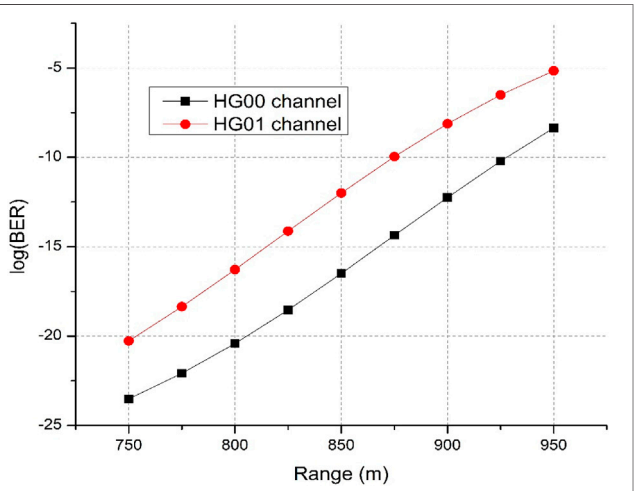


**FIGURE 7 |** log (BER) v/s transmission distance for light dust.

which has been designed using the Optisystem™ photonic software. Two independent 10 GHz RF signals are modulated over different HG mode beams, that is, HG00 and HG01 and transported over the FSO channel. **Eq. 4** mathematically describes the intensity profiles of HG modes (**Figures 2A,B**) as [29]:

$$\psi_{p,q}(x,y) = H_p\left[\left(\frac{\sqrt{2}x}{w_{ox}}\right)\exp\left(-\frac{x^2}{w_{ox}^2}\right)\exp\left(j\frac{\pi x^2}{\lambda R_{ox}}\right)\right] \times H_q\left[\left(\frac{\sqrt{2}y}{w_{oy}}\right)\exp\left(-\frac{y^2}{w_{oy}^2}\right)\exp\left(j\frac{\pi y^2}{\lambda R_{oy}}\right)\right], \quad (4)$$

where $p$ and $q$ denote mode dependencies on the $x$ and $y$ axes, R signifies the radius of curvature, $w_o$ indicates the spot size, and $H_p$ and $H_q$ represent Hermite polynomials. In our proposed design, a continuous wave (CW) laser at 193.1 THz together with an MMG is used to generate two different HG modes. **Figure 2** depicts the spatial profile of HG modes. **Figure 2C** demonstrates the spatial profile of the 2×10 Gb/s-10 GHz MDM-RoFSO transmitted signal.

A 10 Gb/s information-carrying signal is produced by a pseudorandom bit sequence generator (PRBS) for distinct channels and encoded using RZ/NRZ schemes. In RZ-encoded signal, bit "1" is transported by an optical pulse with half bit period. Whereas in NRZ-encoded signal, bit "1" is transported through an optical signal of entire bit period, while in place of bit "0", no optical signal is conveyed. A Mach–Zehnder modulator (MZM) is utilized to superimpose the encoded information onto a 10-GHz RF signal and a distinct HG mode. This information signal is subsequently communicated into the FSO channel through HG00 and HG01 modes of the 193.1 THz frequency channel.

Mathematically, the signal received after FSO transmission can be modeled as [32]:

$$P_{rx} = P_{tx}\left[\frac{D_{rx}^2}{(D_{tx}+\theta d)^2}\right]10^{-\alpha d/10}, \quad (5)$$

where $P_{rx}$ and $P_{tx}$ denote the received and transmitted optical power, respectively, $D_{rx}$ and $D_{tx}$ denote the receiver and transmitter antenna diameter, and $\theta$ is the divergence angle. The system parameters considered in the proposed link design are listed in **Table 2**. The coefficient of atmospheric attenuation for clear sky is 0.14 dB/km and 6.73 dB/km for very light dust, 25.11 for light dust, 107.66 dB/km for moderate dust, and 297.38 dB/km for dense dust [33]. At the receiver end, separates modes are filtered using a mode filter [34, 35]. A spatial positive-intrinsic-negative (PIN) photodiode converts the received optical signal into its electrical equivalent which is followed by low-pass filtering to retrieve the original baseband signal.

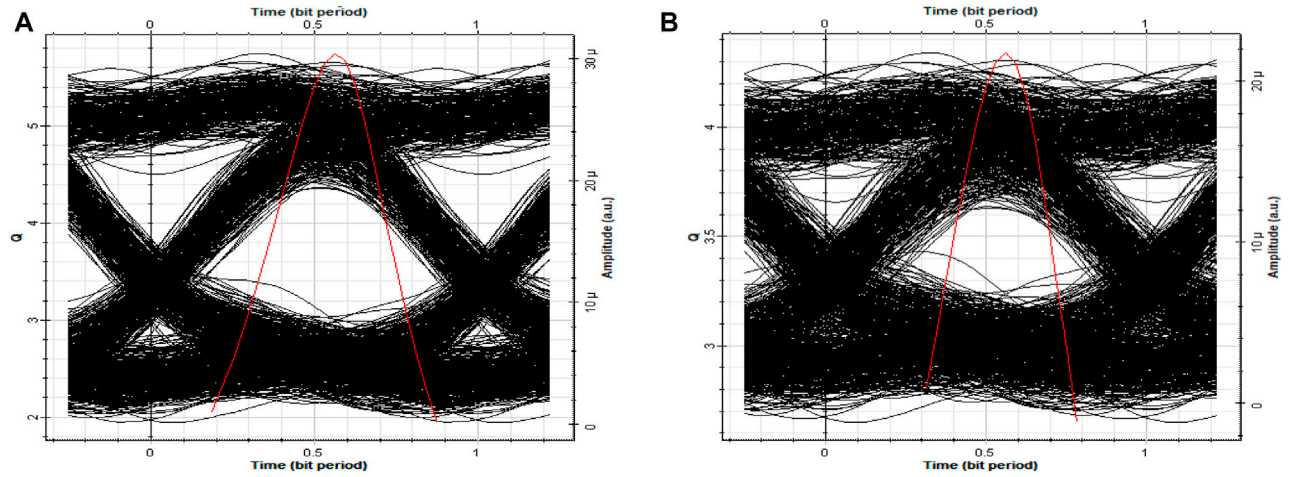


**FIGURE 8 |** Eye diagram using the proposed NRZ-based MDM-RoFSO link at 950 m transmission distance under light dust conditions for the **(A)** HG00 channel and **(B)** HG01 channel.

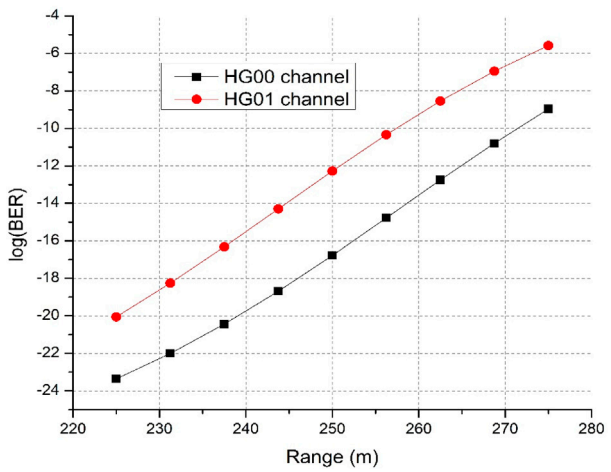


**FIGURE 9 |** log (BER) v/s transmission distance under moderate dust conditions.

## RESULTS AND DISCUSSION

Firstly, we compare the performance of NRZ and RZ modulation-based MDM-RoFSO link under a clear climate. Secondly, we investigate the proposed MDM-RoFSO link utilizing NRZ modulation for four different dust storm conditions. The performance analysis has been carried out with regard to BER, transmission range, and eye diagram.

**Figure 3** presents RZ/NRZ-MDM-RoFSO transmission system performance in terms of BER and range under clear weather conditions where each HG mode (HG00 and HG01) carries independent 10 Gb/s-10 GHz information. Though BER of the system degrades with increasing transmission distance for both the channels, it can be found from **Figure 3A**, using NRZ modulation scheme, the maximum achievable link range is 14.5 km while it decreases to 10 km for RZ modulation in **Figure 3B** under acceptable performance criteria [log (BER) $\approx -6$]. This concludes that NRZ modulation outperforms RZ modulation by a notable increment of 4.5 km FSO link range. Henceforth, we have implemented the NRZ modulation format in the succeeding analysis. The clear eye diagrams at 14.5 km for both the spatial channels as shown in **Figure 4** display a reliable transmission of 20 Gb/s-20 GHz information signal.

To determine how far and well the proposed link can function under four different dust storm situations, we draw the log of BER versus maximum reachable distance graphs. In addition, to demonstrate the reliability of our observations, we report the eye diagrams using the proposed system for each maximum reachable range with regard to specific dust conditions for both the channels.

**Figure 5** shows a log of BER versus range curve under very light dust conditions, that is, $V \leq 10km$. It is evident that the BER performance of the received signals deteriorated from a log (BER) of −21.69 at 2000 m to −9.24 at 2,500 m for the HG00 channel and −17.85 at 2000 m to −5.79 at 2,500 m for the HG01 channel, respectively. **Figure 6** displays the eye diagram of the signals received from the HG00 and HG01 channels at a transmission range of 2,500 m under very light dust circumstances for the proposed design. The outcomes from **Figures 5**, **6** show 20 Gb/s-20 GHz information signal transmission around a distance of 2,500 m under very light dust conditions within standard performance criteria of log (BER) $\approx -6$ and Q factor $\approx 6$.

The proposed NRZ-based MDM-RoFSO system performance in light dust conditions (i.e., $1km < V < 10km$) as a function of the log (BER) and transmission range is presented in **Figure 7**. It can be found that the BER performance of the received signals declines from log (BER) of −23.51 at 750 m to −8.36 at 950 m for the HG00 channel and −20.27 at 750 m to −5.16 at 950 m for the HG01 channel, respectively. **Figure 8** displays an eye diagram of the signals

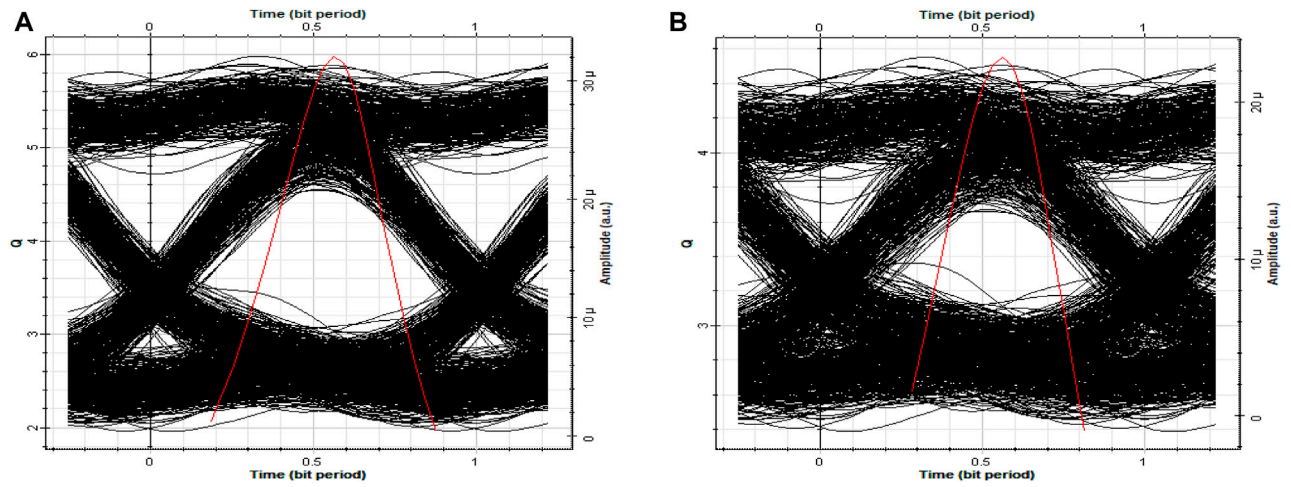


**FIGURE 10 |** Eye diagram using the proposed NRZ-based MDM-RoFSO system at 275 m transmission distance under moderate dust conditions for the **(A)** HG00 channel and **(B)** HG01 channel.

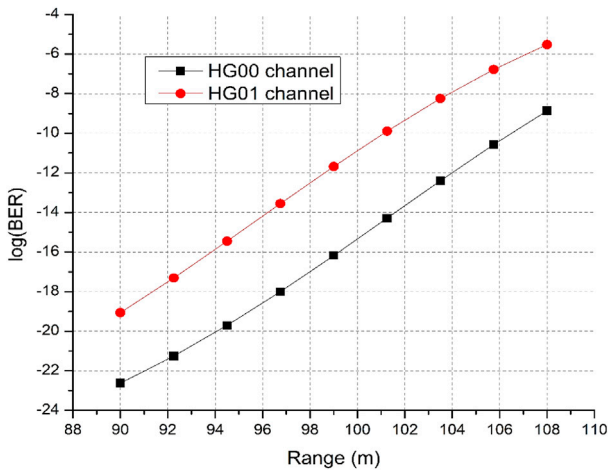


**FIGURE 11 |** log (BER) v/s transmission distance for dense dust.

received at 950 m for light dust conditions. The outcomes from **Figures 7**, **8** show 20 Gb/s-20 GHz information signal transmission around a distance of 950 m under very light dust conditions within standard performance criteria.

**Figure 9** illustrates the log (BER) versus range graph under moderate dust conditions (i.e., 0.2 km < $V$ < 1 km). As can be seen, the BER performance of the received signals reduces from a log (BER) of −23.36 at 225 m to −8.96 at 275 m for the HG00 channel and −20.05 at 225 m to −5.59 at 275 m for the HG01 channel, respectively. **Figure 10** depicts the eye diagram of the two 10 Gb/s-10 GHz received signals from the HG00 and HG01 channels at a transmission distance of 275 m under moderate dust. The outcomes outlined in **Figures 9**, **10** reveal 20 Gb/s-20 GHz data transmission at 275 m in moderate dust situation with log (BER) ≈ − 6 and Q factor ≈ 6.

The transmission performance of the proposed system under dense dust (i.e., $V$ < 0.2 km) as a function of the log (BER) and transmission range is shown in **Figure 11**. As can be noticed, the BER performance of the received signal deteriorates from a log (BER) of −22.62 at 90 m to −8.88 at 108 m for the HG00 channel and −19.06 at 90 m to −5.52 at 108 m for the HG01 channel, respectively. **Figure 12** displays the eye diagram of the two signals transported over HG00 and HG01 channels at a distance of 108 m for a dense dust scenario. As follows from **Figures 11**, **12**, 20 Gb/s-20 GHz information is transported at 108 m under dense dust within acceptable performance limits using the proposed system. Nonetheless, there is no prominent increment in the maximum link reach under dense dust situations. Fortunately, the incident

**TABLE 3 |** Comparison of the transmission performance of the proposed system with recent works.

| Parameter | Reference [7] | Reference [23] | Reference [33] | Proposed work |
|---|---|---|---|---|
| Transmission method | OOK-based FSO link with MIMO and EDFA preamplifier | OOK-based FSO link with single-channel transmission | OOK-based WDM-FSO Link | OOK-based FSO Link employing MDM |
| Data rate | 2.5 Gbps | 2.5 Gbps | 1 Gbps | 20 Gbps |
| Transmission power | 160 mW (22 dBm) | 22 dBm | 50 dBm | 14 dBm |
| Channel conditions and maximum range | Moderate dust- 2.3 km Heavy dust-380 m | Light dust- 1 km Moderate dust- 800 m Heavy dust < 200 m | Very light dust-13.5 km Light dust-4.05 km Moderate dust-1.05 km Heavy dust-0.405 km | Very light dust-2.5 km Light dust- 950 m Moderate dust-275 m Heavy dust- 108 m |

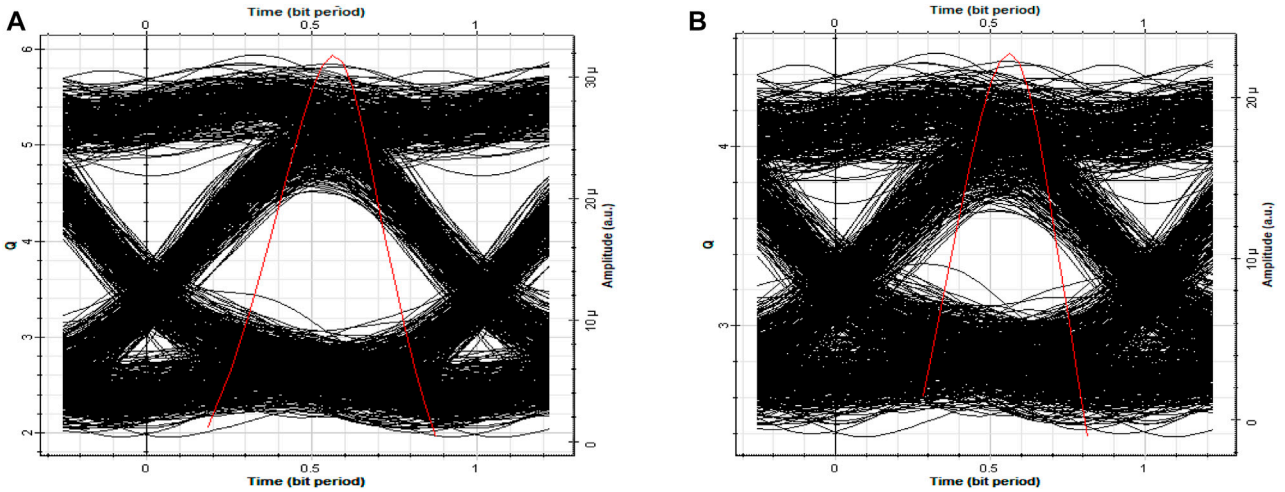


**FIGURE 12 |** Eye diagram using the proposed NRZ-based MDM-RoFSO link at 108 m transmission distance under dense dust for the **(A)** HG00 channel and **(B)** HG01 channel.

of dense dust waves is unusual and accounts for just 0.17% of the year time [36].

**Table 3** compares the transmission performance of the proposed system with recent works and demonstrates that the proposed system achieves higher information capacity. The higher range in recent works can be attributed to the fact that the authors have considered higher transmission power, that is, 22 dBm (Ref [7, 23]) and 50 dBm (Ref. [33]), as compared to 14 dBm in this work.

## CONCLUSION

RoFSO transmission systems integrated with MDM technology can provide a viable solution for providing secure biomedical sensor data transmission in medical facilities. In this work, an NRZ/RZ digital optical modulation schemes based MDM-RoFSO transmission system is proposed and investigated. The outcomes presented demonstrate that NRZ modulation performs significantly better in terms of providing extra 4.5 km coverage as compared to the RZ modulation format. We first investigated the performance reliability and availability of a NRZ-based MDM-RoFSO transmission system in a dust environment. The results obtained show the likelihood of establishing short FSO networks under light and moderate dust circumstances. Nevertheless, rarely encountered dense dust scenarios can significantly affect the performance of MDM-RoFSO links. Additionally, because the 5G network uses ultra-compact cells with modest separation, the proposed NRZ-based MDM-RoFSO link can prove to be a promising substitute to fiber cables in the fronthaul and backhaul sectors of next-generation wireless networks. In future works, the transmission capacity of the proposed system can further be enhanced by incorporating polarization multiplexing along with higher-order modulation schemes.

## DATA AVAILABILITY STATEMENT

The original contributions presented in the study are included in the article/Supplementary Material, and further inquiries can be directed to the corresponding author.

## AUTHOR CONTRIBUTIONS

MS: Conceptualization, methodology, investigation, writing—original draft, supervision, resources, project administration. SP: Methodology, investigation, writing—original draft, supervision. S: Methodology, investigation, data curation, visualization. SD: Investigation, data curation, writing—original draft. R: Investigation, data curation, visualization. AG: Writing—review and editing, validation, conceptualization. AM: Investigation, data curation, visualization. AM: Writing—review and editing, validation, conceptualization.

## REFERENCES

1. Singh M, and Malhotra J. Performance Comparison of M-QAM and DQPSK Modulation Schemes in a 2 × 20 Gbit/s-40 GHz Hybrid MDM-OFDM-Based Radio over FSO Transmission System. *Photon Netw Commun* (2019) 38(3): 378–89. doi:10.1007/s11107-019-00861-z
2. Singh M, and Malhotra J. Performance Comparison of High-Speed Long-Reach Mode Division Multiplexing-Based Radio over Free Space Optics Transmission System Using Different Modulation Formats under the Effect of Atmospheric Turbulence. *Opt Eng* (2019) 58(4):1. doi:10.1117/1.OE.58.4.046112
3. Sharma A, Malhotra J, Chaudhary S, and Thappa V. Analysis of 2 × 10 Gbps MDM Enabled Inter Satellite Optical Wireless Communication under the Impact of Pointing Errors. *Optik* (2021) 227:165250. doi:10.1016/j.ijleo.2020.165250

4. Amphawan A, Chaudhary S, Ghassemlooy Z, and Neo T-K. 2×2-channel Mode-Wavelength Division Multiplexing in Ro-FSO System with PCF Mode Group Demultiplexers and Equalizers. *Opt Commun* (2020) 467:125539. doi:10.1016/j.optcom.2020.125539
5. Amphawan A, Chaudhary S, and Chan V. Optical Millimeter Wave Mode Division Multiplexing of LG and HG Modes for OFDM Ro-FSO System. *Opt Commun* (2019) 431:245–54. doi:10.1016/j.optcom.2018.07.054
6. Chaudhary S, and Amphawan A. Solid Core PCF-Based Mode Selector for MDM-Ro-FSO Transmission Systems. *Photon Netw Commun* (2018) 36: 263–71. doi:10.1007/s11107-018-0778-4
7. Alnajjar SH, Noori AA, and Moosa AA. Enhancement of FSO Communications Links under Complex Environment. *Photonic Sens* (2017) 7(2):113–22. doi:10.1007/s13320-017-0336-1
8. Algamal AA, Fayed HA, Mahmoud M, and Aly MH. Reliable FSO System Performance Matching Multi-Level Customer Needs in Alexandria City, Egypt, Climate: Sandstorm Impact with Pointing Error. *Opt Quant Electron* (2020) 52(18):1. doi:10.1007/s11082-020-02468-5
9. Esmail MA, Ragheb AM, Fathallah HA, Altamimi M, and Alshebeili SA. 5G-28 GHz Signal Transmission over Hybrid All-Optical FSO/RF Link in Dusty Weather Conditions. *IEEE Access* (2019) 7:24404–10. doi:10.1109/ACCESS.2019.2900000
10. Baddock MC, Strong CL, Leys JF, Heidenreich SK, Tews EK, and Mctainsh GH. A Visibility and Total Suspended Dust Relationship. *Atmos Environ* (2014) 89:329–36. doi:10.1016/j.atmosenv.2014.02.038
11. Zhong H, Zhou J, Du Z, and Xie L. A Laboratory Experimental Study on Laser Attenuations by Dust/sand Storms. *J Aerosol Sci* (2018) 121:31–7. doi:10.1016/j.jaerosci.2018.04.004
12. Ghassemlooy Z, Perez J, and Leitgeb E. On the Performance of FSO Communications Links under Sandstorm Conditions. In: Proceedings of the 12th International Conference on Telecommunications, 2013, June 26-28, Zagreb, Croatia. Zagreb (2013). p. 53–8.
13. Chaudhary S, Lin B, Tang X, Wei X, Zhou Z, Lin C, et al. 40 Gbps-80 GHz PSK-MDM Based Ro-FSO Transmission System. *Opt Quant Electron* (2018) 50:321. doi:10.1007/s11082-018-1592-z
14. Chaudhary S, and Amphawan A. High-speed MDM-Ro-FSO System by Incorporating Spiral-Phased Hermite Gaussian Modes. *Photon Netw Commun* (2018) 35:374–80. doi:10.1007/s11107-017-0752-6
15. Chaudhary S, and Amphawan A. High-speed Millimeter Communication through Radio-Over-Free-Space-Optics Network by Mode-Division Multiplexing. *Opt Eng* (2017) 56(11):1. doi:10.1117/1.OE.56.11.116112
16. Chaudhary S, Tang X, and Wei X. Comparison of Laguerre-Gaussian and Donut Modes for MDM-WDM in OFDM-Ro-FSO Transmission System. *AEU - Int J Elect Commun* (2018) 93:208–14. doi:10.1016/j.aeue.2018.06.024
17. Kumar A, and Krishnan P. Performance Analysis of RoFSO Links with Spatial Diversity over Combined Channel Model for 5G in Smart City Applications. *Opt Commun* (2020) 466:125600. doi:10.1016/j.optcom.2020.125600
18. Bohren CF, and Huffman DR. *Absorption and Scattering of Light by Small Particles*. Germany: A Wiley-Interscience publication (1998). doi:10.1002/9783527618156
19. Kim II, Mcarthur B, Korevaar EJ, Street R, and Diego S. Comparison of Laser Beam Propagation at 785 Nm and 1550 Nm in Fog and Haze for Optical Wireless Communications. In: Proceeding SPIE 4214, Optical Communications III, 2001, February 6, Boston, MA, United States (2001). doi:10.1117/12.417512
20. Khalighi MA, Uysal M, Marseille C, and Engineering E. Survey on Free Space Optical Communication: A Communication Theory Perspective. *IEEE Commun Surv Tutorials* (2014) 16(4):2231–58. doi:10.1109/COMST.2014.2329501
21. Hemmati H, Djordjevic IB, and Biswas A. Deep-Space Optical Communications: Future Perspectives and Applications. *Proc IEEE* (2011) 99(11):2020–39. doi:10.1109/JPROC.2011.2160609
22. Ijaz M, Ghassemlooy Z, Pesek J, Fiser O, Le Minh H, and Bentley E. Modeling of Fog and Smoke Attenuation in Free Space Optical Communications Link under Controlled Laboratory Conditions. *J Lightwave Technol* (2013) 31(11): 1720–6. doi:10.1109/JLT.2013.2257683
23. Esmail MA, Fathallah H, and Alouini M-S. Effect of Dust Storms on FSO Communications Links. In: 2016 4th International Conference on Control Engineering & Information Technology (CEIT), 2016, December 16-18, Hammamet, Tunisia. Hammamet (2016). 1–6. doi:10.1109/CEIT.2016.7929046
24. Pierce RM, Ramaprasad J, and Eisenberg EC. Optical Attenuation in Fog and Clouds. In: Proceeding SPIE, 4530, Optical Wireless Communications IV, 2001, November 27, Denver, CO, United States (2001). 58–71. doi:10.1117/12.449815
25. Prokes A. Atmospheric Effects on Availability of Free Space Optics Systems. *Opt Eng* (2009) 48(6):066001. doi:10.1117/1.3155431
26. Cao M, Wang H, Yao Y, and Hou S. Performance Evaluation of FSO Communications under Sand-Dust Conditions. *Int J Antennas Propagation* (2019) 2019:1–11. doi:10.1155/2019/2046896
27. Ricklin JC, Hammel SM, Eaton FD, and Lachinova SL. Atmospheric Channel Effects on Free-Space Laser Communication. *J Optic Comm Rep* (2006) 3: 111–58. doi:10.1007/s10297-005-0056-y
28. Esmail MA, Fathallah H, and Alouini M-S. An Experimental Study of FSO Link Performance in Desert Environment. *IEEE Commun Lett* (2016) 20(9): 1888–91. doi:10.1109/LCOMM.2016.2586043
29. Ghatak A, and Thyagarajan K. *An Introduction to Fiber Optics*. Cambridge: Cambridge University Press (1998). doi:10.1017/CBO9781139174770
30. Nyugen D-N, Bohata J, Spáčil J, Komanec M, Stevens N, Ghassemlooy Z, et al. Polarization Division Multiplexing-Based Hybrid Microwave Photonic Links for Simultaneous mmW and Sub 6-GHz Wireless Transmissions. *IEEE Photon J* (2020) 12(6):1–16. doi:10.1109/JPHOT.2020.3036440
31. Kakati D, and Arya SC. A Full-Duplex Optical Fiber/wireless Coherent Communication System with Digital Signal Processing at the Receiver. *Optik* (2018) 171:190–9. doi:10.1016/j.ijleo.2018.05.140
32. Ghassemlooy Z, and Popoola WO. Terrestrial Free Space Optical Communications. In: S A Fares and F Adachi, editors. *Mobile and Wireless Communication Network Layer and Circuit Level Design*. London, United Kingdom: InTech (2010). doi:10.5772/7698
33. Ali MAA, Shaker FK, and Kadhum HA. Investigation and Analysis of Data Rate for Free Space Optical Communications System under Dust Conditions. *Wirel Pers Commun* (2020) 113:2327–38. doi:10.1007/s11277-020-07328-9
34. Mourka A, Mazilu M, Wright EM, and Dholakia K. Modal Characterization Using Principal Component Analysis: Application to Bessel, Higher-Order Gaussian Beams and Their Superposition. *Sci Rep* (2013) 3:1422. doi:10.1038/srep01422
35. Amphawan A, and O'Brien D. Modal Decomposition of Output Field for Holographic Mode Field Generation in a Multimode Fiber Channel. In: International Conference on Photonics, 2010, July 5-7, Langkawi, Malaysia. Langkawi (2010). 1–5. doi:10.1109/ICP.2010.5604377
36. Alhaider MA. Radio Wave Propagation into Sandstorms-System Design Based on Ten-Years Visibility Data in Riyadh, Saudi Arabia. *Int J Infrared Milli Waves* (1986) 7(9):1339–59. doi:10.1007/BF01012054


**Conflict of Interest:** The authors declare that the research was conducted in the absence of any commercial or financial relationships that could be construed as a potential conflict of interest.

frontiers in Physics

ORIGINAL RESEARCH
published: 07 September 2021
doi: 10.3389/fphy.2021.756232

# Hybrid MDM-PDM Based Ro-FSO System for Broadband Services by Incorporating Donut Modes Under Diverse Weather Conditions

*Sushank Chaudhary[1]*, Lunchakorn Wuttisittikulkij[1]*, Jamel Nebhen[2], Xuan Tang[3], Muhammad Saadi[4], Sattam Al Otaibi[5], Ahmed Althobaiti[5], Abhishek Sharma[6] and Sunita Choudhary[1]*

[1]Wireless Communication Ecosystem Research Unit, Department of Electrical Engineering, Chulalongkorn University, Bangkok, Thailand, [2]College of Computer Engineering and Sciences, Prince Sattam Bin Abdulaziz University, Alkharj, Saudi Arabia, [3]Quanzhou Institute of Equipment Manufacturing, Chinese Academy of Sciences, Quanzhou, China, [4]Department of Electrical Engineering, University of Central Punjab, Lahore, Pakistan, [5]Department of Electrical Engineering, College of Engineering, Taif University, Taif, Saudi Arabia, [6]Department of Electronics and Communication Engineering, Guru Nanak Dev University, Amritsar, India

OPEN ACCESS

**Edited by:**
Santosh Kumar,
Liaocheng University, China

**Reviewed by:**
Tony Jose,
Karunya Institute of Technology and Sciences, India
Madan M. Upadhyay,
Indian Institute of Technology Dhanbad, India

***Correspondence:**
Sushank Chaudhary
sushankchaudhary@gmail.com
Lunchakorn Wuttisittikulkij
Lunchakorn.W@chula.ac.th

**Specialty section:**
This article was submitted to Optics and Photonics, a section of the journal Frontiers in Physics

**Received:** 10 August 2021
**Accepted:** 23 August 2021
**Published:** 07 September 2021

**Citation:**
Chaudhary S, Wuttisittikulkij L, Nebhen J, Tang X, Saadi M, Al Otaibi S, Althobaiti A, Sharma A and Choudhary S (2021) Hybrid MDM-PDM Based Ro-FSO System for Broadband Services by Incorporating Donut Modes Under Diverse Weather Conditions. Front. Phys. 9:756232. doi: 10.3389/fphy.2021.756232

High-speed data demand in sensitive locations has prompted new wireless technologies to grow in areas like hospitals for bio-sensor data transmission between doctors and patients. However, interference of electromagnetic spectrum or highly sensitive medical equipment in such locations can prevent radio waves which can further compromise the health of patients. Radio over Free Space Optics (Ro-FSO) can fulfil high-speed data demand in such locations without any such interference. However, the Ro-FSO performance is highly influenced by different adverse weather conditions, particularly haze and rainfall, which further cause attenuation in the transmission path of Ro-FSO systems. These atmospheric turbulences mainly affect the transmission link range of Ro-FSO systems. In this work, Ro-FSO system is designed by incorporating hybrid mode division multiplexing (MDM) and polarization division multiplexing (PDM) schemes to deliver four independent channels, each carrying 10 Gbps data upconverted to 40 GHz radio signal, over 3.4 km free space optical link operating under clear weather conditions. In addition to this, the proposed Ro-FSO link is subjected to different weather conditions, particularly partially hazy/rainy and dense fog/very rainy. The reported results indicate the achievement of acceptable bit error rate (BER$\approx 10^{-3}$) for all channels up to 3400*m* FSO link under clear weather conditions, 1000*m* under partially haze/rain and 620 m under dense fog/heavy rain.

**Keywords: radio over free space optics, mode division multiplexing, polarization division multiplex, partially hazy, dense fog**

## INTRODUCTION

The current pandemic situation of COVID-19 has not only affected global healthcare in general but also raised questions on the effectiveness of epidemic response mechanisms across the world. In terms of screening the infected individuals and frontline healthcare personnel, communication and data exchange systems have a crucial role to play. Particularly in high-density countries like Thailand,

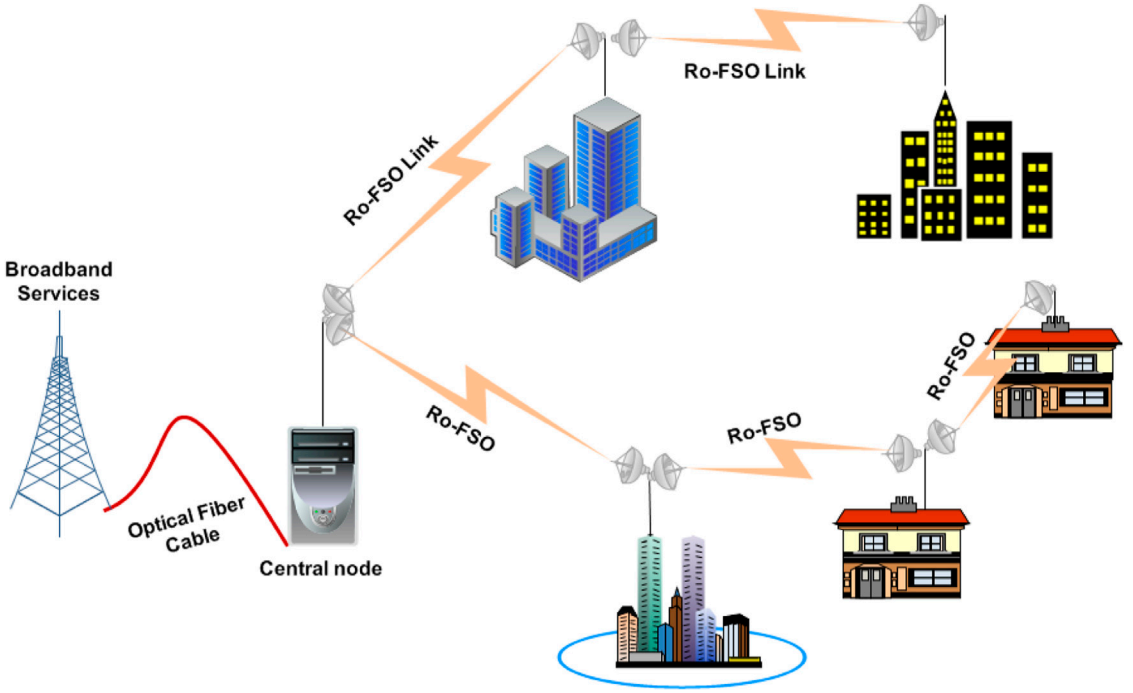


**FIGURE 1 |** Ro-FSO topology for broadband service.

China, and India, it is essential to update such systems for controlling the ongoing pandemic outbreak. Telecommunication operators can install high-speed broadband networks in hospitals by using innovative applications to drive emergency response mechanisms digitally and accurately. Both high and low frequencies can be used by broadband networks to provide highest speeds on millimeter waves with frequencies between 30 and 300 GHz. However, these radio millimeter waves are not permitted in sensitive medical locations since it can interfere with crucial medical equipment which can impact patients' health. Therefore, such sensitive locations are always considered as challenging locations to connect with broadband services. Moreover, growing population has caused substantial increase in data demand which further compels researchers to explore new-generation communication technologies. According to a survey by Ericsson, annual mobile data traffic saw an increase of 65% in 2015 which is assumed to grow ten times bigger by the end of 2021 [1]. The issue of bandwidth increase of the existing wireless radio networks can be resolved by decreasing the cell size to accommodate more users. Spectral congestions can be mitigated by operating frequency bands in microwave or millimeter bands [2]. Because of this, the service area requires multiple base stations resulting in its complexed structure and higher cost. Free Space Optics (FSO) has thrived in application in high-speed wireless networks due to its features for smooth traffic functioning in optical fibers [3–5]. Moreover, another FSO-based study [6] used point-to-point laser signals for negligible interception to secure transmission. Studies [7–9] have also reported features of FSO including its high capacity, less power consumption, light weight, smaller size and cost-effective implementation charges. Radio over Free Space Optical (Ro-FSO) communication can be an excellent solution to fulfill the demands of high-speed data by combining radio technology with optical wireless technology at lower cost [10, 11]. As modern cities are growing bigger and bigger, digging of lands to install optical fiber cables is not feasible. Thus, Ro-FSO can be a potential carrier to deliver various high-speed digital services such as high-speed internet, video on demand, and Triple Play Services (TPS) without using optical fiber cables [12, 13] as shown in **Figure 1**. Ro-FSO can handle the increasing mobile subscribers by transmitting RF signals through high-speed optical carrier that does not cost much or need any licensing.

Some of the major features of Ro-FSO include no license requirement, low power consumption and ease of deployment; however, its performance is limited in atmospheric turbulences such as fog, rain, scintillations, and fog [4, 14, 15]. Atmospheric turbulences cause temporal random fluctuations of the refractive index through the optical channel due to temperature, wind variations, and pressure [16]. This fluctuation in refractive index further results in phase shift of optical signals transmitting through the atmosphere leading to attenuation in the wave front. To improve the performance, many researchers have proposed orthogonal frequency division multiplexing (OFDM) scheme by compromising the complexity and cost of FSO systems. In 2016 [17], authors have transmitted 1.6 Gbps data over 1.8 km FSO link by employing OFDM scheme under heavy rainfall conditions. In 2017 [18], authors have used 16 QAM-OFDM encoding scheme to transmit 20 Gbps data over 10 km single mode fiber link and 300 mm FSO link. In

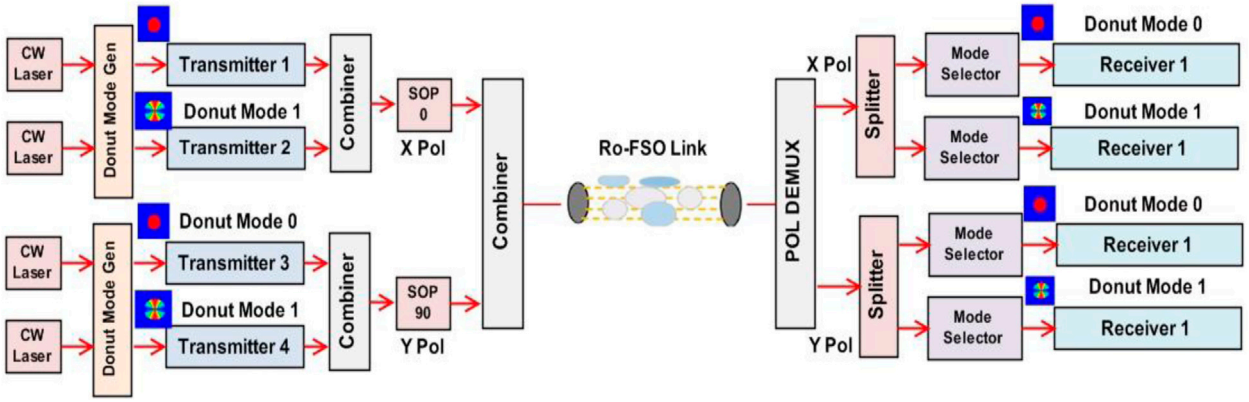


**FIGURE 2 |** MDM-PDM-Ro-FSO transmission system.

2018 [19], authors have proposed OFDM-based FSO link by incorporating non line-of-sight assisted relay. Recently in 2019 [20], authors have proposed hybrid polarization division multiplexing (PDM) and OFDM schemes to transmit data over 5 km FSO link. OFDM can improve the FSO system performance by providing high spectral bandwidth, firmness against multipath path fading effects and narrowband interferences. However, this increases the cost and complexity of FSO transmitter and receiver. On-off key encoding schemes can be an attractive solution to reduce the cost of and simplify FSO communication system. But it also needs to compromise the transmission capacity and distance. Whereas mode division multiplexing (MDM) becomes an attractive solution to increase the transmission capacity of multimode transmission systems by simultaneously transmitting different channels on different modes. The last few years have witnessed remarkable adoption of MDM scheme in FSO systems. It uses eigen modes instead of wavelength which can enhance the capacity of Ro-FSO. Eigen modes can be generated by using mechanisms such as Photonic Crystal Fibers (PCF) or Spatial Light Modulators (SLM). The spectral bandwidth of Ro-FSO can further be increased by incorporating PDM [21] with MDM.

## MODELING OF MDM-PDM-Ro-FSO SYSTEM.

**Figure 2** shows how the hybrid MDM-PDM scheme is designed for transmitting four independent channels by using OptiSystem™ software. Each channel can support the data rate of 10 Gbps upconverted to 40 GHz mm carrier. A continuous wavelength (CW) laser with the wavelength of 1,552.5 *nm* is used to excite the particular donut mode by using donut mode generator. The power of laser is set at 0*dBm*. Transmitter 1 is operated on donut mode 0 and Transmitter 2 is operated on donut mode 1. The output of these transmitters is integrated. The state of polarization controller with azimuth of $0^0$ is used for maintaining the polarization state (X Polarization). Similarly, transmitters 3 and 4 are operated on donut modes 0 and 1, respectively. The output of transmitters 3 and 4 is

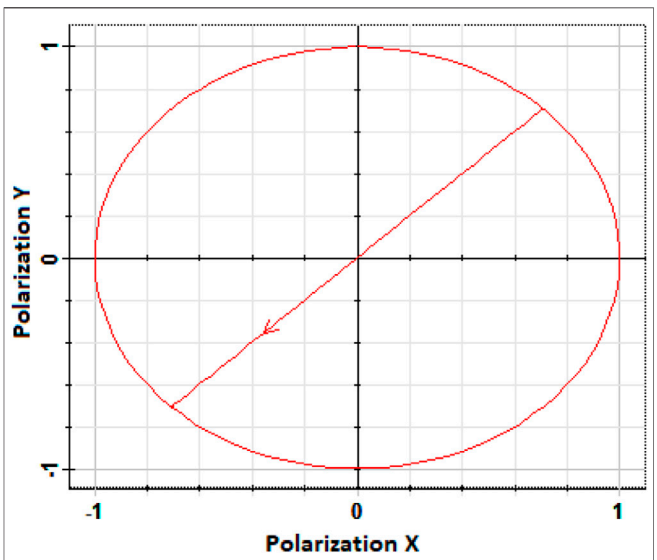


**FIGURE 3 |** Maintained polarization states.

combined and a polarization state (Y Polarization) is maintained by providing azimuth of $90^0$ through the state of polarization controller. The output of the states of polarization controllers is combined and transmitted through free space link. The output of link is amplified by using optical amplifier with the gain of 18dB. **Figure 3** shows the maintained polarization states for X and Y polarizations. X and Y polarizations are separated by using polarization splitter at the receiver side. The polarization states are further split into two parts corresponding to two modes transmitted at the transmitter side. Mode selector is used to select the particular mode required for the receiver side.

**Figure 4** shows the schematic diagram of transmitter and receiver in the proposed MDM-PDM-Ro-FSO system. 10 Gbps data are encoded by employing low-cost NRZ encoding scheme and then upconverted to 40 GHz mm wave by using mixer as shown in **Figure 5**. Sine wave generator is used to generate the 40 GHz mm signal.

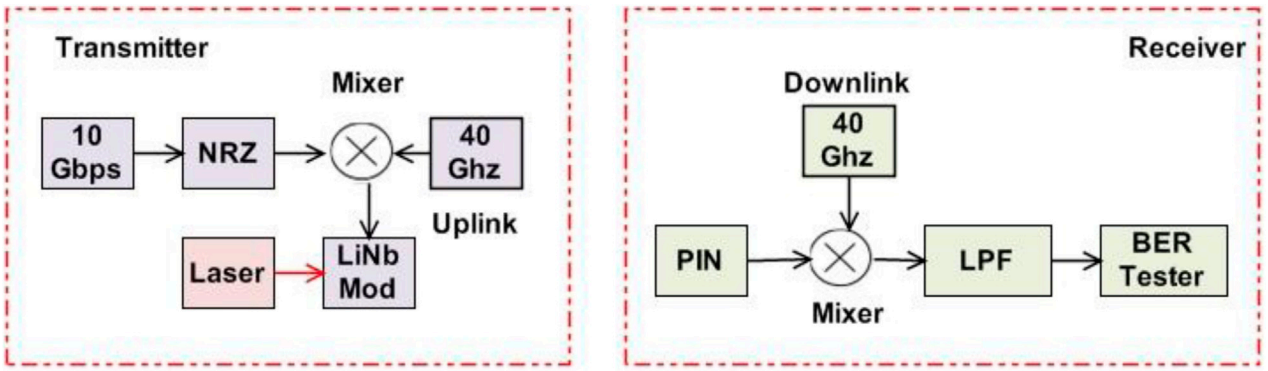


**FIGURE 4 |** Schematic representation of Transmitter and Receive. rThe FSO link can be mathematically described as.

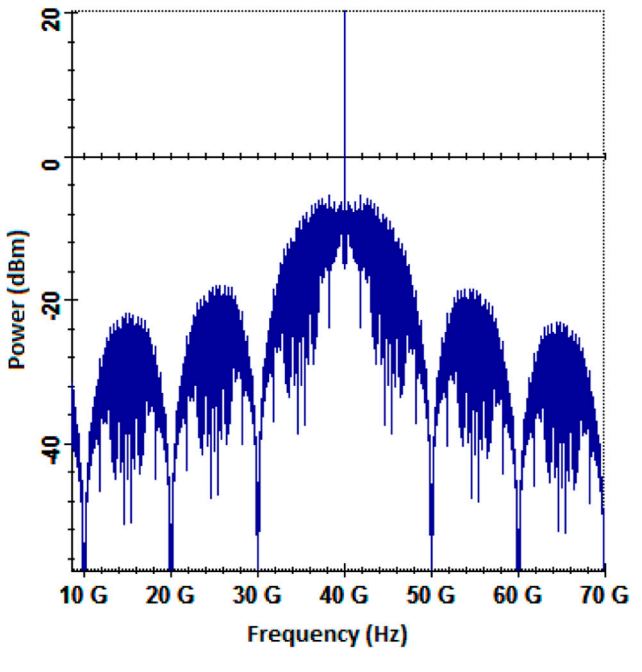


**FIGURE 5 |** Measured Upconverted 40 GHz radio carrier.

Lithium Niobate optical modulator is used for modulating the 40 GHz upconverted wave through optical carrier. The receiver consists of PIN photodiode which further converts the optical signal back to the corresponding electrical signal. The output of photodetector is then mixed with 40 GHz radio signal to attain the process of down conversion.

After the down conversion process, low-pass filter is used to recover the original baseband signal.

$$P_{\text{Received}} = P_{Transmitted}\frac{d_R^2}{(d_T + \vartheta R)^2}10^{-\alpha\frac{R}{10}} \quad (1)$$

In this FSO link equation, $P_{\text{Received}}$ refers to the received power at the receiving end of telescope and $P_{Transmitted}$ the transmitted power at the transmitting end of telescope. $d_T$ is the transmitter's and $d_R$ the receiver's aperture diameters. $\vartheta$ is defined as beam divergence and FSO range is denoted by $R$ and attenuation range is denoted by $\alpha$. Beer-Lambert law is used for calculating the attenuation phenomena which can be represented as follows [22]:

$$H(\lambda, L) = \exp(\lambda, L) \quad (2)$$

In this equation, "λ" refers to wavelength, "L" the propagation distance and "H" the loss coefficient. Another model on FSO attenuation that depends upon visibility factor known as Kim's attenuation model can be represented mathematically as [23]:

$$a(dB/Km) = \frac{3.91}{v}\left(\frac{\lambda}{550}\right)^{-q} \quad (3)$$

where $v$ refers to meteorological visibility, $\lambda$ operating wavelength and $q$ a factor depending on the size distribution of atmospheric particles.

**TABLE 1 |** Attenuation value under different atmospheric turbulences.

| | |
|---|---|
| **Clear sky** | **0.468** |
| Partially Hazy/Rainy | 12 |
| Dense Fog/Very Hazy | 25 |

**TABLE 2 |** MDM-PDM-Ro-FSO modeling parameters.

| Component name | Parameter name | Value |
|---|---|---|
| Spatial Laser | Wavelength | 850 nm |
| | Power | 0 dBm |
| | Mode outer radius | 5 μm |
| | Linewidth | 10 MHz |
| | Noise dynamic | 3 dB |
| MZM Modulator | Extinction Ratio | 30 dB |
| FSO | Transmitter Aperture Diameter | 5 cm |
| | Receiver Aperture Diameter | 20 cm |
| | Beam Divergence | 2 μrad |
| APD | Gain | 3 |
| | Responsivity | 1 A/W |
| | Ionization ratio | 0.9 |

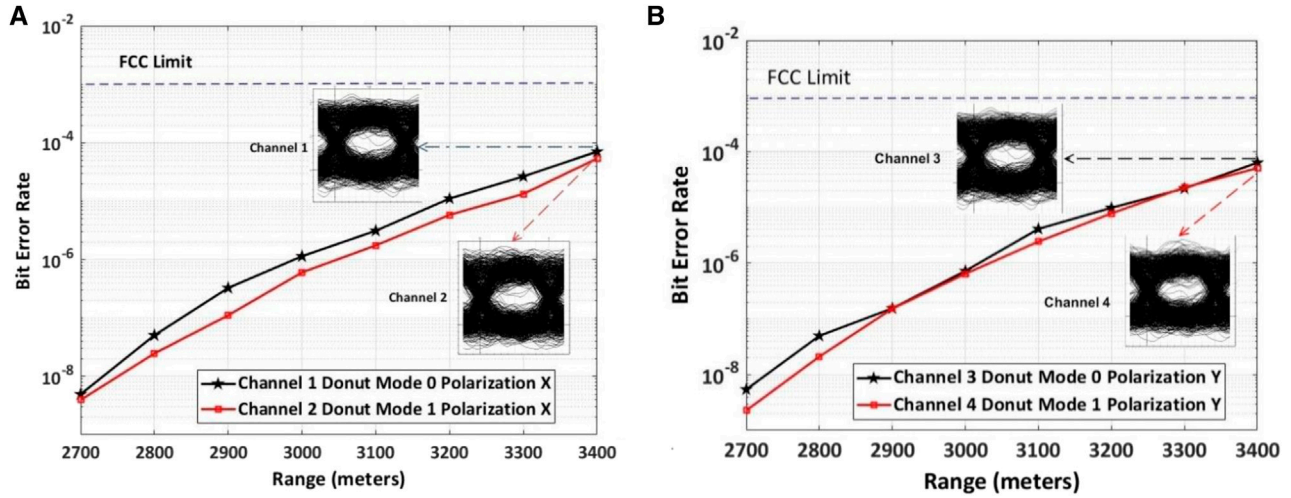


**FIGURE 6 |** Computed BER (clear weather conditions) **(A)** Channel 1 and Channel 2 (X Polarization) **(B)** Channel 3 and Channel 4 (Y Polarization).

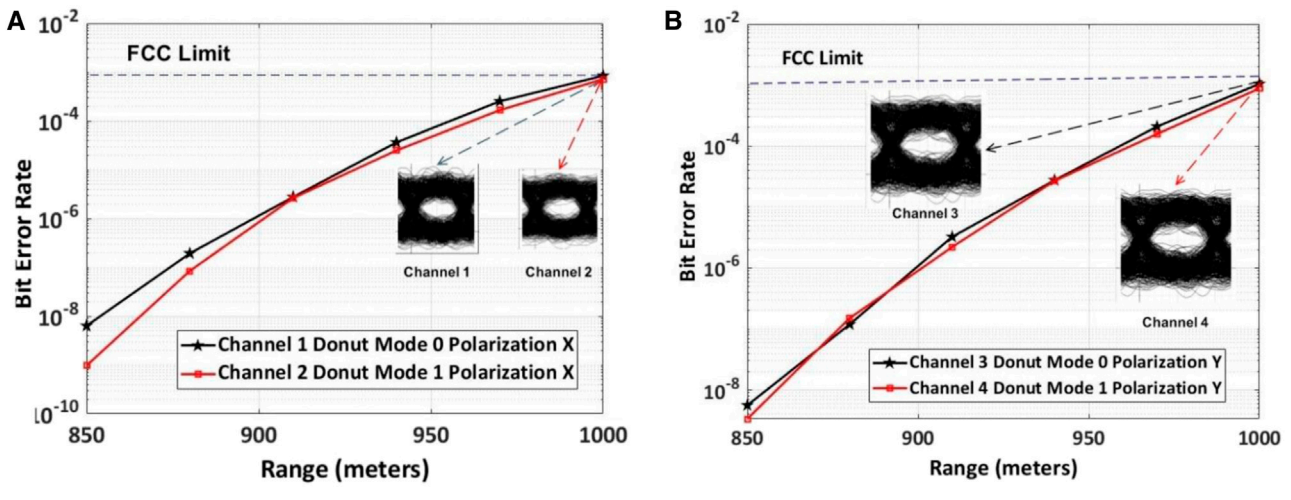


**FIGURE 7 |** Measured BER under partially hazy/rainy atmospheric condition **(A)** Channel 1 and Channel 2 **(B)** Channel 3 and Channel 4

Under the impact of different rainfall, the following equation can calculate the attenuation [24]:

$$\alpha\,(dB/km) = 1.076 \times R^{0.67} \tag{4}$$

where $R$ is the amount of rainfall. **Table 1** shows the different values of atmospheric turbulences [25] and **Table 2** shows the parameters to model the proposed MDM-PDM-Ro-FSO link.

## MODELING OBSERVATIONS AND DISCUSSIONS

The results obtained from the modeling of the proposed MDM-PDM-Ro-FSO system are presented and discussed in this section. **Figure 6** depicts the measured BERs for channels 1 and 2 operated on donut modes 0 and 1, respectively with X polarization as well as for channels 3 and 4 with Y polarization state with respect to Ro-FSO link distance under clear weather conditions. As shown in **Figure 6A**, the computed BER values for Channel 1 and Channel 2 are $10^{-9}$, $10^{-7}$ and $10^{-5}$ at the FSO transmission link of 2,700, 3,200, and 3,400 m. Similarly, for Channel 3 and Channel 4, the BER values are computed as $10^{-9}$, $10^{-6}$ and $10^{-5}$ at the FSO transmission link of 2,700 m, 3,200 m and 3,400 m as shown in **Figure 6B**.

Therefore, under clear weather conditions, all channels achieved the BER of $10^{-4}$ which is below the range of acceptable BER$\approx 10^{-3}$ (FCC limit) at the FSO link of 3400 m with required opening of eye diagrams. However, Channel 2 and Channel 4 operated on donut mode 1 are slightly affected more as compared to Channel 1 and Channel 3 operated on donut mode 0. In another case, the Ro-FSO link is subjected to partially hazy/rainy atmospheric conditions and computed BER is shown in **Figure 7**. The values of BER for Channel 1

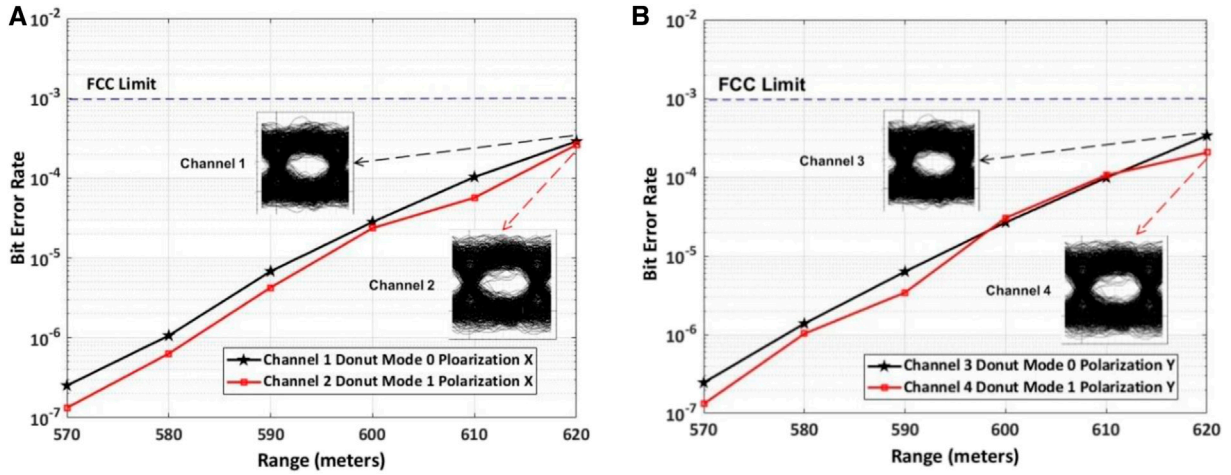


**FIGURE 8 |** Computed BER (dense fog/very hazy atmospheric conditions) **(A)** Channel 1 and Channel 2 (X Polarization) **(B)** Channel 3 and Channel 4 (Y Polarization).

are computed as $10^{-7}$, $10^{-5}$ and $10^{-3}$ at the FSO transmission link of 850, 940 and 1000 m. Similarly for Channel 2, it is computed as $10^{-9}$, $10^{-5}$ and $10^{-3}$ at the FSO transmission link of 850, 940 and 1000 m. As shown in **Figure 7B**, the values of computed BER for Channel 3 and Channel 4 are $10^{-9}$, $10^{-5}$ and $10^{-3}$ at the FSO transmission link of 850, 940 and 1000 m.

**Figure 8** shows the measured BER for all channels under the influence of dense fog/very hazy atmospheric conditions. For Channel 1 and Channel 2, the values of BER are computed as $10^{-7}$, $10^{-5}$, and $10^{-4}$ at the FSO transmission link of 570, 600 and 620 m.

Similarly as shown in **Figure 8B**, for Channel 3 and Channel 4, the values of BER are computed as $10^{-7}$, $10^{-5}$ and $10^{-4}$ at the FSO transmission link of 570, 600 and 620 m.

Thus, when the proposed Ro-FSO link is operated in clear weather conditions, the computed BER shows transmission of all the channels up to 3400 m FSO link with acceptable BER $\approx 10^{-3}$ and eye diagrams. After the FSO transmission distance, BER value increases beyond the FCC limit. Moreover, when the proposed Ro-FSO link is operated in partial haze/rain, the FSO transmission distance reduces to 1000 m with acceptable BER and eye diagrams. Furthermore, when the proposed Ro-FSO link is operated in dense fog/heavy rain, the FSO transmission distance reduces to 620 m with acceptable BER and eye diagrams.

## CONCLUSION

In this work, Ro-FSO link is designed for transmission of broadband services by employing hybrid MDM and PDM schemes. Donut modes 0 and 1 were used for MDM scheme whereas NRZ scheme was used for encoding the pseudorandom data. The designed MDM-PDM-Ro-FSO link could transmit four independent channels each with 10 Gbps data upconverted to 40 GHz radio signal. Under the clear weather condition, the proposed MDM-PDM-Ro-FSO link can transmit 40 Gbps data up to 3400 m with acceptable BER $\approx 10^{-3}$. However, when the weather condition changed to partial haze/rain, the proposed MDM-PDM-Ro-FSO link could withstand only up to 1000 m due to attenuation. Furthermore, when the atmospheric condition changed from partial haze/rain to dense fog/heavy rain, the proposed link could withstand up to 650 m only with acceptable BER.

## DATA AVAILABILITY STATEMENT

The raw data supporting the conclusion of this article will be made available by the authors, without undue reservation.

## AUTHOR CONTRIBUTIONS

SC: Conceptualization, methodology, investigation, writing—original draft. LW: supervision, resources, project administration, funding acquisition. JN and XT: supervision, funding acquisition. MS , SA, and AA: Methodology, Funding Acquisition, resources. AS and SC: data curation and visualization.

## FUNDING

This research project is supported by the Second Century Fund (C2F), Chulalongkorn University, Thailand. This research work is also funded by TSRI Fund (CU_FRB640001_01_21_8).

## ACKNOWLEDGMENTS

The authors also would like to thank Taif University Researchers supporting project number (TURSP-2020/228), Taif University, Taif, Saudi Arabia.

## REFERENCES


1. de la Fuente A, Leal RP, Armada AG. New Technologies and Trends for Next Generation Mobile Broadcasting Services. *IEEE Commun Mag* (2016) 54: 217–23. doi:10.1109/mcom.2016.1600216rp
2. Zin A, Bongsu M, Idrus S, Zulkifli N. An Overview of Radio-Over-Fiber Network Technology. In International Conference On Photonics (2010). p. 1–3. doi:10.1109/icp.2010.5604429
3. Henniger H, Wilfert O. An Introduction to Free-Space Optical Communications. *Radioengineering* (2010) 19:203–12.
4. Malik A, Singh P. Free Space Optics: Current Applications and Future Challenges. *Int J Opt* (2015) 2015. doi:10.1155/2015/945483
5. Lim C, Wang K, Nirmalathas A. Optical Wireless Communications for High-Speed In-Building Personal Area Networks. In Transparent Optical Networks (ICTON). Kuching, Sarawak, Malaysia.: International Conference on (20162016). p. 1–4. doi:10.1109/icton.2016.7550662
6. Majumdar AK. Fundamentals of Free-Space Optical (FSO) Communication System. In Advanced Free Space Optics (FSO). Springer (2015). p. 1–20. doi:10.1007/978-1-4939-0918-6_1
7. Siegel T, Chen S-P. Investigations of Free Space Optical Communications under Real-World Atmospheric Conditions. *Wireless Pers Commun* (2021) 116:475–90. doi:10.1007/s11277-020-07724-1
8. Sarangal H, Singh A, Malhotra J, Chaudhary S. A Cost Effective 100 Gbps Hybrid MDM-OCDMA-FSO Transmission System under Atmospheric Turbulences. *Opt Quant Electron* (2017) 49:184. doi:10.1007/s11082-017-1019-2
9. Anandkumar D, Sangeetha R. A Survey on Performance Enhancement in Free Space Optical Communication System through Channel Models and Modulation Techniques. *Opt Quan Elect* (2021) 53:1–39. doi:10.1007/s11082-020-02629-6
10. Amphawan A, Chaudhary S, Neo T-K, Kakavand M, Dabbagh M. Radio-over-free Space Optical Space Division Multiplexing System Using 3-core Photonic crystal Fiber Mode Group Multiplexers. *Wireless Netw* (2021) 27:211–25. doi:10.1007/s11276-020-02447-4
11. Kuppusamy PG, Rajkumar K, Maheswar R, Rani SS, Amiri IS. A Long-Reach Radio over Free Space Optics (Ro-FSO) System Using Hybrid Orthogonal Frequency Division Multiplexing (OFDM)-multibeam Concept with Enhanced Detection. *J Opt Commun* 1:2020.
12. Mandal GC, Mukherjee R, Das B, Patra AS. Next-generation Bidirectional Triple-Play Services Using RSOA Based WDM Radio on Free-Space Optics PON. *Opt Commun* (2018) 411:138–42. doi:10.1016/j.optcom.2017.11.033
13. Chaudhary S, Choudhary S, Tang X, Wei X. Empirical Evaluation of High-Speed Cost-Effective Ro-FSO System by Incorporating OCDMA-PDM Scheme under the Presence of Fog. *J Opt Commun* (2020) 1. doi:10.1515/joc-2019-0277
14. Chaudhary S, Amphawan A. The Role and Challenges of Free-Space Optical Systems. *J Opt Commun* (2014) 35:327–34. doi:10.1515/joc-2014-0004
15. Chaudhary S, Lin B, Tang X, Wei X, Zhou Z, Lin C, et al. 40 Gbps-80 GHz PSK-MDM Based Ro-FSO Transmission System. *Opt Quant Electron* (2018) 50:321. doi:10.1007/s11082-018-1592-z
16. Xiaoming Zhu X, Kahn JM. Free-space Optical Communication through Atmospheric Turbulence Channels. *IEEE Trans Commun* (2002) 50: 1293–300. doi:10.1109/tcomm.2002.800829
17. Rashidi F, He J, Chen L. Performance Investigation of FSO–OFDM Communication Systems under the Heavy Rain Weather. *J Opt Commun* (2017) 39:37–42. doi:10.1515/joc-2016-0085
18. Perez J, Chicharro F, Ortega B, Mora J, "On the Evaluation of an Optical OFDM Radio over FSO System with IM-DD for High-Speed Indoor Communications," in 2017 19th International Conference on Transparent Optical Networks (ICTON), 2017, pp. 1–4.doi:10.1109/icton.2017.8025112
19. Kumar P, Thakor S. Performance of OFDM-FSO Link with Analog Network Coding. *Photon Netw Commun* (2018) 35:210–24. doi:10.1007/s11107-017-0730-z
20. Kaur G, Srivastava D, Singh P, Parasher Y. Development of a Novel Hybrid PDM/OFDM Technique for FSO System and its Performance Analysis. *Opt Laser Tech* (2019) 109:256–62. doi:10.1016/j.optlastec.2018.08.008
21. Sumathi K, Balasaraswathi M, Boopathi C, Singh M, Malhotra J, Dhasarathan V. Design of 3.84 Tbps Hybrid WDM–PDM Based Inter-satellite Optical Wireless Communication (IsOWC) System Using Spectral Efficient Orthogonal Modulation Scheme. *J Ambient Intelligence Humanized Comput* (2020) 1–9.
22. Gebhart M, Leitgeb E, Muhammad SS, Flecker B, Chlestil C, Al Naboulsi M, et al. Measurement of Light Attenuation in Dense Fog Conditions for FSO Applications. In Atmospheric Optical Modeling. Measurement: and Simulation (2005). p. 58910K. doi:10.1117/12.614830
23. Shakir F, Ali MAA, Ameer F. Utilization of MIMO Concept for Optical Communication System under Fog Condition. *ECTI-EEC* (2019) 17:130–5. doi:10.37936/ecti-eec.2019172.219183
24. Kumar Giri R, Patnaik B. Bit Error Rate Performance Analysis of Hybrid Subcarrier Intensity Modulation-Based FSO with Spatial Diversity in Various Weather Conditions. *J Opt Commun* (2019) 40:307–14. doi:10.1515/joc-2017-0073
25. Israr A, Israr A, Khan F, Khan F. Optimal Modulation Technique for MIMO FSO Link. *Wireless Personal Commun* (2019) 1–20. doi:10.1007/s11277-019-06586-6


**Conflict of Interest:** The authors declare that the research was conducted in the absence of any commercial or financial relationships that could be construed as a potential conflict of interest.

**Publisher's Note:** All claims expressed in this article are solely those of the authors and do not necessarily represent those of their affiliated organizations, or those of the publisher, the editors and the reviewers. Any product that may be evaluated in this article, or claim that may be made by its manufacturer, is not guaranteed or endorsed by the publisher.

frontiers in Sensors

ORIGINAL RESEARCH
published: 13 September 2021
doi: 10.3389/fsens.2021.751952

# Nanoparticle-Based FM-MCF LSPR Biosensor With Open Air-Hole

*Chuanhao Yang, Shiyan Xiao, Qi Wang, Hongxia Zhang, Hui Yu* and Dagong Jia**

*Key Laboratory of Micro Opto-Electro Mechanical System Technology, Key Laboratory of Opto-electronics Information Technology Ministry of Education, School of Precision Instrument and Opto-electronics Engineering, Tianjin University, Tianjin, China*

A nanoparticle-based few-mode multi-core fiber (FM-MCF) localized surface plasmon resonance (LSPR) biosensor is proposed and analyzed using the finite element method (FEM). It's critical to narrow the loss spectrum and improve the coupling efficiency, which makes it have high resolution and high sensitivity. With the aid of open air holes, the gold nanoparticles are easily assembled on the surface of this FM-MCF LSPR biosensor. Through multiple investigations, the performance of the sensor can be improved by properly setting gold nanoparticle configurations, such as radius, positions, shapes, and nanoparticle arrays. The simulation results show that when three circular gold nanoparticles with a radius of 150 nm are placed symmetrically in the open air hole and the angle between adjacent nanoparticles is 5°, the maximum sensitivity of 7,351.6 nm/RIU ($LP_{02y}$ mode $n_a$ = 1.38) can be obtained in the sensing range of 1.33–1.38, which covers the refractive index (RI) of biological fluids, such as bovine serum albumin (BSA) solution and human Immunoglobulin G.

**Keywords: biosensor, nanoparticle, localized surface plasmon resonance, few-mode multicore fiber sensor, open air-hole**

OPEN ACCESS

***Edited by:***
*Santosh Kumar, Liaocheng University, China*

***Reviewed by:***
*Kuldeep Choudhary, DIT University, India*
*Kobra–Omidfar, Tehran University of Medical Sciences, Iran*

****Correspondence:***
*Hui Yu*
*yuhui@tju.edu.cn*
*Dagong Jia*
*dagongjia@tju.edu.cn*

***Specialty section:***
*This article was submitted to Biosensors, a section of the journal Frontiers in Sensors*

***Received:*** *02 August 2021*
***Accepted:*** *30 August 2021*
***Published:*** *13 September 2021*

***Citation:***
*Yang C, Xiao S, Wang Q, Zhang H, Yu H and Jia D (2021) Nanoparticle-Based FM-MCF LSPR Biosensor With Open Air-Hole. Front. Sens. 2:751952. doi: 10.3389/fsens.2021.751952*

## INTRODUCTION

Optical biosensors have shown good performance in detecting biological systems and have promoted major advances in clinical diagnosis, drug discovery, food safety, and environmental monitoring (Chiavaioli et al., 2017a; Zanchetta et al., 2017; Sinibaldi et al., 2018; Min Y, 2020) This is due to the high sensitivity, anti-interference, stability, low noise, and other advantages of optical signals. Localized surface plasmon resonance (LSPR) biosensors are extensively employed because they show many significant advantages over conventional optical biosensors, including high refractive index (RI) sensitivity, fast sensor response, real-time detection, and a label-free technique (Chen and Ming, 2012; Cao et al., 2014). With the development of nanotechnology, biosensors based on LSPR have attracted more attention from researchers (Chen et al., 2020; Li et al., 2020; Wang et al., 2020), LSPR phenomenon exists in metal nanoparticles (MNP) rather than bulk metals, the collective oscillation occurs when the conduction electrons in the nanoparticles have the same frequency as the incident photons. When LSPR is excited, the absorption and scattering of photons are greatly enhanced, and a resonance peak appears in the wide spectral range.

Nanoparticles play a vital role in LSPR excitation, when metal particles are in nanoscale size and smaller than the light wavelength, their physical properties change dramatically (Willets and Van Duyne, 2007). Because of the high specific surface area, nanoparticles can be used to overcome the limitations of SPR sensor performance. Moreover, the localized surface plasmon is distributed in a small region near the particle surface, so the LSPR can be controlled by changing the particle

properties, such as particle size, shape, and composition (Chen et al., 2008). Size and shape dependence allows the resonance peak to be adjusted along the entire visible and near-infrared spectrum, meanwhile, it is useful for optimizing surface enhancement, heat treatment, and enhancing the biosensor response of nanoparticles. In addition, LSPR is highly responsive to RI variation around the MNPs, and the resonance peak shift can be used to monitor the local RI changes caused by the interactions of biomolecules around nanoparticles, so LSPR biosensors are suitable for observing very low concentration of biological liquid analytes and molecules of small weight (Cottat et al., 2013).

Optical fiber offers great advantages for LSPR sensor design. It has been confirmed that expanding the area of LSPR is the key to designing efficient biosensors since the size of the LSPR area is directly proportional to sensing abilities of RI variations in the biological liquid analyte (He, 2019). Therefore, fiber sensor with open structure is more feasible, in which the groove channels can be easily covered or coated with nanoparticles. In such design, the LSPR region is enlarged and the contact of the biological liquid analyte with the nanoparticles is unimpeded. Several open structure sensors have been developed. Liu et al. proposed a mid-infrared SPR sensor with two open-ring channels based on PCF, a thin gold film is deposited on the wall of the open-rings and the liquid analyte can penetrate the channels (Liu et al., 2017). Since the core mode simultaneously activates the SPR at two open-ring channels, the sensing channel cannot be selected. Yang et al. presented a concave-shaped PCF combined with square-channel using indium tin oxide (ITO) for SPR sensing (Yang et al., 2019). Although the role of the groove sensing channel is not mentioned and emphasized in the two papers, the distribution of sensing channels provides useful insight for addressing the problems in the detection of liquid biological substances.

To solve the above problems, we propose nanoparticle-based few-mode multi-core fiber (FM-MCF) LSPR biosensor with open air holes. Due to the air holes distribution of the FM-MCF, the six outer open air holes allow the gold nanoparticles to be easily assembled on the surface of the sensor and enlarge the LSPR area. FM-MCF combines the advantages of multi-core fibers (MCFs) and few-mode fibers (FMFs) that aims to narrow the loss spectrum and improve the coupling efficiency (Dong et al., 2019). which make the sensors have high resolution and high sensitivity (Mollah and Islam, 2020; Singh et al., 2020). Furthermore, MCFs are beneficial to realize multi-channel sensing (Wei et al., 2017). Although FM-MCF sensors have been studied (Yang et al., 2017; Wang et al., 2018; Yao et al., 2019), the application in biochemical has been rarely reported. The LSPR biosensor we propose exhibits high sensitivity in liquid analyte detection, and therefore has potential in chemical and biological sensing (Chiavaioli et al., 2018; Zheng et al., 2018; Zubiate et al., 2019).

## PREPARATION SENSING MODEL AND SIMULATION

**Figure 1A** is a schematic diagram of the FM-MCF LSPR sensor system device; the entire system includes light source (Ocean Optics HL-2000), seven-core fiber fan-in/fan-out modules (FAN 7–42,YOFC), FM-MCF sensor, glass tank and spectrometer (Ocean Optics HR4000CG-UV-NIR). The FM-MCF is connected to the light source and the spectrometer through single-mode seven-core optical fibers (SM-SCF). It's a part of a fan-in/fan-out module as shown in **Figure 1B**, and the other end of this module is composed of seven single mode fibers (SMFs). The area with a length of 1cm in the middle of the FM-MCF is made as the sensing area, **Figure 1C** is the cross section of the sensing area, where the seven cores are arranged in a hexagonal shape and each core is surrounded by six air holes to form a hexagon. As seen in **Figure 1D**, the cladding diameter of the FM-MCF without the coating layer is 192 μm, the core diameter is 13.1 μm, the air hole diameter is 9.4 μm, the core pitch is 40 μm, and the air hole pitch is 13.3 μm. In order to fabricate the groove sensing channels which can be seen in **Figure 1C**, the six outermost air holes of FM-MCF are etched to be tangent to the cores using hydrofluoric acid. Then, the six open air holes are used to assemble nanoparticles and hold biological liquid analytes. When gold nanoparticles are filled into these groove sensing channels, our biosensor can detect many kinds of biological liquid analytes.

In order to find the optimized parameters for the FM-MCF LSPR sensor, the finite element method (FEM) software COMSOL Multiphysics is used to numerically simulate the performance. In the model wizard window, we select Frequency Domain (ewfd) in Electromagnetic Waves module and Mode Analysis in Select Study. The simulation model in COMSOL is illustrated in **Figure 2A**. Due to the geometric symmetry and low core-to-core crosstalk (Van Uden et al., 2014), each fiber core is considered to transmit light independently. Hence, only one-sixth of the whole fiber needs to be calculated. As FEM mesh shows, orange lines are periodic boundary conditions, and perfectly matched layer (PML) is set on the outmost layer. Besides, the free triangular mesh is used to segment the computation area. The computational region contains 22,161 domain elements and the number of degrees of freedom is 155,738. **Figure 2B** is the zoom-in of the red square which depicts a gold nanoparticle with a radius of 150 nm attached to the etched open air-hole.

During the simulation, The refractive index of pure silica can be described by Sellmeier equation (Sellmeier, 1871). The dielectric constant of gold in the visible and near-IR region is given by the Drude-Lorentz model and written as follows (Rakić et al., 1998)

$$\varepsilon(\omega) = 1 - \frac{\Omega_p^2}{\omega(\omega - i\Gamma_0)} + \sum_{j=1}^{k} \frac{f_j \omega_p^2}{\left(\omega_j^2 - \omega^2\right) + i\omega\Gamma_j}$$

where $\omega_p$ is the plasma frequency, k is the number of oscillators with frequency $\omega_j$, strength $f_j$, and lifetime $1/\Gamma_j$, while $\Omega_p = \sqrt{f_0}\omega_p$.

Similarly, confinement loss is a crucial parameter for the FM-MCF LSPR sensor, which expresses the excitation of the LSPR. Confinement loss is mainly determined by the imaginary part of

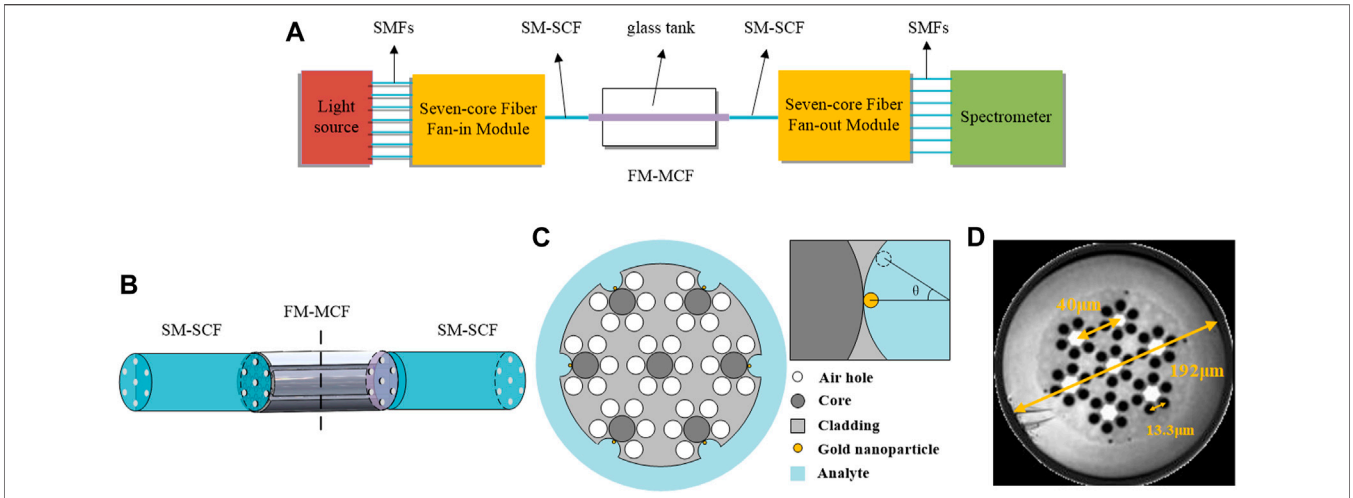


**FIGURE 1 | (A)** Schematic diagram of the FM-MCF LSPR sensor system device; **(B)** Connection between the seven-core fiber fan-in/fan-out module and the FM-MCF; **(C)** Geometric model of the FM-MCF LSPR sensor's sensing area and the structure of gold nanoparticles; **(D)** Cross-section of the FM-MCF. Inset in **Figure 1** depicts the placement of gold nanoparticles.

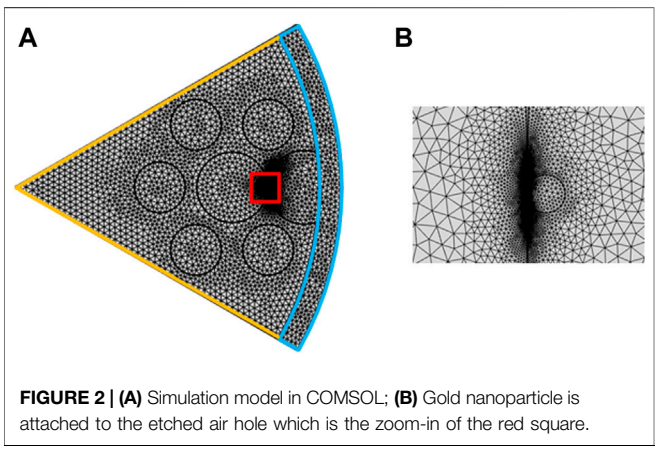


**FIGURE 2 | (A)** Simulation model in COMSOL; **(B)** Gold nanoparticle is attached to the etched air hole which is the zoom-in of the red square.

the core mode effective RI (Im(neff)) and it can be calculated by (Yang et al., 2021)

$$\alpha_{loss}\,(dB/cm) = 8.686 \times \frac{2\pi}{\lambda} \times \mathrm{Im}\,(neff)$$

where λ is the incident wavelength. Therefore, we can discover and discuss the LSPR effect in some loss spectrums and the electric field of Au nano-particles.

The resonant wavelength of FM-MCF LSPR sensor will shift when the biological liquid analyte RI changes slightly. In consequence, the shift of the resonant wavelength can be used for the detection of the RI change of biological liquid analytes. Sensitivity is an important parameter to measure sensor performance. Spectral sensitivity is described as (Yang et al., 2021)

$$S(\lambda) = \frac{\Delta\lambda_{peak}}{\Delta n_a}\,(nm/RIU)$$

where is the resonant wavelength shift of the loss peak, is the change of the biological liquid analyte RI.

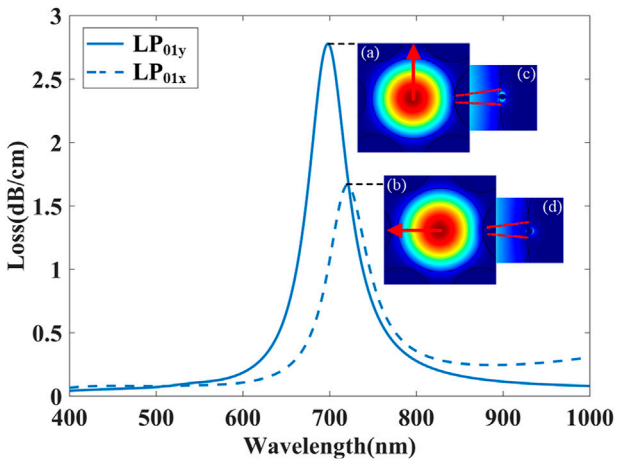


**FIGURE 3 |** Loss spectra excited by $LP_{01y}$ and $LP_{01x}$ mode and corresponding optical field distribution while $n_a = 1.33$. Insets (a), (b), (c) and (d) show the optical field distribution of the core modes and plasmon modes at different resonant wavelengths.

## RESULTS AND DISCUSSION

Our FM-MCF is originally designed to use for transmission of optical signals in telecommunication, so it only supports $LP_{01}$ and $LP_{11}$ two modes in each core at the communication band. Loss spectra of the FM-MCF LSPR sensor excited by fundamental mode ($LP_{01y}$ and $LP_{01x}$) are presented in **Figure 3**, while biological liquid analyte RI ($n_a$) is 1.33 and the radius of the gold nanoparticle is 110 nm. Optical field distribution of $LP_{01y}$ and $LP_{01x}$ (two polarization direction of $LP_{01}$) and corresponding plasmon mode are illustrated in insets (a), (b), (c), and (d), respectively, where the red arrows in the insets (a) and (b) indicate the direction of the electric field. As shown in

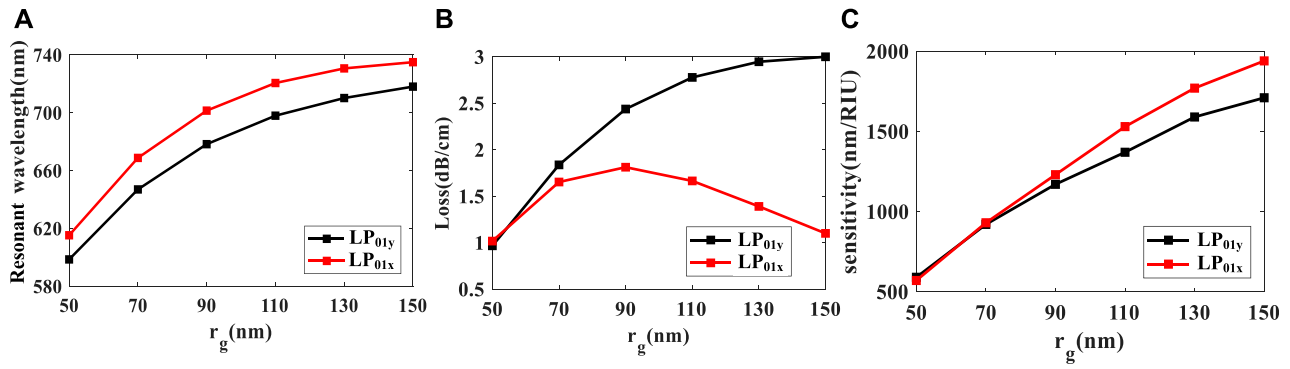


**FIGURE 4 | (A)** Relationship between $r_g$ and resonant wavelength when $n_a$ = 1.33; **(B)** Effect of $r_g$ on spectral loss when $n_a$ = 1.33; **(C)** spectral sensitivity of the FM-MCF LSPR biosensor at different $r_g$ when $n_a$ is from 1.33 to 1.34.

**Figure 3**, not only $LP_{01x}$ but also $LP_{01y}$ mode in the FM-MCF core can excite the LSPR effect. Besides, the resonant wavelength of $LP_{01y}$ is shorter than $LP_{01x}$, though the spectral loss is higher than it. Since the resonant wavelength of plasmon mode is around 700 nm, there are many modes transmitted in the optical fiber core. Similar to LP01 mode, two polarization directions (x and y) of $LP_{11}$, $LP_{21}$, and $LP_{02}$ mode are also able to excite LSPR. Consequently, the influence of transmission modes in the fiber on our biosensor is analyzed in detail, as well as the radius of gold nanoparticle, nanoparticle positions, shapes of nanoparticle, and nanoparticle arrays.

## Effects of the Gold Nanoparticle's Radius

The radius of the nanoparticle plays an important role in the performance of the biosensor. **Figure 4** shows the effect of the nanoparticle's radius $r_g$ on the resonant wavelength, spectral loss, and spectral sensitivity. **Figure 4A** shows the relationship between the resonant wavelength and $r_g$ when $n_a$ is 1.33. With the increase of $r_g$, the resonant wavelength of the FM-MCF LSPR sensor exhibits a red shift, this is because the nanoparticle's radius affects the maximum light coupling between the fiber mode and gold nanoparticle. Although resonant wavelength has a red shift, the change of adjacent resonance peaks gradually decreases. The relationship between $r_g$ and spectral loss when $n_a$ = 1.33 is shown in **Figure 4B**. In **Figure 4B**, the peak loss of $LP_{01x}$ mode increases with the radius of the nanoparticle initially, when $r_g$ = 90 nm, at this moment $LP_{01x}$ has the maximum loss, and then peak loss begins to decrease. However, the peak loss of $LP_{01y}$ mode always increases as the radius increases, when $r_g$ = 150 nm, $LP_{01y}$ has the maximum loss. When $n_a$ varies from 1.33 to 1.34, the spectral sensitivity of FM-MCF LSPR biosensor for different nanoparticle's radius is presented in **Figure 4C**. As the radius increases, the sensitivity continues to increase, reaching its maximum when the radius is 150 nm. Therefore, by changing the radius of the gold nanoparticle, we can adjust the resonant wavelength, spectral loss, and the spectral sensitivity of the biosensor.

## The Influence of Nanoparticle Positions

Meanwhile, the influence of nanoparticle positions on FM-MCF LSPR biosensor performance is also analyzed in this paper. The gold nanoparticle is initially placed tangent to the core, as illustrated in **Figure 1A**. When the nanoparticle rotates clockwise around the center of the open air-hole to the next position, the angle between the original position and the next position is described by $\theta$.

**Figure 5** depicts fundamental mode loss spectra of $n_a$ = 1.33 when $\theta$ is 0°, 5°, 10°, and 15°, respectively. We found that as $\theta$ increases, the peak losses of the two polarizations gradually decrease but the resonant wavelength remains almost the same. The reason is that the evanescent wave has a certain penetration depth, and its amplitude decreases exponentially with the increase of the distance from the interface so peak loss varies when the nanoparticle is placed at different angles (Chiavaioli et al., 2017b).

## Effect of Transmission Modes

The FM-MCF we use only supports two modes ($LP_{01}$ and $LP_{11}$) at the communication band. At visible wavelengths, plenty of high order modes can be transmitted in the fiber core. Transmission mode in the fiber is also a significant factor that affects the performance of the presented biosensor. As mentioned above, we fix the radius of the gold nanoparticle to 150 nm and the best position to $\theta = 0°$. Loss spectra of different modes when biological liquid analyte RI ranges from 1.33 to 1.39 with a step of 0.01 is shown in **Figure 6**, where the dash lines represent the loss spectra of the x polarization while the solid lines represent the y polarization. It can be seen that loss spectra excited by y polarization have higher losses than x polarization in the same mode and the resonant wavelength of x polarization is also longer than that of y. When using high order modes to excite LSPR, high order modes usually have higher losses than the fundamental mode, and hence their LSPR loss curves are steeper than that of the fundamental mode, the narrower the loss curve, the better the resolution of the sensor. Therefore, the performance of LSPR biosensor excited by the high order mode is better than the fundamental mode.

**Figure 7** shows the relations between $n_a$ and the resonant wavelength. The average sensitivity and highest sensitivity can be obtained according to (3). The average sensitivity of the $LP_{01x}$, $LP_{01y}$, $LP_{11x}$, $LP_{11y}$, $LP_{21x}$, $LP_{21y}$, $LP_{02x}$, and $LP_{02y}$ mode is 2467.9, 2257.9, 2528.2, 2310, 2640, 2428.6, 2557.1, and 2313.9 nm/RIU,

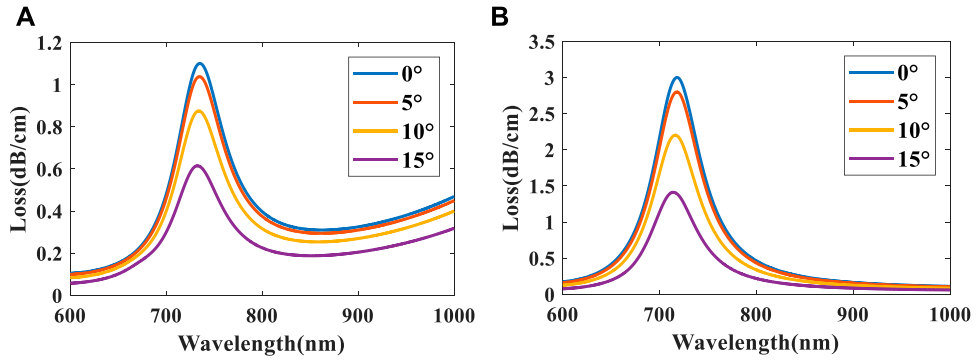


**FIGURE 5 |** Loss spectra excited by gold nanoparticle at different positions. **(A)** $LP_{01x}$; **(B)** $LP_{01y}$.

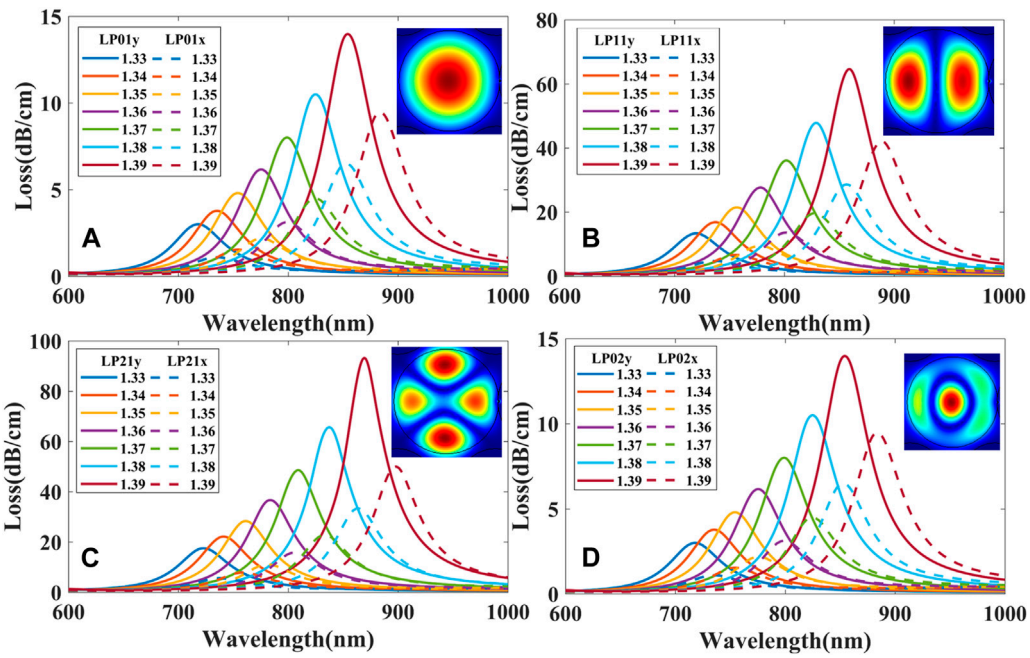


**FIGURE 6 |** Loss spectra excited by different modes: **(A)** $LP_{01x}$ and $LP_{01y}$; **(B)** $LP_{11x}$ and $LP_{11y}$; **(C)** $LP_{21x}$ and $LP_{21y}$; **(D)** $LP_{02x}$ and $LP_{02y}$.

respectively. The $LP_{21x}$ mode has the maximum highest sensitivity of 3478.28 nm/RIU among all modes when $n_a$ = 1.39. It can be seen that x polarization has a higher sensitivity than y polarization in the same mode. In addition, high order modes have higher sensitivity than fundamental mode in the same polarization state. Therefore, using high order mode to excite LSPR can improve the sensitivity of the sensor.

## Effect of Nanoparticle Shapes

It has been shown experimentally that the shape of the gold nanoparticle plays a vital role in determining the sensitivity (Mayer and Hafner, 2011). Several gold nanoparticles with different geometric shapes are illustrated in **Figures 8A–D**, all the nanoparticles are filled in the air hole of the FM-MCF and are tangent to the core. From the previous discussion, when the radius of the circumferential circle is 150 nm, the LSPR excited by gold nanoparticles has the highest sensitivity. When biological liquid analyte RI is set as 1.33, the loss spectra of LSPR excited by four different shapes of gold nanoparticle are shown in **Figure 8E**.

It can be seen that the loss spectra exhibit a red shift as nanoparticle gets sharper in **Figure 8E**. The resonant wavelength of hexagon nanoparticle is close to that of the circular nanoparticle, and the triangle nanoparticle's resonant wavelength is in the near-infrared while circular is in the visible light range. By using different shapes of nanoparticle, we can adjust the resonant wavelength of the FM-MCF LSPR biosensor. **Figure 8** shows the optical field distribution of LSPR excited by different shapes of nanoparticle at the peak of a, b, c, d,

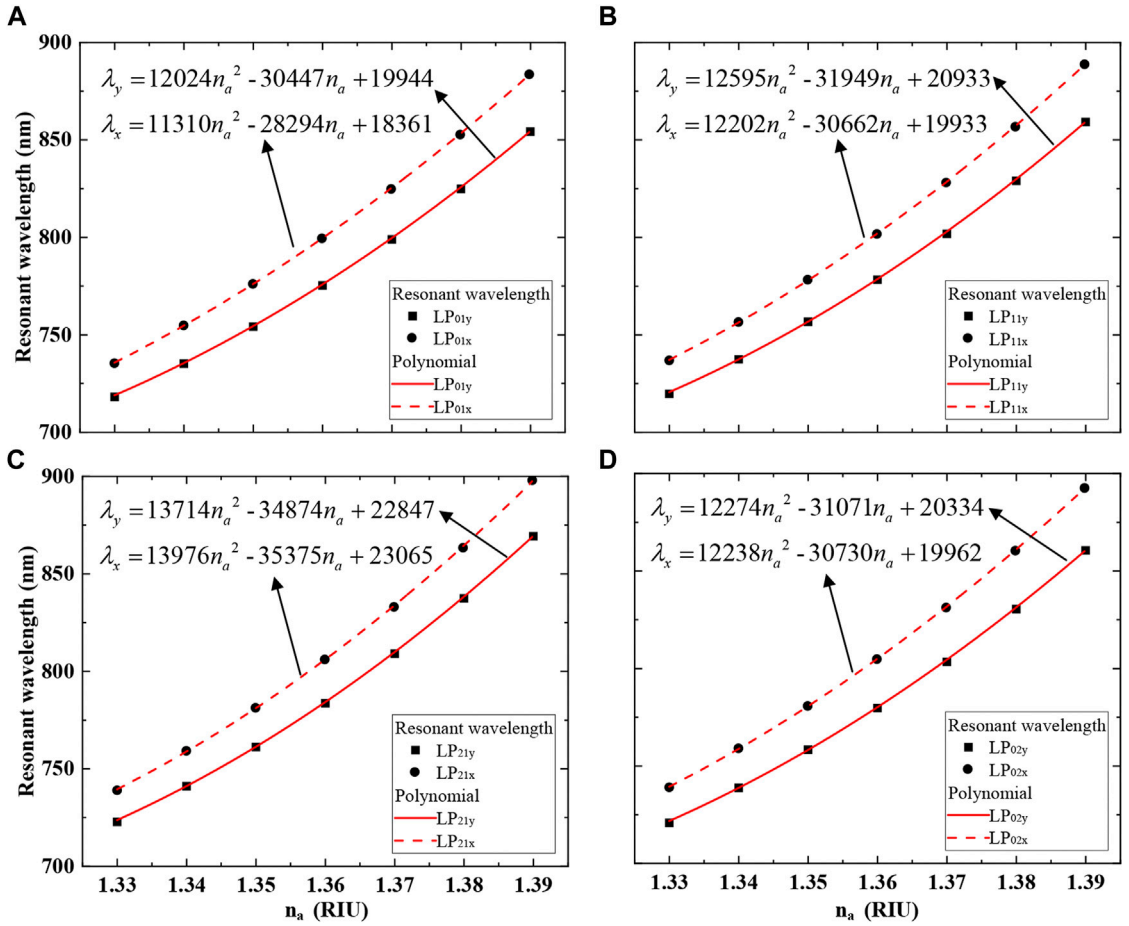


**FIGURE 7 |** Relations between $n_a$ and resonant wavelength. **(A)** $LP_{01x}$ and $LP_{01y}$; **(B)** $LP_{11x}$ and $LP_{11y}$; **(C)** $LP_{21x}$ and $LP_{21y}$; **(D)** $LP_{02x}$ and $LP_{02y}$.

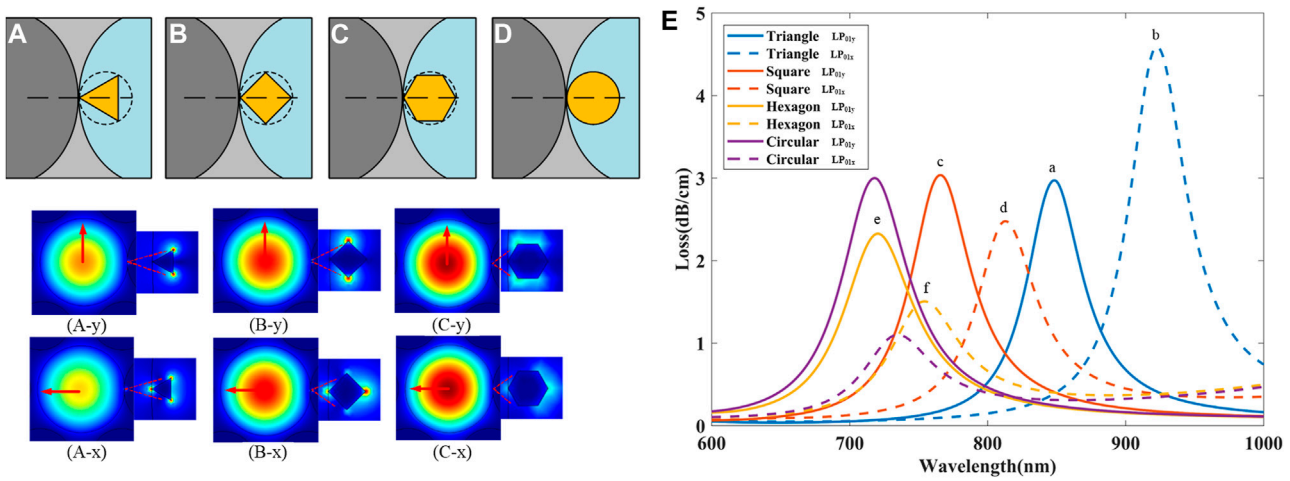


**FIGURE 8 |** Several gold nanoparticles with different geometric shapes. **(A)** triangle nanoparticle; **(B)** square nanoparticle; **(C)** hexagon nanoparticle; **(D)** circular nanoparticle. Optical field distribution of LSPR excited by different shapes of nanoparticle. (A-y) triangle nanoparticle excited by $LP_{01y}$ mode; (A-x) triangle nanoparticle excited by $LP_{01x}$ mode; (B-y) and (B-x) square nanoparticle excited by $LP_{01y}$ mode, $LP_{01x}$ mode, respectively; (C-y) and (C-x) hexagon nanoparticle excited by $LP_{01y}$ mode, $LP_{01x}$ mode, respectively; **(E)** Loss spectra excited by nanoparticle in different shapes for $LP_{01x}$ and $LP_{01y}$ mode.

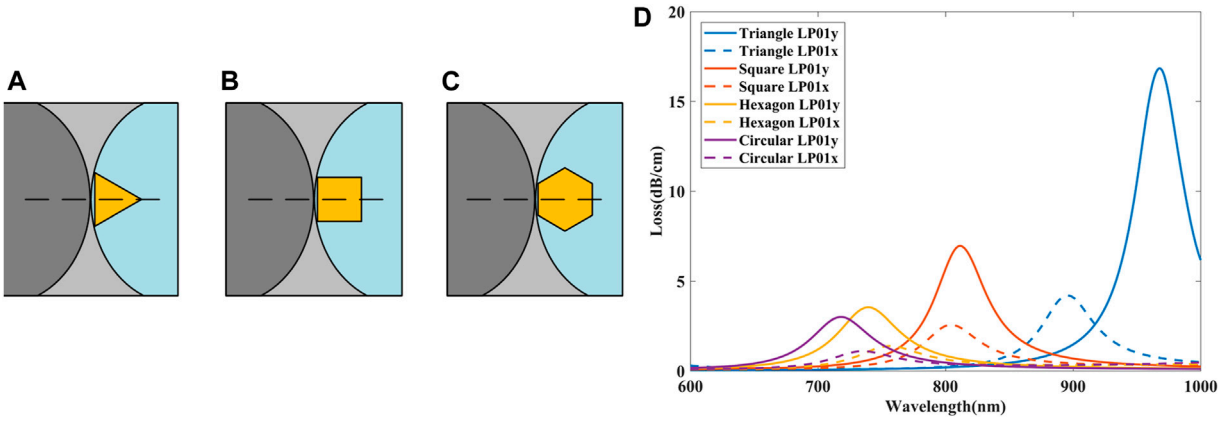


**FIGURE 9 |** Nanoparticles after rotation and moving. **(A)** triangle nanoparticle; **(B)** square nanoparticle; **(C)** hexagon nanoparticle. **(D)** Loss spectra of $LP_{01x}$ and $LP_{01y}$ when different shapes of gold nanoparticles excite LSPR after rotation and moving.

e and f in **Figure 8E**, the red arrows represent the direction of the electric field. When nanoparticles have sharp tips or features, the LSPR energy is mainly concentrated at the tip position. The coupling between $LP_{01}$ mode and SP mode excited by triangle nanoparticle is the best, then square, and finally hexagon nanoparticles. This is because of the sharper the angle, the greater the density of the free electrons at the tip, and the stronger the electric field that can be excited. The strong electric field enhancement at the sharp tips makes it possible to excite surface plasmon resonance with only a small amount of incident light energy, so the sharper the nanoparticle, the longer the resonant wavelength.

In the arrangement shown in **Figures 8A–D**, only one corner of the nanoparticle is in contact with the air hole. For the first three shapes in **Figures 8A–D**, we rotate the nanoparticles 60°, 45°, and 30° counterclockwise along the center as shown in **Figures 9A–C** such that two corners of these nanoparticles are in contact with the air hole. Loss spectra of $LP_{01x}$ and $LP_{01y}$ when different shapes of gold nanoparticles excite LSPR after rotation and moving are shown in **Figure 9D**.

Compare **Figure 9D** with **Figure 8E**, it can be seen that the loss spectra of all shape nanoparticles have changed after rotation and moving. Since the hexagon is closest to the circle, its loss curve does not change significantly after rotation, however, the difference between the triangle and the circle is the largest, so the loss spectra vary obviously. After the triangle nanoparticle rotates 60°, the resonance peak of $LP_{01y}$ moves from 850 to 963 nm (red shift), while the resonance peak of $LP_{01x}$ moves from 950 to 895 nm (blue shift).

## Effect of Nanoparticle Arrays

Nanoparticle arrays also affect the performance of the FM-MCF LSPR biosensor. In **Figure 10** gold nanoparticles with a radius of 150 nm are filled symmetrically in the air hole, the angle between adjacent nanoparticles is represented by $\delta$ and the minimum value is 2.7°, which means that two adjacent nanoparticles are tangent at this time. When $\delta = 2.7°$, the entire air hole can be filled with 81 gold nanoparticles.

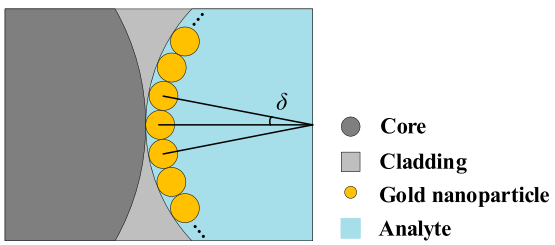


**FIGURE 10 |** Gold nanoparticle arrays excited LSPR at the same time.

Since the air hole range has been determined, the number of nanoparticles n and the angle between adjacent nanoparticles $\delta$ simultaneously affect the property of the gold nanoparticle arrays. The influence of n has been studied at first, the loss curves excited by $LP_{01y}$ mode when $\delta = 2.7°$, $n_a = 1.33$, and n are set as 81, 41, 21, 11, 9, 7, 5, and 3, respectively are shown in **Figure 14**. Because the loss curves of n = 41 and 21 are very close to n = 81, so they are not given in **Figure 11A**. It can be found that compared with single nanoparticle, nanoparticle array has many resonance peaks. When n = 81, the resonant wavelength locates in 680 nm, as n decreases to 11 the loss curves begin to show two peaks, and the resonance peaks at longer wavelength have higher confinement loss. When n = 3, there is an ultra-high loss peak at 1042.4 nm, and the confinement loss can reach 13.5 dB/cm, far exceeding the peak loss at other nanoparticle numbers.

In addition, the loss curves when $n_a = 1.34$ have also been calculated, the resonant wavelength and sensitivity vary with different n, as shown in **Figure 11B**. For the same $n_a$, when n decreases from 81 to 21, the resonance wavelength remains basically unchanged, and as n continues to decrease, the second resonance peak begin to appear at longer wavelength, so the resonant wavelength of n = 11 have a significant red shift. However, as n decrease to 5, the second resonance peak gradually blue shifts so the resonant

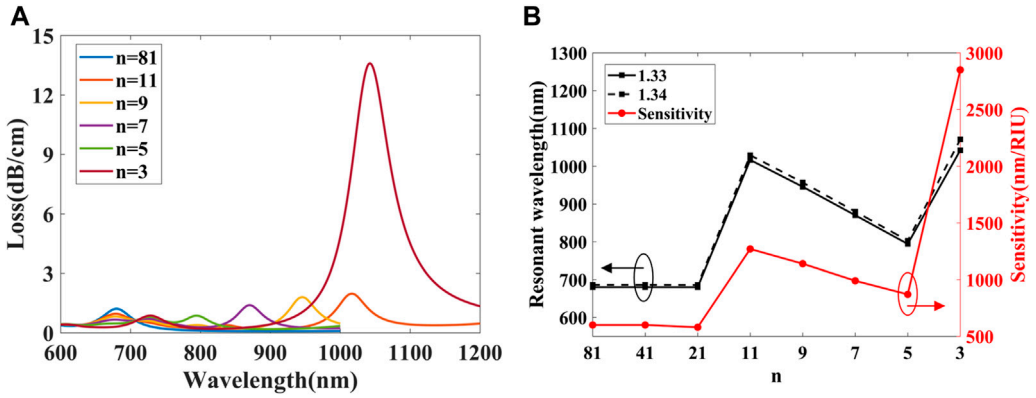


**FIGURE 11 | (A)** spectra of $LP_{01y}$ excited by nanoparticle arrays with different *n*. **(B)** Resonant wavelength and sensitivity vary with different *n*.

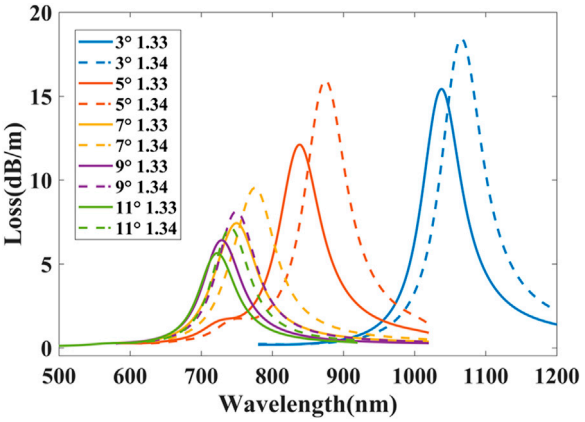


**FIGURE 12 |** Loss spectra of $LP_{01y}$ excited by nanoparticle arrays with different $\delta$.

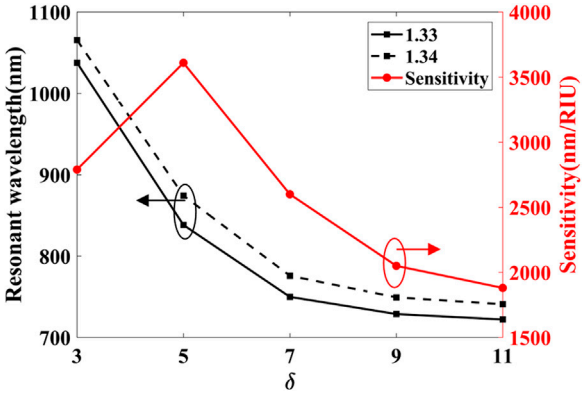


**FIGURE 13 |** Resonant wavelength and sensitivity vary with different $\delta$.

wavelength decreases. The average sensitivity can be calculated by Eq. 3, it can be found that initially when the n decreases, the sensitivity is basically unchanged, when n = 11, the second resonance peak has higher sensitivity but as n continues to decrease the sensitivity decreases. When n = 3, the sensitivity can reach 2850 nm/RIU, which is higher than the sensitivity of other number of nanoparticles. Therefore, the number of nanoparticles n is set to 3.

Secondly, the influence of $\delta$ has been studied. The loss curves for different $\delta$ are shown in **Figure 12** where $\delta = 3^{\circ}, 5^{\circ}, 7^{\circ}, 9^{\circ}$, and $11^{\circ}$. When $\delta$ varies from $11^{\circ}$ to $3^{\circ}$, the resonance peaks have an obvious red shift and the confinement loss gradually increases. It can be interpreted as when $\delta$ is large, each gold nanoparticle can independently excite the LSPR without coupling to each other. With the decrease of $\delta$, the local surface plasmon waves excited by each gold nanoparticle begins to show weak coupling and lead to the red shift of resonance peak. When the distance between gold nanoparticles is close to their own size, the local surface plasmon waves show strong coupling, so the confinement loss gradually increases.

The variation of resonant wavelength and sensitivity with $\delta$ is plotted in **Figure 13**. When $n_a = 1.33$ and $\delta$ increases from $3^{\circ}$ to $5^{\circ}$, the resonant wavelength declines from 1037.7 to 838.2 nm while $\delta$ increases from $9^{\circ}$ to $11^{\circ}$, the resonant wavelength declines from 728.7 to 722 nm. It can be found that although changing $\delta$ can adjust he resonance wavelength's position, the adjustment effect is limited. The sensitivity change with $\delta$ can also be obtained from **Figure 13**. When $\delta = 5^{\circ}$, it reaches the sensitivity of 3610 nm/RIU, which is the largest of all $\delta$. Therefore, the angle between adjacent nanoparticles $\delta = 5^{\circ}$.

The FM-MCF LSPR sensor can work in the RI range of 1.33–1.39 which covers the RI of the BSA solution and human Immunoglobulin G. Therefore, the sensor can be used as a biosensor to detect the biological liquid analytes. The loss curves excited by $LP_{01y}$ and $LP_{11y}$ mode when n = 3, $\delta = 5^{\circ}$ and biological liquid analyte RI is from 1.33 to 1.39 and loss curves excited of $LP_{21y}$ and $LP_{02y}$ mode and biological liquid analyte RI is from 1.33 to 1.38 is shown in **Figure 14**. With the increase of biological liquid analyte RI, the resonance peaks have a red shift and at the same RI, the loss curves of $LP_{11y}$ have a more obvious red shift than that of $LP_{01y}$. **Figure 15** illustrates the relationships between na and resonant wavelengths for $LP_{01y}$

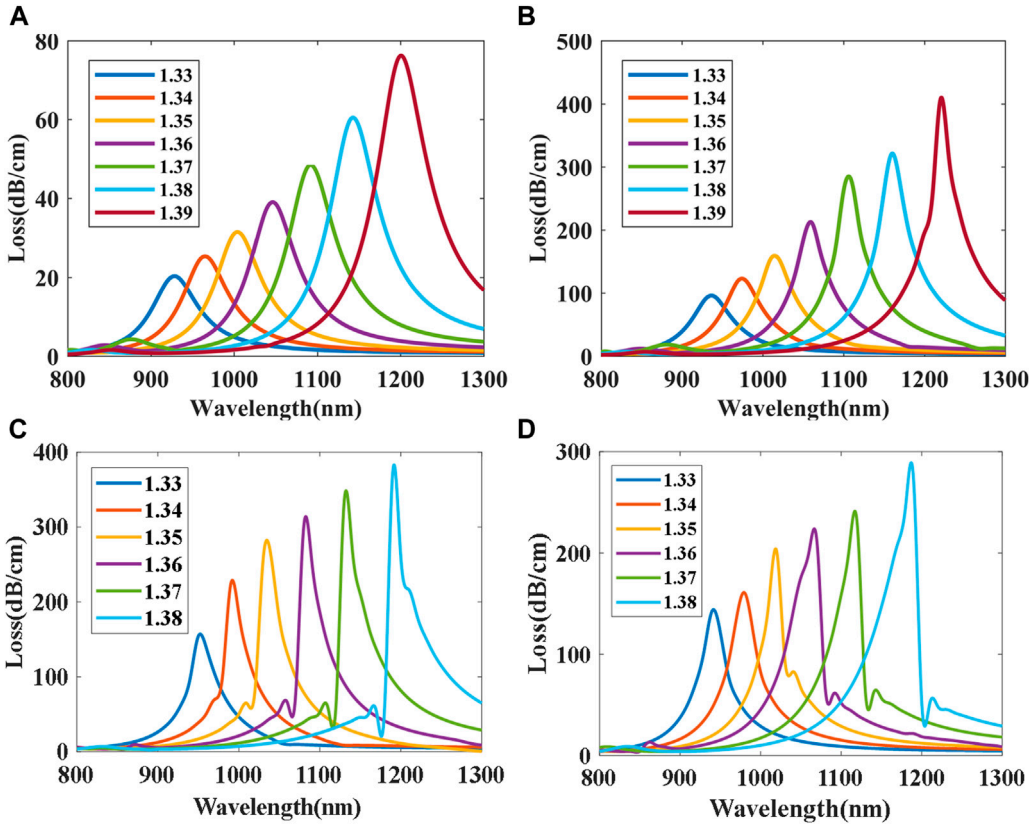


**FIGURE 14 |** Loss curves excited by four different modes. **(A)** $LP_{01y}$; **(B)** $LP_{11y}$; **(C)** $LP_{21y}$; **(D)** $LP_{02y}$.

mode and $LP_{11y}$ mode when $n_a$ = 1.33–1.39. The average sensitivity of $LP_{01y}$ and $LP_{11y}$ mode when $n_a$ is from 1.33 to 1.39 is 4497.1 and 4704.6 nm/RIU, respectively, while the highest sensitivity for each mode is 5732.1 nm/RIU and 6055.36 nm/RIU when $n_a$ = 1.39, respectively. In addition, when the wavelength of incident light along the core is 800–1300 nm, $LP_{21y}$ and $LP_{02y}$ modes can also be transmitted stably, and the RI range at this time is 1.33–1.38. In **Figures 14C,D**, the loss spectra become not smooth, this is mainly because $LP_{21y}$ and $LP_{02y}$ are more likely to resonate with the core mode, and the energy is basically coupled to the plasmon mode. However, when the wavelength has a slight change, the phase matching condition is no longer satisfied. Therefore, the average sensitivity of $LP_{21y}$ and $LP_{02y}$ mode when $n_a$ = 1.33–1.38 is 4888 nm/RIU and 5114 nm/RIU, respectively, and the highest sensitivity for each mode is 6209.6 nm/RIU and 7,351.6 nm/RIU when $n_a$ = 1.38. It is demonstrated that the FM-MCF LSPR biosensor has high sensitivity and is ideal for real-time detection of biological substances.

## CONCLUSION

In this paper, we presented an FM-MCF LSPR biosensor filled with gold nanoparticles in the open air holes. The effect of nanoparticles on the performance of the FM-MCF LSPR biosensor is investigated by using the FEM. The results show that the performance of the sensor can be improved by changing the nanoparticles' configuration. When the radius of gold nanoparticles is 150 nm, three identical gold circular nanoparticles are placed symmetrically in the air hole, and the angle between adjacent nanoparticles is 5°, an average wavelength sensitivity of 4497.1 nm/RIU can be obtained in the sensing range of 1.33–1.39, and the highest sensitivity of $LP_{01y}$ mode is 5732.1 nm/RIU when $n_a$ = 1.39. The FM-MCF can also transmit high order mode stably when the wavelength of incident light is 600–1300 nm. The average sensitivity of $LP_{02y}$ when RI of the biological liquid analyte is 1.33–1.38 is 5114 nm/RIU and the highest sensitivity is 7,351.6 nm/RIU when $n_a$ = 1.38, which is higher than that of the $LP_{01y}$. The proposed sensor can be used in chemical and biological sensing for its excellent properties.

## DATA AVAILABILITY STATEMENT

The original contributions presented in the study are included in the article/supplementary material, further inquiries can be directed to the corresponding author/s.

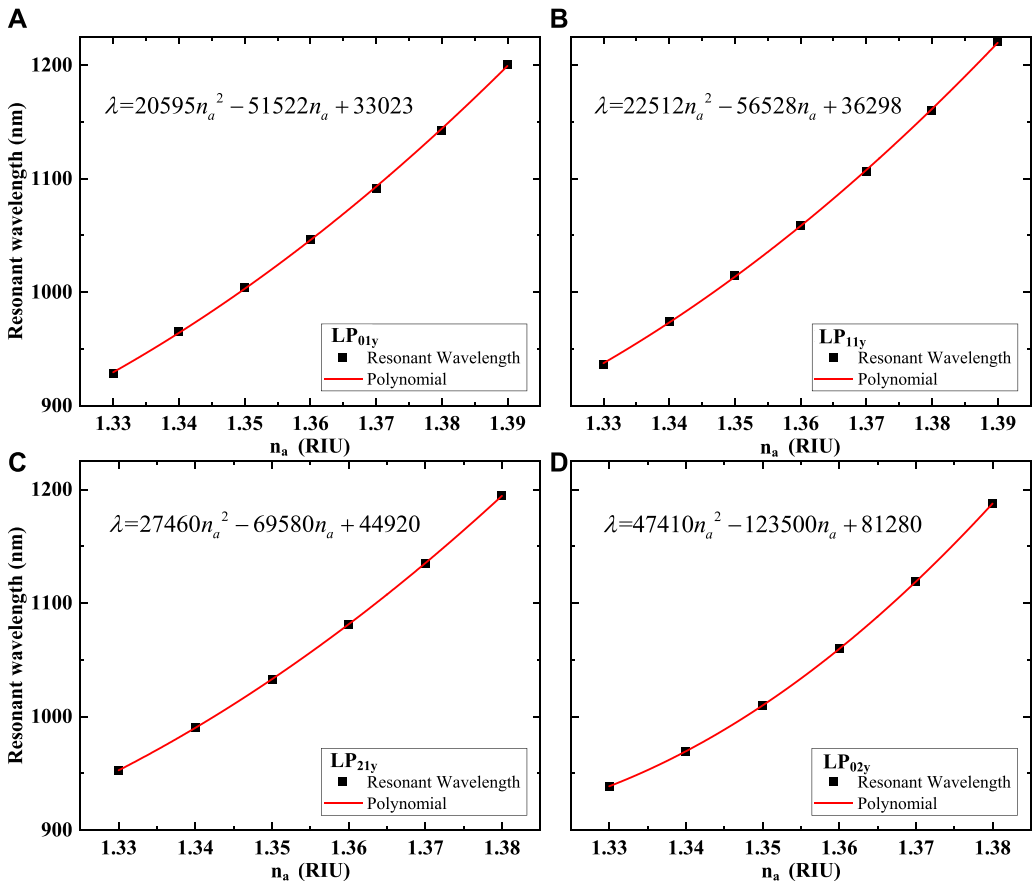


**FIGURE 15 |** Relations between $n_a$ and resonant wavelength. **(A)** $LP_{01y}$; **(B)** $LP_{11y}$; **(C)** $LP_{21y}$; **(D)** $LP_{02y}$.

## AUTHOR CONTRIBUTIONS

All authors listed have made a substantial, direct and intellectual contribution to the work, and approved it for publication.

## FUNDING

This work was supported in part by the National Natural Science Foundation of China (Grant number: U1813207, 61875152) and Key Projects in the Tianjin Science and Technology Pillar Program (Grant number: 20YFZCSY00390).

## ACKNOWLEDGMENTS

The authors would like to thank Prof. Guifang Li from the University of Central Florida for providing the few-mode seven-core fiber, Ruihang Wang and Jing Zhao for revising the paper.

## REFERENCES

Cao, J., Sun, T., and Grattan, K. T. V. (2014). Gold Nanorod-Based Localized Surface Plasmon Resonance Biosensors: A Review. *Sensors Actuators B Chem.* 195, 332–351. doi:10.1016/j.snb.2014.01.056

Chen, H., Kou, X., Yang, Z., Ni, W., and Wang, J. (2008). Shape- and Size-Dependent Refractive Index Sensitivity of Gold Nanoparticles. *Langmuir* 24, 5233–5237. doi:10.1021/la800305j

Chen, S., Liu, Y., Yu, Q., and Peng, W. (2020). Microcapillary-based Integrated LSPR Device for Refractive index Detection and Biosensing. *J. Lightwave Technol.* 38, 2485–2492. doi:10.1109/jlt.2020.2969016

Chen, Y., and Ming, H. (2012). Review of Surface Plasmon Resonance and Localized Surface Plasmon Resonance Sensor. *Photonic Sens.* 2, 37–49. doi:10.1007/s13320-011-0051-2

Chiavaioli, F., Baldini, F., Tombelli, S., Trono, C., and Giannetti, A. (2017). Biosensing with Optical Fiber Gratings. *Nanophotonics* 6, 663–679. doi:10.1515/nanoph-2016-0178

Chiavaioli, F., Gouveia, C., Jorge, P., and Baldini, F. (2017). Towards a Uniform Metrological Assessment of Grating-Based Optical Fiber Sensors: From Refractometers to Biosensors. *Biosensors* 7, 23. doi:10.3390/bios7020023

Chiavaioli, F., Zubiate, P., Del Villar, I., Zamarreño, C. R., Giannetti, A., Tombelli, S., et al. (2018). Femtomolar Detection by Nanocoated Fiber Label-free Biosensors. *ACS Sens.* 3, 936–943. doi:10.1021/acssensors.7b00918

Cottat, M., Thioune, N., Gabudean, A.-M., Lidgi-Guigui, N., Focsan, M., Astilean, S., et al. (2013). Localized Surface Plasmon Resonance (LSPR) Biosensor for the Protein Detection. *Plasmonics* 8, 699–704. doi:10.1007/s11468-012-9460-3

Dong, J., Zhang, Y., Wang, Y., Yang, F., Hu, S., Chen, Y., et al. (2019). Side-polished Few-Mode Fiber Based Surface Plasmon Resonance Biosensor. *Opt. Express* 27, 11348–11360. doi:10.1364/oe.27.011348

He, Y.-J. (2019). Biochemical Sensor Simulation for Rectangular Metal Nanoparticles. *Optik* 195, 163162. doi:10.1016/j.ijleo.2019.163162

Li, C., Li, Z., Li, S., Zhang, Y., Sun, B., Yu, Y., et al. (2020). LSPR Optical Fiber Biosensor Based on a 3D Composite Structure of Gold Nanoparticles and Multilayer Graphene Films. *Opt. Express* 28, 6071–6083. doi:10.1364/oe.385128

Liu, C., Yang, L., Lu, X., Liu, Q., Wang, F., Lv, J., et al. (2017). Mid-infrared Surface Plasmon Resonance Sensor Based on Photonic crystal Fibers. *Opt. Express* 25, 14227–14237. doi:10.1364/oe.25.014227

Mayer, K. M., and Hafner, J. H. (2011). Localized Surface Plasmon Resonance Sensors. *Chem. Rev.* 111, 3828–3857. doi:10.1021/cr100313v

Min Y, W. Y. (2020). Manipulating Bimetallic Nanostructures with Tunable Localized Surface Plasmon Resonance and Their Applications for Sensing. *Front. Chem.* 8, 411. doi:10.3389/fchem.2020.00411

Mollah, M. A., and Islam, M. S. (2020). Novel Single Hole Exposed-Suspended Core Localized Surface Plasmon Resonance Sensor. *IEEE Sensors J.* 21, 2813–2820. doi:10.1109/jsen.2020.3023975

Rakić, A. D., Djurišić, A. B., Elazar, J. M., and Majewski, M. L. (1998). Optical Properties of Metallic Films for Vertical-Cavity Optoelectronic Devices. *Appl. Opt.* 37, 5271–5283.

Sellmeier, W. (1871). Zur Erklärung der abnormen Farbenfolge im Spectrum einiger Substanzen. *Ann. Phys. Chem.* 219, 272–282. doi:10.1002/andp.18712190612

Singh, R., Kumar, S., Liu, F.-Z., Shuang, C., Zhang, B., Jha, R., et al. (2020). Etched Multicore Fiber Sensor Using Copper Oxide and Gold Nanoparticles Decorated Graphene Oxide Structure for Cancer Cells Detection. *Biosens. Bioelectron.* 168, 112557. doi:10.1016/j.bios.2020.112557

Sinibaldi, A., Montaño-Machado, V., Danz, N., Munzert, P., Chiavaioli, F., Michelotti, F., et al. (2018). Real-Time Study of the Adsorption and Grafting Process of Biomolecules by Means of Bloch Surface Wave Biosensors. *ACS Appl. Mater. Inter.* 10 (39), 33611–33618. doi:10.1021/acsami.8b08335

Van Uden, R. G. H., Correa, R. A., Lopez, E. A., Huijskens, F. M., Xia, C., Li, G., et al. (2014). Ultra-high-density Spatial Division Multiplexing with a Few-Mode Multicore Fibre. *Nat. Photon.* 8, 865–870. doi:10.1038/nphoton.2014.243

Wang, Q., Wang, X.-Z., Song, H., Zhao, W.-M., and Jing, J.-Y. (2020). A Dual Channel Self-Compensation Optical Fiber Biosensor Based on Coupling of Surface Plasmon Polariton. *Opt. Laser Techn.* 124, 106002. doi:10.1016/j.optlastec.2019.106002

Wang, R., Jia, D., Zhao, J., Zhang, H., and Liu, T. (2018). Experimental and Analytical Investigation of LP01-LP11 Mode Interference. *Opt. Fiber Techn.* 46, 258–264. doi:10.1016/j.yofte.2018.11.003

Wei, Y., Su, Y., Liu, C., Zhang, Y., Nie, X., Liu, Z., et al. (2017). Segmented Detection SPR Sensor Based on Seven-Core Fiber. *Opt. Express* 25, 21841–21850. doi:10.1364/oe.25.021841

Willets, K. A., and Van Duyne, R. P. (2007). Localized Surface Plasmon Resonance Spectroscopy and Sensing. *Annu. Rev. Phys. Chem.* 58, 267–297. doi:10.1146/annurev.physchem.58.032806.104607

Yang, H., Wang, G., Lu, Y., and Yao, J. (2021). Highly Sensitive Refractive index Sensor Based on SPR with Silver and Titanium Dioxide Coating. *Opt. Quan. Electron.* 53, 1–13. doi:10.1007/s11082-021-02981-1

Yang, K., He, J., Liao, C., Wang, Y., Liu, S., Guo, K., et al. (2017). Femtosecond Laser Inscription of Fiber Bragg Grating in Twin-Core Few-Mode Fiber for Directional bend Sensing. *J. Lightwave Technol.* 35, 4670–4676. doi:10.1109/jlt.2017.2750407

Yang, Z., Xia, L., Li, C., Chen, X., and Liu, D. (2019). A Surface Plasmon Resonance Sensor Based on Concave-Shaped Photonic crystal Fiber for Low Refractive index Detection. *Opt. Commun.* 430, 195–203. doi:10.1016/j.optcom.2018.08.049

Yao, S., Shen, Y., Wu, Y., Jin, W., and Jian, S. (2019). Strain-insensitive Temperature Sensor Based on a Few-Mode Dual-Concentric-Core Fiber. *Opt. Laser Techn.* 111, 95–99. doi:10.1016/j.optlastec.2018.09.046

Zanchetta, G., Lanfranco, R., Giavazzi, F., Bellini, T., and Buscaglia, M. (2017). Emerging Applications of Label-free Optical Biosensors. *Nanophotonics* 6, 627–645. doi:10.1515/nanoph-2016-0158

Zheng, Y., Lang, T., Cao, B., Jin, J., Dong, R., and Feng, H. (2018). Fiber Optic SPR Sensor for Human Immunoglobulin G Measurement Based on the MMF-NCF-MMF Structure. *Opt. Fiber Techn.* 46, 179–185. doi:10.1016/j.yofte.2018.10.015

Zubiate, P., Urrutia, A., Zamarreño, C. R., Egea-Urra, J., Fernández-Irigoyen, J., Giannetti, A., et al. (2019). Fiber-based Early Diagnosis of Venous Thromboembolic Disease by Label-free D-Dimer Detection. *Biosens. Bioelectron. X* 2, 100026. doi:10.1016/j.biosx.2019.100026

**Conflict of Interest:** The authors declare that the research was conducted in the absence of any commercial or financial relationships that could be construed as a potential conflict of interest.

**Publisher's Note:** All claims expressed in this article are solely those of the authors and do not necessarily represent those of their affiliated organizations, or those of the publisher, the editors and the reviewers. Any product that may be evaluated in this article, or claim that may be made by its manufacturer, is not guaranteed or endorsed by the publisher.

frontiers in Physics

ORIGINAL RESEARCH
published: 16 September 2021
doi: 10.3389/fphy.2021.746915

# Improved Dielectric Properties and Grain Boundary Effect of Phenanthrene Under High Pressure

*Xiaofeng Wang[1], Qinglin Wang[1]*, Tianru Qin[2], Guozhao Zhang[1]*, Haiwa Zhang[1], Dandan Sang[1], Cong Wang[3], Jianfu Li[4], Xiaoli Wang[4]* and Cailong Liu[1]*

[1]*Shandong Key Laboratory of Optical Communication Science and Technology, School of Physics Science and Information Technology, Liaocheng University, Liaocheng, China,* [2]*Heilongjiang Province Key Laboratory of Superhard Materials, Department of Physics, Mudanjiang Normal University, Mudanjiang, China,* [3]*College of Mathematics and Physics, Beijing University of Chemical Technology, Beijing, China,* [4]*School of Opto-electronic Information Science and Technology, Yantai University, Yantai, China*

*In situ* impedance measurements, Raman measurements and theoretical calculations were performed to investigate the electrical transport and vibrational properties of polycrystalline phenanthrene. Two phase transitions were observed in the Raman spectra at 2.3 and 5.9 GPa, while phenanthrene transformed into an amorphous phase above 12.1 GPa. Three discontinuous changes in bulk and grain boundary resistance and relaxation frequency with pressure were attributed to the structural phase transitions. Grain boundaries were found to play a dominant role in the carrier transport process of phenanthrene. The dielectric performance of phenanthrene was effectively improved by pressure. A significant mismatch between $Z''$ and $M''$ peaks was observed, which was attributed to the localized electronic conduction in phenanthrene. Theoretical calculations showed that the intramolecular interactions were enhanced under compression. This study offers new insight into the electrical properties as well as grain boundary effect in organic semiconductors at high pressure.

**Keywords: phenanthrene, high pressure, dielectric, grain boundary, phase transition**

OPEN ACCESS

***Edited by:***
*Venugopal Rao Soma, University of Hyderabad, India*

***Reviewed by:***
*Ganapathy Vaitheeswaran, University of Hyderabad, India*
*Feng Ke, Stanford University, United States*

****Correspondence:***
*Qinglin Wang*
*wangqinglin@lcu.edu.cn*
*Guozhao Zhang*
*Z2012GZ@163.com*
*Xiaoli Wang*
*xlwang@ytu.edu.cn*

***Specialty section:***
*This article was submitted to Optics and Photonics, a section of the journal Frontiers in Physics*

***Received:*** *25 July 2021*
***Accepted:*** *03 September 2021*
***Published:*** *16 September 2021*

***Citation:***
*Wang X, Wang Q, Qin T, Zhang G, Zhang H, Sang D, Wang C, Li J, Wang X and Liu C (2021) Improved Dielectric Properties and Grain Boundary Effect of Phenanthrene Under High Pressure. Front. Phys. 9:746915. doi: 10.3389/fphy.2021.746915*

## INTRODUCTION

Organic semiconductors have captured much attention due to their outstanding electronic properties and high mechanical flexibility, which enable improved performance of OLEDs, organic field-effect transistors, or organic solar cells [1–4]. Polycyclic aromatic hydrocarbons (PAHs), as the important class of organic semiconductors, are applied in many areas, such as optoelectronics, electronics, and optical technology [5–7].

Pressure has a significant effect on the structure and properties of PAHs [8–11]. For example, naphthalene is partially oligomerized above 15 GPa at room temperature, and this can be promoted by reducing intermolecular distance with the action of pressure [12]; pressure can effectively reduce the bandgap of oligoacenes, which would affect their electron transport performance [13].

Phenanthrene ($C_{14}H_{10}$) is one of the PAHs and has the simplest flat molecule structure composed of three benzene rings with an armchair configuration. Structure evolution and vibrational features of phenanthrene under high pressure were investigated by x-ray diffraction (XRD) and Raman spectroscopy. Huang *et al.* [14] have reported three phase transitions of phenanthrene under non-hydrostatic conditions with the space group $P2_1$ for phase I (0–2.2 GPa), $P2/m$ for phase II

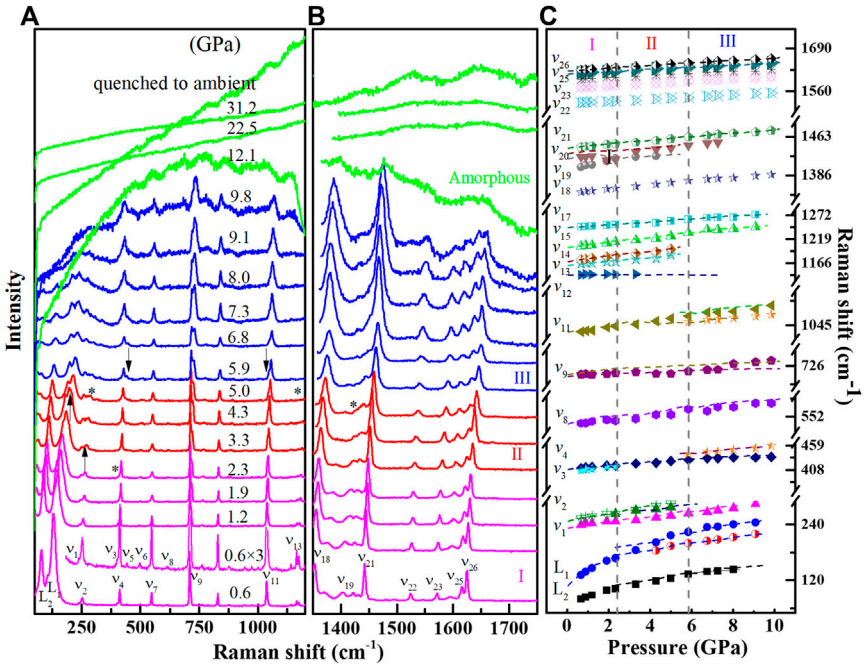


**FIGURE 1 |** High pressure Raman spectra of phenanthrene up to 31.2 GPa. **(A)** Selective Raman spectra in the frequency range of 50–1200 $cm^{-1}$. **(B)** Selective Raman spectra in the frequency range of 1350–1750 $cm^{-1}$. **(C)** Pressure dependence of the Raman shift for the observed modes. The dashed lines are results from Ref. 14. Dashed vertical lines represent phase boundaries, and phases are assigned with Roman numbers. The upper arrows and asterisks denote the new appearance and the disappearance of peaks, respectively.

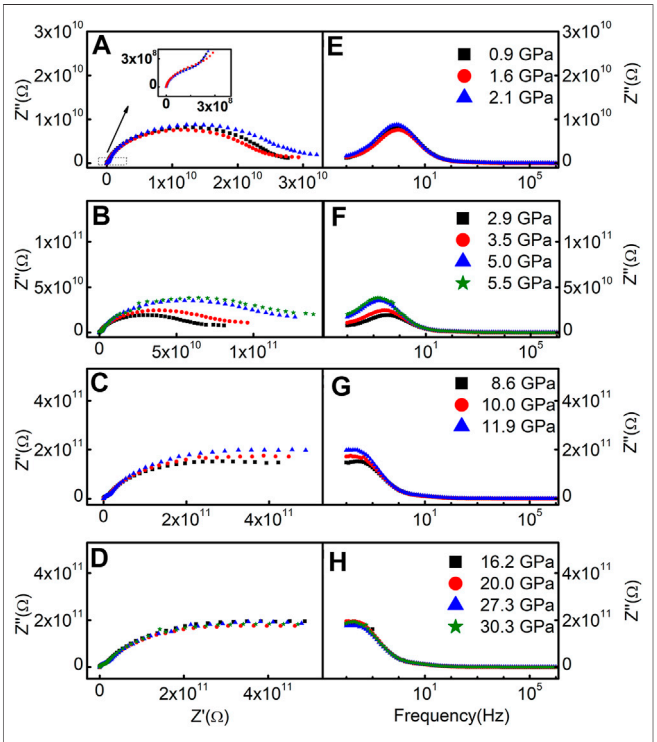


**FIGURE 2 |** Nyquist ($Z''$-$Z'$) plots **(A–D)** and $Z''$-$f$ plots **(E–H)** of the impedance data of phenanthrene under different pressures. Inset: the enlargement of the left arc.

(2.2–5.6 GPa), and $P2/m$ + $Pmmm$ for phase III (5.6–11.4 GPa), whereas the structure has been indexed to the pure $Pmmm$ phase from 11.4 to 20 GPa. Above 20 GPa, it further changed to hydrogenated amorphous carbon structure. Capitani *et al.* [15] have studied the influence of hydrostatic pressure on the structure of phenanthrene by XRD experiment with helium as pressure transmitting medium. They have observed that a phase transition from $P2_1$ to a new phase $P1$ occurred around 8 GPa. Moreover, $P2_1$ and $P1$ phases coexisted from 8 to 13 GPa, then phenanthrene fully transformed to $P1$ phase above 13 GPa. When pressure exceeded 20 GPa, the appearance of amorphization could be detected. Hence, there is an evident influence of non-hydrostatic environment on the phase transition path in phenanthrene.

Transformations in the crystal structure caused by pressure inevitably affect the carrier transport behavior and grain boundary effect in polycrystalline. For example, Li *et al.* [16] have reported the grain boundary effect on the electrical transport properties of $\beta$-boron at high pressure. Qin *et al.* [17] have investigated the dielectric behavior of polycrystalline $CaMoO_4$, and they found that the grain boundaries played a key role in carrier transport process. Zhang *et al.* [18] have studied the correlation between structural phase transition and electrical transport properties of $ZnFe_2O_4$ nanoparticles under high pressure, which concluded that the grain boundary effect was related to the capacity of the charge bounding.

The charge carriers transport in phenanthrene relies on the molecular structure and the form of the molecular packing. Previous studies have clarified the structure and the vibration

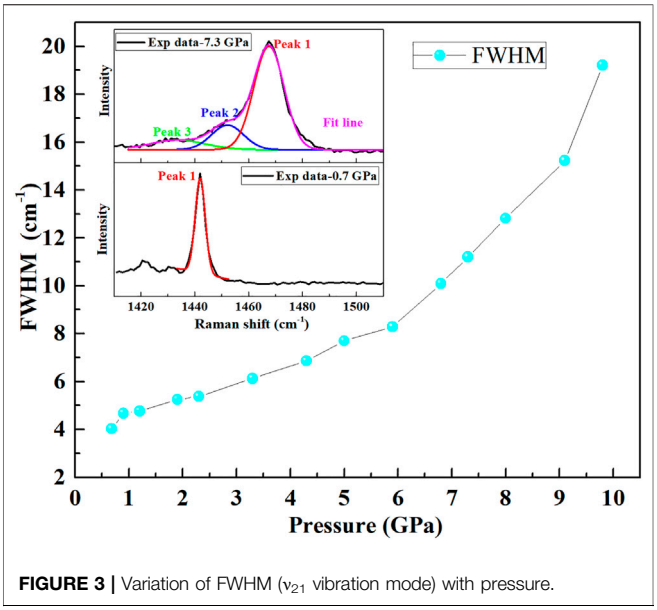


**FIGURE 3 |** Variation of FWHM ($\nu_{21}$ vibration mode) with pressure.

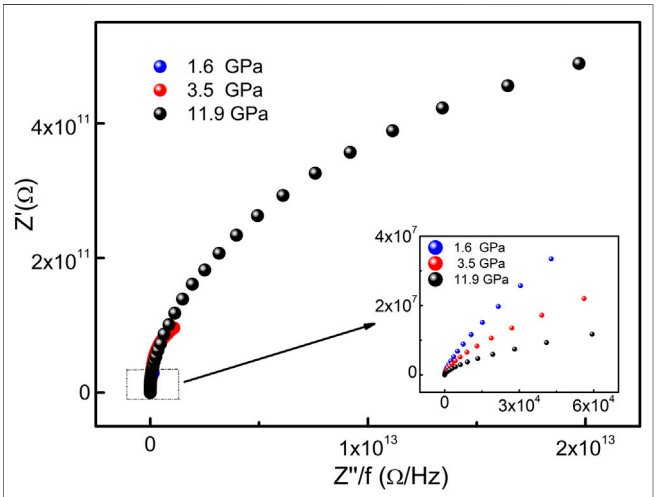


**FIGURE 4 |** Z′- Z″/*f* plots of phenanthrene at different pressures. Inset: the enlargement of the left arc.

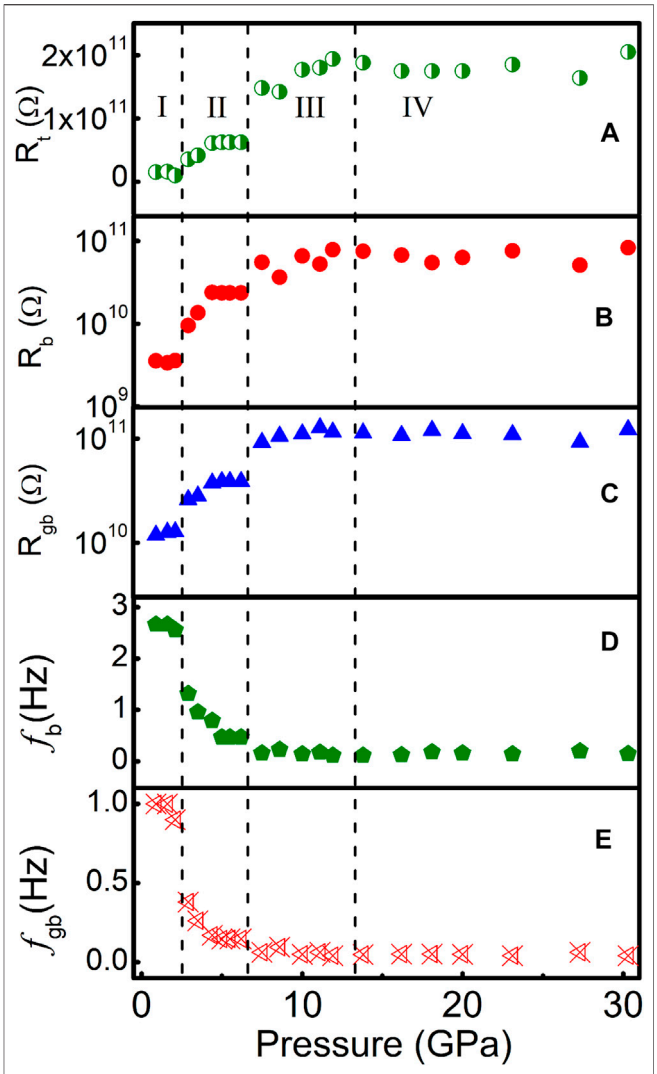


**FIGURE 5 |** Pressure dependencies of **(A)** $R_t$, **(B)** $R_b$, **(C)** $R_{gb}$, **(D)** $f_b$, and **(E)** $f_{gb}$ of phenanthrene.

modes of phenanthrene both at non-hydrostatic/hydrostatic pressure environments. Nevertheless, it remains unclear how pressure regulates the electrical transport behavior of phenanthrene, which limits the design of new phenanthrene-based applications. Meanwhile, another important factor that affects the charge transport processes in polycrystalline phenanthrene is the grain boundary, at which the carrier scattering effect is usually strengthened. However, the studies on the transport properties as well as the grain boundary effect of phenanthrene at high pressure were scarcely tackled. In this work, we investigated the electrical transport behavior of phenanthrene at high pressure by *in-situ* alternating current (AC) impedance measurements. Raman measurements and density-functional theory (DFT) calculations were also conducted. The contributions of bulk and grain boundaries to the electrical transport properties were evaluated. The influence of pressure on resistance, relaxation frequency, activation energy, permittivity, and dielectric loss factor of phenanthrene pressure were discussed.

## EXPERIMENTAL AND COMPUTATIONAL DETAILS

Polycrystalline phenanthrene powders with 99.5% purity were purchased from Sigma-Aldrich. High pressure was generated by a diamond anvil cell (DAC) with anvil culet diameter of 300 $\mu$m. The parallel-plate electrodes configuration was used for impedance measurements. The detailed electrode fabrication procedures were described in our previous works [19–21]. T301 stainless steel was

**TABLE 1 |** Calculated pressure dependence of the bulk activation energy.

| Phase | Pressure region (GPa) | d*H*/dP (meV/GPa) |
|---|---|---|
| I | 0.9–2.1 | 0.58 |
| II | 2.9–6.2 | 8.73 |
| III | 7.5–13.8 | 1.96 |
| IV | 16.2–30.3 | −0.43 |

pre-indented to a thickness of 60 $\mu$m. The mixture of cubic boron nitride powder and epoxy was used as the insulating layer. Pressure was calibrated with the $R_1$ fluorescence peak of the ruby [22].

*In situ* high-pressure AC impedance measurements were carried out by a Solartron 1260 impedance analyzer with a 1296 dielectric interface in the frequency range of $10^{-2}$~$10^{6}$ Hz, and the voltage amplitude was 0.1 V. Impedance measurements were performed at pressures up to 30.3 GPa. In order to avoid the induction of unnecessary additional impedance, pressure transmitting medium was not applied. Raman spectra of phenanthrene were collected during the process from ambient pressure to 31.2 GPa. The excitation source is a laser emitting at 532 nm by a Horiba LabRAM HR Evolution. No pressure medium was used for the Raman measurements to maintain consistency with the impedance experiments.

The calculations for local structural relaxations and electronic properties were performed in the framework of density functional theory within the Perdew-Burke-Ernzerhof generalized gradient approximation (GGA-PBE) [23] and frozen-core all-electron projector-augmented wave (PAW) method [24, 25] as implemented in Vienna *ab initio* simulation package (VASP) [26], the pseudopotentials were taken from the VASP library, in which $2s^2 2p^2$ and $1s^1$ were treated as the valence electrons for C and H atoms, respectively. Cutoff energy of 700 eV and appropriate Monkhorst-Pack [27] *k*-mesh with *k*-points density 0.03 $Å^{-1}$ were chosen to ensure that all the enthalpy calculations were well converged to less than 1 meV/atom. The electron localization function (ELF) was used to describe the charge redistribution and the bonding feature of molecules and solid materials.

## RESULTS AND DISCUSSION

The selected Raman spectra in the frequency region of 50–1800 $cm^{-1}$ were shown in **Figures 1A,B**. With increasing pressure, all the Raman peaks shift to higher frequencies. The vibrational modes can be divided into intermolecular modes ($L_1$, $L_2$) and intramolecular modes, as in Ref. 14. The pressure dependence of all the vibrational modes was displayed in **Figure 1C**. The previous results from Ref. 14 were also drawn together by dashed lines. It can be seen that the phase transitions occurred at 2.3 and 5.9 GPa, which are consistent with the results of Ref. 14. The difference of phase transition paths with Capitani *et al.*[15] was caused by nonhydrostatic/hydrostatic pressure environment. With increasing pressure, the C-C-C bending mode ($\nu_1$) and intermolecular modes ($L_1$) were split, the intramolecular vibration mode ($\nu_3$) disappeared, suggesting that the sample undergoes its first phase transition around

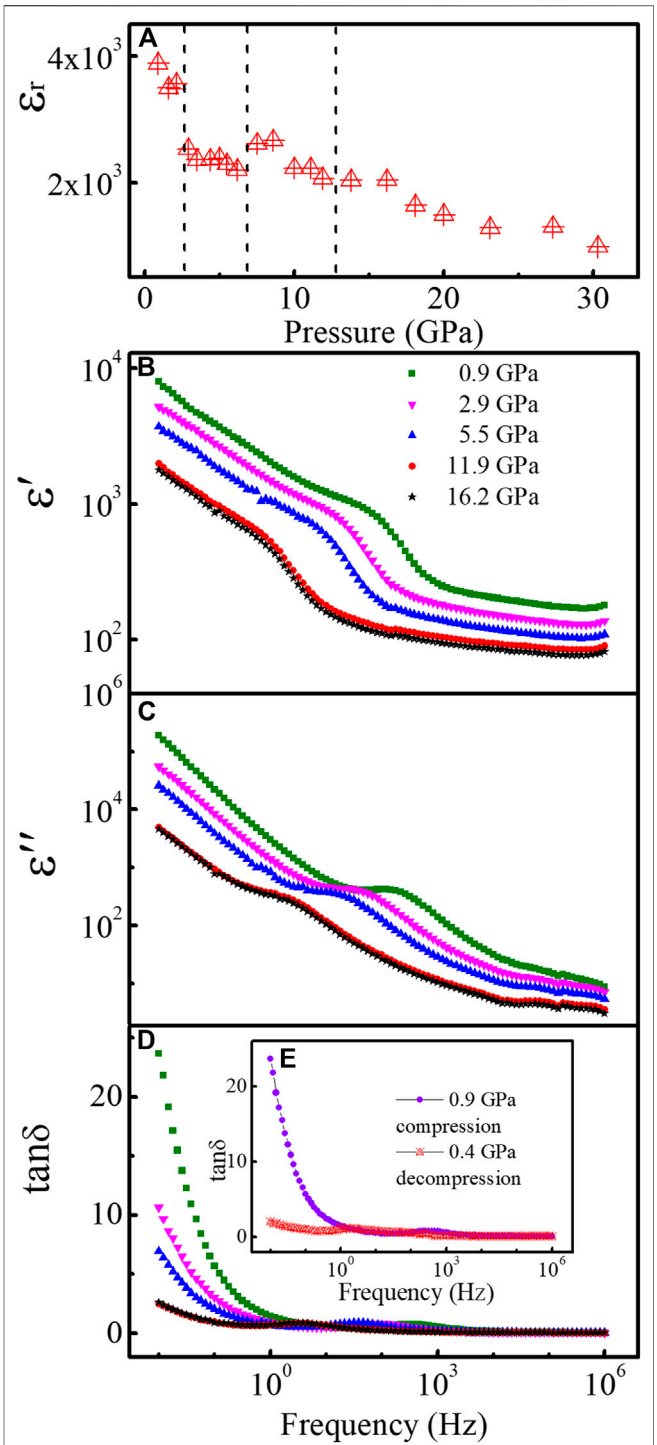


**FIGURE 6 | (A)** Variation of the relative permittivity $\varepsilon_r$ with pressure. **(B–D)** Frequency dependencies of, $\varepsilon'$, $\varepsilon''$ and tan$\delta$ of phenanthrene under different pressures. Inset shows the dielectric loss factor (tan$\delta$) at 0.9 GPa during compression and at 0.4 GPa after decompression.

2.3 GPa. Up to 5.9 GPa, the CCC bending mode ($\nu_4$) and the C-C stretching mode ($\nu_{11}$) were split, several intramolecular vibration modes ($\nu_{12}$, $\nu_{13}$, $\nu_{14}$, $\nu_{19}$, $\nu_{20}$) disappeared, along with

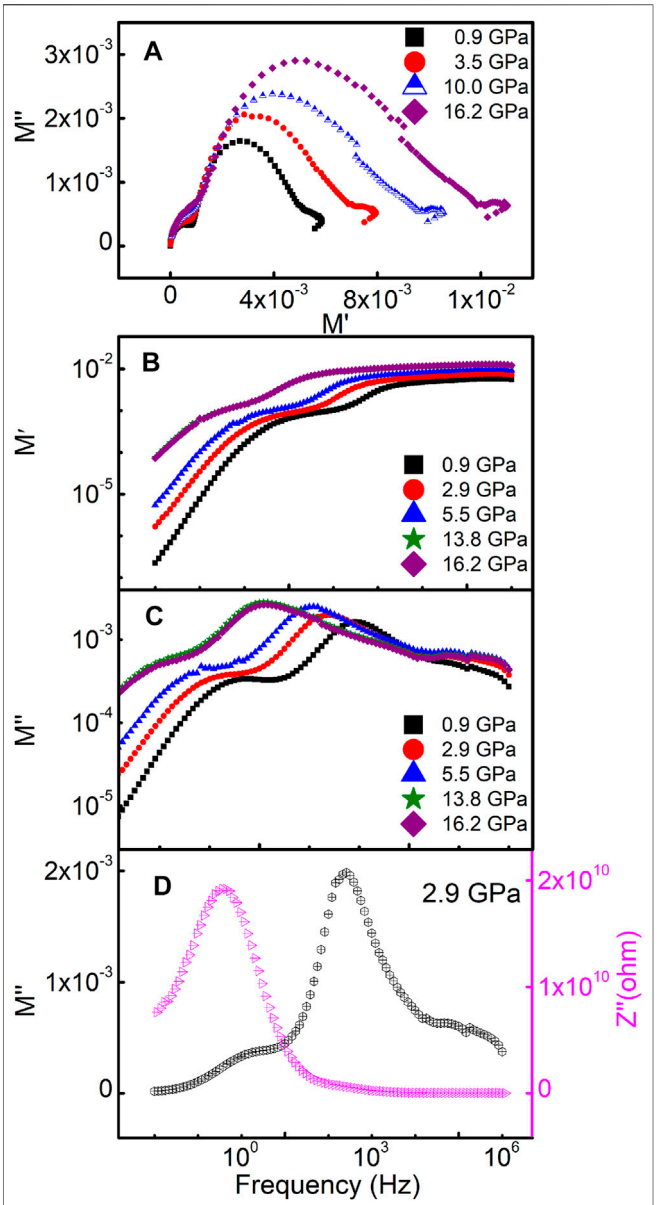


**FIGURE 7 | (A)** Complex modulus plots ($M'' \sim M'$) at different pressures; **(B, C)** variations of $M'$ and $M''$ with frequency at different pressures; **(D)** frequency dependencies of $M''$ and $Z''$ in phenanthrene at 2.9 GPa.

discontinous change in the slope of frequency of the intermolecular modes ($L_1$, $L_2$) around 6.0 GPa (as shown in **Supplementary Figure S1**), which indicates that the sample transforms from phase II to phase III around 5.9 GPa. The stretching vibration of the C-H bond in the high frequency region under different pressures was shown in the **Supplementary Figure S2**). Furthermore, the Raman peak of the intermolecular modes had a large blue shift which was attributed to the reduction of the intermolecular distance and the enhancement of the intermolecular interaction [28]. Above 12.1 GPa, phenanthrene transformed to an amorphous state.

Impedance spectroscopy method can distinguish the contribution of bulk and grain boundaries to electrical transport properties. The impedance spectra of phenanthrene at different pressures were shown in **Figure 2**. There was a big deviation from the ideal semicircle in the Nyquist plots ($Z''\sim Z'$), which was due to the dispersion effect in the process of electron transportation [29]. In Nyquist plots, bulk and grain boundaries had a large difference in frequency responses. Below 8.6 GPa, $Z''$ slowly approached $Z'$ axis in the low-frequency region, and a relatively complete semicircle arc of the grain boundary was shown in **Figures 2A,B**. However, from 8.6 to 30.3 GPa, the grain boundary resistance increased significantly with pressure, so incomplete arcs appeared in the low-frequency region, as shown in **Figures 2C,D**. Nyquist plots of phenanthrene indicated that the contributions of bulk and grain boundaries to the electrical transport properties were significantly different, whereas the grain boundary effect played a dominant role. The relaxation frequency which corresponds to the imaginary impedance peak is equal to the reciprocal of the relaxation time constant. As shown in **Figures 2E,H** the relaxation peaks of the grain boundaries shifted towards lower frequencies with pressure. This indicates that the grain boundary and associated lattice scattering effect on carriers were improved by pressure, which was also convinced by Raman measurements results. Take the $\nu_{21}$ vibration mode (1442 $cm^{-1}$) for example, as shown in **Figure 3**, the FWHM increased with increasing pressure, the crystallinity of the sample was weakened, the defects were increased, and the disorder was increased, indicating that the grain boundary effect enhanced lattice scattering on carriers.

However, due to the large difference in the contribution of bulks and grain boundaries, the bulk relaxation peak was not obvious in the Bode plots ($Z''\sim f$). The separation between bulk and grain boundary relaxation process will be clearly illustrated through the modulus representation later.

Since there was a big difference between the frequency responses from bulk and grain boundaries of phenanthrene, the representation as reported by Abrantes *et al.* was adopted to process the data [30]. The plots of selected impedance data in the Z′- ($Z''/f$) representation were shown in **Figure 4**. Three distinct segments were observed in each plot corresponding to different frequency regions. In the high frequency region,

$$Z' \approx f_b\left(Z''/f\right) \tag{1}$$

In the moderate frequency region, ($f_{gb}<<f<f_b$),

$$Z' \approx R_b + \left(Z''/f\right) f_{gb} \tag{2}$$

In the low frequency region ($f<<f_{gb}$),

$$Z' \approx R_b + R_{gb} + \left(Z''/f\right) f_{el} \tag{3}$$

where $R_b$, $R_{gb}$, $f_b$, $f_{gb}$ represent the resistance and the relaxation frequency of the bulk and grain boundary respectively, and $f_{el}$ corresponds to the electrode relaxation frequency. From **Eq. 1**, **Eq. 2** and **Eq. 3**), the electrical parameters ($R_t= R_b + R_{gb}$, $R_b$, $R_{gb}$, $f_b$, $f_{gb}$) of phenanthrene were obtained by fitting the experimental data, as shown in **Figure 5**.

For each parameter versus pressure, three discontinuous changes can be found at 2.9, 7.5, and 13.8 GPa, respectively, which was

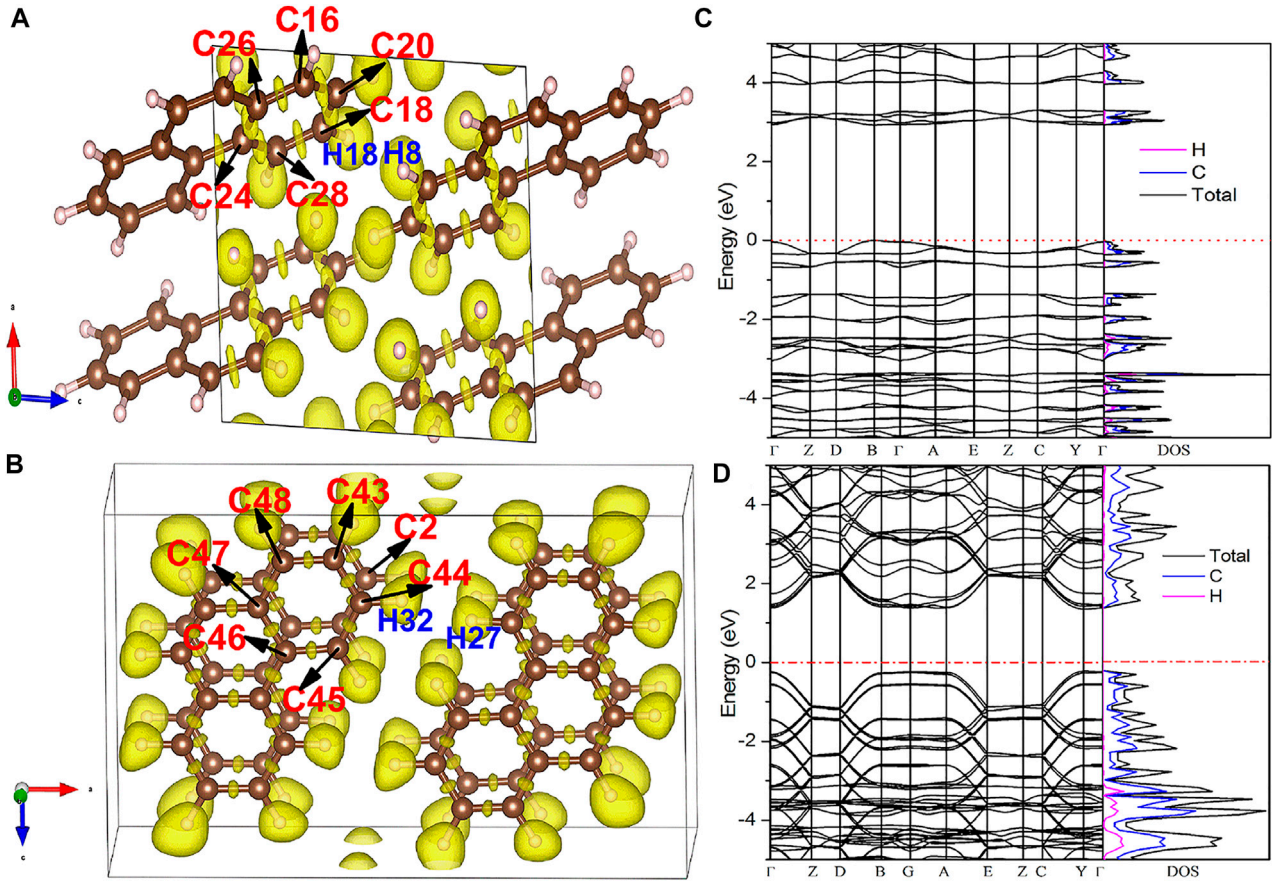


**FIGURE 8 |** Electronic properties of Phase I and Phase II in phenanthrene at 0.5 and 4 GPa. Electron localization function (ELF) **(A, B)**, band structure **(left)**, and Partial DOSs **(right) (C, D)**.

attributed to the pressure-induced structural phase transitions [14]. Below 13.8 GPa, both bulk and grain boundary resistances increased with pressure. The increase in grain boundary resistance probably resulted from the higher grain boundary density under pressure, which consequently generated additional dangling bonds. This statement was consistent with the decreased grain boundary relaxation frequency with pressure, as shown in **Figure 5E**. Above 13.8 GPa, there was no obvious variation in resistance in Phase IV, which was related to the emergence of the amorphous structure. This conclusion was consistent with the Raman results. With the increasing of disorder, the electronic states of the system became more localized [31].

Both bulk and grain boundary relaxation frequencies of phenanthrene decreased significantly with pressure in Phases I and II. Above 7.5 GPa, the relaxation frequency was almost constant as the pressure increases in Phases III and IV. The variation of the relaxation frequencies in both bulk and grain boundary regions below 7.5 GPa indicated that the relaxation time of phenanthrene increased with pressure. The electrical transport parameters ($R_t$, $R_b$, $R_{gb}$, $f_b$, and $f_{gb}$) of Phase III changed slowly with increasing pressure. The electrical transport mechanism of phenanthrene was modulated by pressure, the electrons transport channels became narrower under compression and were finally fully closed in Phase IV (amorphous state).

In order to analyze the relaxation process of phenanthrene under compression, the pressure dependence of the relaxation activation energy was evaluated. According to the Arrhenius equation, the relationship between the relaxation frequency and the activation energy can be depicted as:

$$\boldsymbol{f} = \boldsymbol{f}_0 \exp\left(-\boldsymbol{H}/\boldsymbol{k_B T}\right) \tag{4}$$

where $H$ represents activation energy, $k_B$ is the Boltzmann constant, and $T$ is the temperature. Assume $f$ and $H$ are only the function of pressure, and $f_0$ remains a constant, we have

$$\frac{d\left(\ln f\right)}{dP} = \frac{\partial\left(\mathrm{In} f_0\right)}{\partial P} - \left(\frac{1}{k_B T}\right)\left(\frac{\partial H}{\partial P}\right) \tag{5}$$

By linear fitting to the curve ln$f$-$P$, the pressure dependence of the activation energy was shown in **Table 1**.

Below 13.8 GPa, the d$H$/d$P$ was positive indicating that the required energy for carriers to reach the equilibrium increased with pressure. Therefore, the activation energy increased with increasing pressure. However, in Phase IV, d$H$/d$P$ of phenanthrene turned to be negative (−0.43 meV/GPa). The decreased activation energy indicated that pressure promotes electrical conductivity [32].

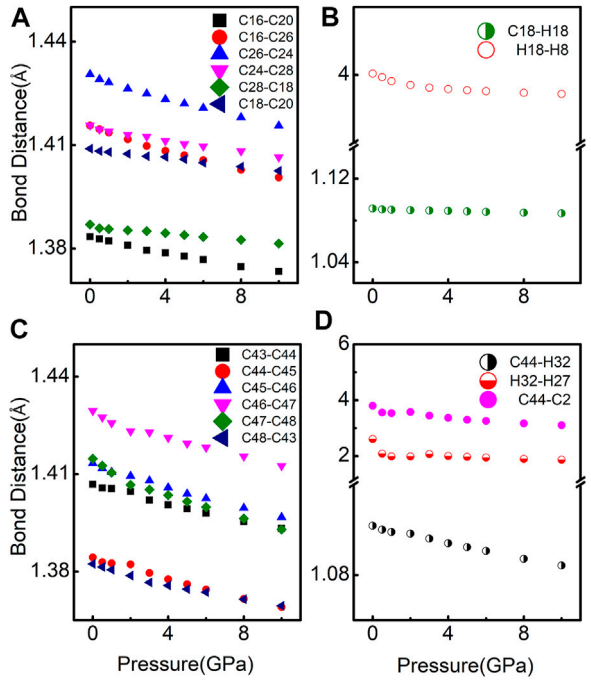


**FIGURE 9 | (A, C)** Intramolecular C-C distances; **(B, D)** intermolecular bond distances of phenanthrene under different pressures at phases I and II.

To obtain a deep insight into the carrier transport process of phenanthrene, the dielectric behavior was investigated. The bulk relative permittivity ($\varepsilon_r$) of phenanthrene can be obtained from:

$$\boldsymbol{\varepsilon}_r(\boldsymbol{P}) = \boldsymbol{d}/(2\pi \boldsymbol{R}_b \boldsymbol{\varepsilon}_0 \boldsymbol{f}_b \boldsymbol{S}) \quad (6)$$

where $d$ is the thickness of a sample, $\varepsilon_0$ is the vacuum permittivity, $S$ is the area of the electrode, and $f_b$ is the bulk relaxation frequency.

As displayed in **Figure 6A**, three discontinuous changes at 2.9, 7.5, and 13.8 GPa were observed in the relative permittivity $\varepsilon_r$ of phenanthrene at different pressures. $\varepsilon_r$ decreased with increasing pressure, which was caused by the decreased dipole moment in alternating electric fields under high pressure. The frequency dependence of both real ($\varepsilon'$) and imaginary ($\varepsilon''$) parts of the complex dielectric permittivity of phenanthrene under high pressure was shown in **Figures 6B,C**. The value of $\varepsilon'$ implies the energy storage and polarization ability [33], whereas the imaginary part ($\varepsilon''$) reflects the dielectric loss. Below $10^5$ Hz, $\varepsilon'$ decreased with increasing frequency at each pressure. However, when the frequency exceeded $10^5$ Hz, $\varepsilon'$ showed gradually reduction with frequency. In high-frequency region, the electric field alternates too fast to affect the rotation of the dipole. Therefore, the polarization of orientation weakened, and the inflection point moved to lower frequencies, while the real and imaginary parts decreased.

At high frequency, the electric field changes so rapidly that there is a time delay (relaxation) between the space charge polarization and the applied electric field, which resulted in the dielectric loss [34]. The frequency-dependent dielectric loss factor (tan$\delta$) at different pressures was illustrated in **Figure 6D**. Moreover, when pressure was released to 0.4 GPa, as shown in the inset of **Figure 6D**, the dielectric loss factor in the low-frequency region became much lower than that at 0.9 GPa under compression. Therefore, the dielectric performance of phenanthrene was effectively improved after a pressure cycle.

The analysis of complex modulus plots ($M^* = j\omega C_0 Z^*$) can help us have a further understanding of the dielectric behavior of phenanthrene. Two representative $Z''$ and $M''$ plots are complementary, the former emphasizes phenomena with large resistance, while the latter shows electrical responses with small capacitance [35, 36]. Two semicircle arcs corresponding to the bulk and grain boundary regions of phenanthrene were shown in **Figure 7A**. The real part $M'$ as a function of frequency at different pressures was displayed in **Figure 7B**. The $M'$ started to increase with increasing frequency, but then kept a constant value in the high-frequency region. The imaginary part $M''$ as a function of frequency was shown in **Figure 7C**. Two peaks in the $M''$-$f$ plots indicated two types of electrical response mechanisms existing in phenanthrene that represent change from long-range to short-range carrier mobility with increasing frequency [17].

The frequency variation of $Z''$ and $M''$ of phenanthrene at 2.9 GPa was shown in **Figure 7D**. High-frequency peak reflects the dipole relaxation at the bulk, whereas the low-frequency peak corresponds to the grain boundary. For an ideal Debye relaxation, the $Z''$and $M''$peaks of a particular *Resistance-Capacitance* component should be coincident on the frequency scale [37]. However, a significant mismatch between $Z''$and $M''$peaks was observed, which can be attributed to the localized electronic conduction in phenanthrene [38].

To obtain a deeper insight into the mechanism of the electrical properties of phenanthrene, DFT theoretical calculations were performed. The electron localization functions (ELF), energy band structure, and densities of states of phenanthrene at different pressures were shown in **Figure 8**. The electron localization function was used to describe the charge redistribution and bonding feature of molecules. **Figures 8A,B** suggested that the bonds in the C6 ring were covalent bonds, whereas intermolecular H atoms formed lone pairs of Phase I and Phase II at 0.5 and 4 GPa. The bandgap of phenanthrene decreased from 2.98 eV (0 GPa in Phase I) to 1.50 eV (4 GPa in Phase II) under compression. Because density functional calculations usually lead to a considerable underestimation of the energy gap, the actual band gaps are expected to be much larger, but we can conclude that the bandgap of phenanthrene decreased significantly with pressure. The decreased bandgap improves the transport of electrons at LUMO to HOMO, giving rise to the holes transfer integral in both directions [39]. According to Marcus theory [40], the hopping process is the exchange of electrons and holes between neighboring molecules and the charge transfer rate between two molecules depends on the recombination energy and charge transfer integral. Thus, the calculated decreased bandgap of phenanthrene was caused by increased charge transfer integral and/or by decreased recombination energy. Compared with the experimental results, the increased bulk resistance with pressure could be due to the increased grain boundary density and/or the pressure-induced disordering, which results in the enhancement of lattice scattering with increasing pressure.

The arrangement of molecules in the crystal structure is mainly determined by molecular conformation and intramolecular interactions. Due to the non-hydrostatic environment, the intramolecular interactions of phenanthrene demonstrated anisotropic changes with pressure. As shown in **Figure 9**, the intramolecular and intermolecular distances of phenanthrene decreased with pressure, leading to enhanced intramolecular interaction. This can provide an explanation for both increased bulk resistance and reduced relaxation frequency. The pressure dependence of intramolecular and intermolecular bond distance was shown in **Supplementary Table S1**. It can be seen that the intermolecular C-C and H-H interaction was more sensitive with pressure than the intramolecular C-C ones.

## CONCLUSION

In summary, the vibrational and electrical properties of phenanthrene were investigated by high-pressure *in situ* impedance spectra measurements, Raman measurements and DFT calculations. Two phase transitions occurred at 2.3 and 5.9 GPa, and then transformed to an amorphous state above 12.1 GPa. Below 13.8 GPa, both bulk and grain boundary resistance increased with pressure. The dielectric performance of phenanthrene was effectively improved after a pressure cycle. A significant mismatch between $Z''$and $M''$peaks was observed, which can be attributed to the localized electronic conduction in phenanthrene. The calculated decreased bandgap of phenanthrene was caused by increased charge transfer integral and/or by decreased recombination energy. Our results provide a better understanding of the correlation between structural modification and electrical transport properties in phenanthrene and establish general guidelines for optimization of the applications of new organic semiconductors.

## DATA AVAILABILITY STATEMENT

The original contributions presented in the study are included in the article/**Supplementary Material**, further inquiries can be directed to the corresponding authors.

## AUTHOR CONTRIBUTIONS

QW and GZ designed and supervised this study. X-F W and QW performed the experiments. X-L W and JL were responsible for the theoretical calculations. X-F W, TQ and QW analyzed the data and wrote the manuscript. HZ, DS, CW and CL contributed to manuscript revision. All authors interpreted data and provided critical insights, while read and approved the content of the manuscript.

## FUNDING

This work was supported by the National Natural Science Foundation of China (Grant Nos. 11604133, 62104090, 11874174, 11974154, and 11674144), the Natural Science Foundation of Shandong Province (Grant Nos. ZR2017QA013, 2019GGX103023, ZR2018JL003, and ZR2018MA038), the Science and Technology Plan of Youth Innovation Team for Universities of Shandong Province (Grant No. 2019KJJ019), the Introduction and Cultivation Plan of Youth Innovation Talents for Universities of Shandong Province, the Heilongjiang Provincial Education Department Project Subsidy (Project No. 1354MSYQN022), the Open Project of State Key Laboratory of Superhard Materials (Jilin University, Grant Nos. 201503 and 201612), the Open Project of Shandong Key Laboratory of Optical Communication Science and Technology (Liaocheng University, SDOC 201902), Fundamental Research Funds for the Central Universities (buctrc 202122) and the Research Funding of Liaocheng University (Grant Nos. 318012016, 318051610, and 318051612).

## SUPPLEMENTARY MATERIAL

The Supplementary Material for this article can be found online at: https://www.frontiersin.org/articles/10.3389/fphy.2021.746915/full#supplementary-material

## REFERENCES

1. Xu C, Liu Z, and lee E-C. Stability and efficiency improved perovskite solar cells through tuning the hydrophobicity of the hole transport layer with an organic semiconductor. *J Mater Chem C* (2021) 9(2):679–86. doi:10.1039/d0tc05113f
2. Tzschoppe M, Huck C, Butkevich A, Günther B, Ulrich C, Rose JN, et al. Interface properties and dopability of an organic semiconductor: TAPP-Br variable as molecule but inert in the condensed phase. *J Mater Chem C* (2020) 8(29):9898–908. doi:10.1039/d0tc01555e
3. Shinar J, and Shinar R. Organic light-emitting devices (oleds) and oled-based chemical and biological sensors: an overview. *J Phys D: Appl Phys* (2008) 41(13):133001. doi:10.1088/0022-3727/41/13/133001
4. Fang AW, Park H, Kuo Y, Jones R, Cohen O, Liang D, et al. Hybrid silicon evanescent devices *Mater Today* (2007) 10(7-8):28–35. doi:10.1016/s1369-7021(07)70177-3
5. Babolghani FM, and Mohammadi-Manesh E. Simulation and experimental study of fet biosensor to detect polycyclic aromatic hydrocarbons. *Appl Surf Sci* (2019) 488:662–70. doi:10.1016/j.apsusc.2019.05.202
6. Cebrián C. Ullazine-based materials: towards novel opportunities in organic electronics. *J Mater Chem C* (2018) 6(44):11943–50.
7. Pazzagli S, Lombardi P, Martella D, Colautti A, Tiribilli B, Cataliotti FS, et al. Self-assembled nanocrystals of polycyclic aromatic hydrocarbons show photostable single-photon emission. *ACS Nano* (2018) 12:4295–303. doi:10.1039/c8tc03573c
8. Farina L, Syassen K, Brillante A, Della Valle RG, Venuti E, and Karl N. Pentacene at high pressure. *High Pressure Res.* (2003) 23(3):349–54. doi:10.1080/0895795031000139145
9. Fanetti S, Citroni M, Malavasi L, Artioli GA, Postorino P, and Bini R. High-pressure optical properties and chemical stability of picene. *J Phys Chem C* (2013) 117(10):5343–51. doi:10.1021/jp4006789
10. Dreger ZA, Balasubramaniam E, Gupta YM, and Joly AG. High-Pressure Effects on the Electronic Structure of Anthracene Single Crystals: Role of Nonhydrostaticity. *J Phys Chem A* (2009) 113(8):1489–96. doi:10.1021/jp808247k
11. Dreger ZA, Lucas H, and Gupta YM. High-Pressure effects on fluorescence of anthracene crystals. *J Phys Chem B* (2003) 107(35):9268–74. doi:10.1021/jp030505m

12. Shinozaki A, Mimura K, Nishida T, Inoue T, Nakano S, and Kagi H. Stability and partial oligomerization of naphthalene under high pressure at room temperature. *Chem Phys Lett* (2016) 662:263–7. doi:10.1016/j.cplett.2016.09.042
13. Schatschneider B, Monaco S, Tkatchenko A, and Liang J-J. Understanding the structure and electronic properties of molecular crystals under pressure: application of dispersion corrected DFT to oligoacenes. *J Phys Chem A* (2013) 117(34):8323–31. doi:10.1021/jp406573n
14. Huang Q-W, Zhang J, Berlie A, Qin Z-X, Zhao X-M, Zhang J-B, et al. Structural and vibrational properties of phenanthrene under pressure. *J Chem Phys* (2013) 139(10):104302. doi:10.1063/1.4820359
15. Capitani F, Höppner M, Malavasi L, Marini C, Artioli GA, Hanfland M, et al. Structural evolution of solid phenanthrene at high pressures. *J Phys Chem C* (2016) 120(26):14310–6. doi:10.1021/acs.jpcc.6b04326
16. Li M, Yang J, Snoussi K, Li L, Wang H, and Gao C. Grain boundary effect on the β-boron electrical transport properties at high pressure. *Appl Phys Lett* (2010) 97(17):174101. doi:10.1063/1.3505751
17. Qin T, Wang Q, Yue D, Shen W, Yan Y, Han Y, et al. High-pressure dielectric behavior of polycrystalline $CaMoO_4$: The role of grain boundaries. *J Alloys Comp* (2018) 730:1–6. doi:10.1016/j.jallcom.2017.09.286
18. Zhang J, Zhang Y, Wu X, Ma Y, Chien S-Y, Guan R, et al. Correlation between Structural Changes and Electrical Transport Properties of Spinel $ZnFe_2O_4$ Nanoparticles under High Pressure. *ACS Appl Mater Inter* (2018) 10(49):42856–64. doi:10.1021/acsami.8b15259
19. Wang Q, Sang D, Guo S, Wang X, Wang W, Zhang B, et al. Dielectric properties and the role of grain boundaries in polycrystalline tetracene at high pressures. *CrystEngComm* (2019) 21(30):4507–12. doi:10.1039/c9ce00961b
20. Zhang X, Wang X, Wang Q, Ma X, Liu C, Li P, et al. Hydride ion ($H^-$) transport behavior in barium hydride under high pressure. *Phys Chem Chem Phys* (2018) 20(13):8917–23. doi:10.1039/c7cp08386f
21. Wang Q, Liu C, Gao Y, Ma Y, Han Y, and Gao C. Mixed conduction and grain boundary effect in lithium niobate under high pressure. *Appl Phys Lett* (2015) 106(13):132902. doi:10.1063/1.4916828
22. Piermarini GJ, Block S, Barnett JD, and Forman RA. Calibration of the pressure dependence of theR1ruby fluorescence line to 195 kbar. *J Appl Phys* (1975) 46(6):2774–80. doi:10.1063/1.321957
23. Perdew JP, Burke K, and Ernzerhof M. Generalized gradient approximation made simple. *Phys Rev Lett* (1996) 77(18):3865–8. doi:10.1103/physrevlett.77.3865
24. Blöchl PE. Projector augmented-wave method. *Phys Rev B* (1994) 50(24):17953–79. doi:10.1103/physrevb.50.17953
25. Kresse G, and Joubert D. From ultrasoft pseudopotentials to the projector augmented-wave method. *Phys Rev B* (1999) 59(3):1758–75. doi:10.1103/physrevb.59.1758
26. Kresse G, and Furthmüller J. Efficient iterative schemes for ab initiototal-energy calculations using a plane-wave basis set. *Phys Rev B* (1996) 54(16):11169–86. doi:10.1103/physrevb.54.11169
27. Monkhorst HJ, and Pack JD. Special points for Brillouin-zone integrations. *Phys Rev B* (1976) 13(12):5188–92. doi:10.1103/physrevb.13.5188
28. Goncharov AF, Manaa MR, Zaug JM, Gee RH, Fried LE, and Montgomery WB. Polymerization of formic acid under high pressure. *Phys Rev Lett* (2005) 94(6):065505. doi:10.1103/PhysRevLett.94.065505
29. Schmidt R, Wu J, Leighton C, and Terry I. Dielectric response to the low-temperature magnetic defect structure and spin state transition in polycrystalline $LaCoO_3$. *Phys Rev B* (2009) 79:125105. doi:10.1103/physrevb.79.125105
30. Abrantes JCC, Labrincha JA, and Frade JR. An alternative representation of impedance spectra of ceramics. *Mater Res Bull* (2000) 35(5):727–40. doi:10.1016/s0025-5408(00)00269-5
31. Anderson PW. Absence of diffusion in certain random lattices. *Phys Rev* (1958) 109(5):1492–505. doi:10.1103/physrev.109.1492
32. Wang Q, Liu C, Ma B, Gao Y, Fitzpatrick M, Li Y, et al. High pressure study of $B_{12}As_2$: Electrical transport behavior and the role of grain boundaries. *J Appl Phys* (2015) 117(4):045302. doi:10.1063/1.4906462
33. Zhang Y, Gao S, Xing H, and Li H. *In situ* carbon nanotubes encapsulated metal nickel as high-performance microwave absorber from Ni-Zn metal-organic framework derivative. *J Alloys Comp* (2019) 801:609–18. doi:10.1016/j.jallcom.2019.06.164
34. Chahar D, Taneja S, Thakur P, and Thakur A. Remarkable resistivity and improved dielectric properties of Co-Zn nanoferrites for high frequency applications. *J Alloys Comp* (2020) 843:155681. doi:10.1016/j.jallcom.2020.155681
35. Kagdi AR, Pullar RC, Meena SS, Jotania RB, and Mujasam Batoo K. Studies of structural, magnetic and dielectric properties of X-type Barium Zinc hexaferrite $Ba_2Zn_2Fe_{28}O_{46}$ powder prepared by combustion treatment method using ginger root extract as a green reducing agent. *J Alloys Comp* (2020) 842:155120. doi:10.1016/j.jallcom.2020.155120
36. Bhowmik RN, and Panneer Muthuselvam I. Dielectric properties of magnetic grains in $CoFe_{1.95}Ho_{0.05}O_4$ spinel ferrite. *J Magnetism Magn Mater* (2013) 335:64–74. doi:10.1016/j.jmmm.2013.01.041
37. Sinclair DC, and West AR. Impedance and modulus spectroscopy of semiconducting $BaTiO_3$ showing positive temperature coefficient of resistance. *J Appl Phys* (1989) 66(8):3850–6. doi:10.1063/1.344049
38. Li W, and Schwartz RW. Maxwell-Wagner relaxations and their contributions to the high permittivity of calcium copper titanate ceramics. *Phys Rev B* (2007) 75(1):012104. doi:10.1103/physrevb.75.012104
39. Nguyen TP, and Shim JH. Hydrostatic pressure effect on charge transport properties of phenacene organic semiconductors. *Phys Chem Chem Phys* (2016) 18(20):13888–96. doi:10.1039/c6cp00127k
40. Marcus RA. Electron transfer reactions in chemistry. Theory and experiment. *Rev Mod Phys* (1993) 65(3):599–610. doi:10.1103/revmodphys.65.599


**Conflict of Interest:** The authors declare that the research was conducted in the absence of any commercial or financial relationships that could be construed as a potential conflict of interest.

The reviewer (FK) declared a past co-authorship with one of the authors (DS) to the handling editor.

frontiers in Physics

ORIGINAL RESEARCH
published: 16 September 2021
doi: 10.3389/fphy.2021.747598

# A Cost-Effective Photonic Radar Under Adverse Weather Conditions for Autonomous Vehicles by Incorporating a Frequency-Modulated Direct Detection Scheme

*Abhishek Sharma[1]*, Sushank Chaudhary[2]*, Jyoteesh Malhotra[3], Muhammad Saadi[4], Sattam Al Otaibi[5], Jamel Nebhen[6] and Lunchakorn Wuttisittikulkij[2]**

*[1]Department of Electronics Technology, Guru Nanak Dev University, Amritsar, India, [2]Wireless Communication Ecosystem Research Unit, Department of Electrical Engineering, Chulalongkorn University, Bangkok, Thailand, [3]Department of Electronics and Communication Engineering, Regional Campus-Guru Nanak Dev University, Jalandhar, India, [4]Department of Electrical Engineering, University of Central Punjab, Lahore, Pakistan, [5]Department of Electrical Engineering, College of Engineering, Taif University, Taif, Saudi Arabia, [6]Prince Sattam bin Abdulaziz University, College of Computer Engineering and Sciences, Alkharj, Saudi Arabia*

OPEN ACCESS

**Edited by:**
*Santosh Kumar,*
*Liaocheng University, China*

**Reviewed by:**
*Sneha Kumari,*
*Indian Institute of Technology Patna, India*
*Rahul Kumar Gangwar,*
*Peking University, China*

***Correspondence:**
*Abhishek Sharma*
*er.abhisheksharma07@gmail.com*
*Sushank Chaudhary*
*sushankchaudhary@gmail.com*
*Lunchakorn Wuttisittikulkij*
*lunchakorn.w@chula.ac.th*

**Specialty section:**
*This article was submitted to Optics and Photonics, a section of the journal Frontiers in Physics*

**Received:** *26 July 2021*
**Accepted:** *03 August 2021*
**Published:** *16 September 2021*

**Citation:**
*Sharma A, Chaudhary S, Malhotra J, Saadi M, Al Otaibi S, Nebhen J and Wuttisittikulkij L (2021) A Cost-Effective Photonic Radar Under Adverse Weather Conditions for Autonomous Vehicles by Incorporating a Frequency-Modulated Direct Detection Scheme. Front. Phys. 9:747598. doi: 10.3389/fphy.2021.747598*

In recent years, there have been plenty of demands and growth in the autonomous vehicle industry, and thus, challenges of designing highly efficient photonic radars that can detect and range any target with the resolution of a few centimeters have been encountered. The existing radar technology is unable to meet such requirements due to limitations on available bandwidth. Another issue is to consider strong attenuation while working under diverse atmospheric conditions at higher frequencies. The proposed model of photonic radar is developed considering these requirements and challenges using the frequency-modulated direct detection technique and considering a free-space range of 750 m. The result depicts improved range detection in terms of received power and an acceptable signal-to-noise ratio and range under adverse climatic situations.

**Keywords: photonic radar, frequency-modulated direct detection, signal-to-noise ratio, adverse weather conditions, autonomous vehicle**

## INTRODUCTION

The photonic radar, also known as LiDAR (light detection and ranging), has been recognized for its use in multifarious spaces—be it a smart self-governing transport system, topography sensors, remote sensing, landscape ecosystem, flood monitoring, militia surveillance, wireless confined localizing scheme, biomass survey, and under water instabilities [1–4]. The existing and established navigation schemes remain limited toward insignificant precision scope that may result in conveying unpredictable performance, especially in the metropolitan zone, thus ruling out the possibility of their applications in self-driving vehicles mostly known as autonomous vehicles (AVs) [5, 6]. The current demand of the automotive industry is to afford high-range and finer resolution-based radar systems that can trace and distinguish mobile or immobile objects with great meticulousness in any atmospheric circumstance. Nowadays, self-driving vehicles are equipped with contemporary equipment to support the driver, namely, 3-D cameras, microwave radars, GPS systems, and signal processing units, at a very high cost yet offers an inadequate discernibility range of a few meters. In addition to it, self-driving demands high-security requirements for unwanted and

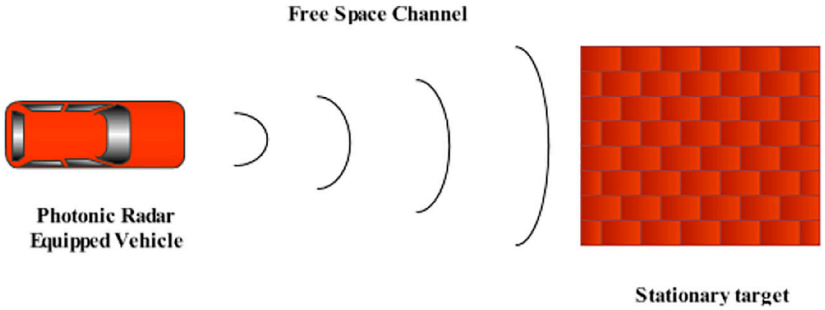


**FIGURE 1 |** Vehicle to stationary target (vehicle) scenario.

mutually affirmative dimensions. This becomes problematic to realize meticulous dimensions under severe atmospheric instabilities. Most of these functions in AVs are reliant upon the radar that can provide precise range detection and visibility with high image perseverance, particularly amid 100–500 m distance. Another factor to be considered is limited power availability in autonomous vehicles, and thus, power requirement should be minimally possible [7]. Keeping in view the different utilities and requirements of the self-driving features, the photonic radar upturns a significant alternative to a traditional radar and has been gaining popularity since its early stage from researchers and AV manufacturers worldwide. The photonic radar delivers finer range resolution and high image resolution compared to the traditional radar with high precision [8–10]. Generally, a low-power continuous wave (CW) laser along with moderately extended reflection interval is engaged to design LiDAR having adequate precision as well as perseverance [11–13]. Triangular sweep is preferred in high-speed target detection because it offers smaller sweep time than the pulsed sweep [13]. Along with it, a frequency-modulated RF signal with a saw-tooth (triangular) modulation function is established to determine the object range and velocity [14]. Besides this, the developed FM-modulated photonic radars are engaged in direct detection formation with an advantage of more sensitivity to the echoes on the expense of a shorter detection range. An alternative protuberant solution is heterodyning mixing which is also known as coherent detection with advantages of high receiver sensitivity, longer ranges, and minimal signal fading than direct detection at the expense of scheme complexity [15, 16]. **Figure 1** shows the representation of a photonic radar–equipped vehicle to detect stationary targets.

Besides challenges in designing a transceiver, the signal must be broadcasted using an extra high–frequency (EHF) band more commonly called the millimeter band (mm band) as RF poses a limit of a small range of few miles as well as incompetence to breach through solid materials [17]. In addition to it, the millimeter band can provide adept spectrum exploitation besides protected communication by allowing supplementary compactly packed waveforms. During transmission through an atmospheric channel, RF signal endures 6 *dB* variance in attenuation for each octave variation in occurrence. On the contrary, circumstances turn out to be complex once the mm-band signal travels through these atmospheric channels under hostile climatic conditions. These high-frequency signals of the mm-band experience high attenuation under various atmospheric influences, for example, air temperature, air compression and dampness, immersion particles as well as dust, and other atmospheric elements [18]. This again puts hindrance in realizing the elongated target detection–centered use and limits operation to a shorter range. For existing equipment, the absorption peaks transpire at 24 and 60 *GHz* which is rather high, and providentially, some broadcast openings are available for securing transmission of signals between these peaks. Furthermore, the mm-band–based radar signal has a substantial effect of precipitation attenuation due to scintillation, foliage blockage, rainfall, scattering, and diffraction. Generally, in a mm band, the wavelengths become shorter; thus, mellow echoes are received that result in feeble signal response.

Nevertheless, still in its early stages, some substantial work reported on AVs has been discussed here. An impact of smoulder and dirt particles in air over the operations of self-driving vehicles is described [19]. Another target simulation was developed under unsystematic atmospheric circumstances exploiting electro-optical LiDAR with irregular visibility variances [20]. A comprehensive study of the photonic radar [21] is demonstrated at 950 and 1550 *nm*. The effect of atmospheric gases has been premeditated to comprehend turbulences due to low ambient temperature [22]. The impact of various fog conditions and experimental evaluation of the working of LiDAR is studied via exhausting foggy conditions in a vacuum chamber [23]. Consequently, the reported work consents the impact of various attenuations due to atmospheric conditions upon the operational efficiency of the photonic radar particularly at high frequency. However, there are limited studies considering the waning effects of atmospheric channels such as rain, haze, and fog that confirm the efficacy of the frequency-modulated continuous wave (FMCW)–driven photonic radar system.

The frequency stands another measure aspect to be considered while designing photonic radars. A laser operates in a 24 *GHz* band more commonly known as the ISM (industrial, scientific, and medical) band with an unlicensed narrow band (NB) bandwidth of 250 *MHz* (24–24.5 *GHz*) and includes a bandwidth of 5 *GHz* known as ultra-wideband (UWB). While the NB-ISM band is used for detecting blind spots, UWB-ISM is

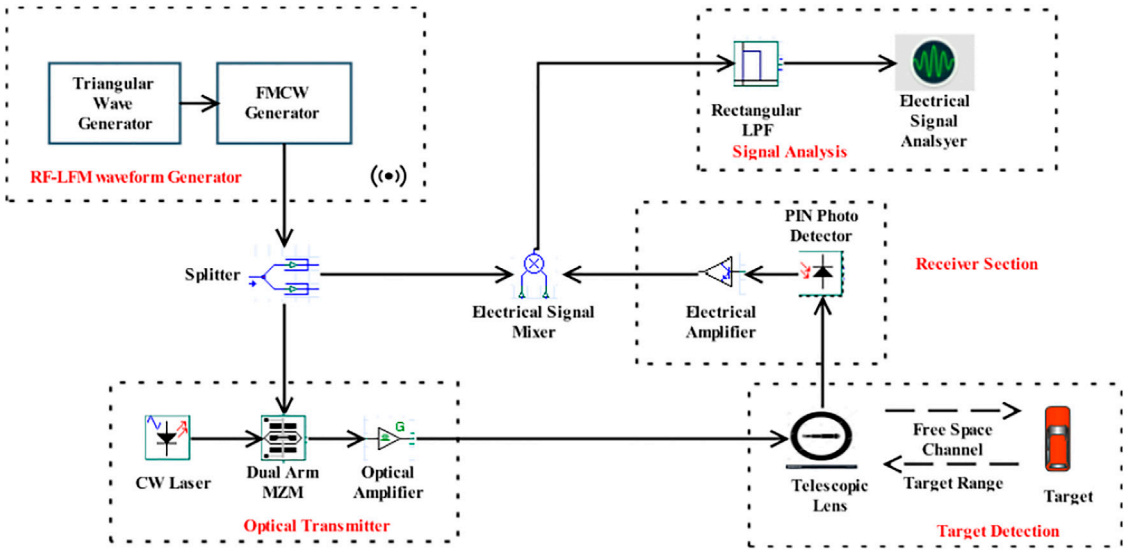


**FIGURE 2 |** Proposed FMCW photonic radar for autonomous vehicles.

used for higher resolution. As per the new regulation, UWB will be phased out soon, and hence, the ISM band may not be attractive for AV applications. The traditional radar operates in a 70 *GHz* band, and 70–77 *GHz* is available for vehicular applications. The 77–81 *GHz* (with 4 *GHz* bandwidth) band is known as the short-range radar (SRR) band. The key benefit offered is highly allowed equivalent isotopic radiated power (EIRP) which enables adaptive cruise control [24]. The range resolution offered at 77 *GHz* with frequency using 4 *GHz* bandwidth is 4 cm compared to range resolution of 75 *cm* offered at 24 *GHz* with the bandwidth of 250 *MHz*. For simplicity of operation, we have used the linear frequency-modulated continuous-wave radar system using direct detection configuration (FMCW–DD). In a FMCW-DD scheme, a transmitted pulse is intensity modulated by a LFM chirp, and de-chirping is accomplished by comprehensible mixing with a modulated local oscillator (LO) [25, 26].

Based on these facts, authors intend to apply the FMCW-based photonic radar at 77 *GHz* to detect the range as well as range frequency of a stationary target using a computer-based simulation model and test the simulation model under the influence of varied atmospheric conditions to attain the elongated target range with an adequate SNR (signal-to-noise ratio). The article is organized as follows: The Introduction section explains the necessities, concerns, and contemporary advancements in the field of photonic radars and self-driving vehicles. The Working Principle section elaborates the working principle of the proposed system. The System Description section explains modeling of the proposed system besides comprehensive constraints used in simulation. The Results and Discussion section presents the correlated results of the theory in addition to simulation of the modeled photonic radar and tests the system under adverse weather, and the presented work is concluded in the Conclusion section.

## WORKING PRINCIPLE

The schematic of the proposed FMCW-based photonic radar is shown in **Figure 2** under direct detection configuration which is also known as noncoherent detection. The start frequency of 77 *GHz* with the sweep bandwidth of 600 MHz is generated using a radio frequency–linear frequency modulator (RF-LFM) driven by a pseudo random sequence generator in conjunction with the saw-tooth modulation function. The carrier signal is generated using a continuous-wave laser light source which is then fed to a dual-arm lithium-niobate (Li-Nb) Mach–Zhander interferometer (MZI) external modulator along with the RF-LFM signal. A D.C. bias generator is used with the modulator to generate second-order sidebands along with the suppression of supplementary bands.

The output-modulated signal from MZM depends upon the operating point, that is, if it operates in a quadrature or at a null point [25, 27]. This RF-LFM signal modulated with light is then transmitted over the free-space optics (FSO) network. The FSO channel is expected to assess the efficiency of the proposed scheme under the impact of atmospheric fluctuations as their impact upsurges with an increase in the operating frequency [17, 18, 28]. The resonance signal replicated from the irradiated target is accepted with a transmission delay time given by $(\frac{2\times R}{C})$, where $R$ is the range of the object and $c$ is the velocity of light.

The received signal is then fed to a photo detector to obtain the required electrical signal from the optical signal. Furthermore, this electrical signal is amplified and mixed with reference to the signal received from the LFM generator and fed to a low-pass filter with a cut-off frequency of 1 *GHz*. The filtered signal is analyzed using an RF spectrum analyzer. The proposed system is modeled and simulated using Optisysem™ while the target model is designed using MATLAB™.

**TABLE 1 |** System parameter.

| Constraint | Value |
|---|---|
| Start frequency | 77 *GHz* |
| Bandwidth | 600 *MHz* |
| PRF (pulse repetition frequency) | 200 *KHz* |
| RF spectrum resolution | 1 *MHz* |
| CW laser wavelength | 1550 *nm* |
| Output power | 40 *mW* |
| Laser line width | 100 *KHz* |
| OSA resolution | 0.02 *nm* |
| Range | 750 *m* |
| Transmitter aperture lens | 5 *cm* |
| Receiver aperture lens | 15 *cm* |
| Additional losses | 2 *dB* |
| Transmission losses | 1 *dB* |
| Turbulence | High |
| Geometrical losses | 2 *dB* |
| Index refractive structure | $10^{-15}\ m^{-2/3}$ |
| Optical detector | PIN |
| Responsivity | 1 $A/W^{-1}$ |
| Sampling rate | 4 *GHz* |
| Photo-detector bandwidth | 40 *GHz* |
| Receiver noise temperature | 290 *k* |
| Load resistance | 50 Ω |
| Bandwidth (shot) | 4 *MHz* |
| Thermal noise | $10^{-24}\ WHz^{-1}$ |
| Optical amplifier | 20 *dB* |
| Electrical amplifier | 40 *dB* |
| DMZM | -ve quadrature point |
| Switching RF voltage | 4 *v* |
| Switching bias voltage | 4 *v* |
| Extinction ratio | 30 *dB* |

## SYSTEM DESCRIPTION

The proposed photonic radar is modeled using the FMCW direct detection technique as illustrated in **Figure 2** to evaluate the distance of an immobile object in the fluctuating weather situations. The radar-armed automobile estimates the range between itself and the immobile target and updates the vehicle accordingly. Unlike the pulsed radar, the FMCW radar is favored due to its cost-effectiveness, small size, and its minimal input power requirement. Complete significant parameters are listed in **Table 1**.

As shown in **Figure 2**, the RF-LFM waveform generator is used to generate 77 *GHz* of the FMCW signal. Frequency variance is measured via a trilateral sweep for approximating the target distance as well as for evaluating the interval time amid the transmitted signal and received echo. Considering that $f_c$ is the carrier frequency, $T_m$ is the sweep time, $B$ is the bandwidth, and $R$ is the distance between the target and radar-equipped vehicle, the range frequency $f_r$ is given by [29]

$$f_r = \frac{2 \times R \times B}{T_m \times C} \tag{1}$$

A larger quality parameter (Q-factor) of the RF-LFM modulator is achieved by matching the trip time of the local oscillator and the sweep rate of frequency [30]. The transfer function of the modulator is given in **Eq. 2** as [31–33]

$$\frac{E_{out}}{E_{in}} = \cos\left(\varnothing_o + \frac{\pi S(t)}{2v_\pi}\right) \tag{2}$$

where $E_{out}$ and $E_{in}$ are the input and output optical fields, $v_\pi$ is the voltage required to change the optical power transfer function [32], $\varnothing_i$ is the initial phase, and S(t) is the RF-LFM signal power that can be expressed as [32]

$$S(t) = A_c \cos\left(2\pi f_c t + \frac{\pi B}{T_m} t^2\right) \tag{3}$$

where $f_c$ is the start frequency, $B$ is the sweep bandwidth, and $Ac$ is the amplitude of the LFM signal. For direct detection schemes, MZI modulator output power is stated as [32]

$$E_{Tx}(t) = \sqrt{\frac{P_t}{2}}\left[1 + \frac{\beta}{2}\cos\left(2\pi f_c t + \frac{\pi B}{T_m} t^2\right)\right].e^{\left(j\omega_o t + \theta_o(t)\right)} \tag{4}$$

where $\beta$ is the modulation index ($\beta$ <<1), $\omega_o$ is the angular frequency of the transmitted signal, and $\theta_o(t)$ is the random-phase component. Sweep bandwidth $B$ of the system is 600 *MHz*.

The output-modulated signal is focused on the target via a free-space channel using a transmitting and receiving telescope lens with corresponding aperture sizes of 5 and 15 *cm*. This free-space network is demonstrated via MATLAB™ to spot the immobile object. Several factors, specifically angular dispersion, atmospheric transmission, and target reflectivity, affect the echo signal from the target at the receiver section. The received power of the echo signal $P_r$ is calculated as [29]

$$P_r = \begin{cases} P_t \dfrac{\rho_t D^2 \tau_{opt} \tau_{atm}^2}{4R^2} & for\ extended\ target \\ P_t \dfrac{\rho_t A_t D^2 \tau_{opt} \tau_{atm}^2}{4R^2 A_{ill}} & for\ any\ target \end{cases} \tag{5}$$

where $D$ is the receiver aperture diameter, $\rho_t$ is the target reflectivity, $A_t$ is the target area, $\tau_{opt}$ is the transmission loss in the optical domain, $\tau_{atm}$ is the atmospheric loss factor, $A_{ill}$ is the illuminated area at the target, and $R$ is the target range. The echoed signal power $E_{ref}$ at the receiver is given as [29]

$$E_{ref}(t) = \sqrt{P_r}\left[1 + \frac{\beta}{2}\cos\left(2\pi f_c\ (t-\tau) + \frac{\pi B}{T_m}(t-\tau)^2\right)\right].e^{\left(j(\omega_o - \omega_d)t + \theta_{o(t)}\right)} \tag{6}$$

where $\tau$ is the propagation delay given as $\tau = 2 \times R/c$. With the range of 750 *m*, the delay time is computed as 5 $\mu s$ at the pulse repetition frequency (PRF) of 200 *kHz*. In the receiver section, as there is no optical mixing performed in the direct detection method, it depends upon square-law photo detection. The output current of the photodiode having the responsivity $\mathfrak{R}$ is expressed as [34]

$$i_{ph}(t) = \mathfrak{R}.P_r\left(1 + \frac{\beta}{2}\cos\left(2\pi f_c\ (t-\tau) + \frac{\pi B}{T_m}(t-\tau)^2\right)\right)^2 \tag{7}$$

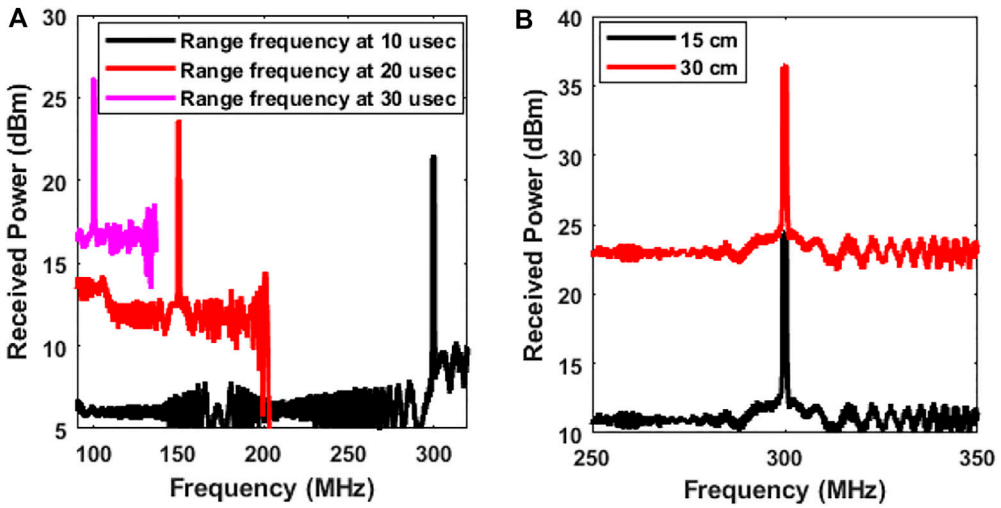


**FIGURE 3 |** Target detection in clear weather at range 750 m. **(A)** Range frequency measurement at different sweep times of 30, 20, and 10 μsec; **(B)** target detection with different receiver aperture sizes.

The filtered photocurrent signal to acquire the baseband signal is given as [32]

$$i_{ph}(t) = I_{dc} + i_{sig}(t) \approx \Re.P_r\left(1 + \frac{\beta}{2}\cos\left(2\pi f_c\,(t-\tau) + \frac{\pi B}{T_m}(t-\tau)^2\right)\right)^2 \quad (8)$$

where $I_{dc}$ and $i_{sig}$ are the dc and ac photo-detected current signals, respectively.

The photo detector used in this work is a PIN-type photo diode with a bandwidth of 40 *GHz* with considered device constraints such as amplified spontaneous noise (ASE), shot noise, and thermal noise. The output signal from the photo detector is then amplified using an electrical amplifier with the gain of 40 *dB* and the mixture using a multiplier with the RF-LFM signal. The mixed signal is fed into a rectangular low-pass filter (LPF) with the cut-off frequency of 1 *GHz*. The beat signal after LPF is given as [29]

$$S_b(t) = A_c\Re P_r\beta\cos\left(2\pi f_c\tau - \frac{\pi B}{T_m}\tau^2 + 2\pi f_r t\right) \quad (9)$$

Responsivity of the PIN photo detector employed in the system is 1 $AW^{-1}$. The performance of the system in terms of signal-to-noise ratio (SNR) is measured using an electrical signal analyzer after a photo detector as [29]

$$SNR_{dir} = \frac{\beta^2\Re^2P_r^2/2}{2q\Re P_rB_{rx} + 4k_bT_rB_{rx}/R_L} \quad (10)$$

where $B_{rx}$ is the receiver bandwidth, $q$ is the electrical charge ≈1.6 × $10^{-19}$ c, $k_b$ is the Boltzmann constant ≈1.38 × $10^{-23}$ J/K, $T_r$ is the receiver noise temperature, and $R_L$ is the load resistance.

## RESULTS AND DISCUSSION

The photonic radar system is designed using OptiSystem™ software, and a free-space path propagation model using MATLAB™ software is first tested for clear weather conditions for a target range of 750 m. An immobile target is considered with 10% reflectivity that means only 10% of the transmitted power is received from echoes for processing and rest of the 90% is either scattered or absorbed. **Figure 3** depicts the target detection and range frequency observed from echoes reflected by the stationary target.

Range frequency ($f_r$) is calculated theoretically using **Eq. 3** as 300 *MHz* at a sweep time of10 *μsec*. The same is shown using the simulated results in **Figure 3A** where the peak is observed at 300 *MHz* frequency at the power level of 22.5 dBm. Similarly, the theoretical values of 150 *MHz* range frequency at 20 *μsec* and 100 *MHz* at 30 *μsec* are calculated, and similar peaks can be observed in **Figure 3A**. Subsequently, the target range can further be measured if range frequency is known by simply reversing **Eq. 1** as $R = \frac{f_r \times T_m \times c}{2 \times B}$; for example, the range at a range frequency of 150 *MHz* will be 375 *m*, and at 150 *MHz*, the range will be 250 *m*.

The measured value of the range and range-frequency using mathematical as well as simulation methods affirms that the demonstrated photonic radar system has precisely reported detection and ranging of the stationary target. Likewise, the received power measured using an electrical analyzer as 23.10 *dBm* and 26.51 *dBm* at 10 and 30 *μsec*, respectively, confirms sufficient signal strength at the photodiode. Consequently, SNR is measured as 68 *dB* and 74 *dB* at 10 and 30 *μsec*, respectively. Likewise, range frequency can be premeditated keeping the range static and varying the time sweep and bandwidth. **Figure 3B** depicts the effect of increasing the aperture area of the telescopic lens. The proposed system observes an increase of 13 *dBm* in the signal strength of the received echoes. The signal strength of 23 *dBm* and 36 *dBm* is measured using the receiver lens with an aperture area of 15 and 30 *cm*, respectively. Thus, the size of the receiver can be kept as per the requirements of the received echo signal strength if the total size is not of much concern. In this work, the size of aperture lens at the transmitter is fixed as 5 *cm*, and at the receiver, as 15 *cm*.

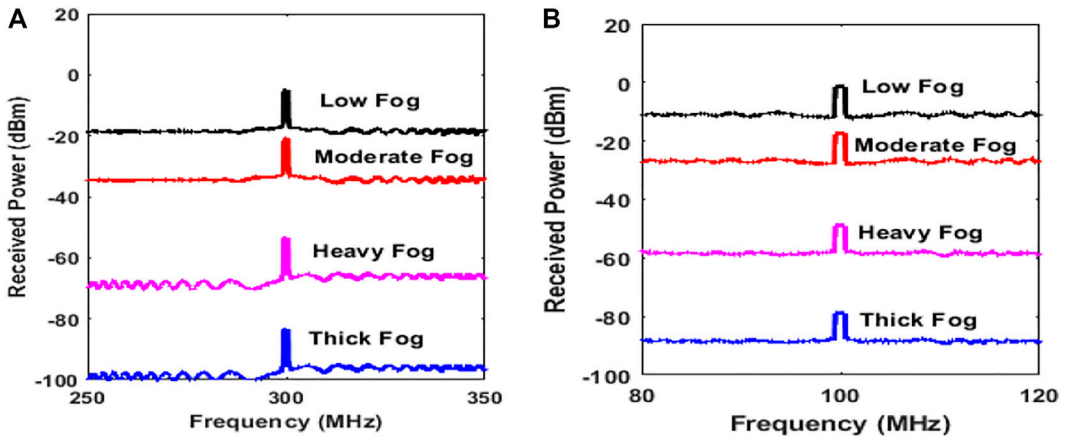


**FIGURE 4 |** Target detection under foggy weather at range 750 *m* with range frequency at different attenuation levels with sweep times **(A)** 10 *μsec* and **(B)** 30 *μsec*.

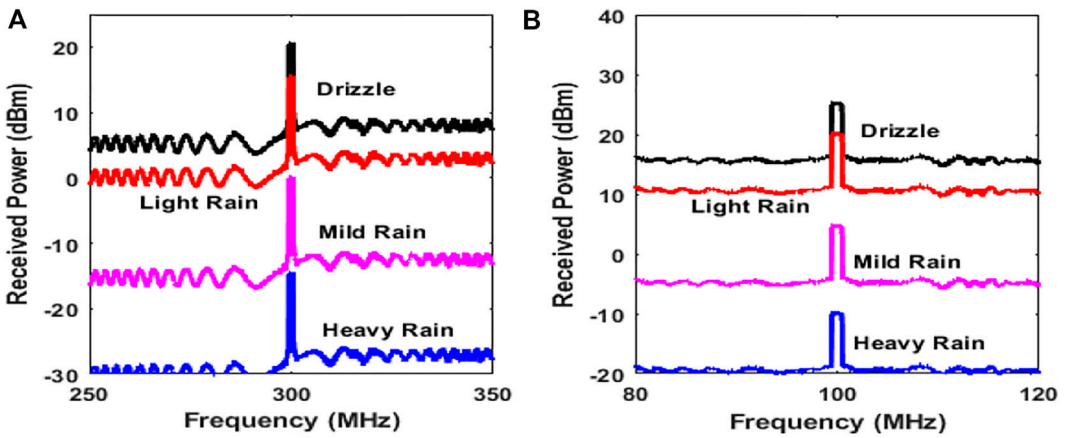


**FIGURE 5 |** Target detection under rainy weather at range 750 *m* with range frequency at different attenuation levels with sweep times **(A)** 10 *μsec* and **(B)** 30 *μsec*.

Autonomous vehicles are reliant upon photonic radars on behalf of most of the conveniences, and hence, they should be able to deliver extended range visibility for precise recognition of the target even under severe atmospheric conditions. Usually, zero visibility in the AV segment is the visibility of fewer than 50 *m* under adverse atmospheric conditions such as fog, snow, or rain and may possibly lead to mishaps [35]. Therefore, the performance of the proposed photonic radar system is further studied under the effects of fog and rain. Fog is the amalgamation of several rudiments that result in dispossession of overall system performance [36, 37]. Usually, the range in foggy surroundings is in hundreds of meters (less than 1 *km*) but can be abridged to a few meters in the course of dense foggy conditions. For the proposed photonic radar, the system is subjected to 4 different fog conditions as per the international visibility code [38], i.e., thick fog with the visibility of 200 *m* and the attenuation value of 70 *dB/km*, heavy fog with the visibility of 350 *m* and the attenuation value of 50 *dB/km*, moderate fog with the visibility of 500 *m* and the attenuation value of 28.9 *dB/km,* and light fog with the visibility of 770 *m* and the attenuation value of 18.3 *dB/km*.

Rain is another key-degrading aspect on the effectiveness of photonic radar, particularly at the mm-wave band. Hence, the effect of heavy rain and its droplet size is obligatory to be considered on the competence of the proposed system, particularly in the AV applications. The attenuation due to rain is dependent upon the droplet size and rate of pouring, and it can be computed as [39]

$$A_{rain} = k.R_o^{\alpha} \tag{11}$$

where $A_{rain}$ is the attenuation due to rain, $R_o$ is the rate of rainfall in mm/hr, and $k$ and $\alpha$ are the power law factors of dependent variables such as droplet size, frequency, and

**TABLE 2 |** Power and SNR values obtained at different attenuation levels.

| Attenuation level | Power | | SNR | |
|---|---|---|---|---|
| | 10 μsec | 30 μsec | 10 μsec | 30 μsec |
| Thick fog (70 dB/km) | −82.89 | −78.91 | 21.10 | 25.08 |
| Heavy fog (50 dB/km) | −54.89 | −49.91 | 51.10 | 55.08 |
| Moderate fog (28.9 dB/km) | −20.24 | −16 | 67.18 | 72.77 |
| Low fog (18.3 dB/km) | −4.34 | −0.1 | 66.11 | 73.92 |
| Heavy rain (24 dB/km) | −9.89 | −5.91 | 67 | 71.09 |
| Mild rain (14.25 dB/km) | 4.72 | 8.70 | 71.01 | 74.36 |
| Light rain (4 dB/km) | 16.5 | 20.08 | 71.04 | 74.93 |
| Drizzle (0.6 dB/km) | 20.05 | 24.87 | 71.83 | 75.48 |

temperature and can be computed using the Marshall–Palmer distribution [40]. At 77 *GHz* operating frequency, the corresponding values of $k$ and $\alpha$ are computed as 1.210 and 0.772. Considering the heavy rain condition at 55 *mm/h*, the attenuation $A_{rain}$ comes out as 24 *dB/km*. Likewise, computed attenuation for mild rain at 25 *mm/h* is 14.25 *dB/km*, for light rain at 5 mm/h is 4 *dB/km,* and for drizzle at 0.25 *mm/h* attenuation is 0.6 *dB/km*.

Another important factor to be considered in photonic radar modeling is the selection of optimal operating wavelength and frequency bands as the higher frequency used in the mm-wave band tends to be affected by atmospheric fluctuations especially in the AV sector. Authors have considered designing target models such as losses viz. geometric loss, transmission loss, and pointing and scintillation loss. The system is further exposed to refractive index variation by utilizing the gamma–gamma distribution model [41].

As shown in **Figures 4A** and **B**, different fog conditions with corresponding attenuation are summed up at 10 and 30 μsec, respectively. Similarly, in **Figures 5A** and **B**, strong-to-weak rainy conditions with corresponding attenuation are summed up at 10 and 30 *μsec*, respectively. The improvement of ≈ 4–5 *dBm* received power is observed at increased sweep time, and the improvement of ≈ 3–5 *dB* is observed in the SNR value.

The comprehensive values of the received power (*dBm*) and SNR (*dB*) observed by the electrical analyzer at different attenuation levels are specified in **Table 2**.

**Figure 6** depicts the SNR value under the influence of atmospheric fluctuations (varying attenuation levels) over a wide transmission range (up to 3000 *m*) detected via the photo detector at different sweep times. For successful reception of signals, the minimum acceptable SNR value is fixed at 20 *dB*. With a sweep time of 10 *μsec* under thick fog conditions (70 dB/Km), the echo is received at 905 *m*, while at a sweep time of 30 *μsec*, the echo is received at 950 m. Similarly, ≈ 40–50 *m* of improvement can be seen in other conditions as well. Due to the limitation of the designed system and parameter constraints, the maximum range observed was 3000 *m*, while mild rain to drizzle conditions were still to be verified for the maximum transmission range. Hence, it can be concluded that the proposed photonic radar can sense the maximum distance at severe atmospheric conditions, whereas the maximum transmission range can be well above 10000 *m* for light rain conditions (4 *dB/km*).

**Figure 7** shows the relation between SNR and attenuation at 10 and 30 *μsec* sweep times to understand the corresponding variations between the signal and noise with respect to the attenuation. Initially, for an attenuation level up to 30 *db/km* at a sweep time of 10 and 30 *μsec*, the SNR value holds good up to 70 *dB* and 74 *dB*, respectively, but, as the attenuation increases from 30 *dB/km* to 75 *dB/km,* the SNR linearly decreases toward zero. The graph clearly indicates that beyond 70 *dB/km*, the SNR falls below the 20 *dB* value which is minimally acceptable [42]. The graph also testifies the proposed model signal reception up to 70 *db/km* of attenuation conditions.

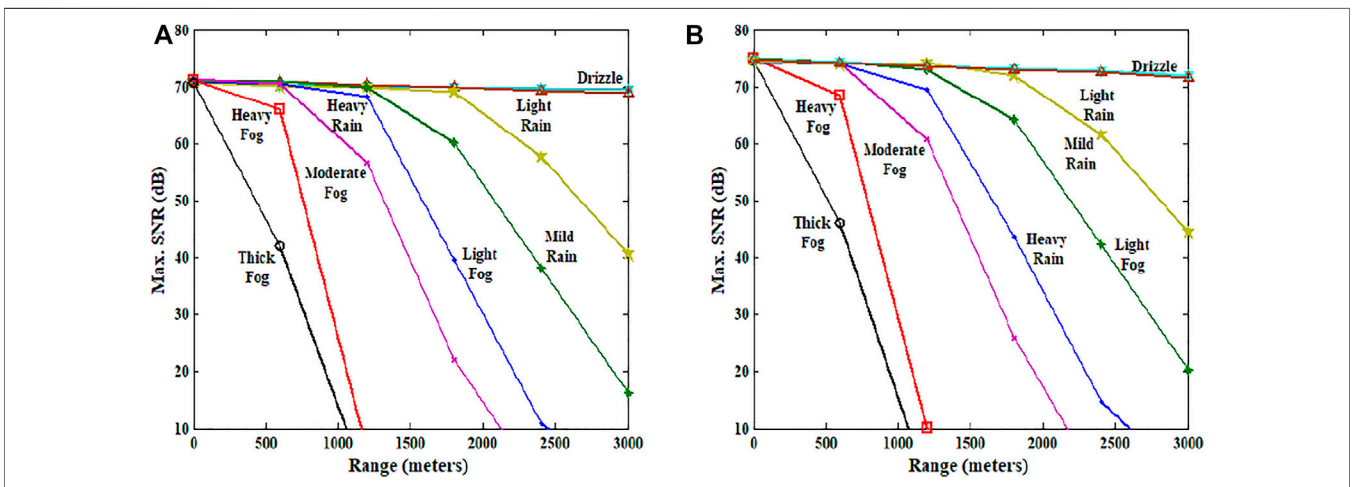


**FIGURE 6 |** SNR (dB) vs range at different attenuation levels (atmospheric conditions) at **(A)** 10 μsec and at **(B)** 30 μsec.

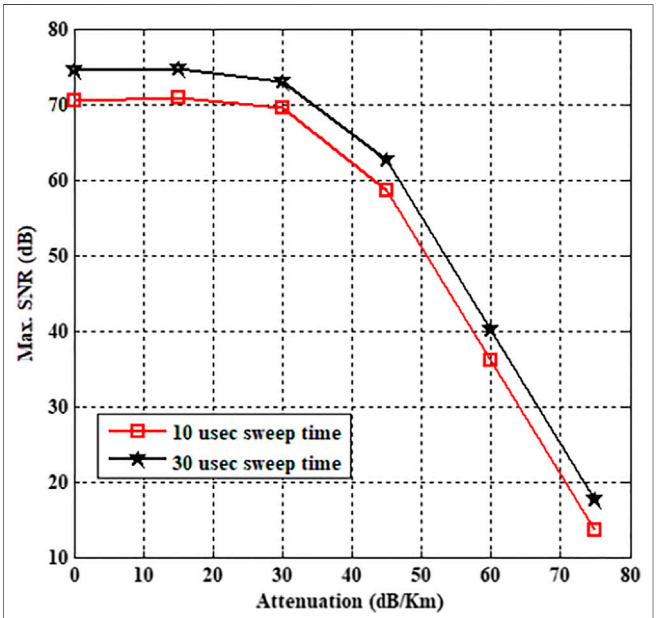


**FIGURE 7 |** Measured SNR at 10 and 30 *μsec* sweep times.

## CONCLUSION

In this article, the frequency-modulated continuous wave (FMCW)–driven photonic radar was modeled for range detection of stationary targets by sensing reflected echoes under the influence of atmospheric fluctuations in terms of attenuation using the direct detection method. Successful target detection and ranging have been reported, and furthermore, the system is verified under weak-to-strong turbulences. Outcomes of the proposed system achieve an enhanced target range of 905 *m* under thick fog condition, 1090 *m* with heavy fog, 1920 *m* with moderate fog, and 2280 *m* with heavy rain. Presented results conclude that atmospheric fluctuations (70 *dB/km* and above) affect the range resolution of the photonic radar. Furthermore, augmentation in the attenuation due to smog (smoke + fog) conditions of cities may affect the working of AVs which must be considered along. It can further be extended to a range and detect moving targets with multiple-object tracking.

## DATA AVAILABILITY STATEMENT

The raw data supporting the conclusions of this article will be made available by the authors, without undue reservation.

## AUTHOR CONTRIBUTIONS

AS: writing original draft, methodology, and simulations; SC: writing review and editing, software; JM: writing review and editing, supervision; MS: visualization; SA: resources; JN: formal analysis; LW: data curation.

## FUNDING

This research work is funded by TSRI Fund (CU_FRB640001_01_21_8).

## ACKNOWLEDGMENTS

The authors would like to thank Guru Nanak Dev University, Amritsar for supporting the research work. The authors would also like to thank Optiwave corporation, Canada specially Dr. Ahmad Atieh for providing the technical support as well as valuable software OptiSystemTM to carry this research work. The authors also would like to thank Taif University Researchers supporting project number (TURSP-2020/228), Taif University, Taif, Saudi Arabia.

## REFERENCES

1. Zhang H, Li J, Wang T, Lin H, Zheng Z, Li Y, et al. A Manifold Learning Approach to Urban Land Cover Classification with Optical and Radar Data. *Landscape Urban Plann* (2018) 172:11–24. doi:10.1016/j.landurbplan.2017.12.009
2. Tong X, Luo X, Liu S, Xie H, Chao W, Liu S, et al. An Approach for Flood Monitoring by the Combined Use of Landsat 8 Optical Imagery and COSMO-SkyMed Radar Imagery. *ISPRS J Photogrammetry Remote Sensing* (2018) 136: 144–53. doi:10.1016/j.isprsjprs.2017.11.006
3. Shen W, Li M, Huang C, Tao X, and Wei A. Annual forest Aboveground Biomass Changes Mapped Using ICESat/GLAS Measurements, Historical Inventory Data, and Time-Series Optical and Radar Imagery for Guangdong Province, China. *Agric For Meteorology* (2018) 259:23–38. doi:10.1016/j.agrformet.2018.04.005
4. Poggio L, and Gimona A. Assimilation of Optical and Radar Remote Sensing Data in 3D Mapping of Soil Properties over Large Areas. *Sci Total Environ* (2017) 579:1094–110. doi:10.1016/j.scitotenv.2016.11.078
5. Skog I, and Handel P. In-Car Positioning and Navigation Technologies-A Survey. *IEEE Trans Intell Transport Syst* (2009) 10:4–21. doi:10.1109/tits.2008.2011712
6. Mautz R. Combination of Indoor and Outdoor Positioning. In: 1st International Conference on Machine Control & Guidance (2008). p. 1–9.
7. Kutila M, Pyykönen P, Ritter W, Sawade O, and Schäufele B. Automotive LIDAR Sensor Development Scenarios for Harsh Weather Conditions. In: 2016 IEEE 19th International Conference on Intelligent Transportation Systems (ITSC). IEEE (2016). p. 265–70. doi:10.1109/itsc.2016.7795565
8. Haykin S. Cognitive Radar: a Way of the Future. *IEEE Signal Process Mag* (2006) 23:30–40. doi:10.1109/msp.2006.1593335
9. Tsui JB. *Digital Techniques for Wideband Receivers*. Stevenage: SciTech Publishing (2004).
10. Scheer JA. Coherent Radar System Performance Estimation. In: IEEE International Conference on Radar. IEEE (1990). p. 125–8.
11. Allen CT, Chong SK, Cobanoglu Y, and Gogineni S. *Development of a 1319-nm Laser Radar Using Fiber Optics and RF Pulse Compression*. Kansas: University of Kansas Technical Report ITTC-RSL-FY2002-TR-18680-01 (2002).

12. Yang W-j., Zhao J-g., Du X-p., Zeng Z-y., and Wang Q. Laser Diode Transmitter for Laser Radar Based on FM Ranging Principles. In: International Symposium on Photoelectronic Detection and Imaging 2007: Optoelectronic System Design, Manufacturing, and Testing. IEEE (2008). p. 662408.
13. Karlsson CJ, and Olsson FÅA. Linearization of the Frequency Sweep of a Frequency-Modulated Continuous-Wave Semiconductor Laser Radar and the Resulting Ranging Performance. *Appl Opt* (1999) 38:3376–86. doi:10.1364/ao.38.003376
14. Ghassemlooy Z, Popoola W, and Rajbhandari S. *Optical Wireless Communications: System and Channel Modelling with Matlab®*. London: CRC Press (2019).
15. Harris M, Young RI, Köpp F, Dolfi A, and Cariou J-P. Wake Vortex Detection and Monitoring. *Aerospace Sci Tech* (2002) 6:325–31. doi:10.1016/s1270-9638(02)01171-9
16. Dolfi-Bouteyre A, Canat G, Valla M, Augere B, Besson C, Goular D, et al. Pulsed 1.5-$\mu$m LIDAR for Axial Aircraft Wake Vortex Detection Based on High-Brightness Large-Core Fiber Amplifier. *IEEE J Select Top Quan Electron.* (2009) 15:441–50. doi:10.1109/jstqe.2008.2010463
17. Itu-R P. *Specific Attenuation Model for Rain for Use in Prediction Methods*. Switzerland: Recommendation P. 838-3, ITU-R Recommendations, P Series (2005).
18. Series P. *Attenuation by Atmospheric Gases* (2016).
19. Peynot T, Underwood J, and Scheding S. Towards Reliable Perception for Unmanned Ground Vehicles in Challenging Conditions. In: 2009 IEEE/RSJ International Conference on Intelligent Robots and Systems. IEEE (2009). p. 1170–6. doi:10.1109/iros.2009.5354484
20. Rasshofer RH, Spies M, and Spies H. Influences of Weather Phenomena on Automotive Laser Radar Systems. *Adv Radio Sci* (2011) 9:49–60. doi:10.5194/ars-9-49-2011
21. Wojtanowski J, Zygmunt M, Kaszczuk M, Mierczyk Z, and Muzal M. Comparison of 905 Nm and 1550 Nm Semiconductor Laser Rangefinders' Performance Deterioration Due to Adverse Environmental Conditions. *Opto-Electronics Rev* (2014) 22:183–90. doi:10.2478/s11772-014-0190-2
22. Hasirlioglu S, Riener A, Huber W, and Wintersberger P. Effects of Exhaust Gases on Laser Scanner Data Quality at Low Ambient Temperatures. In: 2017 IEEE Intelligent Vehicles Symposium (IV). IEEE (2017). p. 1708–13. doi:10.1109/ivs.2017.7995954
23. Bijelic M, Gruber T, and Ritter W. A Benchmark for Lidar Sensors in Fog: Is Detection Breaking Down? In: 2018 IEEE Intelligent Vehicles Symposium (IV). IEEE (2018). p. 760–7.
24. Ramasubramanian K, and Ramaiah K. Moving from Legacy 24 GHz to State-Of-The-Art 77-GHz Radar. *ATZ Elektron Worldw* (2018) 13:46–9. doi:10.1007/s38314-018-0029-6
25. Adany P, Allen C, and Rongqing Hui R. Chirped Lidar Using Simplified Homodyne Detection. *J Lightwave Technol* (2009) 27:3351–7. doi:10.1109/jlt.2009.2016220
26. Pierrottet D, Amzajerdian F, Petway L, Barnes B, Lockard G, and Rubio M. Linear FMCW Laser Radar for Precision Range and Vector Velocity Measurements. *MRS Online Proc Libr (Opl)* (2008) 1076. 1. doi:10.1557/proc-1076-k04-06
27. Elghandour A, and Dianren C. Study on Detection Techniques of Distance and Velocity by Chirped LIDAR. In: 2012 International Conference on Optoelectronics and Microelectronics. IEEE (2012). p. 354–8. doi:10.1109/icoom.2012.6316290
28. Nguyen D-N, Bohata J, Komanec M, Zvanovec S, Ortega B, and Ghassemlooy Z. Seamless 25 GHz Transmission of LTE 4/16/64-QAM Signals over Hybrid SMF/FSO and Wireless Link. *J Lightwave Technol* (2019) 37:6040–7. doi:10.1109/jlt.2019.2945588
29. Elghandour AH, and Ren CD. Modeling and Comparative Study of Various Detection Techniques for FMCW LIDAR Using Optisystem. In: International Symposium on Photoelectronic Detection and Imaging 2013: Laser Sensing and Imaging and Applications. IEEE (2013). p. 890529. doi:10.1117/12.2034878
30. Zhou P, Zhang F, and Pan S. Generation of Linear Frequency-Modulated Waveforms by a Frequency-Sweeping Optoelectronic Oscillator. *J Lightwave Technol* (2018) 36:3927–34. doi:10.1109/jlt.2018.2854713
31. Coutinho OL, Almeida VR, and Oliveira JEB. Analysis of Analog Fiber Optical Links Based on DSB+ C and SSB+ C Modulation Techniques. In: SBMO/IEEE MTT-S International Conference on Microwave and Optoelectronics. IEEE (2005). p. 439–43.
32. Hui R, and O'Sullivan M. *Fiber Optic Measurement Techniques*. Academic Press (2009).
33. Agrawal GP. *Fiber-optic Communication Systems*. John Wiley & Sons (2012).
34. Keiser G. *Optical Communications Essentials*. McGraw-Hill Education (2003).
35. Miclea R-C, Dughir C, Alexa F, Sandru F, and Silea I. Laser and LIDAR in A System for Visibility Distance Estimation in Fog Conditions. *Sensors* (2020) 20:6322. doi:10.3390/s20216322
36. Anbarasi K, Hemanth C, and Sangeetha RG. A Review on Channel Models in Free Space Optical Communication Systems. *Opt Laser Tech* (2017) 97:161–71. doi:10.1016/j.optlastec.2017.06.018
37. Al Naboulsi M, Sizun H, and de Fornel F. Fog Attenuation Prediction for Optical and Infrared Waves. *Opt Eng* (2004) 43:319–29. doi:10.1117/1.1637611
38. Awan MS, Marzuki EL, Hillbrand B, Nadeem F, and Khan MS. Cloud Attenuations for Free-Space Optical Links. In: 2009 International Workshop on Satellite and Space Communications. IEEE (2009). p. 274–8. doi:10.1109/iwssc.2009.5286364
39. Rashidi F, He J, and Chen L. Spectrum Slicing WDM for FSO Communication Systems under the Heavy Rain Weather. *Opt Commun* (2017) 387:296–302. doi:10.1016/j.optcom.2016.11.070
40. Olsen R, Rogers D, and Hodge D. The aRbrelation in the Calculation of Rain Attenuation. *IEEE Trans Antennas Propagat* (1978) 26:318–29. doi:10.1109/tap.1978.1141845
41. Bekkali A, Ben Naila C, Kazaura K, Wakamori K, and Matsumoto M. Transmission Analysis of OFDM-Based Wireless Services over Turbulent Radio-On-FSO Links Modeled by Gamma-Gamma Distribution. *IEEE Photon J.* (2010) 2:510–20. doi:10.1109/jphot.2010.2050306
42. Carlson AB. *Communication System*. Tata McGraw-Hill Education (2010).


**Conflict of Interest:** The authors declare that the research was conducted in the absence of any commercial or financial relationships that could be construed as a potential conflict of interest.

**Publisher's Note:** All claims expressed in this article are solely those of the authors and do not necessarily represent those of their affiliated organizations, or those of the publisher, the editors, and the reviewers. Any product that may be evaluated in this article, or claim that may be made by its manufacturer, is not guaranteed or endorsed by the publisher.

frontiers in Physics

ORIGINAL RESEARCH
published: 20 September 2021
doi: 10.3389/fphy.2021.746779

# Performance Evaluation of a 4 × 20-Gbps OFDM-Based FSO Link Incorporating Hybrid W-MDM Techniques

*Mehtab Singh*[1,2], *Saleh Chebaane*[3,4], *Sana Ben Khalifa*[5,6]*, *Amit Grover*[7], *Sanjeev Dewra*[7] *and Mohit Angurala*[8]

[1]Department of Electronics and Communication Engineering, SIET Amritsar (IKG-PTU, Kapurthala), Amritsar, India, [2]Department of Electronics and Communication Engineering, Guru Nanak Dev University, Regional Campus, Jalandhar, India, [3]Department of Physics, College of Science, University of Ha'il, Ha'il, Saudi Arabia, [4]Laboratoire d'électronique et micro-électronique (LAB-IT06) Faculté des Sciences de Monastir, Monastir, Tunisia, [5]Department of Physics, College of Science and Arts, Qassim University, Ar Rass, Saudi Arabia, [6]Laboratory of Energy and Materials (LabEM), ESSTHS, University of Sousse, H. Sousse, Tunisia, [7]Department of Electronics and Communication Engineering, Shaheed Bhagat Singh State University, Ferozepur, India, [8]Department of Computer Science and Engineering, Chitkara University, Rajpura, India

Free space optics (FSO) has been recognized as a crucial technique to meet the high-bandwidth requirements in future wireless information transmission links. It provides a feasible solution to the last-mile bottleneck problem due to its merits that include high-speed data transportation and secure and low-latency networks. Due to these merits, FSO is a reliable technology for future health-care and biomedical services like the transmission of biomedical sensor signals. But the main limiting factor in the data transmission employing FSO links is adverse atmospheric weather conditions. This research work reports the designing and simulative evaluation of the performance of a high-speed orthogonal frequency division multiplexing–based free space optics link by incorporating wavelength division multiplexing of two independent frequency channels (193.1 THz and 193.2 THz) along with mode division multiplexing of distinct spatial laser Hermite–Gaussian modes (HG01 and HG03). Four independent 20-Gbps quadrature amplitude-modulated data signals are transported simultaneously under different atmospheric weather conditions using the proposed link. Also, the link performance has been investigated for an increasing beam divergence angle.

**Keywords: FSO, WDM, MDM, HG modes, atmospheric weather conditions, beam divergence, biomedical services**

OPEN ACCESS

***Edited by:***
*Santosh Kumar,*
*Liaocheng University, China*

***Reviewed by:***
*Sushank Chaudhary,*
*Quanzhou Institute of Equipment manufacturing, (CAS), China*
*Ayyanar Natesan,*
*Ton Duc Thang University, Vietnam*

***Correspondence:**
*Sana Ben Khalifa*
*s.benkhalifa@qu.edu.sa*

***Specialty section:***
*This article was submitted to Optics and Photonics, a section of the journal Frontiers in Physics*

***Received:*** *24 July 2021*
***Accepted:*** *31 July 2021*
***Published:*** *20 September 2021*

***Citation:***
*Singh M, Chebaane S, Ben Khalifa S, Grover A, Dewra S and Angurala M (2021) Performance Evaluation of a 4 × 20-Gbps OFDM-Based FSO Link Incorporating Hybrid W-MDM Techniques. Front. Phys. 9:746779. doi: 10.3389/fphy.2021.746779*

## INTRODUCTION

Recent years have seen a significant increase in network traffic due to growth in the use of multimedia applications consuming high channel bandwidth like video conferencing, fast Internet, and live streaming. This has challenged the limited and congested radio frequency (RF) spectrum–based conventional wireless transmission systems [1]. Free space optics (FSO) is considered a promising solution to meet the high capacity and large transmission rate demand of the users. Optically modulated carrier signals are used to carry data signals over the free space medium between tightly aligned transmitter and receiver units. FSO technology has numerous merits, such as quick and easy installation, high channel bandwidth, immunity to electromagnetic interference, a high-speed

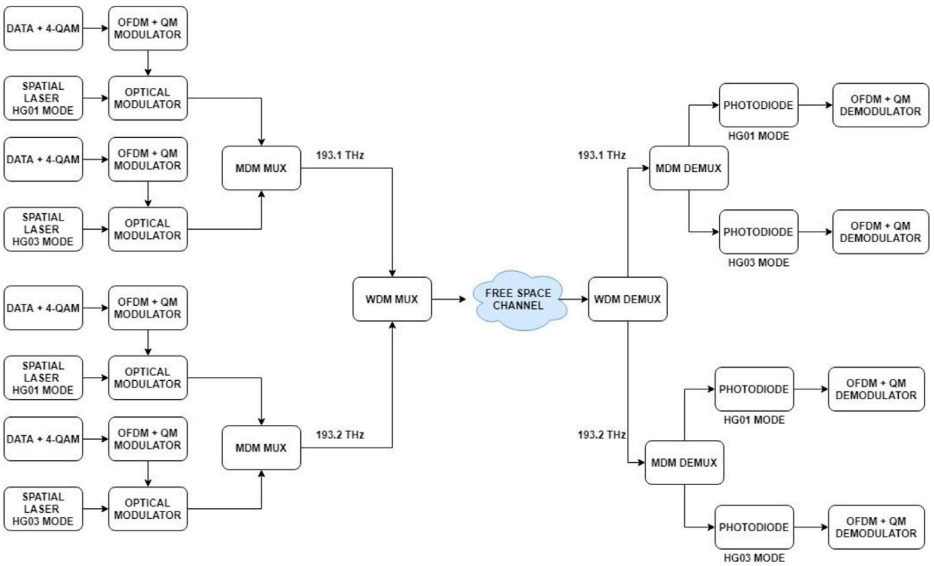


**FIGURE 1 |** Schematic design of the proposed link.

network, secure data transmission, and license-free spectrum availability [2–5]. Orthogonal frequency division multiplexing (OFDM) is a subset of multi-carrier modulation techniques using which a high–bit rate signal is transported over several low-speed subcarriers, which are spaced closely in the frequency domain and are orthogonal to each other, thus eliminating the inter-carrier interference [6, 7]. By incorporating OFDM technology with FSO links, highly reliable long-reach data transmission links can be realized. Here, the authors in references [8–10] report the design and performance investigation of the OFDM-based FSO terrestrial link under the effect of different atmospheric conditions. To increase the data-carrying capacity of the link, wavelength division multiplexing (WDM) can be used which transmits multiple information signals at the same time over the same medium using different wavelengths [11–14].

Mode division multiplexing (MDM) is an important and evolving transmission technique that capitalizes on different spatial modes of a single laser beam to transport independent data signals over the same channel. The authors in references [15–17] report optical signal–processing techniques to generate and de-multiplex different laser modes. The application of a spatial light modulator to multiplex and de-multiplex optical spatial laser beams has been reported in references [18, 19]. Y. Jung et al. proposed the application of dual-fused optical fiber for MDM transmission applications in reference [20]. A. Amphawan et al. report the application of a photonic crystal fiber with a single core to generate different linear polarized (LP) modes. In recent years, the incorporation of MDM in optical fiber links has been extensively investigated to realize high-speed transmission [21]. A. Juarez et al. reported an MDM system capable of realizing high-speed data transmission in multi-mode fiber (MMF) links using linear polarized (LP) modes [22]. The authors reported feasible transportation of 120-Gbps data with 3 GHz-km bandwidth–length product over an MMF link of 50 km length

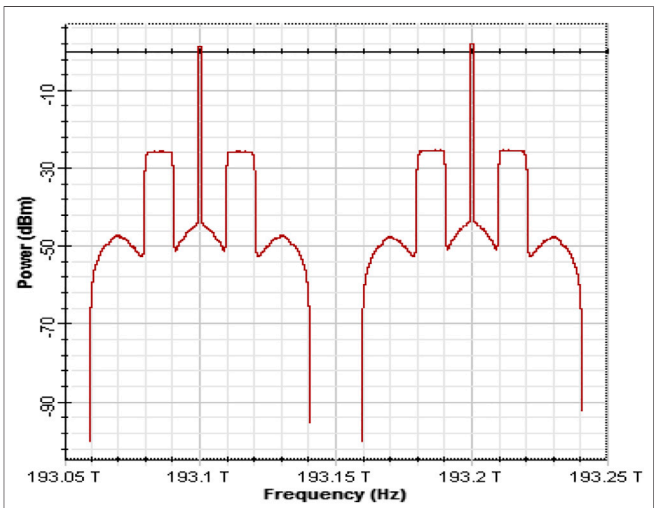


**FIGURE 2 |** Optical spectrum of the transmitted signal.

using a multi-mode erbium-doped fiber amplifier (EDFA) at the receiver unit. T. Kodama et al. reported a novel hybrid all-optical MDM code division multiplexed system to realize future generation optical access networks [23]. The authors experimentally reported feasible transmission of 2 LP modes × 4 phase-shift–keyed optical codes × 10-Gbps on–off–keyed data streams over a 42 km fiber length using a single-mode and a multi-mode fiber without the application of dispersion compensation. T. Masunda et al. proposed hybrid MDM and WDM architecture to realize high-speed MMF interconnects[24]. Six independent vertical-cavity surface-emitting laser diodes are used, where each wavelength generates three distinct Laguerre–Gaussian (LG) modes to realize 18 parallel channel transmissions. The authors report feasible 60 Gbps transmission

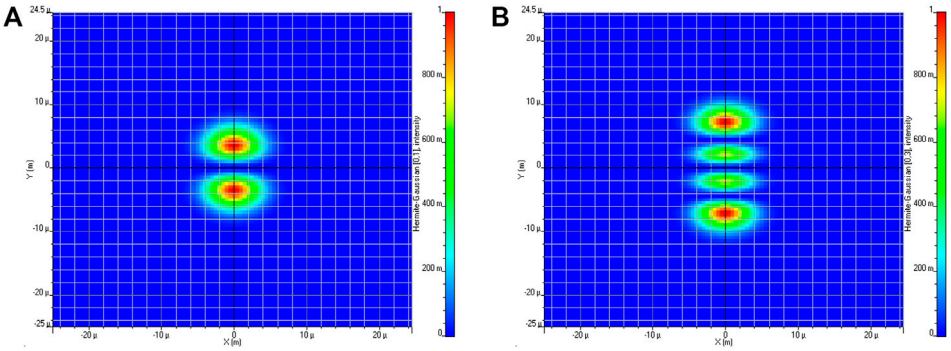


**FIGURE 3 |** Mode intensity profile of **(A)** HG01 and **(B)** HG03.

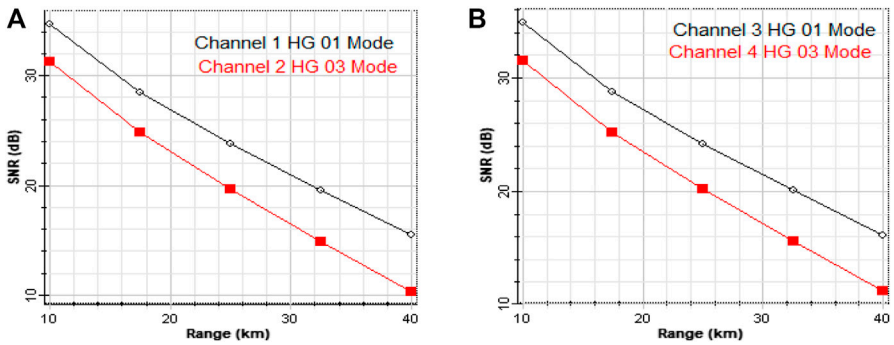


**FIGURE 4 |** SNR for **(A)** 1931. THz channel and **(B)** 193.2 THz channel under clear weather.

over a 2.5-km MMF link by using a novel tap configuration in a feed-forward equalizer to mitigate the effects of inter-mode coupling.

R. Murad et al. reported a high-capacity MDM system using hybrid modes for high-capacity optical interconnects in data centers [25]. The authors reported feasible transportation of 44-Gbps data using two helical-phased ring modes over a 1,550.12-nm channel and two radially offset Hermite–Gaussian (HG) modes over a 1,551.72-nm channel along an MMF of 1,500 m range with an acceptable bit error rate of the system. E. Hamed et al. reported the performance comparison of three different types of optical fibers, that is, a step-index few-mode fiber (FMF), graded-index FMF, and transversal index-FMF in a spectral-efficient MDM system [26]. Three distinct LP modes, where each mode carries 10-Gbps quadrature amplitude-modulated (QAM) data signals are transmitted over all the three optical fiber types. The authors reported that transversal index-FMF performs the best and demonstrated a feasible 500 km transmission of 30-Gbps QAM data with good performance. Z. Feng et al. reported an ultra-high channel capacity optical access network based on hybridization of MDM and WDM technologies with advanced modulation formats [27]. The incorporation of the 200-Gbps polarization division multiplexed (PDM)-16-level-QAM-OFDM data signal has been proposed in the system. The authors reported feasible data transmission of 4 wavelength channels × 6 spatial modes × 200 Gbps QAM data signals along a 37-km MMF with seven cores with acceptable performance.

The application of the orbital angular momentum (OAM) dimension of the optical signal to carry different independent information channels for realizing high-speed optical networks has been reported by many research groups in the last few years. The design of a hollow-core optical fiber capable of transporting 16 distinct OAM modes to realize high-capacity long-range MDM transmission has been reported by C. Brunet et al. in reference [28]. X. Zhang et al. reported the fabrication of a circular photonic crystal fiber capable of supporting 14 distinct OAM modes with low confinement losses and low nonlinear coefficients [29]. Also, the authors reported the fabrication of a multi-mode EDFA based on the circular photonic crystal fiber capable of reliably amplifying all 14 modes with 20 dB gain. The designing of a novel photonic crystal fiber, capable of supporting 26 OAM modes with low confinement loss, low nonlinear coefficient, and high bandwidth for long-haul spectrum-efficient MDM transmission in future optical access networks, has been reported by M. Hassan et al. in reference [30]. K. Ingerslev et al. reported feasible

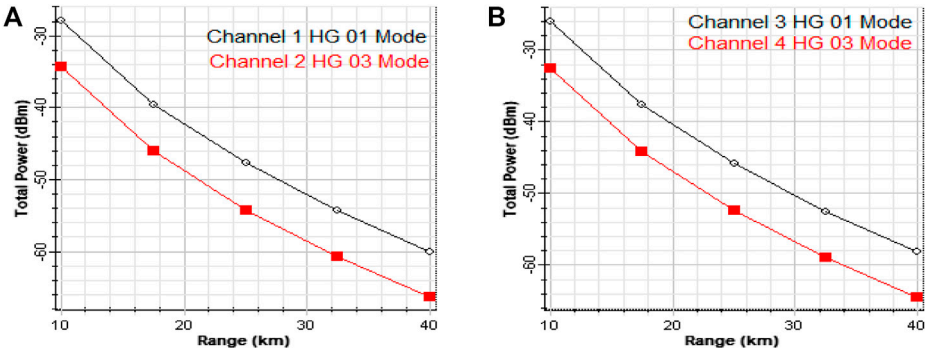


**FIGURE 5 |** Signal power for **(A)** 1931. THz channel and **(B)** 193.2 THz channel under clear weather.

transportation of 12 OAM modes, where each mode carries 10 Gbaud quadrature phase-shift–keyed (QPSK) signals over a 1.2-km MMF link with good performance [31]. Further, the authors have demonstrated ultrahigh capacity reliable transmission by using 60 independent wavelength channels with a channel spacing of 25 GHz. A. Tatarczak et al. reported an experimental demonstration of feasible transportation of three distinct OAM modes, where each mode transported a 10-Gbps on–off–keyed signal over a 400-m MMF link for short-reach links and high-capacity data centers [32]. F. Al-Zahrani et al. reported the development and analysis of a ring-core photonic crystal fiber with high refractive index separation, capable of supporting 76 OAM modes and six LP modes for large-speed high-range optical communication networks [33]. The free space transmission of OAM modes showing a spectral efficiency of 95.7 bit/sec/Hz with a net information rate of 100.8 Tbps and a 1.1 km MMF transmission of OAM modes to realize a 1.6 Tbps optical fiber network has been discussed by J. Wang et al. in reference [34].

The application of OAM modes to realize high-speed FSO links has also been reported by different research groups [35–39]. The designing and evaluation of a low-density parity check coded FSO link incorporating high-capacity transmission under strong turbulence conditions using OAM multiplexing has been discussed by Z Qu. et al. in reference [35]. The use of OAM multiplexing for deep space applications and multi-gigabit near-Earth optical networks has been reported by I. Djordjevic in reference [36]. Z. Qu. et al. reported a multi-gigabit capacity FSO link incorporating hybrid OAM multiplexing and WDM techniques [37]. Further, the link performance under strong turbulent conditions has been improved by deploying adaptive optics and channel coding techniques. L. Li et al. reported an OAM-multiplexed FSO communication system, where 80-Gbps information is transmitted between two ground terminals separated at 100 m *via* an unmanned aerial vehicle (UAV) using two independent 40-Gbps QPSK-modulated OAM beams [38]. Z. Zhao et al. reported an ultrahigh capacity FSO communication system over strong atmospheric turbulence conditions by incorporating hybridization of OAM multiplexing, polarization multiplexing, and frequency multiplexing [39]. The research works in references [40–44] report the simulative analysis of MDM-based high-capacity radio over fiber (RoF) links.

The main motivation here is to model an FSO link capable of securely transmitting biosensor data in health-care facilities under different atmospheric conditions at high bit rates. We discuss the simulation designing and evaluation of the OFDM-FSO link with high-speed data transmission capabilities using WDM and MDM techniques under different atmospheric conditions. The link design is reported in *Link Design of Wavelength-Mode Division Multiplexing-Orthogonal Frequency Division Multiplexing-Based Free Space Optics Link* Section, and the simulative evaluation results are discussed in *Numerical Results* Section. *Conclusion* Section concludes this research work.

## LINK DESIGN OF WAVELENGTH-MODE DIVISION MULTIPLEXING–ORTHOGONAL FREQUENCY DIVISION MULTIPLEXING–BASED FREE SPACE OPTICS LINK

**Figure 1** presents the schematic design of the proposed FSO link. Optisystem™ simulation software v.15 has been used for designing and evaluating the FSO link.

Four 20-Gbps OFDM-encoded data signals are transported over the FSO channel under different weather conditions. Two channels (1 and 2) are transmitted at 193.1-THz frequency over HG01 and HG03 modes, and another two channels (3 and 4) are transmitted at 193.2 THz frequency over HG01 and HG03 modes. A WDM multiplexer is used to combine the two frequencies at the transmitter side. **Figure 2** presents the optical spectrum of the transmitted signal.

The HG modes can be mathematically described using the equation [45]:

$$\varphi_{r,s}(x,y) = H_m\left(\frac{\sqrt{2}x}{\omega_{0,x}}\right)\exp\left(-\frac{x^2}{\omega_{ox}^2}\right)\exp\left(j\frac{\pi x^2}{\lambda R_{ox}}\right) \times H_n\left(\frac{\sqrt{2}y}{w_{o,y}}\right)\exp\left(-\frac{y^2}{w_{oy}^2}\right)\left(j\frac{\pi y^2}{\lambda R_{oy}}\right), \quad (1)$$

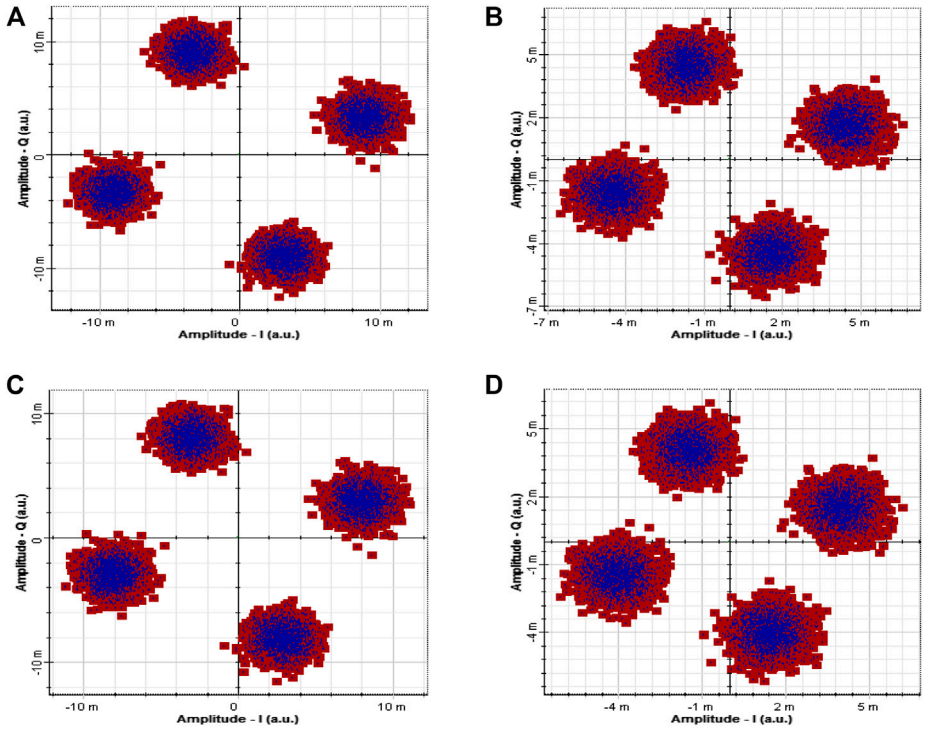


**FIGURE 6 |** Constellation plots after 32 km range for 193.1 THz channel **(A)** HG01 mode and **(B)** HG03 mode; for 193.2 THz channel **(C)** HG01 mode and **(D)** HG03 mode.

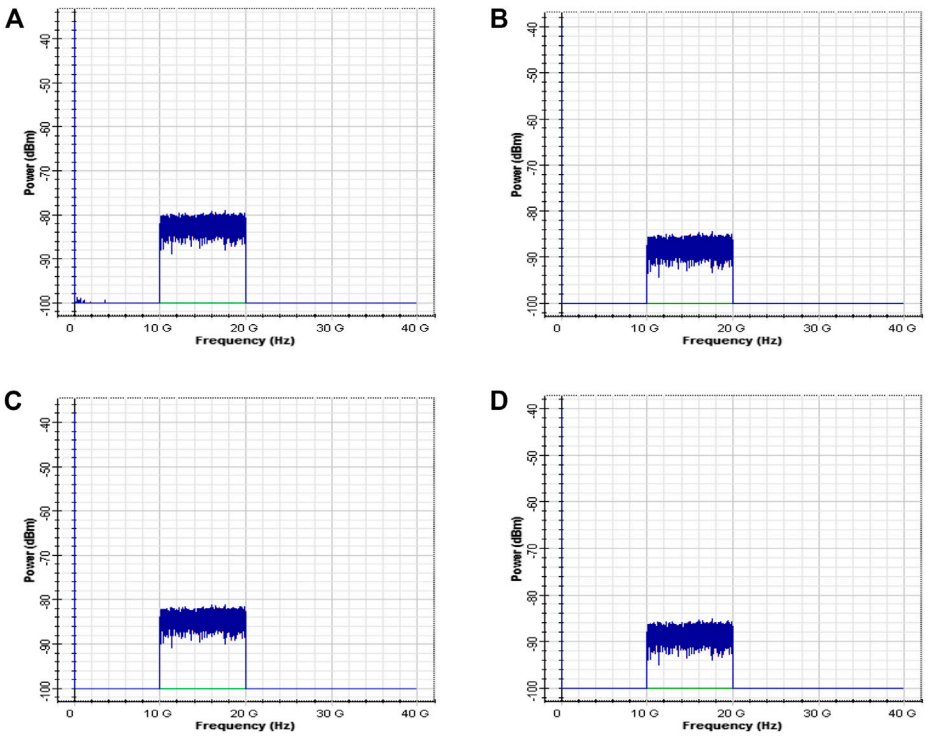


**FIGURE 7 |** RF power after 32 km range for 193.1 THz channel **(A)** HG01 mode and **(B)** HG03 mode; for 193.2 THz channel **(C)** HG01 mode and **(D)** HG03 mode.

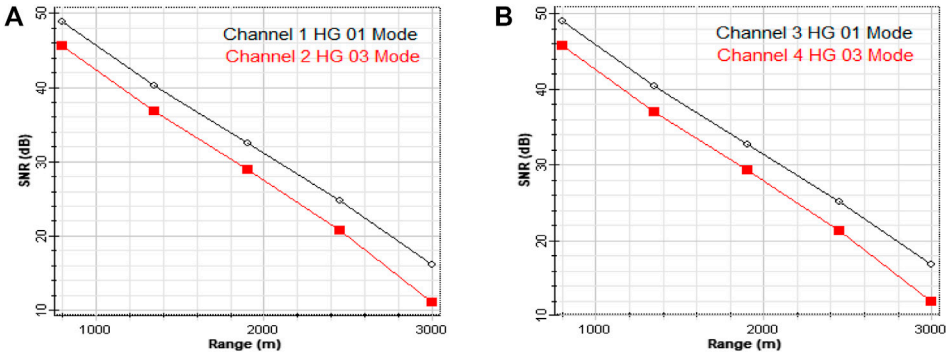


**FIGURE 8 |** SNR plots for **(A)** 1931. THz channel and **(B)** 193.2 THz channel under low fog.

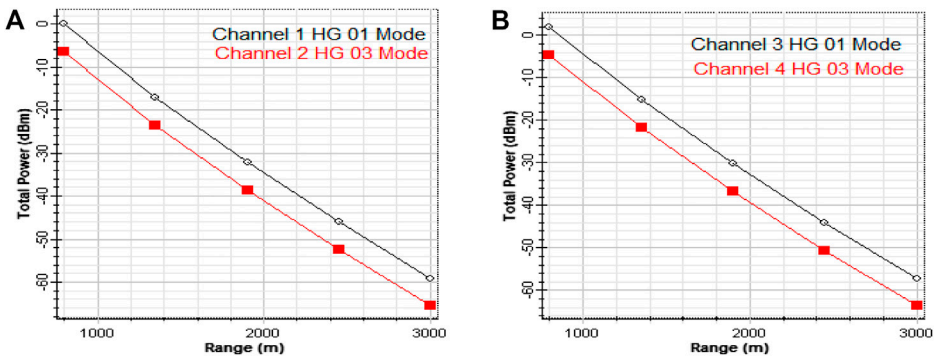


**FIGURE 9 |** Signal power plots for **(A)** 1931. THz channel and **(B)** 193.2 THz channel under low fog.

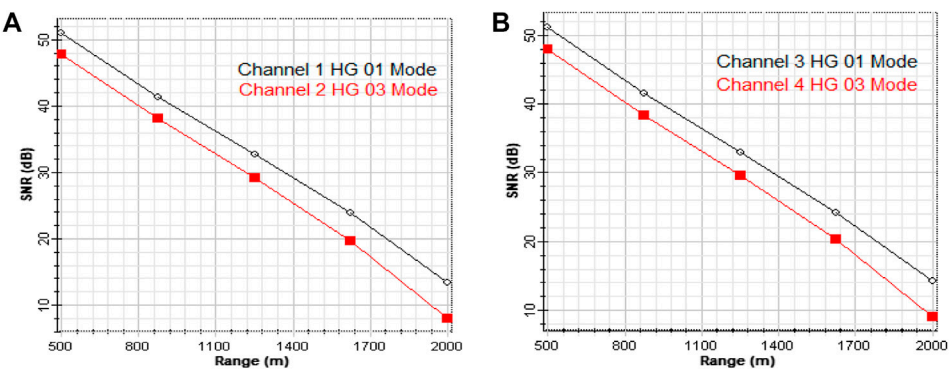


**FIGURE 10 |** SNR plots for **(A)** 1931. THz channel and **(B)** 193.2 THz channel under heavy fog.

where $r$ is the dependency of mode profile on the $X$-axis, $s$ is the dependency of mode profile on the $Y$-axis, the radius of the beam is denoted by $R$, the size of the optical beam at the waist is denoted by $\omega_0$, and $H_m$ *and* $H_n$ denote Hermite polynomials. Different HG modes are excited using a spatial laser, and the mode intensity profiles are illustrated in **Figure 3**.

For each channel, 20-Gbps data from the information source is mapped onto 4-QAM symbols, where two bits are transmitted per symbol. This signal is further OFDM modulated in the electrical domain. The specification of the OFDM modulator is 1,024 inverse fast Fourier transformation points, 512 orthogonal subcarriers, a cyclic prefix of value 32, and average power of 15 dBm. This signal is up-converted using a 7.5-GHz quadrature amplitude (QM) modulator. For each frequency channel, the 4-QAM-OFDM spatially modulated signals are combined using an MDM multiplexer (MUX). The distinct frequency channels are then

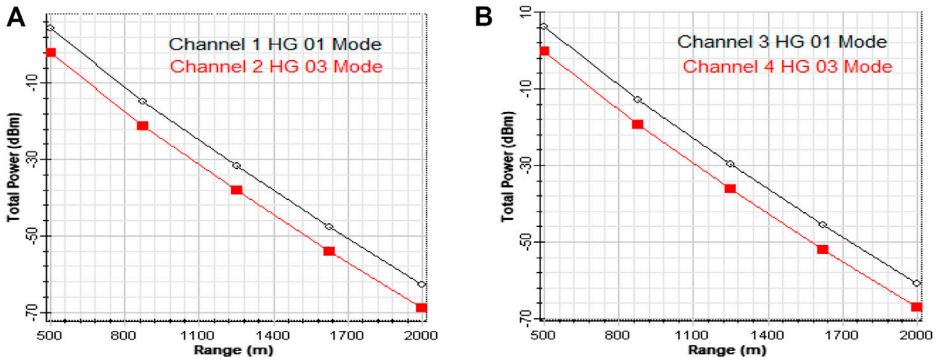


**FIGURE 11 |** Signal power plots for **(A)** 1931. THz channel and **(B)** 193.2 THz channel under heavy fog.

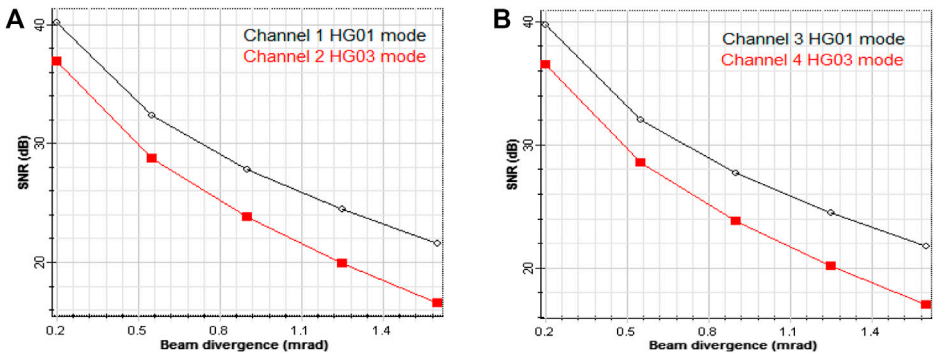


**FIGURE 12 |** SNR plots for **(A)** 1931. THz channel and **(B)** 193.2 THz channel under the effect of the beam divergence angle.

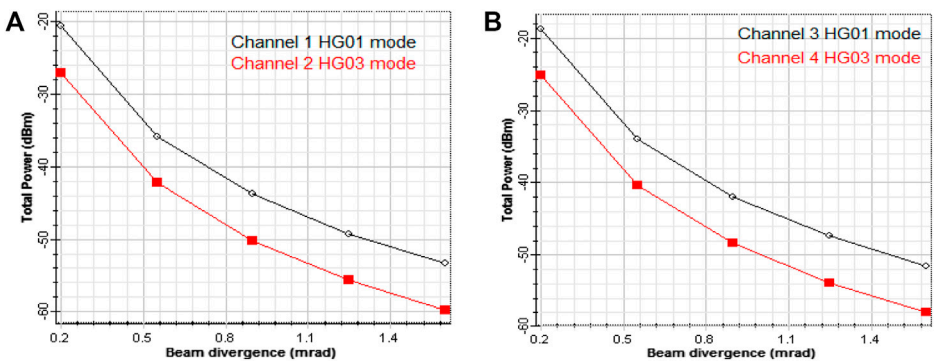


**FIGURE 13 |** Signal power plots for **(A)** 1931. THz channel and **(B)** 193.2 THz channel under the effect of the beam divergence angle.

multiplexed using a WDM MUX (**Figure 2**), and the information signal is transmitted using a transmitter lens.

The link equation can be described as [46]:

$$P_{Received} = P_{Transmitted}\left(\frac{d_R^2}{(d_T + \theta Z)^2}\right)10^{-\sigma Z/10}, \qquad (2)$$

where $d_R$ denotes the aperture diameter of receiver lens (100 mm), $d_T$ denotes aperture diameter of transmitter lens (100 mm), $\theta$ denotes the size of the optical beam/divergence angle (0.25 mrad), Z denotes the FSO range, and $\sigma$ is the attenuation coefficient for varying climate conditions. The attenuation coefficient for low fog, heavy fog, and clear conditions is 9, 22, and 0.14 dB/km, respectively [47]. At the receiver, individual frequency channels are separated using the WDM de-multiplexer (DEMUX), and for each frequency channel, independent spatial channels are separated using

MDM DEMUX. An APD photodiode converts the optical signal into its electrical equivalent. Originally transmitted message bits are recovered using OFDM and QM demodulator sections.

## NUMERICAL RESULTS

**Figures 4**, **5** illustrate plots for SNR and the signal power with an increasing range in the proposed link under clear weather. **Figure 4A** shows that channel 1 transmitted over the HG01 mode performs notably better than channel 2 transmitted over the HG03 mode at 193.1 THz frequency. For channel 1, the SNR value at the receiver terminal is measured as 34.67, 23.75, and 15.44 dB, whereas for channel 2, SNR is reported as 31.29, 19.62, and 10.31 dB at 10, 25, and 40 km, respectively. **Figure 4B** shows that for channel 3, the SNR value is 34.88, 24.14, and 16.16 dB, whereas for channel 4, the SNR value is 31.52, 20.16, and 11.23 dB at 10, 25, and 40 km, respectively. It can be seen that for the 193.2 THz frequency channel, the HG01 mode outperforms the HG03 mode.

**Figure 5A** shows that for the channel 1, the signal power is −27.93, −47.78, and −60.02 dBm, whereas for channel 2, the signal power is −34.39, −54.22, and −66.32 dBm at 10, 25, and 40 km, respectively. **Figure 5B** shows that for channel 3, the signal power is −26.03, −45.88, and −58.14 dBm, whereas for channel 4, the signal power is −32.49, −52.33, and −64.49 dBm at 10, 25, and 40 km, respectively. A feasible transmission of 4 × 20 Gbps information at 32 km with fair performance metrics (SNR ~ 20 dB) [40] is observed from the results presented. **Figure 6** reports constellation plots, and **Figure 7** reports the RF power of the signals at 32 km.

Further, the W-MDM-OFDM–based FSO link is evaluated for low and heavy fog conditions. **Figures 8**, **9** report SNR and signal power plots for different channels under low fog conditions in the proposed link. **Figures 8A,B** show that the SNR reduces from 48.83, 45.59, 49.01, and 45.77 dB to 16.13, 11.07, 16.82, and 11.96 dB for channels 1, 2, 3, and 4, respectively, for the link range increasing from 800 to 3,000 m under low fog conditions. Similarly, **Figure 9A,B** show that the signal power reduces from 0.04, −6.41, 1.94, and −4.51 dBm to −59.12, −65.44, −57.23, and −63.60 dBm for channels 1, 2, 3, and 4, respectively, for the link range increasing from 800 to 3,000 m under low fog conditions.

**Figures 10**, **11** present SNR and signal power plots for different channels under heavy fog conditions. **Figures 10A,B** show that the SNR reduces from 50.96, 47.72, 51.14, and 47.90 dB to 13.36, 8.01, 14.17, and 9.01 dB for channels 1, 2, 3, and 4, respectively, for the link range increasing from 500 to 2000 m under heavy fog conditions. Similarly, **Figures 11A,B** show that the signal power reduces from 4.29, −2.16, 6.18, and −0.26 dBm to −62.67, −68.87, −60.81, and −67.09 dBm for channels 1, 2, 3, and 4, respectively, for the link range increasing from 500 to 2000 m under heavy fog conditions. It can be observed that for low fog, the link prolongs to 2,800 m, whereas for heavy fog, 1750 m range is supported with fair performance (SNR ~ 20 dB).

In this study, we also discuss the impact of the increasing beam divergence angle on the performance of the proposed link. **Figures 12**, **13** demonstrate SNR and signal power plots, respectively, with an increasing angle of beam divergence. From the results presented, it can be seen that SNR varies from 39.73, 36.85, 40.12, and 36.49 dB to 21.57, 17.10, 21.75, and 16.57 dB as the beam divergence angle increases from 0.2 to 1.6 mrad for channels 1, 2, 3, and 4 respectively. Alternatively, the signal power reduces from −20.59, −27.05, −18.73, and −25.19 dBm to −53.35, −59.76, −51.50, and −57.92 dBm as the beam divergence angle increases from 0.2 to 1.6 mrad for channels 1, 2, 3, and 4, respectively. Degradation in the received signal quality with the increasing angle of beam divergence can be observed from the reported results. This is because increasing beam size results in lesser optical power collected at the receiver plane and higher power lost to the surroundings, thus degradation in the link performance.

## CONCLUSION

In this study, an FSO link is proposed for providing biomedical services, and we report a successful transmission of 4 × 20-Gbps data over an OFDM-based FSO link by incorporating hybrid WDM and MDM techniques under different atmospheric conditions. From the results presented, it can be concluded that the proposed link prolongs to 32 km with acceptable performance (SNR ~ 20 dB) under clear weather conditions which reduces to 2,800 m and 1750 m under low fog and heavy fog conditions, respectively. Also, the HG01 mode performs better than the HG03 mode since the former has more immunity against fading effects due to adverse weather conditions. Also, the performance of the proposed link under an increasing beam divergence angle has been discussed. From the results presented, it can be observed that the performance of the proposed link degrades in terms of SNR and signal power of the received signal on increasing the beam divergence angle. In future studies, dual-polarization transmission along with digital signal processing techniques at the receiver side can be incorporated in the proposed system to further enhance the information capacity and link performance under adverse climate conditions.

## DATA AVAILABILITY STATEMENT

The original contributions presented in the study are included in the article/Supplementary Material; further inquiries can be directed to the corresponding author.

## AUTHOR CONTRIBUTIONS

All authors listed have made a substantial, direct, and intellectual contribution to the work and approved it for publication.

## ACKNOWLEDGMENTS

The researchers would like to thank the Deanship of Scientific Research, Qassim University for funding the publication of this project.

## REFERENCES


1. Khalighi MA, and Uysal M. Survey on Free Space Optical Communication: A Communication Theory Perspective. *IEEE Commun Surv Tutorials* (2014) 16(4):2231–58. doi:10.1109/comst.2014.2329501
2. Chaudhary S, Sharma A, Tang X, Wei X, and Sood P. A Cost Effective 100 Gbps FSO System under the Impact of Fog by Incorporating OCDMA-PDM Scheme. *Wireless Pers Commun* (2021) 116:2159–68. doi:10.1007/s11277-020-07784-3
3. Nykolak G, Szajowski PF, Tourgee G, and Presby H. 2.5 Gbit/s Free Space Optical Link over 4.4 Km. *Electron Lett* (1999) 35(7):578–9. doi:10.1049/el:19990377
4. Singh M, and Malhotra J. 4×20Gbit/s-40GHzOFDM Based Radio over FSO Transmission Link Incorporating Hybrid Wavelength Division Multiplexing-Mode Division Multiplexing of LG and HG Modes with Enhanced Detection. *Optoelectronics Adv Mater - Rapid Commun* (2020) 14:5233–6243.
5. Ramezani A, Noroozi MR, and Aghababaee M. Analyzing Free Space Optical Communication Performance. *Int J Eng Adv Technol* (2014) 4(1):46–51.
6. Singh J, and Kumar N. Performance Analysis of Different Modulation Format on Free Space Optical Communication System. *Optik - Int J Light Electron Opt* (2013) 124(20):4651–4. doi:10.1016/j.ijleo.2013.02.014
7. Saruchi Attri S, Charu Narula C, and Sanjiv Kumar S. Performance Analysis of FSO Link Using CO-OFDM under the Effect of Atmospheric Turbulence. In: *Proc. Of International Conference on Intelligent Communication, Control, Devices*. Dehradun, India: Springer (2017). p. 167–72. doi:10.1007/978-981-10-1708-7_18
8. Amphawan A, Chaudhary S, and Chan VWS. 2 X 20 Gbps - 40 GHz OFDM Ro-FSO Transmission with Mode Division Multiplexing. *J Eur Opt Soc - Rapid publications* (2014) 9:14041. doi:10.2971/jeos.2014.14041
9. Cvijetic N, Qian D, and Wang T. 10 GB/s Free-Space Optical Transmission Using OFDM. In: OFC/NFOEC; 24-28 February 2008; San Diego, CA, USA (2007). p. 1–3.
10. Gill HK, Dhaliwal BS, and Singh K. Performance of OFDM FSO System Using ODSB, OSSB, and OVSB Modulation Schemes by Deploying Spatial Diversity. *Int J Eng Develop Res* (2015) 3(2):1384–9.
11. Chaudhary S, Tang X, Ghassemlooy Z, Lin B, Wei X, and Liaw KS. A 3 × 25 Mbps WDM-Ro-VLC System for Amateur Radio Applications. In: 2019 2nd West Asian Colloquium on Optical Wireless Communications (WACOWC); 27-28 April 2019; Tehran, Iran (2019). p. 6–10. doi:10.1109/WACOWC.2019.8770208
12. Sharma A, Kaur S, and Chaudhary S. Performance Analysis of 320 Gbps DWDM-FSO System under the Effect of Different Atmospheric Conditions. *Opt Quant Electron* (2021) 53:239. doi:10.1007/s11082-021-02904-0
13. Chaudhary S, Chauhan P, and Sharma A. High Speed 4 × 2.5 Gbps-5 GHz AMI-WDM-RoF Transmission System for WLANs. *J Opt Commun* (2019) 40(3):285–8. doi:10.1515/joc-2017-0082
14. Chaudhary S, Chaudhary N, Sharma S, and Choudhary B. High Speed Inter-Satellite Communication System by Incorporating Hybrid Polarization-Wavelength Division Multiplexing Scheme. *J Opt Commun* (2017) 39(1):87–92. doi:10.1515/joc-2016-0107
15. Randel S, Ryf R, Sierra A, Winzer PJ, Gnauck AH, bolle CA, Essiambre RJ, et al. Space-division Multiplexing over 10 Km of Three-Mode Fiber Using Coherent 6_ 6 MIMO Processing. In: proceedings to Optical Fiber Communication Conference and Exposition (OFC/NFOEC), 2011 and the National Fiber Optic Engineers Conference; 6–10 March 2011; Los Angeles. IEEE (2011). p. 1–3.
16. Amphawan A, and Dominic O. Modal Decomposition of Output Field for Holographic Mode Field Generation in a Multimode Fiber Channel. In: proceedings to Photonics (ICP), 2010 International Conference; 5-7 July 2010; Langkawi. IEEE (2010). doi:10.1109/icp.2010.5604377
17. Amphawan A, Mishra V, Nisar K, and Nedniyom B. Real-time Holographic Backlighting Positioning Sensor for Enhanced Power Coupling Efficiency into Selective Launches in Multimode Fiber. *J Mod Opt* (2012) 59:1745–52. doi:10.1080/09500340.2012.739713
18. Amphawan A. Binary Encoded Computer Generated Holograms for Temporal Phase Shifting. *Opt Express* (2011) 19:23085–96. doi:10.1364/oe.19.023085
19. Amphawan A. Binary Spatial Amplitude Modulation of Continuous Transverse Modal Electric Field Using a Single Lens for Mode Selectivity in Multimode Fiber. *J Mod Opt* (2012) 59:460–9. doi:10.1080/09500340.2011.636486
20. Jung Y, Chen R, Ismaeel R, Brambilla G, Alam S-U, Giles IP, et al. Dual Mode Fused Optical Fiber Couplers Suitable for Mode Division Multiplexed Transmission. *Opt Express* (2013) 21:24326–31. doi:10.1364/oe.21.024326
21. Amphawan A, Benjaporn N, and Nashwan MAS. Selective Excitation of LP01 Mode in Multimode Fiber Using Solid-Core Photonic crystal Fiber. *J Mod Optic* (2014) 60:1–9. doi:10.1080/09500340.2013.827249
22. Juarez AA, Warm S, Bunge C-A, Krummrich PM, and Petermann K. Perspectives of Principal Mode Transmission in a Multi-Mode Fiber. In: 36th European Conference and Exhibition on Optical Communication; 19-23 Sept. 2010; Torino (2010). p. 1–3. doi:10.1109/ECOC.2010.5621235
23. Kodama T, Isoda T, Morita K, Maruta A, Maruyama R, Kuwaki N, et al. First Demonstration of a Scalable MDM/CDM Optical Access System. *Opt Express* (2014) 22:12060–9. doi:10.1364/oe.22.012060
24. Masunda T, and Amphawan A. Feedforward Equalizers for MDM-WDM in Multimode Fiber Interconnects. *J Opt Commun* (2018) 39(2):147–53. doi:10.1515/joc-2016-0037
25. Murad R, Amphawan A, Fazea Y, Sajat M, and Alias H. MDM of Hybrid Modes in Multimode Fiber. In: Proceeding of International Conference on Electrical Engineering, Computer Science and Informatics, Indonesia; 19-20 August 2015; alembang, Indonesia (2015). p. 117–22.
26. Hamed EK, Munshid MA, and Hmood JK. Effect of Few-Mode Fiber Profile on Long-Haul MDM Transmission. *AIP Conf Proc* (2020) 2213(1):020137. doi:10.1063/5.0000088
27. Feng Z, Xu L, Wu Q, Tang M, Fu S, Tong W, et al. Ultra-high Capacity WDM-SDM Optical Access Network with Self-Homodyne Detection Downstream and 32QAM-FBMC Upstream. *Opt Express* (2017) 25(6):5951–61. doi:10.1364/OE.25.005951
28. Brunet C, Ung B, Messaddeq Y, LaRochelle S, Bernier E, and Rusch LA. Design of an Optical Fiber Supporting 16 OAM Modes. In: OFC 2014; 9-13 March 2014; San Francisco, CA (2014). p. 1–3. doi:10.1364/OFC.2014.Th2A.24
29. Zhang X, Zhang H, and Li H. The OAM Transmission Fiber Based on Circular Photonic crystal Fiber Structure. In: 2017 16th International Conference on Optical Communications and Networks (ICOCN); 7-10 Aug. 2017; Wuzhen, China (2017). p. 1–3. doi:10.1109/ICOCN.2017.8121421
30. Hassan MM, Kabir MA, Hossain MN, Biswas B, Paul BK, and Ahmed K. Photonic crystal Fiber for Robust Orbital Angular Momentum Transmission: Design and Investigation. *Opt Quant Electron* (2020) 52:8. doi:10.1007/s11082-019-2125-0
31. Ingerslev K, Gregg P, Galili M, Da Ros F, Hu H, Bao F, et al. 12 Mode, WDM, MIMO-free Orbital Angular Momentum Transmission. *Opt Express* (2018) 26:20225–32. doi:10.1364/OE.26.020225
32. Tatarczak A, Usuga AM, and Monroy IT. OAM-enhanced Transmission for Multimode Short-Range Links. In: Proc. SPIE 9390, Next-Generation Optical Networks for Data Centers and Short-Reach Links II; 9 March 2015; San Francisco, California, United States (2015). p. 93900E. doi:10.1117/12.2079795
33. Al-Zahrani FA, and Ahmed K. Novel Design of Dual Guided Photonic crystal Fiber for Large Capacity Transmission in High-Speed Optics Communications with Supporting Good Quality OAM and LP Modes. *Alexandria Eng J* (2020) 59:4889–99. doi:10.1016/j.aej.2020.09.004
34. Wang J, and Willner AE. Using Orbital Angular Momentum Modes for Optical Transmission. In: Optical Fiber Communication Conference; 9-13 March 2014; San Francisco, CA, USA. San Francisco: Optical Society of America (2014). OSA Technical Digest (online) paper W4J.5. doi:10.1364/ofc.2014.w4j.5
35. Qu Z, and Djordjevic IB. LDPC-coded OAM Based FSO Transmission System in the Presence of strong Atmospheric Turbulence. In: 2015 49th Asilomar Conference on Signals, Systems and Computers; 8-11 Nov. 2015; Pacific Grove, CA (2015). p. 999–1002. doi:10.1109/ACSSC.2015.7421288
36. Djordjevic IB. Deep-space and Near-Earth Optical Communications by Coded Orbital Angular Momentum (OAM) Modulation. *Opt Express* (2011) 19:14277–89. doi:10.1364/OE.19.014277
37. Qu Z, and Djordjevic IB. Orbital Angular Momentum Multiplexed Free-Space Optical Communication Systems Based on Coded Modulation. *Appl Sci* (2018) 8:2179. doi:10.3390/app8112179
38. Li L, Zhang R, Zhao Z, Xie G, Liao P, Pang K, et al. High-Capacity Free-Space Optical Communications between a Ground Transmitter and a Ground Receiver via a UAV Using Multiplexing of Multiple Orbital-Angular-Momentum Beams. *Sci Rep* (2017) 7:17427. doi:10.1038/s41598-017-17580-y

39. Zhao L, Liu H, Hao Y, Sun H, and Wei Z. Effects of Atmospheric Turbulence on OAM-POL-FDM Hybrid Multiplexing Communication System. *Appl Sci* (2019) 9:5063. doi:10.3390/app9235063
40. Amphawan A, Chaudhary S, and Gupta B. Secure MDM-OFDM-Ro-FSO System Using HG Modes. *Int J sensors, wireless Commun Control* (2015) 5: 13–8. doi:10.2174/2210327905999150521110316
41. Sharma A, Chaudhary S, Thakur D, and Dhasratan V. A Cost Effective High Speed Radio over Fiber System for Millimeter Wave Applications. *J Opt Commun* (2017) 41:177–80. doi:10.1515/jjoc-2017-0166
42. Almogahed A, Amphawan A, and Fazea Y. Mitigation of Atmospheric Turbulences Using Mode Division Multiplexing Based on Decision Feedback Equalizer for Free Space Optics. *J Opt Commun* (2017) 41: 185–93. doi:10.1515/joc-2017-0169
43. Amphawan A, Fazea Y, Murad R, Alisa H, and Sajat M. MDM of Hybrid Modes in Multimode Fiber, Electrical Engineering. In: Computer Science and Informatics (EECSI); August 2015; Palembang, Indonesia (2015).
44. Fazea Y, and Amphawan A. 25 Gbit/s WDM-MDM. *J Opt Commun* (2016) 36: 327–33. doi:10.1515/joc-2014-0091
45. Ghatak A, and Thyagarajan K. *An Introduction to Fiber Optics*. Cambridge: Cambridge University Press (1998).
46. Kolev DR, Wakamori K, and Matsumoto M. Transmission Analysis of OFDM-Based Services over Line-Of-Sight Indoor Infrared Laser Wireless Links. *J Lightwave Technol* (2012) 30:3727–2735. doi:10.1109/jlt.2012.2227456
47. Sarangal H, Singh A, Malhotra J, and Chaudhary S. A Cost Effective 100 Gbps Hybrid MDM-OCDMA-FSO Transmission System under Atmospheric Turbulences. *Opt Quant Electron* (2017) 49:184. doi:10.1007/s11082-017-1019-2


**Conflict of Interest:** The authors declare that the research was conducted in the absence of any commercial or financial relationships that could be construed as a potential conflict of interest.

**Publisher's Note:** All claims expressed in this article are solely those of the authors and do not necessarily represent those of their affiliated organizations, or those of the publisher, the editors, and the reviewers. Any product that may be evaluated in this article, or claim that may be made by its manufacturer, is not guaranteed or endorsed by the publisher.

frontiers in Physics

ORIGINAL RESEARCH
published: 04 October 2021
doi: 10.3389/fphy.2021.749497

# Coherent Detection-Based Optical OFDM, 60 GHz Radio-over-Fiber Link Using Frequency Quadrupling, and Channel and Carrier Phase Estimation

*Sunil N Thool*, Devendra Chack and Amitesh Kumar*

*Department of Electronics Engineering, Indian Institute of Technology (ISM), Dhanbad, Jharkhand, India*

The optical orthogonal frequency division multiplexing (OFDM) is proven to be a most promising technology for the next-generation high-capacity and ultra-wide bandwidth 5G communication systems. 60 GHz millimeter-wave (mm-wave) frequency band is also becoming a most popular upcoming frequency spectrum due to today's available dense frequency spectrum used for mobile, multimedia, and data communication, etc. We propose a system comprised of 60 GHz radio-over-fiber (RoF) model using optimized optical frequency quadrupling, coherent detection, channel estimation, and carrier phase correction techniques for ultra-wide bandwidth 16-quadrature amplitude modulation (QAM) OFDM baseband signal. The proposed RoF system's outcomes have shown relatively better bit error rate (BER) of $3.1 \times 10^{-3}$ to enable successful transmission of 110 Gbps data for more than 105 km optical link comprising of standard single-mode fiber (SSMF). System performance and obtained results show a potential to fulfill the requirements of 5G and cellular communication system.

**Keywords: ultra-wide band optical OFDM, radio over fiber, 16-QAM, frequency quadrupling, coherent detection, 60 GHz (mm-wave)**

OPEN ACCESS

***Edited by:***
*Santosh Kumar,*
*Liaocheng University, China*

***Reviewed by:***
*Akhilesh Pathak,*
*Chulalongkorn University, Thailand*
*Yogendra Kumar Prajapati,*
*Motilal Nehru National Institute of Technology Allahabad, India*
*Vibhutesh Kumar Singh,*
*Intel, Ireland*

****Correspondence:***
*Sunil N Thool*
*sunilthool.18dp000388@ece.iitism.ac.in*

***Specialty section:***
*This article was submitted to Optics and Photonics, a section of the journal Frontiers in Physics*

***Received:*** *29 July 2021*
***Accepted:*** *23 August 2021*
***Published:*** *04 October 2021*

***Citation:***
*Thool SN, Chack D and Kumar A (2021) Coherent Detection-Based Optical OFDM, 60 GHz Radio-over-Fiber Link Using Frequency Quadrupling, and Channel and Carrier Phase Estimation. Front. Phys. 9:749497. doi: 10.3389/fphy.2021.749497*

## INTRODUCTION

The RoF has grown expressively and achieved good technical maturity in the past 3 decades. The research is focused on generating, transporting, and distributing radio signal in mm-wave band over optical fiber to meet the requirement of next-generation broadband 5G technology [1, 2]. In mm-wave, 60 GHz is the unlicensed spectrum which is becoming popular and would be a most promising band for 5G communication. Though it has disadvantage of huge propagation loss and caters for small distance communication, still it is found to be the most suitable wireless communication link ultra-wide bandwidth access. Inline to the above, it also shows the capability to fulfill the requirements of upcoming 5G network access [3]. OFDM-based RoF system has been widely studied and verified performance in terms of spectral signal purity and system robustness characteristics against optical fiber chromatic dispersion (CD), polarization mode dispersion (PMD), etc. [4–8]. Some of the studies represented the hybrid mm-wave RoF system optical OFDM signal transmission using various techniques such as POLMUX, double-lens scheme, and polarization multiplexing technique over 50 km over SSMF and 20 m wireless link [9, 10]. Performance of any RoF system mainly depends on the characteristics and design implementation of the elements used. These elements are laser source and its power level, optical modulator, optical fiber channel, and linear and nonlinear irregularities such as

chromatic dispersion, PMD, bit rate/data rate, and modulation and demodulation scheme. In some studies, it is represented as OFDM transmission using M-ary QAM with in-phase (I) and quadrature (Q) modulator and transmitted carrier frequency ranging from 2.4–10 GHz over a SSMF achieved reasonable data rate transceiver performance. The observed BER and error vector magnitude (EVM) of such implementation scheme is quite good, but it is limited to very short range/distance [4, 6, 8, 13–15]. The M-ary QAM digital modulation and demodulation technique used in any optical OFDM system represents better spectral efficiency and achieved good BER for high-capacity data transmission as compared to the other modulation technique [11–18]. In addition to this, the robust performance of the optical transceiver is achieved against the SSMF linear and nonlinear effect of chromatic dispersion, PMD, using Mach-Zehnder modulator (MZM) as an external modulator as compared with the direct modulator [19, 20]. The main challenge of 60 GHz RoF system is the generation of 60 GHz mm-wave due to the limitation of radio frequency (RF) signal sources. There are various methods available in the optical domain for the generation of 60 GHz mm-wave such as frequency quadrupling and optical heterodyne [21, 22]. A frequency quadrupling and optical heterodyning is a cost-effective solution for the generation of 60 GHz mm-wave signal.

This paper proposes a 60 GHz RoF system implementation using 16-QAM, OFDM with training and pilot symbol. It is also realized with optical heterodyning, coherent detection, channel estimation and carrier phase estimation, and corrections techniques. It consists of central station (CS) which generates the optical OFDM signal at input data rate of 100 Gbps to 120 Gbps using 16-QAM modulator. OFDM modulation is carried out with training and pilot symbol insertion for channel estimation and carrier phase estimation and correction, respectively. A 60 GHz mm-wave signal generation is required a highly expensive optical modulator and extremely stable phase noise local oscillator. In the proposed system, a 60 GHz mm-wave generation is designed through the optical frequency quadrupling process. In this technique, frequency multiplication of input radio frequency (RF) source over a LiNbO3 Mach-Zehnder modulator- (LiNbO3-MZM-) based linear modulation is used to produce high-frequency mm-wave signal generation [23–27]. This process provides a cost-effective solution and tradeoff for the frequency generation of the 60 GHz RF signal and hence becoming more reliable and economical.

The baseband OFDM signal to optical conversation is achieved by two orthogonal arms of LiNbO3-MZM. The laser source input to the two arms of MZM modulators are given by upper optical oscillators (UOO) frequency generated using the optical frequency quadrupling technique. The lowest optical oscillator (LOO) frequency with 60 GHz offset is directly combined with an optical modulated OFDM signal. The generated two UOO and LOO frequencies are orthogonally polarized, parallel polarization with 60 GHz frequency spacing away with respect to the continuous wave (CW) laser carrier. At the base station (BS), a coherent detection technique is used to detect a 60 GHz RF signal. It has the advantage to retrieve the phase information of the transmitted optical signal [28]. The reference oscillator frequency for coherent detector is set same as the LLO frequency to convert the optical signal into 60 GHz RF signal. The generated RF signal is then propagated over a wireless channel, and it is intercepted by a remote radio terminal (RRT). The RRT consists of I-Q demodulator comprising mixer where the mixing of locally generated 60 GHz signal with received RF signal is taking place. The mixer output is passed through low pass filter with cut-off frequency less than 0.2 × data rate/bit rate to eliminate intermodulation product generated during mixing process. The output of I-Q demodulator is the baseband OFDM signal which is highly contaminated by optical channel impartments and passed through the OFDM demodulator. The same training sequence and pilot symbols are used in OFDM demodulator for channel estimation and carrier phase estimation and correction. The chromatic dispersion compensation technique is used to combat the effect of dispersion while transmission is over SSMF. The phase corrected 16-QAM symbols are passed through the demodulator to detect the received bit stream at the symbol rate of 4 bits/symbol. The results obtained through the numerical simulation have been analyzed and discussed at the various stages of designed system. The frequency spectrums at baseband OFDM, optical frequency quadrupling-based 60 GHz frequency spacing of optical oscillator frequencies, transmitted optical frequency spectrum, and received 60 GHz RF spectrum at RRT are analyzed. The 16-QAM constellation diagram before and after channel estimation and the carrier phase correction signal processing block are also analyzed for EVM% and BER estimation. The reliability and robustness of the proposed design have been verified through the result obtained and discussed in terms of achieved BER with respect to the received optical power of SSMF at various lengths varying from 85 to 130 km. The obtained results are also discussed in terms of EVM% against the received optical power for the input data rate up to 120 Gbps. The proposed RoF system would be the best solution to successfully transmit the data for more than 105 and 110 km SSMF. The BER of $3.1 \times 10^{-3}$ and $2.9 \times 10^{-3}$ is achieved at EVM <15% for input data rates of 110 Gbps and 100 Gbps, respectively, against the received optical power at BS which is measured around −13 dBm. This optical power is used to transmit the 60 GHz RF for connecting different RRTs. This paper is organized as *Proposed 60 GHz RoF System* which is describing the proposed 60 GHz RoF system for OFDM with 16-QAM optical-based link. *Simulation Setup, Results, and Discussion* is addressing the verification and feasibility study of simulation setup, test results, analysis, and discussion. At last, a conclusion is drawn and discussed.

# PROPOSED 60 GHZ ROF SYSTEM

## Radio over Fiber

The RoF system is very favorable and prominent technique for today's wireless access network. It is mainly consisting of CS, BS, and RRT connected over fiber optic link and RF link. A larger distance transmission is done for optical signal which is transmitted between CS and BS while smaller distance communication is carried out between BS and RRT via RF wireless link. The OFDM baseband signal is modulated with UOO generated by using frequency

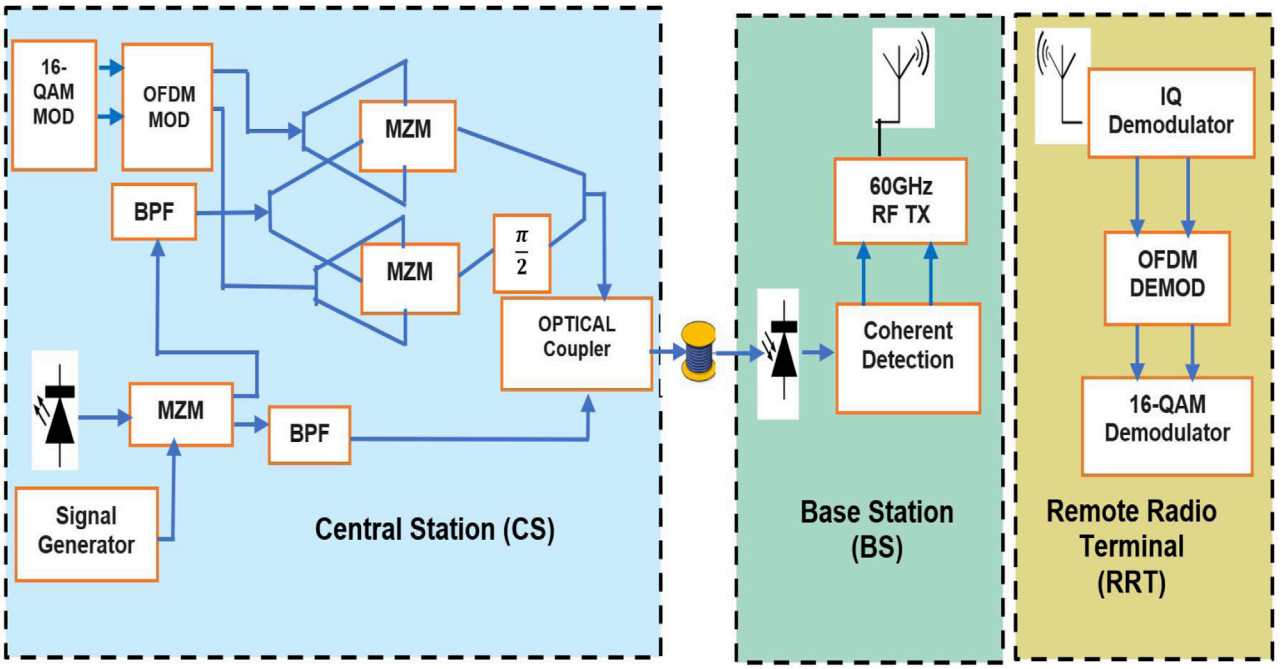


**FIGURE 1 |** Block diagram of the proposed 60 GHz radio-over-fiber system.

quadrupling at CS and subsequently it is transmitted through SSMF. The wireless RF signal transmission between BS and RRT is taking place. The RRT intercepts the RF signal, demodulates it, and generates the desired data stream. The block diagram and complete setup of proposed 60 GHz RoF link are represented in **Figure 1** and **Figure 2**, respectively.

## Central Station (CS)

Following are the major modules at the CS which are integrated to realize the proposed RoF system.

### 16-QAM Modulator

A 16-QAM modulator is used to convert the input data stream into baseband I-Q symbols with 4 bits/symbol. The 16-QAM modulator is implemented by splitting the bit sequence into two parallel subsequences, each transmitted in two arms of I and Q subcarrier. When transmitting the information, amplitude of a signal is varied according to the source symbol input.

### OFDM Modulator

The 16-QAM I-Q signal is passed through the OFDM modulator. The OFDM modulator consists of serial to parallel converter, inverse fast Fourier transform (IFFT), cyclic prefix (CP) insertion, and parallel to serial (S/P) with digital to analog (DAC) conversion with smoothing filter. In OFDM modulator, an S/P converter block takes the coded serial data from 16-QAM modulator and the insertion of training and pilot symbol at the specific symbol interval for channel estimation and carrier phase correction. The digital input data stream is arranged into optical symbols allocated by the 16-QAM modulated subcarrier. This subcarrier signal is passed through the IFFT algorithm through which all subcarriers are converted into time domain OFDM symbols and maintain the orthogonality. The OFDM symbols are again converted into frequency domain to reduce the dispersive effect of the optical channels. It is achieved by adding a guard extension called cyclic prefix (CP) to each OFDM time-domain symbol. It is used to reduce the inter symbol interference (ISI) and inter channel interference (ICI). Each time-domain OFDM symbol is again converted into a serial stream using parallel to serial (P/S) converter, followed by DAC with interpolation factor, to maintain the desired sampling rate.

### Frequency Quadrupling

A CW laser diode ran at fundamental frequency of $f_0 = 2\pi/\omega_0$ and emitted the light wave of $E_0(t) = E_0 \exp(j\omega_0 t)$. The RF local oscillator with clock of $V_{RF} = V_{RF} \sin(2\pi RFt)$ is being modulated with light wave generated by laser source using LiNbO3-MZM. LiNbO3-MZM is biased at maximum transmission point to produce even-order side bands along with carrier. In this system, first-order sidebands $(f_0 \pm 2fm)$ are extracted to generate the quadruple frequency at the photo-detector. The resultant RF frequency at photo-detector is $4f_m$ quadruple signal $((f_0 + 2fm) - (f_0 - 2fm))$. The biasing voltages of LiNbO3-MZM are optimized to modulate the RF signal and light wave signal to suppress odd-order sideband generation and canceled out completely. When the modulation index is more than 2.405, the CW laser carrier frequency gets suppressed. The optimized biasing of two arms of LiNbO3-MZM generates a higher-order sideband carrier with a small amplitude. It is mainly consisting of positive and negative second-order harmonics with reference to the fundamental carrier [29]. **Eq. 1** represents modulating carrier signal generated at LiNbO3-MZM output,

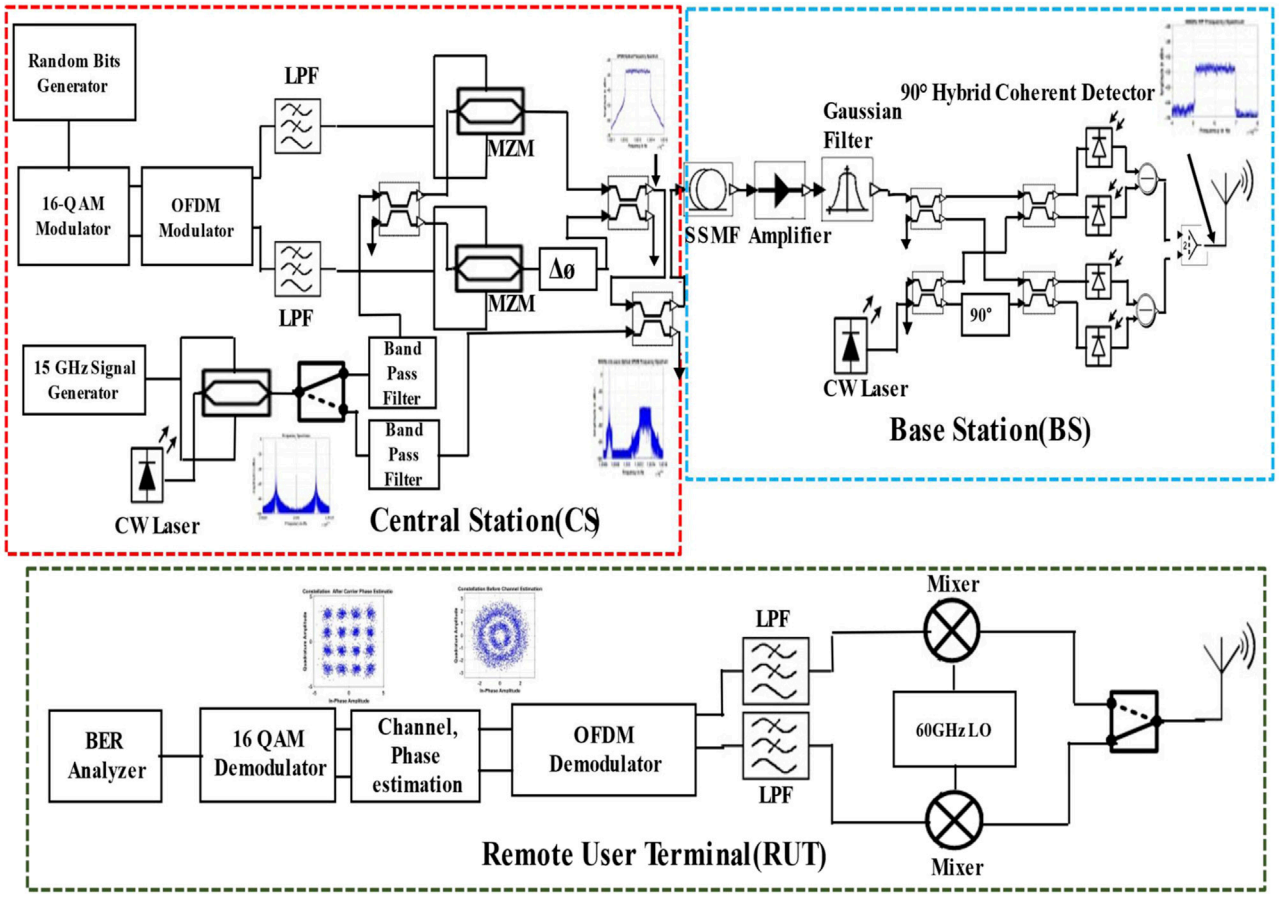


**FIGURE 2 |** Proposed setup of 60 GHz RoF system.

$$E_1(t) = \frac{\gamma_1}{2} E_0 \exp(j\omega_0 t)\left[\exp\left(j\frac{\pi}{V_\pi} V_{Rf}\cos\omega RFt\right) + \exp\left(-j\frac{\pi}{V_\pi} V_{Rf}\cos\omega RFt\right)\right]$$
$$\propto \gamma_1 E_0 J_{2(m_h)}\left[\exp j\,(\omega_0 - 2\omega RF)t + (\omega_0 + 2\omega RF)t\right], \quad (1)$$

where $\gamma_1$ is the insertion loss of MZM and $m_h$ is the modulation index and $J_n(m_h)$ is the $n^{th}$ order Bessel function. The two optical carrier is separated by using two independent band pass filter (BPF) with bandwidth of 10 GHz. The UOO frequency $(\omega_0 - 2\omega RF)$ is represented by

$$E_2(t) = \gamma_1 E_0 J_2(m_h) \exp j(\omega_0 - 2\omega RF)t. \quad (2)$$

The LOO frequency is transmitted without modulating signal, while the UOO is used to modulate optical OFDM signal.

## Optical OFDM Generation

The baseband I and Q signal of OFDM modulator is represented as

$$S(t) = I(t)\sin\omega_{RF}t + Q(t)\cos\omega_{RF}t. \quad (3)$$

The single side band (SSB) modulation using two orthogonal arms of LiNbO3-MZM modulator is used. Theoretically, it configured with bias voltages of $\frac{V_\pi}{2}$ and phase difference of $\frac{\pi}{2}$. The modulation index is chosen as $\alpha = \pi I(t)/V_\pi$ and $\beta = \pi Q(t)/V_\pi$. The SSB optical modulated signal is represented as

$$E_3(t) = \gamma_1\gamma_2 E_0 J_2(m_h)\left\{\exp j(\omega_0 + 2\omega_{RF})t + \frac{\pi}{V_\pi}\left[I(t) + jQ(t)\right]\exp j(\omega_0 + 2\omega_{RF} + \omega_{IF})t\right\}, \quad (4)$$

where $\gamma_2$ is the insertion loss of MZM. After combining two optical oscillators, the combiner output is expressed as

$$E_{equ}(t) = E_2(t) + E_3(t)$$
$$= \gamma_1 E_0 J_2(m_h)\left\{\frac{1}{2}\exp j(\omega_0 - 2\omega_{RF})t + \gamma_2 \exp j(\omega_0 + 2\omega_{RF})t\right\}$$
$$+ \gamma_1 E_0 J_2(m_h) \times \left\{\frac{1}{2}\exp j(\omega_0 - 2\omega_{RF})t + \gamma_2\frac{\pi}{V_\pi}\left[I(t) + jQ(t)\right]\right.$$
$$\left.\times\exp j(\omega_0 + 2\omega_{RF} + \omega_{IF})t\right\}. \quad (5)$$

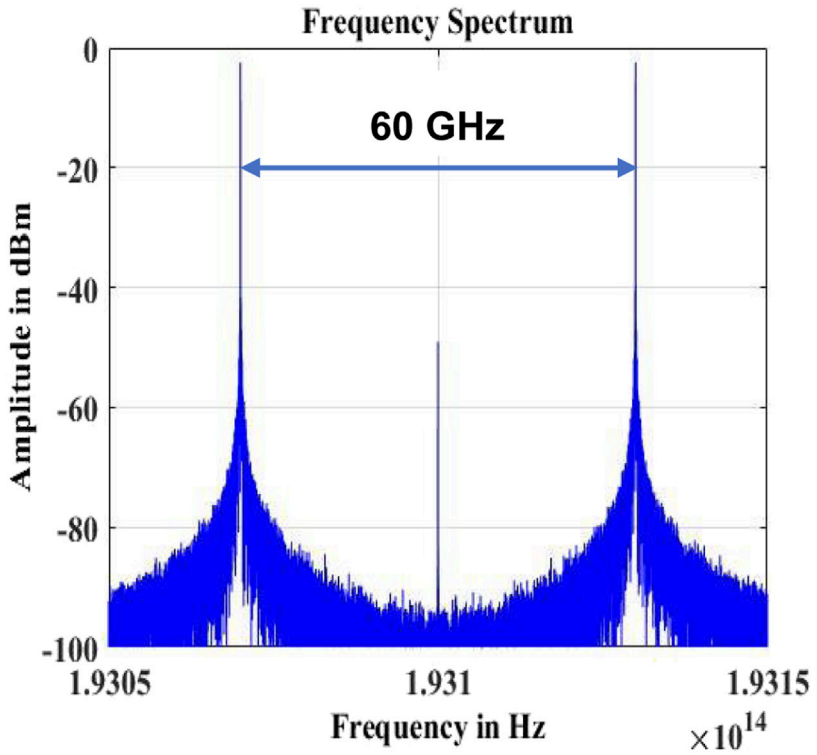


**FIGURE 3 |** 193.07 THz LOO and 193.13 THz UOO Frequencies generation using frequency quadrupling.

This $E_{equ}(t)$ is generated at CS and transmitted over SSMF with standard dispersion and attenuation factor.

## Base Station (BS)

The BS is realized with coherent detection and band pass filter (BPF). The optical coherent detection consists of four high-speed photo-detectors PIN to convert optical signal into 60 GHz RF signal. The amount of the current flow through it mainly depends on the PIN responsivity characteristics. It also preserves the phase information of the incoming signal which is the main advantage over the direct detection technique. The optical coherent receiver consists of a heterodyne receiver design, in which a set of 3 dB optical couplers, local oscillator (LO) laser, and balanced detection is used. A 60 GHz mm-wave RF signal generation is done by detecting optical signal which is received at the end of SSMF. The beating LO laser frequency is set with 60 GHz frequency offset of transmitted optical OFDM signal. Due to coherency nature of this process, it preserves the phase information of the optical signal. Hence, large distance communication coverage without any dispersion compensation technique can be achieved to some extent.

## Remote Radio Terminal (RRT)

The RRT consists of the following major blocks.

### IQ Demodulator

The detected 60 GHz RF signal from BS is transmitted to RRT for a short-range coverage over a wireless link. The RF signal is intercepted by RRT terminal where the I-Q demodulator process is carried out. The I-Q demodulator consists of mixer, RF LO, and low pass filter (LPF). The intercepted RF signal is mixed with 60 GHz LO generated locally, followed by LPF with the cut-off frequency 0.2 × bit rate to discard the intermodulation product generated by mixing process.

### OFDM Demodulator

OFDM demodulator is accomplished by the analog to digital (ADC) conversion with down-sampling factor to convert signal into global symbol rate. Dispersion compensation, removal of CP, fast Fourier transform (FFT), training, and pilot symbol insertion for channel estimation and carrier phase noise estimation and correction are used in the OFDM demodulator. Digital filtering is used to combat dispersion compensation generated due to propagation over a SSMF. It is implemented in the frequency domain indicated in Ref. [30].

$$G(z,w) = exp\left(-j.\frac{D.\lambda^2.z}{4.\pi.c}.w^2\right), \tag{6}$$

where $z, w, \lambda, c, S, \lambda 0, D = Do + S\ x\ (\lambda - \lambda o)$ are the distance coverage, angular frequency, wavelength, speed of light, dispersion slope, reference wavelength, and dispersion coefficient of the fiber for wavelength, respectively.

To reduce ISI and ICI, CP is added during OFDM modulator, hence CP is removed at CP removal stage.

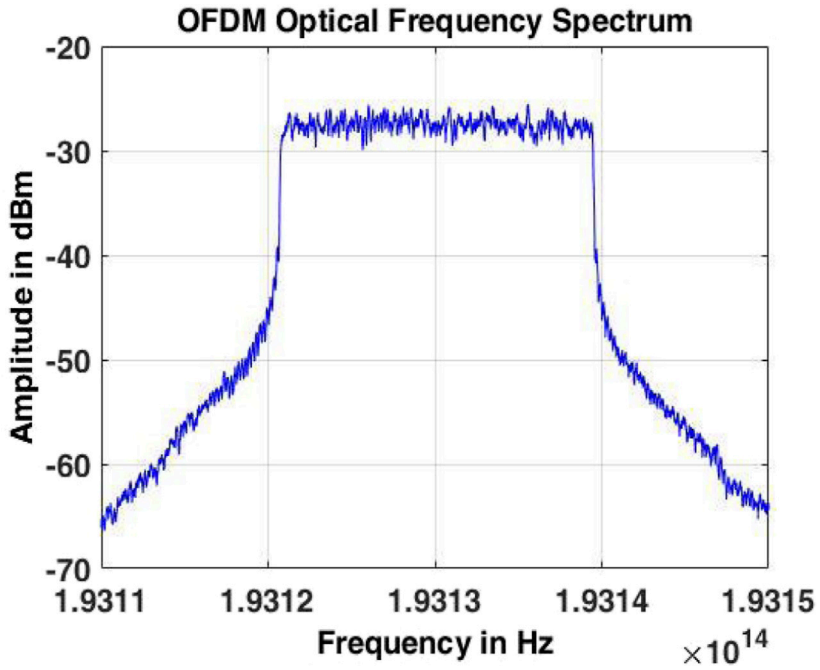


**FIGURE 4 |** Optical OFDM frequency spectrum.

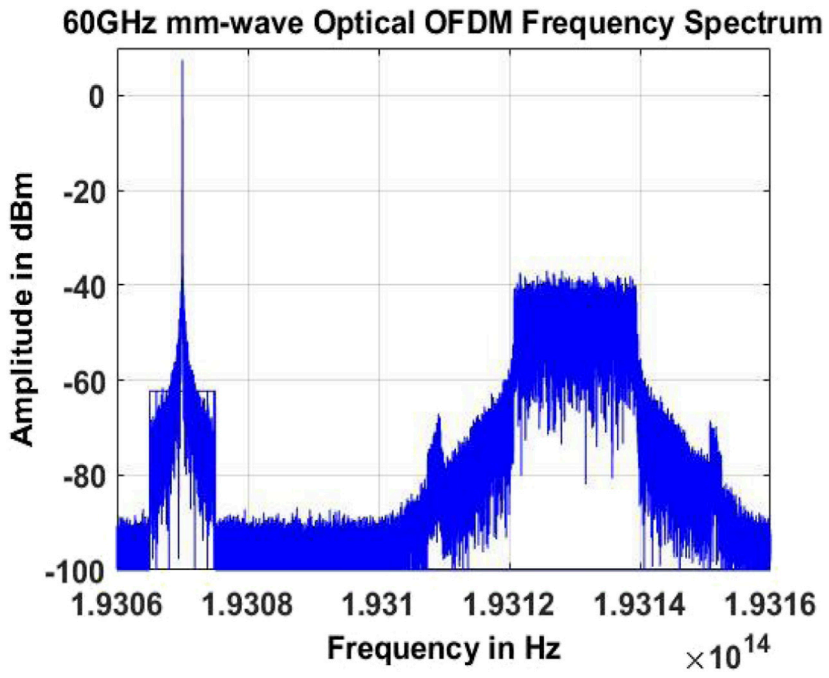


**FIGURE 5 |** Transmitted 60 GHz optical OFDM frequency spectrum.

Each time domain OFDM subcarrier is converted back to a symbol stream by performing FFT, consisting of useful symbols, pilot symbols, and training symbols. A constructed transfer function is used to compensate for CD, fiber non-linearities, PMDs, and polarization-dependent loss. It also improves the symbol error rate (SER). The transfer function for dispersion in the frequency domain can be characterized as

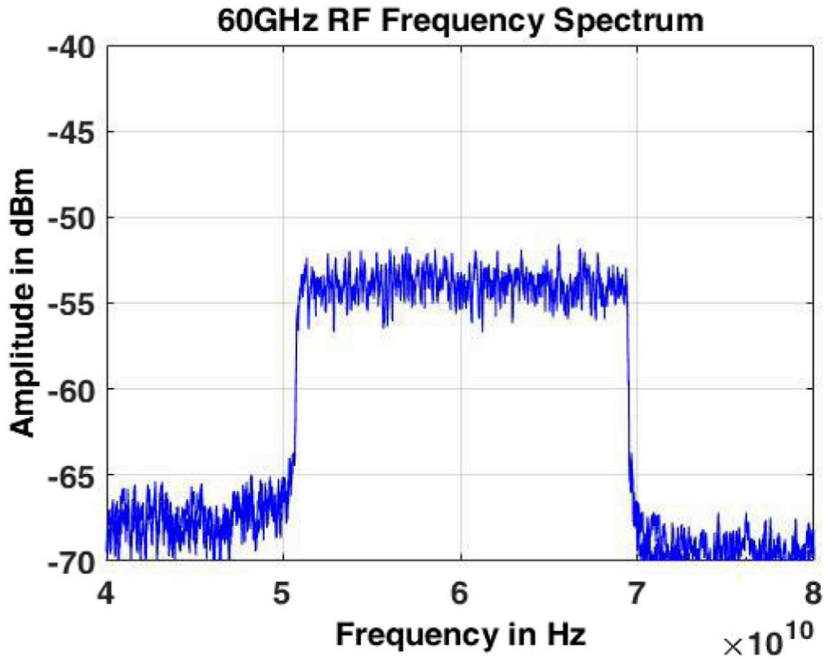


**FIGURE 6 |** 60 GHz RF spectrum.

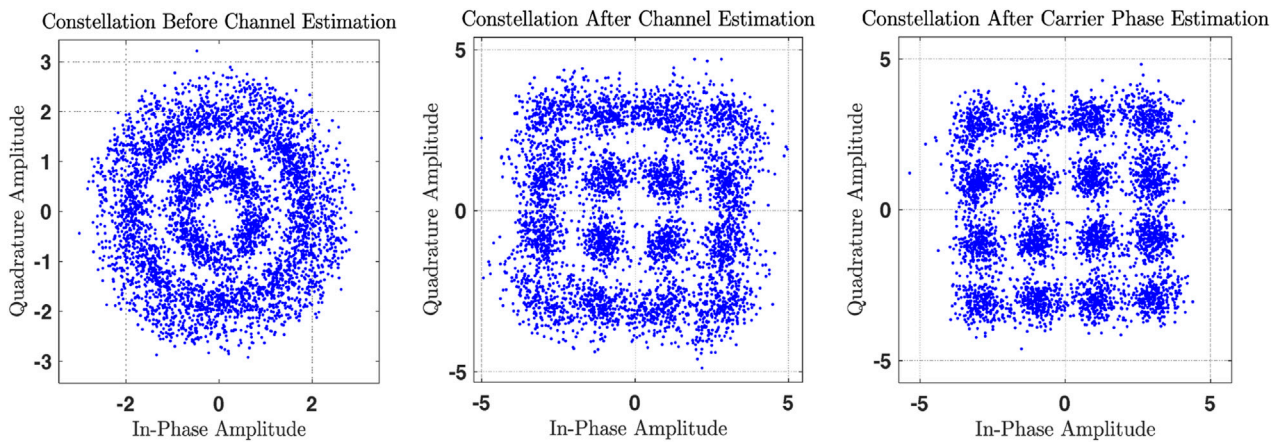


**FIGURE 7 |** 16-QAM constellation at 110 km SSMF for 120 Gbps data rate.

$$H_k = \frac{\langle t_{k,training} \rangle}{t_{k,Rx}} = \frac{\sum_{t_{k,Rx}}^{t_{k,training}}}{N_{training}} \tag{7}$$

where $k$ is the sub-carrier index, $i$ is the training symbol index, $N_{training}$ is the number of training symbols, and $t_k$, $Rx$ are the received symbols in the training symbol locations and $t_k$, training at the original symbols. In case of any receiver conFigureuration, the carrier phase will drift over time. It is usually assuming that the drift remains relatively constant over each OFDM symbol but changes from one OFDM symbol to the next. This is compensated by modifying the transfer function above to one that varies between OFDM symbols [31].

$$H_{K,l} = \exp(-j\varphi_l)\frac{|H_k|^2}{\dot{H}_k}, \tag{8}$$

where $l$ is the OFDM symbol index and $\phi_l$ is the estimated phase over each OFDM symbol.

$$\varphi_l = \frac{1}{N_p}\sum_{n=1}^{N_p}\{\arg(y_{ln}) - \arg(x_{ln})\}, \tag{9}$$

where the index $n$ which goes over the $Np$ pilot symbols is used within each OFDM symbol, $y_{ln}$ is the received pilot

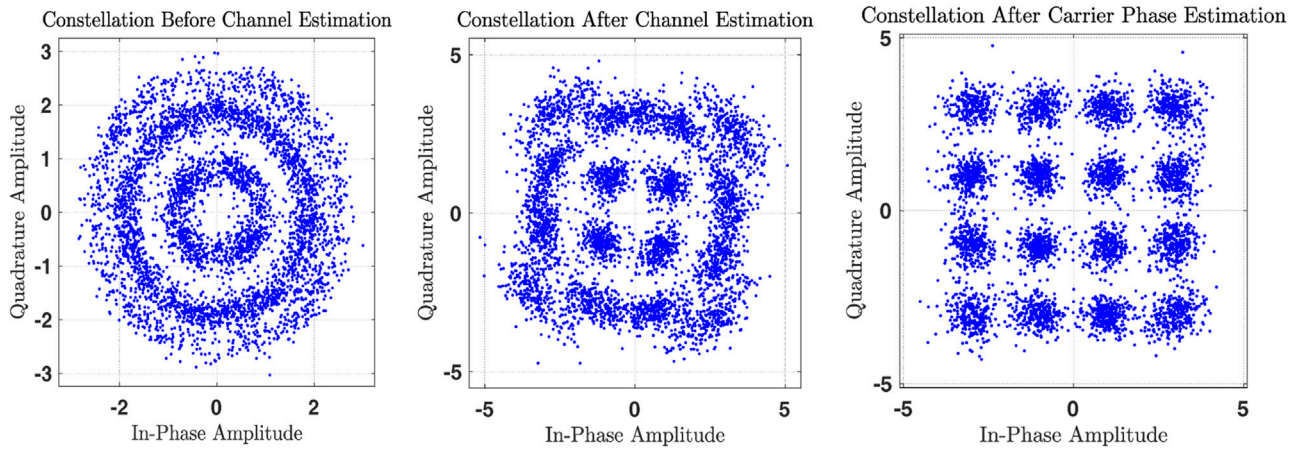


**FIGURE 8 |** 16-QAM constellation at 115 km SSMF for 110 Gbps data rate.

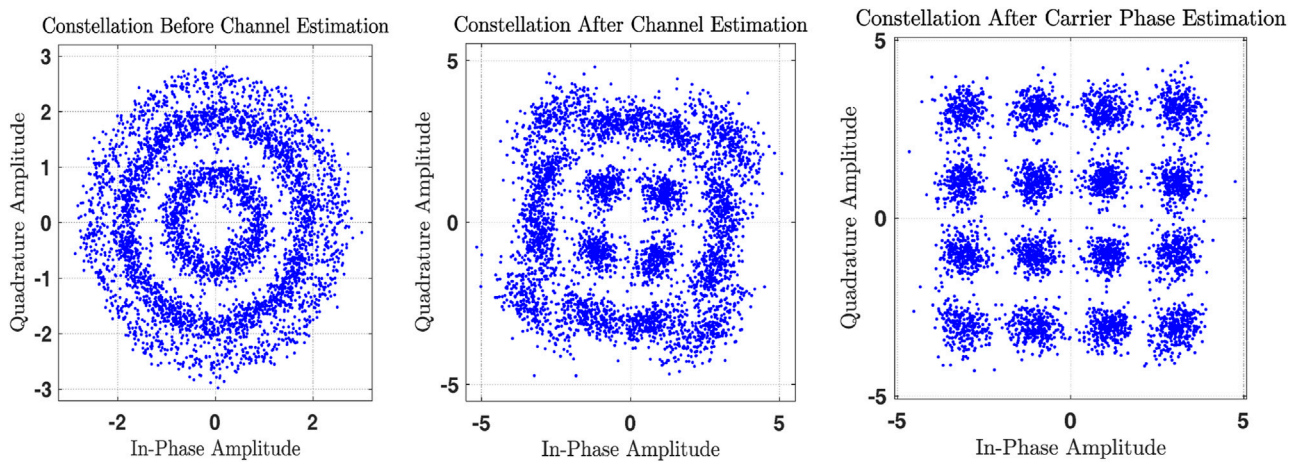


**FIGURE 9 |** 16-QAM constellation at 115 km SSMF for 100 Gbps data rate.

symbol, and $x_{ln}$ is the original transmitted pilot symbol. Since it is assumed that the phase drift is approximately constant over each OFDM symbol, an average over the pilots is taken for calculation. The I and Q symbols are normalized on each channel to their respective 16-QAM constellation grid based on normalized threshold decision setting. Once the decision is set, then the EVM is calculated as

$$EVM = \frac{\sqrt{\overline{|s - \lfloor s \rfloor_D|^2}}}{\overline{|S_D|^2}} \times 100\%, \tag{10}$$

where $s$ is the symbol sequence $\overline{(\ldots)}$ which indicates the mean value and $\lfloor s \rfloor_D$ is the decision of $s$. The received signals after decision are compared with the originally transmitted symbols and count the symbol error and subsequently bit error. The BER for 16-QAM is estimated as

$$BER_{16-QAM} = \frac{3}{8} erfc\left(\sqrt{\frac{SNR_{16-QAM}}{10}}\right). \tag{11}$$

## SIMULATION SETUP, RESULTS, AND DISCUSSION

The proposed 60 GHz mm-wave RoF link implementation is built by using optisystem tool and the obtained results are analyzed in MATLAB. A simulation setup diagram for the proposed system is depicted in **Figure 2**. At the CS, a CW laser is tuned with frequency of 193.1 THz with linewidth of 10 MHz. It is used as light source of LiNbO3-MZM modulator. A 15 GHz LO signal is applied as the RF input to the LiNbO3-MZM modulator and amplitude of RF source is set as 6 V peak-peak. The extinction ratio and bias voltage of LiNbO3-MZM modulator are set as 30 dB and 4 V, respectively. The output of LiNbO3-MZM modulator generates two optical

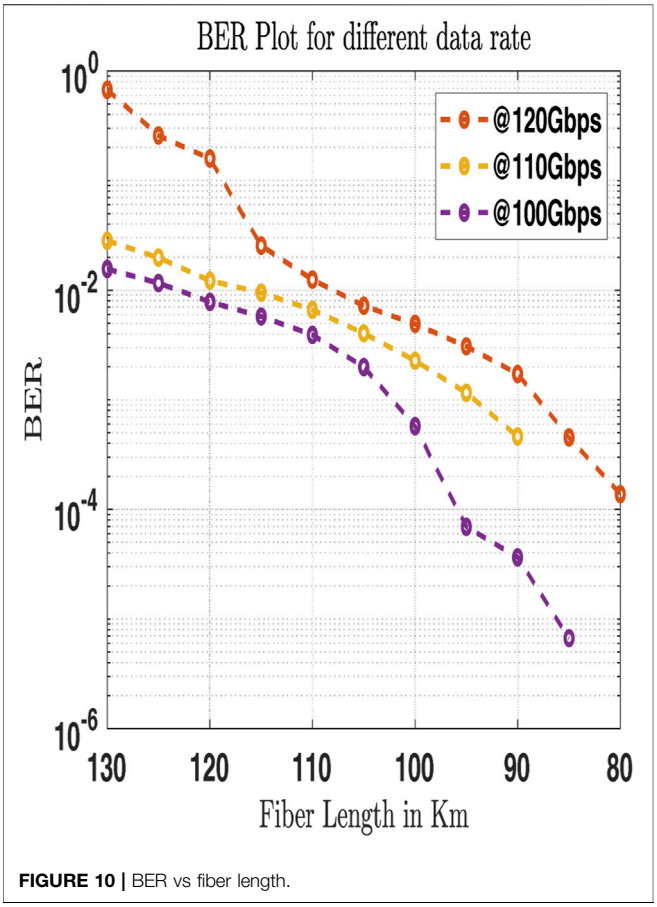


**FIGURE 10 |** BER vs fiber length.

oscillator frequencies by frequency quadrupling of 15 GHz with respect to CW laser carrier frequency of 193.1 THz. The generated optical oscillator frequencies 193.07 THz, LOO, and 193.13 THz, UOO, maintained the frequency offset of 60 GHz, as shown in **Figure 3**. The amplitude of both optical oscillators is amplified by an optical amplifier with 30 dB gain to compensate the losses governed during the modulation process. The signal amplitude at amplifier stage output is measured around −1 dBm.

The two independent rectangular band pass filter (BPF) centered at the frequency of 193.07 THz and 193.13 THz is used to separate out two optical oscillators with BW of 10 GHz. A 16-QAM modulator with 4 bits/symbol is used to map the input pseudo-random data stream at the different data rates of 100 Gbps, 110 Gbps, and 120 Gbps and generates the baseband I-Q signal. The 16-QAM, I-Q signals are passed through the OFDM modulator with 10 training and pilot symbols located at 25, 44, 64, 84, and 104 OFDM symbols location which is used for channel estimation and carrier phase estimation. The total number of 128 OFDM symbols per frame are generated through the modulation process. It is observed that the amplitude of OFDM signal generated as −15 dBm for all input data rates with variation in occupied channel band width (BW) depends on the input data rate chosen from 100 Gbps to 120 Gbps.

The baseband OFDM, I-Q signal is passed through optical conversion block. This block consists of two orthogonal pairs of LiNbO3-MZM in which the I and Q signals are separately modulated in optical domain with 90° phase shift. The input laser source for this optical modulation process is chosen as the highest UOO 193.13 THz. The optical OFDM spectrum generated by two arm LiNbO3-MZM is depicted in **Figure 4**.

The amplitude of the optical OFDM is observed as −27 dBm which is further combined with the LOO 193.07 THz and generates 60 GHz mm-wave optical OFDM signal transmitted over SSMF. The combine output of the 60 GHz mm-wave optical OFDM is shown in **Figure 5**.

The generated mm-wave optical signal is propagated over SSMF optical link with the power loss of 0.2 dB/km with chromatic dispersion of 16.75 ps/km/nm. To compensate for the loss of SSMF, an optical amplifier and Gaussian optical filter are used with 10 dB gain and 60 GHz BW, receptively, connected between CS and BS. The BS consists of optical coherent receiver which is designed with two arms of high-speed photo diode with reference CW laser operated at 193.07 THz. The amplitude of CW laser is set at +10 dBm. The detected 60 GHz RF signal at the coherent detector output is shown in **Figure 6**.

The 60 GHz RF from BS is propagated to the RRT. The RRT mainly consists of I-Q demodulator in which the signal is converted into baseband by mixing the incoming RF signal with locally generated 60 GHz RF signal. The mixer output is passed through the LPF with cutoff frequency 0.2 × bit rate which discards the unwanted harmonics and intermodulation products generated during the mixing process. The output of I-Q

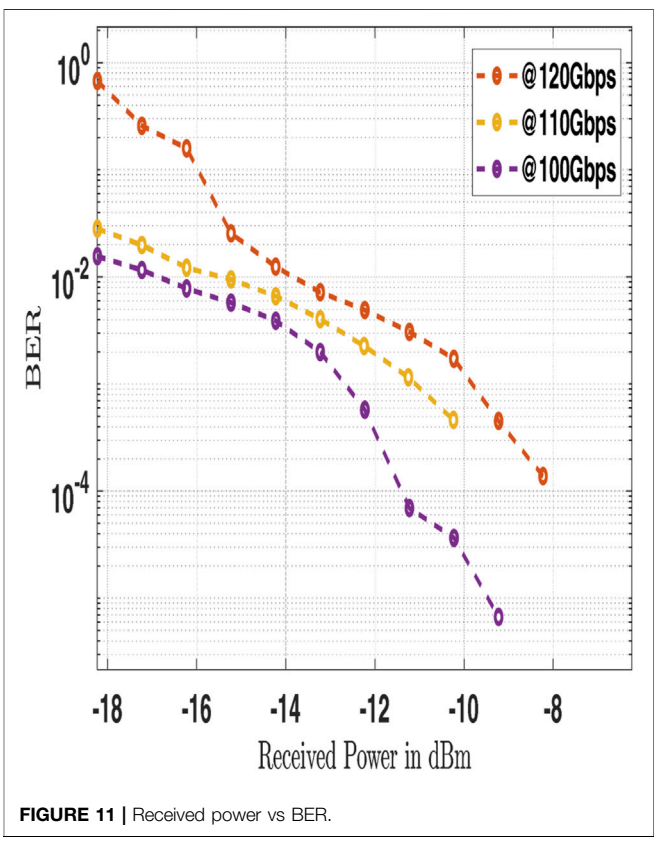


**FIGURE 11 |** Received power vs BER.

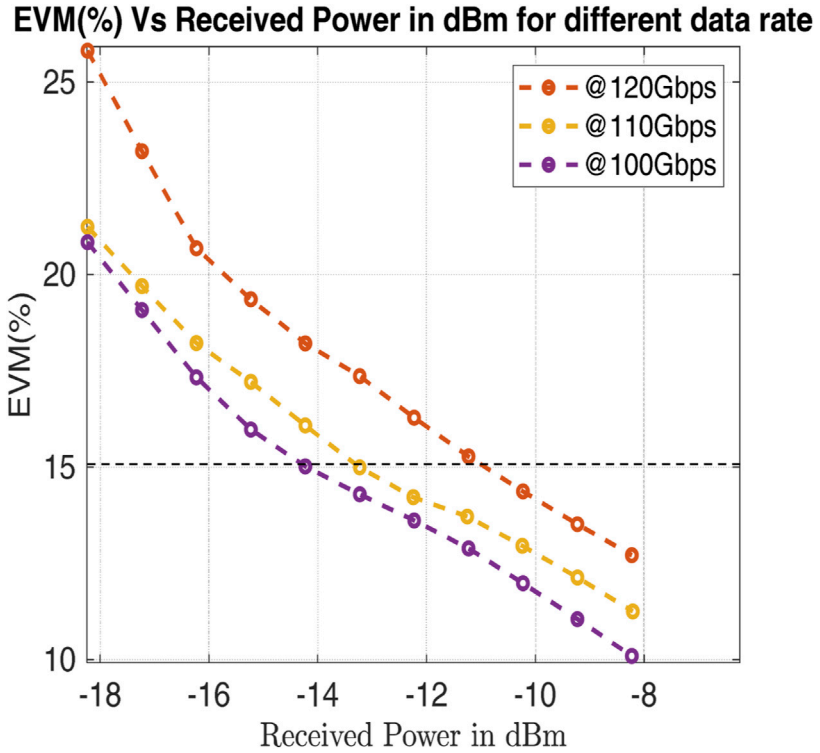


**FIGURE 12 |** Received power vs EVM%.

**TABLE 1 |** Comparison of the pervious implementation with the proposed 60 GHz mm-wave OFDM RoF.

| Parameters/ Ref. No. | Reference [4]$^{y}$ 2012 | Reference [6]$^{x}$ 2015 | Reference [8]$^{y}$ 2015 | Reference [13]$^{y}$ 2014 | Reference [14]$^{y}$ 2017 | Reference [15]$^{x}$ 2017 | Proposed implementation |
|---|---|---|---|---|---|---|---|
| Input data rate | 3.84 Gbps | 10 Gbps | 25 Gbps | 25 Gbps | 4.56 Gbps | 10 Gbps | 110 Gbps, 100 Gbps |
| Modulation scheme | 16-QAM | 16-QAM | 16-QAM | 16-QAM | 64-QAM | 4-QAM | 16-QAM |
| OFDM parameter | MBOFDM | OFDM | OFDM | OFDM | UF OFDM | OFDM | OFDM (channel and carrier phase estimation) |
| Fiber length | 48 km | 100 km | 50 km | 50 km | 25 km | 25 km | 105 km, 110 km |
| BER | -- | -- | $7.8 \times 10^{-4}$ | $8.3 \times 10^{-4}$ | $10^{-4}$ | $10^{-9}$ | $3.1 \times 10^{-3}$, $2.9 \times 10^{-3}$ |
| EVM | 15.84% | 19.4% | 10.9% | 14.6% | 6.3% | -- | <15% |

*x, simulation results; y, experimental results.*

demodulator is passed through OFDM demodulator with chromatic dispersion compensation using digital filtering, a frequency domain technique for the desired optical fiber length.

The OFDM demodulator also estimated the channel characteristics as per the 10-training sequence symbol inserted at the same symbol instances of transmitter training symbols.

A typical 16-QAM constellation mapping symbols diagram before and after channel estimation is shown in **Figure 7**, **Figure 8**, and **Figure 9** for 120 Gbps, 110 Gbps, and 100 Gbps input data rates, respectively. In addition to this channel estimation, carrier phase estimation and correction with a known training pilot symbol are used in the proposed system. The OFDM demodulator training pilot symbol's location is set at the position of 25, 44, 64, 84, and 104 among total 128 OFDM symbols. The constellation diagram after carrier phase estimation is shown in **Figures 7–9** for 110 km, 110 km , and 115 km for input data rates of 120 Gbps, 110 Gbps, and 100 Gbps, respectively.

It is highlighted that carrier phase estimation and correction are calculated properly, maintaining less BER between received and transmitted bits stream. After channel estimation and carrier phase estimation and correction of received OFDM symbols, the baseband I-Q signal is passed through the QAM demodulator with 4 bits/symbol setting. Finally, the BER is estimated between input and received data stream using offline method. **Figure 10** represents the BER performance with respect to SSMF fiber lengths from 80 to 130km for the data rates of 120Gbps, 110Gbps, and 100Gbps. A typical

BER of $9.1 \times 10^{-4}$, $3.1 \times 10^{-3}$ and $2.9 \times 10^{-3}$ is achieved at the approximate fiber lengths of 90km, 105 km , and 110km for the data rates of 120Gbps, 110Gbps, and 100Gbps, respectively.

The received power at the end of SSMF based on its length is varied between −8.2 dBm and −18.23 dBm for 80–130 km fiber length, respectively. The received power vs BER performance is shown in **Figure 11**. It is observed that for the higher data rate of 120 Gbps, the BER of $10^{-4}$ to $10^{-2}$ is achieved against the received power from −8.2 dBm to −15 dBm. Similarly, for the data rate of 100 Gbps, the BER of $10^{-5}$ to $10^{-3}$ is achieved against received input power from −9 dBm to −15 dBm. **Figure 12** shows the EVM in % against the received optical power at the end of SSMF for the different input data rates. It can be seen that EVM increases with the reduction in received power and increases with reference to fiber distance/length increases.

It is also observed that <15% EVM is measured at the SSMF length for 105 and 110 km, but due to novel and effective channel estimation and carrier phase estimation and correction method, the system maintains the BER less than $3.1 \times 10^{-3}$ and $2.9 \times 10^{-3}$ at the input rates of 110 Gbps and 100 Gbps, respectively.

**Table 1** highlights the comparison on the implementation of 60 GHz mm-wave RoF system for optical OFDM with some variations in baseband modulation technique. It is observed that the proposed implementation is supported for longer distance communication by using effective utilization of coherent detection, channel estimation, and carrier phase correction technique and maintaining the BER $3.1 \times 10^{-3}$ and $2.9 \times 10^{-3}$ for SSMF at a distance of 105 and 110 km, respectively, with EVM <15%. As per **Figure 12**, it can be seen that BER is achieved at a threshold value of EVM <15%. The EVM performance degrades with larger optical fiber distances due to fiber irregularities and path loss effect.

## CONCLUSION

The proposed implementation of the 60 GHz mm-wave RoF system is designed and verified through numerical simulation. Also, it is optimized and simplified considerably for the generation of 60 GHz mm-wave signal using frequency quadrupling technique, which would be economical compared to expensive instrumentation. Similarly, the system also uses the optical heterodyning and coherent detection technique for regeneration of 60 GHz RF signal propagated to remote radio terminal. The implemented design also represents its superior performance using channel estimation and carrier phase estimation and correction method, which maintains the desired BER of $3.1 \times 10^{-3}$ and $2.9 \times 10^{-3}$ at EVM <15% for SSMF at 105 and 110 km distance with the input data rates of 110 Gbps and 100 Gbps, respectively. Furthermore, the proposed RoF model is most suitable for the ultra-wide bandwidth requirement to satisfy future communication needs.

## DATA AVAILABILITY STATEMENT

The raw data supporting the conclusions of this article will be made available by the authors, without undue reservation.

## AUTHOR CONTRIBUTIONS

All authors have equally contributed to the proposed RoF system design architecture. DC and AK supervised the entire work. SNT carried out the numerical simulation and analysis. All authors contributed to the writing of the manuscript.

## REFERENCES


1. Li X, Yu J, and Chang GK. Photonics-Assisted Technologies for Extreme Broadband 5G Wireless Communications. *J Light Technol* (2019) 37(12): 2851–65. doi:10.1109/jlt.2019.2906498
2. Fernando XN. *Radio over Fiber for Wireless Communications: From Fundamentals to Advanced Topics* (2014). Hoboken, NJ: John Wiley & Sons.
3. Stöhr A, Akrout A, Buß R, Charbonnier B, van Dijk F, Enard A, et al.60 GHz Radio-Over-Fiber Technologies for Broadband Wireless Services. *J Opt Netw* (2009) 8(5):471. doi:10.1364/jon.8.000471
4. Omomukuyo O, Thakur MP, and Mitchell JE. Simple 60-GHz MB-OFDM Ultrawideband RoF System Based on Remote Heterodyning. *IEEE Photon Technol. Lett.* (2013) 25(3):268–71. doi:10.1109/lpt.2012.2234735
5. Ji W, Li X, Kang Z, and Xue X. Design of WDM-RoF-PON Based on Improved OFDM Mechanism and Optical Coherent Technology. *J Opt Commun Netw* (2015) 7(2):74. doi:10.1364/jocn.7.000074
6. Khwandah SA, Cosmas JP, Glover IA, Lazaridis PI, Prasad NR, and Zaharis ZD. Direct and External Intensity Modulation in OFDM RoF Links. *IEEE Photon J* (2015) 7(4):1–10. doi:10.1109/jphot.2015.2456499
7. Lin CT, Chen WE, and Huang HT. Simple 60-GHz Radio-Over-Fiber System with Transmission Distance Improvement Employing Signal-To-Signal Beat Noise Compensation. *IEEE J Sel Areas Commun* (2013) 31(12):773–9. doi:10.1109/jsac.2013.sup2.1213009
8. Martin EP, Shao T, Vujicic V, Anandarajah PM, Browning C, Llorente R, et al.25-Gb/s OFDM 60-GHz Radio over Fiber System Based on a Gain Switched Laser. *J Light Technol* (2015) 33(8):1635–164. doi:10.1109/jlt.2015.2391994
9. Mallick K, Mandal P, Mandal GC, Mukherjee R, Das B, and Sekhar Patra A. Hybrid MMW-Over Fiber/OFDM-FSO Transmission System Based on Doublet Lens Scheme and POLMUX Technique. *Opt Fiber Technol* (2019) 52:101942. doi:10.1016/j.yofte.2019.101942
10. Mallick K, Mandal P, Mukherjee R, Mandal GC, Das B, Patra AS, et al.Generation of 40 GHz/80 GHz OFDM Based MMW Source and the OFDM-FSO Transport System Based on Special fine Tracking Technology. *Opt Fiber Technol* (2020) 54:102130. doi:10.1016/j.yofte.2019.102130
11. Singh G, and Alphones A. OFDM Modulation Study for a Radio-Over-Fiber System for Wireless LAN (IEEE 802.11a). In: ICICS-PCM 2003 - Proceedings of the 2003 Joint Conference of the 4th International Conference on Information, Communications and Signal Processing and 4th Pacific-Rim Conference on Multimedia, 15-18 Dec 2003, Singapore (2003).
12. Nasoha H, and Idrus SM. Modeling and Performance Analysis of WCDMA Radio over Fiber System. In: Asia-Pacific Conference on Applied Electromagnetics Proceedings, 4-6 Dec. 2007, Melaka, Malaysia. APACE2007 (2007). doi:10.1109/apace.2007.4603973
13. Shao T, Martin E, Anandarajah PM, Browning C, Vujicic V, Llorente R, et al.Chromatic Dispersion-Induced Optical Phase Decorrelation in a 60 GHz OFDM-RoF System. *IEEE Photon Technol. Lett.* (2014) 26(20):2016–9. doi:10.1109/lpt.2014.2344314
14. Browning C, Martin EP, Farhang A, and Barry LP. 60 GHz 5G Radio-Over-Fiber Using UF-OFDM with Optical Heterodyning. *IEEE Photon Technol Lett* (2017) 29(23):2059–62. doi:10.1109/lpt.2017.2763680
15. Zhang R, and Ma J. Full-duplex Link with a Unified Optical OFDM Signal for Wired and Millimeter-Wave Wireless Accesses Based on Direct Detection.

*J Opt Switching Networking.*Vol. 25. Pg. 33–9. 2017. doi:10.1016/j.osn.2017.02.001
16. Khair F, Fakhriy HP, Mustika IW, Setiyanto B, and Idrus SM. Modeling and Simulation of OFDM Scheme for Radio over Fiber (RoF). In: ICITACEE 2015 - 2nd International Conference on Information Technology, Computer, and Electrical Engineering: Green Technology Strengthening in Information Technology, Electrical and Computer Engineering Implementation, Proceedings, 16-18 Oct. 2015, Semarang, Indonesia (2016).
17. Tsai C-T, Lin C-H, Lin C-T, Chi Y-C, and Lin G-R. 60-GHz Millimeter-Wave over Fiber with Directly Modulated Dual-Mode Laser Diode. *Sci Rep* (2016) 6: 27919. doi:10.1038/srep27919
18. Tsai C-T, Li C-C, Lin C-H, Lin C-T, Chi S, and Lin G-R. Long-reach 60-GHz MMWoF Link with Free-Running Laser Diodes Beating. *Sci Rep* (2018) 8: 13711. doi:10.1038/s41598-018-32058-1
19. Tsai C-T, Li C-C, Chen C-W, Chi Y-C, Lin C-T, Chi S, et al.Incoherent Laser Heterodyned Long-Reach 60-GHz MMWoF Link with Volterra Filtered 16-QAM OFDM beyond 13 Gbps. *IEEE J Select Top Quan Electron.* (2021) 27(2): 1–11. March-April 2021. Art no. 7600211. doi:10.1109/JSTQE.2020.2991736
20. Tsai C-T, Wang H-Y, Chi Y-C, Cheng C-H, and Lin G-R. Quad-Mode VCSEL Optical Carrier for Long-Reach Ka-Band Millimeter-Wave over Fiber Link. *IEEE J Select Areas Commun* (2021) 39:2838–48. doi:10.1109/JSAC.2021.3064644
21. Jiang WJ, Lin C-T, Ng'oma A, Shih P-T, Chen J, Sauer M, et al.Simple 14-Gb/s Short-Range Radio-Over-Fiber System Employing a Single-Electrode MZM for 60-GHz Wireless Applications. *J Light Technol* (2010) 28(16):2238–46. doi:10.1109/jlt.2010.2045341
22. Yang H, Zeng J, Zheng Y, Jung H-D, Huiszoon B, van Zantvoort JHC, et al.Evaluation of Effects of MZM Nonlinearity on QAM and OFDM Signals in RoF Transmitter. In: IEEE International Meeting on Microwave Photonics jointly held with the 2008 Asia-Pacific Microwave Photonics Conference, 9 Sept.-3 Oct. Gold Coast, QLD, Australia (2008). MWP2008/APMP2008. 2008. doi:10.1109/mwp.2008.4666642
23. Ma J, Zhan Y, Zhou M, Liang H, Shao Y, and Yu C. Full-duplex Radio over Fiber with a Centralized Optical Source for a 60 GHz Millimeter-Wave System with a 10 Gb/s 16-QAM Downstream Signal Based on Frequency Quadrupling. *J Opt Commun Netw* (2012) 4(7):557–64. doi:10.1364/jocn.4.000557
24. Ma J. 5 Gbit/s Full-Duplex Radio-Over-Fiber Link with Optical Millimeter-Wave Generation by Quadrupling the Frequency of the Electrical RF Carrier. *J Opt Commun Netw* (2011) 3(2):127–34. doi:10.1364/jocn.3.000127
25. Ma J, Xin X, Yu J, Yu C, Wang K, Huang H, et al.Optical Millimeter Wave Generated by Octupling the Frequency of the Local Oscillator. *J Opt Netw* (2008) 7(10):837–45. doi:10.1364/jon.7.000837
26. Jiang W-J, Lin C-T, Huang H-S, Shih P-T, Chen J, and Chi S. 60 GHz photonic vector signal generation employing frequency quadrupling scheme for radio-over-fiber link OSA/OFC/NFOEC, 22-26 March 2009, San Diego, CA. (2009). OWF1. doi:10.1364/ofc.2009.owf1
27. Chun-Ting Lin C-T, Po-Tsung Shih P-T, Chen JJ, Wen-Qiang Xue W-Q, Peng-Chun Peng P-C, and Sien Chi S. Optical Millimeter-Wave Signal Generation Using Frequency Quadrupling Technique and No Optical Filtering. *IEEE Photon Technol Lett* (2008) 20(12):1027–9. doi:10.1109/lpt.2008.923739
28. Kikuchi K. Fundamentals of Coherent Optical Fiber Communications. *J Lightwave Technol* (2016) 34:157–79. doi:10.1109/jlt.2015.2463719
29. Ma J, Chen L, Xin X, Yu J, Yu C, Dong Z, et al.Transmission of a 40 GHz Optical Millimeter Wave Generated by Quadrupling a 10 GHz Local Oscillator via a Mach-Zehnder Modulator. *J Opt A: Pure Appl Opt* (2009) 11(6):065406. doi:10.1088/1464-4258/11/6/065406
30. Savory SJ. Digital Filters for Coherent Optical Receivers. *Opt Express* (2120) 16(2):804–17. doi:10.1364/oe.16.000804
31. Yi X, Shieh W, and Tang Y. Phase Estimation for Coherent Optical OFDM. *IEEE Photon Technol Lett* (2007) 19:919–21. doi:10.1109/lpt.2007.897572

**Conflict of Interest:** The authors declare that the research was conducted in the absence of any commercial or financial relationships that could be construed as a potential conflict of interest.

frontiers in Physics

ORIGINAL RESEARCH
published: 06 October 2021
doi: 10.3389/fphy.2021.707113

# $GeO_2$ Doped Optical Fiber Plasmonic Sensor for Refractive Index Detection

*Rahul Kumar Gangwar*[1], *Rui Min*[1]*, *Santosh Kumar*[2] *and Xiaoli Li*[1]

[1]Center for Cognition and Neuroergonomics, State Key Laboratory of Cognitive Neuroscience and Learning, Beijing Normal University at Zhuhai, Zhuhai, China, [2]Shandong Key Laboratory of Optical Communication Science and Technology, School of Physics Science and Information Technology, Liaocheng University, Liaocheng, China

In this article, a D-shaped optical fiber refractive index (RI) sensor based on surface plasmon resonance effect is demonstrated. The gold film is placed at the flat portion of the optical fiber along with the sensing analytes of the different RIs to excite the plasmonic interactions. Sensing properties are investigated by using the finite element method. The maximum sensitivity of the proposed sensor is achieved as high as 20863.20 nm/RIU with the maximum resolution of $4.79 \times 10^{-6}$ RIU and figure of merit of 308.38 $RIU^{-1}$ for an analyte with RI 1.43 by optimizing the different parameters of the sensor with maximum phase matching between the core mode and surface plasmon mode. The high sensitivity of the sensor offers a promising approach for the detection of unknown RI analyte in chemical and biological fields in the near-infrared region.

OPEN ACCESS

**Edited by:**
*Venugopal Rao Soma,*
*University of Hyderabad, India*

**Reviewed by:**
*Satyendra Mishra,*
*Laval University, Canada*
*Xin Yan,*
*Northeastern University, China*

***Correspondence:**
*Rui Min*
*ruimin@bnu.edu.cn*

**Specialty section:**
*This article was submitted to Optics and Photonics, a section of the journal Frontiers in Physics*

**Received:** *09 May 2021*
**Accepted:** *23 August 2021*
**Published:** *06 October 2021*

**Citation:**
*Gangwar RK, Min R, Kumar S and Li X (2021) $GeO_2$ Doped Optical Fiber Plasmonic Sensor for Refractive Index Detection. Front. Phys. 9:707113. doi: 10.3389/fphy.2021.707113*

**Keywords: optical fiber sensor, surface plasmon resonance, gold, refractive index sensor, $GeO_2$ doped silica, sensitivity**

## INTRODUCTION

While considerable progress has been made over the last decade in the field of surface plasmon resonance (SPR)–based optical fiber refractive index (RI) sensors, the steady increase in the application of these sensors in several fields such as biological, chemical, and health monitoring etc., always sets a new limit for the research communities [1–3]. SPR is a label-free sensing technology in which surface plasmon can be excited when an incident polarized light couples with the surface plasmon wave (SPW) at the interface of the metal-dielectric surface. The wave vector of the SPW depends on the RI of the surrounding medium which leads to make SPR a very sensitive technique to detect the variations in refractive indices (RIs) that are primarily caused by the interactions or binding of the surrounding molecules to the metal surface [4–8]. In traditional SPR configuration, a total internal reflection–based theory is proposed by Kretschmann and Otto in 1968, in which the base of a coupling prism is coated with the thin metal (Au or Ag) and the incident p-polarized light wave excites the surface plasmons at the metal-dielectric interface [9, 10]. However, this configuration has many limitations and disadvantages like bulk in size, poor reliability, not suitable for remote sensing, and requires mechanical instruments which limit its uses.

To overcome these issues, SPR-based micro and nanostructured optical fiber sensors (OFSs) have drawn great attention because of their unique characteristics such as robustness, compact size, fast response, high sensitivity, online real-time monitoring, electromagnetic immunity etc. Because of these advantages, the effect to propose new kinds of SPR sensors in different areas of biosensing, chemical analysis, and environmental control has been expanded exceptionally quickly [11–15]. The first SPR-based OFS, in which a thin gold film is coated on the fiber core for the excitation of the surface plasmon, was proposed by Jorgenson in 1993, and till now, different kinds of fiber such as tapered fiber [16], multicore fiber [17], fiber grating [18], and photonic crystal fiber (PCF) have been

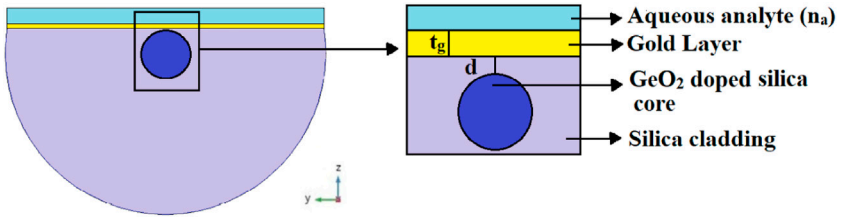


**FIGURE 1 |** Cross-sectional view of the proposed D-shaped optical fiber RI sensor.

proposed and utilized for the SPR-based sensing components. The waveguide property of an optical fiber is altered by some suitable technique to make it sensitive to the external environment (generally by removing the cladding). An alternative to removing the entire cladding of an optical fiber for a certain length, which reduces power, sustainability, and reliability, is to use a D-shaped optical fiber sensor, which is comparatively strong and durable without sacrificing the sensing properties of the device.

In all of these reported sensors, D-shaped OFS has more attractive features such as less fragile structure, easy fabrication process, high sensitivity, and easy access to the large evanescent field for efficient sensing applications [19]. In 2006, Wang et al. presented D-shaped optical fiber sensor based on the SPR effect. In this configuration, a gold film is coated on the fiber and RI sensitivity increases significantly [20]. A magnetic field sensor based on the D-shaped optical fiber Bragg grating with the sensitivity of 1.4403 pm/G was proposed by Lanza et al. in 2011 [21]. In 2015, a D-shaped PCF temperature sensor with a thin gold film coated on the cladding surface realizing a sensitivity of 11.6 nm//°C was reported by Shi et al. [22]. Nayak et al. proposed a D-shaped fiber SPR sensor, in which fiber is coated with silver followed by the graphene layer, with the maximum sensitivity of 6,800 nm/RIU in the RI from 1.33 to 1.37 [23]. Recently, Pathak et al. presented a concave-shaped OFS covered with multiple Au nanowires for RI sensing. The gold nanowires are coated on the concave-shaped channel, located at the D-shaped portion of the fiber perpendicular to the core. The maximum sensitivity of the sensor is 4,471 nm/RIU for analyte RI varying between 1.33 and 1.38 [24]. It is observed that D-shaped OFSs based on the SPR effect have the advantage of good flexibility and high sensitivity.

To improve the detection limit and sensitivity of the OFSs, an SPR-based D-shaped optical fiber RI sensor with a thin gold film coating on the flat surface of the fiber is presented. The finite element method (FEM) is used to characterize the sensing properties of the sensor. The influence of the doping concentration of the germanium ($GeO_2$) in silica for the fiber core, thickness of the gold film, and coating distance of gold film from the fiber core have been studied. By using the wavelength interrogation method, the maximum sensitivity of 20863.20 nm/RIU with the resolution of the order of $10^{-6}$ has been achieved for the analyte 1.43 which is the highest compared to the reported works [23–28].

## MATERIALS AND METHODS

For a D-shaped optical fiber plasmonic sensor, observing the interaction between the evanescent waves (EWs) with surrounding medium is essential and hence it is required to investigate the structure very well. The cross-sectional view of the proposed D-shaped fiber sensor is illustrated in **Figure 1**. The metallic film of thickness "$t_g$" is placed on the flat surface of the optical fiber at a distance "d" from the core of the fiber. Laser micromachine and side polishing technique can be used to fabricate this kind of structure. The polishing depth can be controlled very well [28–30].

The fiber is a conventional single-mode fiber with a core and cladding diameter of 8.2 and 125 μm. The fiber core (with RI, $n_{co}$) and cladding is made up with $GeO_2$ doped silica and fused silica, respectively. Generally, the core of a fiber is doped with X percentage $GeO_2$ in silica. The RI as a function of the wavelength of silica doped with X percentage of $GeO_2$ and fused silica is calculated from the Sellmeier relation as follows [31]

$$n^2(\lambda) = 1 + \frac{[B_1^S + X(B_1^G - B_1^S)]\lambda^2}{\lambda^2 - [C_1^S + X(C_1^G - C_1^S)]^2} + \frac{[B_2^S + X(B_2^G - B_2^S)]\lambda^2}{\lambda^2 - [C_2^S + X(C_2^G - C_2^S)]^2} + \frac{[B_3^S + X(B_3^G - B_3^S)]\lambda^2}{\lambda^2 - [C_3^S + X(C_3^G - C_3^S)]^2} \quad (1)$$

In **Eq. 1**, $\lambda$ is the wavelength and $B_1^S$= 0.696166300, $B_2^S$= 0.407942600, $B_3^S$= 0.897479400, $C_1^S$= 0.068404, $C_2^S$= 0.116241, and $C_3^S$ = 9.896161 are the Sellmeier coefficients for the silica and $B_1^G$ = 0.8068664, $B_2^G$ = 0.7181585, $B_3^G$ = 0.8541683, $C_1^G$ = 0.06897261, $C_2^G$ = 0.1539661, $C_3^G$ = 1.841193 are the Sellmeier coefficients for the $GeO_2$, respectively.

Gold (thickness of $t_g$) is used as a metallic film and is placed at a distance (d) from the core boundary. Drude model has been used to obtain the dielectric constant of gold as follows [23]

$$\mathcal{E}_m(\lambda) = \mathcal{E}_{mr} + i\mathcal{E}_{mi} = 1 - \frac{\lambda^2\lambda_c}{\lambda_p^2(\lambda_c + i\lambda)} \quad (2)$$

Here, $\lambda_p = 1.6826 \times 10^{-7}$ m and $\lambda_c = 8.9342 \times 10^{-6}$ m are the plasma wavelength and the collision wavelength of gold, respectively.

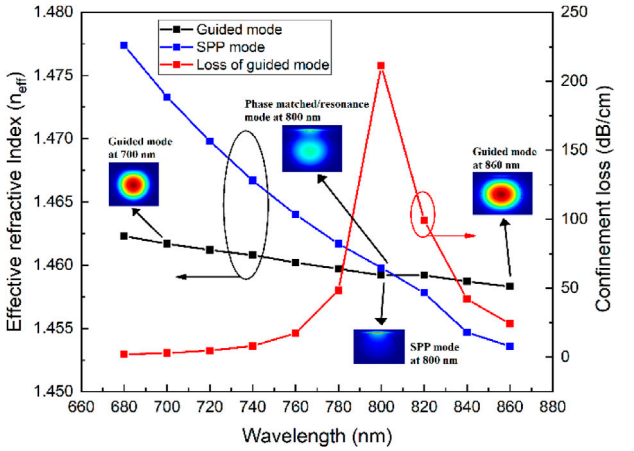


**FIGURE 2 |** Dispersion relations of the fundamental core-guided mode (black), SPP mode (red), and confinement loss spectra (black) for d = 5 nm, $t_g$= 40 nm, and $n_a$ = 1.41 with 5% $GeO_2$ doped silica core.

The COMSOL Multiphysics based on the FEM is an advanced simulation software and widely used for scientific calculation and research in various fields. Here, wave optics module, in the COMSOL Multiphysics, is used for analyzing the sensing properties of the proposed sensor. The whole structure is divided into a small subdomain and surrounded by the perfectly matched layer (PML) boundary which is applied for absorbing the light radiated toward the surface during the whole simulation process.

## RESULTS AND DISCUSSION

The proposed D-shaped plasmonic OFS for the RI sensing is based on the simple SPR effect. In SPR phenomena, the evanescent field of TM mode (p-polarized) wave excites the free electrons on the metal surface which produces the surface plasmon (SP) wave propagating through the metal-dielectric interface. There is a phase matched condition, at which the TM mode loses most of its energy to the SP wave, at given wavelength. This is known as resonance condition and this wavelength is called resonance wavelength. This resonance wavelength directly depends on the surrounding medium's RI. This resonance wavelength is changed as the RI of the surrounding medium changing. Hence, by measuring this resonance wavelength, we can easily obtain the RI of the medium. Throughout the simulation process of the proposed sensor, TM mode is considered. During the simulation process, it is considered that light propagates in the z-axis and all the model investigation is executed in the XY plane. As the overlap between the electric field and the metallic film is increased, an increase in confinement loss appears. The model loss or confinement loss of the proposed sensor is obtained from the imaginary part of the effective RI [$Im(n_{eff})$] of the guided mode, with the help of the following relation

$$\alpha = 8.686 \times \frac{2\pi}{\lambda} \times \mathrm{Im}(n_{eff}) \times 10^4 \quad (\mathrm{dB/cm}) \qquad (3)$$

where $\lambda$ is the operating wavelength in microns.

**Figure 2** shows the dispersion spectrum, the real part of the effective RI of the fundamental TM polarized core-guided mode (black line with square), surface plasmon mode (blue line with square), and the confinement loss (red line with square) of the core-guided mode for d = 5 nm, $t_g$ = 40 nm, and $n_a$ = 1.41 of the proposed sensing device. As can be seen, at the resonance wavelength of 800 nm, the core mode and SPP mode match which excites the SPP mode. The dielectric core mode is not lossy but the SPP mode is highly lossy when they are phase matched at the resonance wavelength. The interaction of the core mode and SPP mode results a maximum power transfer from the core mode to the plasmonic mode. It leads a sharp increase in the confinement loss of the core-guided mode, which is shown in **Figure 2** by the red line with square. The inset of **Figure 2** shows the electric field distributions of TM polarized core mode at wavelength of 700 nm, surface plasmon polariton (SPP) mode and resonance mode at 800 nm, and core-guided mode at 860 nm, respectively. From the distribution of electric field of the resonance mode, it can be seen very clearly that most of the electric field is present at the metal/dielectric layer.

Apart from the influence of the RI of the surrounding medium, other parameters such as the thickness of gold film ($t_g$), the distance (d) between the gold film and the core, and the doping concentration of the $GeO_2$ in core also affect the performance of the proposed sensor. The distance of the gold film has an impact as it decides the strength of the EWs on the surface plasmon and the phase matching of the SPP with the guided mode. **Figure 3** shows the variation of the resonance wavelength and corresponding confinement loss with the distance of the metallic layer from the core at a fixed gold film thickness of 40 nm and the surrounding analyte with a RI of 1.35

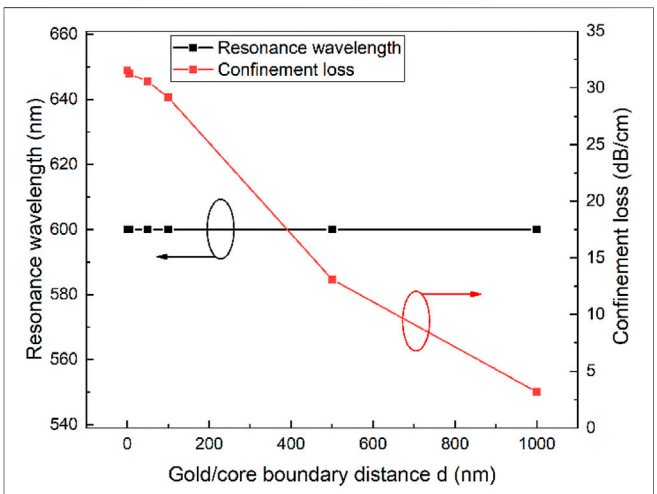


**FIGURE 3 |** Evolution of the resonance wavelength and confinement loss with gold/core boundary distance (d), for $t_g$ = 40 nm, 5% $GeO_2$ doping concentration and $n_a$ = 1.35.

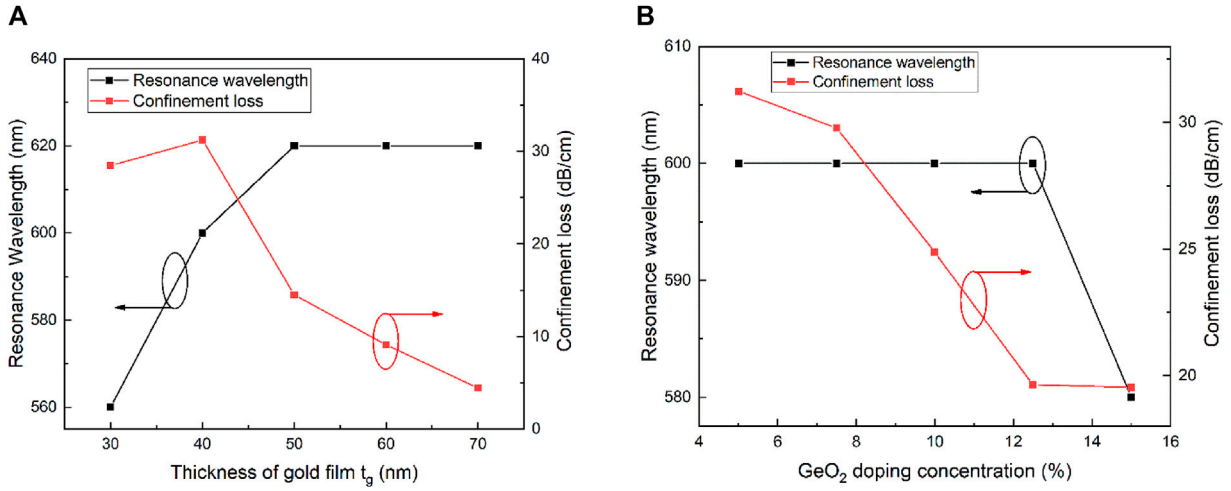


**FIGURE 4 |** Variation of resonance wavelength and confinement loss with **(A)** gold thickness **(B)** $GeO_2$ concentration in silica core for distance at d = 5 nm and $n_a$ = 1.35.

and 5% $GeO_2$ doped silica core. As intended, the resonance wavelength kept constant while the maximum loss at resonance wavelength decreases continuously. The confinement loss decreases as the distance increases. At d = 0 and 5 nm, the confinement loss is 31.53 and 31.23 dB/cm while at d = 1,000 nm, it becomes 3.17 dB/cm at the wavelength of 600 nm, respectively. For the rest of the calculation, d = 5 nm has been considered as the optimized value. These depths can be experimentally achieved by the physical polishing, chemical etching, or the combination of these two techniques as previously reported [33].

After optimizing the coating distance, the thickness of the gold film and the doping concentration of the $GeO_2$ are also optimized. **Figure 4A** shows the variation of the resonance wavelength and corresponding confinement loss with gold thickness varying from 30 to 70 nm at d =5 nm, and 5% $GeO_2$ doped silica core and $n_a$ = 1.35, respectively. It is observed from the spectrum that resonance wavelength shifts toward the higher wavelength and after 50 nm it becomes constant. The corresponding value of confinement loss also first increases from 28.45 to 31.23 dB/cm for the thickness $t_g$ = 30–40 nm, and after $t_g$ = 40 nm, it starts decreasing rapidly to 4.43 dB/cm for the $t_g$ = 70 nm. The increase in metallic layer thickness is responsible for the higher damping loss which decreases the penetration of the evanescent fields toward the surrounding analyte. Here, when the thickness of the gold film is higher than the 40 nm, the higher damping loss causes the overall decrease in the confinement loss of the guided mode. Therefore, the optimized thickness of the gold layer is determined to be 40 nm for the sensor. Variation of the resonance wavelength and confinement loss with doping concentration of $GeO_2$ for the d = 5 nm, $t_g$ = 40 nm, and $n_a$ = 1.35 is shown in **Figure 4B**. As seen from **Figure 4B**, there is no variation in resonance wavelength till 12.5% of doping concentration, and at 15% doping concentration, the resonance wavelength shifts toward the shorter wavelength. While the confinement loss at corresponding resonance wavelength decreases continuously from 31.23 dB/cm to 19.55 dB/cm, the doping concentration of the $GeO_2$ in silica increased from 5 to 15%. On considering higher model loss, the optimized value of $GeO_2$ doping concentration is chosen to be 5%.

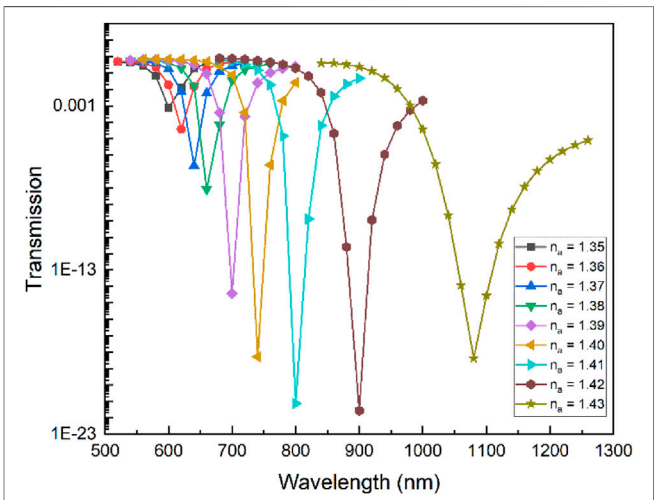


**FIGURE 5 |** Evolution of the confinement loss as a function of wavelength for analytes with different RIs for 5% $GeO_2$ doped silica core, d = 5 nm, and $t_g$ = 40 nm.

After getting all the optimized structural parameters, the proposed sensor is tested for the sensing capabilities and the transmission spectra (logarithmic) are obtained for the broad range of the analytes with RI varying from 1.35 to 1.43 as shown in **Figure 5**. Transmission spectrum of the proposed sensor has been obtained by the following relation [34]

$$T(L, \lambda) = \exp\left(-\frac{4\pi}{\lambda} Im\left(n_{eff}\right) L\right) \quad (4)$$

where Im ($n_{eff}$) is the imaginary part of the effective refractive index and L is length of the sensing fiber. For calculating the transmission

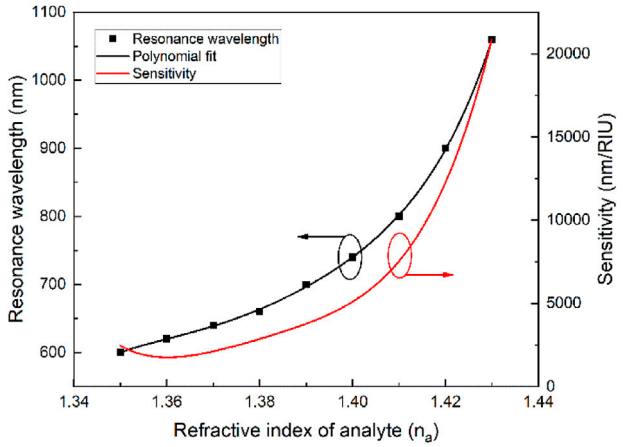


**FIGURE 6 |** Variation of the resonance wavelength and sensitivity with the RI of the analyte ($n_a$) for d = 5 nm with $t_g$ = 40 nm and 5% $GeO_2$ doped silica core. The lines represent a polynomial fit made to the simulated values.

spectrum, we have put L = 1 cm. Here, we can clearly observe a red-shift in the resonance wavelength with respect to the analyte's RI, that is, as the RI of the analytes increases, the confinement loss peak is shifted toward the higher wavelength.

**Figure 6** delineates the variation of the resonance wavelength and sensitivity as a function of the analyte's RI ($n_a$). The sensitivity is obtained by the polynomial fit of the derivative of resonance wavelength with the analyte's RI. The sensitivity of the proposed sensor is denoted by "S" and can be obtained by the following relation

$$S = \frac{d\lambda}{dn_a} \tag{5}$$

As it can be seen that the sensitivity increases non-linearly from 2458.98 nm/RIU to 20863.20 nm/RIU for the analyte's RI which ranges from $n_a$ = 1.35 to $n_a$ = 1.43.

Resolution is another important parameter that describes the ability of the proposed device to detect a small variation in analyte's RI. It is obtained by the following relation

$$R = \frac{\Delta\lambda_{min}}{S} \tag{6}$$

where $\Delta\lambda_{min}$ is the minimum spectral resolution and S is the sensitivity of the device. By choosing $\Delta\lambda_{min}$ = 0.1 nm, the maximum resolution of the proposed sensor is found to be around $4.79 \times 10^{-6}$ RIU for an analyte with a RI of 1.43. It means that the proposed sensor can detect a very small change up to $10^{-6}$ in RI of the analyte.

For the comprehensive analysis of a SPR-based sensor, the figure of merit (FOM) is also a very important and necessary parameter. It is obtained from the following equation

$$\text{FOM} = \frac{\text{S}}{\text{FWHM}} \ \text{RIU}^{-1} \tag{7}$$

where S is the sensitivity and FWHM is the resonance's full width at half maximum. The FWHM is of interest as a larger FWHM will introduce larger uncertainty in detecting the resonance wavelength which causes a lower resolution. **Figure 7** depicts the FOM and FWHM as a function of the analyte's RI ($n_a$). The FOM is varying from the 67.53 $RIU^{-1}$ to 356.83 $RIU^{-1}$ while the FWHM first decreases from 36.41 to 21.99 and then increases up to 67.65 nm. This kind of behavior of the FOM is mainly the result of the non-linear behavior of the sensitivity. The FWHM of the different loss spectrum of the analyte's RI is not constant, that is, it is low for some sets of $n_a$ and high for other sets of $n_a$ which also has an effect on the non-linear variation of the FOM. The increase in the analyte's RI ($n_a$) provides the comparative lower index contrast which causes the broadening in FWHM of each loss spectrum associated with the analyte's RI. **Table 1** provides a detailed comparison of the proposed sensor with other previously reported sensors in terms of sensitivity, resolution, and FOM. From the comparison, we can conclude that the proposed D-shaped optical fiber plasmonic–based RI sensor performs with a higher sensitivity, higher FOM, better resolution, and a larger sensing range. Therefore, the presented sensor based on SPR effect shows great potential for the measurement of different liquids in different fields such as chemical, biochemical, and biosensing film.

## CONCLUSION

A D-shaped optical fiber RI sensor based on the SPR effect is proposed and numerically investigated by using the FEM. The structure of the proposed sensing device consists of a gold layer deposited on the flat surface of the fiber. All structural parameters of the device are optimized and their influence on the sensing characteristics of the device have been systematically analyzed. The sensing device with a gold film of 40 nm thickness deposited at a 5 nm distance from the core boundary has a very good sensitivity which varies from 2458.98 nm/RIU to 20863.20 nm/RIU for the RI ranges from 1.35 to 1.43 with a maximum resolution of $10^{-6}$ RIU. The FOM of the proposed sensor has a maximum value of 356.83 $RIU^{-1}$ from 67.53 $RIU^{-1}$ for the same

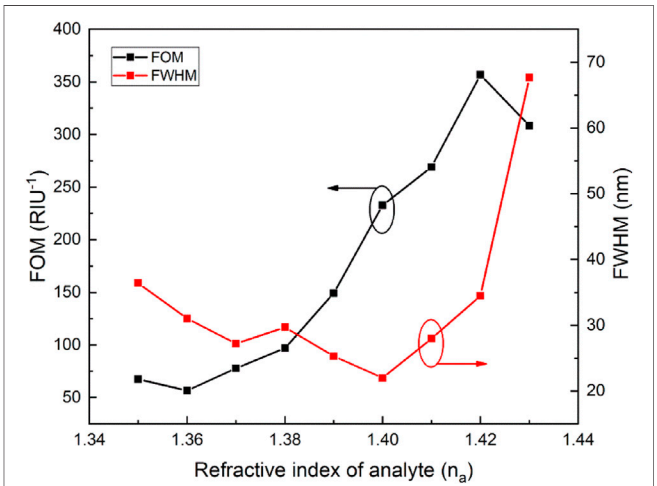


**FIGURE 7 |** Variation of the FOM and FWHM as a function of the RI of the analyte for d = 5 nm with $t_g$ = 40 nm and 5% $GeO_2$ doped silica core.

**TABLE 1 |** D-shaped SPR-based sensor performance comparison using the wavelength interrogation method.

| References | Sensitivity (nm/RIU) | Resolution (RIU) | FOM ($RIU^{-1}$) | Refractive index range |
|---|---|---|---|---|
| [23] | 6,800 | $8.05\times10^{-5}$ | N/A | 1.34–1.37 |
| [24] | 4,471 | N/A | 214 | 1.33–1.38 |
| [25] | 1,566 | N/A | 1021.2 | 1.3–1.335 |
| [26] | 4,122 | N/A | N/A | 1.333–1.398 |
| [27] | 2344.93–8860.93 | N/A | 69 | 1.33–1.39 |
| [28] | 11000 | N/A | 39.85 | 1.41–1.43 |
| This work | 2458.98–20863.20 | $4.07\times10^{-5}$–$4.79\times10^{-6}$ | 67.53–356.83 | 1.35–1.43 |

sensing range. Due to these benefits and considering the latest microfabrication technology, the proposed sensor can be very useful for a broad range of applications such as medical diagnosis, food safety, and chemical and biochemical sensing.

## DATA AVAILABILITY STATEMENT

The raw data supporting the conclusions of this article will be made available by the authors, without undue reservation.

## AUTHOR CONTRIBUTIONS

RK: Methodology, Conceptualization, Formal analysis, Validation, Funding acquisition, Writing - original draft. RM: Conceptualization, Formal analysis, Validation, Funding acquisition, Supervision, Writing - review and editing. SK: Formal analysis, Validation, Writing - review and editing, XL: Validation, Writing - review and editing.

## FUNDING

National Natural Science Foundation of China (62003046, 6211101138); Guangdong Basic and Applied Basic Research Foundation (2021A1515011997); Guangdong Recruitment Program of Foreign Experts (2020A1414010393); Special project in key field of Guangdong Provincial Department of Education (2021ZDZX1050); The Innovation Team Project of Guangdong Provincial Department of Education (2021KCXTD014); Double-Hundred Talent Plan of Shandong Province.

## REFERENCES

1. Yi Z, Huang J, Cen C, Chen X, Zhou Z, Tang Y, et al. Nanoribbon-ring Cross Perfect Metamaterial Graphene Multi-Band Absorber in THz Range and the Sensing Application. *Results Phys* (2019) 14:102367. doi:10.1016/j.rinp.2019.102367
2. Tong H, Xu Y, Su Y, and Wang X. Theoretical Study for Fabricating Elliptical Subwavelength Nanohole Arrays by Higher-Order Waveguide-Mode Interference. *Results Phys* (2019) 14:102460. doi:10.1016/j.rinp.2019.102460
3. Cen C, Zhang Y, Liang C, Chen X, Yi Z, Duan T, et al. Numerical Investigation of a Tunable Metamaterial Perfect Absorber Consisting of Two-Intersecting Graphene Nanoring Arrays. *Phys Lett A* (2019) 383:3030–5. doi:10.1016/j.physleta.2019.06.028
4. Chen H, Huang ZF, and Duan ZY. SPR Biosensor and its Application Progress, Chin. *J Biol Eng* (2003) 23:46–9.
5. Homola J, Yee SS, and Gauglitz G. Surface Plasmon Resonance Sensors: Review. *Sensors Actuators B: Chem* (1999) 54:3–15. doi:10.1016/s0925-4005(98)00321-9
6. Hoa XD, Kirk AG, and Tabrizian M. Towards Integrated and Sensitive Surface Plasmon Resonance Biosensors: A Review of Recent Progress. *Biosens Bioelectron* (2007) 23:151–60. doi:10.1016/j.bios.2007.07.001
7. Cen C, Yi Z, Zhang G, Zhang Y, Liang C, Chen X, et al. Theoretical Design of a Triple-Band Perfect Metamaterial Absorber in the THz Frequency Range. *Results Phys* (2019) 14:102463. doi:10.1016/j.rinp.2019.102463
8. Gangwar RK, Amorim VA, and Marques PVS. High Performance Titanium Oxide Coated D-Shaped Optical Fiber Plasmonic Sensor. *IEEE Sensors J* (2019) 19(20):9244–8. doi:10.1109/jsen.2019.2927728
9. Otto A. Excitation of Nonradiative Surface Plasma Waves in Silver by the Method of Frustrated Total Reflection. *Z Physik* (1968) 216:398–410. doi:10.1007/bf01391532
10. Kretschmann E, and Raether H. Notizen: Radiative Decay of Non Radiative Surface Plasmons Excited by Light. *Z Naturforsch A* (1968) 23:2135–6. doi:10.1515/zna-1968-1247
11. Wang X, Zhu J, Tong H, Yang X, Wu X, Pang Z, et al. A Theoretical Study of a Plasmonic Sensor Comprising a Gold Nano-Disk Array on Gold Film with a SiO 2 Spacer. *Chin Phys. B* (2019) 28:044201. doi:10.1088/1674-1056/28/4/044201
12. Gangwar RK, and Singh VK. Highly Sensitive Surface Plasmon Resonance Based D-Shaped Photonic crystal Fiber Refractive index Sensor. *Plasmonics* (2017) 12(5):1367–72. doi:10.1007/s11468-016-0395-y
13. Wang X, Zhu J, Wen X, Wu X, Wu Y, Su Y, et al. Wide Range Refractive index Sensor Based on a Coupled Structure of Au Nanocubes and Au Film. *Opt Mater Express* (2019) 9:3079–88. doi:10.1364/ome.9.003079
14. Yasli A, and Ademgil H. Geometrical Comparison of Photonic crystal Fiber-Based Surface Plasmon Resonance Sensors. *Opt Eng* (2018) 57:030801. doi:10.1117/1.oe.57.3.030801
15. Yi Z, Liang C, Chen X, Zhou Z, Tang Y, Ye X, et al. Dual-band Plasmonic Perfect Absorber Based on Graphene Metamaterials for Refractive index Sensing Application. *Micromachines* (2019) 10:443. doi:10.3390/mi10070443
16. Korposh S, James S, Lee S-W, and Tatam R. Tapered Optical Fibre Sensors: Current Trends and Future Perspectives. *Sensors* (2019) 19:2294. doi:10.3390/s19102294
17. Barrera D, Madrigal J, Delepine-Lesoille S, and Sales S. Multicore Optical Fiber Shape Sensors Suitable for Use under Gamma Radiation. *Opt Express* (2019) 27(20):29026–33. doi:10.1364/OE.27.029026
18. Lobry M, Loyez M, Hassan EM, Chah K, DeRosa MC, Goormaghtigh E, et al. Multimodal Plasmonic Optical Fiber Grating Aptasensor. *Opt Express* (2020) 28(5):7539–51. doi:10.1364/OE.385747
19. Sharma AK, Jha R, and Gupta BD. Fiber-optic Sensors Based on Surface Plasmon Resonance: a Comprehensive Review. *IEEE Sensors J* (2007) 7:1118–29. doi:10.1109/jsen.2007.897946
20. Wang S-F, Chiu M-H, and Chang R-S. Numerical Simulation of a D-type Optical Fiber Sensor Based on the Kretchmann's Configuration and Heterodyne Interferometry. *Sensors Actuators B: Chem* (2006) 114(1):120–6. doi:10.1016/j.snb.2005.04.012
21. Lanza G, Breglio G, Giordano M, Gaddi A, Buontempo S, and Cusano A. Effect of the Anisotropic Magnetostriction on Terfenol-D Based Fiber Bragg Grating

Magnetic Sensors. *Sensors Actuators A: Phys* (2011) 172(2):420–7. doi:10.1016/j.sna.2011.10.005
22. Shi WH, You CJ, and Wu J. D-shaped Photonic crystal Fiber Refractive index and Temperature Sensor Based on Surface Plasmon Resonance and Directional Coupling. *wlxb* (2015) 64(22):224221–1. doi:10.7498/aps.64.2242215
23. Nayak JK, and Jha R. Numerical Simulation on the Performance Analysis of a Graphene-Coated Optical Fiber Plasmonic Sensor at Anti-crossing. *Appl Opt* (2017) 56:3510–7. doi:10.1364/ao.56.003510
24. Pathak AK, Rahman BMA, Singh VK, and Kumari S. Sensitivity Enhancement of a Concave Shaped Optical Fiber Refractive Index Sensor Covered with Multiple Au Nanowires. *Sensors* (2019) 19:4210–112. doi:10.3390/s19194210
25. Del Villar I, Zubiate P, Zamarreño CR, Arregui FJ, and Matias IR. Optimization in Nanocoated D-Shaped Optical Fiber Sensors. *Opt Express* (2017) 25(10):10743–56. doi:10.1364/oe.25.010743
26. Tien CL, Lin HY, and Su SH. High Sensitivity Refractive Index Sensor by D-Shaped Fibers and Titanium Dioxide Nanofilm. *Adv Condens Matter Phys* (2018) 6.
27. Fu H, Zhang M, Ding J, Wu J, Zhu Y, Li H, et al. A High Sensitivity D-type Surface Plasmon Resonance Optical Fiber Refractive index Sensor with Graphene Coated Silver Nano-Columns. *Opt Fiber Technology* (2019) 48:34–9. doi:10.1016/j.yofte.2018.12.017
28. Pathak AK, Singh VK, Ghosh S, and Rahman BMA. Investigation of a SPR Based Refractive index Sensor Using a Single Mode Fiber with a Large D Shaped Microfluidic Channel. *OSA Continuum* (2019) 2(11):3008–18. doi:10.1364/osac.2.003008
29. Xie Q, Chen Y, Li X, Yin Z, Wang L, Geng Y, et al. Characteristics of D-Shaped Photonic crystal Fiber Surface Plasmon Resonance Sensors with Different Side-Polished Lengths. *Appl Opt* (2017) 56(5):1550–5. doi:10.1364/ao.56.001550
30. Del Villar I, Arregui FJ, Matias IR, Cusano A, Paladino D, and Cutolo A. Fringe Generation with Non-uniformly Coated Long-Period Fiber Gratings. *Opt Express* (2007) 15:9326–40. doi:10.1364/oe.15.009326
31. Tien CL, Lin HY, and Su SH. High Sensitivity Refractive Index Sensor by D-Shaped Fibers and Titanium Dioxide Nanofilm. *Adv Condensed Matter Phys* (2018) 6:2303740. doi:10.1155/2018/2303740
32. Fleming JW. Dispersion in GeO_2-SiO_2 Glasses. *Appl Opt* (1984) 23(24):4486–93. doi:10.1364/ao.23.004486
33. Esmaeilzadeh H, Arzi E, Légaré F, and Hassani A. Controllable Hybrid Side-Polishing Method (CHPM) for Optical Fibers by Combination of Polishing and Etching. *J Mod Opt* (2013) 60(20):1813–20. doi:10.1080/09500340.2013.863401
34. Zhang S, Li-S G, Wu J, Li J, Liu Q, Guo Y, et al. Surface Plasmon Resonance Sensor Based on D-Shaped Photonic crystal Fiber with Two Micro-openings. *J Phys D: Appl Phys* (2018) 51:305104. doi:10.1088/1361-6463/aace72

**Conflict of Interest:** The authors declare that the research was conducted in the absence of any commercial or financial relationships that could be construed as a potential conflict of interest.

**Publisher's Note:** All claims expressed in this article are solely those of the authors and do not necessarily represent those of their affiliated organizations, or those of the publisher, the editors and the reviewers. Any product that may be evaluated in this article, or claim that may be made by its manufacturer, is not guaranteed or endorsed by the publisher.

frontiers in Physics

ORIGINAL RESEARCH
published: 18 October 2021
doi: 10.3389/fphy.2021.747030

# Large Tunable 16-Tupled Millimeter Wave Generation Utilizing Optical Carrier Suppression With a Tunable Sideband Suppression Ratio

*Asha* and Sandeep Dahiya*

*Department of ECE, Faculty of Engineering and Technology, BPS Women University, Khanpur Kalan, Sonepat, India*

Coping up with the rising bandwidth demands for 5G ultra-high speed applications, utilizing millimeter (MM) wave spectrum for data transmission over the radio over a fiber-based system is the ideal approach. In this study, a highly conversant and spectrally pure photonic generation of a 16-tupled MM wave signal using a series-connected DD-MZM with a lower modulation index, a splitting ratio, and a wider tunable range is presented. A 160-GHz MM wave is generated through a double sideband optical carrier suppression technique having an optical sideband suppression ratio (OSSR) of 69 dB and a radio frequency sideband suppression ratio (RSSR) of 40 dB. However, the OSSR and the RSSR are tunable with values greater than 15 dB when the modulation index (M.I.) varies from 2.778 to 2.873, ±8° phase drift, and a 15-dB enhancement in the OSSR with a wider nonideal parameter variation range giving acceptable performance can be seen in the model as compared with previous research works.

**Keywords: millimeter wave generation, radio over fiber system, 16 tupling, OSSR, RSSR, filterless, optical carrier suppression**

OPEN ACCESS

***Edited by:***
*Santosh Kumar,*
*Liaocheng University, China*

***Reviewed by:***
*Sharda Vashisth,*
*The NorthCap University, India*
*Dhramendra Yadav,*
*Bikaner Technical University, India*

****Correspondence:***
*Asha*
*ashabalhara89@gmail.com*

***Specialty section:***
*This article was submitted to Optics and Photonics, a section of the journal Frontiers in Physics*

***Received:*** *25 July 2021*
***Accepted:*** *17 August 2021*
***Published:*** *18 October 2021*

***Citation:***
*Asha and Dahiya S (2021) Large Tunable 16-Tupled Millimeter Wave Generation Utilizing Optical Carrier Suppression With a Tunable Sideband Suppression Ratio. Front. Phys. 9:747030. doi: 10.3389/fphy.2021.747030*

## INTRODUCTION

For supporting multi gigabit per second (gbps) wireless connectivity and resolving spectrum shortage, 5G uses higher frequencies from an MM wave range (30–300 GHz) for signal transmission. However, the generation and transmission of MM wave signals is a troublesome process as these high-frequency signals apart from providing a wide bandwidth limits the transmission distance due to propagation losses. So, in order to cope up with this issue, the MM wave signal is first generated by modulating a low-frequency electrical signal over an optical carrier coming from a light source at a central station (CS) and then transmitting it to the base station (BS). This technique is named as millimeter wave–based radio over the fiber (i.e., MMoF) system. This fiber-based system provides low insertion and transmission losses with being immune toward electromagnetic interference.

The basic requirement for designing an efficient MMoF system is to modulate the RF signal for generating a desired MM wave signal with suppressing all other unwanted signals. The MM waves can be generated in two domains: 1) electrical and 2) optical or photonic. However, MM wave signal generation in a photonic domain is best suited in comparison to their electrical counterparts due to lower phase noise, lower equipment requirement, higher spectral purity, a wider tunable range, and a larger transmission distance [1]. Several different techniques have been discussed in the past for photonic MM wave signal generation which include a direct

**TABLE 1 |** Literature review of frequency 16-tupled MM wave generation based on different parameters.

| Author (Year) | Working Principle | Parameters | | | | | | | |
|---|---|---|---|---|---|---|---|---|---|
| | | OSSR (dB) | RSSR (dB) | Filters | Modulation index | Cost effective | Power efficient | Tunability | O/P freq Generated (GHz) |
| Zihang Zhu [6] (2015) | Two-cascaded dual parallel MZM | 21.5 | 38 | No | 2.265 | No | No | Low | 60 |
| K. Esakki Muthu [10] (2016) | Parallel combination of two-cascaded MZM | 20 | 28 | Yes | 3.14 | Yes | Yes | Low | 60 |
| M. Baskaran [14] (2018) | Cascaded MZM | 54 | 42 | No | 2.827 | Yes | No | High | 80 |
| Dongfei Wang [13] (2019) | Two-cascaded MZM | 31.35 | 24.11 | Yes | 7.59 (very high) | Yes | Yes | Low | 160 |
| Aasif Bashir Dar [9] (2020) | Cascaded parallel MZM | 64 | 31 | No | 2.79–2.86 | No | No | Low | 80 |
| Proposed Scheme (2021) | Series MZM configuration | 69 | 40 | No | 2.778–2.873 | Yes | Yes | High | 160 |

modulation [1], an external modulation [2], optical heterodyning [3], Stimulated brillouin scattering (SBS) [4] etc.

Among the above-stated techniques, the generation method utilizing an external modulation through a Mach–Zehnder Modulator (MZM) is the most reliable one as it offers optical harmonics generation with a higher frequency multiplication factor (FMF), stability, and greater tunability as mentioned in our previous review study in [5]. When an RF signal drives an external modulator, several optical harmonics are generated due to its nonlinear transfer function. By the beating of these harmonics at photodetector, MM wave signals are generated. The main technical challenge in the frequency multiplication (FM) approach is generating required optical harmonics while eliminating unwanted optical harmonics with higher conversion efficiency. So far, FMF of 2, 4, 6, 8, 10, 12, 14, and 16 have been proposed. However, MM wave generation utilizing a high FMF is quite efficient as it eliminates the requirement of high-frequency operated local oscillator (LO) operating at CS.

Recently, several generation techniques have been reported with a 16 FMF utilizing a two-cascaded dual parallel MZM configuration [6–8], parallel combination of two cascaded MZM [9], cascaded parallel MZM [10, 11], and a feedforward modulation [12]. Dongfei wang [13] proposed a generation method with a two-cascaded MZM but with a higher modulation index (>>7) requiring a high voltage radio frequency signal which in turn increases the system sensitivity. These schemes employ a filter for generating desired harmonics which not only increases system complexity but also reduces its tunability range and conversion efficiency. A filterless method has been proposed by the authors of reference [14] using cascaded MZM with an infinite extinction ratio which is not practically realizable. These techniques lead to partial cancellation of undesired harmonics and thus provide a lower sideband suppression ratio (SBSR) at the transmitting side leading to detect unwanted MM waves which deteriorate the system performance and also lower the spectral purity that is not desired for MM wave applications. The detailed review of these configurations is provided in **Table 1**.

In the present study, a cost-effective and spectrally pure 16-tupled MM wave frequency is generated by completely suppressing all the other undesired harmonics except eighth-order sideband (SB) using a series connection of a quad dual drive MZM (DD-MZM) and electrical phase shifters for optimizing biases of MZM and enhancing the OSSR and the RSSR by utilizing a lower modulation index and the extinction and the splitting ratio. A Theoretical analysis along with designing a simulation model is also carried out for understanding the cancellations of all other harmonics. The OSSR of 69 dB and the RSSR of 40 dB are obtained. The effectiveness of the 16-tupled generated MM wave is assessed by analyzing the effect of the MZM extinction ratio, the splitting ratio, the modulation index, and modulating frequency of the RF signal on the OSSR and the RSSR. The rest of the paper is structured as follows. The design principle of the proposed frequency 16 tupled structure is described in **Section 2**. The simulation results with the impact of non-ideal parameter variation on the SBSR are discussed in **Section 3** and finally the conclusion is presented in **Section 4**.

## DESIGN PRINCIPLE

The MWPL is built using the OptiSystem version 17.0.0. **Figure 1** shows a schematic diagram of the proposed filterless MM wave generation with frequency 16 tupling. For generating MM wave with FMF of 16, ±eighth-order SBs must hit the photodetector (PD). In order to obtain this, MZM should be biased at MXTP which provides a carrier and only even order SBs after modulation. Furthermore, obtaining pure ±eighth-order SBs is quite challenging because several other unwanted spurious SBs are also generated.

For suppressing all other spurious harmonics, subsequent measures are adopted in the proposed scheme as: 1) setting MZM at MXTP for suppressing all the odd order SBs and generating only even order SBs, 2) controlling the M.I. of the MZM to let the power of sidebands greater than ±10th order sidebands return to zero or is negligible, and 3) adjusting the electrical phase shift of the RF driving signal between the MZM and insertion loss of modulator so as to suppress the carrier and eliminate all the other $(2n\text{-}2)^{th}$ order sidebands except ±eighth-order SBs. The detailed principle of the proposed scheme is mentioned below.

It utilizes a laser diode (LD), an RF signal generator, electrical phase shifters, a photodiode, optical amplifiers, and a DD-MZM. A continuous wave laser (CWL) with frequency $\omega_c$ emits the light signal which acts as a carrier signal defined as follows:

$$V_{in} = V_c\ (Cos\ \omega_c t). \tag{1}$$

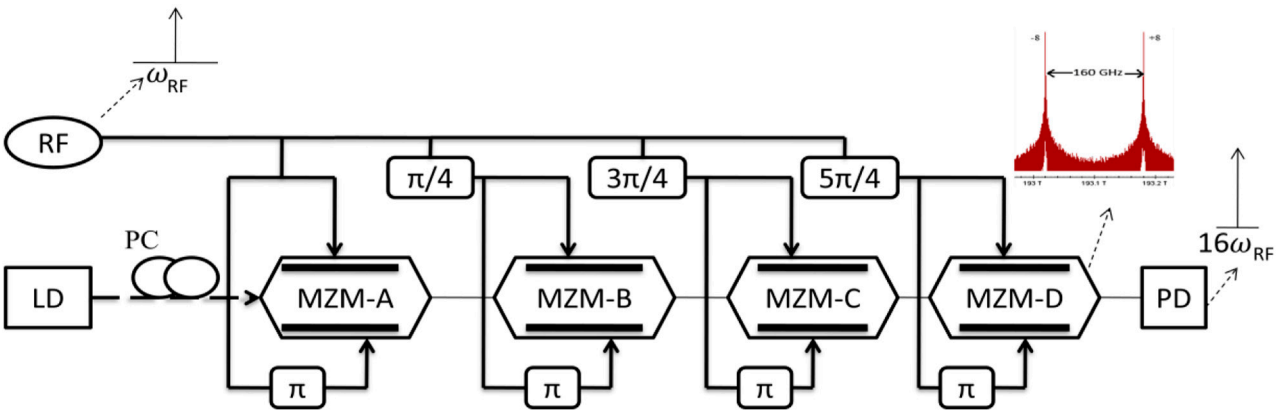


**FIGURE 1 |** Proposed structure for generating a 16-tupled MM wave signal.

Here, $V_c$ is the amplitude of the carrier signal.

This light carrier wave after being polarization controlled (PC) is transmitted to the first intensity modulator, that is, MZM-A triggered by RF LO which produces a single RF tone of frequency, $\omega_{rf}$, given by the following:

$$V_1 = V_{rf}\left(Cos\,\omega_{rf}t\right), \tag{2}$$

where $V_{rf}$ is the amplitude of the input RF signal.

## Odd order Harmonics Elimination

The transfer function of a DD-MZM is expressed as follows:

$$E_{MZM-A}(t) = \frac{\beta}{2}E_c e^{j\omega_c t}\left\{\chi\, e^{-jm_a \sin\omega_{RF}t} + \left(1-\chi\right)e^{jm_a \sin\omega_{RF}t}\right\}, \tag{3}$$

where $m_a = \frac{\pi V_{RF}}{V_\pi}$ is the M.I.,

$V_{RF}$ is the switching RF voltage, $V_\pi$ is the half wave voltage of MZM, and $\beta$ is the insertion loss of MZM.

$x = \frac{\left(1-\frac{1}{\sqrt{\mu_r}}\right)}{2}\left\{\mu_r = 10^{(MZM\ extinction\ ratio)/10}\right\}$ is the splitting ratio of upper and lower arms of MZM.

However, using the Jacobi–Anger expansion,

$$\begin{aligned} e^{jmsin\Phi} &= \sum_{k=-\infty}^{k=\infty} J_k(m)e^{jk\Phi} \text{ and } e^{jmcos\Phi} \\ &= \sum_{k=-\infty}^{k=\infty} (-1)^k J_k(m)e^{jk\Phi}. \end{aligned} \tag{4}$$

The transfer function can be rewritten as follows:

$$E_{MZM}(t) = \beta E_c\left[\sum_{k=-\infty}^{k=\infty}(-1)^k J_k(m)e^{j\{(\omega_c + k\omega_{RF})t\}}\right], \tag{5}$$

$$\begin{aligned} E_{MZM}(t) = \beta E_c\big[ & J_0(m_a)e^{j\omega_c t} - J_1(m_a)\{e^{j(\omega_c-\omega_{RF})t} + e^{j(\omega_c+\omega_{RF})t}\} \\ & + J_2(m_a)\{e^{j(\omega_c-2\omega_{RF})t} + e^{j(\omega_c+2\omega_{RF})t}\} \\ & - J_3(m_a)\{e^{j(\omega_c-3\omega_{RF})t} + e^{j(\omega_c+3\omega_{RF})t}\} + \ldots\ldots\ldots\big]. \end{aligned} \tag{6}$$

As the Li-$NbO_3$ DD-MZM has a nonlinear characteristic response, the modulated output optical signal consists of a carrier along with multiple sidebands symmetrically located around it as depicted in **Eq. 6**. The amplitude and number of sidebands generated around the carrier can be controlled by varying $m_a$ which in turn depends on $V_{RF}$ and $V_\pi$. In order to suppress the odd order SBs, the first modulator is biased at MXTP by applying the bias voltages to the upper and lower arms of the modulator such that $V_{bias} = V_{bias1} - V_{bias2} = 0$ with a $\pi$ phase difference between the RF signals fed to the arms of the modulator.

$$\begin{aligned} E_{MZM-A}(t) = \beta E_c e^{j\omega_c t}\big[ & J_0(m_a) + J_2(m_a)\left\{e^{j2\omega_{RF}t} + e^{-j2\omega_{RF}t}\right\} \\ & + J_4(m_a)\left\{e^{j4\omega_{RF}t} + e^{-j4\omega_{RF}t}\right\} + J_6(m_a)\left\{e^{j6\omega_{RF}t}\right. \\ & \left. + e^{-j6\omega_{RF}t}\right\} + J_8(m_a)\left\{e^{j8\omega_{RF}t} + e^{-j8\omega_{RF}t}\right\}. \end{aligned} \tag{7}$$

The above equation clearly depicts that there are $2n^{th}$ order, that is, even SBs generated from the first modulator, and the corresponding optical spectrum is shown in **Figure 2**.

## Suppressing $(2n\text{-}2)^{th}$ Order Sidebands

For suppressing $(2n\text{-}2)^{th}$ order sidebands, except the desired ±eighth sidebands, an MZM-A output is fed to the second one, which in turn goes to the third and then to the fourth in such a manner that all the modulators are driven with the RF signal with a suitable phase shift between the two consecutive modulators such that the output from the last modulator only contains the desired ±eighth-order SB and the separation between the desired sidebands is the 16th multiple of input RF.

The modulated output from MZM-A is sent to MZM-B which is triggered by an RF signal with a 45° phase difference such that $V_2 = V_{rf}\ (Cos\,\omega_{rf}t + \pi/4)$ is mathematically expressed in **Eq. 6** as follows:

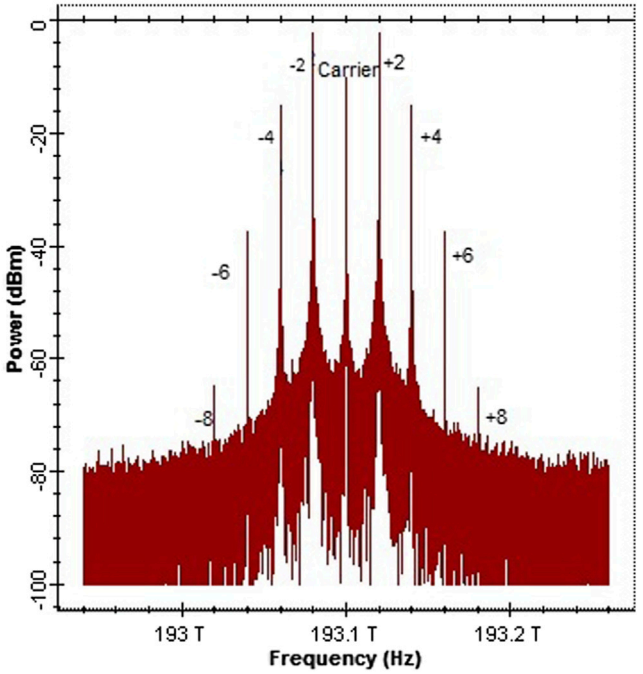


**FIGURE 2 |** Optical spectrum output from MZM-A containing only even order sidebands.

$$E_{MZM-B}(t) = \frac{\beta^2}{2} E_c e^{j\pi/4} \left[ \sum_{k=-\infty}^{k=\infty} J_k^2(m_a) e^{j\{(\omega_c + 2k\omega_{RF})t + k\pi\}} \right]. \quad (8)$$

This output from MZM-B is an input to the third MZM triggered by the RF signal with an electrical phase difference of 135°.

$$\begin{aligned} E_{MZM-c}(t) = \beta E_{MZM-B}(t)\{J_0(m_a) - J_2(m_a)\}\{e^{j2\omega_{RF}t} + e^{-j2\omega_{RF}t}\} \\ + J_4(m_a)\{e^{j4\omega_{RF}t} + e^{-j4\omega_{RF}t}\} - J_6(m_a)\{e^{j6\omega_{RF}t} \\ + e^{-j6\omega_{RF}t}\} + J_8(m_a)\{e^{j8\omega_{RF}t} + e^{-j8\omega_{RF}t}\} \\ - J_{10}(m_a)\{e^{j10\omega_{RF}t} + e^{-j10\omega_{RF}t}\} + J_{12}(m_a)\{e^{j12\omega_{RF}t} \\ + e^{-j12\omega_{RF}t}\}. \end{aligned} \quad (9)$$

This output is fed to the last modulator, that is, MZM-D which is driven by the RF signal phase shifted by 225°. By providing this phase shift, $J_2(m_a)$, $J_4(m_a)$, and $J_6(m_a)$ terms turn into zero and other higher order harmonics, such as $J_{10}(m_a)$ and $J_{12}(m_a)$, have extremely low power which can be neglected.

## Tunable Optical Carrier Suppression

By properly adjusting the modulation index, the carrier could be suppressed completely which results into power saving and efficient transmission leaving behind the optical spectrum with only the eighth-order SB as depicted in **Figure 3**. The MZM-D output can be stated mathematically as follows:

$$E_{MZM-D}(t) = \frac{\beta^4}{2} J_8^2(m_a) E_c e^{j\omega_c t} \{e^{j8\omega_{RF}t} + e^{-j8\omega_{RF}t}\}. \quad (10)$$

This output is then detected at the receiver side through the PIN photodiode whose photocurrent is given by the following equation:

$$I_{ph}(t) = \mu_{ph} |E_{MZM-D}(t)| * |E_{MZM-D}(t)|^*, \quad (11)$$

$$\begin{aligned} I_{ph}(t) = \mu_{ph} \left\{ \frac{\beta}{2} E_c \left[ J_{-8}(m_a) e^{j(\omega_c - 8\omega_{RF})t} + J_8(m_a) e^{j(\omega_c + 8\omega_{RF})t} \right] \right\} \\ * \left\{ \frac{\beta}{2} E_c \left[ J_{-8}(m_a) e^{j(\omega_c - 8\omega_{RF})t} + J_8(m_a) e^{j(\omega_c + 8\omega_{RF})t} \right] \right\}^*, \end{aligned} \quad (12)$$

where $\mu_{ph}$ is the responsivity of the photodiode. The above equation can be further simplified as follows:

$$I_{ph}(t) = \frac{\mu_{ph} \beta^2 |E_{MZM-D}(t)|^2}{4} Cos\ (16\ \omega_{RF} t). \quad (13)$$

Thus, it can be seen mathematically through **Eq. 13** that the photo-detected output consists of an electrical signal of frequency 160 GHz as shown in the **Figure 4** which is 16 times the RF signal frequency, that is, 10 GHz being utilized at the CS.

## RESULTS AND DISCUSSION

A polarization-controlled CWL emitting a light signal of frequency 193.1 THz is sent to MZM-A biased at MXTP and triggered through a 10 GHz RF signal. As MZM-A is biased at MXTP, its output contains only even order sidebands. The output from the first modulator is sent to the second, then to the third,

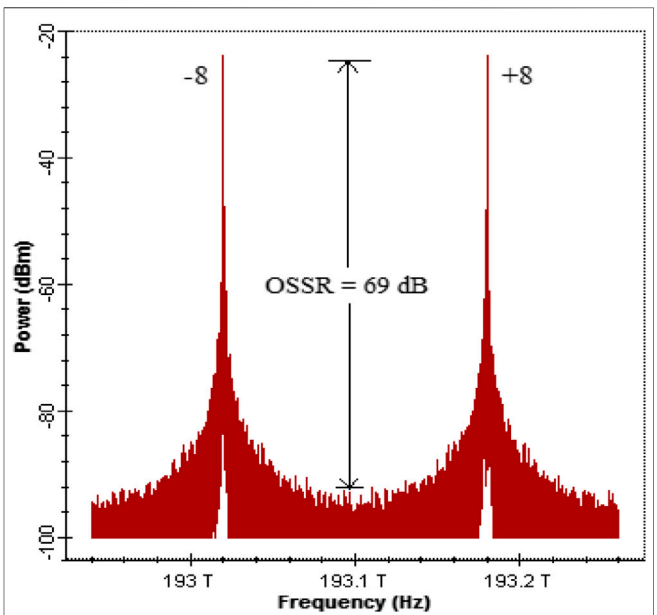


**FIGURE 3 |** Optical spectrum analyzer output from MZM-D.

**TABLE 2 |** Simulation parameters employed for the present scheme of frequency 16 MM wave signal generation.

| System block | Simulation parameters | Parameters value |
|---|---|---|
| Fiber link | Length | 60 km |
| | Attenuation | 0.22 dB/km |
| | Dispersion | 16.75 ps/nm-km |
| | Dispersion slope | 0.075 ps/nm$^2$/k |
| CW laser Diode | Frequency | 193.1 THz |
| | Power | 8 dBm |
| Local oscillator | RF signal | 10 GHz |
| MZM modulator | MZM-A, B, and C extinction ratio | 60 dB |
| | MZM-D extinction ratio | 55 dB |
| | Insertion loss | 3 dB |
| | Switching bias voltage | 3.2 |
| | Switching RF voltage | 3.2 |
| EDFA 1 | Gain | 10 dB |
| | Noise figure (NF) | 3 dB |
| Amplifier | Gain | 12 dB |
| | Noise figure | 2 dB |
| PIN photodiode | PIN photodiode responsivity | 0.9 |
| | PIN dark current | 9 nA |

and at last to the fourth modulator in such a manner that the electrical phase shift of the RF local oscillator (LO) signal between first two consecutive MZMs is 45° and next two MZMs is 90°, and all the four modulators are biased at MXTP. By arranging the electrical phase shift, the modulation index, and the MZM in this manner, the output from the last modulator suppresses the carrier with all other spurious harmonics and contains only eighth-order SBs at $\omega_c + 8\omega_{RF}$, that is, 193.18 THz, and $\omega_c - 8\omega_{RF}$, that is, 193.02 THz with −22.4 dBm power. It can be seen that the difference between +eighth (193.18 THz)- and −eighth (193.02 THz)-order SBs is the 16th multiple of the input electrical signal. These sidebands are then sent to the BS through a 60-km standard single-mode fiber (SSMF) with parameters mentioned in **Table 2**. At the BS, a hybrid configuration of cascaded amplifiers consisting of EDFA with gain of 10 dB and optical amplifier having 15 dB gain is utilized to mitigate the losses incurred during transmission over the fiber, and then a PIN photodiode with a responsivity of 0.9 A/W is utilized to detect the modulated signal by converting it back to electrical form and hence a 160-GHz signal is detected using the RF spectrum analyzer with tan output power of −50 dBm.

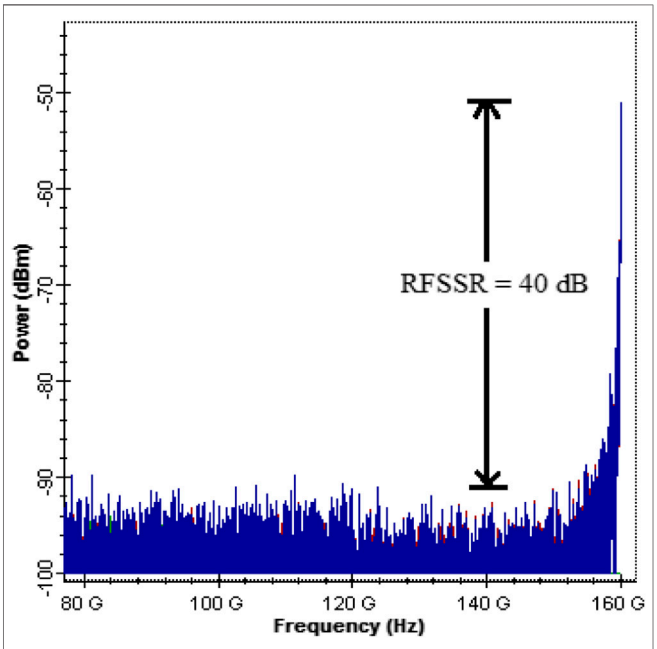


**FIGURE 4 |** RF spectrum of the photo-detected signal from the PIN photodiode.

## Impact of Nonideal Parameters on the OSSR and the RSSR

The above-mentioned results are based on the simulation carried over the OptiSystem software by assuming ideal parameters as mentioned in **Table 2**. However, these parameters might deviate from their desired values and thus it is crucial to analyze the impact of several nonideal parameters, such as RF voltage variation, the MZM extinction ratio, a cascaded amplifier configuration, and phase drift is analyzed over the OSSR and the RSSR.

### Extinction Ratio and Splitting Ratio

For evaluating the proposed system performance, the impact of the extinction ratio (E. R.) or the splitting ratio of each MZM is studied over the OSSR and the RSSR, as shown in **Figure 5**. It is observed that as the extinction ratio varies from its ideal value, the system is not able to suppress the odd order SBs as P8/P1 is 57 dB when it deviates by 0.010 from the ideal value with 30 dB RSSR, and the eighth-order SBs are 26 dB greater than seventh order SBs when it deviates by a value of 0.045 with the 16-tupled MM wave being only 13 dB higher than the 15-tupled signal deteriorating the system performance, as shown in **Figure 5**. This states that the OSSR and the RSSR rises with an increasing splitting ratio/extinction ratio, as the splitting ratio is dependent on the extinction ratio of the MZM. Both the sideband suppression ratio (SSR) are maximum at 0.4995 splitting ratio, as calculated from **Eq. 3** under *Odd Order Harmonics Elimination*, and the unwanted sidebands are completely eliminated when the MZM extinction ratio is set to 60 dB being independent of the extinction ratio exceeding 60 dB, as clearly depicted in **Figures 6**, **7**.

### Modulation Index

The optical and RF spectrum when M.I. deviates 0.0588 from the ideal value is depicted in **Figure 8** where the $P_8$ is 14 dB higher than $P_0$ and 62 dB from $P_3$, respectively. However, the 16-tupled MM wave is 11 dB greater than the octupling wave (eighth multiple of RF), which is quite less for the applications requiring MM wave for their operation. Besides this, the impact of the modulation index on the sideband power ratio (SBPR) ($P_8/P_0$) is depicted in **Figure 9**, which shows that the system provides ($P_8/P_0$) greater than 5 dB

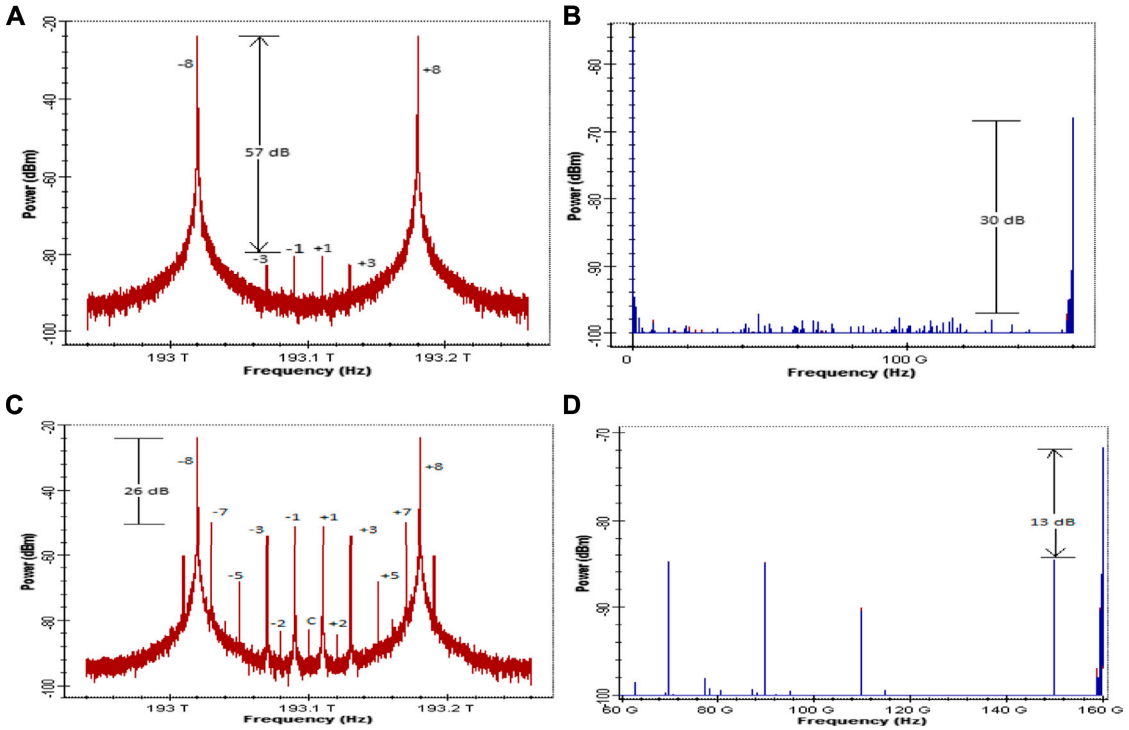


**FIGURE 5 | (A)** Optical spectrum when E.R. deviates by 0.010, **(B)** RF spectrum when E.R. deviates by 0.010, **(C)** optical spectrum when E.R. deviates by 0.045, and **(D)** RF spectrum when E.R. deviates by 0.045 value.

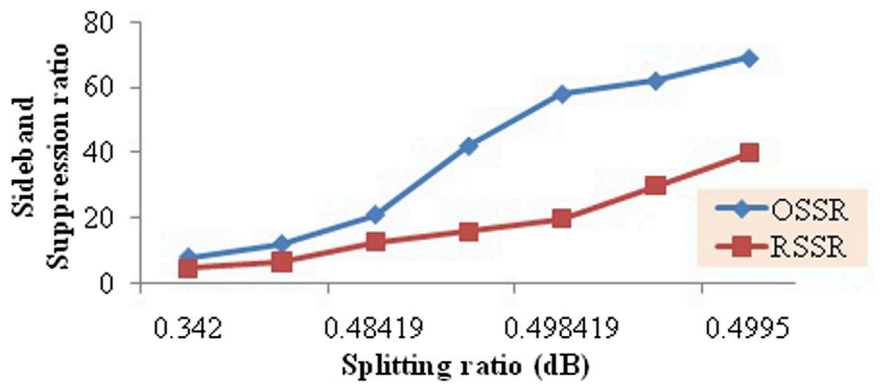


**FIGURE 6 |** Impact of the splitting ratio on the sideband suppression ratio.

and the RSSR greater than 2 dB (**Figure 10**) in the M.I. range of 2.678–2.945 by providing the peak of the OSSR {i.e., ($P_8/P_0$)} and the RSSR at an M.I. of 2.8258 with an RF voltage of 2.87989. The system provides an acceptable and tunable SSR which is greater than 15 dB in the M.I. ranging from 2.778 to 2.873.

## Phase Drift Analysis of the OSSR

The effect of phase drift can be analyzed over the system by studying the OSSR deviation over the phase drift in PS. It can be noticed that for ±10° phase drift between MZM upper arm and lower arms OSSR is above 25 dB which means that the system is less sensitive as far as MZM arms' phase drift is considered, while it is sensitive toward the phase drift in the phase shifters of the RF signal which drives the DD-MZM modulator, as depicted in **Figure 11**. However, the system provides acceptable performance for ±8° phase drift.

## Cascaded Hybrid Amplifier Configuration

Amplifiers are used in the system so as to compensate the losses which are inserted while the signal travels through the optical

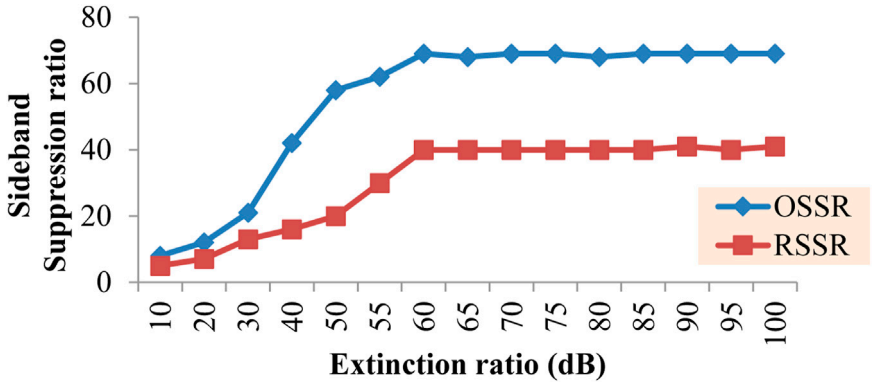


**FIGURE 7 |** Impact of the MZM extinction ratio on the sideband suppression ratio.

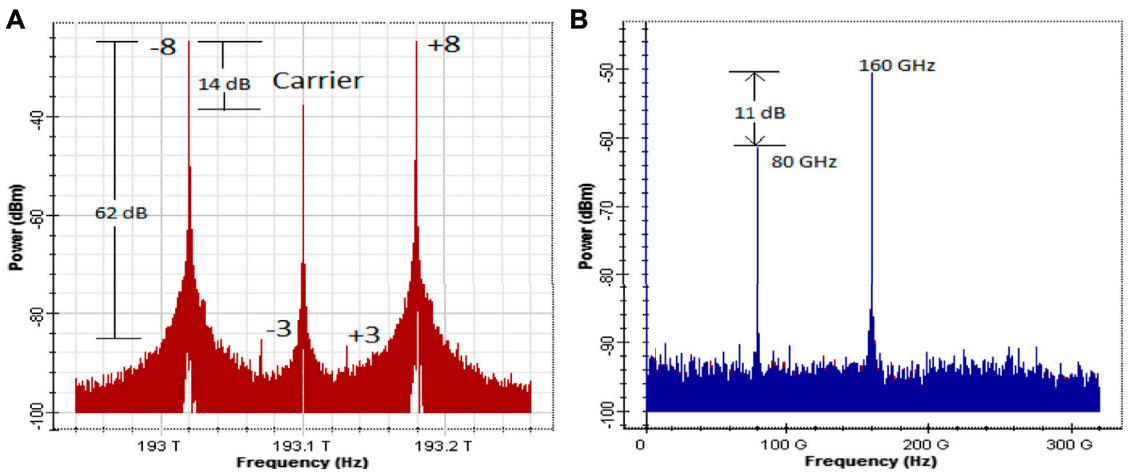


**FIGURE 8 | (A)** Optical spectrum and **(B)** RF spectrum output at M. I of 2.776.

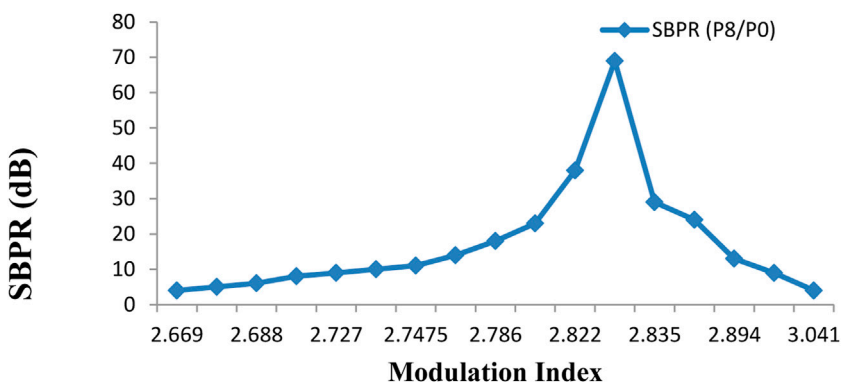


**FIGURE 9 |** SBPR variation with the modulation index.

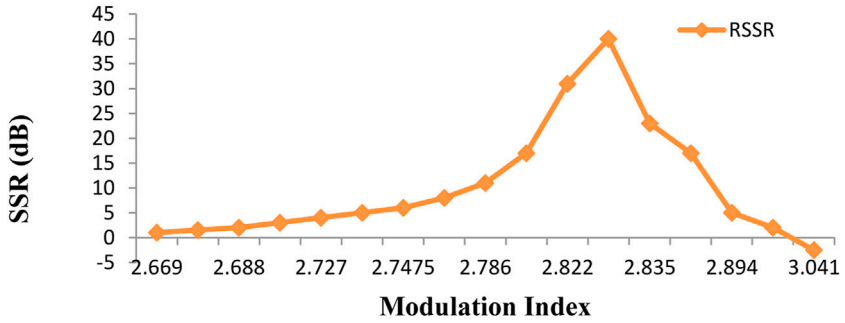


**FIGURE 10 |** RSSR variation with the modulation index.

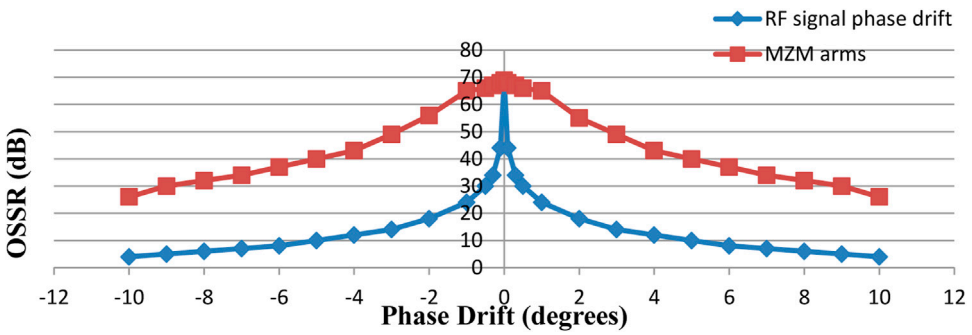


**FIGURE 11 |** OSSR variation with phase drift in the RF signal driving MZM and MZM arms.

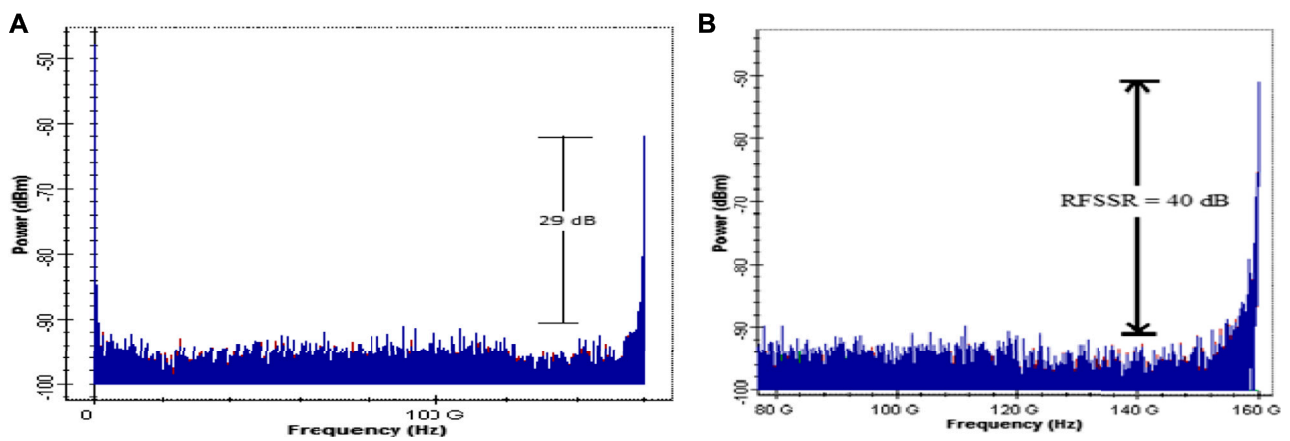


**FIGURE 12 |** RSSR for the system with **(A)** a single amplifier and **(B)** a cascaded amplifier.

fiber. The impact of using a cascaded amplifier configuration having EDFA 1 connected with optical amplifier with their parameters mentioned in **Table 2** enhances the RFSSR by 11 dB in comparison to a single amplifier configuration with a 20-dB gain and NF of 4 dB when detected by the PIN photodiode generates a 160-GHz with a 29-dB RFSSR, as shown in **Figure 12**. It can be noted that the cascaded amplifier configuration results in the improved RFSSR.

## CONCLUSION

A photonic generation scheme of a frequency 16-tupled MM wave signal is presented and demonstrated using a series-connected DD-MZM with a double sideband optical carrier suppression modulation offering efficient power transmission. With appropriate adjustment of internal parameters, such as the modulation index, DC biasing, the splitting ratio, and electrical phase difference, and utilizing a hybrid amplifier configuration, a 160-GHz MM wave signal is generated from a 10-GHz RF signal with an OSSR of 69 dB and an RSSR of 40 dB. This system does not require any additional circuitry such as a mixer, a filter, and a digital signal processor. In comparison to the previous approaches, the proposed structure optically generates a highly conversant, spectrally pure 16-tupled MM wave signal with a better tunable OSSR and an RSSR and with a wider tunable range from 1–15 GHz, as there is no filter required in this scheme. Further, the system provides acceptable performance with a wider range of M.I. variation 2.778–2.873, ±8° phase drift between MZM arms, and electrical phase shifters and is independent of the extinction ratio beyond 60 dB.

## DATA AVAILABILITY STATEMENT

The original contributions presented in the study are included in the article/Supplementary Material; further inquiries can be directed to the corresponding author.

## AUTHOR CONTRIBUTIONS

SD proposed the idea and supervised the whole work. Asha carried out the modeling and simulation. Both authors contributed to the writing of the manuscript.

## REFERENCES


1. Zeb K. *Photonic generation of spectrally pure Millimeter wave signals for 5G applications*. Ottawa, Canada: IEEE International Topical Meeting on Microwave Photonics (2020). p. 1–4.
2. Perez Galacho D, Sartiano D, and Sales S. Analog radio over fiber links for future 5G radio access networks. *IEEE ICTON* (2019) 1–4. doi:10.1109/icton.2019.8840516
3. He X. Linear analog photonic link enabled RoF-5G front haul transmission system. *Optik* (2019) 183(3):99–104. doi:10.1016/j.ijleo.2019.02.056
4. Kamissoko D, Jing H, Ganame H, and Tall M. Performance investigation of W-band Millimeter wave radio over fiber system employing optical heterodyne generation and self homodyne detection. *Opt Commun* (2020) 474(1):1–8. doi:10.1016/j.optcom.2020.126174
5. Asha SD. A Comprehensive Review of Millimeter wave based radio over fiber for 5G front haul transmissions. *Ijst* (2021) 14(1):86–100. doi:10.17485/ijst/v14i1.2177
6. Zhu Z, Zhao S, Chu X, and Dong Y. Optical generation of millimeter-wave signals via frequency 16-tupling without an optical filter. *Opt Commun* (2015) 354(1):40–7. doi:10.1016/j.optcom.2015.05.035
7. Li X, Zhao S, Zhu Z, Gong B, Chu X, Li Y, et al. An optical millimeter-wave generation scheme based on two parallel dual-parallel Mach-Zehnder modulators and polarization multiplexing. *J Mod Opt* (2015) 62(18): 1502–9. doi:10.1080/09500340.2015.1045948
8. Ying X, Xu T, Li W, Weng H, and Zhang X. Photonic generation of millimeter-wavesignal via frequency 16-tupling based on cascaded dual – parallel MZM. *J Optoelectronics – Laser* (2017) 28(11):1212–7.
9. Dar AB, Ahmad F, and Jha RK. Filterless 16-Tupled Optical Millimeter-wave Generation Using Cascaded Parallel Mach-zehnder Modulators with Extinction Ratio Tolerance. *PIER Lett* (2020) 91(1):129–35. doi:10.2528/pierl20031009
10. Muthu K, Raja A, and Shanmugapriya G. Frequency16-tupled optical millimeter wavegeneration using dual cascaded MZMs and 2.5 Gbps RoF tr ansmission. *Optik* (2017) 14(1):338–46.
11. Esakki Muthu K, and Sivanantha Raja A. Bidirectional MM-Wave Radio over Fiber transmission through frequency dual 16-tupling of RF local oscillator. *J Eur Opt Soc – Rapid Publications.* (2016) 12(24):1–9. doi:10.1186/s41476-016-0028-2
12. Chen H, Ning T, Jian W, Pei L, and Li J. D-band millimeter-wave generator based ona frequency 16-tupling feed-forward modulation technique. *Opt Eng* (2013) 52(1):0761041–4. doi:10.1117/1.oe.52.7.076104
13. Wang D, Tang X, Xi L, Zhang X, and Fan Y. A filterless scheme of generating frequency 16-tupling millimeter-wave based on only two MZMs. *Opt Laser Tech* (2019) 116(1):7–12. doi:10.1016/j.optlastec.2019.03.009
14. Baskaran M, and Prabakaran R. Optical Millimeter wave signal generation with frequency 16 tupling using cascaded MZMs and no optical filtering for radio over fiber system. *J Eur Opt Society-Rapid Publications* (2018) 14(13): 1–8. doi:10.1186/s41476-018-0080-1


**Conflict of Interest:** The authors declare that the research was conducted in the absence of any commercial or financial relationships that could be construed as a potential conflict of interest.

frontiers in Physics

ORIGINAL RESEARCH
published: 25 October 2021
doi: 10.3389/fphy.2021.690588

# Modeling and Performance Analysis of Simplified Two-Diode Model of Photovoltaic Cells

*Saripalli Bhanu Prakash*, Gagan Singh and Sonika Singh*

*Department of Electrical and Electronics & Communication Engineering, DIT University, Dehradun, India*

For a quick and consistent photovoltaic (PV) module design, an effective, fast, and exact simulator is crucial to examine the performance of the photovoltaic cell under partial or quick variation of temperature and irradiance. The most prevalent modeling strategy is to apply an equivalent (electrical) circuit that encompasses together non-linear and linear mechanisms. This work proposes the modeling and analysis for a four-parameter two-diode photovoltaic cell model based on the manufacturer's data-sheet. The proposed model needs only four parameters compared to the previously developed seven-parameter two-diode model to reduce the computational complexity. To develop a specific model of photovoltaic cells, the fundamental requirement is the data of temperature and irradiance. The variation of these variables totally affects the output constraints like current, voltage, and power. Thus, it is substantial to design a precise model of the photovoltaic cell module with a reduced computation period. The two-diode photovoltaic module with four constraints is identified to be more accurate and have improved performance compared to a one-diode model particularly at lower irradiance. To confirm the accuracy of the proposed model the method is applied on two different photovoltaic modules. The proposed model and modeling method are helpful for power electronic designers who require a fast, accurate, simple, and easy to implement method for use in photovoltaic system simulation. The electrical equivalent circuit and standard equations of photovoltaic cells are analyzed and the proposed two-diode model is simulated using MATLAB/Simulink software and validated for poly-crystalline and mono-crystalline solar cells under standard test conditions.

**Keywords: one-diode photovoltaic model, two-diode photovoltaic model, poly-crystalline solar cell, circuit constraints, mono-crystalline solar cell**

OPEN ACCESS

***Edited by:***
*Carlos Marques,*
*University of Aveiro, Portugal*

***Reviewed by:***
*Rahul Kumar Gangwar,*
*Peking University, China*
*Dharmendra Kumar,*
*Madan Mohan Malaviya University of Technology, India*

****Correspondence:***
*Saripalli Bhanu Prakash*
*sb.prakash@dituniversity.edu.in*

***Specialty section:***
*This article was submitted to Optics and Photonics, a section of the journal Frontiers in Physics*

***Received:*** *03 April 2021*
***Accepted:*** *15 April 2021*
***Published:*** *25 October 2021*

***Citation:***
*Prakash SB, Singh G and Singh S (2021) Modeling and Performance Analysis of Simplified Two-Diode Model of Photovoltaic Cells. Front. Phys. 9:690588. doi: 10.3389/fphy.2021.690588*

## INTRODUCTION

In recent years, several models have been developed including the single-diode $R_S$ model, $R_P$ model, and double-diode and triple-diode model [1–3]. The most modest scheme is a one-diode PV model (ideal case) as it involves only three variables: current at short circuit, voltage at open circuit, and diode ideality factor. The enhanced type of the model includes the insertion of series resistance $R_s$ to the equivalent circuit [4]. While this model suffers from inconsistencies with the change in the temperature values as it does not considered the voltage temperature coefficient. The upgraded version is the $R_P$ model by the insertion of a shunt resistor to the equivalent circuit [5]. Though this model has improved accuracy, with the insertion of $R_P$ the computational parameters are increased to five which leads to more computation time.

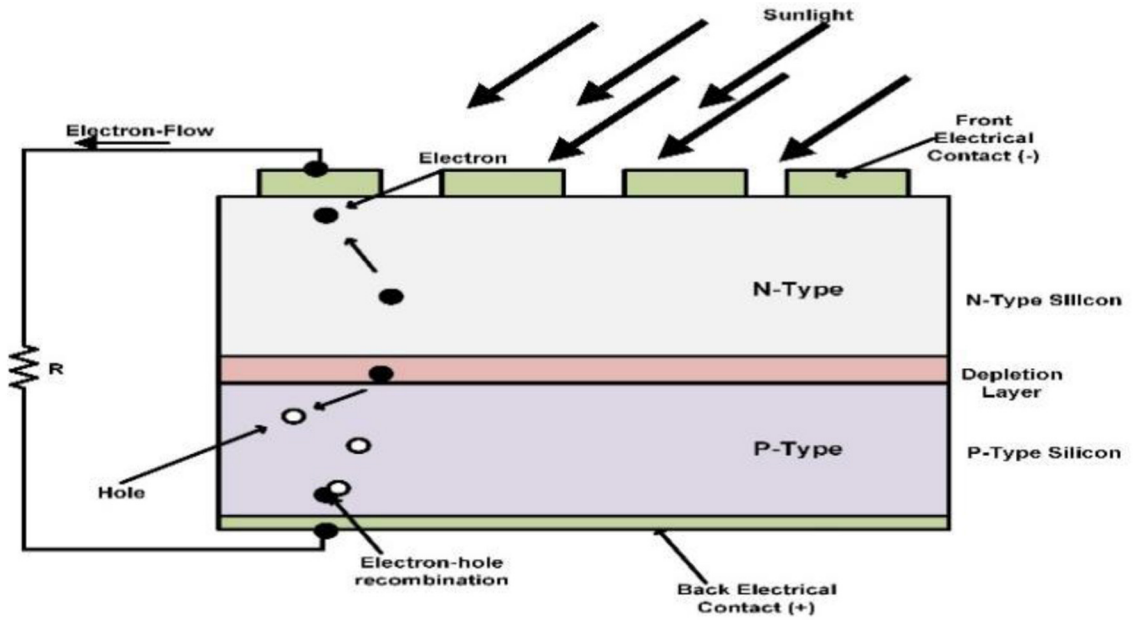


**FIGURE 1 |** Structure of a photovoltaic cell [9].

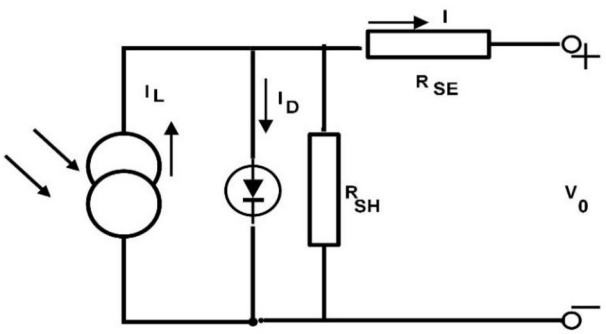


**FIGURE 2 |** Equivalent circuit model: one-diode photovoltaic (PV) model [3].

In general, most of the constructors only provide data about constraints like voltage at open circuit ($V_o$), current at short circuit ($I_{SC}$), peak or maximum power ($P_{mpp}$), current at $P_{mpp}$ ($I_{mpp}$), and voltage at $P_{mpp}$ ($V_{mpp}$) at standard operating conditions and inappropriately these data are far away from what is essential for modeling because a PV cell is used to functioning at various ecological conditions. The non-linear performance of current-voltage characteristics requires the alteration of constraints by using the manufacturer data sheet [6, 7].

So far, many researchers have developed a single-diode model by making an assumption that nonappearance of recombination loss occurs in the depletion layer. In reality, it is not possible to satisfactorily model by using a single diode. Consideration of this loss results in a more exact model, identified as the two-diode model [8]. But, with the insertion of the extra diode it increases the constraints to seven and the new constraints include reverse saturation current $I_{DS2}$ and ideality factor $C_2$ of the second diode. The main task is now to evaluate the values of the model constraints while keeping a realistic computational energy. The key knowledge of this paper, to develop a detailed model of a two-diode PV cell module, is by simplifying the current equation and thereby reducing the constraints to four. The precision of this PV model is confirmed by two different solar PV cells from the constructor information sheet and behavior performance is compared with a one-diode $R_{SH}$ model. This enhanced model can be useful for researchers who work on the precise modeling of photovoltaic (PV) modules.

## FUNDAMENTALS AND CIRCUIT MODEL OF PHOTOVOLTAIC CELLS

### Effective Principle of Photovoltaic Cells

A basic structure of a typical photovoltaic cell is represented in **Figure 1**. A photovoltaic cell essentially consists of two films doped in a different way and behaves as a semiconductor diode through its p-n junction, which is exposed to incident light [9]. When the photovoltaic cell is exposed to this light, electron-hole pairs are generated which initiates the flow of the electric current if the circuit is closed from cathode (N type) to anode (P type).

By this convention, the electric current direction is always chosen with reference to the direction of movement of positive charges. Consequently, the direction of current in the load circuit is shown from a positive to negative terminal.

### Electrical Equivalent Circuit of One-Diode Photovoltaic Cell Model

The one-diode model with a series and parallel resistor is represented in **Figure 2** [3]. For practical reasons, we cannot

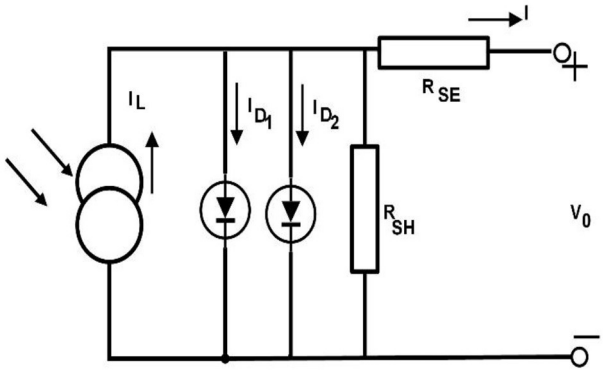


**FIGURE 3 |** Equivalent circuit model: two-diode photovoltaic (PV) model [2].

neglect the $R_{SE}$ and $R_{SH}$ resistor in photovoltaic cell modeling. With the addition of these resistors, the constraints are now increased to five which also lengthens the computation time. This model is the most popular due its ease, accuracy, and easy of implementation. Despite of its advantages, the model's accuracy will worsen at lower irradiance [10].

# MODELING OF A PHOTOVOLTAIC CELL AND DETERMINATION OF CONSTRAINTS

## Modeling of a Two-Diode Photovoltaic Cell

The two-diode PV model is represented in **Figure 3** [2]. Obviously, two more new constraints now need to be considered: the reverse saturation diode current $I_{DS2}$ and ideality factor $C_2$. The current $I_{DS2}$ compensates for the consequence of recombination loss in the depletion area [11].

By applying KVL to **Figure 3**, we get the expression for current I:

$$\begin{aligned} I &= I_L - I_{D1} - I_{D2} - I_{SH} \\ I &= I_L - I_{D1} - I_{D2} - \frac{V_0 + IR_{SE}}{R_{SH}} \end{aligned} \tag{1}$$

$I_L$ is the light or photo current, $I_{D1}$ and $I_{D2}$ is the current through diode 1 and diode 2, $I_{SH}$ is the current through the shunt resistor $= \frac{V_0 + IR_{SE}}{R_{SH}}$, $R_{SE}$ and $R_{SH}$ are series and shunt resistances, $V_0$ is applied voltage across diode, and $I$ is module output current [12].

Currents through diodes 1 and 2 are given by

$$\begin{aligned} I_{D1} &= I_{Ds1}[(e^{\frac{V_o + IR_{SE}}{C_1 V_T N_{SE}}}) - 1] \\ I_{D2} &= I_{Ds2}[(e^{\frac{V_o + IR_{SE}}{C_2 V_T N_{SE}}}) - 1] \\ I &= I_L - I_{Ds1}[(e^{\frac{V_o + IR_{SE}}{C_1 V_T N_{SE}}}) - 1] \\ &\quad -I_{Ds2}[(e^{\frac{V_o + IR_{SE}}{C_2 V_T N_{SE}}}) - 1] - \frac{V_0 + IR_{SE}}{R_{SH}} \end{aligned} \tag{2}$$

$I_{Ds1}$ and $I_{Ds2}$ are reverse saturation diode current, $C_1$ and $C_2$ are the diode ideality factor of 1 and 2, $N_{SE}$ is series-connected PV cells, $V_T$ is thermal voltage $= \frac{K\,T_{Ac}}{q}$, $V_T$ is approximately 25.856 mV at 300 Kelvin, $q$ is $(1.602\ X\ 10^{-19})$, C is electron charge, $K$ – $(1.38\ X\ 10^{-23})\ \frac{Joule}{Kelvin}$ is a Boltzmann constant, and $T_{Ac}$ is the cell's absolute temperature in Kelvin.

Light or photo current [9] is given by

$$I_L = (I_{SC} + \gamma_{SC}\Delta T_{Ac})\frac{G_{ir}}{G_{SC}} \tag{3}$$

$G_{ir}$ – irradiance in $\frac{W}{m^2}$, $G_{SC}$ – irradiance at the standard test condition (STC) = 1,000 $\frac{W}{m^2}$, $T_{Ac} = T_{Ac} - \Delta T_{Ac,ref}$ (Kelvin), $T_{Ac,ref} - (25 + 273 = 298\ Kelvin)$, $I_{SC}$ is the cell's short circuit current at STC (25°), and $\gamma_{SC}$ is the current temperature coefficient (A/K).

$$I_{DS} = I_{DS1} = I_{DS2} = \frac{I_{SC} + \gamma_{SC}\Delta T_{Ac}}{(e^{V_{\Delta T}[\frac{C_1+C_2}{P}]} - 1)} \tag{4}$$

where $\gamma_V$ – voltage temperature coefficient (V/K).

In making the model simple for analysis, the seven constraints are reduced to four by assuming the $I_{DS} = I_{DS1} = I_{DS2}$ and $\frac{(C_1+C_2)}{p}) = 1$ as described in [12] Therefore.

$$I_{DS} = I_{DS1} = I_{DS2} = \frac{I_{SC} + \gamma_{SC}\Delta T_{Ac}}{(e^{\frac{V_0+\gamma_V\Delta T_{Ac}}{V_{\Delta T}}} - 1)} \tag{5}$$

## Determination of Photovoltaic Module Constraints

Owing to its complication in analysis and constraints estimation, the analysis and simulation of the PV cell in the two-diode model is not so simple. To make it easier to study the following assumptions are considered: the $I_{DS} = I_{DS1} = I_{DS2}$ and $\frac{(C_1+C_2)}{p}) = 1$. By inputting the temperature and irradiance in Equations (3) and (5), the light current and diode saturation currents are estimated by using the constructor datasheet. By setting the values of ideality factors $C_1 = 1$ and $C_2 = 1.2$ yields the best suitable outcomes in the current-voltage curve of the PV cell module. These alterations make the two-diode model into its simplified form and therefore attractive for PV system simulation. In general, the constructor gives data of current at short circuit ($I_{SC}$), voltage at open circuit ($V_o$) and peak or maximum power ($P_{mpp}$). Now we will evaluate the current equation shown below for three conditions: current ($I_{SC}$) at short circuit, voltage ($V_o$) at open circuit, and peak or maximum power ($P_{mpp}$) point condition.

$$I = I_L - I_{D1} - I_{D2} - \frac{V_0 + IR_{SE}}{R_{SH}}$$

At the short circuit condition

$$\begin{aligned} &I = I_{SC,STC};\ V_0 = 0 \\ I_{SC,STC} &= I_{L,STC} - I_{D1,STC} - I_{D2,STC} - \frac{I_{SC,STC}R_{SE}}{R_{SH}} \end{aligned} \tag{6}$$

where, $I_{D1,STC} = I_{Ds1,STC}[(e^{\frac{I_{SC,STC}R_{SE}}{C_1 V_T N_{SE}}}) - 1]$ and $I_{D2,STC} = I_{Ds2,STC}[(e^{\frac{I_{SC,STC}R_{SE}}{C_2 V_T N_{SE}}}) - 1]$

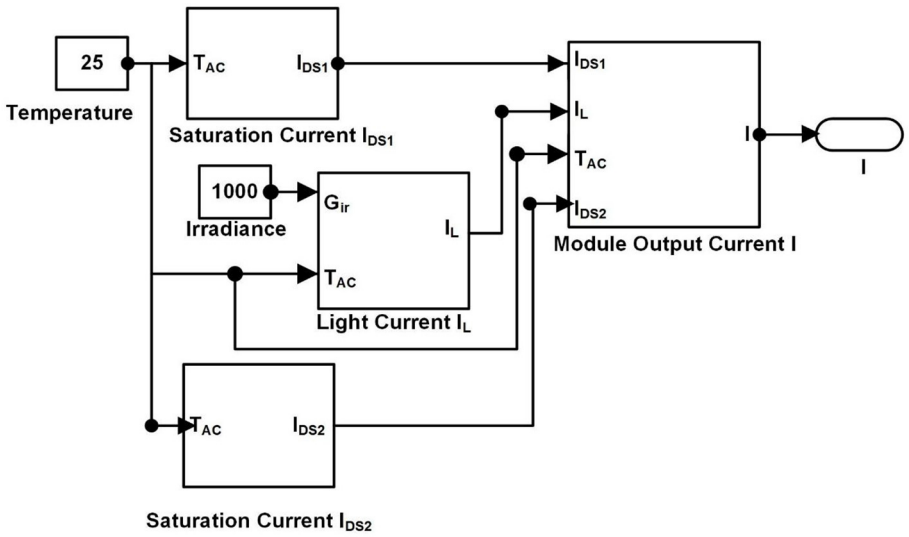


**FIGURE 4 |** Complete sub-system model of proposed two-diode photovoltaic (PV) model.

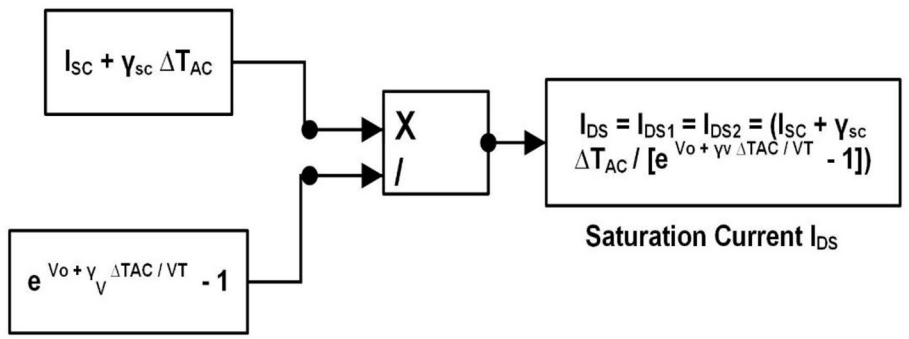


**FIGURE 5 |** Saturation current ($I_{DS}$) of proposed two-diode model.

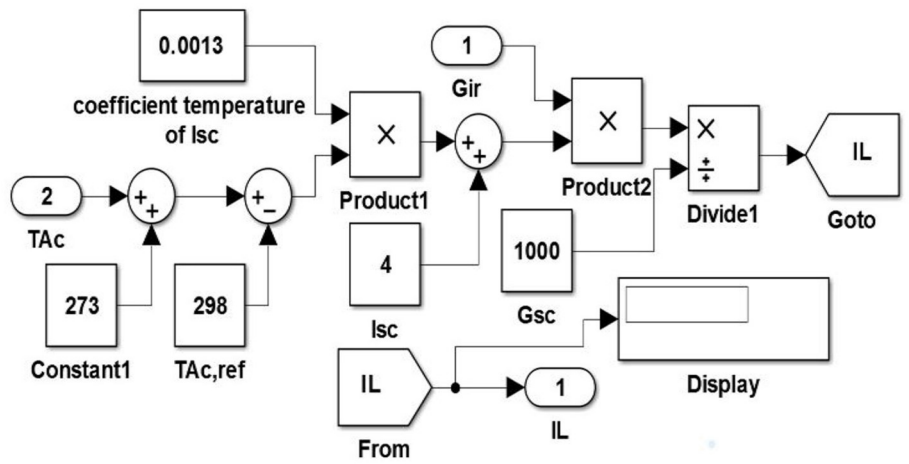


**FIGURE 6 |** Light current ($I_L$) of proposed two-diode model.

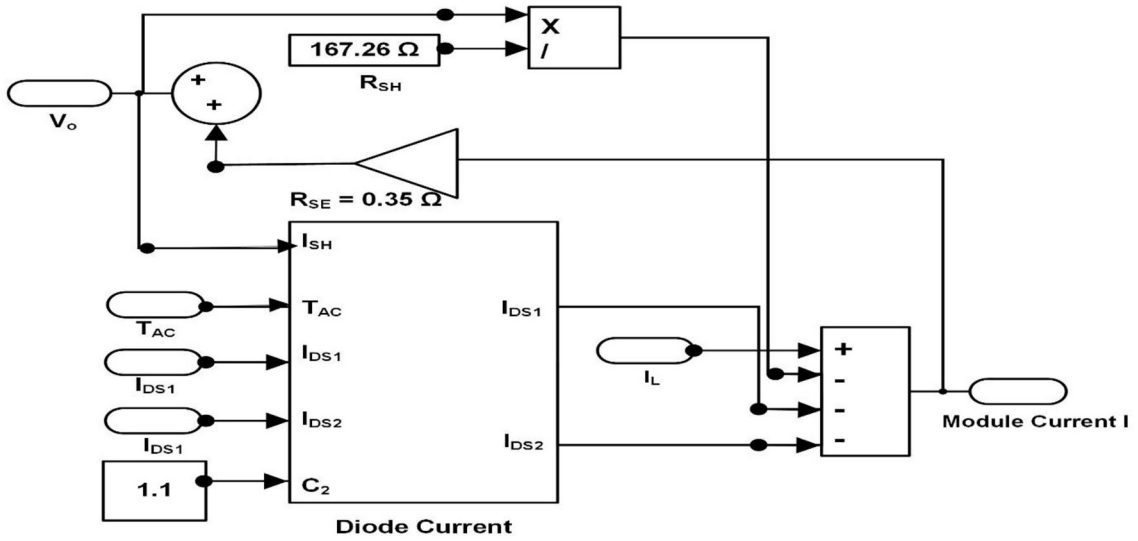


**FIGURE 7 |** Module output current (I) of proposed two-diode model.

**TABLE 1 |** Component specifications from constructor data sheet.

| Constraints | Mono-crystalline DS-A1-80 solar panel | Poly-crystalline Solarex MSX-64 |
|---|---|---|
| Maximum power ($P_{mpp}$) | 80 W | 64 W |
| Voltage at $P_{mpp}$ ($V_{mpp}$) | 17.2 V | 17.5 V |
| Current at $P_{mpp}$ ($I_{mpp}$) | 4.66 A | 3.66 A |
| Voltage at open circuit ($V_o$) | 21.3 V | 21.3 V |
| Current at short circuit ($I_{SC}$) | 5.29 A | 4 A |
| Series-connected cell ($N_{SE}$) | 36 | 36 |
| Voltage temperature coefficient ($\gamma_V$) | −0.38 V/°C | −80 mV/°C |
| Voltage temperature coefficient ($\gamma_{SC}$) | 0.13°C | 0.65°C |

**TABLE 2 |** Estimated values of proposed two-diode model.

| Constraints | Mono-crystalline DS-A1-80 solar panel | Poly-crystalline Solarex MSX-64 |
|---|---|---|
| Maximum power ($P_{mpp}$) | 80.08 W | 64.159 W |
| Voltage at $P_{mpp}$ ($V_{mpp}$) | 17.04 V | 17.46 V |
| Current at $P_{mpp}$ ($I_{mpp}$) | 4.69 A | 3.67 A |
| Voltage at open circuit ($V_o$) | 21.3 V | 21.3 V |
| Current at short circuit ($I_{SC}$) | 5.29 A | 4 A |
| Light current ($I_L$) | 5.29 A | 4.01 A |
| Saturation currents ($I_{DS1} = I_{DS2}$) | $5.207 \times 10^{-10}$ A | $3.937 \times 10^{-10}$ A |
| Series resistance ($R_{SE}$) | 0.34 Ω | 0.3 Ω |
| Shunt resistance ($R_{SH}$) | 157.22 Ω | 160.4 Ω |

At the open circuit condition

$$I = 0;\ V_0 = V_{o,STC}$$
$$0 = I_{L,STC} - I_{D1,STC} - I_{D2,STC} - \frac{V_{o,STC}}{R_{SH}} \quad (7)$$

From Equation (7)

$$I_{L,STC} = I_{D1,STC} + I_{D2,STC} + \frac{V_{o,STC}}{R_{SH}} \quad (8)$$

where $I_{D1,STC} = I_{Ds1,STC}[(e^{\frac{V_{o,STC}}{C_1 V_T N_{SE}}}) - 1]$ and $I_{D2,STC} = I_{Ds2,STC}[(e^{\frac{V_{o,STC}}{C_2 V_T N_{SE}}}) - 1]$

At the maximum power condition

$$I_{mpp,STC} = I_{L,STC} - I_{D1,STC} - I_{D2,STC} - \frac{V_{mpp,STC} + I_{mpp,STC}R_{SE}}{R_{SH}} \quad (9)$$

**TABLE 3 |** Estimated values of one-diode $R_{SH}$ model.

| Constraints | Mono-crystalline DS-A1-80 solar panel | Poly-crystalline Solarex MSX-64 |
|---|---|---|
| Maximum power ($P_{mpp}$) | 80.07 W | 63.55 W |
| Voltage at $P_{mpp}$ ($V_{mpp}$) | 16.61 V | 17.46 V |
| Current at $P_{mpp}$ ($I_{mpp}$) | 4.67 A | 3.64 A |
| Voltage at open circuit ($V_o$) | 21.3 V | 21.3 V |
| Current at short circuit ($I_{SC}$) | 5.29 A | 4 A |
| Light current ($I_L$) | 5.28 A | 4.01 A |
| Saturation currents ($I_{DS1} = I_{DS2}$) | $2.423 \times 10^{-8}$ A | $1.82 \times 10^{-8}$ A |
| Diode ideality factor (C) | 1.2 | 1.2 |
| Series resistance ($R_{SE}$) | 0.22 Ω | 0.2 Ω |
| Shunt resistance ($R_{SH}$) | 282.33 Ω | 310 Ω |

**TABLE 4 |** Comparison of estimated values at maximum power ($P_{mpp}$) of the two-diode model and one-diode ($R_{SH}$) model for a mono-crystalline (DS-A1-80) solar cell.

| Constraints | Manufacturer aata at STC | Two-diode model | One-diode ($R_{SH}$) model | % relative error of two-diode model | % relative error of one-diode model |
|---|---|---|---|---|---|
| Maximum power ($P_{mpp}$) | 80 W | 80.08 W | 80.07 W | 0.099 | 0.087 |
| Voltage at $P_{mpp}$ ($V_{mpp}$) | 17.2 V | 17.04 V | 16.61 V | 0.938 | 3.552 |
| Current at $P_{mpp}$ ($I_{mpp}$) | 4.66 A | 4.69 A | 4.67 A | 0.639 | 0.214 |
| Voltage at open circuit ($V_o$) | 21.3 V | 21.3 V | 21.3 V | 0.00 | 0.00 |
| Current at short circuit ($I_{SC}$) | 5.29 A | 5.29 A | 5.29 A | 0.00 | 0.00 |

**TABLE 5 |** Comparison of estimated values at maximum power ($P_{mpp}$) of the two-diode model and one-diode ($R_{SH}$) model for a poly-crystalline solar cell (MSX-64).

| Constraints | Manufacturer data at STC | Two-diode model | One-diode ($R_{SH}$) model | % relative error of two-diode model | % relative error of one-diode model |
|---|---|---|---|---|---|
| Maximum power ($P_{mpp}$) | 64 W | 64.159 W | 63.55 W | 0.247 | 0.708 |
| Voltage at $P_{mpp}$ ($V_{mpp}$) | 17.5 V | 17.47 V | 17.47 V | 0.171 | 0.171 |
| Current at $P_{mpp}$ ($I_{mpp}$) | 3.66 A | 3.67 A | 3.64 A | 0.272 | 0.549 |
| Voltage at open circuit ($V_o$) | 21.3 V | 21.3 V | 21.3 V | 0.00 | 0.00 |
| Current at short circuit ($I_{SC}$) | 4 A | 4 A | 4 A | 0.00 | 0.00 |

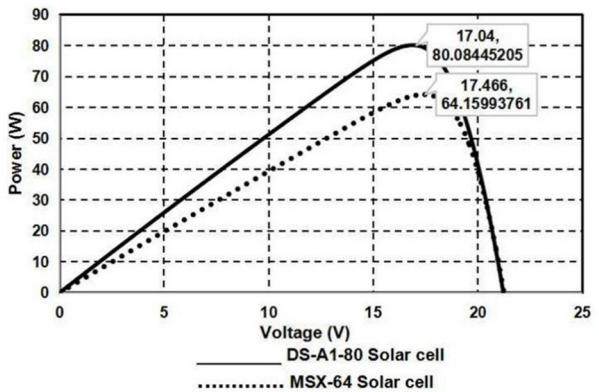


**FIGURE 8 |** Power (W) vs. voltage (V) curve of proposed two-diode model for DS-A1-80 and MSX-64 at STC (25°C and 1,000 KW/m$^2$).

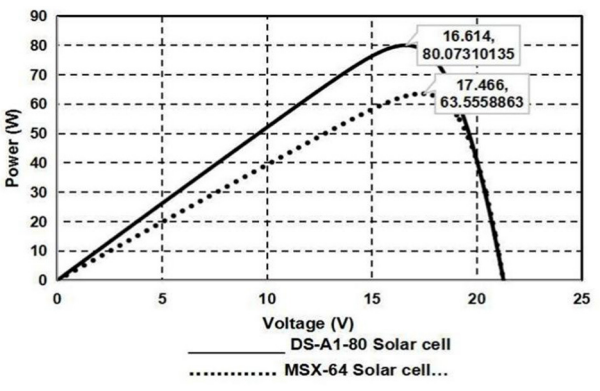


**FIGURE 9 |** Power (W) vs. voltage (V) curve of one-diode $R_{SH}$ for DS-A1-80 and MSX-64 at STC (25°C and 1,000 KW/m$^2$).

From Equation (12)

$$\frac{V_{mpp,STC} + I_{mpp,STC}R_{SE}}{R_{SH}} = I_{L,STC} - I_{D1,STC} - I_{D2,STC} - I_{mpp,STC}$$

$$R_{SH} = \frac{V_{mpp,STC} + I_{mpp,STC}R_{SE}}{I_{L,STC} - I_{D1,STC} - I_{D2,STC} - I_{mpp,STC}} \quad (10)$$

where $P_{mpp}$ is the peak or maximum power, $V_{mpp,STC}$ is the voltage at $P_{mpp}$, and $I_{mpp,STC}$ is the current at $P_{mpp}$, diode saturation currents at the maximum power condition is given by the relation as shown below:

$$I_{D1,STC} = I_{Ds1,STC}[(e^{\frac{V_{mpp,STC} + I_{mpp,STC}R_{SE}}{C_1 V_T N_{SE}}}) - 1]$$

$$I_{D2,STC} = I_{Ds2,STC}[(e^{\frac{V_{mpp,STC} + I_{mpp,STC}R_{SE}}{C_2 V_T N_{SE}}}) - 1]$$

## Determination of $R_{SE}$ and $R_{SH}$ Constraints

Several analytical and numerical approaches [3, 6, 7, 9, 13–15] have been proposed in the literature to evaluate the constraints of one-diode and two-diode models. In this analysis the constraints $R_{SE}$ *and* $R_{SH}$ are estimated by the same method as described previously [9]. By using effective iteration process the value of $R_{SE}$ *and* $R_{SH}$ can be estimated with the help of Equation (10). The main takeaway is that the value of $R_{SE}$ *and* $R_{SH}$ are selected such that calculated power $P_{mpp}$ must be equal to experimental power provided by the constructor data sheet $P_{mpp,STC}$. This iteration procedure initiates from $R_{SE} = 0$ which must vary in directive until it matches the calculated maximum power of $P_{mpp,STC}$, and simultaneously $R_{SH}$ is calculated.

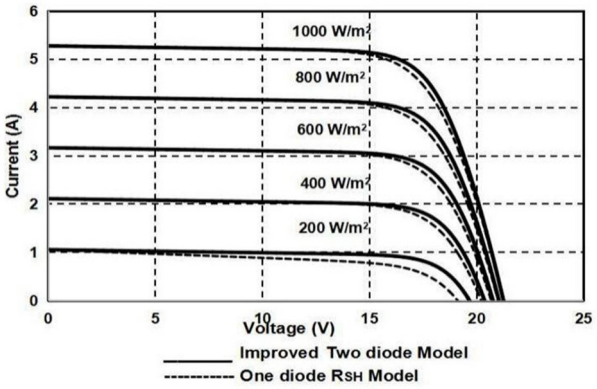


**FIGURE 10 |** Comparative analysis of current (A) vs. voltage (V) curve for one-diode $R_{SH}$ and proposed two-diode model for DS-A1-80 with different irradiance points at STC (25°C).

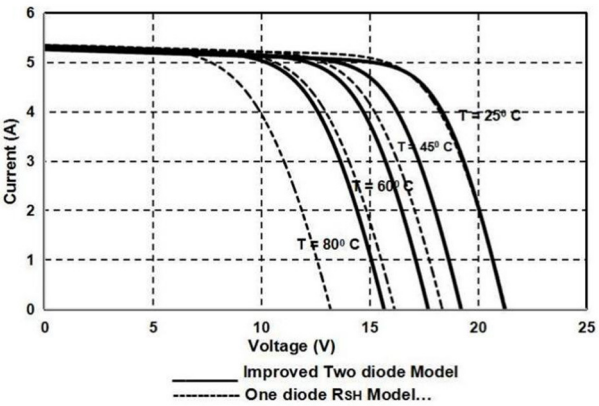


**FIGURE 11 |** Comparative analysis of current (A) vs. voltage (V) curve for one-diode $R_{SH}$ and proposed two-diode model for DS-A1-80 with different temperature points at STC (1,000 KW/m$^2$).

## SIMULATION OF PROPOSED TWO-DIODE MODEL

The complete sub-system group model of the proposed two-diode photovoltaic (PV) module is represented in **Figure 4**. By using Equations (2)–(5), detailed simulation models were developed in MATLAB/Simulink. The simulation block diagram of diode saturation current is represented in **Figure 5**, light current is represented in **Figure 6**, and module output current is represented in **Figure 7**. The component specifications of both mono-crystalline and poly-crystalline PV modules are shown in **Table 1**. **Table 2** illustrates the determined values of the proposed two-diode model and **Table 3** shows the constraints for the one-diode $R_{SH}$ model. **Tables 4**, **5** summarize the study of relative error of $P_{mpp}$, $V_{mpp}$, $I_{mpp}$, $V_o$, and $I_{SC}$ of both mono and poly-crystalline solar cells. The proposed two-diode model actually requires only four constraints because saturation current $I_{DS1} = I_{DS2} = I_{DS}$ whereas $C_1 = 1$, $C_2$ is chosen >1.2 and the value of $p$ is recommended to be a value larger than 2.2 [12].

## SIMULATION RESULTS AND DISCUSSION

The modeling technique characterized in this work is confirmed by measured constraints of certain photovoltaic (PV) cell modules. Two different PV modules; mono-crystalline DS-A1-80[1] and poly-crystalline MSX-64[2] are employed for verification. We can observe that the calculated values slightly deviate from the manufacturer data sheet value at STC. However, the poly-crystalline (MSX-64) cell exactly fits the manufacturer data for the proposed two-diode model. **Figures 8**, **9** characterize the power vs. voltage curve of $R_{SH}$ and the proposed two-diode model for mono-crystalline and poly-crystalline solar cells at STC. Comparative analysis of the current vs. voltage curve of $R_{SH}$ and the proposed two-diode model for the DS-A1-80 solar cell at various temperatures and irradiance levels are represented in **Figures 10**, **11**. Comparative analysis of the current vs. voltage curve of $R_{SH}$ and proposed two-diode model for the MSX-64 solar cell at various temperatures and irradiance levels are represented in **Figures 12**, **13**. From the results we can observe that both models exhibited the same performance at STC. However, the proposed two-diode model showed better performance compared to the $R_{SH}$ model precisely at lesser irradiance levels especially for open circuit voltage**.** The comparison of estimated values at maximum power ($P_{mpp}$) of the two-diode model and one-diode ($R_{SH}$) model for mono-crystalline (DS-A1-80) and poly-crystalline (MSX-64) solar cells are shown in **Tables 4**, **5**.

## CONCLUSION

For a quick and consistent photovoltaic module design, an effective, fast, and exact simulator is crucial to examine the performance of the photovoltaic cell under a partial or quick variation of temperature and irradiance. The most prevalent modeling strategy is to apply an equivalent (electrical) circuit that encompasses both non-linear and linear mechanisms. In the proposed work, an improved typical two-diode system aimed at photovoltaic cell modules was developed. Distinct from past photovoltaic modules recommended by many researchers, the developed work only needed the calculation of four constraints. A modest and fast iterative technique was used to estimate $R_{SE}$ and $R_{SH}$ resistances. The accuracy of the developed model was examined by using experimental data provided by the constructors of two different photovoltaic cell modules. Its performable behavior was compared with one-diode $R_{SH}$ models. It was observed that the proposed two-diode model had improved performance specifically at open circuit voltage and short circuit current and maximum power point conditions irrespective of variations in temperature and irradiance. Specifically, it showed better performance and accuracy at lesser irradiance situations. The proposed model was validated for mono-crystalline and poly-crystalline solar cells under standard test conditions.

[1]Available online at: http://www.posharp.com/ds-a1-80-solar-panel-from-anji-dasol-solarenergysciencetechnology_p462201154d.aspx (accessed January 31, 2021).

[2]Available online at: https://www.solarelectricsupply.com/media/custom/upload/Solarex-MSX64.pdf (accessed January 31, 2021).

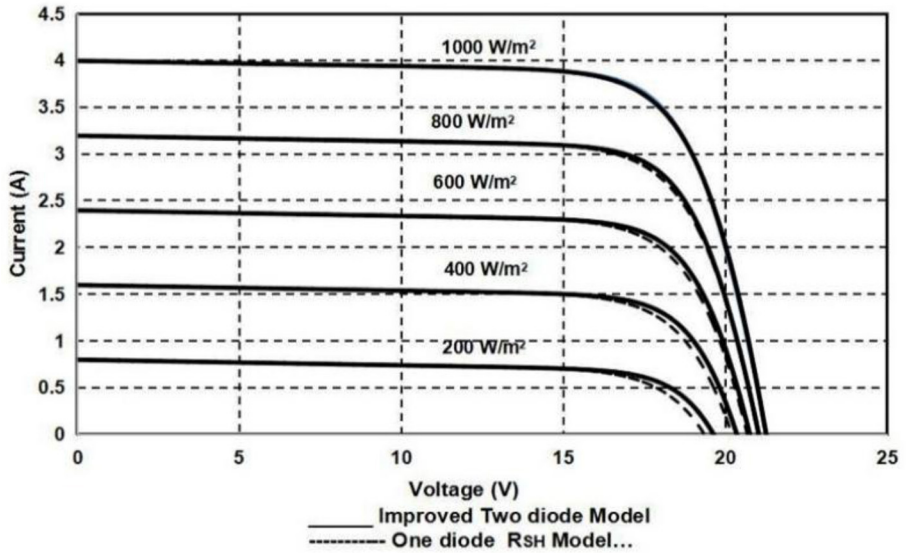


**FIGURE 12 |** Comparative analysis of current (A) vs. voltage (V) curve for one-diode $R_{SH}$ and proposed two-diode model for MSX-64 with different irradiance points at STC (25°C).

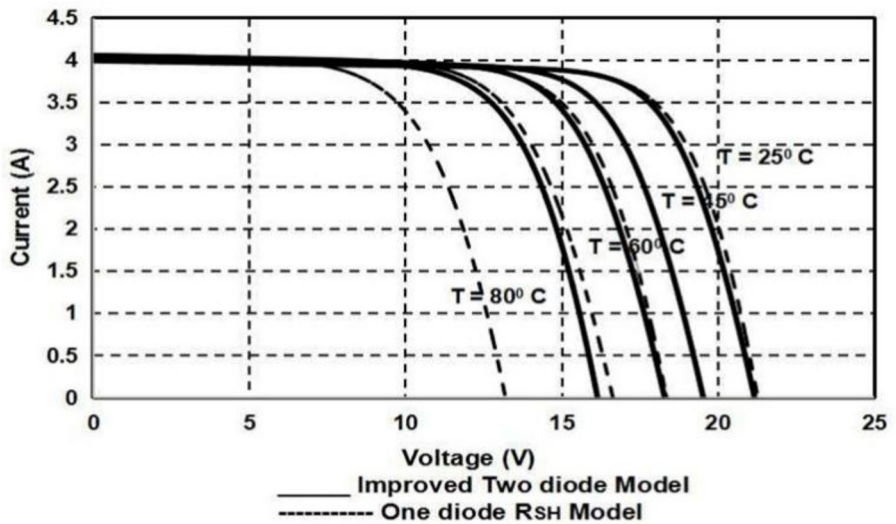


**FIGURE 13 |** Comparative analysis of current (A) vs. voltage (V) curve for one-diode $R_{SH}$ and proposed two-diode model for MSX-64 with different temperature points at STC (1,000 KW/m$^2$).

## DATA AVAILABILITY STATEMENT

The original contributions presented in the study are included in the article/supplementary material, further inquiries can be directed to the corresponding author/s.

## AUTHOR CONTRIBUTIONS

All authors listed have made a substantial, direct and intellectual contribution to the work, and approved it for publication.

## REFERENCES


1. Khanna V, Das BK, Bisht D, Singh PK. A three-diode model for industrial solar cells and estimation of solar cell parameters using PSO algorithm. *Renew Energy.* (2015) 78:105–13. doi: 10.1016/j.renene.2014.12.072
2. Shannan NM, Yahaya NZ, Singh B. Single-diode and two-diode model of PV modules: A comparison. In: *IEEE International Conference on Gontrol System, Computing and Emerging* (Penang). (2013). p. 210–4.
3. Lo Brano V, Orioli A, Ciulla G, Di Gangi A. An improved five-parameter model for photovoltaic modules. *Solar Energy Mater Solar Cell.* (2010) 94:1358–70. doi: 10.1016/j.solmat.2010.04.003
4. Chenni R, Makhlouf M, Kerbache T, Bouzid A. A Detailed modeling method for photovoltaic cells. *Energy.* (2007) 32:1724–30. doi: 10.1016/j.energy.2006.12.006
5. Sera D, Teodorescu R, Rodriguez P. PV panel model based on datasheet values. In: *Proceedings of the IEEE International Symposium on Industrial Electronics (ISIE)* (Vigo). (2007). p. 2392–6.
6. Singh P, Ravindra NM. Analysis of series and shunt resistance in silicon solar cells using single and double exponential models. *Emerg Mater Res.* (2011) 1:33–8. doi: 10.1680/emr.11.00008
7. AlRashidi MR, AlHajri MF, El-Naggar KM, Al-Othman AK. A new estimation approach for determining the I–V characteristics of solar cells. *Solar Energy.* (2011) 85:1543–50. doi: 10.1016/j.solener.2011.04.013
8. Chih-Tang S, Noyce RN, Shockley W. Carrier generation and recombination in p–n junctions and p–n junction characteristics. *Proceedings of IRE, Vol. 90.* (1957) 45:1228–43. doi: 10.1109/JRPROC.1957.278528
9. Villalva MG, Gazoli JR, Filho ER. Comprehensive approach to modeling and simulation of photovoltaic arrays. *IEEE Transact Power Electron.* (2009) 24:1198–208. doi: 10.1109/TPEL.2009.2013862
10. Salam Z, Ishaque K, Taheri H. An improved two-diode photovoltaic (PV) model for PV system. In: *International Conference on Power Electronics, Drives and Energy Systems (PEDES) Power India* (New Delhi). (2010). p. 1–5.
11. Mcintosh K, Pietro Altermatt P, Heiser G. Depletion-region recombination in silicon solar cells: when does m_DR = 2? In: *Proceeding of the 16th European Photovoltaic Solar Energy Conference* (Glasgow). (2000). p. 251–4.
12. Chin VJ, Salam Z, Ishaque K. Cell modelling and model parameters estimation techniques for photovoltaic simulator application: a review. *Appl Energy.* (2015) 154:500–19. doi: 10.1016/j.apenergy.2015.05.035
13. Alonso-Gracia MC, Ruiz JM, Chenlo F. Experimental study of mismatch and shading effects in I-V characteristics of a PV module. *Solar Energy Mater Solar Cells.* (2006) 90:329–40. doi: 10.1016/j.solmat.2005.04.022
14. Hejri M, Mokhtari H, Azizian MR, Ghandhari M, Söder L. On the parameter extraction of five parameter double-diode model of photovoltaic cell and modules. *IEEE J Photovolt Cells.* (2014) 4:915–23. doi: 10.1109/JPHOTOV.2014.2307161
15. Sulyok G, Summhammer J. Extraction of a photovoltaic cell's double-diode model parameters from data sheet values. *Energy Sci Eng.* (2018) 6:424–36. doi: 10.1002/ese3.216


**Conflict of Interest:** The authors declare that the research was conducted in the absence of any commercial or financial relationships that could be construed as a potential conflict of interest.

frontiers in Physics

ORIGINAL RESEARCH
published: 03 November 2021
doi: 10.3389/fphy.2021.770752

# Exploring Optimality of Piecewise Polynomial Interpolation Functions for Lung Field Modeling in 2D Chest X-Ray Images

*Rohit Kumar*, Subrata Bhattacharya and Govind Murmu*

*Department of Electronics Engineering, Indian Institute of Technology (ISM), Dhanbad, India*

In this paper, a landmark based approach, using five different interpolating polynomials (linear, cubic convolution, cubic spline, PCHIP, and Makima) for modeling of lung field region in 2D chest X-ray images have been presented. Japanese Society of Radiological Technology (JSRT) database which is publicly available has been used for evaluation of the proposed method. Selected radiographs are anatomically landmarked using 17 and 16 anatomical landmark points to represent left and right lung field regions, respectively. Local, piecewise polynomial interpolation is then employed to create additional semilandmark points to form the lung contour. Jaccard similarity coefficients and Dice coefficients have been used to find accuracy of the modeled shape through comparison with the prepared ground truth. With the optimality condition of three intermediate semilandmark points, PCHIP interpolation method with an execution time of 5.04873 s is found to be the most promising candidate for lung field modeling with an average Dice coefficient (DC) of 98.20 and 98.54% (for the left and right lung field, respectively) and with the average Jaccard similarity coefficient (JSC) of 96.47 and 97.13% for these two lung field regions. While performance of Makima and cubic convolution is close to the PCHIP with the same optimality condition, i.e., three intermediate semilandmark points, the optimality condition for the cubic spline method is of at least seven intermediate semilandmark points which, however, does not result in better performance in terms of accuracy or execution time.

**Keywords: cubic convolution, cubic spline, Makima, PCHIP, piecewise polynomial, chest X-ray, linear interpolation, lung shape modeling**

OPEN ACCESS

***Edited by:***
*Santosh Kumar,*
*Liaocheng University, China*

***Reviewed by:***
*Sushank Chaudhary,*
*Quanzhou Institute of Equipment manufacturing, (CAS), China*
*Sneha Kumari,*
*Indian Institute of Technology Patna, India*
*Anurag Singh,*
*IIIT Naya Raipur, India*

****Correspondence:***
*Rohit Kumar*
*rohit148@gmail.com*

***Specialty section:***
*This article was submitted to Optics and Photonics, a section of the journal Frontiers in Physics*

***Received:*** *04 September 2021*
***Accepted:*** *13 September 2021*
***Published:*** *03 November 2021*

***Citation:***
*Kumar R, Bhattacharya S and Murmu G (2021) Exploring Optimality of Piecewise Polynomial Interpolation Functions for Lung Field Modeling in 2D Chest X-Ray Images. Front. Phys. 9:770752. doi: 10.3389/fphy.2021.770752*

## 1 INTRODUCTION

The chest X-ray imaging is still one of the most preferred techniques that radiologists and medical practitioners use to diagnose the lung diseases in their daily routine checkups due to its low cost and easy availability. Due to this reason, the accurate detection and segmentation of the lung field region are of prime importance for any biomedical image analysis procedures [1–3]. Delineation of the lung field is a prerequisite for any chest-image analysis procedure. However, delineation is a very tedious and time-consuming procedure that may be prone to subjective bias. Therefore, an automated solution for the lung field segmentation is needed [4]. The development of an automated solution for the lung field segmentation is challenging due to intensity variations across the edges and overlapping of the other anatomical structures. As chest X-rays are low contrast images, the lung regions cannot be differentiated from the background and hence the classical approaches

like thresholding and edge detection algorithms are not sufficient enough for the lung field segmentation. The author in Ref. [5] provided an intuitive method to solve this problem by representing a shape as a set of discrete labeled points and referred to these points as landmarks. Each labeled point represents a particular part of the shape or its boundary and captures certain distribution in the shape space. But in practice, it is very time-consuming. Labeling a set of landmark points to model a shape in the shape space is referred as point distribution model (PDM) [6,7]. The modeled shape takes a considerable amount of landmark points to form a curve. Thus, the point distribution model inevitably reduces the number of points that may use to represent a shape. Clearly, these labeled sets or the number of landmark points do not represent any salient feature of anatomical significance, but a part of the curve or boundary of the anatomical shape. However, this method (PDM) has some undesirable consequences. First, users are forced to put many landmark points to smooth out the curve in every training example. Second, the landmark points may lose their characteristics as true landmark point as they do not represent any salient feature of the object. The above said problem can be minimized by taking only a few landmark points that must characterize some anatomical significance of the lung field region. These significant anatomical landmark points are then interpolated to get a close approximation of the original lung field shape. The accurate delineation of the lung field requires the anatomical knowledge of chest radiography to incorporate the expected shape that may work as a priori information in active shape modeling (ASM).

To delineate the lung fields, the author in Ref. [8] used 50 landmark points for the left lung and 44 landmark points for the right lung representation. They also used 26 landmark points for the heart shape representation and a pair of 23 landmark points for the left and right clavicle's (left and right) representation. Each object and landmark point was defined by manual annotation, and no interpolation method was employed. The author in Ref. [9] proposed a lung segmentation methodology by capturing salient points around the lung fields by subsequent application of simple intensity and edge feature extraction techniques. The detected salient points are then interpolated using Bezier curves to approximate the lung field boundaries. In Ref. [10], Shao et al. presented a joint shape and appearance sparse learning method to segment out lung field from the chest radiographs. They used a total of 14 labeled points (6 for the right lung and 8 for the left lung) to get a rough idea of both the lung regions. They termed these labeled sets as "landmarks." Few more points were also annotated between these landmark points, and they termed these labeled sets as "points." However, the authors did not provide any information about the number of points they used to represent the lung field regions. The author in Ref. [11] presented a customized active shape model to extract the lung regions from the chest X-ray images. They employed an average active shape model, gray scale projection, and affine registration to obtain the initial lung contours. After that, an objective function is defined to push the vertices of the active shape model to the real lung edges to get a more balanced distance distribution of vertices. They used 44 and 50 landmark points to represent the left and the right lung regions for the lung field segmentation. The annotated set of landmark points was manually defined and interpolation was not employed. The author in Ref. [12] presented an automatic lung field segmentation method using an improved statistical shape and appearance model. They used 6 landmark points to locate each lung region and then applied a gray-level intensity based method to locate and initialize the lung shape model. They used the intensity profile model to create boundary landmark points and later these landmark points were interpolated by a cubic spline interpolation method. In Ref. [13], the authors used the set of labeled points to train their algorithm for the automatic lung field segmentation using active shape modeling (ASM) in the single-photon emission computerized tomography (SPECT) images and validated this automatic SPECT segmentation against computed tomography (CT) images as well as manually delineated SPECT images. But the method does not explain the type of interpolation mechanism that they used. In Ref. [14], the authors used 144 annotated boundary points (72 per left/right lung) to construct a statistical shape model of the lung field. Specifically, they used six manually annotated primary landmark points based on the appearance of the lung field and then secondary landmarks were estimated along the lung contour using interpolation between the manually annotated primary landmarks. However, it is noted that the other anatomical structures that overlap with the lung field region were not excluded in their method, and the type of the interpolation method was not defined. All these authors used the landmark selection method to segment out lung field regions from the chest radiographic images. However, these authors could not explain the number of interpolating points (secondary landmarks) that is needed to approximate the lung field regions with the highest similarity index.

The landmarking method is also employed to delineate other anatomical structures like the heart, liver, femur, etc., in CT, SPECT, and other medical imaging techniques. The authors in Ref. [15] reported a general multi-resolution framework for the statistical modeling of multi-object structures. The authors in Ref. [16] proposed a dual active shape model for the segmentation of heart's right ventricle (RV) boundary. The authors in Ref. [17] presented an automatic liver segmentation method using the shape modeling methods in computed tomography (CT) images. The authors in Ref. [18] used landmark based method for extracting prostate boundaries from the 2D transrectal ultrasound (TRUS) images by using a partial active shape model (PASM). The authors in Ref. [16] introduced an ASM-based framework for motion correction of myocardial T1 mapping in magnetic resonance imaging (MRI). Clearly, landmarking is the first stage of any automated computer aided diagnostic (CAD) system that tries to identify the anatomical region. The landmark based method's major strength is that it represents a shape as a set of discrete labeled points. The landmark based method is highly applicable for the cases where the visibility of the boundary is obscured or cannot be differentiated from the background, which is always the case of low contrast imaging like X-ray and ultrasound imaging. The landmark based point distribution model finds numerous applications in active shape modeling

(ASM), active appearance modeling, deep learning (DL), and machine learning (ML) models for the registration and segmentation applications in medical imaging. However, there are some limitations of this method that preclude their accurate clinical application. The model based methods assume that the shape information and intensity information between the training images and the new image to be segmented are similar to each other. Unfortunately, this assumption can often be invalid due to the variability of the lung's anatomy among the individuals in the application stages.

In this paper, a set of landmark points based on the anatomical properties of the left lung region and right lung field regions are explored. Our contributions in this paper are 1) identification of the number of anatomical landmark points in the thorax region for the left and right lung field modeling, 2) identification of the optimality condition of each of the interpolating polynomial to model left and right lung field region, and 3) identification of the most suited interpolating polynomial that models the left and right lung field region with highest similarity index by producing least number of secondary landmark points. Exploring the optimality of piecewise polynomials has an added advantage over selecting a random number of semilandmark points. It minimizes the number of interpolating points and hence reduces the computational complexity of the processing algorithm. Knowing the minimum number of interpolating points is highly beneficial in real-time medical imaging applications requiring less computational complexity. However, one disadvantage of landmark based study is that the number of available landmark points can sometimes be insufficient to capture the shape of an object.

The remainder of this paper is organized as follows: **Section 2** provides the mathematical foundation of the lung shape modeling and **Section 3** discusses the interpolation methods that mainly highlight the different categories of piecewise cubic interpolating polynomial that we have used in this literature. **Section 4** discusses the methods under which the images are landmarked, and, finally, **Section 5** and **Section 6** discuss the simulation results and conclusion, respectively.

## 2 LUNG SHAPE MODELING

Let each shape in the training set be represented by a set of $K$ number of landmark positions that must be consistent from one shape to the next. Here, the consistency employs that each particular landmark point must be placed on the same site as it was on the first image. That means, each particular landmark point represents a specific location of the lung field boundary.

To model a lung field shape, let each annotated landmark point be represented by the coordinate position $(x_j, y_j)$ in the two dimensional space $\mathbb{R}^2$. If each shape is annotated by $K$ number of landmark points, then the modeled shape in terms of coordinate positions for the $i$th shape is defined by [19]

$$S_i = (x_{ij}, y_{ij}); \quad where \;\; j = [1 \cdots K] \tag{1}$$

These coordinate position $S_i = ((x_{i1}, y_{i1}), (x_{i2}, y_{i2}), \ldots, (x_{ik}, y_{ik}))$ in a shape vector form can be represented as

$$\mathbf{S_i} = \left[\mathbf{x_{i1}}, \mathbf{y_{i1}}, \mathbf{x_{i2}}, \mathbf{y_{i2}}, \ldots, \mathbf{x_{ik}}, \mathbf{y_{ik}}\right] \tag{2}$$

that is further rearranged as a set of $2K$ vector:

$$\mathbf{S_i} = \left[\mathbf{x_{i1}}, \mathbf{x_{i2}}, \ldots, \mathbf{x_{ik}}, \mathbf{y_{i1}}, \mathbf{y_{i2}}, \ldots, \mathbf{y_{ik}}\right]^{\mathbf{T}} \tag{3}$$

$$or \;\; \mathbf{S_i} = \left[\mathbf{S_{ix}}, \mathbf{S_{iy}}\right]^{\mathbf{T}} \in \mathbb{R}^{2K\times 1} \tag{4}$$

where

$$\mathbf{S_{ix}} = [\mathbf{x_{i1}}, \mathbf{x_{i2}}, \ldots, \mathbf{x_{ik}}] \in \mathbb{R}^{K\times 1} \tag{5}$$

$$\mathbf{S_{iy}} = [\mathbf{y_{i1}}, \mathbf{y_{i2}}, \ldots, \mathbf{y_{ik}}] \in \mathbb{R}^{K\times 1} \tag{6}$$

If there are $L$ number of training examples, then the configuration matrix $S \in \mathbb{R}^{2K\times L}$ can be written as

$$\mathbf{S} = [\mathbf{S_1}, \mathbf{S_2}, \ldots, \mathbf{S_L}] \in \mathbb{R}^{2K\times L} \tag{7}$$

## 3 INTERPOLATION METHODS

Modeling or building a shape requires the function to be continuous. This creates a real problem if the modeling function consists of a set of discrete data points (landmark points). Therefore, it requires to construct a continuous function based on discrete data points. Here, an attempt is made to examine different interpolation techniques that fit the shape in a continuous manner from a set of discrete landmark points. Interpolation helps to construct a continuous function from a set of discrete data points. It is to be noted that, these interpolation techniques [20] only provide the conditions under which the lung field regions are modeled. The methods do not provide any solution to the explained techniques.

Given $K$ number of landmark points $(x_j, y_j)$ in the 2D-plane $\mathbb{R}^2$, the interpolating polynomial is defined as

$$P(x_j) = y_j; \qquad j = (1, \ldots, k) \tag{8}$$

where $x = (x_1, \ldots, x_k)$ are the interpolation points and $P(x_j)$ is the interpolating polynomial of the landmark point $(x_1, y_1)$, $(x_2, y_2)$, $\ldots$, $(x_k, y_k)$. Solving a fitting polynomial $P(x_j)$ that fits the landmark point $(x_j, y_j)$ is equivalent to solving a system of linear equation

$$\mathbf{AS_{ix}} = \mathbf{S_{iy}} \tag{9}$$

where $\mathbf{A}$ is a Vandermonde matrix.

### 3.1 Piecewise Polynomial Interpolation

A quite natural and different approach to approximate a function on an interval is to first split the interval into subintervals and then approximate the function by a polynomial of fairly low degree on each subinterval.

Given $K$ number of landmark point $(x_j, y_j) \in \mathbb{R}^2$ with the condition $x_1 < x_2 < \cdots < x_k$, the one dimensional piecewise interpolant in terms of piecewise function can be defined as

$$P(x) = P_j(x), \qquad x \in \left[x_j, x_{j+1}\right] \tag{10}$$

where $P_j(x)$ is at least continuous everywhere in $[x_j, x_{j+1}]$. Continuity condition should hold at every data point,

$$P_j(x_{j+1}) = P_{j+1}(x_{j+1}) \tag{11}$$

A piecewise polynomial function is defined as

$$P_j(x) = \sum_{r=1}^{k} a_r^j \left(x - x_j\right)^r \tag{12}$$

Hence, the piecewise polynomial interpolation problem is to determine the coefficients $a_r^j$ for all of the intervals such that the resulting interpolant has desirable properties.

## 3.2 Linear Interpolation

Piecewise linear interpolation [21] is by far the most popular interpolation technique that finds numeral application in signal and image processing due to its faster performance.

If $t$ is the local variable given by $t = x - x_j$, $x \in [x_j, x_{j+1}]$, then the divided difference $\delta_j$ is

$$\delta_j = \frac{y_{j+1} - y_j}{x_{j+1} - x_j}; \qquad j = 1 \cdots (k-1) \tag{13}$$

The piecewise linear interpolation is then piecewise straight lines connecting two consecutive points of the interval $(x_j, x_{j+1})$. The interpolant in the interval $(x_j, x_{j+1})$ is then

$$P(x) = y_j + \left(x - x_j\right)\frac{y_{j+1} - y_j}{x_{j+1} - x_j} \tag{14}$$

or

$$P(x) = y_j + t\delta_j \tag{15}$$

clearly, this equation represents a function of straight line that passes through the landmark positions $(x_j, y_j)$ and $(x_{j+1}, y_{j+1})$.

## 3.3 Cubic Convolution Interpolation

The cubic convolution interpolation [22–24] function is obtained by imposing certain conditions on the interpolation kernel. The kernel is mainly composed of piecewise cubic polynomials defined over the unit subintervals [−2, 2].

For equally spaced data, the interpolation function can be defined as

$$P(x_j) = \sum c_j u\left(\frac{x - x_j}{h}\right); \qquad j = 1, 2, \ldots, k \tag{16}$$

where $c_j$ are the coefficients to be determined and depend on the sampled data, $u_j$ is the kernel basis function, and $h$ is the sampling interval. The cubic convolution interpolation is obtained by setting certain conditions on the kernel to maximize the accuracy. Keys [22] defined the cubic convolution interpolation kernel in terms of piecewise cubic polynomials over the subintervals (−2, −1), (−1, 0), (0, 1), and (1, 2). Outside this interval, the interpolation kernel is assumed to be zero. By imposing this condition, the number of data samples that evaluates the interpolation function is reduced to four. Therefore, the kernel $u$ will have the form:

$$u(s) = \begin{cases} (a+2)|s^3| - (a+3)|s|^2 + 1, & 0 \le |s| \le 1 \\ a|s|^3 - 5a|s|^2 + 8a|s| - 4a, & 1 \le |s| \le 2 \\ 0, & 2 \le |s| \end{cases} \tag{17}$$

with $u(0) = 1$ and $u(n) = 0$ where $n$ is a nonzero integer. As $h$ is the sampling interval between two nodes, the difference between the two interpolating nodes say $x_j$ and $x_r$ will be $(j—r)h$. Now, if $x$ is substituted by $x_j$ in **Equation 16**, then **Eq. 16** will take the form:

$$P(x_j) = \sum c_j u(j - r); \qquad j = 1, 2, \ldots, k \tag{18}$$

Now, if $x_r = x_{j+1}$, then **Eq. 19** will have the form:

$$P(x_j) = \sum c_j u(j - (j+1)); \qquad j = 1, 2, \ldots, k \tag{19}$$

## 3.4 Cubic Spline Interpolation

Among the spline functions, the cubic spline functions [25–28] are the most preferred functions. The cubic spline functions fit the data very smoothly. More importantly, they do not have an oscillatory behavior that is common for higher order degree polynomials associated with interpolation, as the cubic Lagrange interpolation polynomial produce. A cubic spline is defined by

$$Q_4(x) = a_j + b_j x + c_j x^2 + d_j x^3 \tag{20}$$

where $x_{j-1} \le x \le x_j$ for $j = 1, 2, \ldots, K$.

Clearly, the above equation contains four unknowns for each spline, $a_j$, $b_j$, $c_j$, and $d_j$, for a total of $4K$ unknowns over the whole interval.

The cubic spline interpolation must have a second order derivative and should satisfy the continuity condition

$$P_j''\left(x_{j+1}\right) = P_{j+1}''\left(x_{j+1}\right) \tag{21}$$

over the interval $[x_j, x_{j+1}]$. This requires that $P(x_j)$, $P'(x_j)$, and $P''(x_j)$ are continuous over the interval $[x_j, x_{j+1}]$. To find the interpolating function, the coefficients $a_j$, $b_j$, $c_j$, and $d_j$ must be determined for each of the cubic function. For $K$ number of landmark points, there will be $(-1)$ cubic functions and each cubic function requires four coefficients. Hence, there is a total of $4(K–1)$ unknowns. So, to get all the coefficients $4(K–1)$, independent equations are required. To get these coefficients, certain conditions need to be assumed. The first two conditions for each spline are as follows:

1) The piecewise cubic function $Q(x)$ must intersect each and every landmark data points (left and right). This requires

$$Q(x_j) = y_j, j = 1, \ldots, (K-1) \tag{22}$$

2) Moreover, $Q(x)$ must be continuous on the interval $[x_1, x_k]$ which conclude that each sub-function must join at the landmark data points, i.e.,

$$Q_j(x_j) = Q_{j-1}(x_j), j = 1, \ldots, (K-1) \tag{23}$$

These two assumptions give 2($K$–1) equations. As each cubic function has to join smoothly to its nearest neighbors, the first and second derivatives are constrain to be continuous.

3) $Q'(x)$ must be continuous on the interval $[x_1, x_k]$ to make the curve smooth across the interval, i.e.,

$$Q'_j(x_j) = Q'_{j-1}(x_j), j = 1, \ldots, (K-2) \tag{24}$$

4) $Q"(x)$ will be continuous on the interval $[x_1, x_k]$. Therefore,

$$Q''_j(x_j) = Q''_{j+1}(x_j), j = 1, \ldots, (K-3) \tag{25}$$

which gives us 2($K$–2) equations. Hence, we get a total of (4$K$–2) equations and is therefore under-determined. In order to get a cubic spline function, two other conditions must be imposed to get 4$K$ equations.

As our purpose is to get a closed contour of the lung field, the following periodic constraints are imposed (also known as periodic conditions).

5)

$$Q'_1(x_1) = Q'_{k-1}(x_k) \tag{26}$$

6)

$$Q''_1(x_1) = Q''_{k-1}(x_1) \tag{27}$$

## 3.5 Piecewise Cubic Hermite Interpolation

Piecewise cubic Hermite interpolation polynomial (PCHIP) [29,30] is a third order polynomial which has a shape preserving characteristic by matching only the first order derivatives at the data points with their neighbors (before and after) [31]. This characteristic makes it differ from the cubic spline function.

If $h_j$ is the length of $j$th subinterval given by

$$h_j = x_{j+1} - x_j \tag{28}$$

then the divided difference $\delta_j$ will be

$$\delta_j = \frac{y_{j+1} - y_j}{h_j} \tag{29}$$

If $\zeta_j$ is the slope of the interpolant at $x_j$, then

$$\zeta_j = P'(x_k) \tag{30}$$

In shape preserving PCHIP function, the idea is to restrict the overshoot locally by determining the slope $d_j$.

It is to be noted that, if $\delta_j$ and $\delta_{j-1}$ are of opposite signs or either of the term is zero, then $x_j$ will be a discrete local minimum or discrete local maximum. So, we constrain the $\zeta_j$ to be zero, i.e., $\zeta_j$ = 0, and, if $\delta_j$ and $\delta_{j-1}$ are of the same sign and are of the same interval size, then $\zeta_j$ is calculated using harmonic mean

$$\frac{1}{\zeta_j} = \frac{1}{2}\left(\frac{1}{\delta_{j-1}} + \frac{1}{\delta_j}\right) \tag{31}$$

However, if $\delta_j$ and $\delta_{j-1}$ are of the same sign but of different interval lengths, the $\delta_j$ will be a weighted harmonic mean lead by the expression

$$\frac{w_1 + w_2}{\zeta_k} = \frac{w_1}{\delta_{j-1}} + \frac{w_2}{\delta_j} \tag{32}$$

where $w_1 = 2h_j + h_{j-1}$ and $w_2 = h_j + 2h_{j-1}$.

## 3.6 Makima Piecewise Cubic Hermite Interpolation

The Akima interpolation [32] between the interval $[x_j, x_{j+1}]$ mimimizes the wiggling by selecting the derivatives as a linear combination of nearest slopes

$$\zeta_j = \frac{|\delta_{j+1} - \delta_j|\delta_{j-1} + |\delta_{j-1} - \delta_{j-2}|\delta_j}{|\delta_{j+1} - \delta_j| + |\delta_{j-1} - \delta_{j-2}|} \tag{33}$$

where $\delta_j = \frac{y_{j+1}-y_j}{x_{j+1}-x_j}$ is the slope of the interval $[x_j, x_{j+1}]$.

For any landmark point $x_j$, the Akima takes five neighbors landmark point $x_{j-2}$, $x_{j-1}$, $x_j$, $x_{j+1}$, and $x_{j+2}$ to calculate the Akima derivative. However, the Akima interpolant function suffers from two major problems. First, if lower and upper slopes become equal, i.e., $\delta_{j-2}$ =, $\delta_{j-1}$, and $\delta_j = \delta_{j+1}$, both the numerator and denominator become zero and hence Akima derivative will have no solution. Second, the Akima interpolant produces overshoot or undershoot when the data are constant for the two consecutive nodes. To overcome these two problems, a modified Makima interpolation was introduced [33].

To avoid these two conditions, **Eq. 33** is later modified to

$$\zeta_j = \frac{w_1}{w_1 + w_2}\delta_{j-1} + \frac{w_2}{w_1 + w_2}\delta_j \tag{34}$$

where

$$w_1 = \frac{|\delta_{j+1} - \delta_j| + |\delta_{j+1} + \delta_j|}{2} \tag{35}$$

and

$$w_2 = \frac{|\delta_{j-1} - \delta_{j-2}| + |\delta_{j-1} + \delta_{j-2}|}{2} \tag{36}$$

Clearly, $\zeta_j = 0$ when $\delta_j = \delta_{j+1} = 0$, i.e., $\zeta_j = 0$ when $y_j = y_{j+1} = y_{j+2}$ and hence the conditions prevent the equation from an overshoot or undershoot in case of constant data for more than two consecutive nodes [34].

# 4 METHODS

In our method, the radiographs which are anatomically similar in all aspects are chosen to study the performance of the different interpolating polynomials in modeling of the lung field region. A publicly available JSRT dataset [35] has been used to study performance of each interpolating polynomial.

1) JSRT dataset: this dataset contains 247 posteroanterior (PA) chest X-ray images compiled by the Japanese Society of Radiological Technology (JSRT). Out of the 247 chest X-ray images, set of 154 images has lung nodules (100 malignment cases, 54 benign cases) and set of 93 images has no lung nodules. These images are of the size of 2048 × 2048 pixels with a gray scale

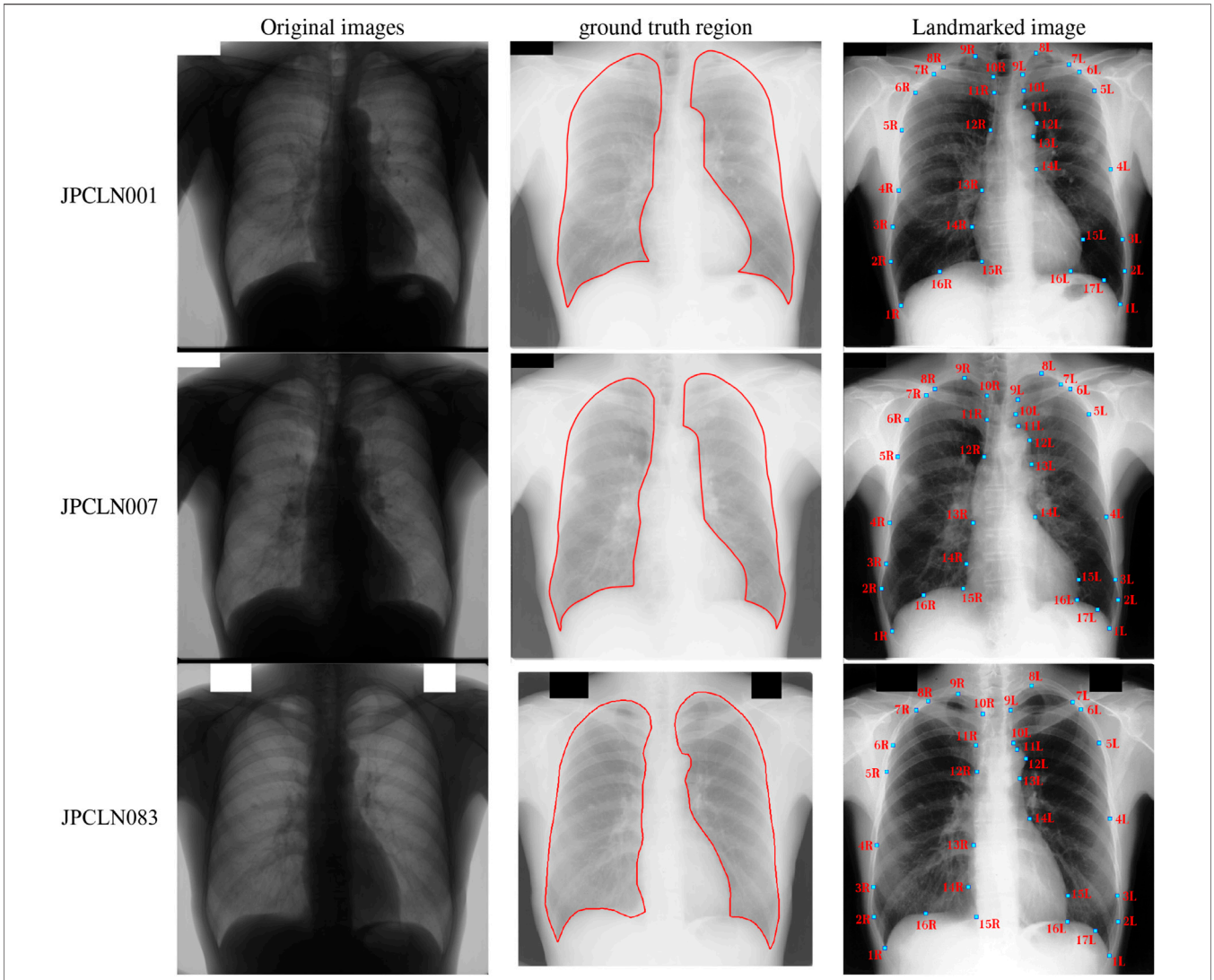


**FIGURE 1 |** Selected images from JSRT dataset, ground truth of the left and right lung field regions, and the placement of manually annotated anatomical landmark points after negative transformation.

color depth of 12 bits and a pixel spacing of 0.175 mm in the horizontal and vertical directions.

The selected posteroanterior (PA) chest X-ray images are first downsampled to a pixel size of 512 × 512. A negative transformation is then applied to highlight the lung field regions. The images are then annotated using 17 anatomical landmark points for the left lung and 16 landmark points for the right lung field region, as shown in **Figure 1**. The ground truth of the lung field regions are prepared for the selected set of images to compare the performance of different interpolating polynomials. The annotation of the ground truth is done by a clinical radiologist using the Image Segmenter application present in the Image Processing and Computer Vision toolbox in the MATLAB R2018b. The annotation is done by tracing the curve around the lung field regions in the Image Segmenter application. The landmark points defined for the left lung region are grouped into the set of left costal edge (1L–5L), left apical region (5L, 6L, 8L, 9L, and 10L), descending aorta/aortic arc (11L–14L), heart's left ventricle boundary (14L–16L) and the left hemidiaphragm (16L, 17L and 1L) for the left lung region. Similarly, the landmark points defined for the right lung are grouped into the set of right coastal edge (1R–6R), right apical region (6R, 7R, 9R, 10R, and 11R), superior vena cava (11R–13R), heart's right ventricle boundary (13R–15R), and right hemidiaphragm (15R, 16R, and 1R) for the right lung field region. Here, the landmark points 7L and 9L are used to represent the left clavicle in combination with the landmark points 6L and 10L. Similarly, the landmark points 8R and 10R in combination with 7R and 11R are used to represent the right clavicle region. These two regions, the left clavicle and the right clavicle (each of which includes four landmark points), are included mainly for the study of landmark based post-processing. It may be noted here that the region above the lung apices, region below the hemidiaphragms, and the

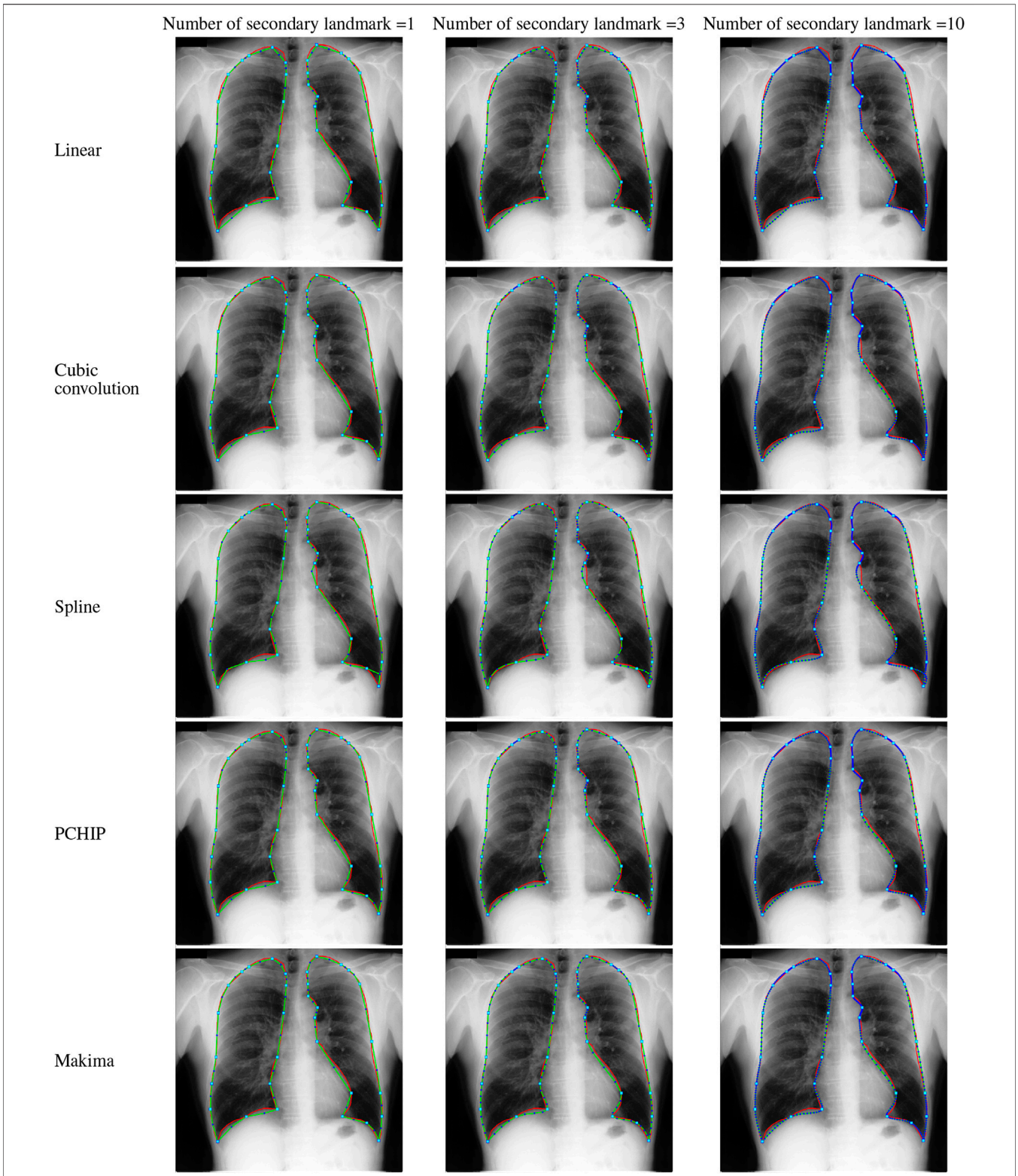


**FIGURE 2 |** Lungs region formation: ground truth (red) and the modeled shape (green) using different interpolating polynomials with 1, 3, and 10 intermediate semilandmark point(s) of the selected image dataset JPCLN001.

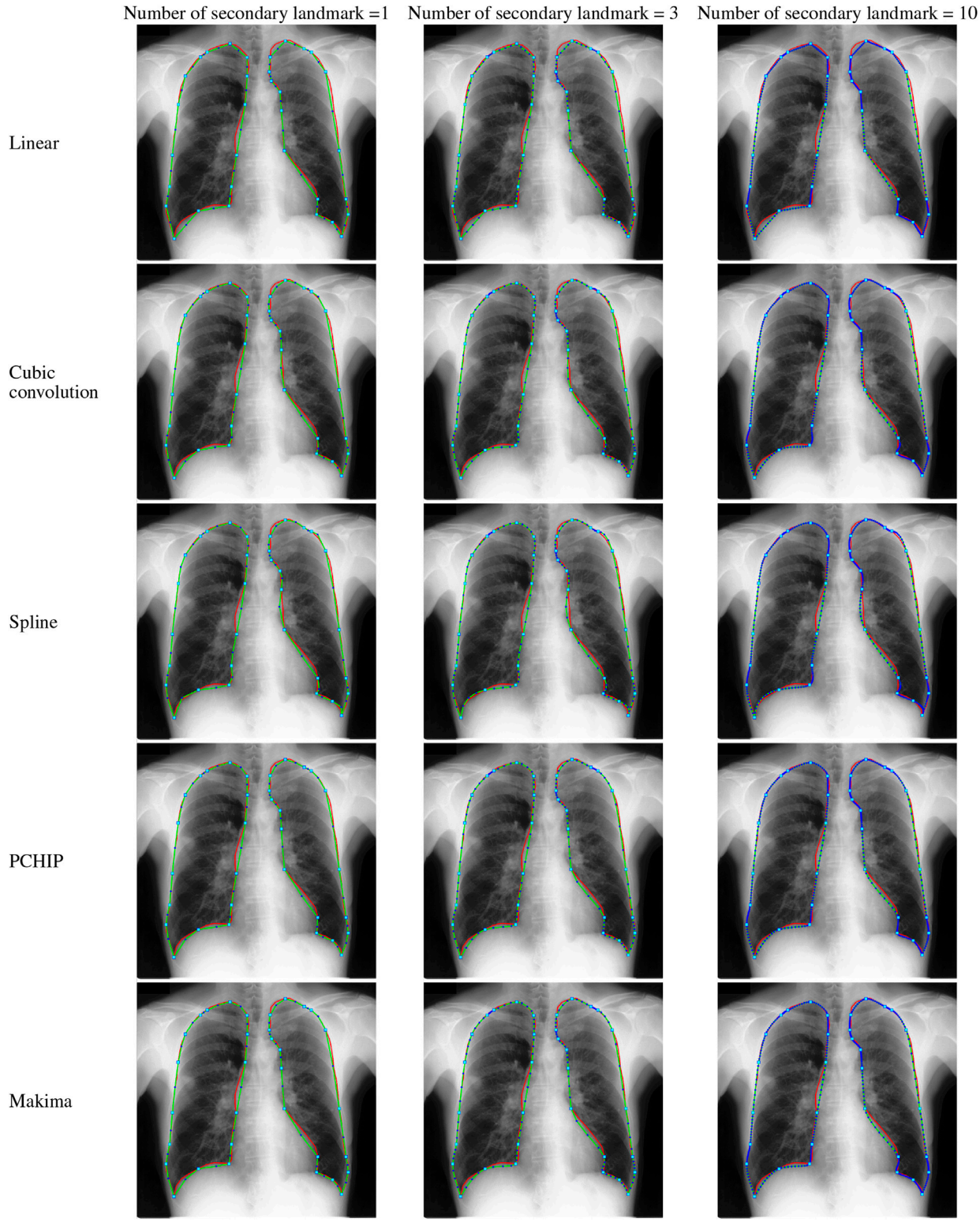


**FIGURE 3 |** Lungs region formation: ground truth (red) and the modeled shape (green) using different interpolating polynomials with 1, 3, and 10 intermediate semilandmark point(s) of the selected image dataset JPCLN007.

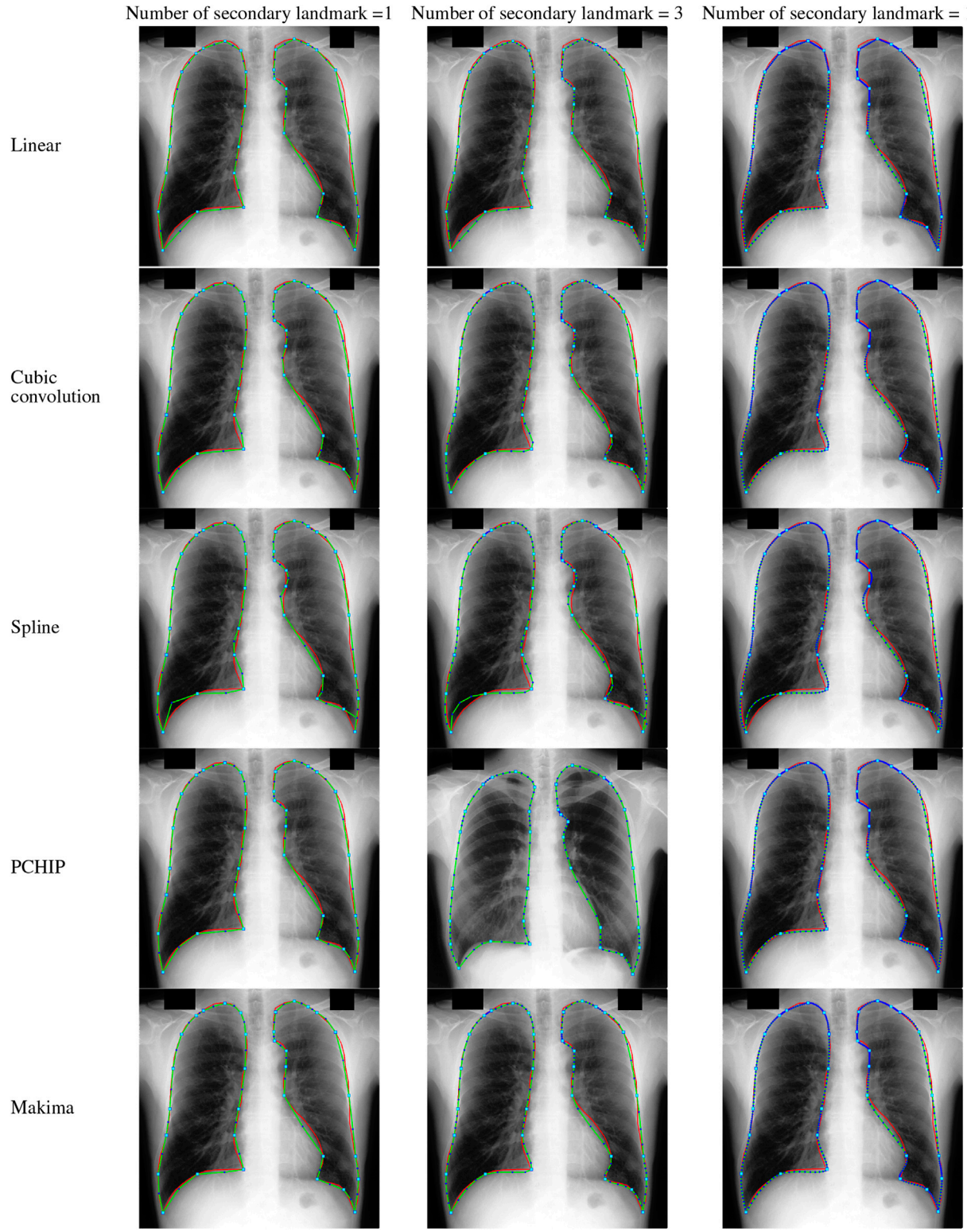


**FIGURE 4 |** Lungs region formation: ground truth (red) and the modeled shape (green) using different interpolating polynomials with 1, 3, and 10 intermediate semilandmark point(s) of the selected image dataset JPCLN083.

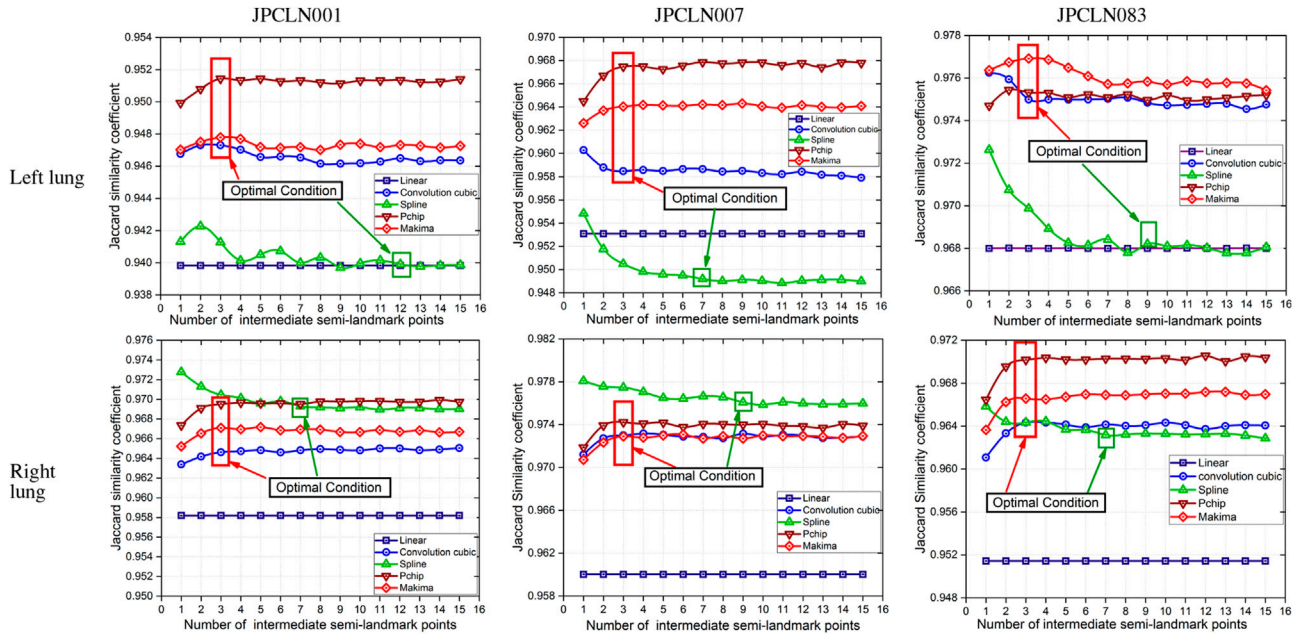


**FIGURE 5 |** Jaccard similarity coefficients of the modeled shape with different piecewise polynomial interpolation methods of the left and right lung field regions of the image datasets JPCLN001, JPCLN007, and JPCLN083.

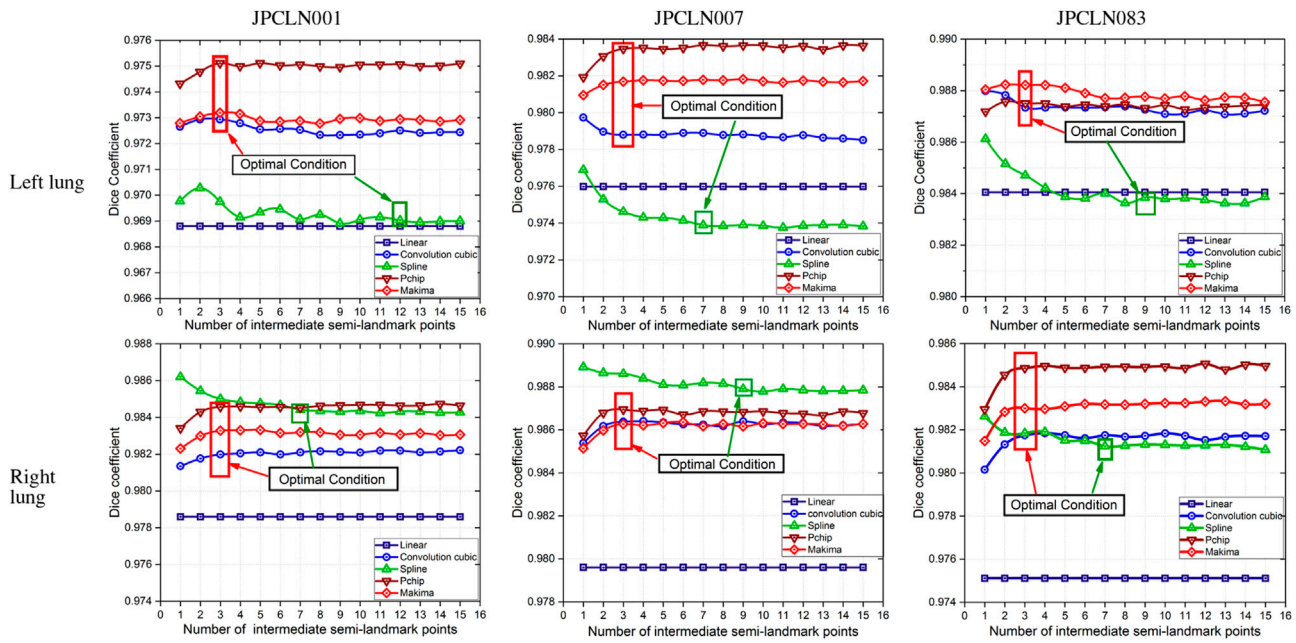


**FIGURE 6 |** Dice similarity coefficients of the modeled shape with different piecewise polynomial interpolation methods of the left and right lung field regions of the image datasets JPCLN001, JPCLN007, and JPCLN083.

mediastinum that encloses the heart, superior vena cava, descending aorta, etc., are not included in the present study. A side by side comparison of one lung region to the other gives important information about the shape dissimilarity like lung's contraction or expansion that helps to analyze different lung diseases [36,37]. Subdividing these regions into different segments may give a better analysis of the diseases. To make these regions independent, the lung regions can be subdivided into three different regions, namely, the apex and medial and lower regions, by defining few co-linear landmark points at the

**TABLE 1 |** Jaccard's and Dice's coefficients of different interpolation schemes with their optimality condition.

| Sl. No. | Interpolation type | No. of intermediate semilandmarks to meet optimality condition | Image dataset | | | | | | | | | | | |
|---|---|---|---|---|---|---|---|---|---|---|---|---|---|---|
| | | | JPCLN001 | | | | JPCLN007 | | | | JPCLN083 | | | |
| | | | Left lung | | Right lung | | Left lung | | Right lung | | Left lung | | Right lung | |
| | | | JSC | DC | JSC | DC | JSC | DC | JSC | DC | JSC | DC | JSC | DC |
| 1 | Linear | NA | 0.9396 | 0.9689 | 0.9581 | 0.9786 | 0.9528 | 0.9758 | 0.9601 | 0.9796 | 0.9685 | 0.9840 | 0.9513 | 0.9751 |
| 2 | Cubic Convolution | 3 | 0.9471 | 0.9728 | 0.9645 | 0.9819 | 0.9590 | 0.9790 | 0.9728 | 0.9862 | 0.9755 | 0.9876 | 0.9635 | 0.9814 |
| 3 | Cubic Spline | ≥7 | 0.9400 | 0.9691 | 0.9695 | 0.9845 | 0.9493 | 0.9740 | 0.9765 | 0.9881 | 0.9683 | 0.9839 | 0.9632 | 0.9812 |
| 4 | PCHIP | 3 | 0.9514 | 0.9751 | 0.9694 | 0.9845 | 0.9675 | 0.9835 | 0.9742 | 0.9869 | 0.9753 | 0.9875 | 0.9702 | 0.9849 |
| 5 | Makima | 3 | 0.9478 | 0.9732 | 0.9671 | 0.9833 | 0.9640 | 0.9817 | 0.9729 | 0.9863 | 0.9763 | 0.9880 | 0.9666 | 0.9830 |

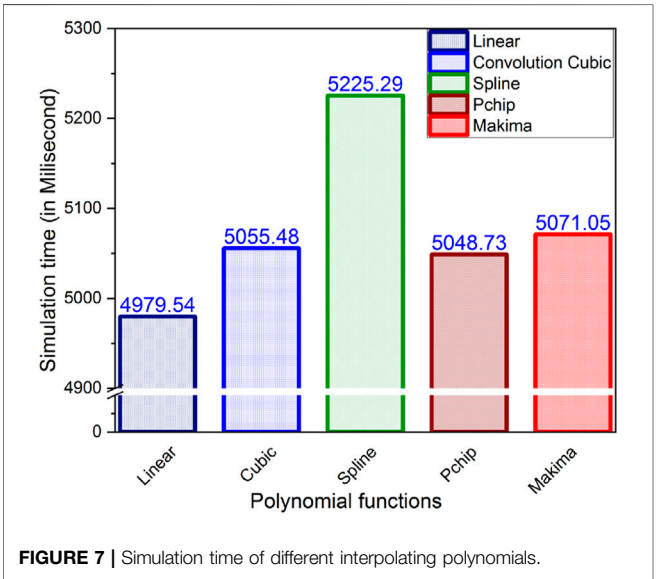


**FIGURE 7 |** Simulation time of different interpolating polynomials.

coastal edges. To fulfil these criteria, the landmark points 2L, 3L, 4L, and 5L that belong to the left coastal edge are made co-linear with the landmark points 16L, 15L, 14L, and 10L, respectively. Similarly, the landmark points 2R, 3R, 4R, 5R, and 6R that belonging to the right coastal edge are made co-linear with the landmark points 15R, 14R, 13R, 12R, and 11R, respectively.

## 4.1 Evaluation Metrics

In order to compare the different interpolation techniques, two different performance measures, namely, Jaccard similarity coefficient and Dice similarity coefficient [38], are used that evaluate the quality of delineation and interpolation.

1) Jaccard similarity coefficient (JSC): the Jaccard similarity coefficient or Jaccard index (J) between the ground truth shape and the interpolated shape is defined as

$$J = \frac{|S_{IS} \cap S_{GT}|}{|S_{IS} \cup S_{GT}|} \tag{37}$$

2) Dice coefficient (DC): the Dice coefficient between the ground truth shape and interpolated shape is defined as

$$D = 2\frac{|S_{IS} \cap S_{GT}|}{|S_{IS}| + |S_{GT}|} \tag{38}$$

where $S_{GT}$ is the region enclosed by the ground truth shape and $S_{IS}$ is the region enclosed by the interpolated shape. The Jaccard coefficient and Dice coefficient between the two shape instances give us an idea of how similar the two sets are. The JSC and DC take a value between $[0, 1]$. The zero indicates that the two shape instances do not coincide with each other, whereas one indicates that the two shape instances completely coincide with each other.

3) Execution time: estimating the execution time often becomes mandatory when evaluating the performance of an algorithm. Knowledge about the execution time of program is of utmost importance in selecting an appropriate method that models the lung field shape within a specified amount of time. The polynomials that take a longer time than the specified amount of time cannot be preferred for the lung field modeling.

# 5 SIMULATION RESULT

In this work, five different interpolating polynomials are studied for the left and right lung field modeling using a set of discrete labeled points called anatomical landmark points. For this purpose, three similar radiographs from the publicly available JSRT dataset are selected. We identified and selected 17 anatomical landmark points for the left lung region and 16 anatomical landmark points for the right lung region in the selected set of images, as shown in **Figure 1**. As the selected landmark points are not sufficient to form the lung contour, piecewise interpolating polynomials are used to create additional intermediate semilandmark points between each pair of the consecutive landmark points. Our intention is to get a shape of highest similarity index by interpolating minimum number of the secondary landmark points (i.e., intermediate semilandmarks). Hence, an analysis is made to find a shape

of highest similarity index by interpolating a minimum number of intermediate semilandmark points. For this purpose, the piecewise interpolating polynomials are used for obtaining 1–15 intermediate semilandmark points between each pair of the consecutive landmark points. Performance of each interpolating polynomial is evaluated for intermediate semilandmarks—varying in number from 1 to 15—formed between each pair of the consecutive landmark points. **Figure 2** shows the lung shape modeling of the image data set JPCLN001 using selected interpolating polynomials with linear, cubic convolution, cubic spline, PCHIP, and Makima interpolation methods, respectively, using one, three, and ten intermediate semilandmark point(s). A similar attempt is also made to represent two other sets of images in **Figures 3**, **4** with the selected interpolating polynomials using one, three, and ten secondary landmark point(s). Here, red and green contours are used to represent ground truths and lung field boundaries obtained using different interpolating polynomials, respectively. Performance of each interpolation method is evaluated, for the left and right lung field modeling, against the number of intermediate semilandmark points, in terms of Jaccard similarity coefficient and Dice coefficient. **Figure 5** shows the performance of each interpolating polynomial in terms of Jaccard similarity coefficient and **Figure 6** is used to represent their performance in terms of Dice coefficient. A tabular form of the different interpolating polynomials for which Jaccard's and Dice's coefficients remain optimal with the minimum required condition is shown in **Table 1**. Here, optimality refers to a situation in which JSC and DC attain the best or most favorable value beyond which no such significant change is sought. The optimality condition refers to a condition that is required (in terms of the minimum number of intermediate semilandmark points between each consecutive anatomical landmark pair) for the JSC and DC to attain the best or most favorable value. The execution time of these interpolating polynomials is evaluated for the three intermediate semilandmark points and is shown and compared in **Figure 7**. The simulation work is carried out using MATLAB R2018b installed under the Fedora Linux kernel version 5.6.13-300.fc32.x86_64 in HP ENVY 15-k004tx Notebook PC with the configuration of 1.7 GHz Intel Core i5-4210U processor having Intel HD Graphics 4400 and 8 GB of RAM.

## 6 CONCLUSION

Here, we have presented an effective method of anatomical landmark point selection and their minimization and modeling of the lung field shape using five different interpolation techniques, namely, linear, cubic convolution, cubic spline, PCHIP, and Makima. Each interpolation method is applied locally with a certain number of intermediate semilandmark point(s) between each consecutive anatomical landmark pair. We measured and compared the modeling performance of each interpolation technique with the prepared ground truth in terms of Jaccard similarity coefficient (JSC) and Dice coefficient (DC). The modeled shape using linear interpolation method with an execution time of 4.97954 s ensures a shape of minimum similarity index (with an average JSC of 95.36 and 95.65% and with an average DC of 97.62 and 97.78% for the left and right lung fields, respectively) and has no impact of increasing the number of intermediate semilandmark points. Therefore, optimality condition for the linear interpolation method cannot be defined. However, for PCHIP and Makima interpolation methods, an incremental change in JSC and DC is observed as the number of intermediate semilandmark points between each consecutive anatomical landmark pair increases from one to three intermediate semilandmark point(s). As soon as the number of intermediate semilandmark points increases beyond three, no significant change in JSC and DC is observed. Hence, with a minimum of three intermediate semilandmark points, the JSC and DC reach the optimal value in case of PCHIP and Makima interpolation methods with an execution time of 5.04873 and 5.07105 s, respectively. The case with cubic convolution is no exception to this and here also the optimal values of JSC and DC are attained with a minimum of three intermediate semilandmark points with an execution time of 5.05548 s irrespective of the incremental or decremental change between one and three intermediate semilandmark point(s). The cubic spline method, however, does not follow the same trend and a gradual decrease or damping is observed in JSC and DC when the number of intermediate semilandmark points is below seven. The cubic spline method takes at least seven intermediate semilandmark points to produce an optimum result. From the experimentation, it is concluded that the PCHIP interpolation method is the most promising candidate for shape modeling of the lung field region with an average JSC of 96.47 and 97.13% and with an average DC of 98.20 and 98.54% for the left and right lung fields, respectively, with the optimality condition of three intermediate semilandmark points. The Makima interpolation method is not far behind and it modeled the shape with an average JSC of 96.27 and 96.87% and with an average DC of 98.10 and 98.42% for the left and right lung fields, respectively, with the optimality condition of three intermediate semilandmark points. The cubic convolution interpolation method takes an average JSC of 96.05 and 96.69% and average DC of 97.98 and 98.32% for the left and right lung field modeling, respectively, with the optimality condition of three intermediate semilandmark points. In contrary to the above stated methods that have the optimality condition of three intermediate semilandmark points, the cubic spline method takes an average JSC of 95.25 and 96.97% and an average DC of 97.56 and 98.46% for the left and right lung field modeling, respectively, with the optimality condition of at least seven intermediate semilandmark points. The cubic spline method remains the weakest candidate for the lung field modeling due to longer execution time of 5.22529 s for the three intermediate semilandmark points and the high optimality condition of at least seven intermediate semilandmark points.

## DATA AVAILABILITY STATEMENT

The original contributions presented in the study are included in the article/Supplementary Material; further inquiries can be directed to the corresponding author.

## AUTHOR CONTRIBUTIONS

RK and SB conceived of the presented idea. RK developed the theory and performed the computations. GM verified the analytical methods. SB investigated (a specific aspect) and supervised the findings of this work. All authors discussed the results and contributed to the final manuscript.

## ACKNOWLEDGMENTS

The authors would like to thank Dr. Rajeev Nayan, MD, Radiology, Relief Diagnostic Centre, Dhanbad, Jharkand (India), for the manual annotation and ground truth preparation of the image dataset.

## REFERENCES

1. Jaeger S, Karargyris A, Candemir S, Folio L, Siegelman J, Callaghan F, et al. Automatic Tuberculosis Screening Using Chest Radiographs. *IEEE Trans Med Imaging* (2013) 33:233–45. doi:10.1109/TMI.2013.2284099
2. Shariaty F, and Mousavi M. Application of CAD Systems for the Automatic Detection of Lung Nodules. *Inform Med Unlocked* (2019) 15:100173. doi:10.1016/j.imu.2019.100173
3. Cao W, Wu R, Cao G, and He Z. A Comprehensive Review of Computer-Aided Diagnosis of Pulmonary Nodules Based on Computed Tomography Scans. *IEEE Access* (2020) 8:154007–23. doi:10.1109/access.2020.3018666
4. Mittal A, Hooda R, and Sofat S. Lung Field Segmentation in Chest Radiographs: A Historical Review, Current Status, and Expectations from Deep Learning. *IET Image Process* (2017) 11:937–52. doi:10.1049/iet-ipr.2016.0526
5. Cootes TF, and Taylor CJ. Active Shape Models - 'Smart Snakes'. *BMVC* (1992) 266–75. doi:10.1007/978-1-4471-3201-1_28
6. Cootes TF, Taylor CJ, Cooper DH, and Graham J. Active Shape Models-Their Training and Application. *Computer Vis Image Understanding* (1995) 61: 38–59. doi:10.1006/cviu.1995.1004
7. Zheng G, Gollmer S, Schumann S, Dong X, Feilkas T, and González Ballester MA. A 2D/3D Correspondence Building Method for Reconstruction of a Patient-Specific 3D Bone Surface Model Using Point Distribution Models and Calibrated X-ray Images. *Med image Anal* (2009) 13:883–99. doi:10.1016/j.media.2008.12.003
8. van Ginneken B, Stegmann MB, and Loog M. Segmentation of Anatomical Structures in Chest Radiographs Using Supervised Methods: A Comparative Study on a Public Database. *Med Image Anal* (2006) 10:19–40. doi:10.1016/j.media.2005.02.002
9. Iakovidis DK, and Papamichalis G. Automatic Segmentation of the Lung Fields in Portable Chest Radiographs Based on Bazier Interpolation of Salient Control Points. In: *2008 IEEE International Workshop on Imaging Systems and Techniques*. IEEE (2008). p. 82–7.
10. Shao Y, Gao Y, Guo Y, Shi Y, Yang X, and Shen D. Hierarchical Lung Field Segmentation With Joint Shape and Appearance Sparse Learning. *IEEE Trans Med Imaging* (2014) 33:1761–80. doi:10.1109/TMI.2014.2305691
11. Wu G, Zhang X, Luo S, and Hu Q. Lung Segmentation Based on Customized Active Shape Model From Digital Radiography Chest Images. *J Med Imaging Hlth Inform* (2015) 5:184–91. doi:10.1166/jmihi.2015.1382
12. Li X, Luo S, Hu Q, Li J, Wang D, and Chiong F. Automatic Lung Field Segmentation in X-ray Radiographs Using Statistical Shape and Appearance Models. *J Med Imaging Hlth Inform* (2016) 6:338–48. doi:10.1166/jmihi.2016.1714
13. Cheimariotis G-A, Al-Mashat M, Haris K, Aletras AH, Jögi J, Bajc M, et al. Automatic Lung Segmentation in Functional SPECT Images Using Active Shape Models Trained on Reference Lung Shapes from CT. *Ann Nucl Med* (2018) 32:94–104. doi:10.1007/s12149-017-1223-y
14. Mansoor A, Cerrolaza JJ, Perez G, Biggs E, Okada K, Nino G, et al. A Generic Approach to Lung Field Segmentation From Chest Radiographs Using Deep Space and Shape Learning. *IEEE Trans Biomed Eng* (2019) 67:1206–20. doi:10.1109/TBME.2019.2933508
15. Cerrolaza JJ, Reyes M, Summers RM, González-Ballester MÁ, and Linguraru MG. Automatic Multi-Resolution Shape Modeling of Multi-Organ Structures. *Med image Anal* (2015) 25:11–21. doi:10.1016/j.media.2015.04.003
16. El-Rewaidy H, Nezafat M, Jang J, Nakamori S, Fahmy AS, and Nezafat R. Nonrigid Active Shape Model-Based Registration Framework for Motion Correction of Cardiac T1mapping. *Magn Reson Med* (2018) 80:780–91. doi:10.1002/mrm.27068
17. Spinczyk D, and Krasoń A. Automatic Liver Segmentation in Computed Tomography Using General-Purpose Shape Modeling Methods. *Biomed Eng Online* (2018) 17:65–13. doi:10.1186/s12938-018-0504-6
18. Pingkun Yan P, Sheng Xu S, Turkbey B, and Kruecker J. Discrete Deformable Model Guided by Partial Active Shape Model for TRUS Image Segmentation. *IEEE Trans Biomed Eng* (2010) 57:1158–66. doi:10.1109/tbme.2009.2037491
19. Kumar R. Analysis of Shape Alignment Using Euclidean and Manhattan Distance Metrics. In: 2017 International Conference on Recent Innovations in Signal processing and Embedded Systems. RISE IEEE (2017). p. 326–31. doi:10.1109/rise.2017.8378175
20. Lehmann TM, Gönner C, and Spitzer K. Survey: Interpolation Methods in Medical Image Processing. *IEEE Trans Med Imaging* (1999) 18:1049–75. doi:10.1109/42.816070
21. Blu T, Thévenaz P, and Unser M. Linear Interpolation Revitalized. *IEEE Trans Image Process* (2004) 13:710–9. doi:10.1109/TIP.2004.826093
22. Keys RG. Cubic Convolution Interpolation for Digital Image Processing. *IEEE Trans Acoust Speech, Signal Process* (1981) 29. doi:10.1109/tassp.1981.1163711
23. Zhou D, Dong W, and Shen X. Image Zooming Using Directional Cubic Convolution Interpolation. *IET Image Process* (2012) 6:627–34. doi:10.1049/iet-ipr.2011.0534
24. Meijering E, and Unser M. A Note on Cubic Convolution Interpolation. *IEEE Trans Image Process* (2003) 12:477–9. doi:10.1109/TIP.2003.811493
25. Hsieh Hou HS, and Andrews H. Cubic Splines for Image Interpolation and Digital Filtering. *IEEE Trans Acoust Speech, Signal Process* (1978) 26:508–17. doi:10.1109/TASSP.1978.1163154
26. Dyer SA, and Dyer JS. Cubic-Spline Interpolation. 1. *IEEE Instrum Meas Mag* (2001) 4:44–6. doi:10.1109/5289.911175
27. Abdul Karim SA, and Voon Pang K. Shape Preserving Interpolation Using Rational Cubic Spline. *J Appl Mathematics* (2016) 2016. doi:10.1155/2016/4875358
28. Karim S. Rational Cubic Spline Interpolation for Monotonic Interpolating Curve With C2 Continuity. *MATEC Web Conferences (EDP Sciences)* (2017) 131:4016. doi:10.1051/matecconf/201713104016
29. Fritsch FN, and Carlson RE. Monotone Piecewise Cubic Interpolation. *SIAM J Numer Anal* (1980) 17:238–46. doi:10.1137/0717021
30. McGregor G, and Nave J-C. Area-preserving Geometric Hermite Interpolation. *J Comput Appl Mathematics* (2019) 361:236–48. doi:10.1016/j.cam.2019.03.005
31. Rabbath CA, and Corriveau D. A Comparison of Piecewise Cubic Hermite Interpolating Polynomials, Cubic Splines and Piecewise Linear Functions for the Approximation of Projectile Aerodynamics. *Defence Technology* (2019) 15. doi:10.1016/j.dt.2019.07.016
32. Akima H. A New Method of Interpolation and Smooth Curve Fitting Based on Local Procedures. *J Acm* (1970) 17:589–602. doi:10.1145/321607.321609

33. Ionita C, and Moler C. Makima Piecewise Cubic Interpolation. *Cleve's Corner: Cleve Moler On Mathematics And Computing MATLAB & Simulink* (2019). (Accessed: Mar 10, 2020)
34. Moler CB. Numerical Computing with Matlab, Chapter: 3. Interpolation. Society for Industrial and Applied Mathematics (SIAM). Philadelphia. (Accessed: March 10, 2020), (2000) 93–116. doi:10.1137/1.9780898717952.ch3
35. Shiraishi J, Katsuragawa S, Ikezoe J, Matsumoto T, Kobayashi T, Komatsu K-i., et al. Development of a Digital Image Database for Chest Radiographs with and without a Lung Nodule. *Am J Roentgenology* (2000) 174:71–4. doi:10.2214/ajr.174.1.1740071
36. Coche EE, Ghaye B, de Mey J, and Duyck P. *Comparative Interpretation of CT and Standard Radiography of the Chest*. New York, NY: Springer Science & Business Media (2011).
37. Tack D, and Howarth N. Missed Lung Lesions: Side-By-Side Comparison of Chest Radiography with MDCT, 15th International Annual Conference, CNCERT 2018 (2019), Beijing, China:17, 26. doi:10.1007/978-3-030-11149-6_2
38. Yang W, Liu Y, Lin L, Yun Z, Lu Z, Feng Q, et al. Lung Field Segmentation in Chest Radiographs From Boundary Maps by a Structured Edge Detector. *IEEE J Biomed Health Inform* (2017) 22:842–51. doi:10.1109/JBHI.2017.2687939

**Conflict of Interest:** The authors declare that the research was conducted in the absence of any commercial or financial relationships that could be construed as a potential conflict of interest.

frontiers in Physics

BRIEF RESEARCH REPORT
published: 25 January 2022
doi: 10.3389/fphy.2021.752943

# Remote Chemical Sensing by SERS with Self-Assembly Plasmonic Nanoparticle Arrays on a Fiber

*Xin Zhang[1], Kunyi Zhang[1], Hasso von Bredow[2], Christopher Metting[2], George Atanasoff[2], Robert M. Briber[1] and Oded Rabin[1,3]**

[1]Department of Materials Science and Engineering, University of Maryland, College Park, MD, United States, [2]Accustrata, Inc., Rockville, MD, United States, [3]Institute for Research in Electronics and Applied Physics, University of Maryland, College Park, MD, United States

An optical fiber was modified at the tip with a self-assembled plasmonic metamaterial that acts as a miniature surface-enhanced Raman spectroscopy (SERS) substrate. This optical fiber-based device co-localizes the laser probe signal and the chemical analyte at a distance remote from the spectrometer, and returns the scattered light signal to the spectrometer for analysis. Remote SERS chemical detection is possible in liquids and in dried samples. Under laboratory conditions, the analyte SERS signal can be separated from the background signal of the fiber itself and the solvent. An enhancement factor greater than 35,000 is achieved with a monolayer of the SERS marker 4-aminothiophenol.

**Keywords: surface enhanced Raman spectroscopy, remote sensing, fiber optics, gold nanoparticles, self-assembly, optical metamaterial, fused silica fiber, enhancement factor**

OPEN ACCESS

***Edited by:***
*Carlos Marques,*
*University of Aveiro, Portugal*

***Reviewed by:***
*Ana-Maria Craciun,*
*Babes-Bolyai University, Romania*
*Carlos Ferrer,*
*University of Aveiro, Portugal*

****Correspondence:***
*Oded Rabin*
*oded@umd.edu*

***Specialty section:***
*This article was submitted to Optics and Photonics, a section of the journal Frontiers in Physics*

***Received:*** *03 August 2021*
***Accepted:*** *29 November 2021*
***Published:*** *25 January 2022*

***Citation:***
*Zhang X, Zhang K, von Bredow H, Metting C, Atanasoff G, Briber RM and Rabin O (2022) Remote Chemical Sensing by SERS with Self-Assembly Plasmonic Nanoparticle Arrays on a Fiber. Front. Phys. 9:752943. doi: 10.3389/fphy.2021.752943*

## INTRODUCTION

Plasmonic metamaterials obtain their unique optical properties from the combined action of plasmonic and dielectric components of sub-wavelength dimensions [1]. Plasmonic metamaterials are useful in a variety of surface-enhanced spectroscopy techniques, enabling detection of chemicals through their spectral signatures with lower detection limits and higher spatial resolution compared to the standard spectroscopy techniques[2–4]. Among the most studied surface-enhanced spectroscopy techniques is surface-enhanced Raman scattering spectroscopy (SERS) [5,6,7]. In SERS, the plasmonic metamaterial increases the scattering cross-section of the probed molecule by a large factor (called the *SERS enhancement factor*), allowing for the possibility of single molecule detection [8]:[9].

Remote chemical sensing by optical methods has many applications in health care, oil and gas exploration, environmental monitoring, and law enforcement [10]:[11]. A number of these applications allow for the installation of a plasmonic metamaterial at the detection site for signal enhancement [12]:[13]. Of particular interest is addressing said metamaterial *via* an optical fiber such that (1) optical sensing is possible even without a direct line-of-sight between the spectrometer and the site of interest, and (2) the measurement can be performed through scattering media such as biological tissue, smoke, and soil. Techniques for localizing a plasmonic metamaterial on the optical fiber tip involve self-assembly methods and/or nanolithography tools [14–24].

Previously, a plasmonic metamaterial consisting of a non-close packed monolayer of metallic nanospheres with controllable inter-particle gaps was demonstrated as a reliable and reproducible SERS substrate [25]. That SERS substrate had been investigated using laser light propagating in free space. Here we report on the implementation of said metamaterial as a component of an optical fiber-based SERS spectroscopy system for remote sensing. The merits of this approach include facile and

economic fabrication based on self-assembly techniques, and quantitative evaluation of the SERS enhancement factor.

## MATERIALS AND METHODS

The metamaterial was produced on the polished tip of an optical fiber (Edmund Optics, 200 μm core diameter 0.22 NA VIS/NIR fused silica fiber, polyimide coating) to demonstrate remote sensing by sending and receiving the optical signals through the fiber. The fiber was ~0.5 m in length. A detailed procedure of the fabrication of the metamaterial was reported elsewhere [26]. Briefly, the optical fiber was equipped with SMA905 connectors and the tips were polished. A drop of solution of the block-copolymer polystyrene-b-poly(4-vinylpyridine) (PS-b-P4VP) in propylene glycol methyl ether acetate was spin coated on one polished tip of the optical fiber for 60 s at 3,000 rpm using a custom-designed holder. The block-copolymer film was annealed in THF vapor for 3 h. The P4VP blocks were crosslinked by exposure to 1,4-dibromobutane (DBB) vapor for 4 h. The fiber tip was immersed in a gold nanoparticle solution (BBI Solutions, citrate-capped, 15 nm) for 12 h, resulting in a non-closed packed monolayer of nanoparticles. The diameter of the nanoparticles was adjusted from ~15 to ~32 nm by soaking the fiber tip in an electroless gold plating solution (prepared by mixing solutions of CTAB (6 ml, 0.2 M), $HAuCl_4$ (0.384 ml, 0.04 M), $AgNO_3$ (0.228 ml, 0.01 M), ascorbic acid (0.96 ml, 0.1 M), and deionized water (11 ml)) for 8 min[25]. The metamaterial was characterized by optical microscopy (Olympus BX60 microscope with an Olympus UMPlanFI 20X/0.46 BD objective lens), by scanning electron microscopy (Hitachi SU-70 Schottky FE-SEM working at 10 kV accelerating voltage) and by atomic force microscopy (DI Nanoscope III multimode AFM, tapping mode, TESP tip (42 N/ m)).

Raman and SERS: The measurements were carried out using a LabRAM ARAMIS Horiba Yvon-Jobin micro-Raman spectrometer, operating at a wavelength of 633 nm and equipped with an Olympus BX41 microscope. The proximal bare tip of the fiber was placed near the focal point of the objective lens (Olympus MPlan, ×10 NA = 0.25 WD = 10.6 mm) of the Raman microscope. For SERS, the metamaterial functionalized tip of the fiber was soaked in the analyte solution for 15 min. Measurements were taken with the functionalized distal tip immersed in the solution in the dark, or for quantitative determination of the enhancement factor, the tip was soaked in a solvent to remove excess analyte, and was let dry in the dark prior to the measurements. Reference spectra were collected using normal Raman spectroscopy with the optical fiber. For normal Raman spectroscopy, no metamaterials were constructed on the optical fiber, and measurements were taken with the distal tip of the fiber immersed in the analyte solution in the dark.

## RESULTS

The SERS system consisted of the 633-nm CW laser, the spectrometer, and the silica optical fiber modified on its distal end with the metamaterial (**Figure 1A**). The laser light was guided through a beam-splitter to a lens that focused the light into the proximal end of the optical fiber. After traveling through the fiber, the light coupled to the metamaterial and the surface-enhanced Raman scattering process took place. A portion of the Stokes-shifted (back-scattered) light was collected by the fiber and was guided back towards the lens and the beam-splitter, making its way to the notch filter and the detector in the spectrometer. The structure of the functionalized distal end of the optical fiber is shown schematically in **Figure 1B**. Over the polished tip of the silica fiber is a thin (<50 nm) film of PS-b-P4VP. This polymer is typically not involved in the Raman process. It is chosen because the P4VP and the PS components microphase separate upon solvent-vapor annealing and self-assemble into hexagonally-ordered P4VP cylindrical domains in a PS matrix, serving as a template for the nanoparticle adsorption process. Over the polymeric film is a monolayer of gold nanoparticles of uniform diameter ($d$~32 nm) arranged in a hexagonal pattern at the microscale. Because the center-to-center distance of the hexagonal pattern ($d$+δ, δ~8 nm) is slightly larger than the nanoparticle diameter, nanoscale gaps are present between pairs of adjacent nanoparticles. This metamaterial of evenly-spaced metallic nanoscale particles and dielectric nanoscale gaps of controlled dimensions generates strong, localized optical fields that give rise to the enhanced Raman signal.

The SERS optical fibers were characterized during fabrication by optical microscopy, SEM and AFM in order to confirm and evaluate the formation of a hexagonal array of gold nanoparticles on the polished surface at the distal end of the fiber. The optical images in **Figure 2** show that the block copolymer film and the nanoparticle metamaterial covered almost the entire cross-sectional area of the fiber and displayed good uniformity, particularly at the center of the fiber core. SEM imaging of the tip of the fiber confirmed the presence of a layer of gold nanoparticles on the entire circular area of the silica core, however, due to the poor electrical conductivity of the sample the resolution and quality of the images were compromised (**Figure 3A**). High-resolution height profile images were obtained by AFM (**Figure 3B**), scanning the AFM tip over a few square-microns of the fiber core in tapping mode. The AFM images indicated that the silica surface and the polymer film on top of it were smooth and that the gold nanoparticles were dispersed as a monolayer over the film. Most nanoparticles were separated from their neighbors by a nanoscale gap (~25 nm), and were locally arranged in hexagonal patterns, as expected for 15 nm nanoparticles adhering to the hydrophilic columnar domains of the (PS-b-P4VP) polymer film[26]. Some sites were not covered by adsorbed nanoparticles. These locations appear to have not formed cylindrical P4VP domains normal to the surface. These defects may be remedied by a longer annealing time and/or a longer immersion time in the nanoparticle solution.

SERS spectra of 4-aminothiophenol (4-ATP) were collected by immersing the functionalized optical fiber in an ethanoic solution of the thiol. To quantify the SERS enhancement factor, the number of molecules probed needs to be known. This was achieved by rinsing the analyte off the fiber, such that only a monolayer of chemisorbed thiol molecules is present on the

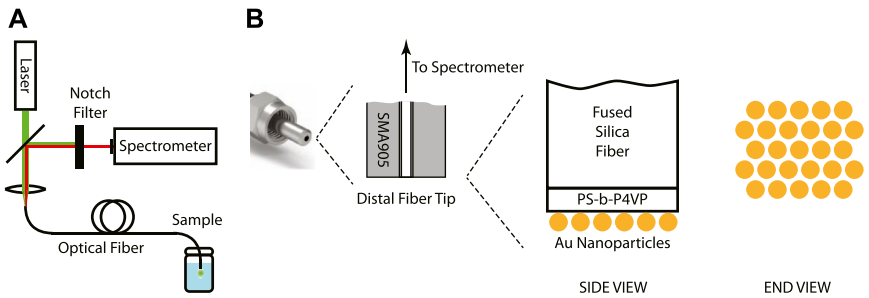


**FIGURE 1 | (A)** Schematic of the SERS remote spectroscopy system. **(B)** Schematic of the structure of the metamaterial-functionalized optical fiber tip.

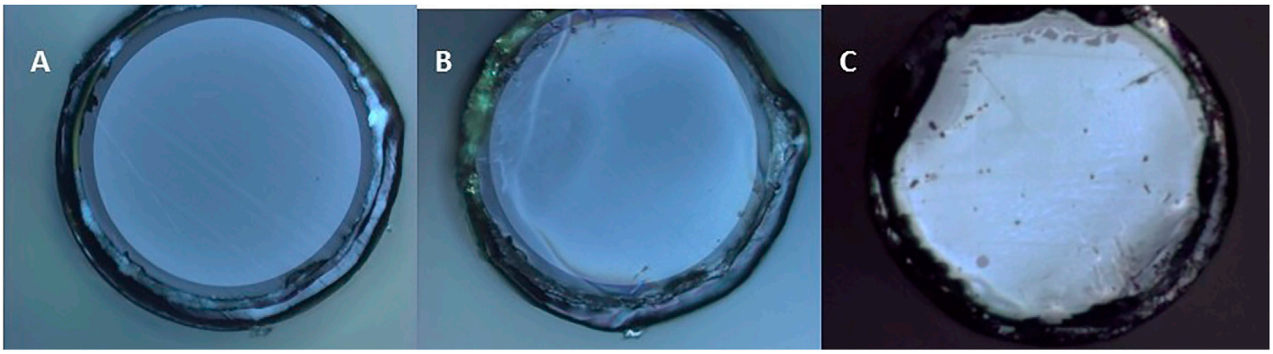


**FIGURE 2 |** Optical images of the silica core of the optical fiber at different stages of the SERS optical fiber fabrication. **(A)** Polished tip fiber mounted on SMA905 connector. **(B)** Same fiber as in **(A)** after spin-coating the block copolymer. **(C)** A different fiber with the block-copolymer film and a monolayer of gold nanoparticles. The metamaterial structure appears uniform at the center. Irregularities are more common toward the edge of the silica core, likely due to height differences between the silica core and the polyimide coating.

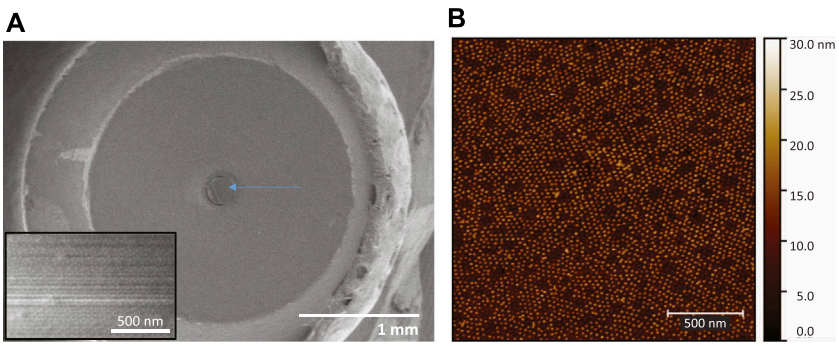


**FIGURE 3 | (A)** Low-magnification SEM image of the fiber mounted on the SMA905 connector, after 15 nm gold nanoparticle absorption and before electroless plating. The arrow points at the silica core surface where the metamaterial is located. Inset: High magnification SEM image of the fiber core surface. **(B)** AFM topography image of the gold nanoparticle array self-assembled on the block-copolymer film on the fiber tip. Short-range hexagonal ordering is observed. There are nanoscale gaps between the nanoparticles.

surface of the gold nanoparticles. The SERS spectrum of "dry" 4-ATP is shown in **Figure 4A**. This spectrum was obtained by subtracting the signals collected before and after exposing the fiber to the chemical solutions. Six peaks associated with the SERS spectrum of 4-ATP can be identified. The SERS spectra obtained in "wet" conditions are qualitatively the same. In **Figure 4B**, the reference Raman spectrum of 4-ATP obtained with the same spectrometer using an optical fiber without the metamaterial is shown. Here, the distal end of the fiber was immersed in a 200 mM solution of 4-ATP in 1,5-pentanediol, and the spectra were collected with the fiber end in the liquid. The spectrum has been baseline-corrected by subtracting the signal collected from pure pentanediol under the same experimental conditions. In the Raman spectrum, the two strong peaks associated with 4-ATP

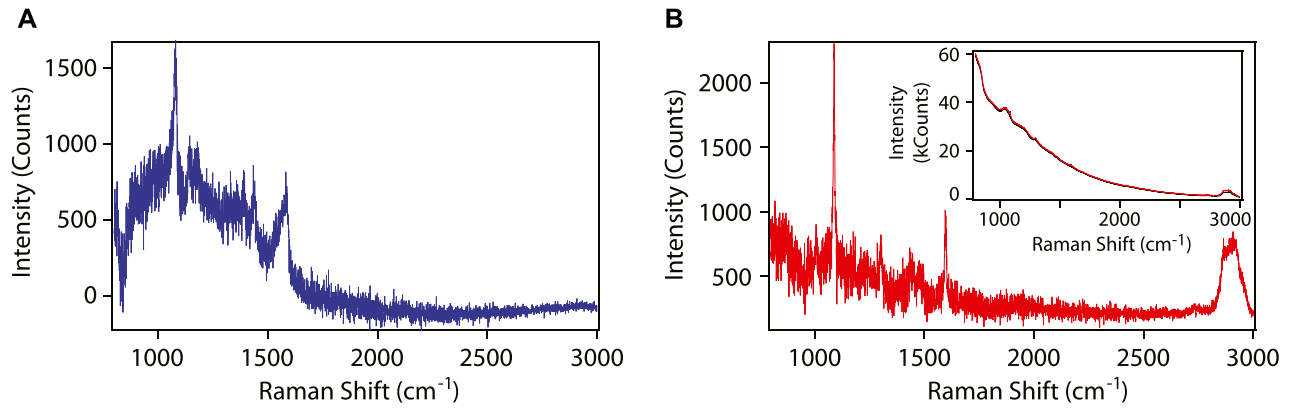


**FIGURE 4 | (A)** SERS spectrum of 4-ATP using the metamaterial functionalized optical fiber. **(B)** Raman spectrum of 4-ATP using a bare optical fiber. The spectrum contains also residual signals from the solvent: three peaks in the range 1300–1500 $cm^{-1}$ and a broad peak at 2850–2940 $cm^{-1}$. Inset: Raw Raman spectra of the bare fiber in pentanediol (black) and in pentanediol with 0.2 M 4-ATP (red). In the measurements, the laser power incident on the proximal end of the fiber was 2 mW. The acquisition time was 45 s for the SERS spectrum, and 60 s for the Raman spectrum.

can be recognized, however, four peaks of pentanediol also remain in the spectrum due to imperfect background subtraction.

The SERS enhancement factor *EF* is calculated using **Eq. 1** where $N_i$ is a function of the number of molecules probed and the signal collection efficiency of the fiber (see **Supplemental Material** for calculation details), $t_i$ is the data acquisition time, and $I_i$ is the intensity of the peak near 1070 $cm^{-1}$. The subscript *i* corresponds to either the SERS experiment or the Raman experiment. The number of molecules probed in the SERS experiment is estimated using the known surface density of the nanospheres in the array, the diameter of the nanospheres and the density of 4-ATP in monolayers on gold surfaces (5 molecules/$nm^2$). The number of molecules probed in the Raman experiment is estimated using the known analyte concentration in the solution.

$$EF = \frac{I_{SERS}}{I_{Raman}} \frac{N_{Raman}}{N_{SERS}} \frac{t_{Raman}}{t_{SERS}} \quad (1)$$

The SERS enhancement factor of the metamaterial-functionalized optical fiber was determined to be ~37,000. This value is comparable to the SERS enhancement factors obtained for large-area (>1 $cm^2$) versions of the metamaterials on glass slides.

The raw data showed a strong Raman and fluorescence signal originating from the fused silica fiber (inset in **Figure 4**). For the purpose of the experiments described above, this signal remained constant throughout the measurements, and was satisfactorily removed using standard background subtraction techniques.

## DISCUSSION

There are a number of technical considerations specific to SERS measurements through optical fibers. First, the optical fiber can channel photons that originate from light sources other than the incident laser (e.g. sunlight, room lighting) back to the spectrometer. Therefore, samples must be measured in the dark. Second, the fiber itself is a source of fluorescence and Raman scattering. These features must be recognized in the recorded spectra and not mistaken for analyte signals. Therefore, the method is limited to analytes with Raman signals that do not overlap with the Raman signals of fused silica (420, 485, 600, and 790 $cm^{-1}$). The method also necessitates post-measurement analysis, such as background subtraction, peak fitting and principal component analysis. The fused silica background signal can be mitigated by employing a Raman spectrometer that operates at a longer wavelength (e.g. 785 nm), or by using specialty optical fibers such as hollow-core photonic crystal fibers [27]. Third, the sensitivity of the optical fiber-based SERS measurement may be limited by losses associated with inserting the incident laser light into the fiber and near-field coupling the light scattered by the molecules in the metamaterial back into the fiber. Interestingly, using macroscopic samples of the metamaterial on quartz slides, we have determined that more photons back-scatter inelastically when the sample is illuminated from the quartz side than from the air side[28]. The permittivity contrast at the interface may be responsible for this effect, as has been previously theorized [29]. Consequently, optical fiber SERS of dry samples (i.e. in air) often results in better sensitivity than SERS performed with solutions.

Despite the technical challenges listed above, remote detection of SERS-active molecules through the optical fiber is practical thanks to the tremendous enhancements in the Raman scattered light intensity by the plasmonic metamaterial, estimated to be of the order of $10^5$ for this metamaterial using a 633-nm input laser light. Through the analysis of the spectrum in **Figure 4A**, it is possible to unambiguously assign 6 SERS peaks (1070, 1140, 1180, 1390, 1435 and 1580 $cm^{-1}$) to 4-ATP adsorbed on the gold nanoparticles at the fiber tip. In contrast, only 2 Raman peaks were recorded in the spectrum collected without the assistance of the metamaterial despite the very-high concentration of 4-ATP in the sample, with 2 other peaks possibly masked by the solvent Raman peaks and the baseline noise.

Optical fiber-based plasmonic sensors using the SERS effect gain their sensitivity from the co-localization of the optical field and the molecules at the surface of the plasmonic nanostructures. The metamaterial-functionalized optical fiber used in this study distinguishes itself from other optical fiber-based plasmonic sensors. The whole diameter of the silica fiber tip surface is

covered with the gold nanoparticle array, providing a maximal functional surface. At the same time, the structure of the metamaterial is sufficiently uniform that, for practical purposes, the enhancement factor is homogenous across the device, without local hot-spots dominating the plasmonic response. The fabrication process can be standardized such that the enhancement factor of all the fibers in a batch is the same, as was achieved with macroscopic SERS substrates. This combination of a predictable SERS enhancement factor and a large functional area is highly desirable among SERS users. The metamaterial functionalized optical fiber is expected to be biocompatible, and operational in aqueous environments, where SERS-based chemical sensing benefits from water molecules being Raman inactive and SERS inactive.

## DATA AVAILABILITY STATEMENT

The raw data supporting the conclusions of this article will be made available by the authors, without undue reservation.

## AUTHOR CONTRIBUTIONS

OR, RB, CM, and GA contributed to conception and design of the study. HvB, KZ, and XZ fabricated the optical fibers. KZ, XZ performed the Raman measurements and the data analysis. OR wrote the manuscript. OR and XZ prepared the figures. All authors read and approved the submitted version of the manuscript.

## FUNDING

This work was supported by the National Science Foundation (Grant No. DMR-1151614) and by the UM Ventures Seed Grant Program of the University of Maryland.

## ACKNOWLEDGMENTS

We acknowledge the support of the Maryland NanoCenter and its AIMLab. The authors thank Dr. Karen Gaskell and Prof. Seung Yong Lee (KIST) for valuable discussions.

## SUPPLEMENTARY MATERIAL

The Supplementary Material for this article can be found online at: https://www.frontiersin.org/articles/10.3389/fphy.2021.752943/full#supplementary-material

## REFERENCES

1. Wang P, Nasir ME, Krasavin AV, Dickson W, Jiang Y, Zayats AV. Plasmonic Metamaterials for Nanochemistry and Sensing. *Acc Chem Res* (2019) 52(11): 3018–28. doi:10.1021/acs.accounts.9b00325
2. Camden JP, Dieringer JA, Wang Y, Masiello DJ, Marks LD, Schatz GC, et al. Probing the Structure of Single-Molecule Surface-Enhanced Raman Scattering Hot Spots. *J Am Chem Soc* (2008) 130(38):12616–7. doi:10.1021/ja8051427
3. Adato R, Yanik AA, Amsden JJ, Kaplan DL, Omenetto FG, Hong MK, et al. Ultra-sensitive Vibrational Spectroscopy of Protein Monolayers with Plasmonic Nanoantenna Arrays. *Proc Natl Acad Sci* (2009) 106(46): 19227–32. doi:10.1073/pnas.0907459106
4. Neubrech F, Beck S, Glaser T, Hentschel M, Giessen H, Pucci A. Spatial Extent of Plasmonic Enhancement of Vibrational Signals in the Infrared. *ACS Nano* (2014) 8(6):6250–8. doi:10.1021/nn5017204
5. Albrecht MG, Creighton JA. Anomalously Intense Raman Spectra of Pyridine at a Silver Electrode. *J Am Chem Soc* (1977) 99(15):5215–7. doi:10.1021/ja00457a071
6. Stiles PL, Dieringer JA, Shah NC, Van Duyne RP. Surface-Enhanced Raman Spectroscopy. *Annu Rev. Anal. Chem.* (2008) 1:601–26. doi:10.1146/annurev.anchem.1.031207.112814
7. Pilot R, Signorini R, Durante C, Orian L, Bhamidipati M, Fabris L. A Review on Surface-Enhanced Raman Scattering. *Biosensors* (2019) 9(2):57. doi:10.3390/bios9020057
8. Weiss A, Haran G. Time-dependent Single-Molecule Raman Scattering as a Probe of Surface Dynamics. *J Phys Chem B* (2001) 105(49):12348–54. doi:10.1021/jp0126863
9. Doering WE, Nie S. Single-molecule and Single-Nanoparticle SERS: Examining the Roles of Surface Active Sites and Chemical Enhancement. *J Phys Chem B* (2002) 106(2):311–7. doi:10.1021/jp011730b
10. Hoge FE, Swift RN. Oil Film Thickness Measurement Using Airborne Laser-Induced Water Raman Backscatter. *Appl Opt* (1980) 19(19):3269–81. doi:10.1364/ao.19.003269
11. Mirell D, Chalus O, Peterson K, Diels J-C. Remote Sensing of Explosives Using Infrared and Ultraviolet Filaments. *J Opt Soc Am B* (2008) 25(7):B108–B111. doi:10.1364/josab.25.00b108
12. Connatser RM, Prokes SM, Glembocki OJ, Schuler RL, Gardner CW, Lewis SA, et al. Toward Surface-Enhanced Raman Imaging of Latent Fingerprints*. *J Forensic Sci* (2010) 55(6):1462–70. doi:10.1111/j.1556-4029.2010.01484.x
13. Vo-Dinh T, Liu Y, Fales AM, Ngo H, Wang HN, Register JK, et al. SERS Nanosensors and Nanoreporters: Golden Opportunities in Biomedical Applications. *Wiley Interdiscip Rev Nanomed Nanobiotechnol* (2015) 7(1): 17–33. doi:10.1002/wnan.1283
14. Hankus ME, Li H, Gibson GJ, Cullum BM. Surface-enhanced Raman Scattering-Based Nanoprobe for High-Resolution, Non-scanning Chemical Imaging. *Anal Chem* (2006) 78(21):7535–46. doi:10.1021/ac061125a
15. Dhawan A, Muth JF. Engineering Surface Plasmon Based Fiber-Optic Sensors. *Mater Sci Eng B* (2008) 149(3):237–41. doi:10.1016/j.mseb.2007.09.076
16. Oo MKK, Han Y, Martini R, Sukhishvili S, Du H. Forward-propagating Surface-Enhanced Raman Scattering and Intensity Distribution in Photonic crystal Fiber with Immobilized Ag Nanoparticles. *Opt Lett* (2009) 34(7): 968–70. doi:10.1364/ol.34.000968
17. Smythe EJ, Dickey MD, Bao J, Whitesides GM, Capasso F. Optical Antenna Arrays on a Fiber Facet for *In Situ* Surface-Enhanced Raman Scattering Detection. *Nano Lett* (2009) 9(3):1132–8. doi:10.1021/nl803668u
18. Ma X, Huo H, Wang W, Tian Y, Wu N, Guthy C, et al. Surface-Enhanced Raman Scattering Sensor on an Optical Fiber Probe Fabricated with a Femtosecond Laser. *Sensors* (2010) 10(12):11064–71. doi:10.3390/s101211064
19. Jayawardhana S, Kostovski G, Mazzolini AP, Stoddart PR. Optical Fiber Sensor Based on Oblique Angle Deposition. *Appl Opt* (2011) 50(2):155–62. doi:10.1364/ao.50.000155
20. Zhu Y, Dluhy RA, Zhao Y. Development of Silver Nanorod Array Based Fiber Optic Probes for SERS Detection. *Sensors Actuators B: Chem* (2011) 157(1): 42–50. doi:10.1016/j.snb.2011.03.024
21. Yap FL, Thoniyot P, Krishnan S, Krishnamoorthy S. Nanoparticle Cluster Arrays for High-Performance SERS through Directed Self-Assembly on Flat Substrates and on Optical Fibers. *ACS Nano* (2012) 6(3):2056–70. doi:10.1021/nn203661n

22. Huang Z, Lei X, Liu Y, Wang Z, Wang X, Wang Z, et al. Tapered Optical Fiber Probe Assembled with Plasmonic Nanostructures for Surface-Enhanced Raman Scattering Application. *ACS Appl Mater Inter* (2015) 7(31): 17247–54. doi:10.1021/acsami.5b04202
23. Micco A, Ricciardi A, Pisco M, La Ferrara V, Cusano A. Optical Fiber Tip Templating Using Direct Focused Ion Beam Milling. *Sci Rep* (2015) 5:15935. doi:10.1038/srep15935
24. Kwak J, Lee W, Kim JB, Bae SI, Jeong KH. Fiber-optic Plasmonic Probe with Nanogap-Rich Au Nanoislands for On-Site Surface-Enhanced Raman Spectroscopy Using Repeated Solid-State Dewetting. *J Biomed Opt* (2019) 24(3):6. doi:10.1117/1.JBO.24.3.037001
25. Lee W, Lee SY, Briber RM, Rabin O. Self-Assembled SERS Substrates with Tunable Surface Plasmon Resonances. *Adv Funct Mater* (2011) 21(18):3424–9. doi:10.1002/adfm.201101218
26. Lee W, Lee SY, Zhang X, Rabin O, Briber RM. Hexagonally Ordered Nanoparticles Templated Using a Block Copolymer Film through Coulombic Interactions. *Nanotechnology* (2013) 24(4):045305. doi:10.1088/0957-4484/24/4/045305
27. Han Y, Tan S, Oo MKK, Pristinski D, Sukhishvili S, Du H. Towards Full-Length Accumulative Surface-Enhanced Raman Scattering-Active Photonic Crystal Fibers. *Adv Mater* (2010) 22(24):2647–51. doi:10.1002/adma.200904192
28. Rabin O, Zhang X, Zhang K, Briber RM, von Bredow H, Metting C, et al. Integrated Surface-Enhanced Raman Spectroscopy Sensors for Process Monitoring. *TechConnect Briefs* (2017) 4:214–7.
29. Engheta N, Papas CH, Elachi C. Radiation Patterns of Interfacial Dipole Antennas. *Radio Sci* (1982) 17(6):1557–66. doi:10.1029/rs017i006p01557

**Conflict of Interest:** Authors HvB, CM, and GA, were employed by the company Accustrata, Inc.

The remaining authors declare that the research was conducted in the absence of any commercial or financial relationships that could be construed as a potential conflict of interest.

**Publisher's Note:** All claims expressed in this article are solely those of the authors and do not necessarily represent those of their affiliated organizations, or those of the publisher, the editors and the reviewers. Any product that may be evaluated in this article, or claim that may be made by its manufacturer, is not guaranteed or endorsed by the publisher.

# Advantages of publishing in Frontiers

**OPEN ACCESS**
Articles are free to read for greatest visibility and readership

**FAST PUBLICATION**
Around 90 days from submission to decision

**HIGH QUALITY PEER-REVIEW**
Rigorous, collaborative, and constructive peer-review

**TRANSPARENT PEER-REVIEW**
Editors and reviewers acknowledged by name on published articles

**Frontiers**
Avenue du Tribunal-Fédéral 34
1005 Lausanne | Switzerland

**Visit us:** www.frontiersin.org
**Contact us:** frontiersin.org/about/contact

**REPRODUCIBILITY OF RESEARCH**
Support open data and methods to enhance research reproducibility

**DIGITAL PUBLISHING**
Articles designed for optimal readership across devices

**FOLLOW US**
@frontiersin

**IMPACT METRICS**
Advanced article metrics track visibility across digital media

**EXTENSIVE PROMOTION**
Marketing and promotion of impactful research

**LOOP RESEARCH NETWORK**
Our network increases your article's readership